代表的な研究論文

雑誌名	活動報告
巻	H14
ページ	25-270
発行年	2003-07
URL	http://hdl.handle.net/10097/00108957

KINETICS, CATALYSIS, AND REACTION ENGINEERING

Ortho-Selective Alkylation of Phenol with 2-Propanol without Catalyst in Supercritical Water

Takafumi Sato, Gaku Sekiguchi, Tadafumi Adschiri, and Kunio Arai*

Department of Chemical Engineering, Tohoku University, 07 Aoba Aramaki-Aza, Aoba-ku, Sendai 980-8579, Japan

The highly ortho-selective alkylation of phenol with 2-propanol could be achieved without catalyst in supercritical water at 673 K. The dehydration of 2-propanol gave propene and was followed by the reaction with phenol to produce 2-isopropylphenol as the main alkylphenol product. The ortho/para ratio of alkylphenols was above 20, and the yield of alkylphenols was 83.1%. Both the dehydration and the alkylation were accelerated with increasing water density, and this acceleration could not be attributed to the proton concentration alone. In supercritical water, the hydroxy group of phenol plays an important role for both dehydration and alkylation, and the reaction proceeds around the hydroxy group of phenol. In the dehydration of 2-propanol, phenol protonates 2-propanol and abstracts a hydrogen atom from 2-propanol. In the alkylation of phenol with propene, phenol provides a proton to propene and forms 2-isopropylphenol via an unsaturated ketone.

Introduction

Supercritical water is expected to play an increasingly important role in developing synthetic reaction routes that embrace the principles of green chemistry.[1] Supercritical water is an alternative solvent for organic syntheses.[1−3] Supercritical water (T_c = 647.3 K and P_c = 22.1 MPa) is completely miscible with light gases, hydrocarbons, and aromatics. The solvent properties of supercritical water, such as the ion product[4] and dielectric constant,[5] can be changed greatly by small changes in pressure and temperature, which can be used to influence reaction rates and equilibria.[6] The hydrolysis of ethers,[1,6] dehydration of alcohols,[7] rearrangement reactions,[8] and disproportionation reactions[9] proceed in the absence of catalyst in supercritical water. The mechanism of noncatalytic organic reactions in supercritical water has attracted attention regarding the role of water as a proton and hydroxide ion donor as well as reactant.

The Friedel−Crafts reaction is an aromatic electrophilic reaction that proceeds through the formation of electrophilic substitution products such as carbocations and essentially requires strong acids such as Lewis acids ($AlCl_3$, BF_3) and mineral acids (HF, H_2SO_4).[10] Further, in the alkylation reaction between a phenol and alcohol, the hydroxy group of the phenol strongly activates the reactivity of the ring substituents, particularly at the ortho and para positions, and thus, it is difficult to obtain high positional selectivity. This means that a large number of undesirable byproducts are produced.

Positional selectivity is influenced by the acidity of the solvent. Sartori et al.[11] reported that the ratio of ortho to para increased with increasing ratio of PhOK to PhOH with $AlCl_3$ in $CHCl_3$ solvent. However, this method requires the use of chlorinated solvents, which would mean substantial environmental considerations. Heterogeneous catalysts provide an environmentally acceptable alternative to strong acids such as $AlCl_3$ and H_2SO_4.[12,13] This chemistry can be used in supercritical CO_2, as shown by Gray et al.,[14] who reported that the yield of ortho alkylphenols was over 3 times larger than the yield of para substituents.

The Friedel−Crafts reaction occurs in sub- and supercritical water without a catalyst. Chandler et al.[15,16] reported that the alkylation of phenol with several alcohols occurs without any catalyst in subcritical water at 523−573 K. In a preliminary communication, we reported that both the alkylation of phenol with 2-propanol and the dehydration of 2-propanol occur in supercritical water under noncatalytic conditions.[17] However, the reaction mechanism of Friedel−Crafts-type alkylation and dehydration in the presence of phenol in supercritical water is still unknown.

In this paper, we demonstrate the noncatalytic dehydration of 2-propanol and the alkylation of phenol in the presence of phenol in supercritical water, where phenol acts as a good catalyst for alkylation and dehydration. We tested other alkylating agents such as propene and added acid. In addition, we conducted the conversion of the alkylphenols as the reverse reaction. First, we determine the positional selectivity for the noncatalytic alkylation of phenol in supercritical water, elucidate the reaction pathways, and evaluate the effect of the water density on the dehydration and alkylation kinetics. Next, we show that the influence of the hydroxy group of phenol on the alkylation and dehydration reactions is predominant over that of the proton concentration in the system. Finally, we propose a

* To whom correspondence should be addressed. E-mail: karai@arai.che.tohoku.ac.jp. Tel.: +81-22-217-7245. Fax: +81-22-217−7246.

10.1021/ie0200712 CCC: $22.00
Published on Web 05/30/2002

reaction mechanism that explains the role of the hydroxy group in dehydration and alkylation and consider the dependence of the kinetics on the water density.

Experimental Section

Phenol and 2-propanol were purchased from Wako Pure Chemical Industries and had purities of >99.0%, and 99.5%, respectively. 2-Isopropyl phenol, 4-isopropylphenol, 2-propylphenol, and 2,6-dimethylphenol were obtained from Tokyo Chemical Industry Co., Ltd., and their purity were >98.0%, >99.0%, >98.0%, and >99.0%, respectively. Propene (>99.0%) of was obtained from Nippon Sanso Co., Ltd. All chemicals were used without further purification. The analytical reagents used were tetrahydrofuran (THF, >97%), with 2,6-di-*tert*-butyl-4-methylphenol as an inhibitor, and naphthalene (>99%), which were obtained from Wako Pure Chemical Industries.

Experiments were conducted with stainless steel (316) batch-type reactors whose internal volume was 6 cm^3. One side of the tube served as a thermocouple well for measuring the reactor temperature, and the other side was sealed. To analyze gases or take gas samples, we used a second type of reactor that had a $^1/_{16}$-in. tube that was connected to the high-pressure valve.

In the experiments, the reactor was loaded with a certain amount of reactants and water. The air in the reactor was replaced with argon or propene via successive purgings, and the reactor was sealed. The amount of water ranged from 1.2 to 3 g, corresponding to a solution density range of 0.2–0.5 g/cm^3. We also conducted the experiment without water. After the reactors had been loaded, they were submerged into a fluidized sand bath (Takabayashirika Co., model TK-3) at 673 K. The heating time was about 3 min, and the reaction pressure was estimated from the pure-water data of Haar et al.[18] The phase behavior inside the reactor in the presence of various organic compounds has not been revealed clearly. However, calculations can be one of the methods used to predict the phase behavior of supercritical water solutions. Here, we estimated the phase behavior inside the reactor from the properties of main components, that is, water and phenol. We performed calculations of the critical locus of the water–phenol system by the method of Heidemann and Khalil[19] with the SRK equation of state assuming no interaction between two components. The calculations predicted a single phase under the experimental conditions in the presence of water.

After a given length of time, including the heating time, the reactors were removed from the fluidized sand bath, and the reaction was rapidly quenched in a water bath at 293 K. After being cooled, the reactors were submerged in an ultrasonic water bath for 5 min to degas the liquid. For the analysis of produced gases, the high-pressure valve at the end of the reactor was connected to sampling loops and a syringe. By opening the valve gently, gas samples could be collected in the syringe through the sampling loop attached to GC-TCD. We measured the compositions of the gases because of the difficulties with the accurate collection of gaseous products. For the product gas, H_2 was analyzed by GC-TCD (Hitachi, model Hitachi163) with a molecular sieve 13X column and Ar carrier gas. Methane was measured with another GC-TCD setup (Shimadzu, model GC-7A) with a molecular sieve 13X column and He carrier gas. The C_2–C_4 hydrocarbons and CO_2 were analyzed by GC-TCD (Shimadzu, model GC-7A) with a Porapak Q column and He carrier gas. After the gases had been sampled or displaced, the reactor was opened and washed with THF. The compounds in the THF solutions were identified by GC-MS (Japan Electron Optics Laboratory, model Automass20; with an HP-5MS column and He carrier gas) and by comparison of the GC retention time with standards. The concentration of product was routinely determined by GC-FID (Hewlett-Packard, model HP6890) with an HP-5 column with naphthalene as the internal standard. The alkylation reaction was usually conducted without the high-pressure valve to improve reproducibility.

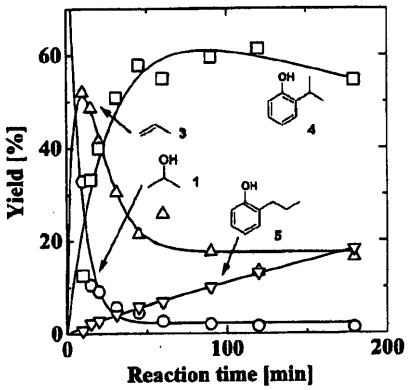

Figure 1. Time dependence of the product yields after reactions at a temperature of 673 K and a water density of 0.5 g/cm^3 with $[2\text{-propanol}]_0$ = 0.33 mol/L and $[\text{phenol}]_0$ = 1.65 mol/L.

The yield of the products for the reaction of alcohol with phenol was evaluated on the basis of the alkyl chains as

$$\text{yield (\%)} = \{\text{moles of carbon atoms in the alkyl chain (excluding the benzene ring) of the product/(moles of carbon atoms in the alkyl chain loaded)}\} \times 100 \quad (1)$$

The conversion of 2-propanol was also evaluated according to

$$\text{conversion (\%)} = \frac{\text{moles of 2-propanol remaining}}{\text{moles of 2-propanol loaded}} \times 100 \quad (2)$$

The yield of the products for the reaction of alkylphenols was evaluated in terms of the introduced benzene structure from

$$\text{yield (\%)} = \frac{\text{moles of benzene structure of the product}}{\text{moles of alkyl phenol loaded}} \times 100 \quad (3)$$

Results and Discussion

Reaction Pathway for Phenol with 2-Propanol. Typical reactant loadings were as follows: 2-propanol, **1**, 0.33 mol/L; phenol, **2**, 1.65 mol/L; and water, 27.7 mol/L (0.5 g/cm^3). The temperature was set at 673 K, and the reaction time ranged from 10 to 180 min. Figure 1 shows the yields of the main products with reaction time. The conversion of **1** occurred rapidly, and the yield of propene, **3**, rapidly increased before 10 min of reaction and then decreased with reaction time. The yield of

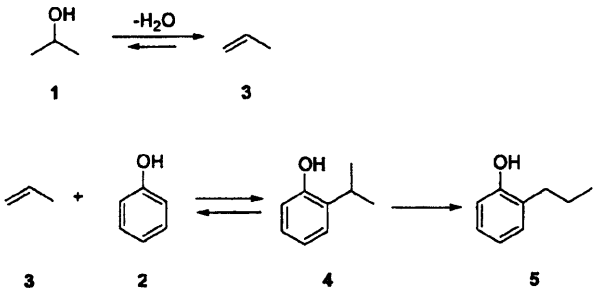

Figure 2. Main reaction pathway for 2-propanol in the presence of phenol in supercritical water at 673 K.

2-isopropylphenol, **4**, increased with reaction time, reached a level equal to that of **3** at around 20 min, leveled off after 45 min, and then decreased slightly at 180 min. The yield of 2-propylphenol, **5**, slightly increased with reaction time. In the reaction, 2,6-diisopropylphenol, 4-isopropylphenol, and 2-isopropyl-6-propylphenol were also produced, but the sum of their yields was below 9.7%. The maximum alkylphenol yield was greater than 80% at 120 min of reaction time.

In Figure 1, the yield of **3** evaluated from the carbon balance is shown. To confirm the formation of **3**, we conducted a series of experiments for gas analysis using the shut-off valve under the same conditions. The molar ratio of **3** to all gases was above 89.9% before 60 min, which means that the main gaseous product was **3**. The other gases detected were hydrogen, methane, propane, and CO_2. The gaseous product was almost **3** at the early part of the reaction.

Judging from these results, we propose the reaction pathway in supercritical water shown in Figure 2. Additional experiments were performed to confirm the reaction pathway, as described below. In the presence of phenol, the dehydration of **1** to **3** occurs and this reaction is considered reversible with the equilibrium being on the dehydration side. Alkylation of **2** with **3** leads to the formation of **4**. Then, **4** dealkylates into **2** and **3** and rearranges to form **5**.

The alkylphenol obtained was almost only the ortho substituent. The ratio of the sum of the yields of ortho substituents (**4**, **5**, 2,6-diisopropylphenol and 2-isopropyl-6-propylphenol) to the sum of the yields of para substituents (4-isopropylphenol) ranged from 20 to 37. A high ortho selectivity was always obtained, and this trend was the same as reported previously for the same reaction in subcritical water without catalyst.[15] The isopropylphenyl ether byproduct was not observed, although the yield of 2,4-diisopropylphenyl isopropyl ether was 11% in **1** as the solvent at 388–433 K with BF_3.[20] This is probably because ethers such as benzylphenyl ether and dibenzyl ether are easily hydrolyzed in supercritical water at 653–673 K. [1,6]

We conducted another series of experiment for the reaction of 2-isopropylphenol, **4**, in supercritical water and confirmed the pathway for dealkylation and rearrangement of **4**. The experiments were conducted in supercritical water at a temperature of 673 K and a water density of 0.5 g/cm^3 for 180 min with **4** (0.5 mol/L) and water (27.7 mol/L, 0.5 g/cm^3) being introduced into the reactor. The conversion of **4** increased with reaction time and reached 49.7% at 180 min. The main products were **2** and **5**, and the yields of these compounds increased with reaction time up to 34.5 and 14.6%, respectively. The gaseous product was mainly **3**, whose molar percentage in the gas was always above 93%. Small amounts of para substituents and 2,6-alkylphenols were formed at levels below 2.5%. The dealkylation of **4** gave **2** and **3**, and the rearrangement of **4** to **5** occurred in supercritical water, although **4** is stable in high-temperature water at 548 K.[21]

Table 1. Yield of Products with Reaction Time at a Temperature of 673 K and a Water Density of 0.5 g/cm^3 with [Phenol]$_0$ = 0.33 mol/L and [Propene]$_0$ = 0.28 mol/L or [2-Propanol]$_0$ = 0.33 mol/L

alkylating agent	reaction time (min)	yield (%)		
		1	**4**	**5**
propene[a]	15	0.8	3.4	0.2
	30	2.8	4.4	0.5
	60	0.4	5.7	1.0
	180	1.3	11.8	5.0
2-propanol[b]	15	72.6	1.6	0.1
	30	65.7	2.1	0.2
	60	44.7	8.7	1.1
	180	25.4	16.3	4.8

[a] Initial concentration = 0.28 mol/L. [b] Initial concentration = 0.33 mol/L.

We also examined the alkylation of **2** ([phenol]$_0$ = 0.33 mol/L) with **3** ([propene]$_0$ = 0.28 mol/L) at 673 K and a water density of 0.5 g/cm^3 to determine the alkylation path. Table 1 summarizes the results. For comparison, the data for [2-propanol]$_0$ = 0.33 mol/L are also shown in Table 1. The main liquid products were **4** and **5**, with yields that were almost the same as in the experiment with **1**. This result shows that the alkylation of **2** with **3** occurs in supercritical water.

Effect of Water Density. We conducted a series of experiments with **1** (0.33 mol/L) and **2** (1.65 mol/L) at 673 K over a range of water densities from 0 to 0.4 g/cm^3. The same products were obtained irrespective of the density. The main liquid products were **4** and **5**, and the alkylphenols obtained were almost all ortho substituents.

Table 2 shows that **1** was converted mainly to **3**, as described above. The conversion of **1** in the absence of water was larger than that at a water density of 0.2 g/cm^3. This change of conversion obeyed the direction of the equilibrium between 2-propanol and propene + water, which indicates that the contribution of equilibrium was large in the region of low water density. However, the conversion increased with increasing water density at densities greater than 0.2 g/cm^3. Water greatly increased the dehydration rate, and to examine this rate more closely, the apparent first-order rate constants were evaluated according to

$$k_{\text{dehydro}} = -\ln[(100 - X)/100]/t \qquad (4)$$

where X is the conversion of **1** (%) and t is the reaction time.

Data from the initial stages of the eaction were used to eliminate the effect of the successive reactions. The data before 30 and 10 min of reaction time were used for water densities of 0.4 and 0.5 g/cm^3, respectively. The estimated values k_{dehydro} are shown in Table 2. The rate constant at a water density of 0.5 g/cm^3 was about 20 times larger than that at 0.3 g/cm^3, which indicates that water significantly enhanced the dehydration.

The yield of **4** greatly increased with increasing water density and that of **5** exhibited the same trend. The yield of **5** decreased slightly for an increase in water density

Table 2. Effect of Water Density on the Reaction of Phenol with 2-Propanol at 673 K with [2-Propanol]$_0$ = 0.33 mol/L and [Phenol]$_0$ = 1.65 mol/L

water density (g/cm^3)	reaction time (min)	conversion of 1 (%)	yield of 4 (%)	yield of 5 (%)	$k_{dehydro}$ (min^{-1})	k_4 (mol L^{-1} min^{-1})	k_5 (mol L^{-1} min^{-1})
0	60	13.1	0.3	0.1	–[a]		
0.2	60	0	0.8	0.1	–[a]		
0.3	10	13.4	0.1	0	5.6×10^{-3}	1.4×10^{-4}	1.6×10^{-5}
	30	22.6	0.5	0.3			
	60	24.1	3.1	3.6			
0.4	10	21.5	1.0	0	1.5×10^{-2}	9.4×10^{-4}	1.1×10^{-4}
	30	34.8	7.4	0.6			
	60	41.5	18.0	2.2			
0.5	10	67.1	12.6	0.7	1.1×10^{-1}	6.3×10^{-3}	4.0×10^{-4}
	15	89.5	33.2	2.2			
	60	97.4	55.0	6.9			

[a] Not evaluated because alkylphenol yield was below 1.0%.

from 0.3 to 0.4 g/cm^3 at 60 min within the range of experimental error.

We evaluated the production rates of both **4** and **5**, that is, the alkylation rate, by using the equation

$$k_{4\text{ or }5} = [\text{2-propanol}]_0 \times (y_{4\text{ or }5}/100)/t \qquad (5)$$

To eliminate the effect of the dealkylation, the data before 15 min of reaction time were used at a water density of 0.5 g/cm^3. The alkylation rates, k_4 and k_5, obtained are shown in Table 2. These results show a clear enhancement of alkylation with increasing water (solvent) density.

Effect of Proton Concentration. In general, both dehydration and alkylation are catalyzed in the presence of a specific acid. The hydroxy groups of phenol and alkylphenols dissociate to form protons and phenoxide ions in aqueous solutions and might govern the proton concentration in supercritical water, while alcohols are much weaker acids than phenol. To examine the effect of the proton concentration on dehydration and alkylation, we conducted a series of experiments with and without nitric acid using the following mixtures: (a) 2-propanol and distilled water; (b) 2-propanol and 0.01 M nitric acid aqueous solution; (c) 2-propanol, phenol, and distilled water; and (d) 2-propanol, phenol, and 0.01 M nitric acid aqueous solution. In these experiments, the initial concentrations of 2-propanol and phenol were 0.33 mol/L, and the temperature and water density were set at 673 K and 0.5 g/cm^3, respectively. We estimated the proton concentration of the system using the ion product of water[4] and the dissociation constants of phenol,[22] alkylphenols,[23] and nitric acid[24] in supercritical water. Estimated proton concentrations were (a) 2.0×10^{-7}, (b) 3.6×10^{-4}, (c) 1.4×10^{-6}, and (d) 3.6×10^{-4} mol/L. The detailed method for the estimation is described in the Supporting Information.

Figure 3 shows the conversion of **1** with reaction time, and Figure 4 shows the yields of **4** and **5** with reaction time for the experiments with phenol. First, we compared the results for the dehydration among these four experiments. In the experiments where phenol was loaded, the main liquid products were **4** and **5**. Further, **3** was the main product in the conversion of **1** before 20 min of reaction time, while the sum of the yields of **4** and **5** was small (below 5.9%). We compared the dehydration rate using the data within 20 min of reaction time. In experiment a, **1** was not converted for 30 min of reaction time and then slightly decomposed after 30 min. In experiment b, the conversion of **1** after 15 min of reaction time was 31.2%. The conversions of **1** in experiments b and c were more or less the same, while the conversion in experiment d at 10 min of reaction time was above 60% and much larger. Hence, the order of the reaction rate for the dehydration of **1** was d > c ≈ b ≫ a. The proton provided by the dissociation of strong acid catalyzed the dehydration of **1** as well as that in subcritical water,[25] and phenol also catalyzed the dehydration.

Next, we evaluated the alkylation rates to **4** and **5** from the slopes in Figure 4. For experiment c, the

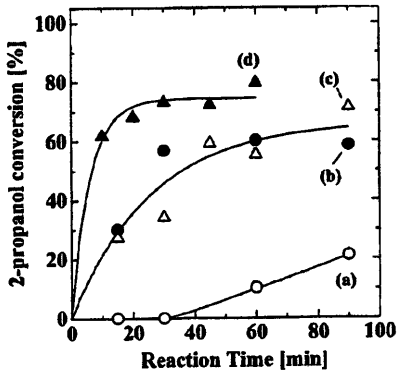

Figure 3. Comparison of conversion of 2-propanol at a temperature of 673 K and a water density of 0.5 g/cm^3, [2-propanol]$_0$ = 0.33 mol/L: (a) in distilled water; (b) in 0.01 M aqueous HNO_3; (c) in distilled water, [phenol]$_0$ = 0.33 mol/L; and (d) in 0.01 M aqueous HNO_3, [phenol]$_0$ = 0.33 mol/L.

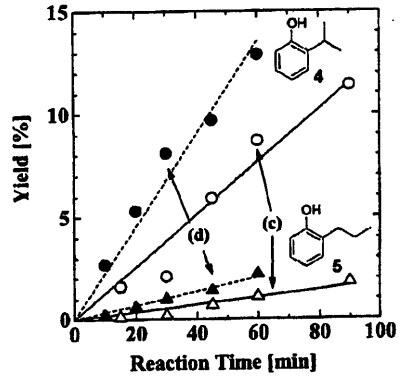

Figure 4. Comparison of yields of 2-isopropylphenol (**4**) and 2-propylphenol (**5**) at a temperature of 673 K and a water density of 0.5 g/cm^3, [2-propanol]$_0$ = 0.33 mol/L: (c) in distilled water, [phenol]$_0$ = 0.33 mol/L; (d) in 0.01 M aqueous HNO_3, [phenol]$_0$ = 0.33 mol/L.

production rates of **4** and **5** were 4.2×10^{-4} and 5.9×10^{-5} mol L^{-1} min^{-1}, respectively. For experiment d, they were 7.5×10^{-4} and 1.1×10^{-4} mol L^{-1} min^{-1}, respectively. The alkylation rates to **4** and **5** in the presence of nitric acid were about 2 times larger than those in the absence of nitric acid.

The proton concentration in experiment b was 4 orders of magnitude larger than that in experiment a, and the proton concentrations in experiments b and d were two orders of magnitude larger than that in experiment c. If the proton-catalyzed reaction controlled the dehydration, the dehydration rate would have been in the order d $\approx$ b > c $\gg$ a , and the alkylation rate would have been d $\gg$ c. Judging from the experimental results, protons enhanced the dehydration of 2-propanol through an acid-catalyzed mechanism. In addition to the protons, phenol also promoted the dehydration. The effect of the proton concentration on the alkylation rate was small. This indicates that the alkylation rate cannot be attributed solely to the proton concentration.

Reactivity of the Para Position. To evaluate the reactivity for alkylation at the para position, we conducted the reaction of **1** with 2,6-dimethylphenol, whose alkylation site should be limited to its para position. The initial concentrations were 0.33 mol/L, and the were a water density of 0.5 g/cm^3, a temperature of 673 K, and a reaction time of 60 min. The conversion of **1** was 41.7%, and 2,6-dimethylphenol did not react.

To determine the reactivity of the para position of alkylphenol, 4-isopropylphenol was reacted under the same conditions for 180 min. No product yield over 1% was observed, and the 4-isopropylphenol concentration in the recovered liquid remained almost constant. The para position of the hydroxy group of **2** had a low reactivity for both alkylation and dealkylation in supercritical water.

Reaction Mechanism. The main experimental findings were that (i) the alkylphenols formed in supercritical water were mainly ortho isomers; (ii) phenol, **2**, enhanced the dehydration of 2-propanol, **1**, and the alkylation of **2** to a greater extent than expected from its proton concentration; and (iii) the para position of the hydroxy group had a low reactivity. From these findings, we concluded that the ordinal acid-catalyzed alkylation is probably not dominant under these conditions and that the hydroxy group of **2** seems to play an important role in the alkylation of **2** and the dealkylation of **4**. Niedeal and Natelson[26] proposed that alkylation can proceed through the rearrangement of isopropylphenyl ether; however, isopropylphenyl ether was not observed at all under the present conditions. Although this reaction pathway cannot be definitively rejected, it is clear that phenol behaves as a catalyst in the present reaction. The dehydration of **1** proceeded through both the ordinal acid-catalyzed mechanism and the phenol-catalyzed one. In this section, we discuss the mechanism, focusing on the phenol-catalyzed reactions for dehydration and alkylation.

Figure 5 illustrates a probable phenol-catalyzed mechanisms for the dealkylation of **1** and alkylation of **2** with propene, **3**, in supercritical water. The mechanism is the dehydration of **1** (Figure 5a), followed by the alkylation of **2** with **3** (Figure 5b). In the dehydration, the hydroxy group of **2** protonates the hydroxy group of **1** and abstracts one hydrogen atom from the methyl group of **1**, yielding **3** and water. The hydrogen of the methyl group of **1** can be easily abstracted by the negatively

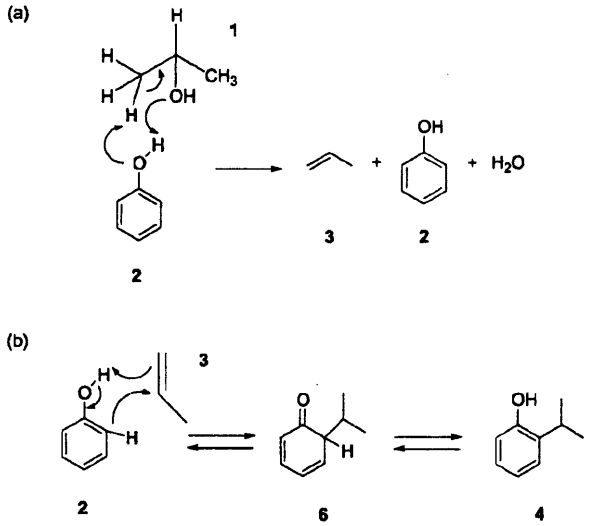

Figure 5. Possible phenol-catalyzed mechanisms for (a) the dehydration of 2-propanol and (b) the alkylation of phenol with propene in supercritical water.

charged phenoxide ion structure. Phenol, **2**, works as an acid and a base catalyst.

In the alkylation, the direct reaction of **2** and **3**, where **2** provides a proton **3** to form the unsaturated ketone **6** as an intermediate, is followed by the conversion of **6** to give 2-isopropylphenol, **4**. The dealkylation of **4** also probably proceeds along the reverse direction. This mechanism via a complex around the hydroxy group of **2** is similar to that proposed by Sartori et al.[27] This mechanism shows that the proton does not participate in the reaction and that the hydroxy group is required for the reaction. Thus, the mechanism in Figure 5b is consistent with the experimental results regarding the effect of the proton concentration on the alkylation rate and the ortho selectivity.

Phenol, **2**, and water molecules can interact by hydrogen bonding. Mikami[28] reported that **2** constructs hydrogen-bonding clusters involving several water molecules, that is, phenol$-(H_2O)_n$, where $n = 2-4$. Gerhards and Kleinermanns[29] reported that the most stable structure of phenol$-(H_2O)_2$ cluster is cyclic with nonlinear hydrogen bonds. Further, the specific solvation of solvent around a solute group often occurs in supercritical fluids,[30] as has been demonstrated for the hydroxy group of **2** in supercritical CO_2.[31] Hoffmann and Conradi[32] reported that there are still 29% as many hydrogen bonds in water at a temperature of 673 K and a water density of 0.52 g/cm^3 as in room-temperature water according to NMR spectroscopic measurements, and some researchers have also reported that hydrogen bonds between water molecules exist in supercritical water on the basis of NMR,[33] Raman,[34] IR adsorption, and X-ray scattering[35] data. Those results support our findings, which indicate that there is an interaction between the phenolic hydroxy group and water and that water molecules probably locate around the hydroxy group of **2** under supercritical conditions. The dehydration of **1** and the alkylation of **2** with **3** were enhanced with increasing water density, which probably means that the number of water molecules around the hydroxy group of **2** increased with increasing water density. This makes the reaction field limited to the hydroxy group.

If there is an increase in the number of water molecules around the hydroxy group, the local dielectric

constant should also increase. Because the electrostatic effect of solvent can be expressed in terms of the dielectric constant of the solvent,[36] if the transition state is more polar than the reactants, the increase in dielectric constant will cause the rate constant to increase. This trend is supported by the experimental data and the transition state of the reactants (Figure 5). The localized water might enhance the dissociation of the hydroxy group. Dimitrova[37] calculated the bond length of hydrogen-bonded clusters of phenol$-(H_2O)_n$ and found that the bond length between hydroxy oxygen and hydrogen increases with increasing number of localized water molecules. The increase in the number of water molecules around the hydroxy group enhances the dissociation of the O−H bond of the hydroxy group, which allows the weakly bonded proton to be donated to the hydroxy group of **1** and to **3** during the dehydration or alkylation reaction.

Conclusions

The dehydration of 2-propanol and alkylation of phenol occurred in supercritical water without the addition of a catalyst, and the alkylphenols obtained were mainly ortho substituents. 2-Propanol was dehydrated to propene, after which phenol was alkylated with propene to form alkylphenols (2-isopropylphenol and 2-propylphenol). In the series of reactions, both dehydration and alkylation were accelerated with increasing water density, and phenol catalyzed the dehydration of 2-propanol. In the dehydration reaction, the hydroxy group of phenol protonates the hydroxy group of 2-propanol and abstracts one hydrogen atom from the methyl group of 2-propanol, yielding propene and water. In the alkylation reaction, the direct reaction of propene and phenol, in which phenol provides a proton to propene, yields an unsaturated ketone as an intermediate, which is followed by the conversion of the unsaturated ketone to 2-isopropylphenol.

Acknowledgment

The authors acknowledge Grants-in-Aid for Scientific Research on Priority Areas (09450281, 10555270, 11450295, and 11694921) from the Ministry of Education, Culture, Sports, Science and Technology of Japan, which supported this research.

Supporting Information Available: Detailed explanation of the method for estimating the proton concentration of the system using the ion product of water and the dissociation constants of phenol, alkylphenols, and nitric acid. This material is available free of charge via the Internet at http://pubs.acs.org.

Literature Cited

(1) Savage, P. E. Organic chemical reactions in supercritical water. *Chem. Rev.* **1999**, *99*, 603.

(2) Katritzky, A. R.; Nichols, D. A.; Siskin, M.; Murugan, R.; Balasubramanian, M. Reactions in high-temperature aqueous media. *Chem. Rev.* **2001**, *101*, 837.

(3) Broll, D.; Kaul, C.; Kramer, A.; Krammer, P.; Richter, T.; Jung, M.; Vogel, H.; Zehner, P. Chemistry in supercritical water. *Angew. Chem., Int. Ed.* **1999**, *38*, 2998.

(4) Marshall, W. L.; Franck, E. U. Ion product of water substance, 0−1000 °C, 1−10 000 bar New international formation and its background. *J. Phys. Chem. Ref. Data* **1981**, *10*, 295.

(5) Uematsu, M.; Franck, E. U. Static dielectric constant of water and steam. *J. Phys. Chem. Ref. Data* **1980**, *9*, 1291.

(6) Savage, P. E.; Gopalan, S.; Mizan, T. I.; Martino, C. J.; Brock, E. E. Reactions at supercritical conditions: Applications and fundamentals. *AIChE J.* **1995**, *41*, 1723.

(7) Akiya, N.; Savage P. E.; Kinetics and mechanism of cyclohexanol dehydration in high-temperature water. *Ind. Eng. Chem. Res.* **2001**, *40*, 1822.

(8) Ikushima, Y.; Hatakeda, K.; Sato, O.; Yokoyama, T.; Arai, M. Acceleration of synthetic organic reactions using supercritical water: Noncatalytic Beckmann and pinacol rearrangements. *J. Am. Chem. Soc.* **2000**, *122*, 1908.

(9) Ikushima, Y.; Hatakeda, K.; Sato, O.; Yokoyama, T.; Arai, M. Structure and base catalysis of supercritical water in the noncatalytic benzaldehyde disproportionation using water at high temperatures and pressures. *Angew. Chem., Int. Ed.* **2001**, *40*, 210.

(10) Olah, G. A. *Friedel−Crafts and Related Reactions*; Interscience Publishers: New York, 1963; Vol. I.

(11) Sartori, G.; Bigi, F.; Maggi, R.; Arienti, A. Acidity effect in the regiochemical control of the alkylation of phenol with alkenes. *J. Chem. Soc., Perkin Trans. 1* **1997**, *3*, 257.

(12) Sato, S.; Takahashi, R.; Sodesawa, T.; Matsumoto, K.; Kamimura, Y. Ortho-Selective Alkylation of Phenol with 1-Propanol Catalyzed by CeO−MgO. *J. Catal.* **1999**, *184*, 180.

(13) Sato, S.; Koizumi, K.; Nozaki, F. Ortho-selective methylation of phenol over CeO2 catalyst. *Appl. Catal. A* **1995**, *133*, L7.

(14) Gray, W. K.; Small, F. R.; Hitzler, M. G.; Ross, S. K.; Poliakoff, M. The continuous acid-catalyzed dehydration of alcohols in supercritical fluids: A new approach to the cleaner synthesis of acetals, ketals, and ethers with high selectivity. *J. Am. Chem. Soc.* **1999**, *12*, 10711.

(15) Chandler, K.; Deng, F.; Dillow, A. K.; Liotta, C. L.; Eckert, C. A. Alkylation reactions in near-critical water in the absence of acid catalysis. *Ind. Eng. Chem. Res.* **1997**, *36*, 5175.

(16) Chandler, K.; Liotta, C. L.; Eckert C. A.; Schiraldi, D. Tuning alkylation reactions with temperature in near-critical water. *AIChE J.* **1998**, *44*, 2080.

(17) Sato, T.; Sekiguchi, G.; Adschiri, T.; Arai, K. Noncatalytic and selective alkylation of phenol with propan-2-ol in supercritical water. *Chem. Commun.* **2001**, *17*, 1566.

(18) *NBC/NRC Steam Tables*; Haar, L., Gallagher, J. S., Kell, G. S., Eds.; Hemisphere Publishing Corp.: New York, 1984.

(19) Heidemann, R. A.; Khalil, A. M. The calculation of critical points. *AIChE J.* **1980**, *26*, 769.

(20) Sowa, F. J.; Hennion, G. F.; Nieuwland J. A. Organic reactions with boron fluoide. IX. The alkylation of phenol with alcohols. *J. Am. Chem. Soc.* **1935**, *57*, 709.

(21) Katritzky, A. R.; Murugan, R.; Siskin, M. Aqueous high-temperature chemistry of carbo- and heterocycles. 9. Aquathermolysis of ortho-substituted, meta-substituted, and multisubstituted phenols in the presence and absence of sodium bisulfite. *Energy Fuels* **1990**, *4*, 538.

(22) Sue, K.; Murata, K.; Matsuura, Y.; Tsukagoshi, M.; Adschiri, T.; Arai, K. Flow-through electrochemical cell for pH measurement of organic acid aqueous solutions at subcritical and supercritical conditions. *Fluid Phase Equilib.* **2002**, *194−197*, 1097.

(23) Xiang, T.; Johnston, K. P. Acid−base behavior of organic compounds in supercritical water. *J. Phys. Chem.* **1994**, *98*, 7915.

(24) Chlistunoff, J.; Ziegler, K. J.; Lasdon, L.; Johnston, K. P. Nitric/nitrous acid equilibria in supercritical water. *J. Phys. Chem. A* **1999**, *103*, 1678.

(25) Antal, M. J., Jr.; Carlsson, M.; Xu, X.; Anderson, D. G. M. Mechanism and kinetics of the acid-catalyzed dehydration of 1- and 2-propanol in hot compressed liquid water. *Ind. Eng. Chem. Res.* **1998**, *37*, 3820.

(26) Niedeal, J. B.; Natelson, S. The rearrangement of saturated alkyl phenyl ethers. Synthesis of isopropyl phenol and cresols. *J. Am. Chem. Soc.* **1931**, *53*, 1928.

(27) Sartori, G.; Maggi, R.; Bigi, F.; Arienti, A.; Porta, C.; Predieri, G. Metal-template ortho-regioselective synthesis of 2′-hydroxyphenylpyridinemethanols. *Tetrahedron* **1994**, *50*, 10587.

(28) Mikami, N. Spectroscopic study of intercluster proton transfer in small size hydrogen-bonding clusters of phenol. *Bull. Chem. Soc. Jpn.* **1995**, *68*, 683.

(29) Gerhards, M.; Kleinermanns, K. Structure and vibrations of phenol$(H_2O)_2$. *J. Chem. Phys.* **1995**, *103*, 7392.

(30) Kajimoto, O. Solvation in supercritical fluids: Its effects on energy transfer and chemical reactions. *Chem. Rev.* **1999**, *99*, 355.

(31) Wada, N.; Saito, M.; Kitada, D.; Smith, R. L., Jr.; Inomata, H.; Arai. K.; Saito, S. Local excess density about substituted benzene compounds in supercritical CO_2 based on FT-IR spectroscopy. *J. Phys. Chem. B* **1997**, *101*, 10918.

(32) Hoffmann, M. M.; Conradi, M. S. Are there hydrogen bonds in supercritical water? *J. Am. Chem. Soc.* **1997**, *119*, 3811.

(33) Nakahara, M.; Matubayashi, N.; Wakai, C.; Tsujino, Y. Structure and dynamics of water: from ambient to supercritical. *J. Mol. Liq.* **2001**, *90*, 75.

(34) Ikushima, Y.; Hatakeda, K.; Saito, N.; Arai, M. An in situ Raman spectroscopy study of subcritical and supercritical water: The peculiarity of hydrogen bonding near the critical point. *J. Chem. Phys.* **1998**, *108*, 5855.

(35) Gorbaty, Y. E.; Kalinichev, A. G. Hydrogen bonding in supercritical water. 1. Experimental results. *J. Phys. Chem.* **1995**, *99*, 5336.

(36) Amis, E. S. *Solvent Effects on Reaction Rates and Mechanisms*; Academic Press: New York, 1966.

(37) Dimitrova Y. Theoretical study of structures and stabilities of hydrogen-bonded phenol−water complexes. *J Mol. Struct. (THEOCHEM)* **1998**, *455*, 9.

Received for review January 23, 2002
Revised manuscript received April 18, 2002
Accepted April 19, 2002

IE0200712

ELSEVIER

Fuel 81 (2002) 1453–1461

FUEL

www.fuelfirst.com

Extraction of Taiheiyo coal with supercritical water–phenol mixtures☆

Taku Michael Aida, Takafumi Sato, Gaku Sekiguchi, Tadafumi Adschiri*, Kunio Arai*

Department of Chemical Engineering, Tohoku University, 07 Aoba, Aramaki, Aza-Aoba-ku,Sendai 980-8579, Japan

Received 7 May 2001; revised 12 October 2001; accepted 8 November 2001; available online 10 April 2002

Abstract

Taiheiyo Japanese sub-bituminous coal was extracted with supercritical water (SCW) and phenol mixtures at 673 K and at over fluid densities ranging from 0 to 0.5 g/cm^3. The extraction yield with SCW was 0.55–0.60, but increased with increasing the ratio of phenol to water, showing a maximum of 0.7 at water–phenol ratio of 4.5:0.5 and then decreased to 0.50–0.55 for pure phenol.

The main products for the SCW–phenol extraction were bisphenol alkyl compounds, while these compounds could not be detected when SCW was used as the solvent. For elucidating the mechanism of SCW–phenol extractions, reactions between phenol and model compounds of hydrolysis products (formaldehyde, acetone, propionic acid, and 2-propanol) were conducted. In SCW, formaldehyde reacted with phenol to produce polymers, while neither acetone nor propionic acid reacted with phenol. The 2-propanol dehydrated to form propene, which reacted with phenol to form 2-isopropylphenol. The reaction rate increased with increasing water density. In SCW–phenol extraction of coal, phenol seems to inhibit reactions that lead to hydrolysis products or those that might cross-link to form the macromolecules. Phenol can be used with SCW to reduce retrograde reactions in residual coals.

Keywords: Supercritical water; Phenol; Coal extraction

1. Introduction

Coal has great potential as an alternate for petroleum as a energy and chemical source for its aromatic structural character and massive stock [1–6]. Various coal conversion techniques such as liquefaction, pyrolysis, and gasification [2] have been developed so far. IG process (Germany) [7], SRC-II process (USA) [7], H-coal process (USA) [7], EDS process (USA) [7–9], and NEDOL process (Japan) [10,11] are coal liquefaction processes that have been conducted on a pilot plant scale [7–11]. In these processes, a large amount of hydrogen is used for liquefying coal, which elevates cost, energy consumption, and CO_2 emission of the process and is one of the reasons that the processes have not been operated on a world-wide scale. A coal liquefaction process that does not require hydrogen would be highly attractive to energy industries. In this work, we examine the potential of supercritical water (SCW)–phenol mixtures as extraction solvents for coal liquefaction. For this type of process, no hydrogen is used in the liquefaction.

Water becomes supercritical fluid, when the temperature and pressure are increased above its critical point (T_c: 647 K, P_c: 22.1 MPa). The reaction rate and equilibrium change greatly around the critical point due to the change of the properties of water [12,13]. In particular, SCW forms a homogeneous phase with light gases like hydrogen or oxygen, which allows one to control whether the reaction environment is oxidizing or reducing. These characteristics of SCW provide unique reaction pathways that are unavailable in other phase or solvents as reported in a recent reviews [14–16]. So far, various processes using these specific features of SCW have been proposed for material processing and chemical recycle [14–16].

Reactions of coal in SCW and some features of SCW coal conversion process have been reported in the literature [17–21]. Hydrolysis of coal occurs in SCW without catalyst, and this promotes coal conversion [19]. For reforming liquid products, effective hydro-treatment can be attained through the partial oxidation of the products in SCW [20]. This is because CO is selectively produced by partial oxidation of hydrocarbons in SCW, which is followed by the production of active hydrogenating species through a water–gas shift reaction ($CO + H_2O = CO_2 + H_2$) [22,23]. Another feature of the SCW coal conversion process is in regard to product separation. Liquid products can be separated from solid residue or ash, and fractionated into some portions according to the molecular weight or affinity with SCW after the reaction stage, because solubility of SCW can be manipulated by temperature and

* Corresponding authors. Tel./fax: +81-22-217-7246. (T. Adschiri).
Tel./fax: +81-22-217-7246 (K. Arai).
E-mail address: Karai@arai.che.tohoku.ac.jp (K. Arai).

☆ Published first on the web via Fuelfirst.com—http://www.fuelfirst.com

0016-2361/02/$ - see front matter
PII: S0016-2361(02)00067-4

Table 1
Proximate and Ultimate analysis of Taiheiyo coal

Proximate analysis (wt. % db)				
Ash	Volatile matter	Fixed carbon		
12.0	45.9	42.1		
Ultimate analysis (wt% daf)				
C	H	S	N	O
65.6	4.6	0.09	0.7	29.0

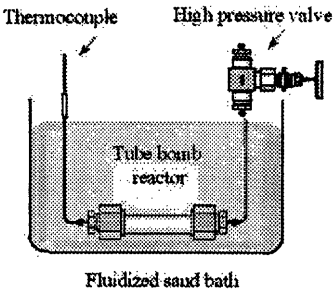

Fig. 1. Experimental apparatus for coal extraction.

pressure. This can reduce the required number of fractionation and separation steps [21].

Coal consists of a number of oxygen functional groups (phenolic compounds, hydroxyl, carboxyl and carbonyl groups [24]), which influence its physical and chemical properties [7]. Fundamental studies on reactions of coal model compounds including oxygen functional groups in sub- and supercritical water have been reported by Townsend [25], Chandler [26], Katritzky [27] and Siskin [28]. They reported that ether or ester bonds were hydrolyzed to produce hydroxyl compounds such as alcohols in sub- and supercritical water without a catalyst, and that hydrolysis rate increased over the pyrolysis rate with increasing water density [25].

Importance of hydrolysis in the extraction of coal in SCW has also been reported. Kershaw [17], Li [18] and Adschiri [19] compared the results of extraction of coal using SCW and supercritical toluene. They reported that coal conversion in SCW was higher than that in supercritical toluene and that hydrolysis products including alcohols and carboxylic acids were produced in SCW. However, according to the literature [17–19], conversion of coal did not exceed 60 wt%. This is probably because of retrograde reactions in the residual coal.

A similar problem has been reported in a research of the decomposition of phenol resin and lignin in SCW, both of which have similar structures as coal [29,30]. Phenolic resin is a condensation polymer produced by dehydration between phenol and formaldehyde. Goto et al. [29] tried to recover phenol from phenolic resin through the hydrolysis in SCW. They reported that a considerable amount of cross-linked residues were formed, while hydrolysis products were recovered. Lignin consists of phenolic structures linked with glycelaldehyde. Yokoyama [30] studied lignin decomposition in SCW and claimed that compounds heavier than the original lignin were formed, while phenolic compounds including guaiacol and catechol were produced. These results suggest coal that also forms cross-linked heavier residues during the SCW extraction.

These results suggest that suppression of cross-linkage reactions during the hydrolysis in SCW is important. Chandler et al. [26] and Katritzky et al. [27] have studied reactions between phenols and alcohols in sub-critical water. They reported that the condensation reaction occurs to form alkylphenols under these conditions. These results suggest that phenol can work as a capping agent for aldehydes and alcohols.

Wayman et al. [31] reported that the condensation of lignin could be prevented by the addition of phenolic compounds during lignin autohydrolysis at 448 K. Ouchi et al. [32] and Kamiya et al. [33] preformed research to elucidate the chemical structure of coal and its reactivity, and suggested that phenol addition could aid in the coal liquefaction. Miura et al. [34] demonstrated that extremely high coal extraction yield could be obtained by using a carbolic oil, which is composed of phenolic compounds, as an extraction solvent. They claimed that the role of this solvent is to dissociate hydrogen bondings between the coal structures, namely the physical effect rather than the chemical effect [35].

Based on the previous research, it seems that phenol addition to SCW extraction of coal could enhance the coal extraction yield due to both the physical effect and chemical capping effect. The first objective of this study is to examine the effect of phenol addition in SCW extraction of Taiheiyo coal. The second objective is to understand the mechanism of coal extraction with SCW–phenol water mixtures.

2. Experimental

2.1. Materials

Taiheiyo coal was employed as a sample. Proximate and ultimate analyses of the coal are shown in Table 1. The particle size of the coal was in the range from 16 to 24 meshes. Phenol (99.0%), toluene (99%) 2-propanol (99.5%), acetone (99.5%), pronionic acid (99.0%), formaldehyde (99%) and hydroxymethylphenol (99%) were purchased from Wako chemicals and were used without further purification as additives.

2.2. Procedures

2.2.1. Coal extraction

The experiments were conducted with a SUS316 tube bomb reactor (10 cm^3) with a thermocouple as shown in Fig. 1. The reactor was loaded with about 0.1 g of coal and 0–6 g of a solvent, purged with Ar gas and sealed. The solvents used in the experiment were water, phenol

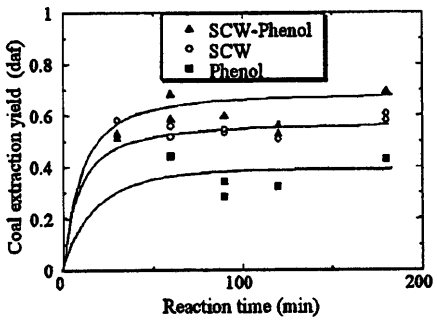

Fig. 2. Coal extraction yield SCW–phenol (5 g:1 g), SCW(5 g), and phenol (5 g) extraction as a function of reaction time at 673 K, 180 min.

and mixtures of water and phenol at various compositions. The reactor was submerged in a fluidized sand bath that was controlled at 673 K. The time required to heat up the reactor from room temperature to 673 K was about 30 s. The extraction was conducted for 0–180 min and ended by quenching the reactor in a water bath at room temperature.

The products were collected by rinsing the reactor with 30 g of acetone and filtering with a 1 μm membrane filter. Acetone soluble products were defined as liquid. An internal standard, naphthalene, was added to the collected liquid products. The compositions of the liquid products were analyzed by the gas chromatography-flame ionized detector (GC-FID Hewlett Packard, model 6890) and a gas chromatography-mass spectroscopy (GC-MS Japan Electron Optics Laboratory, model Auto mass 20). The acetone insoluble products were dried in vacuo at 353 K for 12 h, and then weighed. This product was defined as residue. The ash content of the parent coal and the residue were analyzed by combustion using TGA (Metller, TG50).

The coal extraction yield was evaluated from the following equation:

$$\text{coal extraction yield (daf)} = \frac{W_{coal}(1-\alpha_0) - W_{residue}(1-\alpha)}{W_{coal}(1-\alpha_0)} \quad (1)$$

where W_{coal}, $W_{residue}$, α_0, α are the weight of parent coal (g), weight of residue (g), ash content of the parent coal and ash content of the residue, respectively.

2.2.2. Reaction between phenol and model coal hydrolysis products in supercritical water

For elucidating the role of phenol addition on the SCW extraction of coal, a series of experiments of reactions between phenol and model compounds of hydrolysis products (formaldehyde, acetone, 2-propanol, propionic acid) was conducted. The experiments were conducted in the previously described set up with 6 cm^3 volume tube bomb reactors. Phenol (1.65 mol/l = 0.941 g), the model compound (0.33 mol/l = 0.12 g) and distilled water (0–3 g) were loaded in the reactor, then purged with Ar gas, and sealed. Density of the mixture at supercritical homogeneous state was estimated to be from 0 to 0.5 g/cm^3, according to the amount of water loaded. The reactor was submerged into the fluidized sand bath at 673 K, and quenched as described in the Section 2.2.1. The reaction time was in the range from 0 to 360 min. The reactor was connected to a syringe (50 cm^3) to collect gas produced and measure its volume. The gas was analyzed by a GC-TCD (Shimadzu, model GC-7A and Hitachi, model GC-163). The liquid product in the reactor was washed with 15 g of THF, naphthalene was added as an internal standard, and then the sample was analyzed using GC-FID and GC-MS.

For reaction between phenol and 2-propanol, yields of the liquid products in this experiment were evaluated by the ratio of moles of carbon of products derived from 2-propanol to that in 2-propanol loaded, from the following equation:

$$\text{yield}\,[-] = \frac{\text{carbon of products derived from 2-propanol (mol)}}{\text{carbon in 2-propanol loaded (mol)}} \quad (2)$$

The yield of phenol structure was defined as the total moles of phenol structure in the liquid products to the moles of phenol loaded, using the formula below:

$$\text{yield of phenol structure}\,[-] = \frac{\sum \text{phenol structure in liquid products (mol)}}{\text{phenol loaded (mol)}} \quad (3)$$

3. Results and discussion

3.1. Coal extraction experiments

Fig. 2 shows the results of coal extraction experiments with water, water–phenol and phenol. The extraction yield increased rapidly during the first 60 min and approached a constant value around 120 min. Similar trends were observed for the other solvents. SCW–phenol (5 g:1 g) mixture showed the highest extraction yield of 0.7, followed by the SCW extraction with 0.6 of extraction yield and the phenol extraction with 0.4. According to the results, subsequent experiments were conducted with 180 min of extraction time.

A series of experiments were conducted with SCW–phenol mixtures in more detail. The ratio of water to phenol was changed while keeping the total amount of solvent constant at 5 g. The solvent density, which is a major factor for determining the solubility, was approximately the same (0.5 g/cm^3).

Fig. 3 shows the relation between coal extraction yield and solvent composition. The extraction yield of coal for pure water (5 g) was 0.55–0.60. The extraction yield increased with an increase in the ratio of phenol to water, showing a maximum of 0.67 at water–phenol ratio of

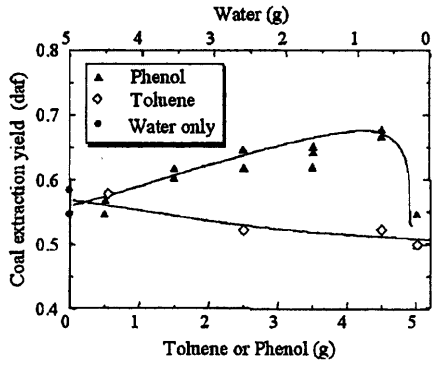

Fig. 3. Coal extraction yield as a function of water to phenol and toluene ration at 673 K, 180 min.

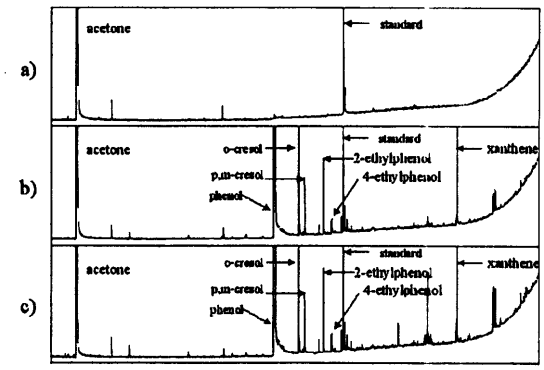

Fig. 4. GC-FID chart of the liquid products of (a) SCW(5 g), (b) SCW–phenol (5 g:1 g) and (c) phenol (5 g) extraction at 673 K, 180 min.

0.5 (g):4.5 (g) and then decreased to 0.50–0.55 at pure phenol (5 g).

Kershaw et al. [36] and Ogo et al. [37] reported a similar trend for the coal extraction yield for a mixed solvent of water and *n*-hexane solvent. They explained the results by considering the hydrophilic and hydrophobic nature of the mixed solvent. Coal decomposition products include both hydrophilic and hydrophobic components. The mixture of water and *n*-hexane should have an affinity for both hydrophilic and hydrophobic compounds, which they thought was one of the reasons for the higher solubility of the mixed solvent versus pure solvents.

To examine the effect of solvent affinity on the extraction of Taiheiyo coal, an experiment using a non-reacting hydrophobic solvent, toluene, instead of phenols was conducted. As shown in Fig. 3, a maximum in the yield was not observed for SCW–toluene. The extraction yield at pure toluene (5 g) was 0.5, and monotonically increased as the ratio of toluene to water decreased, showing a maximum of 0.63 at pure water (5 g). The higher extraction yield in SCW compared with the toluene extraction may be attributed to the effect of hydrolysis at ether or ester bonds in coal as reported in previous research [18–20]. Hydrolysis is promoted by increasing water concentration [13,25,38], which results in an increase in extraction yield. Thus, the effect of hydrophilic and hydrophobic affinity of the mixed solvent seems to be not as important for the Taiheiyo coal extraction under the given conditions. From these results, we could not attribute the higher extraction yield of the SCW–phenol mixed solvent to the hydrophilic and hydrophobicity nature of the mixed solvent.

One possible reason for the high yields may be the reaction of phenol with coal or intermediate products during the coal extraction. Reactions with phenol and alcohols, aldehydes in sub-critical water have been reported by Chandler et al. [26] and Katritzky et al. [27]. Their results lead us to hypothesize that phenol works as an reactant with the hydrolysis products in SCW–phenol extraction of coal. Once an alcohol or aldehyde or such functional groups are formed through hydrolysis, these can react with the phenolic structure of coal to form cross linkages in SCW. When phenol is added, the cross linking reactions might be suppressed, since it is possible for phenol to work as a capping agent to the active aldehyde or OH groups. This will be discussed later.

Fig. 4 shows GC-FID chromatograms of the liquid products obtained at the three conditions, (a) SCW, (b) SCW–phenol (5 g:1 g) and (c) phenol. The peaks were analyzed by GC-MS. For extraction in the presence of phenol ((b) and (c)), alkyl phenols, such as *o*-cresol, *m*-cresol, *p*-cresol, 2-ethylphenol, 4-ethylphenol and xanthene were obtained. As for the SCW extraction (a), the GC-FID chromatogram of the product showed none of the compounds mentioned earlier, which indicated that phenol probably reacted with the extracts or pyrolysis products. The peaks shown in the GC chromatogram are for a light portion of the liquid products, but similar reactions are considered to take place for heavier compounds.

The number of carbon atoms captured by phenol is one for *o*-cresol(CH_3), p-cresol(CH_3) and xanthenes(CH_2) and two for 2-ethylphenol(C_2H_5), 4-ethylphenol(C_2H_5). We evaluated the ratio of the weight of captured carbons to that of carbons in the loaded coal and defined as carbon yield, as shown in Fig. 5. The carbon yield for light liquid products was 0% for SCW (5 g) extractions and 3% maximum for SCW–phenol extractions and 2.7% for phenol extractions. Similar reactions are considered to take place for the heavier liquid products. Thus, reaction with phenol appeared to be a key to bringing about the increase in the extraction yield for SCW–phenol extractions of coal.

As shown in Fig. 5, the total carbon yield in light liquid yield for SCW–phenol experiment was a slightly higher than that in pure phenol, although the loaded amount of phenol in the SCW–phenol experiments (4.5 g) was lower than that in phenol (5 g). One of the reasons for these differences may be the reaction between phenol and hydrolysis products. Another reason might be the effect of water on the reaction rate of phenol and extracts. Phenol in SCW may have acted as an acid, activating the hydrolysis of the esters and ethers bonds of the coal [39,40].

Xanthene was probably formed by a reaction between formaldehyde and phenols as reported by Ouchi [41]. The

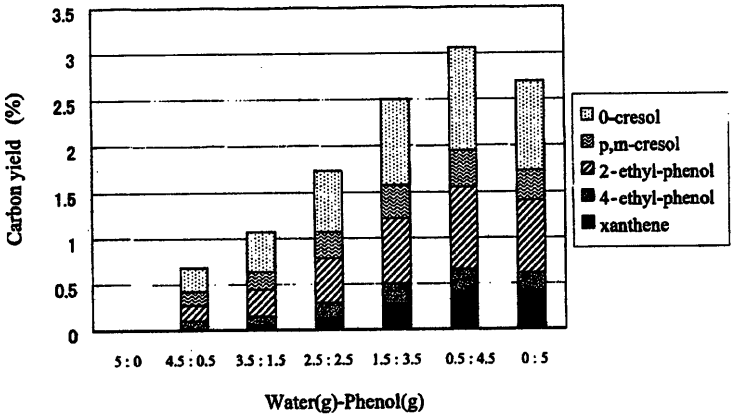

Fig. 5. Ration of the captured carbons by phenols as *o,p,m*-cresol, 2,4-ethylphenol and xanthene as a function of extraction solvent at 673 K, 180 min.

formation of xanthene implies that formaldehyde was produced by the hydrolysis or pyrolysis of coal during the extraction. Formaldehyde is a known cross-linking agent especially for phenolic structures. The formation of xanthene during the coal extraction shows that phenol probably reacted with formaldehyde, resulting in the inhibition of the cross-linking.

Research [14,15] on the reaction in SCW indicates that reaction rates and chemical equilibrium are greatly affected by water density. Experiments were performed at various water densities while holding the phenol concentration constant. Fig. 6 shows the effect of water density on the extraction yield. Experiments without phenol (0 g) and at water density of 0 g/cm^3 was for thermal decomposition. Coal conversion for this experiment was 0.28. There was a tendency for the extraction yield to increase with the amount of phenol added. Although the data are scattered, there is a clear tendency for the extraction yield to increase with increasing water density for all the phenol loadings.

Miura and his colleagues [34] suggested the mechanism of dissociating hydrogen bonds between the coal structures for explaining the solubilization of coal by carbol oils at 573–623 K. This physical factor may also work to elevate the extraction yield. However, the extraction yield obtained for phenol extraction was around 0.4, which is no more than that for supercritical toluene extraction as shown in Fig. 3. The contribution of physical factor of phenol addition appears to be less significant in the present experimental conditions.

Fig. 7 shows TGA experimental results for the residue of the three extraction conditions (SCW, phenol, SCW–phenol (5 g:1 g)). In this figure, the weight changes are expressed on an ash free parent coal basis. At temperatures below 623 K (350 °C), the weight change was insignificant, which implies that moisture or phenol (boiling point: 455 K) content of the samples was not large. A large weight loss was observed between 623 and 900 K. The final residue yield for SCW, phenol, and SCW–phenol extractions were 11, 7, and 6%, respectively, which shows that the SCW–phenol mixture inhibited the cross-linking of the residue during the extraction.

3.2. Reaction between phenol and model coal hydrolysis products in supercritical water

A series of experiments using model compounds were conducted for elucidating the reaction mechanism. We used formaldehyde, acetone, propionic acid and 2-propanol as samples. Experiments were conducted with the same

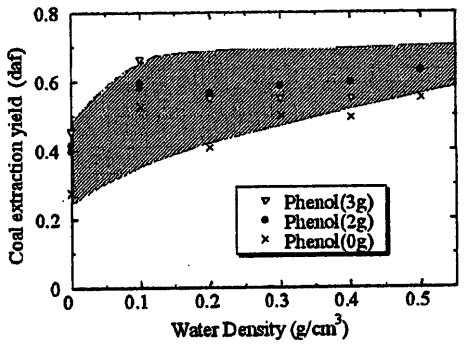

Fig. 6. Coal extraction yield as a function of water density at 673 K, 180 min.

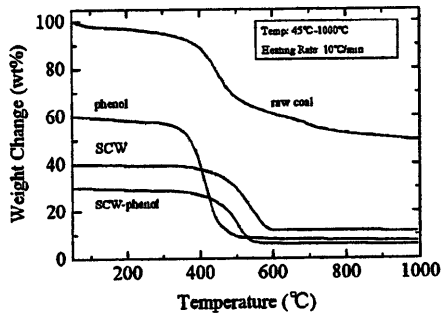

Fig. 7. TGA of residue of SCW(5 g), SCW–phenol (5 g: 1 g) and phenol (5 g) extraction.

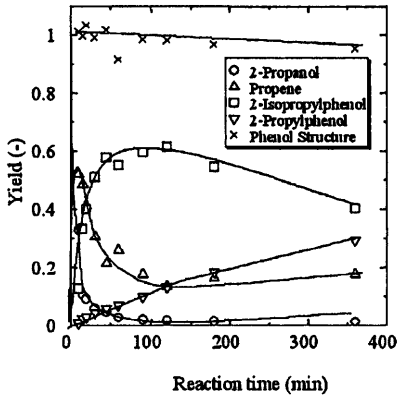

Fig. 8. Product yield of the reaction between 2-isopropylphenol and phenol as a *s* function of reaction time at 673 K in SCW.

apparatus and with the same procedures as the coal extraction experiments. Water density was set at 0 (in Ar atmosphere) or 0.5 g/cm^3 and the reaction time was 60 min. Formaldehyde–phenol reactions produced polymers both in Ar atmosphere and in SCW. We also conducted an experiment of hydroxymethylphenol in SCW, which may be a possible intermediate species formed by the reaction between formaldehyde and phenol. From this experiment, it was confirmed that polymerization took place. On the other hand, reaction between acetone and phenol was negligible both in an Ar atmosphere and in SCW. In our previous study on the decomposition of bis-phenol A in SCW, that can be formed by the acetone–phenol reaction, we found that hydrolysis occurs at high water density conditions [42]. The reaction between propionic acid and phenol produced 40 mol% yield of propionic acid phenyl ester in an Ar atmosphere, but negligible amounts in SCW. An experiment of propionic acid phenyl ester decomposition in SCW (0.5 g/cm^3) was also conducted. The results showed that hydrolysis occurred to produce propionic acid and phenol.

In experiments of 2-propanol-phenol reaction in SCW, the main products obtained were propene, 2-isopropylphenol, 2-propylphenol from GC-MS analysis. As shown in Fig. 8, a high yield of aromatic compounds was obtained. The yield of 2-propanol decreased in very short reaction times, and propene was formed. The yield of propene decreased gradually with an increase in reaction time, while the yield of isopropylphenol increased first up to 0.6 and then decreased gradually. The maximum yield of 2-isopropylphenol was obtained at around 150 min of reaction time. The yield of 2-propylphenol increased gradually over a range of 360 min and this increase corresponded to a decrease in the yield of 2-isopropylphenol. We can propose the following reaction pathways. Probably 2-propanol was dehydrated to form propene. The propene reacted with phenol to form 2-isopropylphenol, which was then converted to 2-propylphenol [43]. Rearrangement of 2-isoproylphenol to 2-propylphenol in SCW has been found in our previous work [43]. We conducted experiments for reaction of phenol and propene to confirm the formation of 2-isopropylphenol.

For the dehydration of secondary alcohols in sub- and supercritical water, Antal and his colleagues [44–46] explained the results by a specific acid catalyzed mechanism by considering the ion product of water. For other reactions in SCW including Friedel–Crafts type reactions, a widely accepted mechanism for non-catalytic reactions in high temperature water has not yet been proposed so far [13,39,47].

Based on the results obtained, a reaction mechanism is shown in Fig. 9 based on our results. The first step is the dehydration of 2-propanol to form propene, followed by the reaction with phenol to form 2-isopropylphenol, which reforms to 2-propylphenol.

As reported previously [14,15], reaction rates and chemical equilibria in SCW can be varied greatly around the critical point with temperature and density The effect of water density on the reaction was examined. Fig. 10 shows that the yield of 2-isopropylphenol increased with an increase in water density. The maximum yield of 2-isopropylphenol reached 60% at $\rho_w = 0.5$ g/cm^3, while the reaction without water ($\rho_w = 0$ g/cm^3) was no more than 5% under these conditions. The 2-propanol decomposition was as low as several percent without water. Fig. 11 shows the yield of 2-propanol at different water density. As shown in Fig. 11, dehydration of 2-propanol was promoted with increasing water density.

3.3. Role of phenol addition in supercritical water extraction of coal

An extraction mechanism was developed as shown in Fig. 12. In SCW, hydrolysis takes place at ether or ester

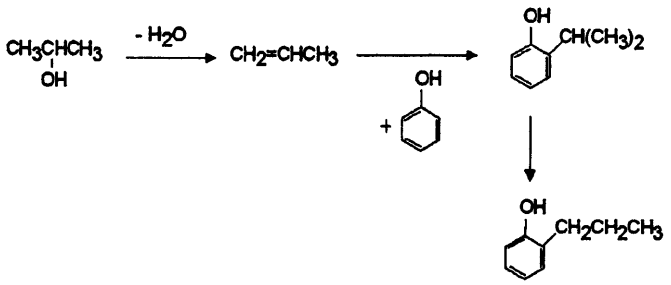

Fig. 9. Reaction mechanism between 2-propanol and phenol in SCW.

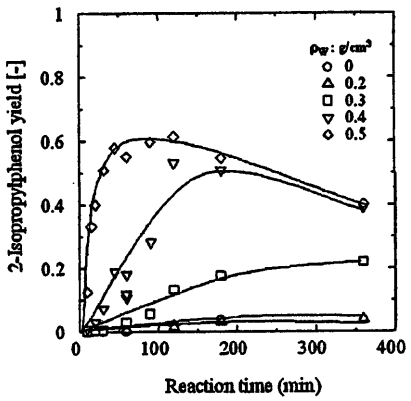

Fig. 10. Product yield of 2-isopropylphenol the reaction between 2-propanol and phenol as a function of reaction time and water density at 673 K in SCW.

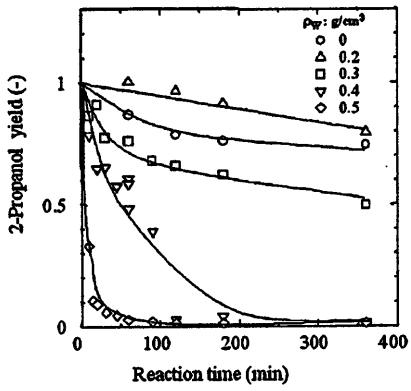

Fig. 11. Product yield of 2-propanol of the reaction between 2-propanol and phenol as a function of reaction time and water density at 673 K in SCW.

bonds in coal structure without catalyst, in parallel with thermal decomposition of coal. Some fragments are extracted by SCW. Some of alcohols, aldehydes, and their functional group (hydroxyl and aldehyde) of the macromolecules formed through hydrolysis, react with the phenolic structures in coal through the dehydration. In particular, aldehyde group act as cross-linking agents between phenolic structures in coal and increase the residue yield.

When phenol is added, phenol traps the hydrolysis products that might react with phenolic structures to make larger molecules (residual). Phenol bounded species, including alkylphenols, are extracted into a SCW–phenol mixture. This is probably the reason for obtaining higher extraction yields with SCW–phenol. An increase in water density enhances both hydrolysis rate of ether or ester bonds in coal structure and the dehydration rate of formed alcohol, which leads to the enhancement of the reaction with phenol. Thus, the extraction yield increased with increasing in water density. If the added amount of phenol against coal were extremely high, bis-phenol alkyl structure would be recovered. Based on this reaction mechanism, alkylphenols that have vacant ortho or para positions, such as cresol, ethylphenol, or catechol can probably be used as capping agents.

Miura et al. [34] reported that extraction of coal with carbol oil probably includes a large amount of phenolic compounds, showed 90% of coal solubilization. In this study, we focused a point of the discussion on the chemical role of phenol, since a clear physical role could not be observed in the pure phenol extraction of Taiheiyo coal. However, we think that dissociation of hydrogen bonds among the macromolecules of coal also takes place during the coal extraction, which supplies a better environment for the chemical reactions with phenol.

A possible process for coal conversion to recover

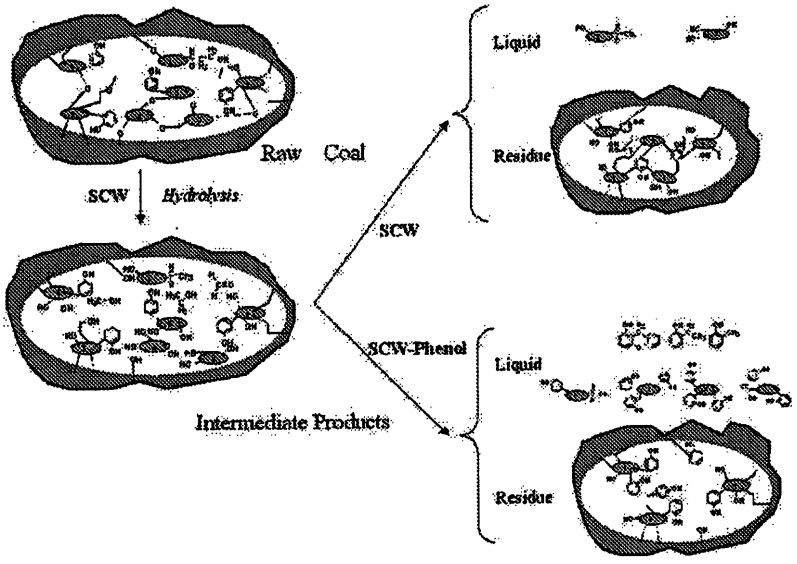

Fig. 12. The extraction mechanism of coal liquefaction in SCW and SCW–phenol mixtures.

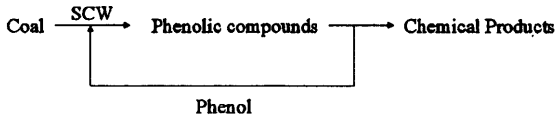

Fig. 13. Chemical production process with SCW–phenol mixtures.

chemicals with SCW is shown in Fig. 13. Phenol or alkyl phenols (phenols) are added to coal water mixtures and the reactive extraction is conducted at 673 K. The recovered extracts are compounds that have phenol-like structures. After the products are recovered in the reforming (partial oxidation or mild gasification in SCW) [23,48,49] and separation process, phenols can be recycled to the feed. Since phenol is a major component of coal structures, especially for low rank coals, a make-up portion of phenol in this process can be supplied from coal. One method to recover phenol or alkyl phenol from the extracts may be the partial oxidation in SCW [23,48].

4. Conclusions

SCW–phenol extraction was conducted at 673 K and at density ranging from 0 to 0.5 g/cm^3. Extraction yield increased with increase in a phenol/water ratio showing the maximum and then decreased. Phenol addition into the SCW extraction showed reduction of the cross linking of the residue. Main products in SCW–phenol extraction were bisphenol alkyl compounds, while these compounds could not be detected in the products of SCW extraction. In SCW, formaldehyde reacted with phenol significantly to produce polymers, while neither acetone nor propionic acid reacted with phenol. 2-propanol was dehydrated to form propylene, which reacted with phenol to form isopropylphenol. The reaction rate increased with increasing the water density. In SCW–phenol extraction of coal, phenol appears to act as a capping agent for reactive hydrolysis products that might cross-link the structure of residual coal. A new process is proposed that provides liquefaction of coal without the use of hydrogen.

Acknowledgements

Authors would like to express their thanks to the grant of the Ministry of Education, Science, Culture and Sports for partial financial support. We would also like to thank Idemitu Kosan Co. Ltd for supplying the Taiheiyo coal.

References

[1] International Energy Outlook, DOE/ETA-0484, 98 Energy Information Administration, 1998. p. 73.
[2] Miura K. Fuel Process Technol 2000;62:119–35.
[3] Nomura M, Matsubayashi K, Ida T, Murata S. Fuel Process Technol 1992;31:169–79.
[4] Shinn JH. Fuel 1984;63:1187–96.
[5] Murakami H. J Fuel Soc Jpn 1987;66:448–51.
[6] Schobert H. 6th Japan–China Symp Coal C1 Chem Zoa 1998:358–61.
[7] Van Krevelen PW. Coal. 3rd ed 1993 p. 750–757
[8] Exxon Research and Engineering. EDS Consolidation Programme, Reactor. Optimization Design Study Phase V. FE-28993-152; 1985.
[9] Irrvine AR, Cochran HD, Culberson OL, Fisher JF, Gambill WR, Salamon R. Direct liquefaction technology assessment. Task 1. Technical readiness of the developing plant functions. Oak Ridge National Laboratory, 1981 ORNL/MIT-326.
[10] Kouzu M, Koyama K, Oneyama M, Aramaki T, Hayashi T, Kobayashi M, Itoh H, Hattori H. Fuel 2000;79:365–71.
[11] Hirano K. Fuel Process Technol 2000;62:109–18.
[12] Jessop PG, Leiter W. Chemical synthesis using supercritical fluids. Wiley-VCH, 1999.
[13] Klein MT, Torry LA, Wu BC, Townsend SH, Paspek SC. J Supercrit Fluids 1990;3:222–7.
[14] Knutson CA, Knutson BL, Debenedetti PG. Nature 1996;383(26):313–8.
[15] Arai K, Adschiri T. Fluid Phase Equilib 1999:158–60, see also pages 673–684.
[16] Savage PE. Chem Rev 1990;99:603–21.
[17] Kershaw JR, Bagnell L. J Supercrit Fluids ACS Symp Ser 1987;329:267.
[18] Li L, Egiebor NO. Energy Fuels 1992;6:35–40.
[19] Adschiri T, Nagashima S, Shibuichi H, Shishido M, Arai K. J Jpn Inst Energy 1996;75(8):742–50.
[20] Adschiri T, Sato T, Shibuichi H, Fang Z, Okazaki S. Arai K. Fuel 2000;79:243–8.
[21] Kershaw JR. J Supercrit Fluids 1989;2:35–45.
[22] Adschiri T, Shibata R, Sato T, Watanabe M, Arai K. Ind Engng Chem Res 1998;378(7):2634–8.
[23] Arai K, Adschiri T, Watanabe M. Ind Engng Chem Res 2000;39:4697–701.
[24] Aida T, Nishisu A, Yamanishi I. Prepr Am Chem Soc Div Fuel Chem 1999;44(3):571–5.
[25] Townsend SH, Abraham MA, Huppert GL, Klein MT, Paspep NC. Ind Engng Chem Res 1988;27:143–9.
[26] Chandler K, Deng F, Dillow A, Liotta CL, Eckert CA. Ind Engng Chem Res 1997;36:5175–9.
[27] Katritzky AR, Balasubramanian M. Energy Fuels 1990;4:499–505.
[28] Siskin M, Katritzky AR. J Anal Appl Pyrolysis 2000;54:193–214.
[29] Goto J, Adschiri T, Arai K. Proceedings of the 1st International Symposium on Feedstock Recycling of Plastics, 1999. p. 231–4.
[30] Yokoyama C, Nishi K, Nakajima A, Seino K. Sekiyu Gakkaishi 1998;41:243–4.
[31] Wayman M, Lora JH. Tappi 1978;61:55–7.
[32] Ouchi K, Imuta K, Yamashita Y. Fuel 1965;44:29–38.
[33] Kamiya Y, Sato H, Yao T. Fuel 1978;57:681–5.
[34] Miura K, Mae K. Proceedings of the Society of Chemical Engineers Japan 63rd Annual Meeting 2000. p. G104.
[35] Miura K, Mae K, Yoshimura T, Masuda K, Hashimoto K. Energy Fuels 1991;5:803–8.
[36] Kershaw JR. Liq Fuels Technol 1984;2:385–94.
[37] Ogo Y, Mizun o K, Bangjouya A. Proc ICCS 1993;1:238–41.
[38] Savage PE, Gopalan S, Mizan TI, Martino CJ, Brock EE. AIChE J 1995;41:1723–78.
[39] Taylor JD, Steinfeld JI, Tester JW. Ind Engng Chem Res 2001;40:67–74.
[40] Penninger JML, Kersten RJA, Baur HCL. J Supercrit Fluids 1999;16:119–32.
[41] Ouchi K, Imuta K, Yamashita Y. Fuel 1959;38:429–43.
[42] Adschiri T, Shibata R, Arai K. Sekiyu Gakkaishi 1997;40:291–7.
[43] Sato T, Sekiguchi G, Saisu M, Watanabe M, Adschiui T, Arai K. Ind Engng Chem res, 2002, in press.
[44] Ramayya S, Andrew B, Antal MJ. Fuel 1987;66:1364–71.

[45] Xiadong X, De Almeida C, Antal MJ. J Supercrit Fluids 1990;3:228–32.
[46] Xiadong X, Antal MJ. Ind Engng Chem Res 1997;36:23–41.
[47] Ikushima Y, Hatakeda K, Sato O, Yokoyama T, Arai M. J Am Chem Soc 2000;122:1908–18.
[48] Watanabe M, Hirakoso H, Sawamoto S, Adschiri T, Arai K. J Supercrit Fluids 1998;13:247–52.
[49] Watanabe M, Mochiduki M, Sawamoto S, Adschiri T, Arai K. J Supercrit Fluids 2001;20:257–66.

Rapid and selective retro-aldol condensation of glucose to glycolaldehyde in supercritical water

Mitsuru Sasaki,*[a] Kohtaro Goto,[b] Kiyohiko Tajima,[b] Tadafumi Adschiri[c] and Kunio Arai[c]

[a] *Genesis Research Institute, Inc, 4-1-35 Noritake-shinmachi, Nishi-ku, Nagoya 451-0051, Japan. E-mail: sasaki@arai.che.tohoku.ac.jp*
[b] *Noguchi Institute, 1-8-1 Yoga, Itabashi-ku, Tokyo 173-0003, Japan*
[c] *Department of Chemical Engineering, Tohoku University, Aza-Aoba 7, Aramaki, Aoba-ku, Sendai 980-8579, Japan*

Received 20th March 2002
First published as an Advance Article on the web 23rd May 2002

Retro-aldol condensation of glucose occurred preferentially relative to dehydration and isomerization under low water density conditions in supercritical water, and glycolaldehyde was successfully produced in a rapid and selective manner without any catalyst.

Glycolaldehyde can be utilized as a raw material of glycolic acid that has recently been focused on as a source material for resin production. This chemical intermediate is produced by various synthetic methods from formaldehyde, allyl alcohol or ethylene glycol. Although the usual glycolaldehyde production techniques are useful as a quantitative manufacturing method, they must use petrochemicals, catalysts and microorganisms, which requires considerable waste treatment. Moreover, from the viewpoint of 'post petrochemistry', research has been directed towards alternative resources, cleaner solvents and non-catalytic reaction routes.

Biomass is an important energy resource that has been focused on as one of alternatives for petroleum. It is possible that carbon dioxide once discharged from biomass can be fixed in biomass again by photosynthesis with water and solar energy. Therefore, chemical synthesis processes using biomass resources have been realized as an environmentally benign technology. Cellulose is one of the major components of biomass and has been utilized in extensive fields such as pulp, paper, fiber, food and cosmetics. Glucose, which is a repeating unit of cellulose, can be also an important chemical intermediate for many synthetic polymers that have been manufactured in the present petrochemical industries.[1]

Supercritical water (T > 647.2 K, P > 22.1 MPa) shows some unique properties and has been considered as a reaction field for the decomposition of organics and for chemical synthesis.[2,3] Solvent properties such as density and dielectric constant can be varied by manipulating temperature and pressure. In our previous work, we clarified that chemical substances such as glucose and cellooligosaccharides can be rapidly and selectively recovered from cellulose in supercritical water.[4] From the study on the phase behaviour of the cellulose–water system, it was found that cellulose can dissolve in high-temperature and high-pressure water.[5] Our recent kinetic studies of glucose and cellobiose indicated that the main reactions of saccharides were hydrolysis, retro-aldol condensation, isomerization and dehydration, and that these reactions can be probably controlled by manipulating temperature and pressure in near-critical and supercritical water.[6] In this study, we aimed to evaluate effects of temperature and pressure on retro-aldol condensation of glucose and to explore an optimal reaction condition in which glycolaldehyde was selectively obtained through non-catalytic glucose decomposition experiments in subcritical and supercritical water.

Reactions of glucose were conducted using a continuous flow-type micro-reactor for high-temperature and high-pressure conditions. The reactor was made from 316 stainless steel tubing (1.59 mm O.D.; 0.50 mm I.D.). Prior to the experiment, distilled water was introduced in a system by a high-performance liquid chromatography (HPLC) pump (Nihon-Seimitsu Industries Co., Ltd., Model NP-AX-15) at a flow rate of 14 g min^{-1}, and subsequently pressurized using a back-pressure regulator (TESCOM, Model 26-1721-24) in the range 25-40 MPa. Then, the distilled water was heated with an electric furnace (Seiwa-Riko Co., Ltd., Model FTO-6), and mixed at the mixing point with a 1.0 mol L^{-1} glucose aqueous solution supplied from the other line at 2 g min^{-1} using a HPLC pump (GL Science Co., Ltd., Model PUS-3). The glucose solution was rapidly heated to the desired reaction temperature (623–723 K). The reactor was submerged into a metal-salt bath that was set at the reaction temperature in advance to keep the temperature uniform. The reaction time was ranged from 0.02 to 1.02 s by replacing the reactor tubing whose length is different in each experiment. At the reactor outlet, the reacted solution was quenched by a cooling jacket, and then collected in a sampling bottle for a fixed time after it was decompressed. Liquid products were identified by NMR, FAB-MS and HPLC-RI, and quantified with HPLC-RI/UV (wavelength of 210 nm in UV). Carbon recovery in the aqueous product solution in each experiment was examined by a total organic carbon analyser (Shimadzu Co., Ltd., Model TOC-5000A). In this study, the analytical error of the quantification of products was in the range 0.5–2.0%, and the carbon recovery ranged from 93 to 102% in all the experiments. Glucose conversion (X), product yield (Y) and selectivity (S) were defined on the carbon basis.

Green Context

The conversion of renewable resources into useful chemical building blocks is of great importance, as petrochemical resources become scarcer. Here, the conversion of glucose into glycolaldehyde using supercritical water is described. The system chosen allows the decomposition of glucose to a range of useful products, primarily *via* retro-aldol reaction to glycolaldehyde, a raw material which can be used in a variety of industrial processes and applications. ***DJM***

DOI: 10.1039/b203968k

The main products obtained in this experiment were erythrose, glycolaldehyde, fructose, glyceraldehyde, dihydroxyacetone, 1,6-anhydro-β-D-glucose (1,6-AHG) and 5-hydroxymethyl-2-furfural (5-HMF), *cf.* the report of Kabyemela *et al.*[7] According to the proposed reaction pathways of glucose decomposition,[8] glucose can primarily be converted to erythrose plus glycolaldehyde, to fructose, and to 1,6-AHG or 5-HMF *via* retro-aldol condensation, isomerization and dehydration, respectively. Fig. 1 shows a typical variation of glucose decomposition products in supercritical water at 673 K and 40 MPa. The yield of erythrose was optimised at 0.1 s and decreased with time, whereas the yield of glycolaldehyde increased with increasing time and reached 48.8% at 0.76 s by retro-aldol condensation of the erythrose formed. Fructose was formed at the initial stage of glucose decomposition and then was converted to form glyceraldehyde, dihydroxyacetone and 5-HMF. Dehydration products such as 1,6-AHG and 5-HMF were also formed, although the product yields were low.

In order to explore an optimal reaction condition for glycolaldehyde production and to determine effect of temperature and pressure on glucose decomposition, we conducted experiments at 623–723 K, 25–40 MPa and 0.02–1.02 s, and results are summarized in Table 1. At 623 K, products of retro-aldol condensation of glucose were mainly obtained, but by-products from dehydration and isomerization of glucose also formed in relatively high yields. In supercritical water, the yield of glycolaldehyde became higher and the contributions of both dehydration and isomerization were lowered. This tendency became dramatic with a decrease in water density of the reaction atmosphere in supercritical water. A dramatic change of the product distribution will occur if supercritical water experiments under lower water density conditions than the conditions reported here are conducted. However, such experiments have not yet been conducted due to some limitations of the experimental setup (*e.g.* limited operating temperatures and pressures) preventing experiments at higher temperatures and lower pressures. It is hoped that such experiments can be conducted in the future.

From the experimental findings, we clarified the main reaction pathways of glucose under low water density conditions in supercritical water as shown in Scheme 1. Antal *et al.*[3] reported that dehydration preferentially took place under hydrothermal conditions in the absence of acid catalyst. Thus, it can be considered that dehydration scarcely takes place in supercritical water. Isomerization of glucose (1) to fructose (2) is also suppressed with a rise of temperature, and therefore, glyceraldehyde (7), dihydroxyacetone (8) and 5-HMF (6) did not form to a significant extent. By contrast, retro-aldol condensation of both glucose (1) and erythrose (4) to form glycolaldehyde (5) becomes dominant under low water density conditions in supercritical water.

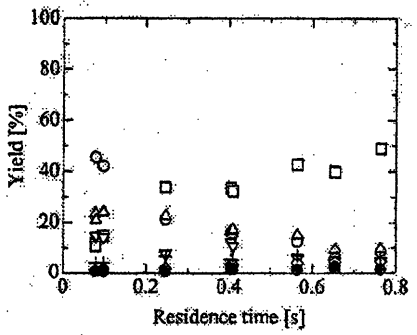

Fig. 1 A typical variation of glucose decomposition products in supercritical water at 673 K and 40 MPa; glucose (○); erythrose (△); glycolaldehyde (□); fructose (▽); dihydroxyacetone (◇); glyceraldehydeal (+); 5-hydroxymethyl-2-furfural (5-HMF) (●); 1,6-anhydro-β-D-glucose (1,6-AHG) (×).

Table 1 Effect of temperature and pressure on the product distribution of glucose decomposition in subcritical and supercritical water at 623–723 K and 25–40 MPa

					Y [C%] (*S* [C%])				
					RA[a]		Iso[a]	DH[a]	
T/K	*P*/MPa	ρ_w/g cm^{-3}	*t*/s	*X* [C%]	5	4	2, 7, 8	3	6
623	40	0.67	1.02	50.8	11.1 (21.9)	16.5 (32.5)	15.4 (30.3)	6.3 (12.4)	3.3 (6.5)
	25	0.63	0.92	45.1	11.8 (26.2)	10.1 (22.4)	16.4 (36.4)	5.2 (11.5)	2.3 (5.1)
673	40	0.52	0.76	91.4	48.8 (53.4)	9.6 (10.5)	15.3 (16.7)	tr. (—)	1.5 (1.6)
	25	0.17	0.24	87.0	48.0 (55.2)	18.3 (21.0)	16.5 (19.0)	tr. (—)	0.3 (0.3)
723	40	0.27	0.34	98.9	59.2 (59.9)	3.4 (3.4)	4.6 (4.7)	tr. (—)	0.5 (0.5)
	35	0.20	0.25	99.4	63.8 (64.2)	4.5 (4.5)	5.4 (5.4)	tr. (—)	0.5 (0.5)

[a] RA: Retro-aldol condensation; Iso: isomerization; DH: dehydration.

The reason why this reaction to form glycolaldehyde is undergone selectively under low water density conditions in supercritical water can be explained as follows. In supercritical water, the contribution of retro-aldol condensation to glucose decomposition increased and that of both isomerization and dehydration decreased as the water density of the supercritical atmosphere was lowered. It is well known that retro-aldol condensation of a saccharide occurs *via* formation of intramolecular hydrogen bond linkages. For a low water density reaction atmosphere, the formation of intramolecular hydrogen bond linkages of the saccharide becomes easier than that of intermolecular hydrogen bond linkages between water and saccharide. As a result, glycolaldehyde is selectively obtained by lowering the water density in supercritical water. Also, from equilibrium considerations, retro-aldol condensation leads to two aldehyde molecules from one saccharide molecule, and a lower hydration energy of the product, thus at higher water densities retro-aldol condensation is suppressed.

In summary, glycolaldehyde was obtained in a relative high selectivity *via* retro-aldol condensation of glucose in supercritical water (maximum selectivity = 64.2% at 723 K, 35 MPa and 0.25 s) without any catalyst. This finding suggests an effective and environmentally benign technique that can produce glycolaldehyde from cellulosic biomass resource with

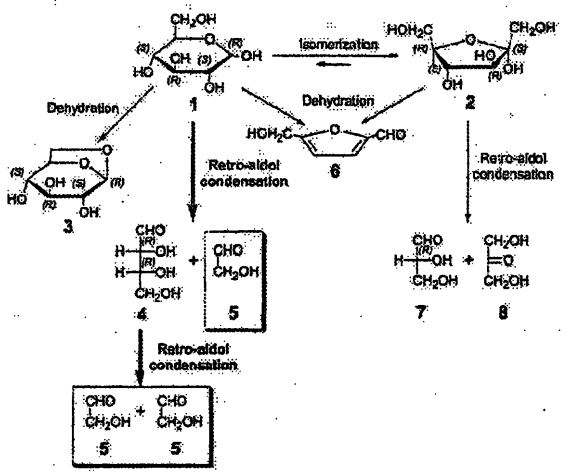

Scheme 1 Reaction pathways for glycolaldehyde production on glucose decomposition under low water density conditions in supercritical water; 1 glucose, 2 fructose, 3 1,6-AHG, 4 erythrose, 5 glycolaldehyde, 6 5-HMF, 7 glyceraldehyde, 8 dihydroxyacetone.

supercritical water as a reaction medium. Additionally, supercritical water can provide an unique atmosphere for chemical synthesis from biomass resources.

The authors gratefully acknowledge support by a Grand-in-Aid for Scientific Research on Priority Area 'Mechanism of hydrolysis in supercritical water' (#11450295) from the Ministry of Education, Culture, Sports, Science and Technology.

References

1 H. Danner and R. Braun, *Chem. Soc. Rev.*, 1999, **28**, 395; K. Tajima, *Biosci. Bioind.*, 1998, **56**(10), 23.

2 P. E. Savage, *Chem. Rev.*, 1999, **99**, 603; J. An, L. Bagnell, T. Cablewski, C. R. Strauss and R. W. Trainor, *J. Org. Chem.*, 1997, **62**, 2505; A. R. Katritzky, S. M. Allin and M. Siskin, *Acc. Chem. Res.*, 1996, **29**, 399; Y. Tsujino, C. Wakai, N. Matsubayashi and M. Nakahara, *Chem. Lett.*, 1989, 287; Y. Ikushima, K. Hatakeda, O. Sato, T. Yokoyama and M. Arai, *J. Am. Chem. Soc.*, 2000, **122**, 1908; H. Ito, J. Nishiyama, T. Adschiri and K. Arai, *Kobunshi Ronbunshu*, 2001, **58**((12)), 679.

3 M. J. Antal, M. Carlsson, X. Xu and D. G. M. Anderson, *Ind. Eng. Chem. Res.*, 1998, **37**, 3820; M. J. Antal and W. S.-L. Mok, *Carbohydr. Res.*, 1990, **199**, 91.

4 T. Adschiri, R. M. Malaluan, S. Hirose and K. Arai, *J. Chem. Eng. Jpn.*, 1993, **26**(6), 676; M. Sasaki, B. M. Kabyemela, R. M. Malaluan, S. Hirose, N. Takeda, T. Adschiri and K. Arai, *J. Supercrit. Fluids*, 1998, **13**, 261.

5 M. Sasaki, Z. Fang, Y. Fukushima, T. Adschiri and K. Arai, *Ind. Eng. Chem. Res.*, 2000, **39**(8), 2883.

6 B. M. Kabyemela, M. Takigawa, T. Adschiri and K. Arai, *Ind. Eng. Chem. Res.*, 1997, **37**(2), 357; B. M. Kabyemela, T. Adschiri, K. Arai and H. Ozeki, *Ind. Eng. Chem. Res.*, 1997, **36**(12), 2025.

7 B. M. Kabyemela, T. Adschiri and K. Arai, *Ind. Eng. Chem. Res.*, 1999, **38**(8), 2888.

8 K. Goto, K. Tajima, M. Sasaki, T. Adschiri and K. Arai, *Kobunshi Ronbunshu*, 2001, **58**(12), 685.

Kinetics and Mechanism of Cellobiose Hydrolysis and Retro-Aldol Condensation in Subcritical and Supercritical Water

Mitsuru Sasaki,[†] Momoko Furukawa,[‡] Kimitaka Minami,[‡] Tadafumi Adschiri,[‡] and Kunio Arai*[,‡]

Research Group II, Genesis Research Institute, Inc., 4-1-35 Noritake-shinmachi, Nishi-ku, Nagoya 451-0051, Japan, Department of Chemical Engineering, Tohoku University, 07 Aza-Aoba, Aramaki, Aoba-ku, Sendai 980-8579, Japan

Reactions of cellobiose in subcritical and supercritical water were studied. Kinetic study on the cellobiose decomposition clarified that the contribution of hydrolysis to the overall cellobiose decomposition rate decreased and that of retro-aldol condensation greatly increased with decreasing pressure in near-critical and supercritical water. It was found that the rate of retro-aldol condensation was expressed as a first-order reaction rate law and the kinetic parameters of this reaction were estimated. With regards to hydrolysis of cellobiose, it was indicated that the rate of hydrolysis was a second-order reaction (first-order reaction of the water concentration) and its activation energy and preexponential factor were determined. Mechanisms of these reactions were discussed based on the experimental findings. It was suggested that hydrolysis of cellobiose mainly took place by the nucleophilic attack of the oxygen atom of the water molecule or by the attack of a proton ion dissociated from supercritical water to the glycosidic carbon atom of the cellobiose molecule under the condition where the density of water was low and that the increase in the local water density around a solute promotes the hydrolysis rate at identical conditions. It was also found that retro-aldol condensation was promoted as the density of water decreased in near-critical and supercritical water. This is probably because this reaction can take place via the intermediate formed by the intramolecular hydrogen bond linkage of cellobiose, resulting in the enhancement of the intermediate formation by the increase of hydrophobic water molecules at lower water densities such as the gas-phase treatment.

Introduction

Various cellulose materials such as paper products, cellulosic fibers, and cellulose derivatives greatly contribute to our cultural life. However, the conventional manufacturing techniques of cellulosic materials cannot be called the "green" one in the environment from the following points: (1) These technologies have utilized alkali and acid aqueous solutions for pulping and bleaching treatments of cellulosic biomass; (2) special solvents must be utilized for the dissolution, regeneration, and chemical modification of cellulose. In this way, the reasons the load of the conventional technology to the environment must increase seem to be mainly the two below. One is the complexity of the internal structure of cellulosic biomass. Fractionation of each component is difficult because the main components (cellulose, hemicellulose, and lignin) in biomass complicatedly intertwine each other. Another is that each cellulose molecular chain has crystallized by intermolecular hydrogen bond linkages. For these reasons, the following materials which have a high impact on the environment must have been employed: special solvents on the cellulose dissolution process and organic solvents, alkali, halide additives, etc., on the cellulose chemical modification process.

As a means for solving such problems, the utilization of supercritical water as a reaction medium can be considered. Supercritical water (T_C = 374.2 °C, P_C = 22.1 MPa, and ρ_c = 0.323 g cm^{-3}) has unique properties (e.g., dielectric constant, density, and ionic product) that are greatly and continuously changed between the gas and liquid by manipulating the temperature and pressure. Moreover, water, oil, and gas, which do not melt at normal conditions, can form a homogeneous phase in supercritical water.

Research on various organic chemical reactions using this characteristic has been carried out. Dehydration condensation polymers with ester, ether, or acid amide bonds, etc., rapidly hydrolyze without acid and base catalysts.[1] In dehydration, it has been confirmed that olefin can be synthesized from various alcohols by intramolecular dehydration in high-temperature and high-pressure water including the supercritical state under catalyst-free conditions and that *tert*-butyl alcohol with one tertiary hydroxyl group can rapidly dehydrate to form isobutylene even under hydrothermal conditions.[2,3] Additionally, it has been reported that decarboxylation,[4] hydration of alcohols to alkenes to alkynes,[5,6] pinacol rearrangement, Beckmann rearrangement, Friedel−Crafts reaction,[7,8] Cannizzaro reaction,[9] etc., can occur in subcritical and supercritical water without catalyst. In this way, various reactions, which do not generally occur, can occur if any catalyst and organic solvent has been used.

We have conducted the research for developing a new method that uses supercritical water as a reaction solvent for the chemical conversion of carbohydrates (e.g., cellulose and glucose) to valuable chemical materials in a rapid and selective manner. We found that the

* Corresponding author. Phone: +81.22.217.7245. Fax: +81.22.217.7246. E-mail: karai@arai.che.tohoku.ac.jp.
[†] Genesis Research Institute, Inc.
[‡] Department of Chemical Engineering, Tohoku University.

10.1021/ie020326b CCC: $22.00
Published on Web 11/19/2002

crystalline cellulose can rapidly and selectively hydrolyzed to water-soluble cellooligosaccharides and glucose in supercritical water,[10,11] which was due to dissolution of cellulose into high-temperature and high-pressure water.[12] It was also found that the main reaction paths of saccharides in subcritical and supercritical water were hydrolysis, retro-aldol condensation, keto–enol tautomerism, and dehydration.[13–17] On the kinetic study of the glucose degradation,[17] it was clarified that keto–enol tautomerism superiorly progressed with an increase of the reaction pressure, while retro-aldol condensation superiorly progressed at low pressures in supercritical water. From the degradation experiment of cellobiose,[18] it was explained that the selectivity of the rate of retro-aldol condensation decreased as the pressure decreased and that of the rate of hydrolysis increased with an increase of the pressure in supercritical water. In this work, however, the temperature and pressure dependences of these reaction rates were evaluated on the basis of limited experimental data at high pressures in near-critical and supercritical water. Also, it has not discussed very much on the reaction mechanism. Therefore, it was necessary to evaluate the effects of several reaction factors (temperature, pressure, etc.) and properties of water (density, ion product, and dielectric constant) on the reaction rates and to elucidate the mechanism of cellobiose degradation in the extensive ranges of temperatures and pressures.

In this study, we conducted cellobiose degradation experiments in subcritical and supercritical water and determined the rates of hydrolysis and retro-aldol condensation of cellobiose. Moreover, we tried to elucidate the mechanism of these reactions at identical conditions.

Experimental and Analytical Methods

Chemicals. The reagents used for cellobiose degradation experiments and high-performance liquid chromatographic (HPLC) analyses are as follows: cellobiose (98+%; Sigma); glucose (99+%), fructose (99+%), erythrose (60+%), dihydroxyacetone (99+%), 1,6-anhydro-β-D-glucose (99+%), glyceraldehyde (97+%), pyruvaldehyde (40%), 5-(hydroxymethyl)-2-furfural (5-HMF) (95+%), 2-furfural (95+%) (Wako Pure Chemicals Industries Ltd.).

Experimental Apparatus and Procedure. Experiments were conducted for cellobiose degradation in subcritical and supercritical water at 325–400 °C, 25–40 MPa, and residence times of 0.01–0.54 s. Figure 1 shows a schematic representation of the continuous flow-type microreactor used in this study. At first, distilled water was fed into a system at a flow rate of 14.0 $cm^3\ min^{-1}$ using a HPLC pump P2 (Nihon-Seimitsu Chem. Co. Ltd., model NP-AX-15), pressurized in the system to a reaction pressure which was controlled in the range between 25 and 40 MPa using a back-pressure regulator (TECSOM, model 26-1721-24), and preheated up to supercritical temperature. The preheated water was then mixed with the cellobiose aqueous solution of 0.2–0.5 mol L^{-1} fed from another line at 2.0 $cm^3\ min^{-1}$ using a pump P1 (GL Science Co. Ltd., model PUS-3) at the mixing point to heat up rapidly to the reaction temperature, T [°C]. The aqueous solution was then introduced to the reactor (316 stainless steel tubing; 0.077 cm i.d.) with a volume of V [cm^3], which had sunk in the preheated molten salt bath (Parker Michael Ind. Co. Ltd., $KNO_3/NaNO_2$ = 45/55 (w/w)). Temperature of

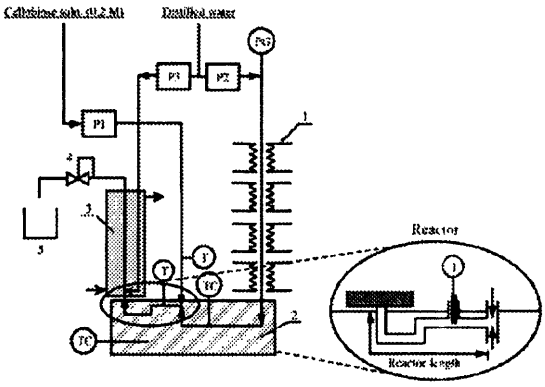

Figure 1. Schematic diagram of a continuous flow-type microreactor for cellobiose degradation in subcritical and supercritical water: (1) preheating unit of distilled water; (2) molten salt bath; (3) cooling jacket; (4) back-pressure regulator; (5) sampling bottle.

the reactor inlet was monitored at a position of 19 mm from the mixing point using a chromel–alumel thermocouple (K type). At the exit of the reactor, the aqueous solution was quickly quenched to below 60 °C to terminate further reaction by injecting water into the line at 14.0 $cm^3\ min^{-1}$ by the pump P3 (Nihon-Seimitsu Chem. Co. Ltd., model NP-AX-15) and externally by a cooling water jacket. If the system reached steady state, the aqueous product solution was depressurized by passing it through the back-pressure regulator and then collected in a sampling bottle for 10–20 min during the experiment.

In this study, we employed the rapid-heating and quick-quenching method. This method permits us to determine the accurate V value from 0.037 to 0.222 cm^3. Using this method, the residence time in the reactor, τ, could be calculated using the following values: the reactor volume, the flow rate of the aqueous solution in the reactor, F, the solution density at the reaction condition, $\rho(T,P)$, and the solution density at ambient temperature and pressure, $\rho(T_0,P_0)$.[16] However, in this method, cellobiose may be decomposed not only in the reactor but also in front of the mixing point or in back of the reactor outlet. The residence time in this region can be defined as an end effect of the reactor. If we consider the effect, we can obtain more accurate kinetic data than that obtained from a simple calculation without considering it. In this study, the end effect of the reactor, τ_0, was decided in the following. From the experiments of cellobiose degradation at various temperatures, pressures, and residence times, we calculated each conversion of cellobiose, X, and plotted the $-\ln(1 - X)$ value against the residence time in the reactor, τ. Under all of the reaction conditions, we observed linear correlations with positive intercepts. Each $\tau_0(T,P)$ value was determined from the intercept in the horizontal axis when the straight line was extrapolated to $-\ln(1 - X) = 0$ and consequently estimated as 0.0434 s by averaging all of the $\tau_0(T,P)$ values. Accordingly, each actual reaction time, τ_{actual}, was calculated as a summation of the residence time in the reactor and the time for the end effect by eq 1.

$$\tau_{actual} = \tau + \tau_0 \tag{1}$$

Analysis. The composition of an aqueous product solution was analyzed by HPLC (Thermoquest Co. Ltd., Model Spectra System AS3000) with a refraction index (RI) detector (ERC, model 7512). Details on the HPLC

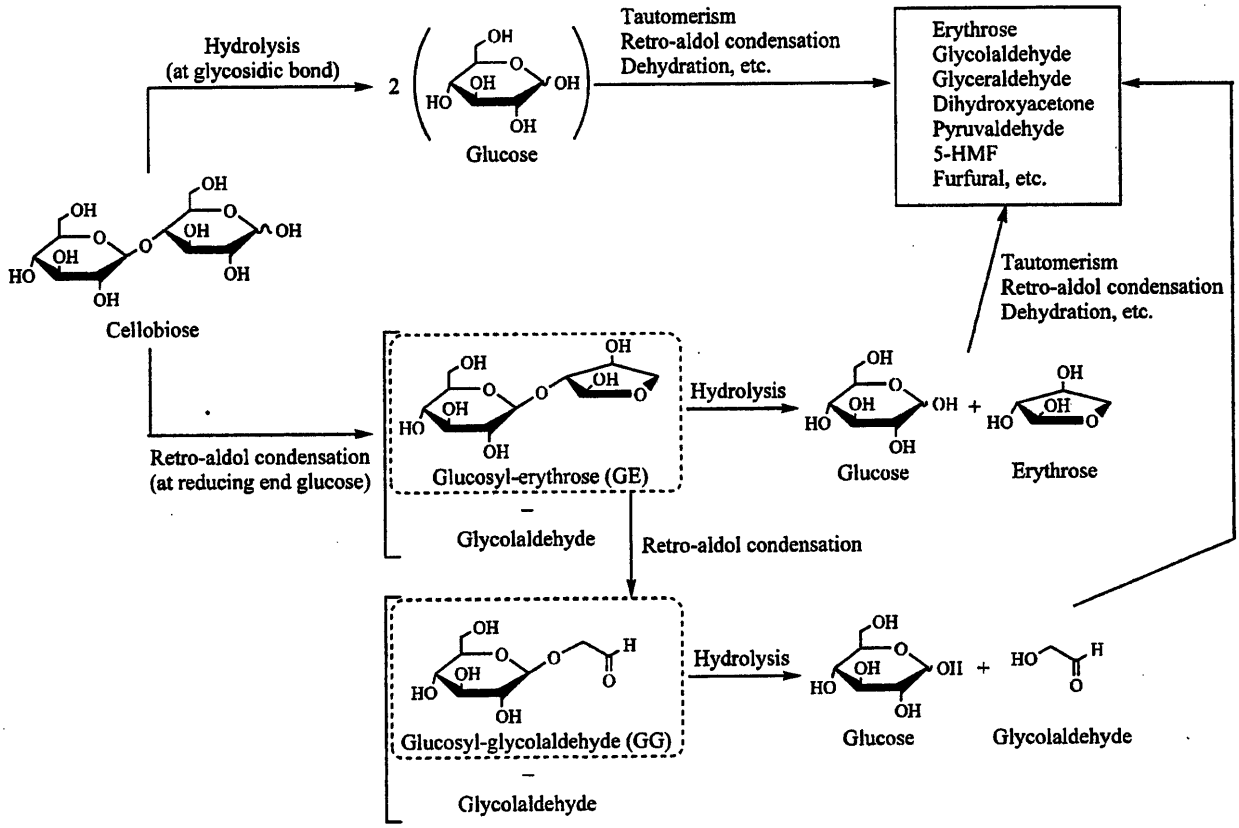

Figure 2. Main reaction pathway of cellobiose degradation in subcritical and supercritical water.

analysis are described on the previous work.[18] Conversion of cellobiose, X, and product yield of component i, Y_i, were calculated by eqs 2 and 3, respectively, where

$$X = \frac{C_{0,CB} - C_{CB}}{C_{0,CB}} \tag{2}$$

$$Y_i = \frac{C_i}{C_{0,CB}} \tag{3}$$

$C_{0,CB}$ is the concentration at the reactor inlet [mol L^{-1}], C_{CB} is the concentration at the exit of the reactor [mol L^{-1}], and C_i is the concentration of product i at the reactor outlet [mol L^{-1}]. Concentrations of the organic carbons in the aqueous solution were measured by a total organic carbon (TOC) analyzer (Shimadzu Ind. Co. Ltd., model TOC-5000A). The carbon balance in every experiment ranged from 91 to 108%. Analysis of gaseous products was not conducted in this study.

Main Reaction Pathway of Cellobiose Degradation. Figure 2 shows a main reaction pathway of cellobiose degradation in subcritical and supercritical water elucidated based on the organic chemical reactions and our earlier work.[18] Cellobiose degradation mainly proceeds through parallel reactions: hydrolysis and retro-aldol condensation. Hydrolysis can take place at the $\beta(1,4)$-glycosidic bond in the cellobiose molecule to form two glucose molecules. Retro-aldol condensation can occur at the reducing end of the cellobiose to form glucosyl–erythrose (GE) and glycolaldehyde. The GE hydrolyzes to glucose plus erythrose or converts to glucosyl–glycolaldehyde (GG) plus glycolaldehyde via retro-aldol condensation. The formed GG subsequently hydrolyzes to glucose plus glycolaldehyde. Glucose can convert to glyceraldehyde, dihydroxyacetone, and some organic acids.[12,18]

Results

Cellobiose Degradation Rate. Parts a–c of Figure 3 show plots of the $-\ln(1 - X)$ value against the actual residence time (τ_{actual}) at temperatures of 350, 380, and 400 °C, respectively. In all of the reaction conditions, linear correlations were observed. Each slope of the straight line shows the first-order rate constant of cellobiose degradation, k, as shown in eq 4. At 350 °C, the rate constant did not increase even if the reaction pressure increased. In near-critical water (380 °C), the rate constant gradually increased with an increase of pressure from 25 to 40 MPa. By contrast, the effect of the reaction pressure on the conversion of cellobiose at 400 °C showed a tendency different from those obtained at other temperatures. Especially in the lower pressures of 25 and 27.5 MPa, the k values became much higher than those at other pressures. In these conditions, the formation of 1,6-anhydro-β-D-glucose, 5-HMF, and 2-furfural, which were typical products of the gas-phase treatment of saccharides,[19-21] at a few percent in yield was confirmed. At higher pressures in supercritical water, however, the formation of these products was not confirmed. This result suggests that the degradation of cellobiose at lower pressures becomes similar to the gas-phase treatment.

$$k\tau_{actual} = -\ln(1 - X) \tag{4}$$

Figure 4 shows the Arrhenius plot of the logarithm of k as a function of the reciprocal temperature. All of the rate constants except for the data at 400 °C and

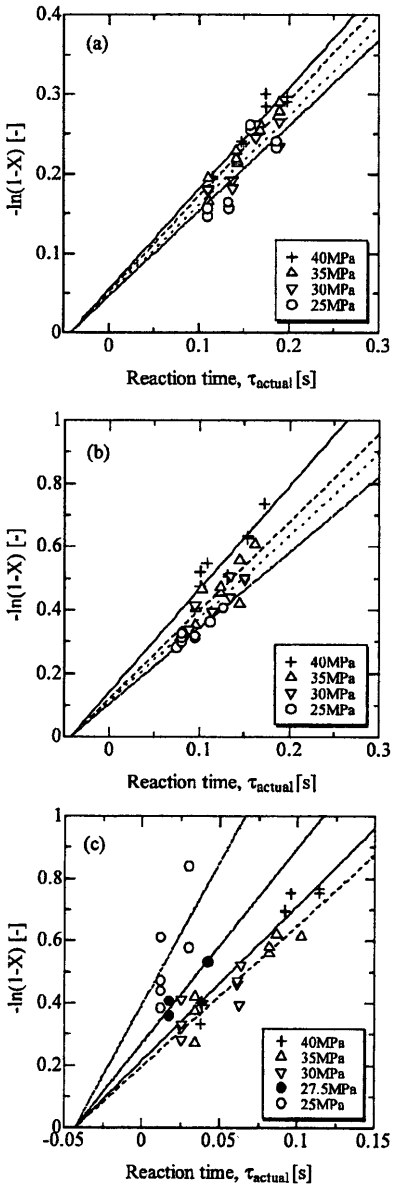

Figure 3. Plot of $-\ln(1 - X)$ versus the actual reaction time: (a) 350 °C; (b) 380 °C; (c) 400 °C.

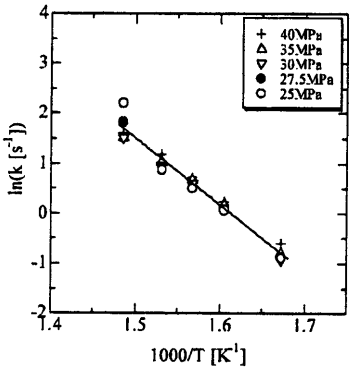

Figure 4. Arrhenius plot of the overall rate constant of cellobiose degradation (k) in subcritical and supercritical water.

lower pressures (25 and 27.5 MPa) apparently approached in a straight line. From this figure, the activation energy and the preexponential factor were found to be 111.2 kJ mol^{-1} and $10^{9.4}$, respectively.

Rates of Hydrolysis and Retro-Aldol Condensation. At the initial stage of cellobiose degradation, glucose was formed via hydrolysis of cellobiose and GE was obtained via retro-aldol condensation. The GE yield primarily increased and then decreased with time, while GG formed via retro-aldol condensation of GE. At first, the yield of glucose increased with time because glucose was formed by hydrolysis of cellobiose, GE, and GG. As the reaction time further increased, however, it gradually decreased by further degradation of glucose to erythrose, glycolaldehyde, etc. This variation of the degradation products of cellobiose was consistent with the result of Kabyemela et al.[18]

(a) Determination of the Rates of Hydrolysis and Retro-Aldol Condensation. The assumption that cellobiose degradation follows the reaction pathway shown in Figure 2 permits us to divide cellobiose degradation into two elemental reactions, namely, hydrolysis and retro-aldol condensation. In this study, these rate constants, k_H and k_{RA}, were estimated as follows. At the initial stage of the degradation, it can be considered that only the two primary reactions take place. Here, we determined the contribution of each reaction path to the overall rate of cellobiose degradation, k_H/k or k_{RA}/k, from the reaction pathway analysis using the Delplot method.[22] According to this method, the values (k_H/k or k_{RA}/k) can be determined by extrapolating each product selectivity of hydrolysis ($S_H = Y_{Glc}/X$) and retro-aldol condensation ($S_{RA} = Y_{GE+GG}/X$) to $X = 0$ as shown in eqs 5 and 6.

$$\frac{k_H}{k} = S_H = \lim_{X \to 0} \frac{Y_{Glc}}{X} \tag{5}$$

$$\frac{k_{RA}}{k} = S_{RA} = \lim_{X \to 0} \frac{Y_{GE+GG}}{X} \tag{6}$$

Parts a and b of Figure 5 show the typical result of each reaction path at 400 °C, respectively. In all of the reaction conditions, the straight relationship between Y_H/X (or Y_{SA}/X) and X was obtained at the conversion region ranging from 23 to 53%. Also, the summation of the two intercepts, k_H/k and k_{SA}/k, in each reaction condition reached nearly 1. This information indicates that hydrolysis and retro-aldol condensation are major reaction paths on the cellobiose degradation in subcritical and supercritical water. Below 380 °C, the intercepts of both of the two lines ranged from 0.5 to 0.65 regardless of temperature and pressure. By contrast, at 400 °C, the intercept of hydrolysis, k_H/k, increased with an increase in the pressure, but that of retro-aldol condensation decreased. Parts a and b of Figure 6 show the Arrhenius plots of the first-order rate constant of hydrolysis, k_H, and retro-aldol condensation, k_{RA}, of cellobiose, respectively. It was found that the hydrolysis rate follows the Arrhenius-type reaction in subcritical water, but in near-critical and supercritical water, the deviation between the experimental value and the rate constant extrapolated from the subcritical data became significant with increasing temperature, especially at lower water densities. On the contrary, it was found that the rate constant of retro-aldol condensation had a linear correlation with the reciprocal temperature. The activation energy and the preexponential factor of this reaction were 122.6 kJ mol^{-1} and $10^{10.1}$, respectively. This activation energy value was nearly the same as

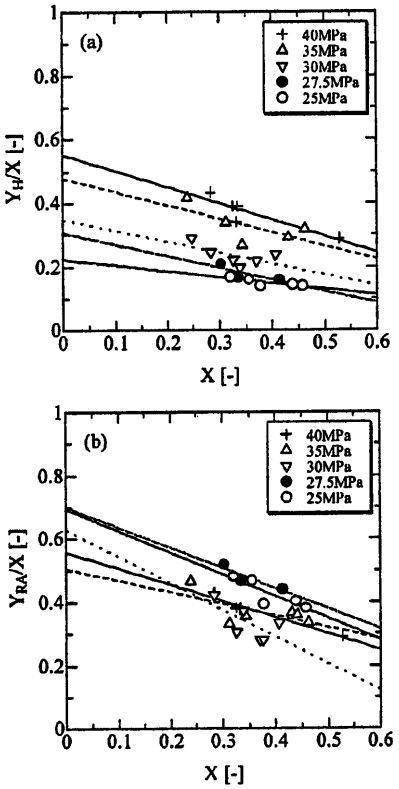

Figure 5. Delplot analysis concerning the reaction rates at 400 °C: (a) hydrolysis; (b) retro-aldol condensation.

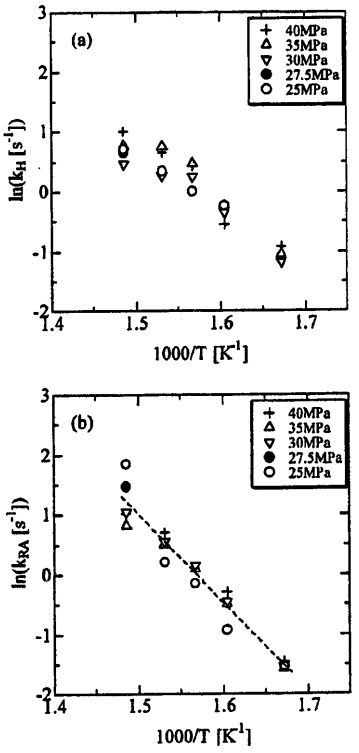

Figure 6. Arrhenius plots of the first-order rate constants of (a) hydrolysis and (b) retro-aldol condensation.

those reported from the previous works at hydrothermal condition (121 kJ mol^{-1})[23] and at subcritical and supercritical conditions (110 kJ mol^{-1}).[18]

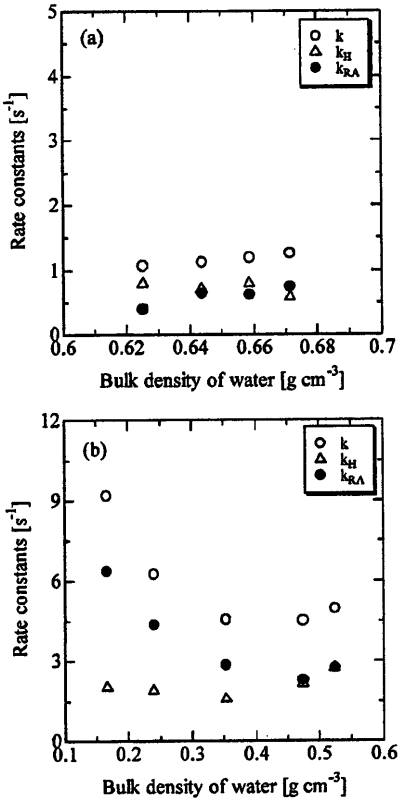

Figure 7. Effect of the density of water on the rates of hydrolysis and retro-aldol condensation: (a) 350 °C; (b) 400 °C.

Discussion

At near-critical and supercritical regions, the properties of water change drastically by manipulating the temperature and pressure, although they do not vary even if pressure varies under constant temperature at the subcritical region. For instance, at 400 °C, the bulk density, the dielectric constant, and the ion product of water are respectively 0.52 g cm^{-3}, 10.5, and 3.31 × 10^{-13} mol^2 L^{-2} at 40 MPa and 0.17 g cm^{-3}, 2.4, and 3.60 × 10^{-20} mol^2 L^{-2} at 25 MPa. This drastic change in the reaction atmosphere will make control of the reaction equilibrium and the rates of the major reactions possible by adjusting the temperature and pressure.

To examine the controllability of the reactions in supercritical water and to clarify the reason the rates of both of the two main reaction paths could vary by manipulating the temperature and pressure in near-critical and supercritical water, we evaluated solvent effects on the hydrolysis rate and the retro-aldol condensation rate of cellobiose. First, we evaluated the effect of the density of water on the two reactions in subcritical and supercritical water. The k_H and k_{RA} values obtained in this study were plotted against the bulk density of water. Parts a and b of Figure 7 show the typical results at 350 and 400 °C, respectively. At the subcritical temperature of 350 °C, both of the k_H and k_{RA} values were almost constant even if the density of water changed. This shows that the reaction rates hardly depend on the reaction pressure in subcritical water. By contrast, in near-critical and supercritical water (e.g., 400 °C), the k_H value did not change at around 2.0 s^{-1} in the range between 0.17 and 0.36 g cm^{-3} and increased with an increase in the bulk density of water from 0.36 to 0.53 g cm^{-3}. The k_{RA} value

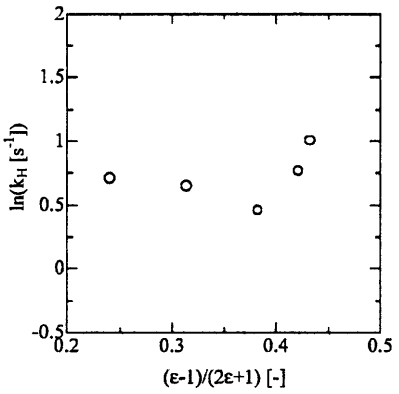

Figure 8. Electrostatic effect on the first-order rate constant of hydrolysis at 400 °C.

monotonically decreased from 6.0 to 2.0 s^{-1} with the bulk density of water. This water density dependence of the rate of retro-aldol condensation of cellobiose was consistent with that of glucose[17] in supercritical water. From this experimental finding, it was suggested that manipulating the temperature and pressure at near-critical and supercritical regions could control the contribution of each reaction path to the overall rate of cellobiose degradation; especially at lower water densities, retro-aldol condensation took place superiorly. As for hydrolysis, however, we found it difficult to make hydrolysis proceed in a selective manner under the present working temperature and pressure. The selective hydrolysis of cellobiose will be achieved under the condition where the density of water is much higher than what we deal with at present.

Next, an electrostatic effect on hydrolysis and retro-aldol condensation of cellobiose was evaluated. Figure 8 illustrates the relationship between the logarithm of k_H and the Kirkwood polarity parameter, $(\epsilon - 1)/(2\epsilon + 1)$, in the case of 400 °C. The $\ln(k_H)$ value slightly decreased with an increase in the polarity parameter from 0.23 to 0.38 and increased with the parameter in the range of 0.38 to 0.43. This trend indicates that the rate of hydrolysis of cellobiose becomes high at both the lower dielectric constant and the higher one. An interesting point in this result is that hydrolysis, which is a kind of ionic reaction, takes place at such low water densities and dielectric constants. We considered that this result was due to the following reasons.

(1) At lower pressures in supercritical water, a hydrophobic water molecule itself works to cleave the $\beta(1,4)$-glycosidic bond linkage in cellobiose as a nucleophilic agent.

(2) At lower pressures in supercritical water, the local density of water around a solute molecule increases compared with the bulk density of water, so hydrolysis is promoted.

The detailed evidence was described in the following. In nature, it can be assumed that hydrolysis proceeds through the formation of a cellobiose–water intermediate (a transition state), which has a higher polarity than the reactant, so the rate of hydrolysis must become slow at the condition where the ion product, the density, and the dielectric constant of water are extremely small. Here, we assumed two mechanisms: (a) hydrolysis by the nucleophilic attack of the hydrophobic water molecule to the $\beta(1,4)$-glycosidic bond linkage in cellobiose and (b) hydrolysis by the attack of the proton (H^+) ion dissociated from the water molecule to the $\beta(1,4)$-glycosidic bond linkage in cellobiose. In each case, the

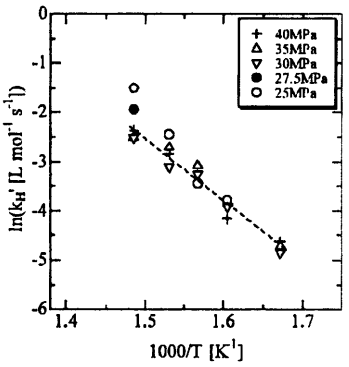

Figure 9. Arrhenius plot of the second-order rate constant of hydrolysis of cellobiose (k_H') in subcritical and supercritical water.

second-order hydrolysis rate constants of cellobiose, k_H' ($=k_H/[H_2O]$) and k_H'' ($=k_H/[H^+]$), were respectively considered to eliminate the effect of the water density or the concentration of the H^+ ion. Some researchers have reported on the mechanism of hydrolysis of ethers in supercritical water. Taylor et al.[24] stated that hydrolysis of methyl *tert*-butyl ether in supercritical water could be successfully explained using an acid-catalyzed mechanism. Penninger et al.[25] also stated that an S_N1 proton-catalyzed mechanism could be adopted for the hydrolysis of diphenyl ether in supercritical water. Thus, the effect of the proton concentration on hydrolysis of cellobiose was at first evaluated with the same technique as that used by Taylor et al.,[24] although the reactivity of the glycosidic bond linkage may differ from that of the ether bond linkage. As a result, it was found that the pressure dependence of the rate constants could not be explained, although the data at each pressure had a straight relationship with reciprocal temperature, which resulted in a rate expression with a first-order dependence on the proton concentration.

Next, Figure 9 shows the Arrhenius plot of the logarithm of k_H' in subcritical and supercritical water. From this figure, we observed a good linear correlation at all of the reaction conditions except for the condition where the density of water was low. This second-order hydrolysis rate can be regarded as the real hydrolysis rate, while the k_H value obtained in Figure 6a shows the apparent hydrolysis rate. Based on the experimental results, the activation energy value and the preexponential factor of the second-order rate constant of cellobiose hydrolysis were found to be 104.5 kJ mol^{-1} and $10^{7.1}$, respectively.

At lower pressures (25 and 27.5 MPa) in supercritical water, the $\ln(k_H')$ values deviated above from the linear correlation. For the density dependence of this solute–solvent interaction, it is well-known that a common pattern exists for different supercritical fluids. This pattern consists of the three density regions: a rapid increase in the low-density region (a reduced density $\rho_r < 0.5$); a plateaulike state in the near-critical density region ($0.5 \le \rho_r < 1.5$); a further increase in the high-density region ($\rho_r \le 1.5$).[26] Actually, the densities of water at 25 and 27.5 MPa were 0.17 g cm^{-3} ($\rho_r = 0.52$) and 0.24 g cm^{-3} ($\rho_r = 0.74$), respectively. Assuming that the difference between each $\ln(k_H')$ value obtained by the experiments and the value of the second-order rate at these pressures in Figure 9 originated from the increase in the local density of water around a solute molecule, each local water density was estimated. As a result, the densities of water were found to be 0.385 g cm^{-3} at 25 MPa and 0.362 g cm^{-3} at 27.5 MPa. These

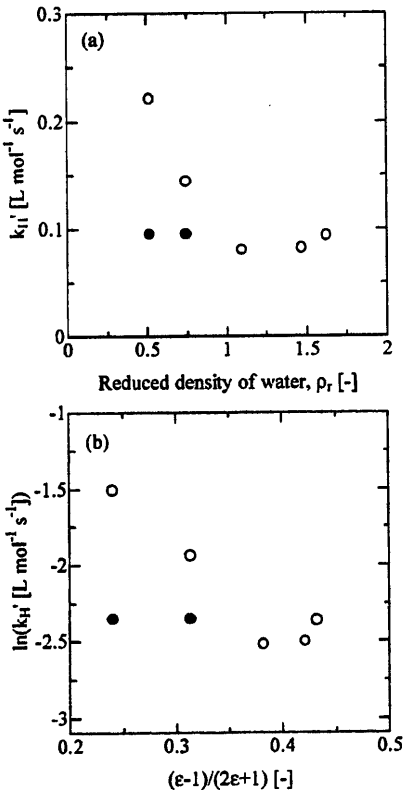

Figure 10. Solvent effects on the second-order rate constant of hydrolysis at 400 °C: (a) the effect of the bulk density of water; (b) the effect of the Kirkwood polarity parameter. Symbols: O, with no consideration of the local density of water; ●, with consideration of the local density of water.

values were similar to the bulk densities of water at higher pressures of 30−31 MPa (0.35−0.390 g cm^{-3}; ρ_r = 1.09−1.21), indicating that the local density of water shows a plateaulike behavior in the near-critical density region. Figure 10 shows the plot of k_H' versus the reduced bulk density of water (a) and of the logarithm of k_H' versus the Kirkwood polarity parameter (b) at 400 °C. When the local density of water was considered for calculating the hydrolysis rate, both of the k_H' and ln(k_H') values seemed to be constant values against the bulk density of water and the polarity parameter. This result suggests that the hydrolysis rate can be promoted even at lower pressures in supercritical water because of the increase in the local density of water around a solute at the near-critical density region.

Next, we considered the mechanism of retro-aldol condensation of cellobiose. Figure 11 shows a relationship between the logarithm of k_{RA} and the Kirkwood polarity parameter. The rate of retro-aldol condensation increased with a decrease of the polarity parameter, indicating that the polarity of the reaction intermediate, namely, GE plus glycolaldehyde, becomes lower than that of the reactant at the condition where the dielectric constant is low. It can be considered that retro-aldol condensation proceeds through the formation of the intermediate with an intramolecular hydrogen bond linkage as shown in Scheme 1.[17] As the reaction pressure increases, hydroxyl groups in the cellobiose molecule can easily interact with water molecules to form intermolecular hydrogen bond linkages. Thus, retro-aldol condensation of cellobiose will be suppressed with an increase of the density of water. Also, from the

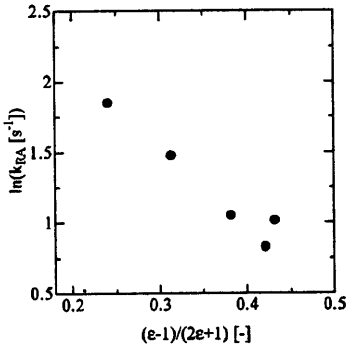

Figure 11. Electrostatic effect on the first-order rate constant of retro-aldol condensation at 400 °C.

Scheme 1. Predicted Reaction Mechanism of Retro-Aldol Condensation of Cellobiose[17]

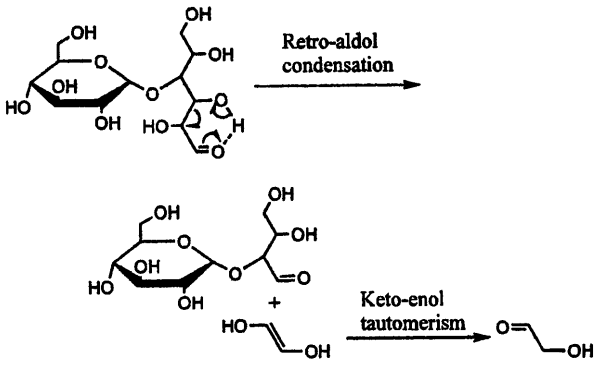

equilibrium point of view, retro-aldol condensation of saccharide is the reaction in which two aldehydes are formed from one saccharide molecule having any hydrophilic hydroxyl group, so hydration of the product occurs in comparison with that of the reactant with an increase of the density of water.[17] Consequently, it can be considered that retro-aldol condensation can be suppressed as the reaction pressure increases in supercritical water.

Conclusions

From the cellobiose decomposition experiments in subcritical and supercritical water, we found the following matters.

(1) At high water densities in supercritical water, hydrolysis of cellobiose was promoted and retro-aldol condensation of cellobiose was suppressed. Each contribution to the overall rate of cellobiose degradation can be controlled by manipulating the temperature and pressure.

(2) The hydrolysis rate of cellobiose was found to be the second-order reaction, that is, the first-order reaction of water concentration. The activation energy and the preexponential factor of this reaction were estimated at 104.5 kJ mol^{-1} and $10^{7.1}$, respectively. In regards to the mechanism of hydrolysis, it was suggested that hydrolysis mainly occurred by the nucleophilic attack of the water oxygen atom of the water molecule to the β(1,4)-glycosidic carbon atom of cellobiose. Moreover, we found that the increase in the hydrolysis rate of cellobiose at lower pressures in supercritical water originated from the increase in the local density of water around a cellobiose molecule in the near-critical density region.

(3) The rate of retro-aldol condensation was the first-order reaction, and the activation energy and the preexponential factor of this reaction were estimated at 122.6 kJ mol^{-1} and $10^{10.1}$, respectively. It also became fast with a decrease in the density of water and the dielectric constant in supercritical water. This is probably because the formation of the intermediate with the intramolecular hydrogen bond linkage of cellobiose can be promoted with a decrease in the density of water.

Acknowledgment

The authors gratefully acknowledge support by a Grand-in-Aid for Scientific Research on Priority Area "Mechanism of Hydrolysis in Supercritical Water" (Grant 11450295) from the Ministry of Education, Culture, Sports, Science and Technology.

Nomenclature

$C_{0,CB}$ = initial concentration of cellobiose fed to the reactor [mol L^{-1}]
C_{CB} = concentration of cellobiose at the exit of the reactor [mol L^{-1}]
F = flow rate [cm^3 min^{-1}]
k = overall decomposition rate constant of cellobiose [s^{-1}]
k_H = first-order hydrolysis rate constant of cellobiose [s^{-1}]
k_H' = second-order hydrolysis rate constant of cellobiose ($=k_H/[H_2O]$) [L mol^{-1} s^{-1}]
k_H'' = second-order hydrolysis rate constant of cellobiose ($=k_H/[H^+]$) [kg mol^{-1} s^{-1}]
k_{RA} = retro-aldol condensation rate constant of cellobiose [s^{-1}]
P = reaction pressure [MPa]
P_0 = ambient pressure [MPa]
T = reaction temperature [°C]
T_0 = ambient temperature [°C]
V = reactor volume [cm^3]
X = conversion of cellobiose
Y_i = product yield of component i

Greek Letters

ϵ = dielectric constant of water
$\rho(T_0,P)$ = water density at the reaction pressure and ambient temperature [g cm^{-3}]
$\rho(T,P)$ = water density at the reaction condition [g cm^{-3}]
ρ_r = reduced water density ($=\rho(T,P)/\rho_c$)
τ = residence time in the reactor [s]
τ_0 = time for the end effect [s]
τ_{actual} = actual reaction time [s]

Literature Cited

(1) Townsend, S. H.; Abraham, M. A.; Huppert, G. L.; Klein, M. T.; Paspek, S. C. Solvent Effects during Reactions in Supercritical Water. *Ind. Eng. Chem. Res.* **1988**, *27* (1), 143–149.

(2) Xu, X. D.; Antal, M. J., Jr.; Anderson, D. G. M. Mechanism and temperature-dependent kinetics of the dehydration of *tert*-butyl alcohol in hot compressed liquid water. *Ind. Eng. Chem. Res.* **1997**, *36* (1), 23–41.

(3) Antal, M. J., Jr.; Carlsson, M.; Xu, X. D.; Anderson, D. G. M. Mechanism and kinetics of the acid-catalyzed dehydration of 1- and 2-propanol in hot compressed liquid water. *Ind. Eng. Chem. Res.* **1998**, *37* (10), 3820–3829.

(4) Carlsson, M.; Habenicht, C.; Kam, L. C.; Antal, M. J., Jr.; Bian, N. Y.; Cunningham, R. J.; Jones, M., Jr. Study of the Sequential Conversion of Citric to Itakonic to Methacrylic Acid in Near-Critical and Supercritical Water. *Ind. Eng. Chem. Res.* **1994**, *33* (8), 1989–1996.

(5) An, J. Y.; Bagnell, L.; Cablewski, T.; Strauss, C. R.; Trainor, R. W. Applications of high-temperature aqueous media for synthetic organic reactions. *J. Org. Chem.* **1997**, *62* (8), 2505–2511.

(6) Crittendon, R. C.; Parsons, E. J. Transformations of Cyclohexane Derivatives in Supercritical Water. *Organometallics* **1994**, *13* (7), 2587–2591.

(7) Ikushima, Y.; Hatakeda, K.; Sato, O.; Yokoyama, T.; Arai, K. Acceleration of synthetic organic reactions using supercritical water: Noncatalytic Beckmann and pinacol rearrangements. *J. Am. Chem. Soc.* **2000**, *122* (9), 1908–1918.

(8) Sato, O.; Ikushima, Y.; Yokoyama, T. Noncatalytic Beckmann rearrangement of cyclohexanone-oxime in supercritical water. *J. Org. Chem.* **1998**, *63* (24), 9100–9102.

(9) Katritzky, A. R.; Allin, S. M.; Siskin, M. Aquathermolysis: Reactions of organic compounds with superheated water. *Acc. Chem. Res.* **1996**, *29* (8), 399–406.

(10) Adschiri, T.; Hirose, S.; Malaluan, M. R.; Arai, K. Noncatalytic Conversion of Cellulose in Supercritical and Subcritical Water. *J. Chem. Eng. Jpn.* **1993**, *26* (6), 676–680.

(11) Sasaki, M.; Kabyemela, B. M.; Adschiri, T.; Malaluan, R. M.; Hirose, S.; Takeda, N.; Arai, K. Cellulose hydrolysis in sub- and supercritical water. *J. Supercrit. Fluids* **1998**, *13* (1–3), 261–268.

(12) Sasaki, M.; Fang, Z.; Fukushima, Y.; Adschiri, T.; Arai, K. Dissolution and Hydrolysis of Cellulose in Subcritical and Supercritical Water. *Ind. Eng. Chem. Res.* **2000**, *39* (8), 2883–2890.

(13) Kabyemela, B. M.; Adschiri, T.; Malaluan, R. M.; Arai, K. Kinetics of Glucose Epimerization and Decomposition in Subcritical and Supercritical Water. *Ind. Eng. Chem. Res.* **1997**, *36* (5), 1552–1558.

(14) Kabyemela, B. M.; Adschiri, T.; Malaluan, R. M.; Arai, K.; Ohzeki, H. Rapid and Selective Conversion of Glucose to Erythrose in Supercritical Water. *Ind. Eng. Chem. Res.* **1997**, *36* (12), 5063–5067.

(15) Kabyemela, B. M.; Adschiri, T.; Malaluan, R. M.; Arai, K. Degradation Kinetics of Dihydroxyacetone and Glyceraldehyde in Subcritical and Supercritical Water. *Ind. Eng. Chem. Res.* **1997**, *36* (6), 2025–2030.

(16) Kabyemela, B. M.; Adschiri, T.; Malaluan, R. M.; Arai, K. Glucose and Fructose Decomposition in Subcritical and Supercritical Water: Detailed Reaction Pathway, Mechanism, and Kinetics. *Ind. Eng. Chem. Res.* **1999**, *38* (8), 2888–2895.

(17) Goto, K.; Tajima, K.; Sasaki, M.; Adschiri, T.; Arai, K. Reaction Mechanism of Sugar Derivatives in Subcritical and Supercritical Water. *Kobunshi Ronbunshu* **2001**, *58* (12), 685–691.

(18) Kabyemela, B. M.; Takigawa, M.; Adschiri, T.; Malaluan, R. M.; Arai, K. Mechanism and Kinetics of Cellobiose Decomposition in Sub- and Supercritical Water. *Ind. Eng. Chem. Res.* **1998**, *37* (2), 357–361.

(19) Antal, M. J., Jr. Biomass Pyrolysis. A Review of the Literature. *Advances in Solar Energy*; Plenum Press: New York, 1982; Part 1, pp 61–111.

(20) Shin, E.-J.; Nimlos, M. R.; Evans, R. J. Kinetic analysis of the gas-phase pyrolysis of carbohydrates. *Fuel* **2001**, *80*, 1697–1709.

(21) Piskorz, J.; Majerski, P.; Radlein, D.; Vladars-Usas, A.; Scott, D. S. Flash pyrolysis of cellulose for production of anhydro-oligomers. *J. Anal. Appl. Pyrolysis* **2000**, *56*, 145–166.

(22) Bhore, N. A.; Klein, M. T.; Bischoff, K. B. The Delplot Technique: A New Method for Reaction Pathway Analysis. *Ind. Eng. Chem. Res.* **1990**, *29* (2), 313–316.

(23) Bobleter, O.; Page, G. Hydrothermal Decomposition of Glucose. *Monatsh. Chem.* **1968**, *99*, 1560.

(24) Taylor, J. D.; Steinfeld, J. I.; Tester, J. W. Experimental Measurement of the Rate of Methyl *tert*-Butyl Ether Hydrolysis in Sub- and Supercritical Water. *Ind. Eng. Chem. Res.* **2001**, *40* (1), 67–74.

(25) Penninger, J. M. L.; Kersten, R. J. A.; Baur, H. C. L. Reactions of diphenyl ether in supercritical water—mechanism and kinetics. *J. Supercrit. Fluids* **1999**, *16* (2), 119–132

(26) Bunker, C. E.; Rollins, H. W.; Sun, Y.-P. Fundamental Properties of Supercritical Fluids. In *Supercritical Fluid Technology in Materials Science and Engineering*; Sun, Y.-P , Ed.; Marcel Dekker: New York, 2002; pp 1–58.

Received for review May 1, 2002
Revised manuscript received October 10, 2002
Accepted October 13, 2002

IE020326B

Ind. Eng. Chem. Res. **2002**, *41*, 3298−3306

Predictive Model for Equilibrium Constants of Aqueous Inorganic Species at Subcritical and Supercritical Conditions

Kiwamu Sue, Tadafumi Adschiri, and Kunio Arai*

Department of Chemical Engineering, Tohoku University, Aoba-07, Aramaki-Aza, Aoba-ku, Sendai 980-8579, Japan

A simple estimation model is proposed for describing dissociation constants of alkali-metal salts and dissolution constants of metal oxides in subcritical and supercritical water. The required parameters of the model are the Gibbs free energy, enthalpy, heat capacity, and conventional Born coefficient of the dissolved species at a given reference state. The *g* function needed for calculation of the temperature- and pressure-dependent conventional Born coefficient was reevaluated by regression with new experimental data of NaCl and KCl dissociation constants. The model shows a good agreement with the recently reported metal salt dissociation constants at near-critical and supercritical regions compared with the revised Helgeson−Kirkham−Flowers model.

Introduction

Production of metal oxide fine particles is greatly affected by the hydrothermal synthesis conditions.[1] In high-temperature water, the reaction equilibrium of metal nitrates shifts toward metal hydroxides or metal oxides, which subsequently precipitate from solution according to the degree of supersaturation.[1] Hydrothermal syntheses at supercritical conditions have been used to produce new functional materials[2,3] and to separate metals from simulated high-level radioactive wastewater.[4] The thermodynamic properties and the solubility of inorganic species at these conditions are essential, not only for these applications but also for geochemistry, inorganic synthesis, corrosion, and other fields. *In this work, we focus on the evaluation of the molal equilibrium constant, K, of aqueous inorganic species at infinite dilution in supercritical water.* There are many methods for estimating the reaction equilibrium but very few predictive models especially for the supercritical region.

Marshall and Franck (1981)[5] proposed a simple empirical model, which is a function of temperature and density of water and has been widely applied for data correlation. Anderson et al. (1991)[6] simplified this model, made a thermodynamic analysis, and related the terms to constants having physical meaning. The three constant parameters for the model can be determined with the equilibrium constant, enthalpy change of a reaction, heat capacity change of a reaction, water density, and thermal expansion of water at the reference state. Although these constant parameters at a given reference state are available in most cases, the density-dependent term in the model is basically empirical. Therefore, prediction of equilibrium constants over a wide range of temperatures and pressures, especially around the critical point, can be unreliable.

The Helgeson−Kirkham−Flowers (HKF) model[7] has been successfully applied to the correlation of the equilibrium constant for hundreds of inorganic aqueous species of interest to geochemistry over a wide range of conditions (25−1000 °C and 1−5000 bar). In this model, the standard partial molal Gibbs free energy of formation, ΔG°_i, at given temperatures and pressures is described by the following relation:

$$\Delta G^\circ_i = \Delta G^\circ_{r,i} + \Delta G^\circ_{s,i} + \Delta G^\circ_{n,i} \qquad (1)$$

where $\Delta G^\circ_{r,i}$ is the Gibbs free energy of formation at the reference state (298.15 K and 1 bar). $\Delta G^\circ_{s,i}$ and $\Delta G^\circ_{n,i}$ are the solvation Gibbs free energy change and the nonsolvation Gibbs free energy change of aqueous species, *i*, from the reference state to given temperatures and pressures, respectively, which are defined as

$$\Delta G^\circ_{n,i} = -S^\circ_{P_r,T_r}(T - T_r) - c_1\left[T\ln\left(\frac{T}{T_r}\right) - T + T_r\right] - c_2\left\{\left[\left(\frac{1}{T-\Theta}\right) - \left(\frac{1}{T_r-\Theta}\right)\right]\left(\frac{\Theta - T}{\Theta}\right) - \frac{T}{\Theta^2}\ln\left[\frac{T_r(T-\Theta)}{T(T_r-\Theta)}\right]\right\} + a_1(P - P_r) + a_2\ln\left(\frac{\Psi + P}{\Psi + P_r}\right) + \left(\frac{1}{T-\Theta}\right)\left[a_3(P - P_r) + a_4\ln\left(\frac{\Psi + P}{\Psi + P_r}\right)\right] \qquad (2)$$

$$\Delta G^\circ_{s,i} = \omega_{P,T}\left(\frac{1}{\epsilon_{P,T}} - 1\right) - \omega_{P_r,T_r}\left(\frac{1}{\epsilon_{P_r,T_r}} - 1\right) + \omega_{P_r,T_r}Y_{P_r,T_r}(T - T_r) \qquad (3)$$

where a_1, a_2, a_3, a_4, c_1, c_2, and ω represent species-dependent parameters and Ψ, Θ, and Y_{P_r,T_r} designate solvent-dependent parameters. For water, Ψ, Θ, and Y_{P_r,T_r} are equal to 2600 bar, 228 K, and -5.8×10^{-5} K^{-1}, respectively.

Sverjensky et al. (1997)[8] reported that each parameter (a_1, a_2, a_3, a_4, c_1, and c_2) in eq 2 could be estimated with heat capacity, partial molal volume, and a conventional Born coefficient at a given reference state.

Tanger and Helgeson (1988)[9] and Shock et al. (1992)[10] proposed a revised HKF model by introducing temperature and pressure dependence into the Born coefficient,

* To whom correspondence should be addressed. E-mail: karai@arai.che.tohoku.ac.jp. Phone/Fax: +81-22-217-7245/7246.

10.1021/ie010956y CCC: $22.00
Published on Web 05/31/2002

$\omega_{P,T}$. The Born coefficients, $\omega_{P,T}$, for ionic species were given by

$$\omega_{P,T} = \eta\left(\frac{Z^2}{r_{e,P_r,T_r} + |Z|g} - \frac{Z}{3.082 + g}\right) \quad (4)$$

where $\eta = 6.946\,57 \times 10^5$ J mol^{-1} and Z refers to *the charge on ionic species*, respectively, and g is a function of the solvent temperature, pressure, and density given by Shock et al. (1992).[10] The r_{e,P_r,T_r} term in eq 4 denotes the effective electrostatic radius of the species at the reference pressure and temperature. For monatomic ions, r_{e,P_r,T_r} is given by

$$r_{e,P_r,T_r} = r_x + |Z|k_Z \quad (5)$$

where r_x designates the crystallographic radius of the ion. In eq 5 k_Z is set equal to zero for anions and 0.94 for cations based on the theory of the HKF model.[7] For nonionic species, the value of the Born coefficient $\omega_{P,T}$ is constant (−12552 J mol^{-1}) as in the revised HKF model. The revised HKF model provides a substantial improvement over previous models in predicting equilibrium constants.

In its application, the empirical part of the revised HKF model has seven parameters for each reaction. These parameters can be estimated through correlation with reference state thermodynamic properties for each species.[8] Thus, in use of the revised HKF model, $\Delta G^\circ_{T_r,P_r}$, $S^\circ_{T_r,P_r}$, $C_P{}^\circ_{T_r,P_r}$, $V^\circ_{T_r,P_r}$, and ω_{T_r,P_r} are required for each species. Shock et al. (1997)[11] provided a database for these parameters. *However, the number of experimentally determined $V^\circ_{T_r,P_r}$ data for inorganics are generally less than that of experimentally determined other data.*

For this reason, in the viewpoint of the prediction for equilibrium constant, K, at supercritical conditions, a more simple and predictive model is needed. Furthermore, the revised HKF model cannot apply to the near-critical region because the applicability range of the g function is not included in the region.[10]

Recently, we demonstrated that the equilibrium constant for dissociation of water and phenol and for dissolution of metal oxides in subcritical and supercritical water could be well described with a simple relation equation:[12,13]

$$\ln K_{T,\rho} = \ln K_{T_r,\rho_r} - \frac{\Delta H^\circ_{T_r,\rho_r}}{R}\left(\frac{1}{T} - \frac{1}{T_r}\right) - \frac{\Delta\omega_{T_r,\rho_r}}{RT}\left(\frac{1}{\epsilon_{T,\rho}} - \frac{1}{\epsilon_{T_r,\rho_r}}\right) \quad (6)$$

where ϵ is the dielectric constant of water. In eq 6, K_{T_r,ρ_r} is the equilibrium constant and $\Delta H^\circ_{T_r,\rho_r}$ is the enthalpy change at the reference state conditions of pure water at 25 °C and 0.997 g cm^{-3}. $\Delta\omega_{T_r,\rho_r}$ in eq 6 represents the change of the Born coefficient at a given reference state. In the work, $\Delta\omega_{T_r,\rho_r}$ was determined from the experimental data. At saturation conditions and temperatures ranging from 25 to 350 °C, the calculated dissociation constants for water were in good agreement with the literature data. Equation 6 was applied to correlate newly measured solubilities of copper oxide and lead oxide in the critical region, and it was found that retrograde behavior could be accurately described.[12]

In this study, we constructed the simple estimation model for the equilibrium constant by simplifying the empirical part of the revised HKF model from the function of temperature and pressure to that of temperature and water density, to eliminate the parameter needed, $V^\circ_{T_r,P_r}$ and to reevaluate the g function to expand the applicability range to the near-critical region.

2. Development and Analysis of the Model

2.1. Theory. To calculate the equilibrium constant, K, at subcritical and supercritical aqueous systems, we begin with the following thermodynamic framework. The equilibrium constant in high-temperature water can be described as follows:

$$\ln K = -\frac{\sum_i n_i \Delta G^\circ{}_i}{RT} = -\frac{\Delta G^\circ_{T_r,\rho_r} + \Delta G^\circ}{RT} \quad (7)$$

where the reference state is 25 °C (T_r) and 0.997 g cm^{-3} (ρ_r). In this state, the pressure P_r is 1 bar. $\Delta G^\circ_{T_r,\rho_r}$ is the Gibbs free energy change of reaction at the reference state, and ΔG° is the Gibbs free energy change of reaction from the reference state to given temperature and density. The terms in eq 7 can be expressed as follows. The electrostatic interaction between the solute and the solvent is determined by the following Born-type equation based on the Born[14] or Amis and Hinton theory.[15]

$$\Delta G^\circ_{s,i} = \omega_{T,\rho}\left(\frac{1}{\epsilon_{T,\rho}} - 1\right) - \omega_{T_r,\rho_r}\left(\frac{1}{\epsilon_{T_r,\rho_r}} - 1\right) \quad (8)$$

where $\omega_{T,\rho}$ is estimated by eq 4. Thus, by using eq 8, ΔG° can be separated into two terms as follows:

$$\Delta G^\circ = \Delta G^\circ_s(T_r,\rho_r \rightarrow T,\rho) + \Delta G^\circ_{res}(T_r,\rho_r \rightarrow T,\rho) \quad (9)$$

where ΔG°_{res} is the other contributions (residual term) including nonelectrostatic solute–solvent or solute–solute interactions and the rearrangement of solvent molecules.

2.2. Evaluation of ΔG°_{res}. At this section, we modified and simplified the empirical part of the revised HKF model by taking two steps: (i) changing the temperature from T_r to T at reference density ρ_r and (ii) changing the density from ρ_r to ρ at a given temperature.

(i) ln K at Constant Density ρ_r. At a constant density, the relation between ln $K_{T,\rho}$ and T can be expressed by the van't Hoff relation over both subcritical and supercritical regions despite the divergence of various properties around the critical point.[5,16,17] For this case, the change in K with temperature can be written as

$$\ln K_{T,\rho_r} = -\frac{\Delta G_{T,\rho_r}}{RT} = -\frac{\Delta G^\circ_{T_r,\rho_r}}{RT_r} - \frac{\Delta H^\circ_{T,\rho_r}}{R}\left(\frac{1}{T} - \frac{1}{T_r}\right) \quad (10)$$

where $\Delta G^\circ_{T_r,\rho_r}$ is estimated from thermochemical data at the reference state. $\Delta H^\circ_{T,\rho_r}$ is a constant and is

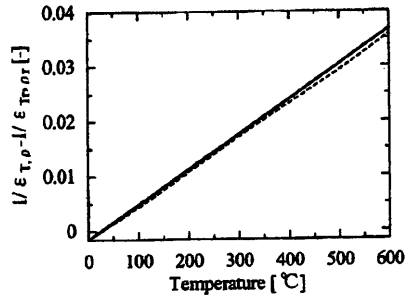

Figure 1. Temperature dependence of the dielectric factor at constant density ρ_r. Dashed line: Johnson and Norton (1991). Solid line: eq 15.

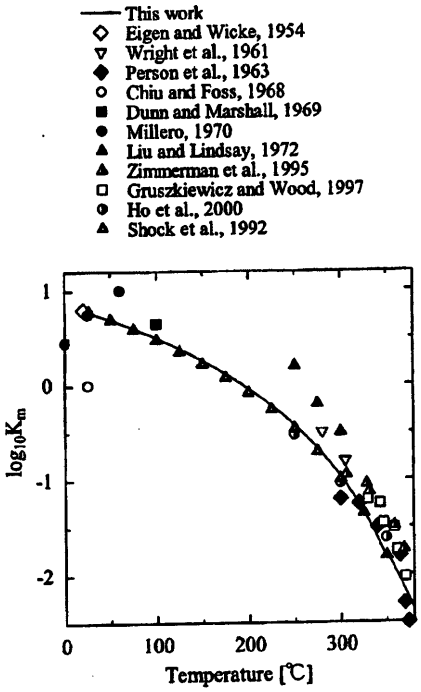

Figure 2. Comparison of the correlation results and literature data for the dissociation constant of NaCl at saturation conditions.

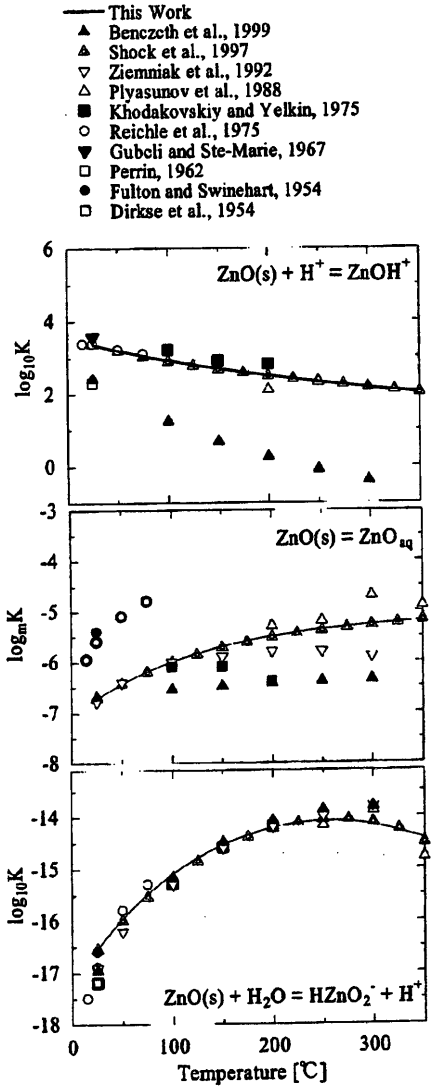

Figure 3. Comparison of the correlation and literature data for the dissolution constant of ZnO at saturation conditions.

evaluated from the reference state T_r to an arbitrary liquid state (T') less than about 100 °C by the following relationship:

$$-\frac{\Delta H^\circ_{T_r,\rho_r}}{R}\left(\frac{1}{T'}-\frac{1}{T_r}\right)=\ln\frac{K_{T'}}{K_{T_r}} \qquad (11)$$

where $\ln K_{T_r}$ is the equilibrium constant at 25 °C and is calculated with the standard state Gibbs free energy, $\Delta G^\circ_{T_r,\rho_r}$. The equilibrium constant at T' is evaluated as follows:

$$\ln K_{T'}=\ln K_{T_r}-\frac{\Delta H^\circ_{T_r,\rho_r}}{R}\left(\frac{1}{T}-\frac{1}{T_r}\right)+\frac{\Delta C_P^\circ{}_{T_r,\rho_r}}{R}\left(\ln\frac{T}{T_r}+\frac{T_r}{T}-1\right) \qquad (12)$$

where, in this work, we selected 50 °C as T'.

A comparison of eqs 7 and 9 with eq 10 gives

$$-\frac{\Delta G^\circ_{T_r,\rho_r}}{RT_r}-\frac{\Delta H^\circ_{T_r,\rho_r}}{R}\left(\frac{1}{T}-\frac{1}{T_r}\right)=-\frac{\Delta G^\circ_{T_r,\rho_r}}{RT}-\frac{\Delta G^\circ_s}{RT}-\frac{\Delta G^\circ_{res}}{RT} \qquad (13)$$

At the constant density of ρ_r and over a range of temperatures from 25 to 600 °C, the g function in eq 4 is negligible.[10] Therefore, the value of $\omega_{T,\rho}$ in eq 4 can be regarded as constant[10] and thus equal to ω_{T_r,ρ_r}, which gives

$$\Delta G^\circ_s=\Delta\omega_{T_r,\rho_r}\left(\frac{1}{\epsilon_{T,\rho_r}}-1\right)-\Delta\omega_{T_r,\rho_r}\left(\frac{1}{\epsilon_{T_r,\rho_r}}-1\right)=\Delta\omega_{T_r,\rho_r}\left(\frac{1}{\epsilon_{T,\rho_r}}-\frac{1}{\epsilon_{T_r,\rho_r}}\right) \qquad (14)$$

At these conditions, the relationship between the value of the dielectric factor, $1/\epsilon_{T,\rho_r}-1/\epsilon_{T_r,\rho_r}$, in eq 14 and

Table 1. Thermodynamic Data at the Reference State and Coefficient β Fitted to the Revised HKF Model at Saturation Conditions

	ΔG (kJ/mol)	ΔH (kJ/mol)	$\Delta\omega$ (kJ/mol)	ΔC_P (J/mol·K)	β (kJ/mol)		ΔG (kJ/mol)	ΔH (kJ/mol)	$\Delta\omega$ (kJ/mol)	ΔC_P (J/mol·K)	β (kJ/mol)
LiCl	−8.6259	−3.3681	828.52	−147.700	−5.0	$SnOH^+$	−245.182	−266.939	108.57	−53.974	−2.0
NaCL	−4.4357	−5.0459	763.41	−120.080	−1.0	SnO_{aq}	−224.262	−251.458	−12.55	−135.562	−13.0
KCl	−9.9960	−11.7278	702.37	−160.670	−2.5	$HSnO_2^-$	−407.103	−510.866	622.33	−189.117	−11.0
RbCl	−5.4804	−13.1922	676.22	−51.463	4.0	Al^{3+}	−483.708	−530.676	1151.86	−128.867	0.1
CsCl	−0.7935	−2.7322	566.26	−48.534	4.5	$AlOH^{2+}$	−692.347	−766.927	721.61	56.066	20.0
LiOH	1.9752	−0.1213	937.55	−105.020	6.0	AlO^+	−661.859	−715.046	400.41	−125.102	0.1
NaOH	−1.1988	−0.4602	872.45	−84.935	10.0	$HAlO_2$	−869.017	−951.860	−12.55	−209.200	−20.0
KOH	−2.5290	20.7234	814.75	−42.258	11.0	AlO_2^-	−831.332	−929.371	728.77	−48.953	0.1
RbOH	−1.2331	−8.3554	796.97	−33.890	13.0	Bi^{3+}	95.730	81.002	949.72	4.184	17.0
CsOH	−9.6477	−18.1878	774.88	−29.288	16.0	$BiOH^{2+}$	−135.143	−187.443	567.02	−62.342	6.0
NaBr	−7.7467	−6.8743	747.43	−121.750	−1.0	BiO^+	−122.591	−126.775	110.21	−345.598	−35.0
KBr	−9.9160	−12.5102	662.54	−84.935	0.1	$HBiO_2$	−331.791	−361.079	−12.55	−621.324	−65.0
RbBr	−6.9475	−13.9327	646.85	−58.994	4.0	BiO_2^-	−258.153	−299.574	395.64	−532.623	−50.0
CsBr	0.1256	−9.2885	620.99	−41.840	8.0	Cr^{3+}	−206.271	−251.040	1146.54	−94.558	5.0
NaI	−8.7914	−8.0835	679.90	−121.750	−3.0	$CrOH^{2+}$	−420.492	−496.222	736.68	65.270	15.0
KI	−9.1225	−8.5395	623.88	−84.935	−2.0	CrO^+	−388.275	−439.320	394.84	−128.449	0.1
RbI	−5.4804	−7.9496	604.42	−58.994	1.0	$HCrO_2$	−577.810	−658.143	−12.55	−157.737	−7.0
CsI	5.6060	10.6692	540.07	−41.840	5.05	CrO_2^-	−524.255	−620.487	725.13	−85.772	0.1
NaF	-5.6973	−7.2090	901.90	−121.750	4.0	Fe^{3+}	−17.238	−49.580	1079.97	−76.567	10.0
RbF	5.4804	−1.9246	810.94	−58.576	8.0	$FeOH^{2+}$	−241.835	−292.880	601.74	−33.890	10.0
Zn^{2+}	−147.277	−153.385	609.78	−22.594	10.0	FeO^+	−222.170	−255.224	300.87	−200.832	−12.0
$ZnOH^+$	−339.699	−363.966	136.40	41.840	10.5	$HFeO_2$	−423.002	−503.335	−12.55	−312.126	−25.0
ZnO_{aq}	−282.085	−327.565	−12.55	−41.840	−1.5	FeO_2^-	−368.192	−463.169	613.46	−234.722	−10.0
$HZnO_2^-$	−463.252	−595.676	781.11	84.517	25.0	Ga^{3+}	−158.992	−211.710	1162.61	−109.621	10.0
Cu^{2+}	65.584	65.689	617.93	−8.786	15.0	$GaOH^{2+}$	−381.162	−488.273	866.09	166.105	30.0
$CuOH^+$	−126.357	−174.473	270.79	67.362	16.0	GaO^+	−362.334	−422.166	417.81	−114.642	−4.0
CuO_{aq}	−87.027	−143.093	308.95	−5.439	8.0	$HGaO_2$	−574.463	−663.582	−18.37	−128.030	−9.0
$HCuO_2^-$	−251.458	−361.079	228.61	−102.926	−5.0	GaO_2^-	−538.481	−643.918	743.79	−57.321	10.0
Ca^{2+}	−552.790	−543.083	517.39	−30.962	5.0	In^{3+}	−97.906	−104.600	1060.48	−64.015	10.0
$CaOH^+$	−716.719	−751.446	188.11	5.858	5.0	$InOH^{2+}$	−312.126	−396.225	726.59	58.576	17.0
Fe^{2+}	−91.504	−92.257	601.74	−32.635	80.	InO^+	−290.370	−321.750	247.15	−241.417	−17.0
$FeOH^+$	−275.516	−326.687	293.01	63.178	15.0	$HInO_2$	−501.243	−565.258	−12.55	−359.824	−30.0
FeO_{aq}	−212.212	−263.383	−12.55	0.000	3.4	InO_2^-	−446.433	−524.255	581.62	−281.165	−18.0
$HFeO_2^-$	−399.154	−525.929	776.72	92.885	25.0	Sc^+	−586.597	−614.211	1046.13	−56.484	12.0
Mg^{2+}	−453.985	−465.960	643.16	−21.757	12.0	$ScOH^{2+}$	−79.914	−839.729	541.58	−80.333	2.0
$MgOH^+$	−624.483	−639.964	353.51	129.286	24.0	ScO^+	−768.182	−794.123	253.68	−236.814	−20.0
Mn^{2+}	−230.538	−221.334	586.01	−16.736	8.0	$HScO_2$	−969.014	−1022.151	−12.55	−384.510	−27.0
$MnOH^+$	−407.103	−446.851	228.61	36.819	11.0	ScO_2^-	−912.530	−979.474	559.36	−309.616	−20.0
MnO_{aq}	−340.996	−414.634	−12.55	−53.137	−3.0	Tl^{3+}	214.639	196.648	951.94	−0.837	15.0
$HMnO_2^-$	−506.264	−627.182	739.94	−12.970	12.0	$TlOH^{2+}$	−18.828	−78.659	593.79	−42.258	5.0
Ni^{2+}	−45.606	−53.974	630.40	−48.116	8.0	TlO^+	−13.389	−21.548	118.49	−338.904	−36.0
$NiOH^+$	−21.124	−283.048	344.01	130.122	23.0	$HTlO_2$	−240.998	−274.470	−12.55	−607.098	−70.0
NiO_{aq}	−164.599	−235.266	−12.55	41.840	10.0	TlO_2^-	−174.054	−219.660	405.81	−518.816	−53.0
$HNiO_2^-$	−343.004	−496.892	906.42	201.669	41.0	Y^{3+}	−685.339	−715.046	1041.40	−52.718	15.0
Pb^{2+}	−23.891	0.920	451.37	−52.718	3.0	YOH^{2+}	−878.640	−924.246	552.33	−73.220	0.1
$PbOH^+$	−225.727	−288.278	293.01	−83.262	−2.0	YO^+	−828.850	−856.046	243.97	−243.509	−15.0
PbO_{aq}	−164.640	−187.025	−12.55	−175.728	−18.0	HYO_2	−1011.273	−1065.246	−12.55	−403.756	−30.0
$HPbO_2^-$	−338.904	−435.973	567.60	−292.462	−24.0	YO_2^-	−951.442	−1019.222	549.99	−323.005	−20.0
Sn^{2+}	−27.489	−8.786	469.28	−64.434	2.0						

temperature can be expressed as a linear function with temperature as shown in Figure 1. In this work, we approximated this by

$$\frac{1}{\epsilon_{T,\rho_r}} - \frac{1}{\epsilon_{Tr,\rho_r}} = \alpha(T - T_r) \tag{15}$$

where the slope α is constant at 6.385×10^{-5} K^{-1} and ϵ is calculated from the equation of Johnson and Norton (1991).[18]

When eqs 13−15 are compared, the residual term can be described as

$$-\frac{\Delta G_{res}}{RT} = -\frac{\Delta H^\circ_{T,\rho_r}}{R}\left(\frac{1}{T} - \frac{1}{T_r}\right) + \frac{\Delta G^\circ_{T_r,\rho_r}}{R}\left(\frac{1}{T} - \frac{1}{T_r}\right) + \frac{\alpha\Delta\omega_{T_r,\rho_r}(T - T_r)}{RT} = -\frac{\Delta H^\circ_{T,\rho_r} - \Delta G^\circ_{T_r,\rho_r} + \alpha\Delta\omega_{T_r,\rho_r}T_r}{R}\left(\frac{1}{T} - \frac{1}{T_r}\right) \tag{16}$$

Therefore, at a given density ρ_r, equilibrium constant K can be expressed with the solvation and the residual terms as follows:

$$\ln K_{T,\rho_r} = -\frac{\Delta G_{T,\rho_r}}{RT} = -\frac{\Delta G^\circ_{T_r,\rho_r}}{RT_r} - \frac{\Delta H^\circ_{T,\rho_r} + \alpha\Delta\omega_{T_r,\rho_r}T_r}{R}\left(\frac{1}{T} - \frac{1}{T_r}\right) - \frac{\Delta\omega_{T,\rho_r}}{RT}\left(\frac{1}{\epsilon_{T,\rho_r}} - 1\right) + \frac{\Delta\omega_{T_r,\rho_r}}{RT}\left(\frac{1}{\epsilon_{T_r,\rho_r}} - 1\right) \tag{17}$$

(ii) Effect of Density ρ on $\ln K$. In eq 17, the density dependence of the solvation term, eq 8, is clearly related to the density dependence by replacing $\Delta\omega_{T,\rho_r}$ and ϵ_{T,ρ_r} with $\Delta\omega_{T,\rho}$ and $\epsilon_{T,\rho}$, respectively. The density dependence of the residual term was determined by comparing eq 17 with the literature data.[7]

To analyze the density dependence of the residual term, the dissociation reaction of sodium chloride at

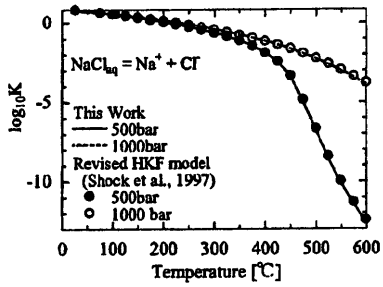

Figure 4. Calculated results of the NaCl dissociation constant. Circles are data calculated by the revised HKF model.

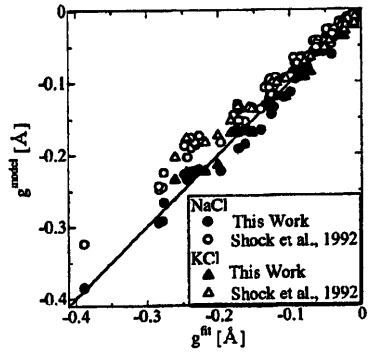

Figure 5. Parity plot of the g values for NaCl and KCl dissociation constants.

saturation conditions was considered because many literature data, including the results from the revised HKF model, were reported over a wide range of conditions including the supercritical region.

When the density was changed from ρ_r to ρ, the density dependence of the residual term was found to correlate as

$$\ln K_{T,\rho,\text{lit}} - \ln K_{T,\rho} = -\frac{\beta(1-\rho^*)^{2/3}}{R}\left(\frac{1}{T}-\frac{1}{T_r}\right) \quad (18)$$

where $\ln K_{T,\rho,\text{lit}}$ shows literature data.

When eq 18 was substituted into eq 17, the following equation was obtained:

$$\ln K_{T,\rho} = \ln K_{T_r,\rho_r} - \frac{\Delta H^\circ_{T_r,\rho_r} + \beta(1-\rho^*)^{2/3} + \alpha\Delta\omega_{T_r,\rho_r}T_r}{R}\left(\frac{1}{T}-\frac{1}{T_r}\right) - \frac{\Delta\omega_{T,\rho}}{RT}\left(\frac{1}{\epsilon_{T,\rho}}-1\right) + \frac{\Delta\omega_{T_r,\rho_r}}{RT}\left(\frac{1}{\epsilon_{T_r,\rho_r}}-1\right) \quad (19)$$

The calculation results of eq 19 are shown in Figure 2 for the NaCl dissociation reaction. The coefficient β fitted with the value from eq 19 was -1.0 kJ mol^{-1}. From the results described above, it was considered that the Gibbs energy of formation of the dissolved species could be estimated with the theory of eq 19.

2.3. Estimation Method of β. In this section, a method to estimate β from the available information will be developed. In general, the database for ω_{T_r,ρ_r} and $C_P^\circ{}_{T_r,\rho_r}$ are sufficient compared with that of $V^\circ{}_{T_r,\rho_r}$. Thus, in the latter part, correlation of β with the available parameters will be examined.

The equilibrium constant for the dissociation of alkali-metal salts and the Gibbs energy of formation for the divalent and trivalent cations and metal hydroxide complexes as shown in Table 1 were calculated with eq 19 at temperatures ranging from 25 to 350 °C and at saturation conditions to use β as a correlation parameter for the results of the revised HKF model. In the calculations, $\Delta G^\circ{}_{T_r,\rho_r}$, $\Delta H^\circ{}_{T_r,\rho_r}$, $\Delta C_P^\circ{}_{T_r,\rho_r}$, and $\Delta\omega_{T_r,\rho_r}$ were evaluated using the database of the standard state parameters of the revised HKF model.[11] The water density was calculated from the equation of Haar et al. (1984),[19] and the dielectric constant was calculated from the equation of Johnson and Norton (1991).[18] The standard deviations in log K in the case of comparison to the revised HKF model are less than 0.126. Correlation results of zinc ions are shown in Figure 3 as ZnO dissolution reactions with the values calculated by the revised HKF model and literature data. The Gibbs energy of formation for zinc oxide was taken from Shock et al. (1998).[11]

For predictions over a wide range of inorganics, it would be preferable to correlate β with $\Delta\omega_{T_r,\rho_r}$ and $\Delta C_P^\circ{}_{T_r,\rho_r}$. This is because the literature data for conventional Born coefficients $\Delta\omega_{T_r,\rho_r}$ and the standard heat capacities $\Delta C_P^\circ{}_{T_r,\rho_r}$ are more extensive than $\Delta V^\circ{}_{T_r,\rho_r}$ tabulated for the revised HKF model. Considering that $\Delta G^\circ{}_{\text{res},\rho,\text{dif}}$ is the perturbation term from the second term of eq 19, we analyzed and found that a linear relation existed between β and $\Delta C_P^\circ{}_{T_r,\rho_r} + \Delta\omega_{T_r,\rho_r}/5000$. Therefore, in this study, the following linear function was employed:

$$\beta = \lambda_1\Delta C_P^\circ{}_{T_r,\rho_r} + \lambda_2\Delta\omega_{T_r,\rho_r} + \lambda_3 \quad (20)$$

where λ_1, λ_2, and λ_3 were determined to be 9.737×10^1 K, 1.947×10^{-2}, and -5.96×10^2 J mol^{-1}, respectively. *The standard deviation of error between the calculated value of β from eq 20 and the fitted value of β is 4.097 kJ mol^{-1}.*

2.4. Comparison of the Estimated Dissociation Constants with Those of the Revised HKF Model at Supercritical Conditions. With the parameters in Table 1, the equilibrium constants of sodium chloride were estimated by eq 19 at supercritical conditions (25–600 °C and 500–1000 bar) as shown in Figure 4. Even though β in eq 19 was obtained by the fitting with the data at saturation conditions, the calculation result showed a good agreement with that of the revised HKF model. Using the correlation function, eq 20, we considered that equilibrium constants of inorganics not only for saturation conditions but also for supercritical conditions could be reliably estimated and predicted.

2.5. Reevaluation of the g Function. Within the framework of the revised HKF model, the range of application of the g function is at pressures from 500 to 5000 bar and densities from 0.35 to 1 g cm^{-3} in the supercritical region and is not included in the near-

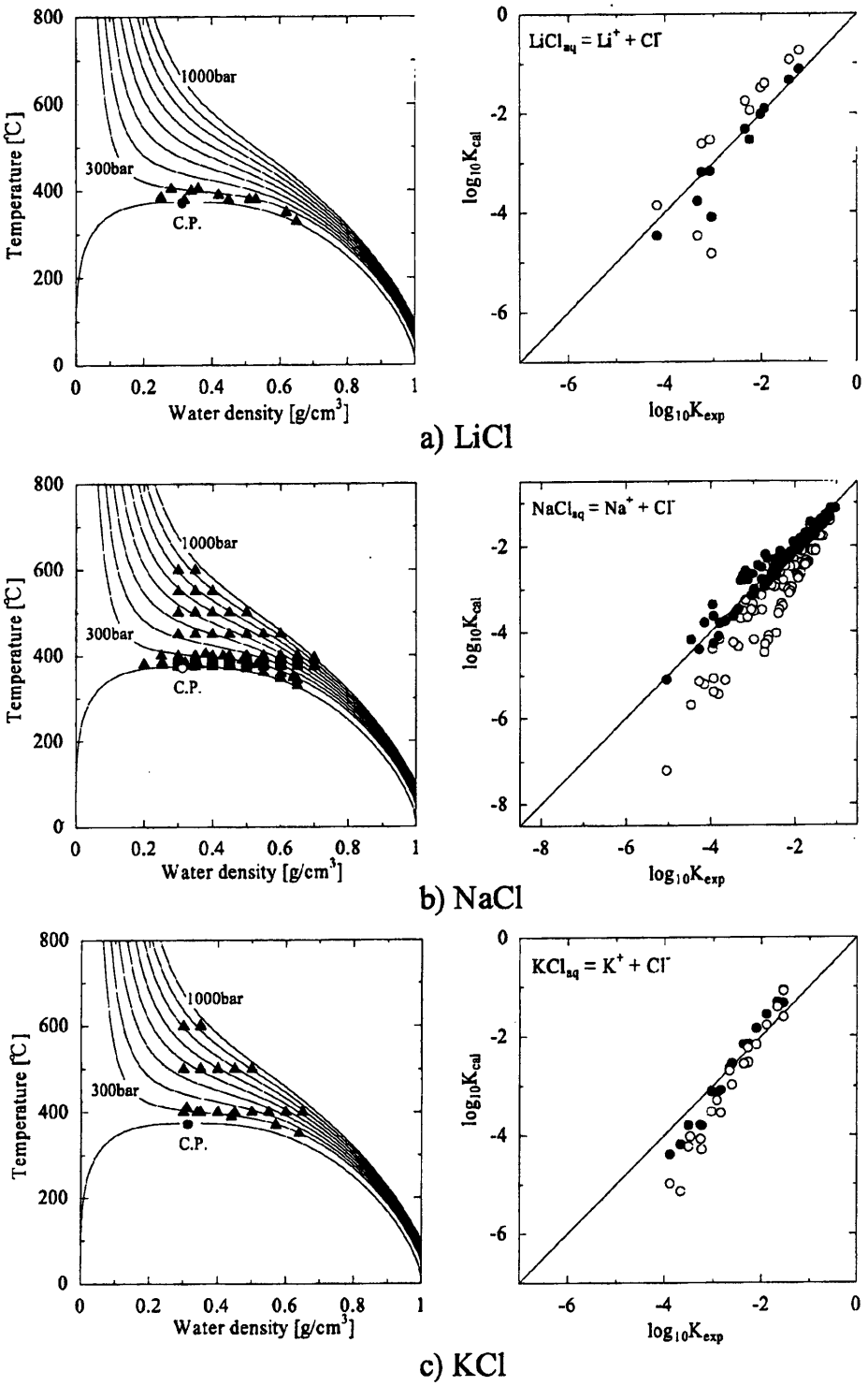

critical region. The g function in the supercritical region is expressed by regression with experimental data of dissociation constants for NaCl by Quist and Marshall (1968).[20] Since the development of the revised HKF model, new NaCl and KCl experimental data have been reported in the near-critical and supercritical regions by Gruszkiewicz and Wood (1997)[21] and Ho et al. (1994, 2000, 1997).[22-24] In the reevaluation of the applicability region of our model, we assumed that the g function in the electrostatic term should be reevaluated because the residual term is not sensitive to changing temperature and density at the supercritical region compared with the electrostatic term.[7-11]

In this part, the g function was evaluated with these experimental data. Data used in the regression were at conditions of temperatures ranging from 250 to 600 °C, pressures ranging from 223 to 998 bar, and densities ranging from 0.20 to 0.81 g cm^{-3}. In the framework of

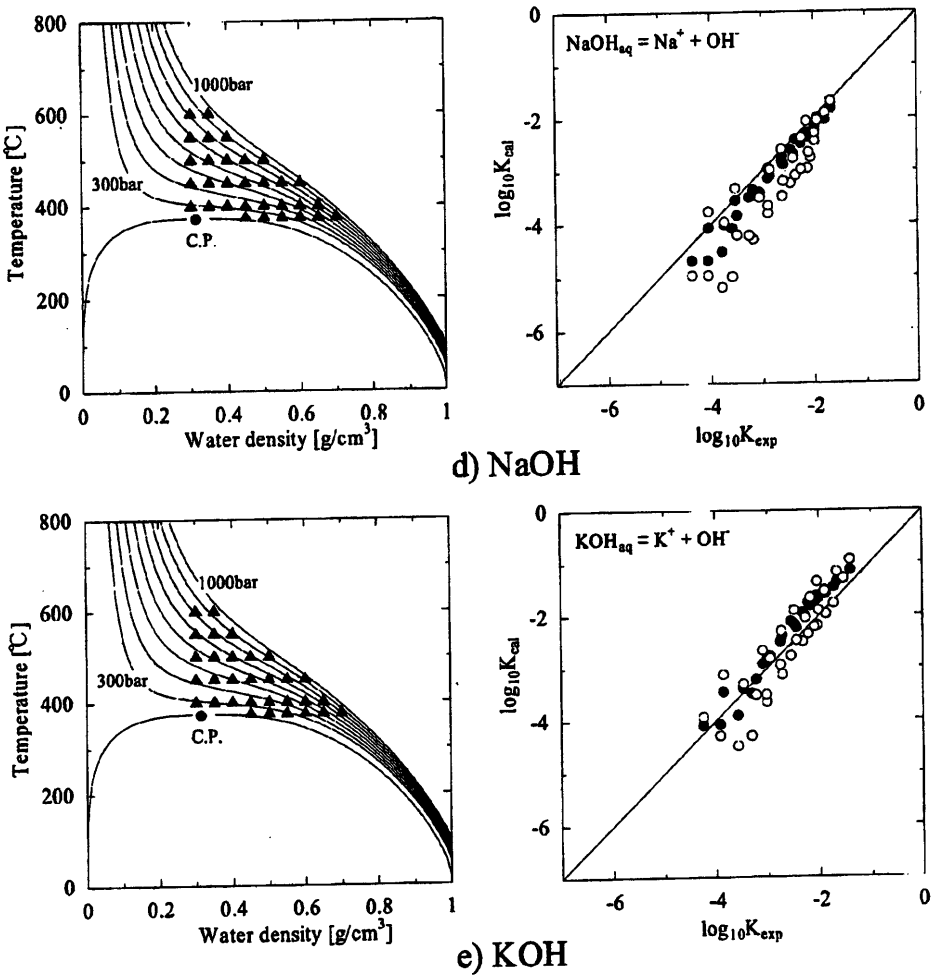

Figure 6. Comparison of the dissociation constant between the literature data and calculated result with the conditions of data. Closed circles: this work. Open circles: the revised HKF model.

the revised HKF model, the g function was given by Shock et al. (1992)[10] as

$$g = a_g(1 - \rho^*)^{b_g} - f(P,T) \tag{21}$$

$$a_g = a_{g1} + a_{g2}T + a_{g3}T^2 \tag{22}$$

$$b_g = b_{g1} + b_{g2}T + b_{g3}T^2 \tag{23}$$

$$f(P,T) = \left[\left(\frac{T-155}{300}\right)^{4.8} + c_{g1}\left(\frac{T-155}{300}\right)^{16}\right][c_{g2}(1000 - P)^3 + c_{g3}(1000 - P)^4] \tag{24}$$

where a_{g1}, a_{g2}, a_{g3}, b_{g1}, b_{g2}, b_{g3}, c_{g1}, c_{g2}, and c_{g3} are constants. In eq 21, ρ^* is a density ratio formed by dividing the pure water density by its density at a reference condition that was chosen to be that of pure water at atmospheric pressure at 25 °C. The function $f(P,T)$ is used at temperatures above 150 °C and pressures under 1000 bar. We analyzed the term $f(T,P)$ in eq 21 and found that the behavior could be described by the following function:

$$f(P,T) = c_{g1}(\rho^*) + c_{g2}(\rho^*)^2 + c_{g3}\ln(\rho^*) \tag{25}$$

In eq 25, c_{g1}, c_{g2}, and c_{g3} are constants that were determined by Marquardt's method correlating to experimental data of dissociation constants of NaCl and KCl. The values of c_{g1}, c_{g2}, and c_{g3} were estimated to have values of 0.18359, −0.18632, and 0.11531, respectively.

A comparison between g^{model} in eq 21 and g^{fit} in eq 25 is shown in Figure 5 with the g values from the revised HKF model. Calculated values, g^{model}, with eq 25 are in good agreement with the values, g^{fit}, fitted with the experimental data. The deviation of the revised HKF model from g^{fit} became larger as the g value became smaller because of the lower densities.

With the new g function defined by eqs 21 and 25, the equilibrium constants of some metal salts (LiCl,[25] NaCl,[21-23] NaOH,[26] KCl,[24] KOH[24]), which were recently determined by electric conductance measurement at supercritical conditions, were estimated. The results of this evaluation are summarized in Figure 6. The results

showed a good agreement with experimental data compared to the results from the revised HKF model.

3. Conclusions

A simple predictive model was developed for describing equilibrium constants for metal salt dissociation and metal oxide dissolution in subcritical and supercritical water. The required parameters of the model are the Gibbs free energy, enthalpy, heat capacity, and conventional Born coefficient of dissolved species at the reference state. The proposed model given by eq 19 with the coefficient β given by eq 20 can be applied to estimate the equilibrium constant of many inorganic species not only for saturation conditions but also for the supercritical region.

Literature Cited

(1) Adschiri, T.; Hakuta, Y.; Arai, K. Hydrothermal synthesis of metal oxide fine particles at supercritical conditions. *Ind. Eng. Chem. Res.* **2000**, *39*, 4901−4907.

(2) Kanamura, K.; Goto, A.; Ho, R. Y.; Umegaki, T.; Toyoshima, K.; Okada, K.; Hakuta, Y.; Adschiri, T.; Arai, K. Preparetion and electrochemical characterization of $LiCoO_2$ particles prepared by supercritical water synthesis. *Electrochem. Solid-State Lett.* **2000**, *3* (8), 256−258.

(3) Hakuta, Y.; Seino, K.; Ura, H.; Adschiri, T.; Takizawa, H.; Arai, K. Production of phosphor (YAG:Tb) fine particles by hydrothermal synthesis in supercritical water. *J. Mater. Chem.* **1999**, *9* (10), 2671−2674.

(4) Smith, R. L., Jr.; Atmaji, P.; Hakuta, Y.; Kawaguchi, M.; Adschiri, T.; Arai, K. Recovery of metals from simulated high-level liquid waste with hydrothermal crystallization. *J. Supercrit. Fluids* **1997**, *11*, 103−114.

(5) Marshall, W. L.; Franck, E. U. Ion product of water substance, 0−1000 °C, 1−10 000 bar; New international formulation and its background. *J. Phys. Chem. Ref. Data* **1981**, *10*, 295−304.

(6) Anderson, G. M.; Castet, S.; Schott, J.; Mesmer, R. E. The density model for estimation of thermodynamic parameters of reactions at high temperature and pressures. *Geochim. Cosmochim. Acta* **1991**, *55*, 1769−1779.

(7) Helgeson, H. C.; Kirkham, D. H.; Flowers, G. C. Theoretical prediction of the thermodynamic behavior of aqueous electrolytes at high pressures and temperatures: IV. Calculation of activity coefficients, osmotic coefficients, and apparent molal and standard and relative partial molal properties to 600 °C and 5 kb. *Am. J. Sci.* **1981**, *281*, 1249−1516.

(8) Sverjensky, D. A.; Shock, E. L.; Helgeson, H. C. Prediction of the thermodynamic properties of aqueous metal complexes to 1000 °C and 5 kb. *Geochim. Cosmochim. Acta* **1997**, *61*, 1359−1412.

(9) Tanger, J. C.; Helgeson, H. C. Calculation of the thermodynamic and transport properties of aqueous species at high pressures and temperatures: Revised equations of state for the standard partial molal properties of ions and electrolytes. *Am. J. Sci.* **1988**, *288*, 19−98.

(10) Shock, E. L.; Oelkers, E. H.; Johnson, J. W.; Sverjensky, D. A.; Helgeson, H. C. Calculation of the thermodynamic and transport properties of aqueous species at high pressures and temperatures: Effective electrostatic radii to 1000 °C and 5 kb. *J. Chem. Soc., Faraday Trans.* **1992**, *88*, 803−826.

(11) Shock, E. L.; Sassani, D. C.; Willis, M.; Sverjensky, D. A. Inorganic species in geologic fluids: Correlations among standard molal thermodynamic properties of aqueous ions and hydroxide complexes. *Geochim. Cosmochim. Acta* **1997**, *61*, 907−950.

(12) Sue, K.; Aida, M. T.; Hakuta, Y.; Smith, R. L., Jr.; Adschiri, T.; Arai, K. Measurement and correlation of metal oxide solubility in sub- and supercritical water. In *Physical and Chemistry: Meeting the Needs of Industry*; Tremaine, P. R., et al., Eds.; NRC Research Press: Ottawa, Ontario, Canada, 2000; pp 782−789.

(13) Sue, K.; Murata, K.; Matsuura, Y.; Tsukagoshi, M.; Adschiri, T.; Arai, K. Flow-through electrochemical cell for pH measurement of organic acid aqueous solutions at subcritical and supercritical conditions. *Fluid Phase Equilib.* **2002**, *194−197*, 1097−1106.

(14) Born, V. M. Vumen und hydratationswarme der inen. *Z. Phys.* **1920**, *1*, 45−48.

(15) Amis, E. S.; Hinton, J. F. *Solvent effects on chemical phenomena*; Academic Press: New York, 1973.

(16) Marshall, W. L. Complete equilibrium constants, electrolyte equilibria, and reaction rates. *J. Phys. Chem.* **1970**, *74* (2), 346−355

(17) Xiang, T.; Johnston, K. P. Acid−base behavior of organic compounds in supercritical water. *J. Phys. Chem.* **1994**, *98*, 7915−7922.

(18) Johnson, J. W.; Norton, D. Critical phenomena in hydrothermal systems: State, thermodynamic, electrostatic, and transport properties of H_2O in the critical region. *Am. J. Sci.* **1991**, *291*, 541−648.

(19) Haar, L.; Gallagher, J. S.; Kell, G. S. *NBC/NRC Steam Tables*; Hemisphere: Washington, DC, 1984.

(20) Quist, A. S.; Marshall, W. L. Electrical conductances of aqueous sodium chloride solutions from 0 to 800°C and at pressures to 4000 bar. *J. Phys. Chem.* **1968**, *72*, 684−702.

(21) Gruszkiewicz, M. S.; Wood, R. H. Conductance of dilute LiCl, NaCl, NaBr, and CsBr solutions in supercritical water using a flow conductance cell. *J. Phys. Chem. B* **1997**, *101*, 6549−6559.

(22) Ho, P. C.; Palmer, D. A.; Mesmer, R. E. Electrical conductivity measurement of aqueous sodium chloride solutions to 600 °C and 300 MPa. *J. Solution Chem.* **1994**, *23*, 997−1017.

(23) Ho, P. C.; Bianchi, H.; Palmer, D. A.; Wood, R. H. Conductivity of dilute aqueous electrolyte solutions at high temperatures and pressures using a flow cell. *J. Solution Chem.* **2000**, *29*, 217−235.

(24) Ho, P. C.; Palmer, D. A. Ion association of dilute aqueous potassium chloride and potassium hydroxide solutions to 600 °C and 300 MPa determined by electrical conductance measurements. *Geochim. Cosmochim. Acta* **1997**, *61*, 3027−3040.

(25) Ho, P. C.; Palmer, D. A. Determination of ion association in dilute aqueous lithium chloride and lithium hydroxide solutions to 600 °C and 300 MPa by electrical conductance measurements. *J. Chem. Eng. Data* **1998**, *43*, 162−170.

(26) Ho, P. C.; Palmer, D. A. Ion association of dilute aqueous sodium hydroxide solutions to 600 °C and 300 MPa by conductance measurements. *J. Solution Chem.* **1996**, *25* (8), 711−729.

(27) Eigen, M.; Wicke, E. The thermodynamics of electrolytes at higher concentrations. *J. Phys. Chem.* **1954**, *58*, 702−714.

(28) Wright, J. M.; Lindsay, W. T.; Druga, T. R. *The behavior of electrolyte solutions at elevated temperatures as derived from conductance measurements*; WAPD-TM-204; U.S. Atomic Energy Commission: Washington, DC, 1961; p 31.

(29) Person, D.; Copeland, C. S.; Benson, S. W. The electrical conductance of aqueous sodium chloride in the range of 300 to 383 K. *J. Am. Chem. Soc.* **1963**, *85*, 1044−1047.

(30) Chiu, Y. C.; Fuoss, R. M. Conductance of the alkali metal halides. XII. Sodium and potassium chlorides in water at 25 °C. *J. Phys. Chem.* **1968**, *72*, 4123−4129.

(31) Dunn, L. A.; Marshall, W. L. Electrical conductances and ionization behavior of sodium chloride in dioxane−water mixtures at 100°. *J. Phys. Chem.* **1969**, *73*, 2619−2622.

(32) Millero, F. J. The apparent and partial molal volumes of aqueous sodium chloride solutions at various temperatures. *J. Phys. Chem.* **1970**, *74*, 356−362.

(33) Liu, C.; Lindsay, W. T., Jr. Thermodynamics of sodium chloride solutions at high temperatures. *J. Solution Chem.* **1972**, *1*, 45−70.

(34) Zimmerman, G. H.; Gruszkiewicz, M. S.; Wood, R. H. New apparatus for conductance measurements at high temperatures: Conductance of aqueous solutions of LiCl, NaCl, NaBr, and CsBr at 28 MPa and water densities from 700 to 260 kg m^{-3}. *J. Phys. Chem.* **1995**, *99*, 11612−11625.

(35) Benezeth, P.; Palmer, D. A.; Wesolowski, D. J. The solubility of zinc oxide in 0.03 m NaTr as a function of temperature, with in situ pH measurement. *Geochim. Cosmochim. Acta* **1999**, *63* (10), 1571−1586.

(36) Ziemniak, S. E.; Jones, M. E.; Combs, K. E. S. Zinc(II) oxide solubility and phase behavior in aqueous sodium phosphate

solutions at elevated temperatures. *J. Solution Chem.* **1992**, *21*, 1153−1176.

(37) Plyasunov, A. V.; Belonozhko, A. B.; Ivanov, I. P.; Khodakovskiy, I. L. Solubility of zinc oxide in alkaline solutions at 200−350 °C under saturated steam pressure. *Geochem. Int.* **1988**, *25*, 77−85.

(38) Khodakovskiy, I. L.; Yelkin, A. Y. Measurement of the solubility of zincite in aqueous NaOH at 100, 150, and 200 °C. *Geochem. Int.* **1975**, 127−133.

(39) Reichle, R. A.; McCurdy, K. G.; Helper, L. G. Zinc hydroxide: Solubility product and hydroxy-complex stability constants from 12.5 to 75 °C. *Can. J. Chem.* **1975**, *53*, 3841−3845.

(40) Gubeli, A. O.; Ste-Marie, J. Stabilite des complexes hydroxo et produtits de solubilite des hydroxides de metaux. I. Argent et zinc. *Can. J. Chem.* **1967**, *45*, 827−832.

(41) Perrin, D. D. The hydrolysis of metal ions. Part III. Zinc. *J. Chem. Soc.* **1962**, 4500−4502.

(42) Fulton, J. W.; Swinehart, D. F. The equilibria of crystalline zinc hydroxide in dilute hydrochloric acid and sodium hydroxide at 25 °C. The first and second acidic dissociation constants of zinc hydroxide. *J. Am. Chem. Soc.* **1954**, *76*, 864−867.

(43) Dirkse, T. P.; Postmus, C., Jr.; Vandenbosch, R. A study of alkaline solutions of zinc oxide. *J. Am. Chem. Soc.* **1954**, *76*, 6022−6024.

Received for review November 26, 2001
Revised manuscript received April 5, 2002
Accepted April 15, 2002

IE010956Y

ELSEVIER

Fluid Phase Equilibria 194–197 (2002) 1097–1106

FLUID PHASE EQUILIBRIA

www.elsevier.com/locate/fluid

Flow-through electrochemical cell for pH measurement of organic acid aqueous solutions at subcritical and supercritical conditions

Kiwamu Sue, Kenji Murata, Yuuki Matsuura, Masayuki Tsukagoshi, Tadafumi Adschiri, Kunio Arai*

Department of Chemical Engineering, Tohoku University, Aoba 07, Aramaki-Aza, Aoba-ku, Sendai 980-8579, Japan

Received 20 May 2001; accepted 26 August 2001

Abstract

The pH of aqueous phenol solutions at subcritical and supercritical conditions was measured for the first time at temperatures from 296.4 to 673.4 K and pressures from 29.8 to 34.9 MPa by using a flow-through electrochemical cell. From the results, we determined the equilibrium constant for the dissociation reaction of phenol (K_{PhOH}). The dissociation constants of phenol varied from 1.0×10^{-12} mol/kg at 673.4 K and 30.2 MPa to 7.9×10^{-10} mol/kg at 473.1 K and 29.9 MPa. The semi-empirical model for correlation of the equilibrium constant in subcritical and supercritical water was applied to correlate the data and to discuss the temperature, pressure and density effects on the phenol dissociation constant.

Keywords: Supercritical water; Phenol; Dissociation constant; pH measurement; Flow-through electrochemical cell; Data; Experimental method

1. Introduction

Supercritical water (SCW) phenomena are gaining interest in the fields of geochemistry, power cycle technology and hydrothermal organic chemistry [1–3]. Although, Brönsted acid–base chemistry plays a central role in these fields, it is not very well understood in near critical and SCW media. Knowledge of the acidity in SCW is necessary to interpret the reaction data and to develop theory for the reaction mechanisms and phase behavior. The present understanding of acidity is mainly based on inorganic acids and bases from electrochemical potentials at subcritical conditions up to 573.2 K [4] and from conductivity measurements up to 1073.2 K and 400 MPa [5,6]. On the other hand, recently, the dissociation constant of β-napthol in SCW was reported by Xiang and Johnston [7] using UV–VIS spectroscopy.

Potentiometric pH measurement in high temperature aqueous systems have been a major challenge in experimentally exploring the thermodynamics of the hydrothermal systems over the past few decades,

* Corresponding author. Tel.: +81-22-217-7245; fax: +81-22-217-7246.
E-mail address: karai@arai.che.tohoku.ac.jp (K. Arai).

0378-3812/02/$ – see front matter
PII: S0378-3812(01)00712-9

because of the lack of an accurate reference electrode. Recently, Lvov et al. [8,9] developed a flow-through technique for pH measurement and demonstrated that it operates successfully in both subcritical and supercritical aqueous environments (HCl + NaCl system) at temperatures up to 673.2 K and pressures up to 25.3 MPa.

We have developed a flow-through electrochemical cell based on the apparatus of Lvov et al. [8] and improved the cell to measure the potential more precisely at subcritical and supercritical conditions (HCl+ NaCl system) [10]. The three major modifications are as follows. First, the cell was made of Hastelloy-B2, which had high corrosion resistance, especially to HCl aqueous solution. Then, a hydrogen platinum electrode was used as both reference and test electrode. And the orifices were placed near the center of the cell to reduce the fluctuation of the concentration around the test electrode for the mixing between the reference and test solutions. For these modifications, the standard deviations of the potential measurements were <0.4 mV at temperatures ranging from 297.2 to 673.2 K and pressures ranging from 25 to 35 MPa. Comparison of experimentally observed and theoretically calculated pH values showed an ability to use our apparatus for high precision potentiometric pH measurements. We concluded that high temperature pH measurements with high accuracy better than ±0.03 logarithmic units could be accomplished.

In this work, our objectives are to measure the dissociation constant of phenol (PhOH) (K_{PhOH}) at subcritical and supercritical conditions and to understand the temperature, pressure and density effects on K_{PhOH} with a previously proposed model [11].

2. Experimental

2.1. Solutions

We used two different solutions (HCl + NaCl and PhOH + NaCl). The first solution consisted of 10^{-5} mol/kg HCl + 0.1 mol/kg NaCl aqueous solution as a reference solution and a standard solution. It was prepared by diluting 0.1 mol/kg HCl standardized solution (Wako Pure Chemicals, Osaka, Japan) with the ultra pure water (resistivity of 18.2 MΩ cm) and then adding precise amount of crystalline NaCl (purity 99.5%, Wako Pure Chemicals, Osaka, Japan). The second solution consisted of 0.01 mol/kg PhOH + 0.1 mol/kg NaCl aqueous solution as a test solution. It was prepared with a precise amount of ultra pure water, phenol (purity 99.5%, Wako Pure Chemicals, Osaka, Japan) and crystalline NaCl. These solutions were continuously purged with pure hydrogen gas (purity 99.99%, Nihon Sanso, Sendai, Japan) for at least a day prior to use, to remove dissolved oxygen and to maintain constant H_2 concentration around the electrodes.

2.2. Construction of the flow-through electrochemical cell

The cell construction is shown in Fig. 1, where $E^{(I)}$ is the emf, φ_L and φ_R the electrostatic potentials of the left and right terminals, respectively, at ambient temperature T_1. T_2 is an elevated temperature that is higher than T_1.

If the solutions are constantly renewed by using flow through technique, the $E^{(I)}$ value is the initial emf (V), which can be expressed on the basis of linear irreversible thermodynamics [8,12] as follows:

$$E^{(I)} = \frac{1}{F}\left(\mu_{H^+}(T_2) + \frac{1}{2}\mu_{H_2}(T_1) - \mu_{H^+}(T_1) - \frac{1}{2}\mu_{H_2}(T_2)\right)$$
$$= \Delta\varphi_{TE} + \Delta\varphi_D + \Delta\varphi_{STR(R)} + \Delta\varphi_{STR(L)} + \Delta\varphi_{TD} \quad (1)$$

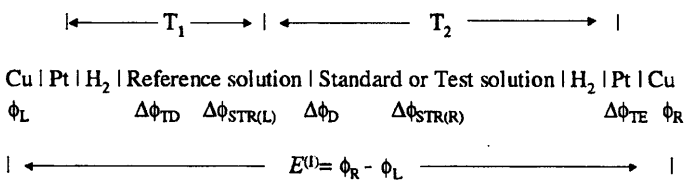

Fig. 1. Design of a flow-through electrochemical cell.

where μ_{H^+} and μ_{H_2} are the chemical potentials of $H^+(aq)$ and $H_2(aq)$, respectively, at given temperature (T_1 or T_2) and F the Faraday constant. In Eq. (1), $\Delta\varphi_{TE}$, $\Delta\varphi_D$, $\Delta\varphi_{STR}$ and $\Delta\varphi_{TD}$ are the thermoelectric, diffusion, streaming and thermal diffusion potentials, respectively.

2.3. Equipment and procedure

The experimental apparatus is the same that reported previously [10]. The cell has the T-type passage and the reference and test electrodes are placed on the left and right side, respectively. These electrodes were sealed by a packing type high-pressure CONAX fitting with Teflon sealant. At the beginning of each experiment, the reference and standard solution were pumped through the cell from the inlet placed on the left and right end of the cell, respectively, until the potentials between the reference and test electrodes attained a steady value within ±0.5 mV. Then, the feed solution was changed from standard solution (HCl + NaCl) to test solution (PhOH + NaCl). The reference and test solution (or standard solution) were mixed in the center of the cell and then, the mixed solution was withdrawn after the cooling and the de-pressurization. The temperatures in the center of the cell and near the tip of the reference electrode were measured by Inconel-sheathed K-type thermocouple and kept to a given value by the electric furnace. The pressure in the cell was controlled by the back pressure regulator. All these measurements were carried out at the flow rate from 1.0 to 4.0 g/min, given pressure and temperature within the accuracy of ±2.0%, ±0.1 MPa and ±0.1 K, respectively.

3. Results and discussion

3.1. Experimental results

The experimental $E^{(I)}$ values were measured for standard solution (HCl + NaCl) and test solution (PhOH + NaCl) at temperatures ranging from 296.4 to 673.4 K and pressures ranging from 29.8 to 34.9 MPa.

A typical potential response, due to change of test solution to standard solution is given in Fig. 2. About 100 min were necessary to stabilize the potential after a solution change at the low flow rate of 1.0 g/min. The standard deviations of the potential measurements were <0.4 mV for the tests at all conditions.

The experimental data obtained for both standard solution and test solution at given temperatures and pressures are shown in Table 1. The potential difference $\Delta E^{(I)}$ is defined as follows:

$$\Delta E^{(I)} = E_t^{(I)} - E_s^{(I)} = \frac{RT_2}{F} \ln \frac{[H^+]_t \gamma_t (a_s^{H_2})^{1/2}}{[H^+]_s \gamma_s (a_t^{H_2})^{1/2}} + \Delta\varphi_D + \Delta\varphi_{STR} \quad (2)$$

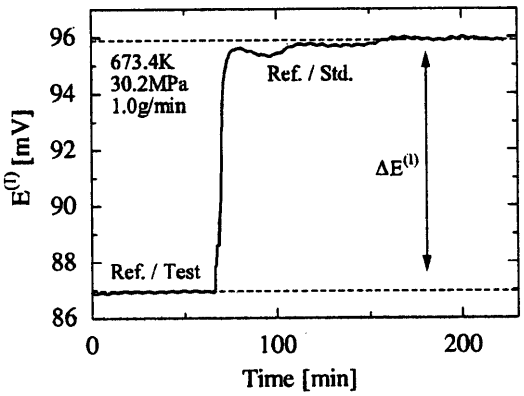

Fig. 2. Sample data for measured $E^{(I)}$ at 673.4 K, 30.2 MPa and 1.0 g/min flow rate.

where $E_s^{(I)}$ and $E_t^{(I)}$ are the emf (V) using standard solution (HCl+NaCl) and test solution (PhOH+NaCl), respectively, at given flow rate, temperature and pressure. In Eq. (2), R is the gas constant (8.314 J/(mol K)) and $[H^+]$ the hydrogen ion concentration (mol/kg). In this work, we assumed that the activity of molecular hydrogen (a^{H_2}) and the activity coefficient of hydrogen ion (γ) were approximately the same for the same concentration of NaCl.

The potential difference ($\Delta E^{(I)}$) as a function of temperature, pressure and flow rate are shown in Fig. 3 and Table 1. Lvov et al. [8] found a reproducible linear dependence of the streaming potential from the flow rate at subcritical and supercritical condition studies and showed that the streaming potential could be deleted by the linear extrapolation of the measured potential differences. In our work, the potential differences also showed a linear dependence on flow rate in a range from 1.0 to 4.0 g/min. Therefore, an extrapolation of the measured potentials of the thermocell shown in Fig. 1 up to zero flow rate value helped to avoid the problem of the streaming potential in our flow-through electrochemical systems.

The diffusion potential between the reference solution and the standard solution can be assumed to be negligible because of the same concentration of HCl and NaCl. The diffusion potential between the reference solution and the test solution exists because of the difference of the concentration and the

Table 1
Experimental potential differences obtained for both standard solution (10^{-5} mol/kg HCl + 0.1 mol/kg NaCl) and test solution (0.01 mol/kg PhOH + 0.1 mol/kg NaCl)

Flow rate (g/min)	$\Delta E^{(I)}$ (mV)						
	$T = 296.4$ K, $P = 30.0$ MPa	$T = 473.1$ K, $P = 29.9$ MPa	$T = 633.3$ K, P = 29.8 MPa	$T = 653.5$ K, $P = 30.1$ MPa	$T = 653.3$ K, $P = 34.8$ MPa	$T = 673.4$ K, $P = 30.2$ MPa	$T = 673.0$ K, $P = 34.9$ MPa
0.0	−57.1	−32.3	25.8	0.6	8.6	−10.3	10.7
1.0	−57.0	−30.7	24.3	0.5	7.4	−8.9	9.4
2.0	−56.7	−29.0	22.9	0.5	5.6	−7.8	7.6
3.0	−56.6	−27.1	21.3	0.2	4.4	−6.6	6.5
4.0	−56.5	−25.6	19.5	0.2	3.2	−5.0	5.0
R^2	0.929	0.998	0.997	0.760	0.993	0.993	0.991

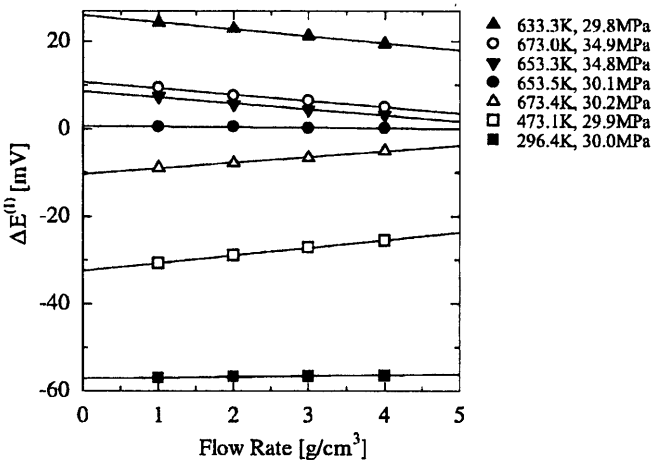

Fig. 3. Voltage difference ($\Delta E^{(I)}$) due to the standard solution (HCl + NaCl) into test solution (PhOH + NaCl) vs temperature and flow rate.

transport number of ions (H^+, Na^+, OH^-, Cl^- and PhO^-). However, because of the lack of the transport number data of phenolate anion (PhO^-) at high temperature conditions, it is difficult to estimate the diffusion potential. In these solutions, the concentration of H^+, OH^- and PhO^- are very low compared with the value of Na^+ and Cl^- at given temperature and pressure because of the low HCl concentration in the reference and standard solutions and the small dissociation constant of phenol. Therefore, we assumed that the effects on the diffusion potential by H^+, OH^- and PhO^- were probably very small.

Considering the above description, the following relationship is lead:

$$\Delta E_0^{(I)} = \frac{RT_2}{F} \ln \frac{[H^+]_t}{[H^+]_s} \tag{3}$$

The potential differences ($\Delta E_0^{(I)}$) were determined from the linear extrapolation of the measured potentials to the zero flow rate. The potential difference data are shown in Table 1 with the extrapolated values to zero flow rates and correlation coefficients (R^2). Relatively high correlation coefficients were obtained for all runs except for measurements at 653.5 K and 30.1 MPa. This is probably due to the higher variation of properties near the critical point of water.

3.2. Thermodynamic calculations

3.2.1. Calculation of hydrogen ion concentration in HCl + NaCl system at subcritical and supercritical conditions

We considered the following dissociation equilibria for standard solution (10^{-5} mol/kg HCl+0.1 mol/kg NaCl) [5]:

$$H_2O = H^+ + OH^-, \qquad K_W = \frac{[H^+]\gamma_{H^+}[OH^-]\gamma_{OH^-}}{a_{H_2O}} \tag{4}$$

$$NaCl(aq) = Na^+ + Cl^-, \qquad K_{NaCl} = \frac{[Na^+]\gamma_{Na^+}[Cl^-]\gamma_{Cl^-}}{[NaCl(aq)]} \tag{5}$$

Table 2
Literature values used for calculations in this work

T (K)	P (MPa)	ρ (g/cm^3)	ε	$\log K_W$	$\log K_{NaCl}$	$\log K_{HCl}$	$\log K_{NaOH}$
296.4	30.0	1.011	80.4	−13.95	1.45	1.33	0.05
473.1	29.9	0.885	35.9	−11.14	0.42	0.43	−0.31
633.3	29.8	0.614	14.3	−11.81	−1.47	−2.48	−1.76
653.5	30.1	0.534	11.1	−12.51	−1.88	−3.24	−2.34
653.3	34.8	0.569	12.3	−12.12	−1.70	−2.98	−2.08
673.4	30.2	0.353	5.8	−14.87	−3.11	−4.67	−3.83
673.0	34.9	0.474	9.0	−13.09	−2.24	−3.83	−2.75

$$HCl(aq) = H^+ + Cl^-, \qquad K_{NaOH} = \frac{[Na^+]\gamma_{Na^+}[OH^-]\gamma_{OH^-}}{[NaOH(aq)]} \tag{6}$$

$$NaOH(aq) = Na^+ + OH^-, \qquad K_{HCl} = \frac{[H^+]\gamma_{H^+}[Cl^-]\gamma_{Cl^-}}{[HCl(aq)]} \tag{7}$$

together with the electroneutrality and mass balance constraints. The ionization constant of water (K_W) was taken from the equation of Marshall and Franck [13] and the dissociation constants of NaCl (K_{NaCl}), HCl (K_{HCl}) and NaOH (K_{NaOH}) were obtained from literature data [5,6,14–16]. The activity coefficients of ions in NaCl aqueous solution were evaluated using ion interaction model of Pabalan and Pitzer [17]. The empirical parameter in the model at supercritical condition was extrapolated using the temperature and pressure function. The activity coefficient of non-charged species (NaCl(aq), NaOH(aq) and HCl(aq)) and the activity of water were assumed equal to one in dilute solution.

The concentrations of dissolved species were calculated from the initial concentration of HCl and NaCl and the literature data (shown in Table 2) of the dissociation. It should be noted that for the case of 0.1 mol/kg NaCl aqueous solutions, the lowest possible pressure without phase separation at 673.2 K is about 27.5 MPa [18]. The calculated results of hydrogen ion concentration, ionic strength and activity coefficient are shown in Table 3.

3.2.2. *Estimation of hydrogen ion concentration in PhOH + NaCl aqueous solution and consideration of acid–base behavior at PhOH + NaCl systems*

The concentration of H^+ (mol/kg) in test solution (PhOH + NaCl) was calculated from Eq. (3) with the calculated concentration of hydrogen ion in standard solution (HCl + NaCl) and the experimentally

Table 3
Calculated results of hydrogen ion concentrations and dissociation constants of phenol determined in this study

T (K)	P (MPa)	$\gamma_\pm$	I (mol/kg)	$[H^+]_s$	$[H^+]_t$	$[H^+]_{NaCl}$	$[H^+]_{H_2O}$	$\log K_{PhOH}$
296.4	30.0	0.946	9.97×10^{-2}	9.96×10^{-6}	1.06×10^{-6}	1.11×10^{-7}	1.14×10^{-7}	−10.0
473.1	29.9	0.841	9.74×10^{-2}	1.05×10^{-5}	4.77×10^{-6}	2.85×10^{-6}	2.70×10^{-6}	−9.1
633.3	29.8	0.527	6.53×10^{-2}	1.82×10^{-6}	2.93×10^{-6}	6.89×10^{-7}	1.24×10^{-6}	−9.6
653.5	30.1	0.440	5.53×10^{-2}	6.01×10^{-7}	6.07×10^{-7}	2.30×10^{-7}	5.55×10^{-7}	−10.7
653.3	34.8	0.477	5.96×10^{-2}	8.76×10^{-7}	1.02×10^{-6}	3.83×10^{-7}	8.80×10^{-7}	−10.1
673.4	30.2	0.273	2.76×10^{-2}	1.06×10^{-7}	8.86×10^{-8}	1.44×10^{-8}	3.67×10^{-8}	−12.0
673.0	34.9	0.375	4.67×10^{-2}	2.55×10^{-7}	3.06×10^{-7}	9.22×10^{-8}	2.85×10^{-7}	−11.0

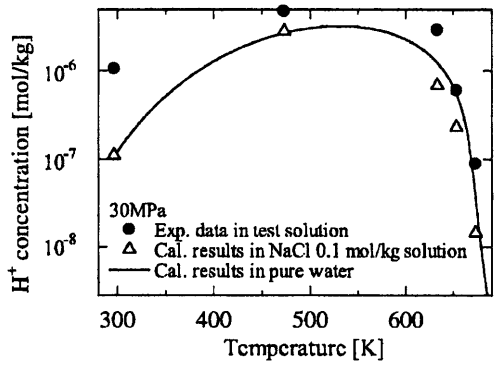

Fig. 4. Measured hydrogen ion concentration in test solution (0.01 mol/kg PhOH + 0.1 mol/kg NaCl) from 296.4 to 673.4 K at 30 MPa.

determined $\Delta E_0^{(I)}$ value at given temperature and pressure. The results are shown in Fig. 4 and in Table 3 together with the H^+ concentration in 0.1 mol/kg NaCl aqueous solution and pure water calculated by the method described above and the equation proposed Marshall and Franck [13]. As shown in Fig. 4 and Table 3, 0.1 mol/kg NaCl aqueous solution behaves as a neutral at low temperature. However, at high temperature (near critical and supercritical conditions), the solution behaves like a weak base solution. This is because H^+ and Cl^- is strongly associated and formed the HCl molecule compared with the association of Na^+ and OH^- at high temperature. For this reason, at 653.5 K and 30.1 MPa, the 0.01 mol/kg PhOH + 0.1 mol/kg NaCl solution behaves like neutral solution.

3.2.3. Determination of phenol dissociation constants

In test solution, the following reactions are occurred with the reaction in Eqs. (4)–(7).

$$\mathrm{PhOH(aq)} = \mathrm{H^+} + \mathrm{PhO^-}, \qquad K_{\mathrm{PhOH}} = \frac{[\mathrm{H^+}]\gamma_{\mathrm{H^+}}[\mathrm{PhO^-}]\gamma_{\mathrm{PhO^-}}}{[\mathrm{PhOH(aq)}]} \tag{8}$$

$$\mathrm{PhONa(aq)} = \mathrm{Na^+} + \mathrm{PhO^-}, \qquad K_{\mathrm{PhONa}} = \frac{[\mathrm{Na^+}]\gamma_{\mathrm{Na^+}}[\mathrm{PhO^-}]\gamma_{\mathrm{PhO^-}}}{[\mathrm{PhONa(aq)}]} \tag{9}$$

We assumed that Eq. (9) was less important reaction under our experimental conditions because the salt of the weak acid was more dissociated compared with the weak acid [19].

Using known initial concentration of NaCl and PhOH, the concentration of H^+ estimated above and the literature data of dissociation constant in Eqs. (4)–(7), the dissociation constants of phenol were determined at given temperature and pressure together with the electroneutrality and mass balance constraints.

The phenol dissociation constants determined in this work are shown in Table 3 and Fig. 5. The literature values [20] at 296.2 to 332.1 K and at the saturation pressure are also shown in same figure. The dissociation constant of phenol determined in this work at 296.4 K was 1.0×10^{-10}, which is in good agreement with the reported value (1.1×10^{-10}) at 296.3 K.

3.3. Dissociation behavior of phenol in subcritical and supercritical water

To discuss the dissociation behavior of phenol, the experimental data was correlated by the following semi-empirical model [11]. In this model, the reference state is 298.2 K and 0.997 g/cm^3 (pure water

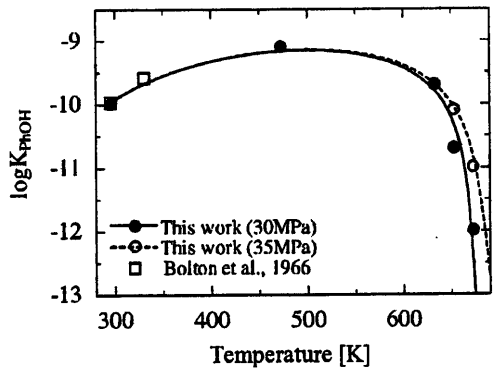

Fig. 5. Comparison of dissociation constants of phenol with correlation results of Eq. (10).

density). At this state, the pressure is 0.1 MPa.

$$\ln K = \ln K_r - \frac{\Delta H_r^0}{R}\left(\frac{1}{T} - \frac{1}{T_r}\right) - \frac{\eta}{T}\left(\frac{Z_{H^+}^2}{r_{H^+}} + \frac{Z_{PhO^-}^2}{r_{PhO^-}}\right)\left(\frac{1}{\varepsilon} - \frac{1}{\varepsilon_r}\right) \tag{10}$$

where Z and r are charge and radius (Å) of the ions, ε dielectric constant and η the constant (83549 (Å K)$^{-1}$). K_r and ΔH_r^0 are the equilibrium constant and the enthalpy of the phenol dissociation reaction at reference state. These values are evaluated from literature data, 1.12×10^{-10} and 22.89 kJ/mol, respectively [20]. In this model, the Born radii were adjusted from the bare ion values to include hydrated water. In this study, we assumed that the change of Gibbs free energy of molecular phenol with changing temperature and density was much smaller than the corresponding changes of the solvation energies of the ionic substances. For the hydrated H^+ ion radius, we used the value of 3.08 Å reported by Helgeson et al. [21]. The radius of phenolate anion (r_{PHO^-}) was determined by Marquardt's method and minimizing differences between the calculated result by Eq. (10) and the experimental data of phenol dissociation constants.

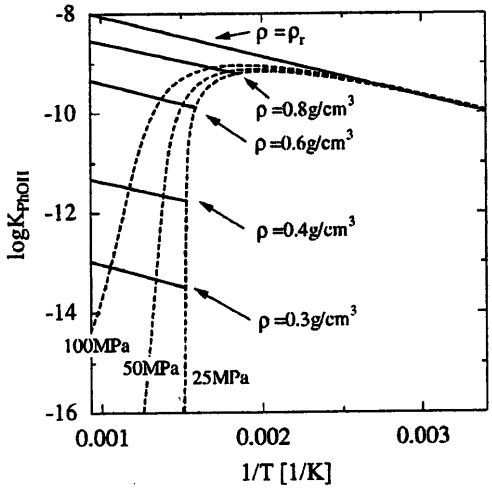

Fig. 6. Comparison of temperature behavior on the dissociation constants of phenol at various conditions.

The fitted value of r_{PHO^-} was determined to be 3.51 Å. The dielectric constant was calculated from the equation given by Johnson and Norton [22] and water density was calculated with an equation from the Steam Tables [23]. The correlation results are shown in Fig. 5 as a solid line (30 MPa) and a dashed line (35 MPa) and was in good agreement with the experimental values.

In Fig. 6, the dissociation constant calculated by Eq. (10) is plotted as a function of $1/T$ at constant pressure and density. The isobar at 25 MPa is closest to the critical pressure (22.1 MPa). All points above and to the left of this isobar are also at supercritical state. At constant density, the dissociation constant of phenol increased with temperature, exhibited endothermic behavior. The slopes did not change significantly from 0.3 to 0.997 g/cm^3. These behaviors are similar to the data of β-naphtol dissociation constant reported by Xiang and Johnston [7].

4. Conclusions

A flow-through electrochemical cell was developed to measure the dissociation constant of phenol in subcritical and supercritical aqueous solutions. The experimentally determined dissociation constants were in good agreement with available literature data. A semi-empirical electrostatic model could correlate the data as a function of water density and temperature.

List of symbols

a	activity
$E^{(I)}$	cell potential (V)
F	Faraday constant (C/mol)
H	enthalpy (J/mol)
I	ionic strength (mol/kg)
K	dissociation constant (mol/kg)
P	pressure (MPa)
r	hydrated ion radius (Å)
R	gas constant (J/(mol K))
R^2	correlation coefficient
T	temperature (°C)
Z	ionic charge

Greek letters

ε	dielectric constant
γ	activity coefficient,
φ	electrostatic potential
μ	chemical potential
ρ	density of water (g/cm^3)

Subscripts

r	reference state (298.2 K, 0.997 g/cm^3)
s	standard solution (10^{-5} mol/kg HCl + 0.1 NaCl)
t	test solution (0.01 mol/kg PhOH + 0.1 mol/kg NaCl)

Acknowledgements

The author wishes to acknowledge the Ministry of Education, Science, Sports and Culture, Japan, Japan Science & Technology Corporation (JST), and Core Research for Evolutional Science and Technology (CREST) for financial support of this research. We are indebted to Professor Richard L. Smith, Jr. of the Research Center of Supercritical Fluid Technology (Tohoku university) for many helpful discussions.

References

[1] K. Arai, T. Adschiri, Fluid Phase Equilib. 158–160 (1999) 673–684.
[2] Y. Ikushima, K. Hatakeda, M. Arai, J. Am. Chem. Soc. 122 (2000) 1908–1912.
[3] R.W. Shaw, T.B. Brill, A.A. Clifford, C.A. Eckert, E.U. Franck, Chem. Eng. News 69 (1991) 26–35.
[4] R.E. Mesmer, W.L. Marshall, D.A. Palmer, J.M. Simonson, H.F. Holmes, J. Solution Chem. 17 (1988) 699–718.
[5] P.C. Ho, D.A. Palmer, R.E. Mesmer, J. Solution Chem. 23 (9) (1994) 997–1018.
[6] P.C. Ho, H. Bianchi, D.A. Palmer, R.H. Wood, J. Solution Chem. 29 (3) (2000) 217–235.
[7] T. Xiang, K.P. Johnston, J. Phys. Chem. 98 (1994) 7915–7922.
[8] S.N. Lvov, X.Y. Zhou, D.D. Macdonald, J. Electroanal. Chem. 463 (1999) 146–156.
[9] S.N. Lvov, H. Gao, D.D. Macdonald, J. Electroanal. Chem. 443 (1998) 186–194.
[10] K. Sue, K. Murata, M. Tsukagoshi, Y. Matsuura, T. Adschiri, K. Arai, Rev. Sci. Instrum., in press.
[11] K. Sue, T.M. Aida, Y. Hakuta, R.L. Smith Jr., T. Adschiri, K. Arai, in: P.R. Tremaine, et al. (Eds.), Physical and Chemistry: Meeting the Needs of Industry, NRC Research Press, Ottawa, 2000, pp. 782–789.
[12] R. Hasse, Thermodynamics of Irreversible Processes, Addison-Wesley, Reading, MA, 1969.
[13] W.L. Marshall, E.U. Franck, J. Phys. Chem. Ref. Data 10 (2) (1981) 295–304.
[14] S.N. Lvov, X.Y. Zhou, S.M. Ulyanov, A.V. Bandura, Chem. Geol. 167 (2000) 105–115.
[15] P.C. Ho, D.A. Palmer, J. Solution Chem. 25 (8) (1996) 711–729.
[16] J.D. Frantz, W.L. Marshall, Am. J. Sci. 284 (1984) 651–667.
[17] R.T. Pabalan, K.S. Pitzer, Geochim. Cosmochim. Acta 51 (1987) 2429–2443.
[18] J.L. Bischoff, K.S. Pitzer, Am. J. Sci. 289 (1989) 217–248.
[19] J.L. Oscarson, S.E. Gillespie, J.J. Christensen, R.M. Izatt, P.R. Brown, J. Solution Chem. 17 (9) (1988) 865–885.
[20] P.D. Bolton, F.M. Hall, I.H. Reece, Spectrochim. Acta 22 (1966) 1149–1155.
[21] H.C. Helgeson, D.H. Kirkham, G.C. Flowers, Am. J. Sci. 281 (1981) 1249–1516.
[22] J.W. Johnson, D. Norton, Am. J. Sci. 291 (1991) 541–648.
[23] L. Haar, J.S. Gallagher, G.S. Kell, NBS/NRC Steam Tables, Hemisphere, Washington, DC, 1984.

PERGAMON

Biomass and Bioenergy 22 (2002) 405–410

BIOMASS & BIOENERGY

www.elsevier.com/locate/biombioe

Catalytic hydrogen generation from biomass (glucose and cellulose) with ZrO_2 in supercritical water

Masaru Watanabe, Hiroshi Inomata *, Kunio Arai

Research Center of Supercritical Fluid Technology, Department of Chemical Engineering, Tohoku University 07, Aoba, Aramaki, Aoba-ku, Sendai 980-8579, Japan

Received 17 April 2001; received in revised form 17 December 2001; accepted 17 December 2001

Abstract

We conducted the batch experiments for hydrogen production from biomass (glucose and cellulose) with ZrO_2 catalyst in supercritical water (673–713 K and 30–35 MPa). For comparison, we also conducted the experiments with alkali and without catalyst at the same conditions. The yield of hydrogen with zirconia was almost twice as much as that without catalyst for all the starting materials (glucose and cellulose). © 2002 Elsevier Science Ltd. All rights reserved.

Keywords: Glucose; Cellulose; Catalyst; Alkali; Zirconia; Hydrogen generation; Biomass

1. Introduction

Generation of hydrogen from biomass is an environmentally benign method to produce energy. In order to generate H_2 from biomass effectively, water is used as a suitable solvent and reactant as follows:

$$C_6H_{10}O_5 + 7H_2O \rightarrow 12H_2 + 6CO_2. \quad (1)$$

For these reasons, many researchers has conducted hydrogen generation from biomass in sub- and supercritical water [1–4]. Yu et al. [1] reported that the effective gasification of biomass must be conducted at low concentration of biomass because at high concentrations of biomass polymerization of the decomposition products occurred. However, higher concentration of biomass must be gasified to be an economical source [2]. For this reason, Xu et al. [2] examined the effect of active carbon on the gasification of high-concentration biomass in supercritical water for achieving high degree of gasification of high-concentration biomass solution. Although the yield of hydrogen was low, biomass was completely decomposed into gas even at a high concentration of biomass (1.2 M). Minowa and Ogi [3] conducted the experiments of gasification of cellulose in hot compressed water using a batch reactor and reported that the rate of gasification was enhanced with a reduced Ni catalyst. However, the yield of CH_4 was also enhanced and the yield of H_2 was suppressed. Kruse et al. [4] studied the effect of alkali (KOH) on the gasification of biomass in supercritical water. The yield of H_2 was almost three times greater with alkali (5 wt%), than without alkali. They considered that the enhancement of H_2 yield by adding alkali was due to the enhancement of water gas shift reaction (Eq. (2)):

$$CO + H_2O \rightleftharpoons CO_2 + H_2. \quad (2)$$

After evaluating the previous work on the high-temperature water gasification of biomass [1,2,4],

* Corresponding author. Tel.: 81-22-217-7282; fax: 81-22-217-7283.

E-mail address: inomata@scf.che.tohoku.ac.jp (H. Inomata).

0961-9534/02/$ - see front matter
PII: S0961-9534(02)00017-X

we considered the most important factors to be: (1) The rate of biomass decomposition to intermediates that form hydrogen has to be much greater than the rate of formation of polymeric unreactive substances; (2) the rate of the water gas shift reaction has to be promoted, and (3) the methanation of either carbon monoxide or carbon dioxide has to be inhibited. Alkali catalyst is one of the suitable catalysts for the gasification of biomass. However, the recovery of homogeneous alkali catalyst such as sodium hydroxide is difficult, and thus, the process using homogeneous catalyst would be expensive. Therefore, a recoverable heterogeneous catalyst such as metal oxide must be selected for the development of a low cost process. Recently, we found that zirconia, which is a solid base catalyst [5] and stable in supercritical water [6], is an effective catalyst for the decomposition of carbonyl compound such as carboxylic acid in supercritical water [7]. Since the decomposition of biomass such as glucose and cellulose in supercritical water produces aldehydes and ketones [8,9] intermediates, the yield of H_2 could be promoted using zirconia as a catalyst for gasification of biomass in supercritical water.

In this paper, the experiments of gasification of glucose and cellulose were conducted with and without catalyst (NaOH and zirconia) using a batch reactor. The effect of catalyst on the gasification of biomass in supercritical water was discussed.

2. Experimental

Zirconia catalyst was prepared by calcination of zirconium hydroxide (purchased from Nakarai Tesque Inc.) at 673 K for 3 h. The catalyst was used in the form of fine powder (67.69 m^2/g of surface area). Glucose was obtained from Wako Chemical. Cellulose (de-ashed microcrystalline cellulose) was purchased from Merck. Glucose and cellulose were used as received. Sodium hydroxide (NaOH, 1 M aqueous solution) was purchased from Wako Chemicals and used without further purification. Pure water, which was distilled after deionization, was obtained by a water distillation apparatus (Yamato Co., model WG-220).

The reaction was carried out in an SS 316 stainless steel tube bomb reactor with an inner volume of 6 cm^3 as described elsewhere [10]. The experimental procedure was also reported elsewhere [10]. The loaded amounts of samples were of 0.1 g, and the loaded amount of water was 1.2 g (0.2 g/cm^3) at 713 K or 2.1 g (0.35 g/cm^3) at 673 K. For the experiments using alkali hydroxide (NaOH), 1.2 g 713 K or 2.1 g (673 K) of 1 M NaOH solution was loaded into a reactor instead of pure water. In the case of the experiments with solid catalysts, 0.3 g of a catalyst was loaded. The reaction temperatures were 673 and 713 K, the reaction times ranged from 10 min (713 K) to 15 min (673 K). Experimental conditions are summarized in Table 1.

Table 1
Experimental conditions

Run (no.)	Reactant[a]	Temperature (K)	Reaction time (min)	Water density (g/cm^3)	Catalyst
1	Glucose	673	15	0.35	—
2	Glucose	673	15	0.35	ZrO_2[b]
3	Glucose	673	15	0.35	NaOH[c]
4	Glucose	713	10	0.2	—
5	Glucose	713	10	0.2	ZrO_2[b]
6	Glucose	713	10	0.2	NaOH[c]
7	Cellulose	673	15	0.35	—
8	Cellulose	673	15	0.35	ZrO_2[b]
9	Cellulose	673	15	0.35	NaOH[c]
10	Cellulose	713	10	0.2	—
11	Cellulose	713	10	0.2	ZrO_2[b]
12	Cellulose	713	10	0.2	NaOH[c]

[a]Loaded weight of reactants to a reactor is 0.1 g.
[b]Loaded weight of zirconia to a reactor is 0.3 g.
[c]1 M of NaOH aqueous solution was loaded to a reactor instead of water.

The identification and quantification of the gas product was conducted by GC-TCD (Shimadzu, model GC-7A, and Hitachi, model GC163). Water insolubles (including the metal oxide catalyst and coke) were divided by filtration with a membrane filter. The amount of carbon in the water solution was evaluated using total organic carbon (TOC) detector, Shimadzu, model TOC-5000A). Zirconia catalyst before and after the reaction were analyzed by X-ray diffractometer (Mac Science, model M18XHF-SRA) with Mo Kα radiation.

The product yield (mol%) of carbon compound was evaluated from carbon base as shown below:

$$\text{Product yield [mol\%]} = \frac{\text{The amount of carbon atom in a product}}{\text{The amount of carbon atom in a loaded starting material}} \times 100. \quad (3)$$

Hydrogen yield (H_2 yield, mol%) was evaluated from hydrogen base of a loaded amount of samples as follows:

$$H_2 \text{ yield [mol\%]} = \frac{\text{The amount of hydrogen atom in a produced } H_2}{\text{The amount of hydrogen atom in a loaded starting material}} \times 100. \quad (4)$$

3. Results and discussion

In this study, the products, which were identified and quantified, were H_2, CO, CO_2, CH_4, C_2–C_4 hydrocarbons (C_2H_4, C_2H_6, C_3H_6, C_3H_8, C_4H_8, C_4H_{10}), and TOC (total organic carbon in the recovered water). The yields of C_1–C_4 hydrocarbons were negligibly small for all the experimental conditions. The lack of mass balance closure, i.e. 100 − (TOC + gaseous carbon (CO, CO_2, and hydrocarbons)) was presumed to be due to the water insoluble products which were not measured.

Zirconia crystal system was a mixture of monoclinic and tetragonal forms before the reaction, after reaction it was changed into almost pure monoclinic structure. As reported previously [7], the stable phase of zirconia was assumed to be monoclinic.

Figs. 1 and 2 show the gas and liquid carbon compounds distribution (C distribution: CO, CO_2, and TOC) and the yield of H_2 from glucose decomposition at 673 K for 15 min with and without catalyst, respectively. Without catalyst, the yield of CO plus CO_2 was only 10% and that of H_2 was about 2%. On the other hand, the gasification efficiency of glucose with zirconia was twice (CO + CO_2: about 20%, H_2: 5%) as much as without catalyst in supercritical water.

In Figs. 3 and 4, the C distribution and the yield of H_2 from cellulose decomposition at 673 K for 15 min with and without catalyst were shown, respectively. As same as the case of glucose, while the yield of CO plus CO_2 was only 15% and that of H_2 was about 2% without catalyst, the gasification of glucose with zirconia was twice as much as without catalyst (CO + CO_2: about 20%, H_2: 5%) in supercritical water.

The effect of temperature on the gasification of glucose and cellulose in supercritical water was also examined. The reaction temperature, the water density, and the reaction time were 713 K, 0.2 g/cm^3, and 10 min, respectively. The results are shown in

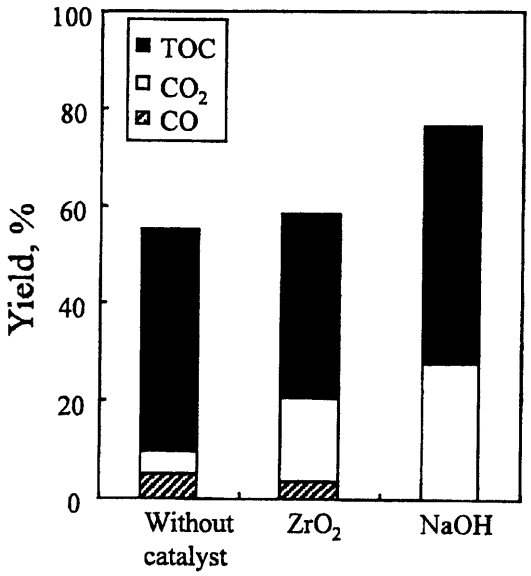

Fig. 1. Gas and liquid carbon compound yield of glucose decomposition in supercritical water (673 K, 15 min, 0.35 g/cm^3 of water density, and 0.1 g of glucose).

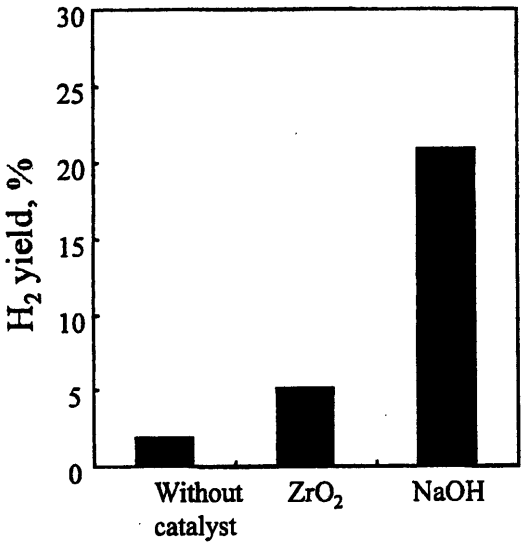

Fig. 2. H_2 yield of glucose decomposition in supercritical water (673 K, 15 min, 0.35 g/cm^3 of water density, and 0.1 g of glucose).

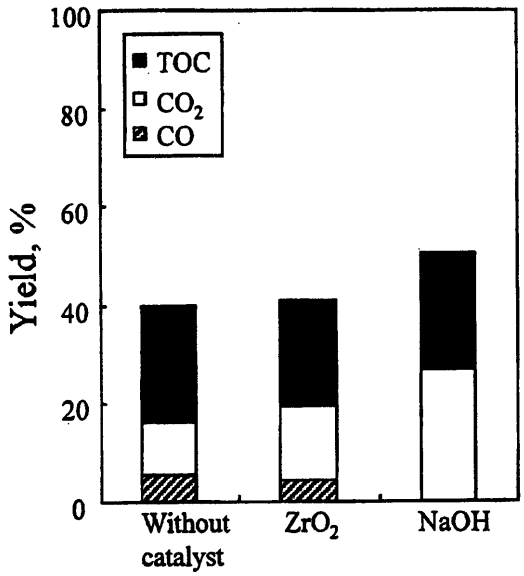

Fig. 3. Gas and liquid carbon compound yield of cellulose decomposition in supercritical water (673 K, 15 min, 0.35 g/cm^3 of water density, and 0.1 g of cellulose).

Figs. 5–8. Figs. 5, 6, 7 and 8 show the C distribution of glucose gasification, the yield of H_2 of glucose gasification, the C distribution of cellulose gasification, and the yield of H_2 of cellulose gasification, respectively.

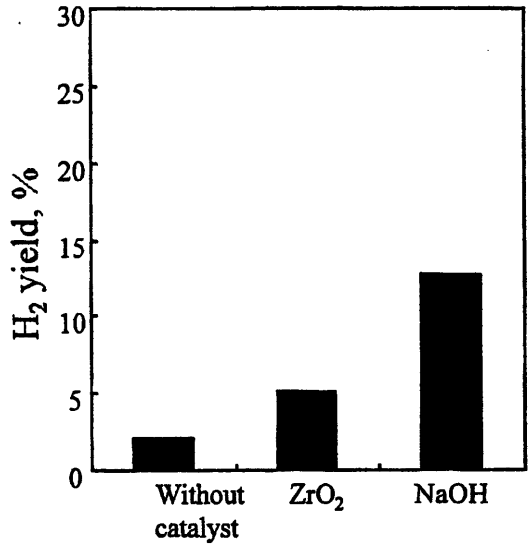

Fig. 4. H_2 yield of cellulose decomposition in supercritical water (673 K, 15 min, 0.35 g/cm^3 of water density, and 0.1 g of cellulose).

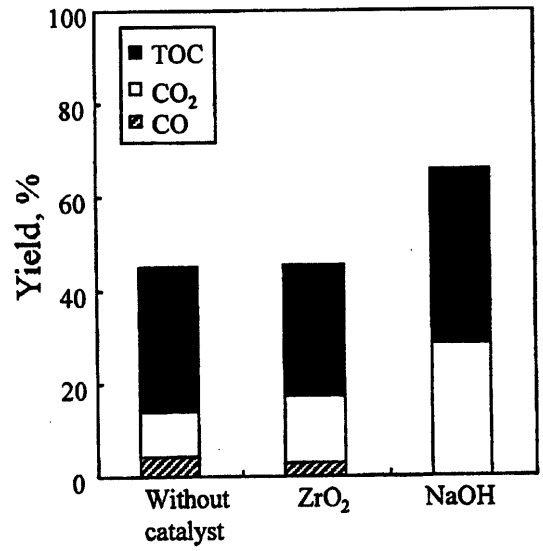

Fig. 5. Gas and liquid carbon compound yield of glucose decomposition in supercritical water (713 K, 10 min, 0.2 g/cm^3 of water density, and 0.1 g of glucose).

Even at a shorter reaction time (10 min) at 713 K than that (15 min) at 673 K, the gasification efficiency at 713 K was almost the same as that at 673 K for all the experiments of glucose and cellulose. This indicates that the rate of gasification has enhanced with

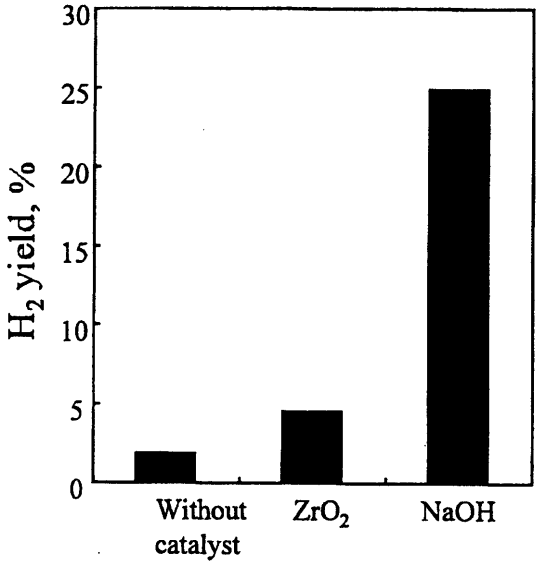

Fig. 6. H_2 yield of glucose decomposition in supercritical water (713 K, 10 min, 0.2 g/cm^3 of water density, and 0.3 g of glucose).

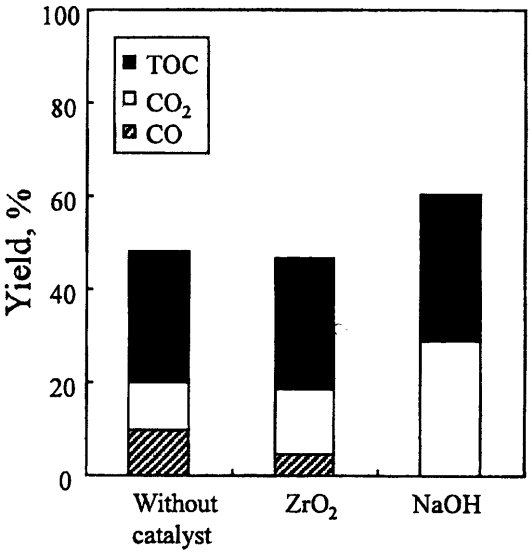

Fig. 7. Gas and liquid carbon compound yield of cellulose decomposition in supercritical water (713 K, 10 min, 0.2 g/cm^3 of water density, and 0.3 g of cellulose).

temperature. At a higher temperature (713 K), the gasification efficiency with zirconia was twice as much as that without catalyst for glucose and cellulose. Thus, the activity of zirconia was found to be still kept even at 713 K.

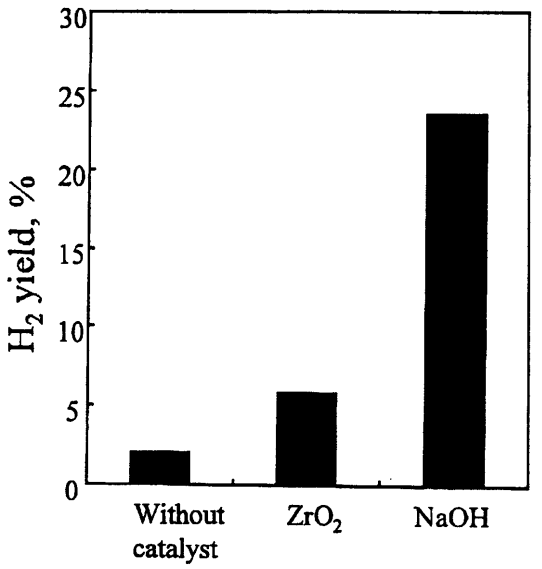

Fig. 8. H_2 yield of cellulose decomposition in supercritical water (713 K, 10 min, 0.2 g/cm^3 of water density, and 0.3 g of cellulose).

For comparison, we conducted the experiments using alkali hydroxide (NaOH) for glucose and cellulose at 673 and 713 K. The results are also shown in Figs. 1–8. For all the experiments, the gasification efficiency with NaOH was the highest. In the case of NaOH, the yield of CO was negligibly small. Thus, it was assumed that CO rapidly reacted with water to produce CO_2 and H_2 (water gas shift reaction: Eq. (2)) as suggested by Kruse et al. [4]. Although the yield of gaseous compounds (CO, CO_2, and H_2) with zirconia was lower than that with NaOH at all the experimental conditions, we believe that we could show the possibility of zirconia as a catalyst for the gasification of biomass in supercritical water.

Zirconia is well known to be an acid–base catalyst [5]. The acidity and/or basidity on the surface of zirconia was controlled with the structure [5,11]. Furthermore, the structure and stabilization of zirconia was controlled by doping Yttrium (the so-called stabilized zirconia), alkali metal [11] and so on, and thus, the catalytic property of zirconia was also controlled. In the near future, we will try the same metal-doped zirconia in the reaction, and we will make clear the relationship between the acid–base property of zirconia and gasification of biomass in supercritical water.

4. Conclusion

In this study, the gasification of biomass (glucose and cellulose) was conducted to examine the effect of zirconia by use of batch-type reactors in supercritical water (0.35 g/cm^3 of water density for 15 min at 673 K and 0.2 g/cm^3 of water density for 10 min at 713 K). As a result, the gasification efficiency of biomass in supercritical water with zirconia was twice as much as that without catalyst at all the experimental conditions.

References

[1] Yu D, Aihara M, Antal Jr. MJ. Energy Fuels 1993;7:574.
[2] Xu X, Matsumura Y, Stenberg J, Antal Jr. MJ. Ind Eng Chem Res 1996;35:2522.
[3] Minowa T, Ogi T. Catal Today 1998;45:411.
[4] Kruse A, Meier D, Rimbrecht P, Schacht M. Ind Eng Chem Res 2000;39:4842.
[5] Tomishige K, Sakaihori T, Ikeda Y, Fujimoto K. Catal Lett 1999;58:225.
[6] Ding ZY, Frisch MA, Li L, Gloyna EF. Ind Eng Chem Res 1996;35:3257.
[7] Watanabe M, Inomata H, Smith Jr. RL, Arai K. Appl Catal A Gen 2001;219:149.
[8] Kabyemela BM, Adschiri T, Malaluan RM, Arai K, Ohzeki H. Ind Eng Chem Res 1997;36:5063.
[9] Sasaki M, Kabyemela B, Malaluan R, Hirose S, Takeda N, Adschiri T, Arai K. J Supercrit Fluids 1998;13:261.
[10] Arai K, Adschiri T, Watanabe M. Ind Eng Chem Res 1998;39:4697.
[11] Parida K, Mishra HK. J Mol Catal A 1999;139:73.

Dealkylation and Rearrangement Kinetics of 2-Isopropylphenol in Supercritical Water

Takafumi Sato, Gaku Sekiguchi, Motofumi Saisu, Masaru Watanabe, Tadafumi Adschiri, and Kunio Arai*

Department of Chemical Engineering, Tohoku University, 07 Aoba, Aramaki-Aza, Aoba-ku, Sendai 980-8579, Japan

The decomposition of 2-isopropylphenol at temperatures of 613−713 K and water densities of 0−0.6 g/cm^3 yielded phenol, propene, and 2-propylphenol. The decomposition was determined to occur via two reaction pathways: (1) dealkylation of 2-isopropylphenol to produce phenol and propene and (2) rearrangement of the propyl functional group from 2-isopropylphenol to 2-propylphenol. The rate constant for dealkylation increased proportionally with increasing water density. The reaction rate for rearrangement was invariant with the water density. The rate constants for dealkylation and rearrangement could be correlated as a function of temperature and water density with a global reaction model.

Introduction

Alkylphenols and phenol are important intermediates in the chemical industry for a great diversity of products, such as pharmaceuticals, dyes, and antioxidants.[1] The industrial production routes for alkylphenols and phenol are through the alkylation of phenol with the corresponding alkenes under acid catalysis or through cumene oxidation. The recovery of alkylphenols and phenol from coal and lignin is expected to become a major source of these compounds, because coal and lignin have many alkylphenol units in their basic structure and can be thought of as polymers of alkylphenol.[2] Further, chemical recycling of alkylphenol related materials including waste plastics has been gaining greater attention in recent years as a means of obtaining valuable products from waste. Alkylphenols and their related compounds are usually recovered by the hydrogenation of waste materials using hydrogen-donor solvents or catalysts.[3] The use of these solvents is expected to be limited, however, as more emphasis is placed on green chemistry.

Water is an inexpensive and environmentally acceptable solvent that offers tremendous opportunities for pollution prevention for a wide variety of chemical reactions.[4] Supercritical water is completely miscible with light gases[5] and hydrocarbons,[6] which suggests the potential of using supercritical water as a reaction medium in place of many organic solvents. Small changes in pressure and temperature greatly affect solvent properties such as the ion product and dielectric constant especially near the critical point. This allows for the manipulation of chemical equilibria and reaction rates.[7] Many reactions such as hydrolysis, substitution, rearrangement, isomerization, and dehydration occur without catalyst in sub- and supercritical water.[4,8−11] Hence, the process of destroying and chemically recycling alkylphenol-related compounds without a catalyst is possible using supercritical water.

For process development, an understanding of the reactions of alkylphenols in supercritical water is essential. Martino and Savage[12,13] reported that cresols and ethylphenols are dealkylated in supercritical water at 733 K to yield phenol as the main product. Suzuki et al.[14] reported that prepolymers of phenol resin decompose in supercritical water at 523−703 K and that methylene bridges could be decomposed. These studies show that supercritical water might be a useful solvent for the conversion of alkylphenols. However, few kinetic studies on the decomposition of alkylphenols in supercritical water have been performed. Further, the dependence on water of the reaction rate and the reaction mechanism have not been elucidated sufficiently.

In this study, we chose 2-isopropylphenol as a model alkylphenol that has a structure similar to the unit structure of lignin and examined its decomposition in the absence and in the presence of water. Experiments were conducted over a wide range of temperature and water density, namely, 613−713 K and 0−0.6 g/cm^3, respectively.

Experimental Section

2-Isopropylphenol (IPP) was purchased from Tokyo Kasei and had a purity of >98%. The analytical reagents used were tetrahydrofuran (THF, >97%), with 2,6-di-*tert*-butyl-4-methylphenol as an inhibitor, and naphthalene (>99%), which were obtained from Wako Chemical. All chemicals were used without further purification.

Experiments at 673 K were conducted with stainless steel (SUS 316) batch-type reactors (6 cm^3) that were fitted with a high-pressure valve (Whitey, model SS-3NBF2). The batch-type reactors were made of SUS 316 tubes (length = 105 mm, i.d. = 8.5 mm, o.d. = 12.7 mm) that had two SUS 316 $^1/_{16}$−$^1/_2$-in. Swagelok reducing unions to a $^1/_{16}$-in. SUS 316 tube (length = 300 mm, i.d. = 0.59 mm, o.d. = 1.59 mm) for ports. One port was connected to a high-pressure valve, and the other served as a thermocouple well for measuring the reactor temperature. Air in the reactor was displaced with argon (Ar) by pressurizing several times to 15−27 bar and then relieving the pressure slowly. The reactor was loaded with 0.204−0.818 g of IPP and 0.3−3 g of distilled water (corresponding to water densities, ρ_W, of 0.05−0.5 g/cm^3). These amounts of water correspond to

* To whom correspondence should be addressed. E-mail: karai@arai.che.tohoku.ac.jp. Tel.: +81-22-217-7245. Fax: +81-22-217-7246.

10.1021/ie010763a CCC: $22.00
Published on Web 05/30/2002

pressures of 12.6–37.0 MPa according to the pure-water data of Haar et al.[15] Experiments in Ar atmosphere without water were also conducted.

Except at 673 K, experiments were conducted without the high-pressure valve. In these experiments, the reactor was loaded with 0.409 g of IPP and 3.6 g (613 K), 3.0 g (633, 653 K), 2.4 g (693 K), or 1.8 g (713 K) of distilled water. Experiments without water were also conducted.

The general procedure was as follows. After the reactor had been loaded, the tube was submerged up to the high-pressure valve into a fluidized sand bath (Takabayashirika Co., model TK-3) that was controlled at the reaction temperature. The heating time was about 3 min. After a given amount of time (10–360 min), including the heating time, the reactor was removed from the bath, and the reaction was rapidly quenched in a water bath at 293 K.

After being cooled, the reactor was submerged in an ultrasonic water bath for 5 min to degas the liquid and allow for the recovery of the gases dissolved in water. The high-pressure valve at the end of the reactor was connected to sampling loops and a syringe. By opening the valve gently and withdrawing the syringe, gas samples could be collected. Gas products were analyzed by gas chromatography with thermal conductivity detection, GC-TCD (Shimadzu, model GC-8A). H_2 was analyzed with a molecular sieve 5A column and Ar carrier gas. CH_4 was analyzed with a molecular sieve 13X column and He carrier gas. C2–C3 hydrocarbons and CO_2 were analyzed with a Porapak Q column and He carrier gas.

After the gases had been sampled or displaced, the reactor was opened and washed with THF. The aromatics in the THF solutions were identified by gas chromatography with flame ionization detection, GC-FID (Hewlett-Packard, model 5890, series II), with an HP-1 column and by gas chromatography–mass spectrometry, GC-MS (Japan Electron Optics Laboratory, model Automass 20), with an HP-5MS column by comparison with peak standards and a mass spectrum library. For some experiments, analyses for detecting aliphatic alcohols were conducted with the HP-5 column. The concentration of products was determined by GC-FID with naphthalene as the internal standard.

The product yield (Y), IPP conversion (X), and product selectivity (S) were evaluated according to

$$Y_{\text{Product}} = \frac{\text{amount of product (mol)}}{\text{amount of IPP loaded (mol)}} \times 100\% \quad (1)$$

$$X = 1 - \frac{\text{amount of product (mol)}}{\text{amount of IPP loaded (mol)}} \quad (2)$$

$$S_{\text{Product}} = \frac{Y_{\text{product}}/100}{X} \quad (3)$$

Results and Discussion

Product Distribution. Figure 1 shows the liquid products that were found, and Table 1 provides a summary of the experimental results for the liquid products at $T = 673$ K, $[\text{IPP}]_0 = 0.5$ mol/L, and water density = 0–0.5 g/cm^3. The sum of the yield of these compounds for each run was above 87.9%. For some experiments, the sum was above 100% because of the difficulty of accurate estimation for large amounts of IPP. The main products were phenol (2) and 2-propylphenol (PP, 3) for all water densities. These yields clearly increased, while the residual yield of 2-isopropylphenol (IPP, 1) decreased with reaction time, which indicates that phenol was produced through the dealkylation of IPP and PP was produced through the rearrangement of the alkyl groups of IPP. Other products detected were 2-cresol (4), 2-ethylphenol (5), 4-isopropylphenol (6), 2,6-diisopropylphenol (7), 2-isopropyl-6-propylphenol (8), and 2,6-dipropylphenol (9), but the yields of these side products were always below 2.5%. IPP rapidly decomposed in supercritical water at 673 K, although Katritzky et al.[16] reported that it was stable in water at 548 K.

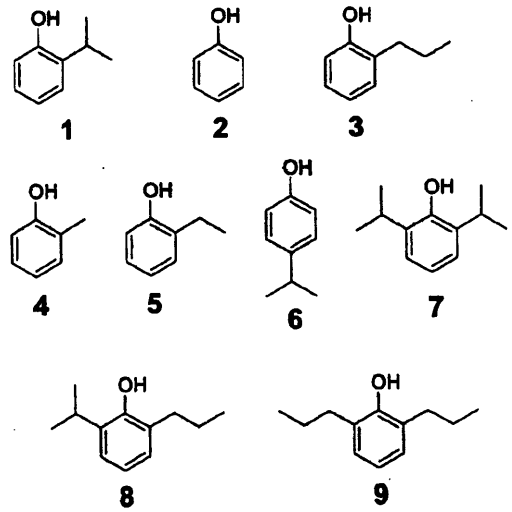

Figure 1. Liquid products of 2-isopropylphenol decomposition in supercritical water.

We conducted gas analysis at water densities of 0 and 0.5 g/cm^3 after 60 min of reaction time. At a water density of 0 g/cm^3, C_3H_6, H_2, and CH_4 were detected, at levels of 87.8, 11.4, and 0.8 mol %, respectively. At a water density of 0.5 g/cm^3, C_3H_6, H_2, CH_4, C_2H_4, and CO_2 were found with a composition of 98.3, 0.4, 0.4, 0.5, and 0.4 mol %, respectively. Thus, propene was the main gas product under the present conditions. We also analyzed aliphatic alcohols for the experiment at 0.5 g/cm^3 from 15 to 60 min of reaction time. The maximum yield of 2-propanol was 1.1% at 60 min of reaction time, whereas that for phenol was 21.5%. Only a small amount of 2-propanol was produced under these conditions, which means that the side chain of IPP was converted mainly to propene by dealkylation. Judging from these results, we propose the main reaction pathway for IPP decomposition shown in Figure 2. Dealkylation of IPP to phenol and propene and rearrangement of IPP to PP appear to occur as parallel reactions.

As shown in Table 1, the effect of water density on the initial product distribution was very small at water densities of 0.1 g/cm^3 and below. In this range of water density, the yield of phenol was 5.0–7.1% and that of PP was 4.0–5.9% at 60 min of reaction time. At water densities of 0.3 and 0.5 g/cm^3, the yield of phenol clearly increased with increasing water density. For example, the yield of phenol increased to 11.2 and 21.5% at 60 min of reaction time and water densities of 0.3 and 0.5 g/cm^3, respectively. On the other hand, the yield of PP was practically constant at 5–6% regardless of the water density. The dealkylation seemed to be enhanced

Table 1. Yields of Liquid Products for 2-Isopropylphenol (IPP) Decomposition at Water Densities of 0–0.5 g/cm³, 673 K and $[IPP]_0$ = 0.5 mol/L

water density (g/cm³)	reaction time (min)	yield (%)									sum of yields
		1	2	3	4	5	6	7	8	9	
0	15	103	1.5	1.4	0.0	0.1	0.7	0.0	0.0	0.0	107
	22	90.8	1.9	1.9	0.0	0.1	0.6	0.1	0.0	0.0	95.4
	30	88.8	3.9	2.8	0.0	0.0	0.8	0.8	0.1	0.1	97.3
	60	83.1	7.1	5.9	0.0	0.0	0.9	1.2	0.3	0.0	98.5
	139	63.7	12.9	13.5	0.0	0.0	0.8	1.7	0.9	0.2	93.7
	180	60.0	14.4	17.0	0.2	0.2	0.6	1.6	1.0	0.2	95.2
	360	41.4	22.4	27.9	0.7	0.4	0.9	1.7	2.3	0.7	98.4
	360	37.3	24.3	27.0	1.0	0.7	0.6	1.6	2.3	0.8	95.6
0.05	15	90.3	0.9	0.3	0.0	0.0	0.4	0.0	0.0	0.0	91.9
	22	94.1	2.8	1.6	0.0	0.1	0.7	0.3	0.1	0.0	99.7
	30	87.4	2.7	2.3	0.0	0.0	0.6	0.3	0.0	0.0	93.3
	60	78.0	5.2	5.0	0.0	0.0	0.6	0.6	0.0	0.0	89.4
	120	69.9	11.5	11.1	0.0	0.0	0.8	1.4	0.6	0.0	95.3
	180	58.4	17.0	16.4	0.0	0.0	0.7	1.9	1.3	0.1	95.8
	360	35.7	24.4	22.6	0.5	0.3	0.7	1.5	2.2	0.7	88.6
	360	37.2	22.6	24.8	0.8	0.4	0.8	1.4	2.2	0.8	91.0
0.1	15	91.4	1.2	0.8	0.0	0.0	0.5	0.1	0.0	0.0	94.0
	15	98.1	2.3	1.3	0.0	0.1	0.7	0.1	0.0	0.0	103
	30	86.8	2.4	2.3	0.0	0.0	0.5	0.1	0.0	0.0	92.1
	60	82.5	5.0	4.6	0.0	0.0	0.6	0.4	0.0	0.0	93.1
	122	70.0	11.6	10.0	0.0	0.0	0.7	1.4	0.5	0.0	94.2
	180	64.4	13.2	13.0	0.0	0.0	0.8	1.2	0.7	0.1	93.4
	360	50.6	19.3	19.0	0.4	0.1	0.6	1.1	1.5	0.4	93.0
	360	43.2	20.9	20.0	0.1	0.0	0.5	1.1	1.7	0.5	88.0
	15	91.6	2.7	1.2	0.0	0.1	0.6	0.0	0.0	0.0	96.2
0.3	22	86.6	5.1	2.1	0.0	0.1	0.6	0.3	0.1	0.0	94.9
	30	89.5	4.7	2.6	0.0	0.0	0.5	0.3	0.0	0.0	97.6
	45	88.0	11.9	4.7	0.0	0.1	0.7	0.9	0.1	0.0	106
	60	74.3	11.2	6.0	0.0	0.0	0.6	1.3	0.2	0.0	93.6
	120	63.6	19.8	10.9	0.1	0.1	0.6	1.9	0.9	0.1	98.0
	180	53.7	22.1	13.8	0.0	0.0	0.5	1.7	1.3	0.2	93.3
	360	38.2	30.0	18.5	0.4	0.2	0.6	1.0	2.1	0.9	91.9
	15	83.4	4.4	1.2	0.0	0.1	0.6	0.3	0.1	0.0	90.1
	22	78.3	6.2	1.9	0.0	0.1	0.6	0.5	0.1	0.1	87.8
0.5	30	87.0	7.8	2.7	0.0	0.0	0.7	0.7	0.0	0.0	98.9
	30	81.9	10.1	3.0	0.0	0.1	0.6	1.0	0.1	0.0	96.8
	45	71.7	11.8	4.0	0.0	0.1	0.6	0.7	0.2	0.0	89.1
	60	78.0	21.5	5.4	0.0	0.1	0.7	2.5	0.5	0.0	109
	120	60.1	23.4	9.7	0.0	0.0	0.7	2.1	1.0	0.1	97.1
	180	50.3	34.5	14.6	0.0	0.0	0.8	2.3	2.0	0.3	105
	360	37.6	35.0	17.5	0.7	0.4	0.7	0.9	2.1	1.1	96.0
	360	36.5	33.9	16.9	0.4	0.3	0.7	0.9	2.1	1.1	92.8

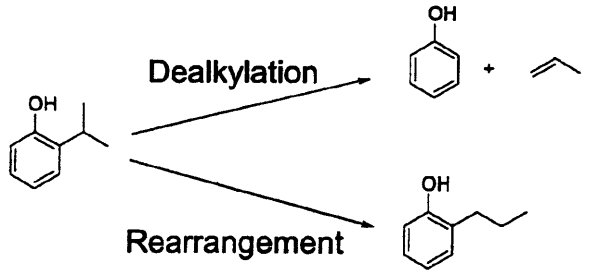

Figure 2. Main reaction pathways of 2-isopropylphnol decomposition.

with increasing water density, whereas the rearrangement reaction did not seem to be affected by the water content.

We conducted another series of experiments at temperatures of 613–713 K and water densities of 0–0.6 g/cm³ as summarized in Table 2. The products obtained were the same as those found at 673 K, with the main products being phenol (**2**) and PP (**3**). Other products did not exceed 4%. At higher temperatures, the yields of phenol and PP increased. At each reaction temperature, the yield of phenol in the presence of water was larger than that without water. The yield of PP was more or less the same with or without water.

Evaluation of the Rate Constant. (a) Effect of Water Density. We determined the rate constant for the dealkylation and rearrangement of IPP from the data at reaction times of less than 60 min so that we could evaluate the kinetics of the primary reactions while eliminating the effect of secondary reactions. Figure 3 shows a plot of $-\ln(1 - X)$ versus t where X was evaluated as the sum of the concentrations of phenol and PP divided by the initial concentration of IPP. The straight line going through the origin indicates that the reaction is probably first-order with respect to IPP at each water density. The slope increased with increasing water density. We also conducted experiments in the range of water density from 0.13 to 0.45 g/cm³ at $[IPP]_0$ = 0.5 mol/L and evaluated the rate constant at each water density.

Table 3 lists the number of data points, the maximum conversion used for the estimation, and the best-fit value of the rate constant for each water density. The rate constant clearly increased with increasing water density, which indicates that water enhanced the decom-

Table 2. Yields of Liquid Products for 2-Isopropylphenol (IPP) Decomposition at 613–713 K and $[IPP]_0$ = 0.5 mol/L

T (K)	water loaded (g)	reaction time (min)	yield (%) 1	2	3	4	5	6	7	8	9	sum of yields
613	0	180	93.4	0.9	0.3	0.0	0.1	0.6	0.1	0.0	0.0	95.4
		360	92.6	1.3	0.5	0.8	0.1	0.6	0.1	0.0	0.0	96.0
		540	99.5	2.3	1.0	1.2	0.1	0.7	0.4	0.0	0.0	105
		720	97.0	3.6	1.6	1.6	0.1	0.7	0.8	0.1	0.0	106
	3.6	180	102	2.1	0.3	1.0	0.1	0.6	0.2	0.1	0.0	106
		360	99.7	4.2	0.5	1.6	0.1	0.7	0.8	0.0	0.0	108
		540	94.1	5.6	0.8	2.0	0.1	0.6	1.3	0.1	0.0	105
		720	94.4	8.3	1.2	3.4	0.1	0.6	2.5	0.2	0.0	111
633	0	60	97.9	0.9	0.4	0.8	0.0	0.7	0.1	0.0	0.0	101
		120	98.1	1.4	0.9	0.9	0.0	0.7	0.2	0.0	0.0	102
		180	90.1	1.7	1.0	0.7	0.0	0.6	0.2	0.0	0.0	94.3
		240	93.4	2.3	1.4	0.9	0.0	0.6	0.3	0.0	0.0	98.9
	3.0	60	95.0	2.0	0.5	0.9	0.0	0.7	0.2	0.0	0.0	99.3
		120	94.4	4.1	0.8	1.1	0.0	0.6	0.5	0.0	0.0	102
		180	94.2	6.0	1.1	1.8	0.0	0.7	1.0	0.1	0.0	105
		240	87.6	7.6	1.4	2.0	0.0	0.6	1.3	0.1	0.0	101
653	0	15	98.4	0.5	0.3	0.7	0.0	0.7	0.0	0.0	0.0	101
		30	99.2	0.9	0.7	0.9	0.0	0.7	0.1	0.0	0.0	103
		45	98.4	1.3	1.1	0.7	0.0	0.7	0.1	0.0	0.0	102
		60	96.7	1.7	1.4	0.8	0.0	0.7	0.1	0.0	0.0	101
	3	15	98.0	1.5	0.4	0.7	0.0	0.6	0.1	0.0	0.0	101
		45	93.9	4.7	1.1	1.1	0.0	0.7	0.4	0.0	0.0	102
		60	92.1	6.0	1.3	1.3	0.0	0.6	0.6	0.0	0.0	102
693	0	10	83.5	1.8	2.0	0.7	0.1	0.6	0.0	0.0	0.0	88.7
		17	87.6	3.5	4.1	0.9	0.1	0.6	0.1	0.0	0.0	96.9
		24	83.9	4.1	5.9	0.9	0.1	0.6	0.2	0.0	0.0	95.7
		30	79.3	5.6	8.2	1.2	0.1	0.6	0.3	0.1	0.0	95.4
	2.4	10	84.7	6.3	2.5	1.1	0.1	0.6	0.3	0.0	0.0	95.6
		17	77.7	11.7	4.8	1.7	0.1	0.6	0.8	0.1	0.0	97.5
		24	71.1	16.3	6.4	2.2	0.1	0.7	1.2	0.3	0.0	98.3
		30	63.3	20.5	8.8	3.3	0.1	0.7	1.9	0.6	0.0	99.2
713	0	10	81.9	5.2	6.9	1.0	0.1	0.6	0.2	0.1	0.0	96.0
		15	74.0	8.3	11.4	1.4	0.1	0.6	0.4	0.2	0.0	96.4
		20	65.2	11.0	15.2	1.9	0.2	0.6	0.6	0.3	0.0	95.0
		25	58.2	13.0	18.4	2.5	0.3	0.6	0.7	0.5	0.1	94.3
	1.8	10	71.7	13.2	8.1	1.6	0.1	0.6	0.7	0.2	0.0	96.2
		20	47.1	25.6	16.8	3.4	0.2	0.6	1.3	0.9	0.1	96.0
		25	38.8	30.2	19.8	4.0	0.3	0.6	1.3	1.2	0.2	96.4

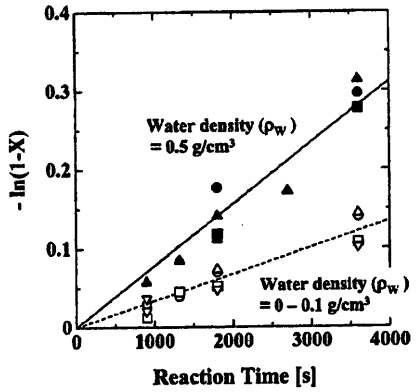

Figure 3. Plot of $-\ln(1 - X)$ versus reaction time at water densities of 0–0.1 and 0.5 g/cm³ and 673 K for 2-isopropylphenol (IPP) decomposition: (○) $[IPP]_0$ = 0.5 mol/L, ρ_W = 0 g/cm³; (△) $[IPP]_0$ = 1.0 mol/L, ρ_W = 0 g/cm³; (□) $[IPP]_0$ = 0.5 mol/L, ρ_W = 0.05 g/cm³; (▽) $[IPP]_0$ = 0.5 mol/L, ρ_W = 0.1 g/cm³; (●) $[IPP]_0$ = 0.25 mol/L; (▲) $[IPP]_0$ = 0.5 mol/L; (■) $[IPP]_0$ = 1.0 mol/L

position of IPP at a water density of 0.5 g/cm³. The rate constant at 0.5 g/cm³ was 2.3 times larger than that at 0–0.1 g/cm³.

According to the experimental results, we proposed a reaction pathway in which the decomposition of IPP consists of dealkylation and rearrangement. Thus, the overall rate constant k is expressed as $k = k_r$ (rearrangement) + k_d (dealkylation). These reaction rate constants, k_r and k_d, can be related to the selectivities of phenol and PP at zero conversion level ($S_{0,Phenol}$, $S_{0,PP}$, respectively) as[17]

$$k_d = S_{0,Phenol}k \quad (4)$$

$$k_r = S_{0,PP}k \quad (5)$$

Figure 4 shows the relationship between the IPP conversion and the selectivities of phenol and PP at water densities of 0–0.1 and 0.5 g/cm³. The solid and dashed lines were obtained by correlations at 0–0.1 and 0.5 g/cm³, respectively. These lines were obtained with the least-squares method. The data at 0.5 g/cm³ exhibited linear behavior, whereas the data at 0–0.1 g/cm³ were scattered. However, the data clearly show that the selectivity of PP at a water density of 0.5 g/cm³ was lower than that at 0–0.1 g/cm³ and that the selectivity of phenol at 0.5 g/cm³ was higher than that at 0–0.1 g/cm³. This means that water enhanced the dealkylation. We also evaluated $S_{0,Phenol}$ and $S_{0,PP}$ at other water densities, as summarized in Table 3.

The values k_r and k_d were determined from eqs 4 and 5. Figure 5 shows k_r and k_d plotted against the water density, where k_r and k_d at 0–0.1 g/cm³ are plotted at 0 g/cm³. The dashed lines were obtained by the least-squares method from correlations for k_d and k_r. The k_r

Table 3. Effect of Water Density on the Rate Constants and Selectivity for 2-Isopropylphenol (IPP) Decomposition at 673 K and $[IPP]_0$ = 0.5 mol/L

water density (g/cm³)	no. of points	maximum conversion	k (10^{-5} s^{-1})	95% CI (10^{-5} s^{-1})	$S_{0,Phenol}$	$S_{0,PP}$	95% CI
0–0.1[a]	14	0.134	3.37	±0.35	0.60	0.40	±0.08
0.13	3	0.174	5.12	±1.28	0.55	0.45	±0.75
0.18	5	0.176	5.35	±0.09	0.69	0.31	±0.03
0.20	3	0.128	5.17	±0.70	0.69	0.31	±0.13
0.30	5	0.172	5.54	±1.15	0.68	0.32	±0.11
0.35	4	0.220	6.96	±1.35	0.86	0.14	±0.36
0.40	5	0.227	7.09	±0.64	0.76	0.24	±0.03
0.45	4	0.228	7.57	±0.77	0.81	0.19	±0.06
0.50[b]	10	0.269	7.70	±0.76	0.74	0.26	±0.09

[a] $[IPP]_0$= 0.5–1.0 mol/L. [b] $[IPP]_0$= 0.25–1.0 mol/L.

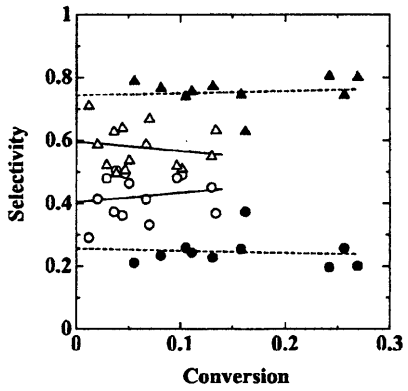

Figure 4. Relationship between 2-isopropylphenol (IPP) conversion and selectivities of 2-propylphenol (PP) and phenol at water densities of 0–0.1 g/cm³ and 0.5 g/cm³ of at 673 K: (○) PP, ρ_W = 0–0.1 g/cm³; (●) PP, ρ_W = 0.5 g/cm³; (△) phenol, ρ_W = 0–0.1 g/cm³; (▲) phenol, ρ_W = 0.5 g/cm³

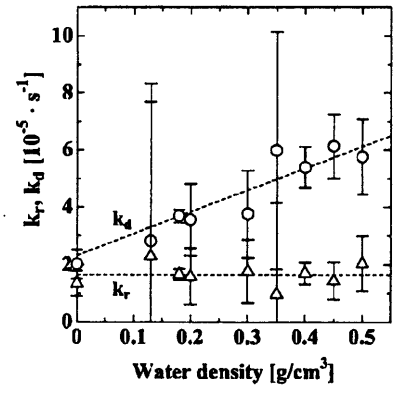

Figure 5. Dependence of rate constant of rearrangement (k_r, △) and dealkylation (k_d, ○) on water density at 673 K.

and k_d values were almost the same at a water density of 0 g/cm³. This might suggest the possibility of the existence of a common intermediate for dealkylation and rearrangement. Although the obtained results can provide some information on the reaction mechanism, we focused on the evaluation of the rate constants for dealkylation and rearrangement rather than the mechanism in this paper. k_r was practically constant (1.65 × 10^{-5} s^{-1}) over the entire range of water densities, and k_d was directly proportional to the water density. At 0.5 g/cm³, k_d was 2.8 times larger than k_r.

To evaluate the effect of water, we assumed that k_d could be expressed as a function of the water density

$$k_d = k_{d0} + k_{dw}[H_2O] \quad (6)$$

where k_{d0} is the value of k_d at a water density of 0 g/cm³ and $[H_2O]$ is the water concentration (mol/L) at the given conditions. The values of k_{dw} and k_{d0} were determined from the slope and intercept of the line for k_d to be $k_{d0} = (1.94 \pm 0.89) \times 10^{-5}$ s^{-1} and $k_{dw} = (1.56 \pm 0.50) \times 10^{-6}$ L mol^{-1} s^{-1}.

The dealkylation of IPP was promoted with increasing water density. Sato et al.[18] reported the formation of IPP by the alkylation of phenol with propene in supercritical water, the reverse route of alkylation, with the alkylation being accelerated with increasing water density as in dealkylation. In supercritical water, an increase in reaction rate with increasing water density often occurs. This phenomenon can be explained by considering electrostatic effects,[7,19] which are described in terms of the solvent dielectric constant.[20] In general, if the transition state is more polar than the reactants, an increase in the dielectric constant causes the rate constant to increase. The dealkylation rate of IPP increased with increasing water density, which implies that the transition state of the rate-determining step was stabilized compared to the corresponding reactants.

(b) Effect of Temperature. We evaluated k_r and k_d from the data at 613–713 K without water in the same way as for the data at 673 K, and Table 4 summarizes the results for k, $S_{0,Phenol}$, $S_{0,PP}$, k_r, and k_d. Figure 6 shows the Arrhenius plot for k_r and k_d. The dashed lines are for k_r and k_d without water and were obtained with the least-squares method. The first-order rate constants were determined to be

$$k_r \text{ (without water)} = 10^{12.8\pm2.8} \exp(-2.28 \pm 0.36 \times 10^5/RT) \text{ (s}^{-1}\text{)} \quad (7)$$

$$k_d \text{ (without water)} = 10^{9.32\pm1.40} \exp(-1.82 \pm 0.18 \times 10^5/RT) \text{ (s}^{-1}\text{)} \quad (8)$$

where R is the gas constant (8.314 J mol^{-1} K^{-1}).

Next, we evaluated k_r and k_d in sub- and supercritical water at 613–713 K in each case. Table 5 shows a summary of the results. Both k_r and k_d increased with increasing temperature, and k_d was larger than k_r. In the presence of water, dealkylation was the dominant pathway.

Figure 6 shows the Arrhenius plot of k_r and k_d in sub- and supercritical water, where the amount of water loaded was not the same at each temperature. k_r in the presence of water was the same as k_r without water.

$$k_r \text{ (in the presence of water)} = k_r \text{ (without water)} \quad (9)$$

However, k_d in the presence of water was clearly larger

Table 4. Rate Constants and Selectivities for Decomposition of 2-Isopropylphenol (IPP) without Water at 613–713 K and $[IPP]_0$ = 0.5 mol/L

T (K)	k (10^{-5} s^{-1})	95% CI (10^{-5} s^{-1})	$S_{0,Phenol}$	$S_{0,PP}$	95% CI	k_r (10^{-5} s^{-1})	95% CI (10^{-5} s^{-1})	k_d (10^{-5} s^{-1})	95% CI (10^{-5} s^{-1})
613	0.11	±0.03	0.72	0.28	±0.04	0.03	±0.01	0.08	±0.02
633	0.27	±0.05	0.70	0.30	±0.18	0.08	±0.07	0.19	±0.10
653	0.89	±0.04	0.63	0.37	±0.07	0.22	±0.08	0.56	±0.09
673[a]	3.37	±0.35	0.60	0.40	±0.08	1.35	±0.44	2.02	±0.51
693	7.79	±0.98	0.51	0.49	±0.11	3.82	±1.44	3.97	±1.46
713	24.8	±1.80	0.44	0.56	±0.01	13.9	±1.30	10.9	±1.10

[a] $[IPP]_0$= 0.5–1.0 mol/L

Table 5. Rate Constants and Selectivities for 2-Isopropylphenol (IPP) Decomposition in the Presence of Water at 613–713 K at $[IPP]_0$ = 0.5 mol/L

T (K)	water density (g/cm³)	k (10^{-5} s^{-1})	95% CI (10^{-5} s^{-1})	$S_{0,Phenol}$	$S_{0,PP}$	95% CI	k_r (10^{-5} s^{-1})	95% CI (10^{-5} s^{-1})	k_d (10^{-5} s^{-1})	95% CI (10^{-5} s^{-1})
613	0.6	0.22	±0.02	0.87	0.13	±0.05	0.03	±0.01	0.19	±0.03
633	0.5	0.67	±0.03	0.81	0.19	±0.05	0.13	±0.04	0.54	±0.06
653	0.5	2.14	±0.12	0.80	0.20	±0.02	0.42	±0.07	1.71	±0.14
673[a]	0.5	7.79	±0.74	0.74	0.26	±0.09	2.03	±0.96	5.76	±1.32
693	0.4	18.4	±1.90	0.72	0.28	±0.04	5.15	±1.34	13.2	±2.18
713	0.3	45.6	±5.50	0.63	0.37	±0.08	16.9	±6.12	28.7	±7.55

[a] $[IPP]_0$ = 0.25–1.0 mol/L.

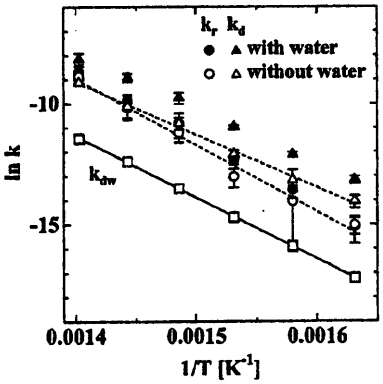

Figure 6. Arrhenius plot for k_r, k_d, and k_{dw} at 613–713 K and water densities of 0–0.6 g/cm³.

than k_d without water. This means that water enhanced the dealkylation over this temperature range. The contribution of water to the dealkyaltion rate constant was described by the difference between k_d in the presence of water from k_d without water. Here, we assumed that the dependence of the dealkyaltion rate constant on water was the first-order in the water concentration

$$k_d \text{ (in the presence of water)} = k_d \text{ (without water)} + k_{dw}[H_2O] \quad (10)$$

We calculated k_{dw} at each temperature where the water density was different, as shown in Figure 6. The plot of k_{dw} shows linearity over the entire temperature range, which means that the magnitude of enhancement of dealkyaltion in the presence of water is first-order in the water density and that the role of water in dealkylation can be explained in the same way at the other temperatures as it can at 673 K.

From the straight line for k_{dw}, we obtained the following expression

$$k_{dw} = 10^{10.5\pm0.3} \exp(-2.11 \pm 0.04 \times 10^5/RT) \quad (\text{L mol}^{-1}\ \text{s}^{-1}) \quad (11)$$

The global reaction model for dealkylation and rearrangement of IPP can be developed by considering of eqs 9–11 to yield

$$-\frac{d[IPP]}{dt} = (k_r + k_{d0} + k_{dw}[H_2O])[IPP]$$
$$= \{10^{12.8\pm2.8} \exp(-2.28 \pm 0.36 \times 10^5/RT) + 10^{9.32\pm1.40} \exp(-1.82 \pm 0.18 \times 10^5/RT) \quad (12)$$
$$+ \{10^{10.5\pm0.3} \exp(-2.11 \pm 0.04 \times 10^5/RT)[H_2O]\}[IPP] \ (\text{mol L}^{-1}\ \text{s}^{-1})$$

Possible Role of the Hydroxy Group. For the alkylation of phenol with propene, IPP is mainly produced, as reported in a recent study.[18] The alkyl side chain of IPP is attached to the neighboring position of a hydroxyl group, and thus, the contribution of the hydroxyl group in this position is supposed to be larger than those of a hydroxyl group attached to the para or meta positions in supercritical water. To examine the effect of the hydroxyl group on the reaction and its reactivity, we performed some experiments with 4-isopropylphenol. At 673 K and a reaction time of 180 min, 4-isopropylphenol was found to be relatively stable at water densities of both 0 and 0.5 g/cm³. At 0 g/cm³, product yields were below 3%. At 0.5 g/cm³, no product yield over 1% was observed. We concluded that the para position of the hydroxyl group had a low reactivity for both rearrangement and dealkylation.

The hydroxy group possibly plays an important role in both dealkylation and rearrangement, although the mechanisms of dealkylation and rearrangement of IPP in supercritical water have not yet been revealed. We believe that a detailed study that clarifies the role of the hydroxy group in dealkylation and rearrangement is needed to elucidate the mechanisms of these reactions in supercritical water.

Conclusions

The main products of the decomposition of 2-isopropylphenol are phenol, propene, and 2-propylphenol.

Water does not affect the main product distribution over the temperature range of 613−713 K and water density range of 0−0.6 g/cm^3. The decomposition rate of 2-isopropylphenol exhibited first-order dependence on the 2-isopropylphenol concentration. The main reaction pathways were dealkylation to phenol and propene and rearrangement to 2-propylphenol. The hydroxyl group of IPP seems to play an important role in the dealkylation and rearrangement processes. The reaction rate of dealkylation increased with increasing water density almost proportionally to the concentration of water. The reaction rate of rearrangement was not influenced by the water density. These results demonstrate that the yield of alkylphenol product can be controlled by manipulating the temperature and pressure (water density) in supercritical water.

Acknowledgment

The authors acknowledge financial support from the Ministry of Education, Culture, Sports, Science and Technology through Grants-in-Aid for Scientific Research on Priority Areas (09450281, 10555270, 11450295, and 11694921).

Literature Cited

(1) Kroschwitz, J. I.; Mary, H.-G. *Kirk−Othmer, Encyclopedia of Chemical Technology*, 4th ed.; Wiley-Interscience: New York, 1991.

(2) Dong, J.-Z.; Ouchi, K. Geochemical origin of long chain alkyl aromatics in coal. *Fuel* **1989**, *68*, 710.

(3) Dorrstijn, E.; Laarhoven, L. J. J.; Arends, I. W. C. E.; Mulder, P. The occurrence and reactivity of phenoxyl linkages in lignin and low rank coal. *J. Anal. Appl. Pyrolysis* **2000**, *54*, 153.

(4) Savage, P. E. Organic chemical reactions in supercritical water. *Chem. Rev.* **1999**, *99*, 603.

(5) Frank, E. U. Special aspects of fluid solution at high pressures and sub- and supercritical temperatures. *Pure Appl. Chem.* **1981**, *53*, 1401.

(6) Schneider, G. M. Phase behavior and critical phenomena in fluid mixtures under pressure. *Ber. Bunsen-Ges. Phys. Chem.* **1972**, *76*, 325.

(7) Savage, P. E.; Gopalan, S.; Mizan, T. I.; Martino, C. J.; Brock, E. E. Reactions at supercritical conditions: Applications and fundamentals. *AIChE J.* **1995**, *41*, 1723.

(8) Katritzky, A. R.; Nichols, D. A.; Siskin, M.; Murugan, R.; Balasubramanian, M. Reactions in high-temperature aqueous media. *Chem. Rev.* **2001**, *101*, 837.

(9) Siskin, M.; Katritzky, A. R. A review of the reactivity of organic compounds with oxygen-containing functionality in superheated water. *J. Anal. Appl. Pyrolysis* **2000**, *54*, 193.

(10) An, J.; Bagnell, L.; Cablewski, T.; Strauss, C. R.; Trainor, R. W. Applications of high-temperature aqueous media for synthetic organic reactions. *J. Org. Chem.* **1997**, *62*, 2505.

(11) Broll, D.; Kaul, C.; Kramer, A.; Krammer, P.; Richter, T.; Jung, M.; Vogel, H.; Zehner, P. Chemistry in supercritical water. *Angew. Chem., Int. Ed.* **1999**, *38*, 2998.

(12) Martino, C. J.; Savage, P. E. Thermal decomposition of substituted phenols in supercritical water. *Ind. Eng. Chem. Res.* **1997**, *36*, 1385.

(13) Martino, C. J.; Savage, P. E. Supercritical water oxidation kinetics and pathways for ethylphenols, hydroxyacetophenones, and other monosubstituted phenols. *Ind. Eng. Chem. Res.* **1999**, *38*, 1775.

(14) Suzuki, Y.; Tagaya, H.; Asou, T.; Kadokawa, J.; Chiba, K. Decomposition of prepolymers and molding materials of phenol resin in subcritical and supercritical water under an Ar atmosphere. *Ind. Eng. Chem. Res.* **1999**, *38*, 1391.

(15) *NBC/NRC Steam Tables*; Haar, L., Gallagher, J. S., Kell, G. S., Eds.; Hemisphere Publishing Corp.: New York, 1984.

(16) Katritzky, A. R.; Murugan, R.; Siskin, M. Aqueous high-temperature chemistry of carbo- and heterocycles. 9. Aquathermolysis of ortho-substituted, meta-substituted, and multisubstituted phenols in the presence and absence of sodium bisulfite. *Energy Fuels* **1990**, *4*, 538−543.

(17) Bhore, N. A.; Klein, M. T.; Bischoff, K. B. The delplot technique: A new method for reaction pathway analysis. *Ind. Eng. Chem. Res.* **1990**, *29*, 313.

(18) Sato, T.; Sekiguchi, G.; Adschiri, T.; Arai, K. Noncatalytic and selective alkylation of phenol with propan-2-ol in supercritical water. *Chem. Commun.* **2001**, *17*, 1566.

(19) Townsend, S. H.; Abraham, M. A.; Huppert G. L.; Klein, M. T.; Paspek, S. C. Solvent effects during reactions in supercritical water. *Ind. Eng. Chem. Res.* **1988**, *27*, 143.

(20) Amis, E. S. *Solvent Effects on Reaction Rates and Mechanisms*; Academic Press: New York, 1966.

Received for review September 10, 2001
Revised manuscript received April 11, 2002
Accepted April 12, 2002

IE010763A

Regioselectivity of phenol alkylation in supercritical water

Takafumi Sato, Gaku Sekiguchi, Tadafumi Adschiri, Richard L. Smith Jr. and Kunio Arai*

Department of Chemical Engineering, Tohoku University, 07 Aoba, Aramaki-Aza, Aoba-ku, Sendai 980-8579, Japan. E-mail: karai@arai.che.tohoku.ac.jp; Fax: +81-22-217-7246; Tel: +81-22-217-7245

Received 19th July 2002
First published as an Advance Article on the web 8th August 2002

Regioselectivity of phenol alkylation with propionaldehyde could be controlled in supercritical water under non-catalytic conditions at 673 K by manipulating water density.

Introduction

Toxicity and risk management of chemical processes can become simplified if environmental fluids such as water or carbon dioxide can be substituted for organic solvents in harmony with the philosophy of Green Chemistry. Water, in a state above its critical point (T_c: 647.3 K, P_c: 22.1 MPa) has many environmental and technological advantages.[1] In the supercritical region, water is completely miscible with many organics and provides a homogeneous reaction field.[2] The change of water density affects the reaction rate and reaction pathway by changing the contribution of ionic reaction pathways.[2] Organic syntheses such as dehydration, Diels–Alder reaction and rearrangements have been examined in supercritical water.[1] We have reported that non-catalytic alkylation of phenol with 2-propanol also occurs in supercritical water.[3,4]

Alkylphenols are important for industrial intermediates and the production of alkylphenols exceeds 450000 tonnes/year on a worldwide basis.[5] The vast majority of alkylphenols are used to synthesize derivatives for pharmaceuticals, antioxidants and polymers. The Friedel–Crafts reaction is one of the major methods for synthesis of alkylphenols and requires strong acids such as Lewis acids ($AlCl_3$, BF_3) and mineral acids (HF, H_2SO_4).[6] In the alkylation of phenol, the hydroxy group of phenol strongly activates the reactivity of both *ortho* and *para* positions.[7]

To control the regioselectivity of alkylation, base reagents or heterogeneous catalysis is used. Sartori *et al.*[8] reported that the ratio of *ortho* to *para* increased with increasing PhOK : PhOH ratio in $CHCl_3$ solvent. Sato *et al.*[9] examined the *ortho*-selective alkylation of phenol with 1-propanol by CeO_2–MgO. Gray *et al.*[10] conducted the reaction of phenol with 2-propanol in supercritical CO_2. They reported that isopropyl phenyl ether was the main product and that the yield of *ortho* alkylphenols was always larger than that of the *para* products. In this work, we examined the regioselectivity of phenol alkylation when the ionic atmosphere of the water solvent was varied. As an example, we show alkylation of phenol with propionaldehyde in supercritical water solvent.

Experimental

Experiments were conducted in stainless 316 tube-bomb reactors (6 cm^3) equipped with a high pressure shut-off valve.[4] For the reaction of propionaldehyde and phenol, 0.002 mol of propionaldehyde, 0.010 mol of phenol and 0.6–3 g of water were loaded into the reactor. The amount of water corresponded to a water density of 0.1–0.5 g cm^{-3}. We also conducted experiments without water (denoted as water densities of 0 g cm^{-3}). After loading samples and purging the reactor with argon, the reactor was submerged into a sand-bath controlled at 673 K. Heat-up time was within 4 min. After a given reaction time, the reactor was quenched in a water-bath. Liquid products were collected by combining the reacted mixtures with THF solvent in sufficient amounts such that a single phase mixture was formed. This allowed complete analysis of the liquid products. Products were identified by GC–MS and quantified by GC–FID. Gas products were analysed by GC–TCD by using a sampling loop attached to GC. The product yield was defined by on a propionaldehyde basis, as: yield (%) = (moles of carbon of the alkyl chains attached to the benzene ring)/(moles of carbon in propionaldehyde loaded) × 100.

Results and discussion

Fig. 1 shows the yield of main products with reaction time for the reaction of phenol (1) and propionaldehyde (2) in supercritical water at 673 K at a water density of 0.5 g cm^{-3}. From the experimental results, we propose the reaction pathway as Scheme 1. Propionaldehyde (2) was converted within 20 min and yielded 2-propenylphenol (3) and 4-propenylphenol (4) through the reaction with phenol (1). Then, cyclization of 2-propenylphenol (3) gave 2,3-dihydro-2-methybenzofuran (5),[11] followed by the dehydrogenation to 2-methylbenzofuran (6). Hydrogenation of both 2-propenylphenol (3) and 4-propenylphenol (4) also occurred and yielded 2-propylphenol (7) and 4-propylphenol (8), respectively. Alkylphenols such as 2-cresol, 4-cresol, 2-ethylphenol and 4-ethylphenol were detected.

Green Context

The ability of supercritical fluids to function as highly tunable solvents is remarkable. In addition to the normal solvent parameters, SCFs have the additional flexibility of variable density. While denser fluids are generally better solvents, the control of density can allow important changes in e.g. selectivity (see for example, C. Rayner, *Green Chem.*, 1999, 1(2), G44). Here the selectivity of phenol alkylation can be dramatically varied by simply controlling the density of the medium. Additionally, no catalyst was required to perform the operation. ***DJM***

DOI: 10.1039/b207100b

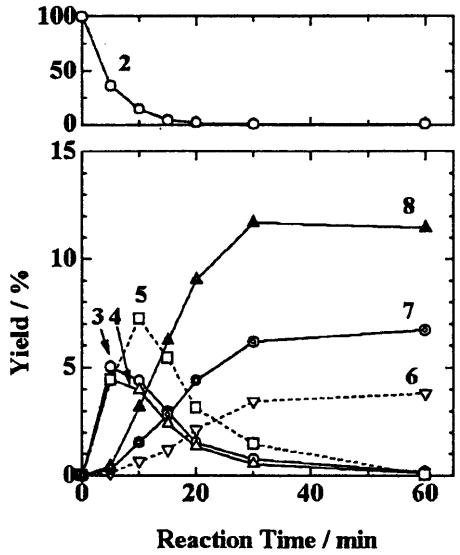

Fig. 1 Yield of propionaldehyde (**2**), 2-propenylphenol (**3**), 4-propenylphenol (**4**), 2,3-dihydro-2-methybenzofuran (**5**), 2-methylbenzofuran (**6**), 2-propylphenol (**7**) and 4-propylphenol (**8**) at 0.5 g cm^{-3} water density and 673 K.

The sum of the yield of the main liquid products was about 30% and almost constant. We conducted gas analyses and found that the main gas products were CO and C_2H_6 as reported in the pyrolysis of propionaldehyde (**2**).[12] There was no solid after the reaction and byproducts from propionaldehyde (**2**), other than gas and alkylphenols, probably yielded oligomers through aldol condensation.[13,14]

We evaluated the product distribution at other ionic atmospheres by changing the water density to confirm the proposed mechanism of Scheme 1. Table 1 shows the product distribution at 673 K and 60 min reaction time at water density of 0–0.5 g cm^{-3}. The ratio of *ortho* to *para* isomers was evaluated from the sum of the product yields of the alkyl side chain attached to the *ortho*-position of hydroxy group of phenol (**3**, **5**, **6**, **7**) and to *para*-positions (**4**, **8**). The sum of the yields of phenolic compounds increased with increasing water density. At 60 min reaction time, the yields of 2-propylphenol (**7**) and 4-propylphenol (**8**) were high, which means that these compounds were relatively stable. The reactivity at both *ortho* and *para* positions of the hydroxy group seemed to be enhanced in the region of high water density. The ratio of *ortho*/*para* product clearly decreased with increasing water density. These results provide strong evidence that the selectivity of the *para* position is a function of the ionic atmosphere of the water solvent.

The dielectric constant and ion product of water increase with increasing water density, which makes the reaction atmosphere have a greater ionic character.[2] Further, phenol dissociates in supercritical water and its dissociation constant increases with water density.[15] At 673 K, the dissociation constant of phenol increases from 10^{-12} to 10^{-11} with increasing water density from 0.36 to 0.47 g cm^{-3}.[15] This means that the proton concentration also increases with increasing water density. The high water density region provides an ionic atmosphere favorable for the formation of ionic species such as protons or carbonium ions.

From the experimental findings, we propose an alkylation mechanism as shown in Scheme 2. Propionaldehyde (**2**) and protons are in equilibrium with the 1-propanol cation $CH_3CH_2CH^+OH$ (**9**) in aqueous solution. With increasing water density, this equilibrium probably shifts to the carbonium ion side through the contribution of solvating power for ionic species and proton concentration. In the experiments, both *ortho* and *para* substituents were formed in an ionic atmosphere due to the high water density. Under such conditions, the reaction proceeds through pathway (a). If 1-propanol cation (**9**) reacted with phenol, electrophilic substitution at the benzene ring of phenol should occur. The 1-propanol cation (**9**) attacked both *ortho* and *para* positions of phenol and yielded both *ortho* and *para* hydroxyalkylphenols in a similar manner as standard Friedel–Crafts reactions.[6] Hydroxyalkylphenols can be formed through the reaction of phenol and aldehyde in high temperature water.[14] The hydroxy group of aliphatic alcohols easily

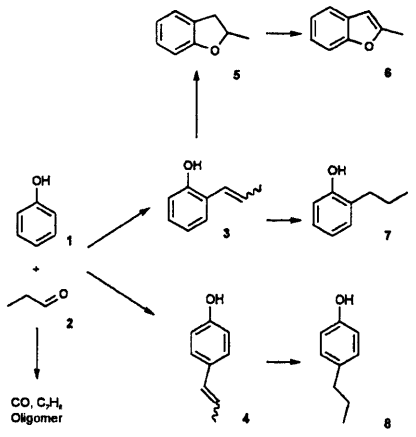

Scheme 1 Reaction pathway for the reaction of phenol and propionaldehyde in supercritical water.

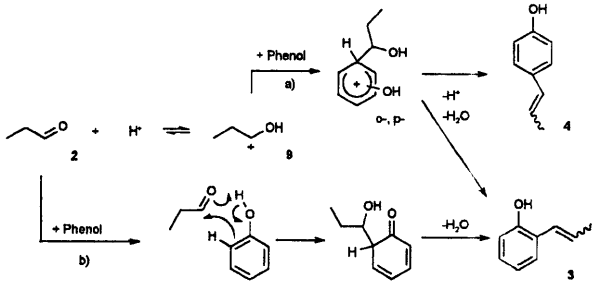

Scheme 2 Mechanism for alkylation of phenol with propionaldehyde in supercritical water.

Table 1 Yield of main liquid products at various water densities (673 K, 60 min, propionaldehyde = 0.002 mol, phenol = 0.01 mol)

	Yield (%)								
		Ortho				*Para*			
Water density/g cm^{-3}	**2**	**3**	**5**	**6**	**7**	**4**	**8**	Sum of alkyl phenols	*Ortho*/*para* ratio[a]
0	0.4	0.1	0.8	0.7	1.4	0.0	0.0	3.4	≫99[b]
0.1	1.6	0.3	1.1	0.3	1.0	0.0	0.2	2.9	14.3
0.3	1.3	1.1	3.6	1.2	2.9	0.8	2.2	11.8	2.94
0.5	0.5	0.2	0.0	3.8	6.7	0.1	11.5	22.3	0.93

[a] (**3** + **5** + **6** + **7**)/(**4** + **8**); [b] No *para* products observed.

dehydrates in high temperature water in the presence of phenol as well as acids.[4] The hydroxy group in the alkyl side chain of alkylphenols can be eliminated by dehydration and yielded the corresponding propenylphenols (**3**, **4**). In the low density region, the *ortho* substituent was the dominant product where the reaction atmosphere has less ionic character. Under these conditions, the equilibrium between propionaldehyde (**2**) and the 1-propanol cation (**9**) was shifted to the propionaldehyde (**2**) and the reaction proceeded through pathway (b). Sartori *et al.*[16] reported that the hydroxy group participates in the reaction mechanism in the catalytic alkylation of phenol. Under these conditions, phenol and propionaldehyde (**2**) probably react directly through the contribution of hydoxy group. Then, dehydration of hydroxyalkylphenol occurs, leading to the *ortho* product 2-propenylphenol (**3**).

In summary, the regioselectivity of phenol alkylation with propionaldehyde could be controlled in supercritical water under non-catalytic conditions. In the high density region of water, alkylation occurred at both *ortho* and *para* positions. A decrease in water density increased the product ratio of the *ortho* substituents.

Acknowledgements

The authors are thankful for the Grant-in-Aid for Scientific Research on Priority Areas (09450281, 10555270, 11450295 and 11694921) the Ministry of Education, Culture, Sports, Science and Technology.

References

1 P. E. Savage, *Chem. Rev.*, 1999, **99**, 603.
2 P. E. Savage, S. Gopalan, T. I. Mizan, C. J. Martino and E. E. Brock, *AIChE J.*, 1995, **41**, 1723.
3 T. Sato, G. Sekiguchi, T. Adschiri and K. Arai, *Chem. Commun.*, 2001, 1566.
4 T. Sato, G. Sekiguchi, T. Adschiri and K. Arai, *Ind. Eng. Chem. Res.*, 2002, **41**, 3064.
5 J. I. Kroschwitz and H.-G. Mary Kirk-Othmer, *Encyclopedia of Chemical Technology*, Wiley-Interscience, New York, 4th edn., 1991.
6 G. A. Olah, *Friedel–Crafts and related reactions*, Interscience Publishers, New York, 1963, vol. I.
7 F. J. Sowa, G. F. Hennion and J. A. Nieuwland, *J. Am. Chem. Soc.*, 1935, **57**, 709.
8 G. Sartori, F. Bigi, R. Maggi and A. Arienti, *J. Chem. Soc., Perkin Trans. 1*, 1997, **3**, 257.
9 S. Sato, R. Takahashi, T. Sodesawa, K. Matsumoto and Y. Kamimura, *J. Catal.*, 1999, **184**, 180.
10 W. K. Gray, F. R. Smail, M. G. Hitzler, S. K. Ross and M. Poliakoff, *J. Am. Chem. Soc.*, 1999, **121**, 10711.
11 L. Bagnell, T. Cablewski, C. R. Strauss and R. W. Trainor, *J. Org. Chem.*, 1996, **61**, 7355.
12 C. H. Bamford and C. F. H. Tipper, *Comprehensive Chemical Kinetics*, Elsevier, Amsterdam, 1972, vol. 5.
13 E. L. Coitino, J. Tomasi and O. N. Ventura, *J. Chem. Soc. Faraday Trans.*, 1994, **90**, 1745.
14 A. R. Katritzky, M. Balasubramanian and M. Siskin, *Energy Fuels*, 1990, **4**, 499.
15 K. Sue, K. Murata, Y. Matsuura, M. Tsukagoshi, T. Adschiri and K. Arai, *Fluid Phase Equilib.*, 2002, **194–197**, 1097.
16 G. Sartori, R. Maggi, F. Bigi, A. Arienti, C. Porta and G. Predieri, *Tetrahedron*, 1994, **50**, 10587.

10 May 2002

ELSEVIER

Chemical Physics Letters 357 (2002) 168–172

CHEMICAL PHYSICS LETTERS

www.elsevier.com/locate/cplett

Local density augmentation from fluorescence lifetime for anthracene *N*,*N*-dimethylaniline exciplex in supercritical carbon dioxide

Takafumi Aizawa [a,*], Yutaka Ikushima [a], Norio Saitoh [a], Kunio Arai [a], Richard L. Smith Jr. [b]

[a] *Supercritical Fluid Research Center, National Institute of Advanced Industrial Science and Technology, Sendai 983-8551, Japan*
[b] *Graduate School of Chemical Engineering, Research Center of Supercritical Fluid Technology, Tohoku University, Sendai 980-8579, Japan*

Received 1 February 2002

Abstract

Local density augmentation around exciplex between anthracene and *N*,*N*-dimethylaniline in supercritical carbon dioxide was measured by fluorescence lifetime at 40 °C and at pressures from 9.3 to 19.1 MPa. In the near-critical (9.3–10.5 MPa) region, the exciplex was more stable than that predicted by Kirkwood analysis, which means strong influence of local density augmentation around the exciplex. © 2002 Published by Elsevier Science B.V.

1. Introduction

Local density augmentation in the near-critical region of fluids has attracted much attention as a phenomena specific to the solvent state, and has been investigated by many techniques such as UV/Visible absorption [1], NMR [2], EPR [3], fluorescence [4,5], and molecular simulation [6]. Recently, we studied the pressure dependence of the formation and decay processes of exciplex between acetophenone (AP) and *N*,*N*,*N*′,*N*′-tetramethylbenzidine (TMB) in supercritical carbon dioxide (SC-CO_2) by a transient absorption technique [7]. The decay of the exciplex was determined by analyzing its lifetime, and was found to be very sensitive to the local environment. Evidence of local density augmentation around AP–TMB exciplex was apparent in the low-pressure region (9.0–10.8 MPa).

The microscopic structure around short-lived intermediate species, such as exciplex, is very important in understanding reaction mechanisms and can be affected by local density augmentation. In particular, the exciplex is a key intermediate of photoinduced electron transfer reactions, and due to its role in photochemical reactions and biological processes, the exciplex has been intensively studied in organic solvents by fluorescence [8], transient dc conductivity [9], and cyclic voltammetry [10]. SC-CO_2 can have significant advanta-

* Corresponding author. Fax: +81-22-237-5224.
E-mail address: t.aizawa@aist.go.jp (T. Aizawa).

0009-2614/02/$ - see front matter © 2002 Published by Elsevier Science B.V.
PII: S0009-2614(02)00526-2

ges over organic solvents, since its properties can be widely controlled with pressure [11]. However, relatively few studies exist on exciplexes in SC-CO_2. It is possible, that in our previous Letter [7], that the local density augmentation effects observed might represent an example specific to the system components. On the other hand, local density augmentation around exciplexes in supercritical fluids might be a more general phenomenon that could have wide implications in determining exciplex reaction rate, pathways, and mechanisms.

For this purpose, we investigated the photochemical reaction between anthracene and *N*,*N*-dimethylaniline (DMA), and used fluorescence lifetime measurements as an alternative technique to transient absorption to explore the possible generality of local density augmentation around exciplexes. Anthracene and DMA were chosen to study, since the anthracene–DMA exciplex has been well-studied in organic solvents [12–14]. Examining the peak shift of fluorescence is a popular method to analyze the local density augmentation of excited molecules in SC-CO_2 [15,16]. However, in this work, a lifetime analysis technique was adapted to anthracene–DMA exciplex, as this system exhibits a very broad fluorescence band. Kirkwood analysis [17] of the decay rate of exciplex provides information on the polarity change around the exciplex, which should be affected by the local density. In the near-critical region, the local density around solute molecules in SC-CO_2 is higher than the bulk density [1–6], and so it can be expected that the decay rate of the exciplex will change with conditions of the solvent.

2. Experimental

To follow exciplex decay, fluorescence lifetime analyses were carried out. Laser excitation was provided from a Nd:YAG laser (Spectra-Physics GCR-130) operated at 355 nm (90 mJ; pulse width 5–6 ns) with the time resolution of the system being limited only by the pulse width of the laser. A streak camera (Hamamatsu Photonics C4880) connected to a spectrometer (Chromex C5094) was used as a detector. Timing of the laser pulse was controlled to locate the scanning area of the streak camera. The high-pressure cell (ca 13 ml) fitted with a 'totsu'-window [18] was controlled to within ±0.1 K by a water-jacket. Anthracene (> 99%) and *N*,*N*-dimethylaniline (> 99%) were obtained from Nacalai Tesque (Tokyo) and used as received. Carbon dioxide (> 99.9%) was supplied by Sogo Sangyo (Sendai). Concentration of acetophenone was fixed at 5×10^{-4} M and two different concentrations (0.016 M and 0.032 M) of DMA were used. Further details on the procedure are given in previous Letter [7].

3. Results and discussion

Exciplex $(A\ DMA)^*$ in SC-CO_2 at 12.1 MPa showed emission over 350–550 nm range (Fig. 1). The excited state of anthracene was observed as shoulders at 375, 392, and 420 nm. For this case, the maximum point of exciplex fluorescence was 465 nm (Fig. 1, inset). Peak shape was similar for all pressures, and the maximum point at each pressure was used for each respective experiment.

Reaction between anthracene and DMA was represented by the following reaction scheme taken from the literature for non-polar solvents [14]:

$$A \xrightarrow{h\nu} A^*, \tag{1a}$$

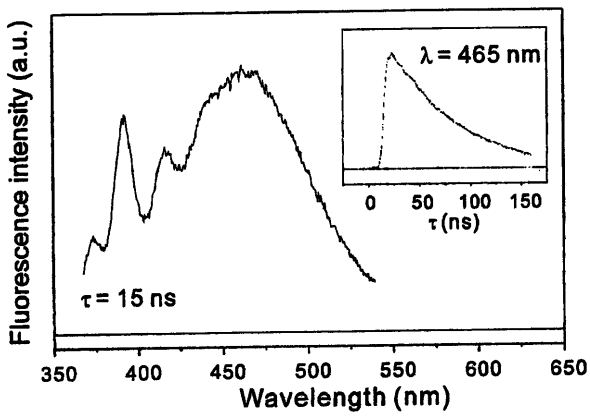

Fig. 1. Fluorescence spectrum of anthracene–DMA exciplex at 40 °C and 12.1 MPa. Concentration of DMA was 0.032 M. Inset shows time profile of emission of exciplex at 465 nm.

$$A^* + DMA \xrightarrow{k_1} (A\ DMA)^* \xrightarrow{k_2} A + DMA. \quad (1b)$$

In our work, excited state anthracene (A^*) was generated from anthracene (A) by laser irradiation at 355 nm. An exciplex $(A\ DMA)^*$ was formed by A^* and DMA, which subsequently underwent decay. In the experiments, fluorescence of each A^* and $(A\ DMA)^*$ were observed, however, radiative decay, which is not included in the scheme, was confirmed to be a minor reaction as described below.

Generation of $(A\ DMA)^*$ is a pseudo first-order reaction and is determined by k_1 and DMA concentration. For the case of exciplex formation being diffusion-controlled ($k_1 \approx 10^{11}\ M^{-1}\ s^{-1}$), formation of exciplex is less than 1 ns, which is well below the system time resolution for a concentration of 0.032 M DMA. Rise of the exciplex fluorescence (Fig. 1, inset) was determined by the laser pulse width. Time profiles of the exciplex were weak functions of DMA concentrations over the ranges examined. The intensity of A^* fluorescence at 0.016 M DMA was greater than that at 0.032 M DMA, but the intensity of $(A\ DMA)^*$ remained about the same, which means that practically the same yield of $(A\ DMA)^*$ was obtained under both conditions. This is strong evidence that radiative deactivation was a minor reaction. We measured A^* fluorescence under conditions of zero concentration DMA in SC-CO_2 at 12.1 MPa, and observed that the intensity was more than 30 times as strong as that in the mixture. Since the fluorescence quantum yield of anthracene in non-polar solvents like cyclohexane is approximately 0.24 [19,20], quantum yield of anthracene fluorescence in our system should be less than 0.01. This is further evidence that radiative deactivation was a minor reaction. Exciplex fluorescence intensity was weaker than that of the anthracene fluorescence, which was confirmed by the anthracene fluorescence remaining at the end of the laser pulse (Fig. 1). From these results, it became apparent that exciplex radiative decay was also a minor reaction under the given conditions.

Since the decay of the exciplex is a monomolecular reaction, reaction rate constant k_2 was obtained from exponential decay fitting of transient data after 30 ns. The decay rate constant k_2 of exciplex $(A\ DMA)^*$ decreased with increasing pressure, which can be attributed to the increase in the permittivity of the reaction medium. Kirkwood analysis was performed in a similar manner as that used in [7]:

$$\log(k_2/k_0) = -\frac{N_A}{4\pi\varepsilon_0 RT}\left(\frac{\mu^2}{r^3} - \frac{\mu^{\ddagger 2}}{r^{\ddagger 3}}\right)\left(\frac{\varepsilon - 1}{2\varepsilon + 1}\right), \quad (2)$$

where N_A is the Avogadro constant, ε_0 is the vacuum permittivity, μ and r are the electric dipole moment and radius of the reactant $(A\ DMA)^*$. In Eq. (2), $\mu^\ddagger$ and $r^\ddagger$ are the electric dipole moment and radius of the transition state, k_0 is the reaction rate constant for the case of no dipole moment change, and ε is the relative permittivity that was obtained from [21] with IUPAC density data [22]. The k_0 was arbitrarily set equal to unity as before [7]. Fig. 2 shows a plot of $\log(k_2/k_0)$ versus $(\varepsilon - 1)/(2\varepsilon + 1)$, where Eq. (2) was fit to the data in the high-pressure (10.5–19.1 MPa) region. Bera et al. [13] determined an exciplex dipole moment of 12.5 D (4.17×10^{-29} C m) with the assumption that both r and $r^\ddagger$ were equal to 4.8 Å according to the fluorescence peak shift in organic solvents. With the same assumption, the $(\mu^2 - \mu^{\ddagger 2})$ term was

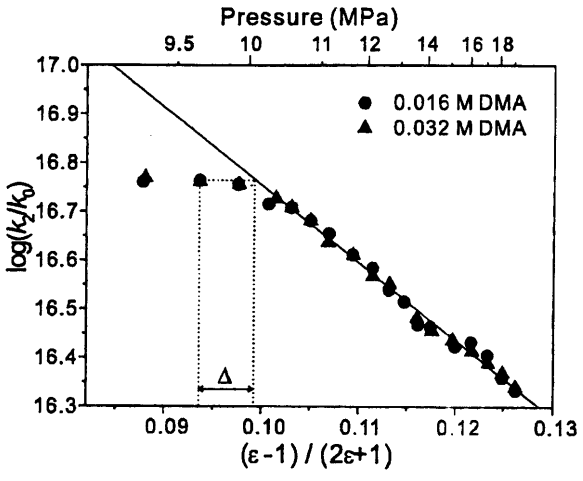

Fig. 2. Plot of $\ln(k_2/k_0)$ against $(\varepsilon - 1)/(2\varepsilon + 1)$. Circles: experimental results at 0.016 M DMA; triangles: experimental results at 0.032 M DMA; solid line: Kirkwood equation (Eq. (2)). The Δ gives the difference between the local environment and the bulk property at 9.6 MPa.

calculated in this work to be 75.9 D^2 (8.45×10^{-58} C^2 m^2). For the combination of μ and $\mu^\ddagger$ equal to 12.5 D (4.17×10^{-29} C m) and 9.0 D (2.99×10^{-29} C m), respectively, the $(\mu^2 - \mu^{\ddagger 2})$ term was calculated to be equal to 75.8 D, which is consistent with their results. In the low-pressure (9.3–10.5 MPa) region, experimental data were lower than calculated values from Eq. (2) using bulk permittivity, which means that the exciplex was in a higher permittivity environment over that of the bulk. This can be attributed to the effect of local density augmentation. The result that the lifetime of the exciplex was longer than that predicted by the Kirkwood analysis is caused by local density augmentation, and for this reason, the exciplex was stabilized. This kind of stability enhancement of solute molecules has also been observed for other systems in the form of an electronic spectral shift [23,24].

The dependence of $\log(k_2/k_0)$ versus $(\varepsilon - 1)/(2\varepsilon + 1)$ determined in this work showed a similar trend to that of our previous transient absorption analysis for AP–TMB exciplex [7], in which the local density augmentation around exciplex in SC-CO_2 occurred. In the anthracene–DMA system of this work, the difference in the polar scale between the local environment and the bulk property (Δ in Fig. 2) at 9.6 MPa was 0.006. In the AP–TMB system as determined by transient absorption analysis [7], this value was 0.003 at a pressure of 9.6 MPa. This shows that solvent aggregation around the anthracene–DMA exciplex was greater than that around the AP–TMB exciplex. It has been reported that local density augmentation around the anthracene molecule is much greater than that for benzene in SC-CO_2 [6]. This could be an additional factor in the higher local density augmentation around the anthracene–DMA exciplex.

4. Conclusions

Local density augmentation could be clearly observed in the fluorescence of anthracene–DMA exciplex decay rates in SC-CO_2. The exciplex was more stable than that predicted by Kirkwood analysis in the low-pressure region (9.3–10.5 MPa), which was caused by local density augmentation around the exciplex. Considering the previous data for the AP–TMB system, results in this work provide conclusive evidence of local density augmentation effects in exciplex decay processes.

Acknowledgements

This study was partially supported by Industrial Technology Research Grant Program in 2000 from the New Energy and Industrial Technology Development Organization (NEDO) of Japan and Core Research for Evolutional Science and Technology (CREST) from Japan Science and Technology Corporation (JST).

References

[1] J. Otomo, S. Koda, Chem. Phys. 242 (1999) 241.
[2] M. Kanakubo, T. Aizawa, T. Kawakami, O. Sato, Y. Ikushima, K. Hatakeda, N. Saito, J. Phys. Chem. B 104 (2000) 2749.
[3] J.L. deGrazia, T.W. Randolph, J.A. O'Brien, J. Phys. Chem. A 102 (1998) 1674.
[4] M. Khajehpour, J.F. Kauffman, Chem. Phys. Lett. 297 (1998) 141.
[5] H. Inomata, H. Hamatani, N. Wada, Y. Yagi, S. Saito, J. Phys. Chem. 97 (1993) 6332.
[6] W. Song, R. Biswas, M. Maroncelli, J. Phys. Chem. A 104 (2000) 6924.
[7] T. Aizawa, S. Janttarakeeree, Y. Ikushima, N. Saitoh, Chem. Phys. Lett. 354 (2002) 298.
[8] R.P. Herbrich, R. Schmidt, J. Photochem. Photobiol. A: Chem. 133 (2000) 149.
[9] S.E. Mylon, S.N. Smirnov, C.L. Braun, J. Phys. Chem. A 102 (1998) 6558.
[10] S. Wang, G.C. Bazan, Chem. Phys. Lett. 333 (2001) 437.
[11] P.G. Jessop, W. Leitner (Eds.), Chemical Synthesis Using Supercritical Fluids, Wiley-VCH, Weinhein, 1999.
[12] N. Ghoneim, Spectrochim. Acta, Part A 57 (2001) 483.
[13] P.K. Bera, D. Nath, A. Misra, M. Chowdhury, J. Photochem. Photobiol. A: Chem. 95 (1996) 127.
[14] U.P. Agarwal, H. Jagannath, D.R. Rao, J. Chem. Soc., Faraday Trans. II 73 (1977) 1020.
[15] R. Biswas, J.E. Lewis, M. Maroncelli, Chem. Phys. Lett. 310 (1999) 485.
[16] K. Takahashi, K. Fujii, S. Sawamura, C.D. Jonah, Radiat. Phys. Chem. 55 (1999) 579.
[17] J.G. Kirkwood, J. Chem. Phys. 2 (1934) 351.
[18] T. Aizawa, Y. Ikushima, N. Saitoh, Rev. Sci. Instrum. (2002) (submitted).

[19] R.P. DeToma, D.O. Cowan, J. Am. Chem. Soc. 97 (1975) 3283.
[20] N.I. Nijegorodov, W.S. Downey, J. Phys. Chem. 98 (1994) 5639.
[21] T. Moriyoshi, T. Kita, Y. Uosaki, Ber. Bunsenges. Phys. Chem. 97 (1993) 589.
[22] PROPATH Group, PROPATH: A Program Package for Thermophysical Properties, version 10.2, July, 1997.
[23] K. Takahashi, K. Abe, S. Sawamura, C.D. Jonah, Chem. Phys. Lett. 282 (1998) 361.
[24] J.K. Rice, E.D. Niemeyer, R.A. Dunbar, F.V. Bright, J. Am. Chem. Soc. 117 (1995) 5832.

New Treatment Method for Dilute Hydrochloric Acid Using Magnesium-Aluminum Oxide

Tomohito Kameda,*# Toshiaki Yoshioka, Miho Uchida, Yoshinori Miyano, and Akitsugu Okuwaki

Department of Applied Chemistry, Graduate School of Engineering, Tohoku University, Aoba 07, Aoba-ku, Sendai 980-8579

(Received July 13, 2001)

Magnesium-aluminum oxide (Mg-Al oxide) was shown to be superior to CO_3^{2-} intercalated hydrotalcite (CO_3-HT) for removing dilute hydrochloric acid. Cl^- in a 0.5 M HCl solution could be quantitatively removed by adding 1.75-times the stoichiometric quantity of $Mg_{0.70}Al_{0.20}O$ at 60 °C for 1 h. The solution after the reaction was weakly alkaline. This reaction could be adequately described as being first order for the HCl concentration, and the apparent activation energy was 49.3 kJ mol^{-1}. The amount of Cl^- removal per 1 g of Mg-Al oxide in the first use was 3.08 meq at a Mg/Al molar ratio of 2.0 and 2.89 meq at a ratio of 3.5.

HT ($[Mg^{2+}_{1-x}Al^{3+}_x(OH)_2](A^{n-})_{x/n}\cdot mH_2O$: $0.20 \leqq x \leqq 0.33$) is a layered double hydroxide with anion-exchange properties.[1] CO_3-HT transforms into Mg-Al oxide when heated to 450–800 °C, as expressed by[2]

$$Mg_{1-x}Al_x(OH)_2(CO_3)_{x/2} \rightarrow (1 + x/2)Mg_{2(1-x)/(2+x)}Al_{2x/(2+x)}O + x/2CO_2 + H_2O. \quad (1)$$

The Mg-Al oxide can intercalate anions in solution, and then the original HT structure can be reconstructed, as expressed by[2-4]

$$(1 + x/2)Mg_{2(1-x)/(2+x)}Al_{2x/(2+x)}O + x/n\,A^{n-} + (1 + x/2)H_2O \rightarrow [Mg_{1-x}Al_x(OH)_2]A_{x/n} + xOH^-. \quad (2)$$

The feature of this reaction is the release of OH^- along with the intercalation of anions, and it is known that the selectivity of anion intercalation into the Mg-Al oxide increases with increasing charge density of the anion.[2] In the case of anions whose charge density is smaller than that of OH^-, $OH^- > F^- > Cl^- > Br^- > NO_3^- > I^-$, the Mg-Al oxide preferentially intercalates the released OH^- rather than those anions in a neutral solution. Therefore, the Mg-Al oxide can not be used as a remover of those anions in a neutral solution. In addition, because the solution after the reaction is strongly alkaline, it is difficult to apply Mg-Al oxide for treating a waste neutral saline solution. Accordingly, we propose that the Mg-Al oxide can be utilized for waste acid treatment as both a neutralizer and a fixative of anions.

There have been many studies on the reaction for such neutral saline solutions as NaCl, Na_2SO_4 and $NaNO_3$.[3-5] In contrast, no study had been made for an acidic solution below pH 2. We have thus reported briefly on this matter recently.[6] In this study, Mg-Al oxide was applied for treating dilute hydrochloric acid. The effects of the time, Mg-Al oxide quantity, HCl concentration, and temperature on Cl^- removal were revealed in detail. The difference on Cl^- removal between CO_3-HT and Mg-Al oxide was also examined.

Experimental

CO_3-HTs were prepared by a common precipitation method.[7] Mixed $Mg(NO_3)_2\cdot 6H_2O$ and $Al(NO_3)_3\cdot 9H_2O$ solutions with Mg/Al molar ratios of 3.5 and 2.0 were added to 1.0 M Na_2CO_3 solutions. When the pH of the mixture was lower than 10, a solution of 2.0 M NaOH was added to maintain the pH at 10.0. The mixture was stirred and aged for a certain period of time, and the resulting product was washed, dried and calcined at 500 °C for 1 h. 0.01–0.5 M HCl solutions (10 mL) and $[Mg_{0.70}Al_{0.20}(OH)_{1.80}](CO_3)_{0.10}$, $Mg_{0.70}Al_{0.20}O$ or $Mg_{0.58}Al_{0.28}O$ of 0.5–2.0 times the stoichiometric quantity, according to Eqs. 3–5, were placed in a 50 ml screw tube and shaken at 25–80 °C for 0.2–3 h.

$$[Mg_{0.70}Al_{0.20}(OH)_{1.80}](CO_3)_{0.10} + 0.20HCl \rightarrow [Mg_{0.70}Al_{0.20}(OH)_{1.80}]Cl_{0.20} + 0.10CO_2 + 0.10H_2O \quad (3)$$

$$Mg_{0.70}Al_{0.20}O + 0.20HCl + 0.80H_2O \rightarrow [Mg_{0.70}Al_{0.20}(OH)_{1.80}]Cl_{0.20} \quad (4)$$

$$Mg_{0.58}Al_{0.28}O + 0.28HCl + 0.72H_2O \rightarrow [Mg_{0.58}Al_{0.28}(OH)_{1.72}]Cl_{0.28} \quad (5)$$

The pH of the solution was measured after the reaction, and the Cl^- concentration was determined by ion chromatography. The degrees of Mg^{2+} and Al^{3+} leaching were determined by ICP-AES. The precipitates were identified by X-ray diffraction (XRD).

Results and Discussion

1. Difference between CO_3-HT and Mg-Al Oxide. Figure 1 shows the effect of time on Cl^- removal using $Mg_{0.70}Al_{0.20}O$ or $[Mg_{0.70}Al_{0.20}(OH)_{1.80}](CO_3)_{0.10}$ of 1.75-times

Present adress; Institute of Multidisciplinary Research for Advanced Materials, Tohoku University, 1,1 Katahira, 2-Chome, Aoba-ku, Sendai 980-8577

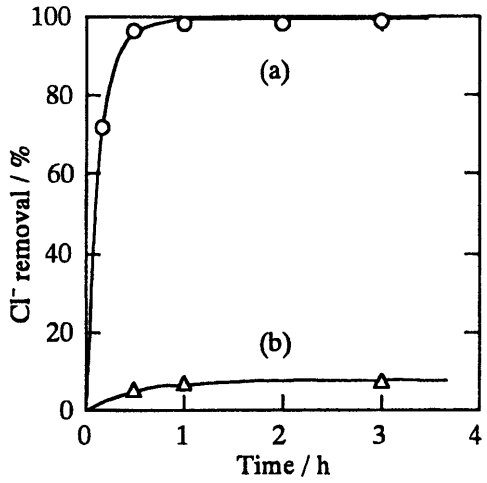

Fig. 1. Effect of time on Cl^- removal using (a) $Mg_{0.70}Al_{0.20}O$ or (b) $[Mg_{0.70}Al_{0.20}(OH)_{1.80}](CO_3)_{0.10}$ of 1.75-times the stoichiometric quantity. HCl concd: 0.5 M, Temp.:60 °C.

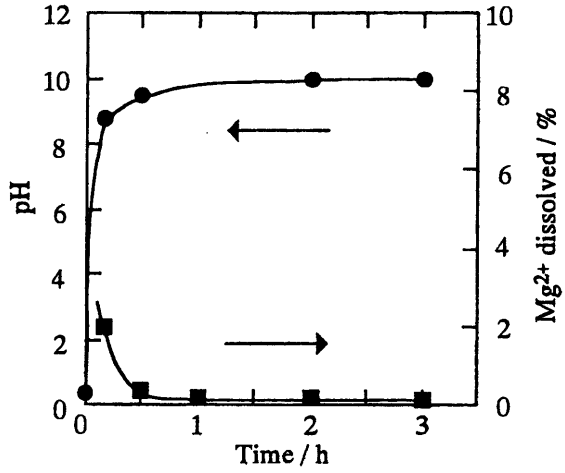

Fig. 2. Effect of time on the pH or Mg^{2+} dissolved using $Mg_{0.70}Al_{0.20}O$ of 1.75-times the stoichiometric quantity. HCl concd: 0.5 M, Temp: 60 °C.

the stoichiometric quantity. The CO_3-HT removed hydrochloric acid slightly. When a 0.1 M HCl solution (20 mL) and CO_3-HT of the stoichiometric quantity were shaken at 37 °C, Cl^- was removed 55% by an exchange reaction of HCl and CO_3^{2-}, as shown in Eq. 3.[8] Because the HCl concentration was high in this study, it is conjectured that the CO_3-HT was mainly dissolved in addition to the slight exchange reaction. From the fact that the solution after the reaction was neutral, it may be deduced that Cl^- could hardly exchange with the CO_3^{2-}.

In contrast, $Mg_{0.70}Al_{0.20}O$ exhibited a much higher degree of Cl^- removal, and Cl^- was quantitatively removed above 1 h. Figure 2 shows the effect of time on the pH or Mg^{2+} dissolved using $Mg_{0.70}Al_{0.20}O$ of 1.75-times the stoichiometric quantity. The pH was rapidly increased and kept constant at about 10. Although Mg from $Mg_{0.70}Al_{0.20}O$ was dissolved at first, the dissolution was not recognized after 1 h. The precipitate after 1 h

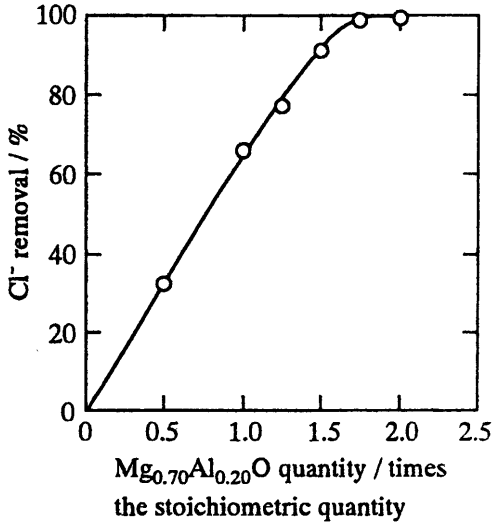

Fig. 3. Effect of the $Mg_{0.70}Al_{0.20}O$ quantity on Cl^- removal. HCl concd: 0.5 M, Temp: 60 °C, Time: 3 h.

was a mixture of HT and a slight amount of $Mg(OH)_2$. The reaction until about 0.2 h was interpreted by both the intercalation of Cl^- and the dissolution of $Mg_{0.70}Al_{0.20}O$, as expressed in Eq. 4 and

$$Mg_{0.70}Al_{0.20}O + H_2O \rightarrow 0.70Mg^{2+} + 0.20Al^{3+} + 2OH^-. \quad (6)$$

It is conjectured that Cl^- was removed as follows at 0.2–1 h:

$$Mg_{0.70}Al_{0.20}O + 0.10Mg^{2+} + 0.20Cl^- + H_2O \rightarrow [Mg_{0.70}Al_{0.20}(OH)_{1.80}]Cl_{0.20} + 0.10Mg(OH)_2. \quad (7)$$

Since the dissolution of Al was not recognized at 0.2 h, it is supposed that Al was promptly hydrolyzed.

In sum, because an increase in the OH^- concentration was prevented by the precipitation of $Mg(OH)_2$, as expressed in Eq. 7, it may be concluded that Cl^- was easily intercalated into $Mg_{0.70}Al_{0.20}O$ for a small amount of OH^-.

2. Dilute Hydrochloric Acid Removal Using Mg-Al Oxide. Figure 3 shows the effect of the $Mg_{0.70}Al_{0.20}O$ quantity on Cl^- removal. Cl^- removal increased with increasing $Mg_{0.70}Al_{0.20}O$ quantity, and Cl^- was removed above 99% adding $Mg_{0.70}Al_{0.20}O$ of 1.75-times the stoichiometric quantity. However, Cl^- was not quantitatively removed at the stoichiometric quantity. This was due to the formation of OH-HT, as expressed by

$$Mg_{0.70}Al_{0.20}O + H_2O \rightarrow [Mg_{0.70}Al_{0.20}(OH)_{1.80}](OH)_{0.20} \quad (8)$$

after the release of OH^-, as expressed by

$$Mg_{0.70}Al_{0.20}O + 0.20Cl^- + H_2O \rightarrow [Mg_{0.70}Al_{0.20}(OH)_{1.80}]Cl_{0.20} + 0.20OH^-. \quad (9)$$

Additionally, this is also attributable to the dissolution of

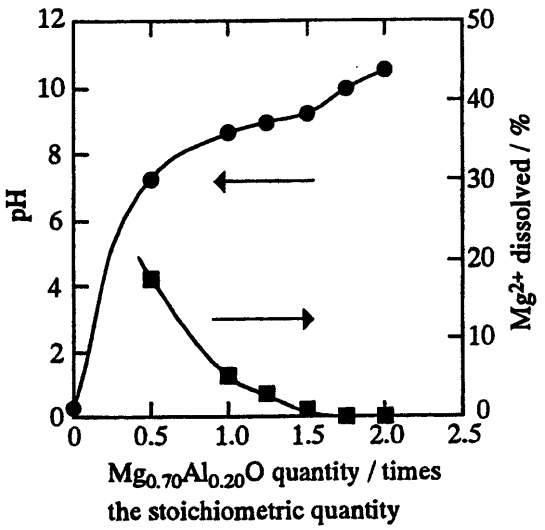

Fig. 4. Effect of the $Mg_{0.70}Al_{0.20}O$ quantity on the pH or Mg^{2+} dissolved. HCl concd: 0.5 M, Temp: 60 °C, Time: 3 h.

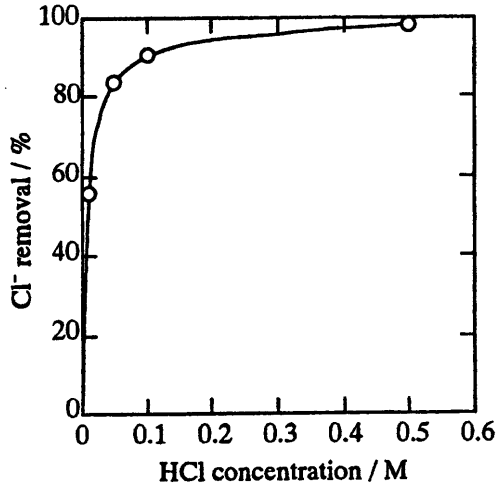

Fig. 5. Effect of the HCl concentration on Cl^- removal using $Mg_{0.70}Al_{0.20}O$ of 1.75-times the stoichiometric quantity. Temp: 60 °C, Time: 1 h.

$Mg_{0.70}Al_{0.20}O$. About 5% of Mg was dissolved at the stoichiometric quantity, as shown in Fig. 4. Considering the formation of OH-HT and the dissolution of Mg, Mg-Al oxide is required above the stoichiometric quantity for a quantitative removal of Cl^-.

Figure 5 shows the effect of the HCl concentration on Cl^- removal using $Mg_{0.70}Al_{0.20}O$ of 1.75-times the stoichiometric quantity. Cl^- removal increased with increasing HCl concentration. With increasing HCl concentration, the concentration of Cl^- should be higher than that of OH^- at the pH at which the once dissolved Mg^{2+} catch the released OH^- to precipitate as $Mg(OH)_2$. Consequently, it can be stated that Cl^- was easily intercalated into $Mg_{0.70}Al_{0.20}O$. The intercalation capacity of Mg-Al oxide for Cl^- has been investigated in a NaCl solution,[3-5] and it is known that Cl^- removal is low, since OH^- is

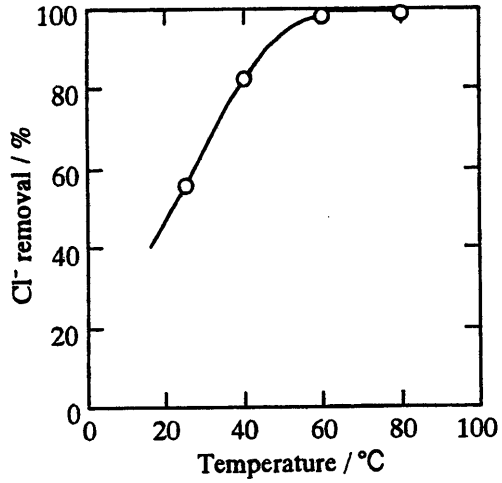

Fig. 6. Effect of the temperature on Cl^- removal using $Mg_{0.70}Al_{0.20}O$ of 1.75-times the stoichiometric quantity. HCl concnd: 0.5 M, Time: 1 h.

mainly intercalated due to an increase in the OH^- concentration due to the formation of NaOH, as expressed by

$$Mg_{0.70}Al_{0.20}O + 0.20NaCl + H_2O \rightarrow [Mg_{0.70}Al_{0.20}(OH)_{1.80}]Cl_{0.20} + 0.20NaOH. \quad (10)$$

It must be emphasized that the capacity of Mg-Al oxide for Cl^- removal could be attained maximally in a strong hydrochloric acid below 0.1 M.

Figure 6 shows the effect of the temperature on Cl^- removal using $Mg_{0.70}Al_{0.20}O$ of 1.75-times the stoichiometric quantity. Cl^- removal increased with increasing temperature, and Cl^- was quantitatively removed above 60 °C. The thermostable temperature of the anion-exchange resin is below 60 °C. It should be noted that a hydrochloric acid treatment at over 60 °C is possible using Mg-Al oxide instead of the resin.

From the fact that the removal rate of Cl^- was fast with increasing temperature, it is implied that this reaction proceeded under chemical reaction control. The Cl^- removal rate at 25–60 °C was arranged according to the following equation using the results shown in Fig. 1 and 6:

$$-\ln(1-x) = kt, \quad (11)$$

where x is the degree of Cl^- removal, and k (min^{-1}) is the apparent rate constant. Figure 7 shows a first-order plot of Cl^- removal using $Mg_{0.70}Al_{0.20}O$ of 1.75-times the stoichiometric quantity. This reaction is described as being first order for the HCl concentration because of the good linearity at each temperature. An Arrhenius plot of k, determined from the slope of the straight lines in Fig. 7, is shown in Fig. 8. The apparent activation energy was 49.3 kJ mol^{-1}. This value confirms that Cl^- removal by Mg-Al oxide proceeded under chemical reaction control.

3. An Application of Mg-Al Oxide to Dilute Waste Hydrochloric Acid Treatment. Table 1 gives the amounts of Cl^- removed per 1 g of Mg-Al oxide in the first use. The Mg-Al oxide has a large capacity for removing Cl^- relatively, be-

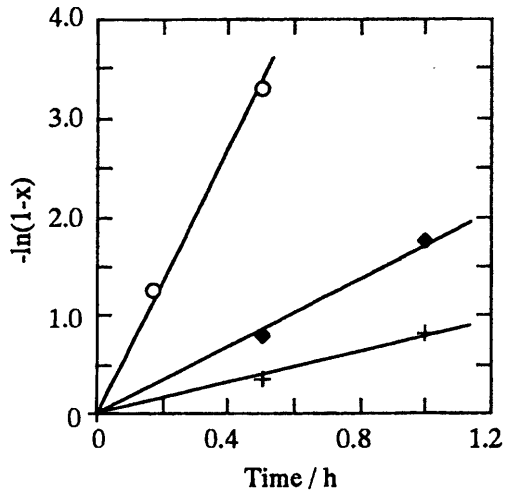

Fig. 7. First-order plot of Cl^- removal using $Mg_{0.70}Al_{0.20}O$ of 1.75-times the stoichiometric quantity. HCl concd: 0.5 M.

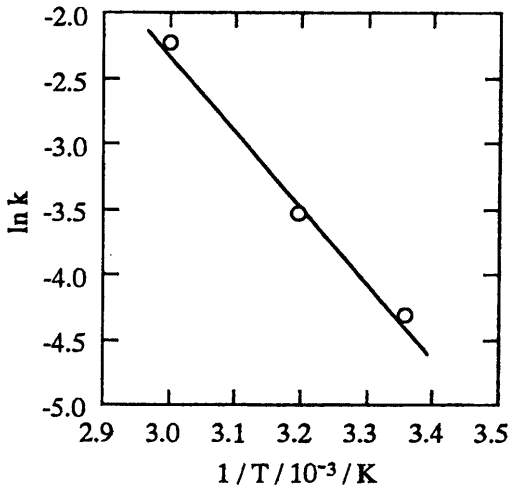

Fig. 8. Arrhenius plot of the apparent rate constant of Cl^- removal using $Mg_{0.70}Al_{0.20}O$ of 1.75-times the stoichiometric quantity. HCl concd: 0.5 M.

Table 1. Amounts of Cl^- Removed per 1 g of Mg-Al Oxide in the First Use

Mg/Al molar ratio in Mg-Al oxide	mg/g	meq/g
2.0	109	3.08
3.5	103	2.89

HCl concd: 0.5 M, Temp: 60 °C, Time: 1 h,
Mg-Al oxide: 1.75-times the stoichiometric quantity.

cause the ion-exchange capacity of the anion-exchange resin is 3.5 (meq/g). A Mg-Al oxide at Mg/Al molar ratio of 2.0 has a larger capacity for removing Cl^- than that at 3.5. However, it is advisable utilizing Mg-Al oxide with a large Mg/Al molar ratio for practical use, since the price of Al is higher than that of Mg.

An exaust gas containing hydrogen chloride from garbage incinerators is generally treated by blowing slaked lime powder, and the produced calcium chloride etc. are discharged into landfill.[9] However, the calcium chloride generates highly concentrated saline leachate, and the leachate becomes a cause of damage from salt to the surrounding water environment.[10,11] We thus propose that Mg-Al oxide can be applied for treating hydrochloric acid produced by washing waste hydrogen chloride with venturis scrubbers. After this treatment and a filtration process, the produced Cl-HT can be used as an ion exchanger for removing phosphorus to prevent eutrophication of surface water by an algae bloom.[12,13] It is known that the use of Cl-HT in various anion intercalated HTs is suitable for treating phosphate ion.[12] In the case of calcining Cl-HT at 450–800 °C, Mg-Al oxide can be reproduced with hydrochloric acid.[14,15] This reproduction method doesn't produce any new drainage, contrary to the reproduction of an ion-exchange resin. The reproduced Mg-Al oxide can be used for another treatment.

Conclusion

From the present results concerning the removal of dilute hydrochloric acid using Mg-Al oxide, the following conclusions may be drawn:

1. Mg-Al oxide was superior to CO_3-HT as a remover of dilute hydrochloric acid.
2. 0.5 M hydrochloric acid could be quantitatively removed by adding 1.75-2 times the stoichiometric quantity of $Mg_{0.70}Al_{0.20}O$ at 60–80 °C over a period of 1 h.
3. The reaction of Cl^- removal by Mg-Al oxide could be adequately described by first order for the HCl concentration. The apparent activation energy was 49.3 kJ mol^{-1}.
4. The amount of Cl^- removal per 1 g of Mg-Al oxide in the first use was 3.08 meq at a Mg/Al molar ratio of 2.0, and 2.89 meq at a ratio of 3.5.

References

1 S. Miyata, *Clays Clay Miner.*, **28**, 50 (1980).
2 S. Miyata, *Clays Clay Miner.*, **31**, 305 (1983).
3 T. Sato, T. Wakabayashi, and M. Shimada, *Ind. Eng. Chem. Prod. Res. Dev.*, **25**, 89 (1986).
4 T. Sato, M. Tezuka, T. Endo, and M. Shimada, *React. Solids*, **3**, 287 (1987).
5 T. Sato, S. Onai, T. Yoshioka, and A. Okuwaki, *J. Chem. Tech. Biotechnol.*, **57**, 137 (1993).
6 T. Kameda, Y. Miyano, T. Yoshioka, M. Uchida, and A. Okuwaki, *Chem. Lett.*, **2000**, 1136.
7 S. K. Yun, and T. J. Pinnavaia, *Chem. Mater.*, **7**, 348 (1995).
8 Y. Takagishi, K. Iwamoto, and H. Maekawa, *Yakuzaigaku*, **38**, 166 (1978).
9 M. Shigaki, "Etokihaikibutsunosyoukyakugijyutsu." Ohmsha, Japan (1998), p.87.
10 F. Takano, T. Shoji, and T. Komatsu, *Haikibutsugakkaishi*, **8**, 523 (1997).
11 Y. Horii, S. Higuchi, T. Shimaoka, and M. Hanashima, *Haikibutsugakkaishi*, **8**, 529 (1997).
12 H. Shin, M. Kim, S. Nam, and H. Moon, *Water Sci. Tech.*, **34**, 161 (1996).
13 A. Kawamoto, A. Ookubo, T. Sato, and T. Suzuki, *Mizu-*

kannkyougakkaishi, **22**, 875 (1999).
14 V. R. L. Constantino, and T. J. Pinnavaia, *Inorg. Chem.*, **34**, 883 (1995).
15 S. Miyata, *Clays Clay Miner.*, **23**, 369 (1975).

Phosphorus, Sulfur and Silicon, 2002, Vol. 177:1503–1506

1042-6507/02 $12.00 + .00
DOI: 10.1080/10426500290093469

SYNTHESIS OF HYDROTALCITE FROM SEAWATER AND ITS APPLICATION TO PHOSPHORUS REMOVAL

Tomohito Kameda,[a,b] *Toshiaki Yoshioka,*[a] *Miho Uchida,*[a] *and Akitsugu Okuwaki*[a]
Department of Applied Chemistry, Graduate School of Engineering, Tohoku University, Aoba 07, Aoba-ku, Sendai 980-8579, Japan[a] *and Institute of Multidisciplinary Research for Advanced Materials, Tohoku University, 1,1 Katahira, 2-Chome, Aoba-ku, Sendai 980-8577, Japan*[b]

(Received July 28, 2001; accepted December 25, 2001)

*10.0 wt% milk of lime was added to seawater containing $AlCl_3$ at Mg/Al molar ratio of 3.0 until pH 10.5 with stirring, and kept at 25°C for 1 h. Hydrotalcite (HT) was precipitated as a single phase, and Mg^{2+} and Al^{3+} were quantitatively precipitated. The chemical composition was $[Mg_{0.75}Al_{0.25}(OH)_2](SO_4)_{0.06}(Cl)_{0.02}(OH)_{0.11}^{*}]\cdot 0.27H_2O^{*}$ (*Balance). A 100 mg-P/L Na_2HPO_4 solution and the HT were shaken at 25°C. Phosphate removal increased with increasing time and the HT quantity, and was the highest at pH 7–9. Phosphate ion could be quantitatively removed, adding 8 times the stoichiometric quantity of the HT at pH 8.7 for 6 h.*

Keywords: Anion exchange; hydrotalcite; milk of lime; phosphorus removal; seawater; synthesis

INTRODUCTION

In order to prevent eutrophication, it is considered to reduce the load of phosphorus to water environment. One method is the removal of phosphate ion by HT ($[Mg^{2+}_{1-x}Al^{3+}_x(OH)_2](A^{n-})_{x/n}\cdot mH_2O$:$0.20 \leqq x \leqq 0.33$), which is a layered double hydroxide with anion exchange property;[1,2] however, HT is an expensive material used as antacid, etc.,[3] and it is necessary to develop new process for inexpensive HT. In this study, HT was synthesized using seawater and milk of lime in consideration for the utilization of plant-producing $Mg(OH)_2$, and the characteristic of phosphate removal by the HT was examined.

Address correspondence to T. Kameda. E-mail: kameda@tagen.tohoku.ac.jp

TABLE I The Compositions of Seawaters (mM)

Seawater	Na^+	K^+	Mg^{2+}	Ca^{2+}	SO_4^{2-}	Cl^-	Br^-
Artificial	466	0	53	10	28	536	0
Natural	424	9	48	11	25	500	1

EXPERIMENTAL

1. Synthesis of HT from Seawater (Seawater-Milk of Lime Process)

Table I shows the compositions of seawaters. 0.7–10.0 wt% $Ca(OH)_2$ slurry or $Ca(OH)_2$ powder were added to artificial or natural seawater containing $AlCl_3$ at Mg/Al molar ratio of 1.0–5.0 until pH 10.5 or stoichiometric amounts with stirring and kept at 25°C or 60°C for 1 h. Precipitates were filtered, washed with water, dried at 105°C for 24 h, and then identified by X-ray diffraction (XRD). Chemical composition of filtrates and precipitates was determined by ICP-AES and ion chromatography.

2. The Application of HT Prepared with the New Process to Phosphorus Removal

The $[Mg_{0.75}Al_{0.25}(OH)_2][(SO_4)_{0.06}(Cl)_{0.02}(OH)^*_{0.11}] \cdot 0.27H_2O^*$ ($HT_{(SW)}$) was applied to phosphorus removal. $HT_{(SW)}$ of 1–8 times the stoichiometric quantity were added to a 100 mg-P/L Na_2HPO_4 solution (15 ml) according to eq. (1) at pH 7.1–13.3, and they were shaken at 25°C for 6 h:

$$[Mg_{0.75}Al_{0.25}(OH)_2][(Cl)_{0.02}(SO_4)_{0.06}(OH)_{0.11}] + 0.125HPO_4^{2-} \rightleftarrows [Mg_{0.75}Al_{0.25}(OH)_2][(HPO_4)_{0.125}] + 0.02Cl^- + 0.06SO_4^{2-} + 0.11OH^-. \quad (1)$$

After the filtration, chemical composition of filtrates was determined by ion chromatography.

RESULTS AND DISCUSSION

1. Synthesis of HT from Seawater (Seawater-Milk of Lime Process)

1-1. The Effect of Mg/Al Molar Ratio in Solution (Artificial Seawater, 0.7 wt% $Ca(OH)_2$ Slurry, 60°C)

HT was precipitated as a single phase at Mg/Al molar ratio of 2.0–4.0, although a small amount of $Al(OH)_3$ was precipitated at 1.0 and

a small amount of $Mg(OH)_2$ was precipitated at 4.5–5.0. As increasing Mg/Al molar ratio in solution, Al^{3+} precipitated increased and Mg^{2+} precipitated decreased. Mg^{2+} and Al^{3+} were quantitatively precipitated at 2.4–3.0.

1-2. The Effect of $Ca(OH)_2$ Slurry Concentration (Artificial Seawater, Mg/Al Molar Ratio of 3.0 in Solution, 25°C)

HT was precipitated as a single phase using 0.7–10.0 wt% $Ca(OH)_2$ slurry and even $Ca(OH)_2$ powder. Mg^{2+} and Al^{3+} were quantitatively precipitated.

1-3. Synthesis of HT from Natural Seawater (Mg/Al Molar Ratio of 3.0 in Solution, 10.0 wt% $Ca(OH)_2$ Slurry, 25°C)

HT ($HT_{(SW)}$) was also precipitated as a single phase from natural seawater, as well as from artificial seawater, and Mg^{2+} and Al^{3+} were quantitatively precipitated. The chemical composition of $HT_{(SW)}$ was $[Mg_{0.75}Al_{0.25}(OH)_2][(SO_4)_{0.06}(Cl)_{0.02}(OH)_{0.11}{}^*] \cdot 0.27H_2O^*$ (*Balance). The ratio of SO_4^{2-} to Cl^- in the interlayer was high. This is because the charge density of SO_4^{2-} is larger than that of Cl^-. Anion is easily intercalated into HT, as the charge density is larger.[4]

2. The Application of HT Prepared with the New Process to Phosphorus Removal

Figure 1 shows the effect of $HT_{(SW)}$ quantity on phosphate removal. Phosphate removal increased with increasing the $HT_{(SW)}$ quantity, and

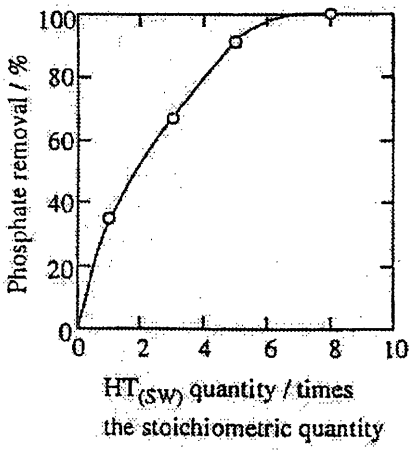

FIGURE 1 Effect of $HT_{(SW)}$ quantity on phosphate removal (pH 8.7).

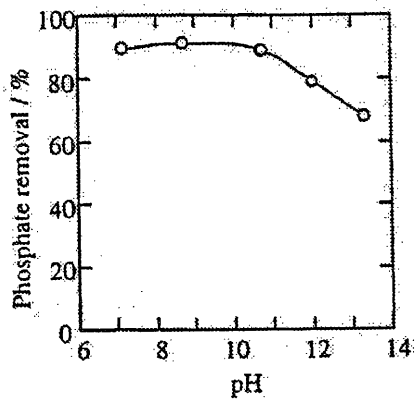

FIGURE 2 Effect of pH on phosphate removal using $HT_{(SW)}$ of 5 times the stoichiometric quantity.

phosphate ion could be quantitatively removed by adding 8 times the stoichiometric quantity of $HT_{(SW)}$; however, phosphate ion was not quantitatively removed at the stoichiometric quantity. The ionic species of phosphate at pH 8.7 are mainly HPO_4^{2-}. Because the anion size of HPO_4^{2-} is almost close to that of SO_4^{2-},[5] it is supposed that HPO_4^{2-} was not much exchanged for SO_4^{2-} in $HT_{(SW)}$. Figure 2 shows the effect of pH on phosphate removal. Phosphate removal was the highest at pH 7–9 and decreased with increasing pH. The ionic species of phosphate at pH 13.3 are mainly PO_4^{3-}. Although the charge density of PO_4^{3-} is larger than that of SO_4^{2-}, the phosphate removal was the lowest. Because of the large amounts of OH^- at the pH, it is supposed that OH^- was mainly intercalated into $HT_{(SW)}$, and the intercalation of PO_4^{3-} was prevented. In contrast, although the existence ratio of HPO_4^{2-} was low since the ionic species at pH 7.1 were a mixture of HPO_4^{2-} (44%) and $H_2PO_4^-$ (56%), the phosphate removal at pH 7.1 was almost as same as that at pH 8.7. This is attributable to the increase in the HPO_4^{2-} in solution with the deintercalation of OH^- in $HT_{(SW)}$.

REFERENCES

[1] A. Kawamoto, A. Ookubo, T. Sato, and T. Suzuki, *Mizukannkyougakkaishi*, **22**, 875 (1999).
[2] H. Shin, M. Kim, S. Nam, and H. Moon, *Water Sci. Tech.*, **34**, 161 (1996).
[3] F. Cavani, F. Trifiro, and A. Vaccari, *Catal. Today*, **11**, 173 (1991).
[4] S. Miyata, *Clays Clay Miner.*, **31**, 305 (1983).
[5] T. Sato, T. Wakabayashi, and M. Shimada, *Ind. Eng. Chem., Process Des. Dev.*, **25**, 89 (1986).

JOURNAL OF MATERIALS SCIENCE LETTERS 21, 2002, 1747–1749

Hydrotalcite synthesis using calcined dolomite as a magnesium and alkali resource

T. KAMEDA*
Department of Applied Chemistry, Graduate School of Engineering, Tohoku University, Aoba 07, Aoba-ku, Sendai, 980-8579, Japan; Institute of Multidisciplinary Research for Advanced Materials, Tohoku University, 1,1 Katahira 2-Chome, Aoba-ku, Sendai, 980-8577, Japan
E-mail: kameda@tagen.tohoku.ac.jp

T. YOSHIOKA, M. UCHIDA, A. OKUWAKI
Department of Applied Chemistry, Graduate School of Engineering, Tohoku University, Aoba 07, Aoba-ku, Sendai, 980-8579, Japan

Hydrotalcite (HT) ($[Mg^{2+}_{1-x}Al^{3+}_x(OH)_2](A^{n-})_{x/n}\cdot mH_2O$) is a layered double hydroxide with anion exchange properties [1–4], and CO_3^{2-} intercalated HT (CO_3^{2-}-HT) has been used as an antacid and a flame retardant [5]. Since HT has excellent heat- and radiation-resisting properties that far exceed its properties as an ion exchange resin, it is thought that it can be used to remove toxic anionic species from wastewater [6–12]. In the industry today, CO_3^{2-}-HT has been produced using the general reagent at temperatures above 80 °C, and furthermore purified [13]. However, because a large amount of HT is required in case of using HT for the preservation of water environment, it is thought that the above process is not suitable for treating wastewater. Additionally, the large charge density of CO_3^{2-}-HT makes it difficult to use as an anion exchanger, since the anion with the lesser charge density will not readily exchange with the larger-charged intercalated anion [14]. CO_3^{2-}-HT can be transformed into magnesium-aluminum oxide (Mg-Al oxide) when heated to 450–800 °C as expressed in Equation 1 [15–18]:

$$Mg_{1-x}Al_x(OH)_2(CO_3)_{x/2} \rightarrow Mg_{1-x}Al_xO_{1+x/2} + x/2CO_2 + H_2O \quad (1)$$
$$0.20 \leqq x \leqq 0.33$$

Once in solution, the Mg-Al oxide can intercalate anions (A^{n-}) leading to regeneration of the original HT structure, as demonstrated in Equation 2 [15–18]:

$$Mg_{1-x}Al_xO_{1+x/2} + x/n\,A^{n-} + (1+x/2)H_2O \rightarrow Mg_{1-x}Al_x(OH)_2(A)_{x/n} + xOH^- \quad (2)$$
$$0.20 \leqq x \leqq 0.33$$

In summary, for anion removal, CO_3^{2-}-HT can only be used as a precursor of Mg-Al oxide. Therefore, a new synthetic process for treating wastewater must be developed.

In the laboratory, HT is usually synthesized by mixing alkali solutions, such as NaOH, with Mg^{2+}-Al^{3+} solutions, such as $MgCl_2$-$AlCl_3$ [19]. A few studies have described commercial-scale production of HT. For example, $Mg(OH)_2$, $MgCO_3$, and MgO were all tested as new magnesium sources and $NaAlO_2$ and $Al(OH)_3$ as new aluminum sources [20–22]. These synthetic processes require very long reaction times at 95–100 °C in order to obtain a single-phase HT precipitate.

This study examined the possibility of synthesizing HT as a single phase using calcined dolomite as a new magnesium and alkali source. Calcined dolomite consists of a mixture of CaO and MgO. The stoichiometric equation describing the synthesis of HT is:

$$(1-x)Mg^{2+} + xAl^{3+} + 2OH^- + (x/n)A^{n-} \rightarrow Mg_{1-x}Al_x(OH)_2(A)_{x/n} \quad (3)$$
$$0.20 \leqq x \leqq 0.33 \quad (A^{n-}: n \text{ valent anion})$$

Theoretically, the synthesis of HT should obey Equation 4 when calcined dolomite is used. It is also expected that the use of calcined dolomite will further reduce the amount of Mg^{2+} in solution by 62.5–75%.

$$(0.5-x)Mg^{2+} + xAl^{3+} + 0.5MgO + 0.5CaO + H_2O + (x/n)A^{n-} \rightarrow Mg_{1-x}Al_x(OH)_2(A)_{x/n} + 0.5Ca^{2+} \quad (4)$$
$$0.20 \leqq x \leqq 0.33 \quad (A^{n-}: n \text{ valent anion})$$

The effects of initial Mg/Al molar ratio, temperature, and time on the formation of HT were investigated.

All general reagents used were purchased from Kanto Chemical Co. Inc. Dolomite was supplied by Ube Material Industries, Ltd. Dolomite ($CaMg(CO_3)_2$) calcination was carried out in an electric furnace at 1000 °C for 1 h. The contents of CaO and MgO in the calcined dolomite were determined to be 59.5 and 39.8%, respectively. $MgCl_2$ was added to 100 ml of 0.1 mol/L $AlCl_3$ solution in $(Mg)_{Cl}$/Al molar ratios of (i) 0.5, (ii) 1.0, and (iii) 1.5, at 25 °C and stirred. The calcined dolomite was added in $(Mg)_D$/Al molar ratios of (i) 1.5,

*Author to whom all correspondence should be addressed.

0261–8028

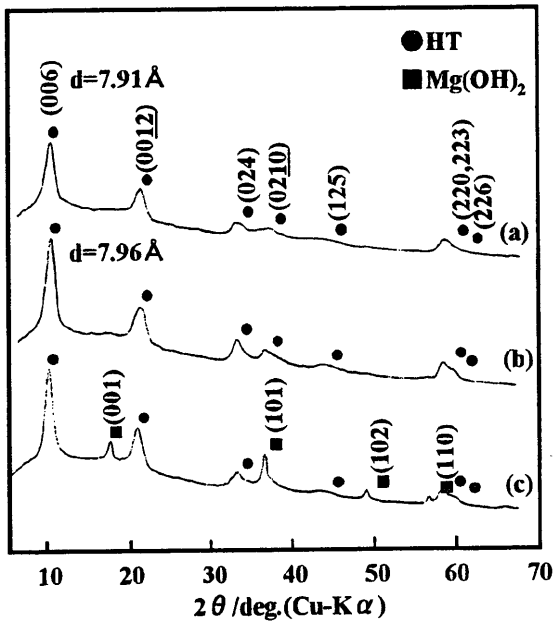

Figure 1 XRD patterns of precipitates at 25 °C for 1 h. $((Mg)_D + (Mg)_{Cl})/Al$ molar ratio: (a) 2.0, (b) 3.0, (c) 4.0.

(ii) 2.0, and (iii) 2.5 in *a burst*. ($(Mg)_{Cl}$: Mg from $MgCl_2$, $(Mg)_D$: Mg from the calcined dolomite) the slurry, prepared in $((Mg)_D + (Mg)_{Cl})/Al$ molar ratios of (i) 2.0, (ii) 3.0, and (iii) 4.0, was stirred at 25 and 90 °C for 1–16 h. The precipitates were filtered, washed with water, and dried at 105 °C for 24 h.

The precipitates were identified using X-ray diffraction (XRD) with a Rigaku Denki Geiger-flex 2013 diffractometer using Ni-filtered Cu K_α radiation at 30 kV and 15 mA and a scanning rate of 2°/min. The Mg^{2+} and Al^{3+} concentrations in the precipitates were determined using ICP-AES (Seiko SPS-2400A) after dissolving the sample in 1 M HNO_3 solution. The Cl^- concentrations were determined using ion chromatography (DIONEX QIC).

Fig. 1 shows XRD patterns of precipitates at 25 °C for 1 h. At $((Mg)_D + (Mg)_{Cl})/Al$ molar ratios of 2.0 and 3.0, HT was precipitated as a single phase, while a small amount of $Mg(OH)_2$ was obtained when a molar ratio of 4.0 was used. It has previously been determined that HT is formed by the reaction of dissolved Mg and Al species [23]. At the completion of the reaction with molar ratios of 2.0 and 3.0, the pH measured was 6.8 and 9.0, respectively. Thus, the formation of HT was attributed to the reaction of the Mg species dissolved from the calcined dolomite and the Al species from $AlCl_3$. In contrast, it is thought that at a molar ratio of 4.0, the rate of hydration of MgO was faster than the formation of HT. This is supported by the fact that the pH measured after the reaction was 10.4, because the amount of the calcined dolomite added is larger than that at molar ratios of 2.0 and 3.0.

Table I shows the contents of cations and anions in HT precipitated from mixed $MgCl_2$ and $AlCl_3$ solutions following addition of calcined dolomite. Precipitation of almost all of the Mg and Al occurred, while 4 wt% of Cl^- remained in both HTs. The interlayer distances calculated by subtracting the 4.77 Å brucite layer

TABLE I Contents of cations and anions in HT precipitated from mixed $MgCl_2$ and $AlCl_3$ solutions following addition of calcined dolomite

$((Mg)_D + (Mg)_{Cl})/Al$ molar ratio	Mg/Al molar ratio	Mg content	Al content	Cl content
(a) 2.0	1.9	22.0	13.4	4.3
(b) 3.0	2.9	25.4	9.8	3.5

All values are in wt%.

from the unit layer distances, $d(006)$, were (a) 3.14 and (b) 3.19 Å, respectively. Since the unit layer distance of Cl^- intercalated HT [14, 16] is roughly 3 Å, it can be deduced that Cl^- was intercalated in both HTs. The anionic charge ratios of Cl^- to all anions in the interlayer of both HTs were found to be around 25%. Since CO_2 contamination was not avoided in this synthesis, it is assumed that not only OH^- but also CO_3^{2-} was intercalated in both HTs. The charge density of both OH^- and CO_3^{2-} is greater than that of Cl^-, and HT has been shown to preferentially intercalate anions with larger charge densities [14].

When calcination of Cl^--HT at 450–800 °C takes place, Mg-Al oxide can be reproduced with hydrochloric acid [19, 24]. Similarly, it is conjectured that HT produced in this synthetic process would be transformed into Mg-Al oxide by calcination at 450–800 °C. We expect that this Mg-Al oxide could be used to treat wastewater.

Fig. 2 shows the XRD pattern of precipitates at $((Mg)_D + (Mg)_{Cl})/Al$ molar ratio of 4.0 at 90 °C. The intensity ratio of $Mg(OH)_2$ to HT decreased with increasing time. It is assumed that acid was released following hydrolysis of amorphous aluminum hydroxide in the product as time increased, and $Mg(OH)_2$ dissolved gradually. Accordingly, HT was gradually regenerated by the reactions of the dissolved Mg and Al species.

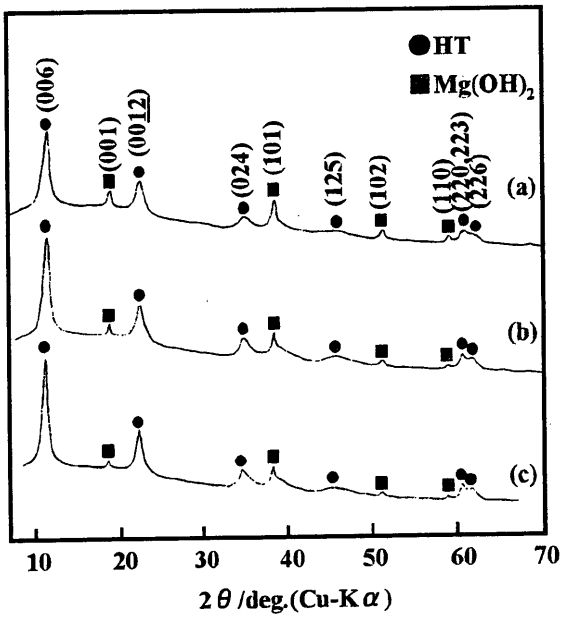

Figure 2 XRD patterns of precipitates at $((Mg)_D + (Mg)_{Cl})/Al$ molar ratio of 4.0 at 90 °C. Time (h): (a) 1, (b) 8, (c) 16.

To date, there have been no reports of HT synthesis as a single phase using salts of low solubility (e.g., $Mg(OH)_2$) at ambient temperature. Therefore, it is noteworthy that HT could be produced as a single phase at 25 °C by the addition of calcined dolomite to mixtures of $MgCl_2$ and $AlCl_3$ at a $((Mg)_D + (Mg)_{Cl})/Al$ molar ratio of 2.0 or 3.0.

References

1. L. INGRAM and H. F. W. TAYLOR, *Mineral. Mag.* **36** (1967) 465.
2. T. HIBINO and A. TSUNASHIMA, *Chem. Mater.* **9** (1997) 2082.
3. A. D. ROY, *Mol. Cryst. Liq. Cryst.* **311** (1998) 173.
4. S. P. NEWMAN and W. JONES, *New J. Chem.* **22** (1998) 105.
5. F. CAVANI, F. TRIFIRO and A. VACCARI, *Catal. Today* **11** (1991) 173.
6. M. C. HERMOSIN, I. PAVLOVIC, M. A. ULIBARRI and J. CORNEJO, *Wat. Res.* **30** (1996) 171.
7. M. J. KANG, S. W. RHEE and H. MOON, *Radiochim. Acta* **75** (1996) 169.
8. M. T. OLGUIN, P. BOSCH, D. ACOSTA and S. BULBULIAN, *Clays Clay Miner.* **46** (1998) 567.
9. G. FETTER, M. T. OLGUIN and P. BOSCH, *J. Radioanal. Nucl. Chem.* **241** (1999) 595.
10. J. SERRANO, V. BERTIN and S. BULBULIAN, *Langmuir* **16** (2000) 3355.
11. T. KAMEDA, Y. MIYANO, T. YOSHIOKA, M. UCHIDA and A. OKUWAKI, *Chem. Lett.* **2000** (2000) 1136.
12. T. KAMEDA, T. YOSHIOKA, M. UCHIDA, Y. MIYANO and A. OKUWAKI. *Bull. Chem. Soc. Jpn.* **75** (2002) 595.
13. T. KUMURA, N. IMATAKI, K. HASUI, T. INOUE and K. YASUTOMI, Jp. patent 46/2280, 1971.
14. S. MIYATA, *Clays Clay Miner.* **31** (1983) 305.
15. *Idem., ibid.* **28** (1980) 50.
16. T. SATO, T. WAKABAYASHI and M. SHIMADA, *Ind. Eng. Chem. Prod. Res. Dev.* **25** (1986) 89.
17. T. SATO, M. TEZUKA, T. ENDO and M. SHIMADA, *React. Solids* **3** (1987) 287.
18. T. SATO, S. ONAI, T. YOSHIOKA and A. OKUWAKI, *J. Chem. Tech. Biotech.* **57** (1993) 137.
19. S. MIYATA, *Clays Clay Miner.* **23** (1975) 369.
20. C. MIRSA, U.S. patent 4 904 457, 1990.
21. T. TSUBOI, T. MIDERA and R. KABEYA, Jp. patent 6/329410, 1994.
22. T. KASAI and T. MIZOTA, *Shigen-to-Sozai* **112** (1996) 131.
23. R. K. VANDERLAAN, J. L. WHITE and S. L. HEM, *J. Pharm. Sci.* **71** (1982) 780.
24. V. R. L. CONSTANTINO and T. J. PINNAVAIA, *Inorg. Chem.* **34** (1995) 883.

Received 22 April
and accepted 7 August 2002

ELSEVIER

Fluid Phase Equilibria 194–197 (2002) 271–280

FLUID PHASE EQUILIBRIA

www.elsevier.com/locate/fluid

Phase behavior and physico-chemical properties of aqueous electrolyte solutions near the critical point via molecular dynamics simulation with gravity perturbation

Tetsuo Honma[a], Shunsuke Kuzuhara[a], Chee Chin Liew[b], Hiroshi Inomata[a,*]

[a] *Department of Chemical Engineering, Research Center of Supercritical Fluid Technology, Tohoku University, Sendai 980-8579, Japan*

[b] *Research Institute for Computational Sciences (RICS), National Institute of Advanced Industrial Science and Technology (AIST), Tsukuba 305-8568, Japan*

Received 12 March 2001; accepted 15 October 2001

Abstract

In molecular dynamics (MD) simulation, large-scale density fluctuations bring about difficulties in evaluating the critical point from coexisting vapor–liquid densities. This study proposes a gravity perturbation method that improves the stability of vapor–liquid coexisting phases near the critical point by introducing gravity and boundary walls. Trial simulations were performed with a modified flexible SPC-TR (Toukan–Rahman) model and a critical point obtained for water (T_C = 377.6 °C, ρ_C = 0.302 g cm^{-3}) was in good agreement with the experimental data (T_C = 374.0 °C, ρ_C = 0.322 g cm^{-3}). The method was also applied to NaCl–water mixtures and it was found that simulations were greatly facilitated with the technique. The gravity perturbation method allows reliable determination of phase behavior in the vicinity of a critical point.

Keywords: Molecular simulation; Critical properties; Vapor–liquid phase equilibrium; Water

1. Introduction

Supercritical and subcritical water have attracted industrial interest as solvents for the production of superfine particle processes and as reaction media of partial oxidation for organic compounds, etc. [1]. Water in its supercritical state has low viscosity, high diffusivity, and other physical properties that change greatly with temperature or pressure. These properties have been related to solution structure via molecular simulation [2]. Molecular dynamics (MD) simulation has been applied to electrolyte aqueous solutions of supercritical conditions to examine changes in solution structure of the solvation free energy of ions [3], the transition between the contact ion-pair and the solvent-shared ion-pairs [4], and the local properties

* Corresponding author. Tel. +81-22-217-7283; fax: +81-22-217-7283.
E-mail address: inomata@scf.che.tohoku.ac.jp (H. Inomata).

0378-3812/02/$ – see front matter
PII: S0378-3812(01)00777-4

around ion species [5]. In these simulations knowledge of the critical point of the model is important for interpretation of the results. One method to estimate the critical point of the model is through vapor–liquid equilibrium simulations.

To estimate vapor–liquid equilibrium by molecular simulation, two general methods have been applied: (i) Gibbs Ensemble Monte Carlo (GEMC) technique [6,7], (ii) direct molecular dynamics (DMD) [8]. The GEMC simulation employs two simulation boxes (one vapor, one liquid), where molecules are moved independently in each box. There are moves involving volume changes in both boxes and molecule exchanges between the boxes. GEMC method greatly facilitates attainment of phase equilibrium. The direct molecular dynamics simulation technique employs a single two-phase simulation box, and can determine vapor–liquid coexisting densities and interfacial properties by observation of density gradients. However, both of these methods have difficulty in estimating vapor–liquid coexisting densities in the vicinity of the critical point because the presence of large density fluctuations. One way to reduce the density fluctuation is to apply weights for the phase densities so that differences in the phases are emphasized. In this work, we develop a gravity perturbation technique that can improve simulations of vapor–liquid equilibrium in the critical region. The new technique can provide reliable estimation of the critical point of simulation models. The systems examined were pure water and aqueous electrolyte (NaCl) solutions.

2. Methods

2.1. Molecular models

The water model used was comprised of an intra- and an inter-molecular potentials [9]. The intra-molecular potential used the angular form of Toukan–Rahman (TR) potential [10]. In our previous work, a modified TR (mTR) intra-molecular potential was proposed [11] that improved high-temperature stability of the original TR potential. The angular form of TR potential was also stable at high-temperature and composed of the Morse and harmonic potentials given by Eqs. (1)–(3).

$$U_{\text{intra}} = U_{\text{OH}} + U_{\text{HOH}} \tag{1}$$

$$U_{\text{OH}} = D_{\text{OH}}([1 - \exp(-\alpha\,\Delta r_{1,2})]^2 + [1 - \exp(-\alpha\,\Delta r_{1,3})]^2) \tag{2}$$

$$U_{\text{HOH}} = 0.5\beta(r_{\text{OH}}\,\Delta\theta)^2 + \gamma(r_{\text{OH}}\,\Delta\theta)(\Delta r_{1,2} + \Delta r_{1,3}) + \Delta(\Delta r_{1,2}\Delta r_{1,3}) \tag{3}$$

where r_{OH} is the O–H distance, and D_{OH} the dissociation energy for O–H bond. Subscripts 1, 2 and 3 denote the oxygen, the first hydrogen and the second hydrogen, respectively. The $\Delta r_{1,2}$ and $\Delta r_{1,3}$ denote the stretch in the O–H bonds and $\Delta\theta$ is the bending for the H–O–H angle from monomer equilibrium geometry. The α, β, γ, and δ are potential parameters.

The inter-molecular interactions preferred SPC potential form that consisted of a Lennard–Jones (LJ) 12-6 potential and a Coulomb potential. The original SPC [12], SPC-TR [10], and SPC-mTR [13] models neglect LJ parameters of hydrogen site. In this work, to improve the stability of the model at high temperatures, the hydrogen site was considered to be a LJ potential site. The intra- and inter-molecular potential parameters used are given in Tables 1 and 2 [9]. The model given by Pettitt–Rossky (PR) [14] was used for ion–water and ion–ion. We adopted the parameters of Cummings et al. [2] for PR model of ion–water interaction with the geometry of SPC charge distribution.

Table 1
Potential parameters for the angular form of TR potential [9]

r_{OH} (Å)	1.0
θ (°)	109.47
D_{OH} (kJ mol^{-1})	426.376
α (Å^{-1})	2.311
β (kJ mol^{-1} Å^{-2})	417.04
γ (kJ mol^{-1} Å^{-2})	124.947
δ (kJ mol^{-1} Å^{-2})	−55.35

Table 2
Lennard–Jones parameters and partial charges [9]

Atoms	m (g mol^{-1})	ε (kJ mol^{-1})	σ (Å)	q (e)
O (1)	16.000	0.6257	3.1757	−0.82
H (2)	1.008	0.0120	0.5700	0.41
H (3)	1.008	0.0120	0.5700	0.41

2.2. System size and run time

MD simulation with a *NVT*-ensemble was employed for system of 1372 molecules. Temperature was varied from 25 to 375 °C. The equation of motion was solved using the velocity Verlet algorithm with the multiple time scale algorithm of Tuckerman et al. [15]. Time steps were 1 fs for the inter-molecular motion and 0.2 fs for the intra-molecular motion. Total simulated time was 300 ps including 100 ps equilibration. Momentum scaling was used for the initial 60 ps and afterwards the Nosé–Hoover thermostat was applied. The long-range force was treated by site–site reaction field method [16] with the cut-off distance being 10 Å.

2.3. Gravity perturbation

In this section, we introduce a method for gravity perturbation. In our proposing method, we add gravity in the z-direction and boundary walls with a LJ potential as shown in Fig. 1. The length of the simulation box, $L_x = L_y = 28.0$ Å and L_z 171 Å, was suitable for representing the critical density. The boundary

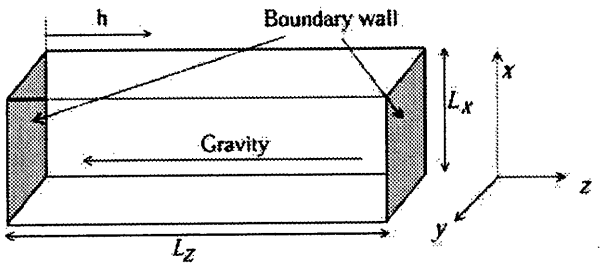

Fig. 1. Simulation box for the direct molecular dynamics method with gravity perturbation.

walls were chosen to be a 10-4 type of LJ potential function:

$$U_{wi} = \sum_{w}^{wallsatoms} \sum_{i} 4\varepsilon_{wi} \left[\left(\frac{\sigma_{wi}}{r_{wi}} \right)^{10} - \left(\frac{\sigma_{wi}}{r_{wi}} \right)^{4} \right] \tag{4}$$

where subscripts w and i denote the walls and the sites on the molecules, respectively. The σ and ε of wall are the same as the flexible SPC water. Periodic boundary conditions were applied along x- and y-axes. The gravity applied to stabilize the interface was described as follows:

$$U_{\text{gravity}} = \sum_{i}^{sites} m_i g' h \tag{5}$$

where

$$g' = 10^A g_0 N_A \tag{6}$$

In Eqs. (5) and (6), m_i is the atomic mass of site i, h the distance from the wall defined in Fig. 1, g_0 is the Earth's gravity, N_A is Avogadro's number, and A is the gravity factor. Water molecules filled in the simulation box. Application of gravity can be expected to promote phase separations if the thermodynamic state is accessible.

We also performed conventional direct MD simulations to compare with the proposed gravity simulations. For these runs, periodic boundary conditions were applied along the x-, y- and z-axes during the simulations. Water molecules were placed in the center of the simulation box at an ambient liquid density.

3. Results and discussion

3.1. Effect of the gravity

For purposes of exploring the behavior of interfacial properties at high temperatures, conventional direct MD simulations were employed at three temperatures. After the system reached equilibrium, the density profiles sliced along z-coordinates were obtained, which were shown in Fig. 2. The liquid layer was stable

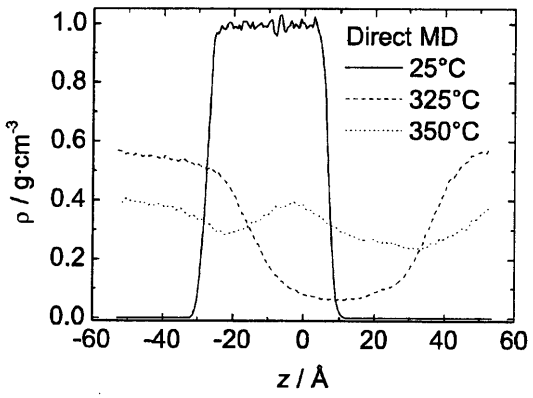

Fig. 2. Density profiles sliced along z-axis.

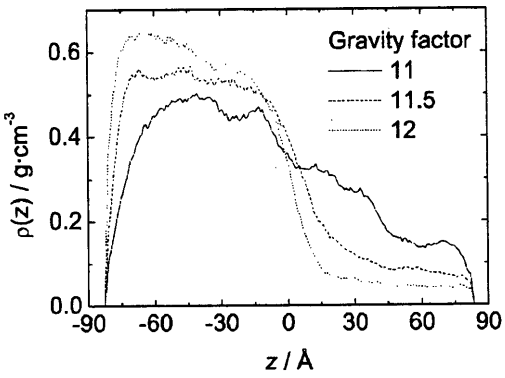

Fig. 3. Density profiles of flexible SPC water (see text) [9] at 350 °C with gravity perturbation.

in the center of the simulation box and the vapor and liquid phase densities could be easily determined. At higher temperatures, the liquid layer diffused and did not form stable vapor–liquid interfaces. Coexisting densities could not be determined for these cases. The effect of gravity on the vapor–liquid interface of water at high temperatures was then examined. Three simulations were performed at 350 °C with gravity factors ranging from $A = 11$ to 12 as shown in Fig. 3. The liquid phase appeared at the left side of the simulation box as expected and the vapor–liquid interface formed in the center of the box. Comparing these three simulations, the vapor–liquid interface could not be clearly determined at the gravity factor of 11. When the gravity factor was 12, the interface became more distinct. It is obvious that the large gravity factors promoted condensation and caused an increase in liquid density. The results in Fig. 3 indicated that a gravity factor of about 11.5 was most appropriate in these runs. It should be noted that the applied gravity ($A = 11.5$) corresponds to only about 1% of the inter-molecular forces.

We also examined the length of the equilibration period. Fig. 4 shows density profiles at the gravity factor of 11.5, where each simulation was made sequentially. In other words, at each initial condition, coordinates and velocities, were supplied from the final conditions of the previous simulation. As shown in Fig. 4, the vapor–liquid interface became clearly distinguishable as equilibration time increased. Pre-equilibration periods of at least 300 ps were used in this study.

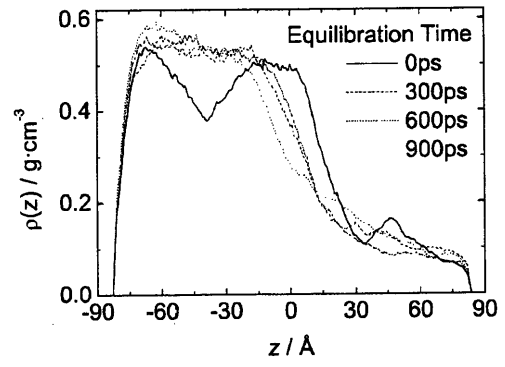

Fig. 4. Time evolution of the density profile of flexible SPC model at 350 °C with gravity perturbation at a gravity factor of 11.5.

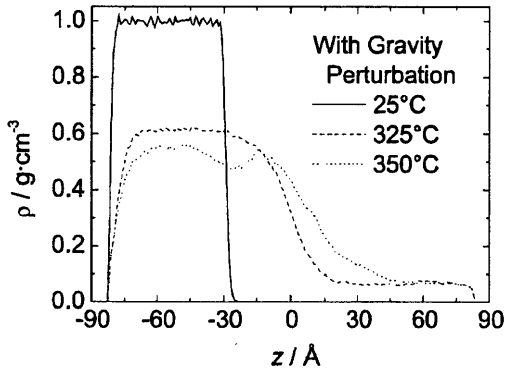

Fig. 5. Density profiles of the flexible SPC model. Temperatures ranged from 25 to 350 °C with the gravity factor 11.5.

3.2. Vapor–liquid phase equilibrium and critical point of flexible SPC water

The density profile estimated from the gravity simulation is shown in Fig. 5. Temperatures were varied between 25 and 350 °C. The liquid phase became clearly stabilized even at the higher temperatures. The vapor–liquid saturated densities were obtained from

$$\rho(z) = \frac{\rho_L + \rho_V}{2} - \frac{\rho_L - \rho_V}{2} \tanh\left(\frac{z - z_0}{d}\right) \tag{7}$$

where ρ_L and ρ_V are the densities at the liquid and the vapor phase, z_0 the position of the Gibbs' dividing surface, and d a parameter for the thickness of the interface. Estimated coexisting densities are plotted against the temperature as shown in Fig. 6. According to the orthobaric density data, we estimated the critical point by fitting them to the law of rectilinear diameters and the appropriate scaling law with scaling exponent of 0.325 [17]. The estimated critical temperature and critical density (DMD-G) are listed in Table 3 along with literature simulation results [8,11,18]. The T_C was about 2% higher and the ρ_C was about 6% lower compared to the experimental data [19]. The presence of gravity, which has significant effect on promoting phase separation, may change the model's critical point. For the purpose

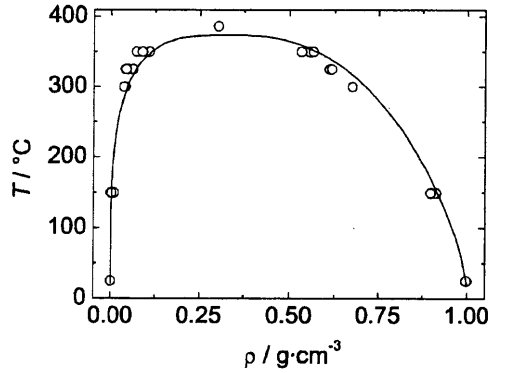

Fig. 6. Vapor–liquid coexistence curve of flexible SPC model compared with experimental data, which obtained from steam table [19]. Gravity factor A (Eq. (6)) was 11.5.

Table 3
Estimated critical point of flexible SPC model. DMD and GEMC indicate direct molecular dynamics method and Gibbs Ensemble Monte Carlo Method, respectively

	Model	Method	N	T_C (°C)	ρ_C (g cm^{-3})
This work	SPC-TR	DMD-G	1372	386.2 ± 5.2	0.302 ±0.006
This work	SPC-TR	DMD-GP	1372	377.6 ±3.2	Not determined
Liew et al. [11]	SPC-mTR	DMD	800	370.3 ± 3.6	0.320 ± 0.006
Alejandre et al. [8]	SPC/E	DMD	500	357.2	0.308
De Pablo et al. [18]	SPC	GEMC	200	317.0 ± 7.8	0.311 ± 0.006
Wagner et al. [19]	Exp.			374.0	0.322

of minimizing the effect of gravity, we introduced *gravity perturbation technique*. In other words, the critical point was determined by extrapolating the simulation results at various gravity factors to a zero gravity factor. The critical temperatures from two-phase simulations with gravities ranging from 11.1 to 11.9 were shown in Fig. 7. The critical temperature approached a constant value as the gravity factor decreased. We used a first-order exponential function to extrapolate the critical temperature to zero gravity. The T_C estimated with gravity perturbation (DMD-GP in Table 3) was in excellent agreement with the experimental value [19]. It should be noted that the gravity perturbation method does not eliminate the effect of gravity on the critical density because the critical densities from the two-phase simulations still have large uncertainties. However, gravity perturbation does provide an additional method to locate the critical point and Fig. 7 confirms the consistency of the procedure.

3.3. Phase behavior of electrolyte solutions

The direct molecular dynamics with gravity was applied to the phase behavior of aqueous electrolyte solutions with our water model and the gravity simulation. The systems contained one or two pairs of sodium chloride ions, which correspond to 0.236 and 0.471 wt.%, respectively. The simulation method used was the same as in the previous direct MD simulations. The ion–wall interaction parameter was the same as the parameter used for ion–oxygen interaction.

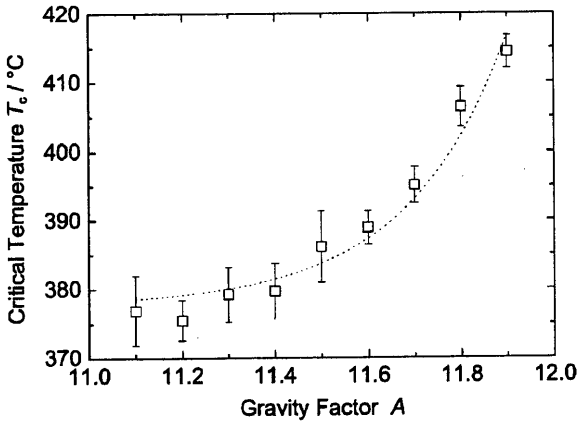

Fig. 7. Gravity factor dependence of the critical temperature. Gravity factor, A, ranged from 11.1 to 11.9.

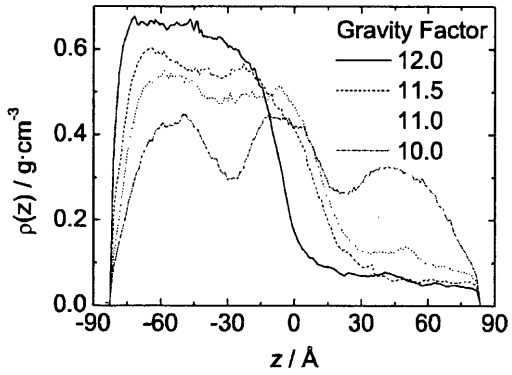

Fig. 8. Density profile of flexible SPC water with 1 pair of NaCl at 350 °C. Gravity factor was ranged from 10 to 12.

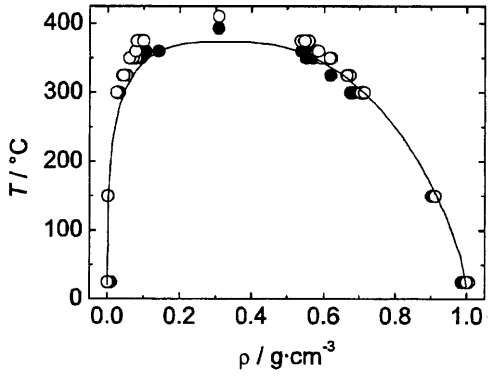

Fig. 9. Vapor–liquid saturated densities of the aqueous electrolyte solutions. Filled circles: one NaCl pair; open ciecles: two NaCl pairs; solid line is the experimental data for pure water [19].

For the case of electrolyte aqueous solutions, one would expect that the critical temperature and density of the electrolyte aqueous solution to be higher than those of pure water, because electrolytes had a strong attractive force which prevented the vaporization of water. As shown in Fig. 8, the density profiles for the gravity factor of 11.5 produced a clear vapor–liquid phase separation for the given conditions. It should be mentioned that other gravity factors higher than 11 gave satisfactory results. The vapor–liquid saturated densities were estimated with Eq. (7) as shown in Fig. 9. The critical points estimated from the simulations (Table 4) were slightly higher than the experimental data [20]. This indicates that the ion–water interactions used are probably too strong at supercritical conditions.

Table 4
Critical temperature and density of aqueous electrolyte solutions

N_w	$N_{ion\text{-}pair}$	C_{NaCl} (wt.%)	T_C (°C)	ρ_C (g cm^{-3})
1372	1	0.236	393.1 ± 4.51	0.3080 ± 0.0035
1372	2	0.471	410.6 ± 3.05	0.3083 ± 0.0026

4. Conclusion

A gravity perturbation was found to stabilize vapor–liquid equilibrium MD simulation at conditions near the critical point. Phase separation as high as 350 °C for pure water could be obtained. The critical point of a flexible SPC water model was found to be in good agreement with the experimental value. The gravity perturbation method could also be applied to electrolyte solutions.

List of symbols

C_{NaCl}	weight concentration of NaCl (wt.%)
d	thickness parameter of liquid (Å)
D	dissociation energy (kJ mol^{-1})
g_0	Earth's gravity
h	distance from side wall (Å)
m	mass of sites (g mol^{-1})
N	number of molecules in a simulation box
N_A	Avogadro's number (mol^{-1})
q	partial charge of sites (e)
r_{ij}	interatomic distances between sites (Å)
Δr_{ij}	difference from equilibrium geometry (Å)
T_C	Critical temperature (°C)
$U_{gravity}$	potential energy due to gravity (kJ mol^{-1})
z	z-axis coordinate (Å)

Greek symbols

α	Morse un-harmonic parameter (Å^{-1})
β, γ, δ	harmonic potential parameter for HOH (kJ mol^{-1} Å^{-2})
ε, σ	Lennard–Jones parameter (kJ mol^{-1} and Å)
θ	H–O–H angle (rad)
$\Delta\theta$	difference from equilibrium geometry (rad)
ρ	saturated density (g cm^{-3})
ρ (z)	density sliced along z-axis (g cm^{-3})

Subscripts

HOH	H–O–H bond
i	interaction sites
intra	intra-molecule
L, V	Liquid or vapor phase
OH	bond between oxygen and hydrogen
wi	between wall and sites

Acknowledgements

This work has been partly supported by CREST of JST (Japan Science and Technology).

References

[1] D. Bröll, C. Kaul, A. Krämer, P. Krammer, T. Richter, M. Jung, H. Vogel, P. Zehner, Chemistry in supercritical water, Angew. Chem. Int. Ed. 38 (1999) 2998–3014.
[2] P.T. Cummings, H.D. Cochran, J.M. Simonson, R.E. Mesmer, S. Karaborni, Simulation of supercritical water and of supercritical aqueous solutions, J. Chem. Phys. 94 (8) (1991) 5606–5621.
[3] P.B. Balbuena, K.P. Johnston, P.J. Rossky, Molecular dynamics simulation of electrolyte solutions in ambient and supercritical water. 1. Ion solvation, J. Phys. Chem. 100 (7) (1996) 2706–2715.
[4] A.A. Chialvo, P.T. Cummings, J.M. Simonson, R.E. Mesmer, Temperature and density effects on the high temperature ionic speciation in dilute Na^+/Cl^- aqueous solutions, J. Chem. Phys 105 (20) (1996) 9248–9257.
[5] A.A. Chialvo, P.T. Cummings, J.M. Simonson, R.E. Mesmer, Solvation in high-temperature electrolyte solutions. I. Hydration shell behavior from molecular simulation, J. Chem. Phys. 110 (2) (1999) 1064–1074.
[6] A.Z. Panagiotopoulos, Direct determination of phase coexistence properties of fluids by Monte Carlo simulation in a new ensemble, Mol. Phys. 61 (4) (1987) 813–826.
[7] J.R. Errington, A.Z. Panagiotopoulos, A fixed point charge model for water optimized to the vapor–liquid coexistence properties, J. Phys. Chem. B 102 (38) (1998) 7470–7475.
[8] J. Alejandre, D.J. Tildesley, G.A. Chapela, Molecular dynamics simulation of the orthobaric densities and surface tension of water, J. Chem. Phys. 102 (11) (1995) 4574–4583.
[9] T. Honma, C.C. Liew, H. Inomata, A flexible molecular model for the critical region of water, J. Chem. Phys., 2002, submitted for publication.
[10] K. Toukan, A. Rahman, Molecular-dynamics study of atomic motions in water, Phys. Rev. B 31 (5) (1985) 2643–2648.
[11] C.C. Liew, H. Inomata, K. Arai, Flexible molecular models for molecular dynamics study of near and supercritical water, Fluid Phase Equil. 144 (1998) 287–298.
[12] H.J.C. Berendsen, J.P.M. Postma, W.F. van Gunsteren, J. Hermans, in: B. Pullman (Ed.), Inter-molecular Forces, Reidel, Dordrecht, 1981.
[13] C.C. Liew, H. Inomata, K. Arai, S. Saito, Three-dimensional structure and hydrogen bonding of water in sub- and supercritical regions: a molecular simulation study, J. Supercrit. Fluids 13 (1998) 83–91.
[14] B.M. Pettitt, P.J. Rossky, Alkali halides in water: ion–solvent correlations and ion–ion potentials of mean force at infinite dilution, J. Chem. Phys. 84 (10) (1986) 5836–5844.
[15] M. Tuckerman, B.J. Berne, G.J. Martyna, Reversible multiple time scale molecular dynamics, J. Chem. Phys. 97 (3) (1992) 1990–2001.
[16] G. Hummer, D.M. Soumpasis, M. Neumann, Pair correlations in an NaCl-SPC water model simulations versus extended RISM computations, Mol. Phys. 77 (4) (1992) 769–785.
[17] J.M.H.L. Sengers, J. Straub, K. Watanabe, P.G. Hill, Assessment of critical parameter values for H_2O and D_2O, J. Phys. Chem. Ref. Data 14 (1) (1985) 193–207.
[18] J.J. de Pablo, J.M. Prausnitz, H.J. Strauch, P.T. Cummings, Molecular simulation of water along the liquid–vapor coexistence curve from 25 °C to the critical point, J. Chem. Phys. 93 (10) (1990) 7355–7359.
[19] W. Wagner, A. Pruß, The IAPWS formulation 1995 for the thermodynamics properties of ordinary water substance for general and scientific use, International association for the properties of water and steam, Sep. 1996.
[20] J.L. Bischoff, K.S. Pitzer, Liquid–vapor relations for the system NaCl–H_2O: summary of the P–T–x surface from 300 to 500 °C, Am. J. Sci. 289 (1989) 217–248.

Pergamon

Materials Research Bulletin 37 (2002) 949–955

Materials Research Bulletin

Preparation and magnetization of hematite nanocrystals with amorphous iron oxide layers by hydrothermal conditions

G.S. Li, R.L. Smith Jr., H. Inomata*, K. Arai

Department of Chemical Engineering, Research Center of Supercritical Fluid Technology, Tohoku University, Sendai 980-8579, Japan

(Refereed)
Received 14 March 2001; accepted 18 January 2002

Abstract

Hematite nanocrystals modified with surface layers of amorphous hydrous iron oxides were prepared by hydrothermal conditions in the absence of alkali. The formation temperature was found to be ca. 130°C. When the temperature was lower than 130°C, no product was formed, while above this temperature, the amount of amorphous hydrous iron oxides at the surface of hematite nanocrystals was drastically decreased. The amorphous layers on the hematite nanocrystals obtained at 130°C were determined to be $Fe_2O_3 \cdot 1.64H_2O$. The coercivity for the hematite nanocrystals with modified layers was 0.534 kOe, which is slightly larger than the values for hematite nanocrystals with few agglomerations.

Keywords: A. Oxides; B. Chemical synthesis; D. Magnetic properties

1. Introduction

Hematite nanocrystals have shown several excellent properties and found a wide field of technological applications including catalysts, pigments, recording medium, and sensors. An agglomerate of hematite particles exhibits a coercivity two times higher than that of commercial hematite [1]. Several synthetic methods have been developed for preparation of hematite nanocrystals including sol–gel, hydrolysis of

* Corresponding author. Tel.: +81-22-217-7283; fax: +81-22-217-7293.
E-mail address: inomata@scf.che.tohoku.ac.jp (H. Inomata).

0025-5408/02/$ – see front matter
PII: S0025-5408(02)00695-5

iron salts, and hydrothermal synthesis [2–4]. Hydrothermal synthesis has shown to be advantageous over other methods in homogeneous nucleation and grain growth of hematite nanocrystals. Preparation conditions such as concentration, reaction temperature and time are the main factors in determining the morphologies and structures of the nanocrystals prepared by hydrothermal conditions.

For example, hydrothermal reactions of an aqueous iron nitrate solution at a wide concentration range produce porous hematite nanocrystals (40–80 nm) containing non-intersecting 5–20 nm pores [5], while lowering the concentration to 0.0027–0.18 M yields some amounts of a second phase that is mainly α-FeOOH (goethite) [6]. Single phase α-Fe_2O_3 (hematite) can be formed in ferric chloride hydrothermal systems [7]. However, the ferric concentration has to be restricted as low as 0.02–0.04 M. Beyond this range, second phase β-FeOOH can be readily formed. It is clear that hematite nanocrystals can be obtained by adjusting hydrothermal conditions, but nanocrystals formed in this manner tend to agglomerate. In a previous work, we [8] demonstrated that nanocomposite technology could be an effective solution to this problem with nonmagnetic amorphous silica matrix allowing homogenous grain growth of nanocrystals. It appears to be very important to study the magnetization of nanocrystals and whether they can be modified by addition of magnetic layers.

In this work, we report on preparation, grain growth, and magnetization of hematite nanocrystals modified with amorphous hydrous iron oxide layers by hydrothermal conditions.

2. Experimental

The samples were prepared by hydrothermal reactions of 0.25 M ferric nitrate solutions in 15 ml stainless steel autoclaves lined by Teflon (<250°C) and 10 ml stainless steel autoclaves (>250°C). Analytical grade reagent $Fe(NO_3)_3 \cdot 9H_2O$ was used as the starting material. The experimental conditions are listed in Table 1. The synthesis process was as follows. An aqueous solution of 0.25 M $Fe(NO_3)_3$ was charged into an autoclave and filled halfway by volume. Each autoclave was sealed and immersed into the molten salt bath at the desired temperatures for a given period. After the reactions, the autoclaves were cooled in air. The products were washed with distilled water and dried in an oven at 50°C.

Table 1
Preparation conditions and particle sizes along four crystallographic directions for hematite nanocrystals

Condition	$D_{(1\,0\,4)}$ (nm)	$D_{(1\,1\,0)}$ (nm)	$D_{(0\,2\,4)}$ (nm)	$D_{(1\,1\,6)}$ (nm)
130°C, 1 h	17.1	15.6	23.5	16.9
150°C, 1 h	21.2	22.8	29.6	24.3
195°C, 1 h	26.6	26.0	29.4	29.2
250°C, 1 h	25.8	27.8	35.9	30.4
400°C, 1 h	25.8	25.3	31.1	28.6

The structures of the products were characterized by X-ray diffraction on a diffractometer with Mo Kα radiation ($\lambda_{K\alpha 1} = 0.70932$ Å). The scan rate was 1°/min. Particle sizes were determined by Scherrer equation. Water content in the samples was detected by TG at a heating rate of 20°C/min in air. The morphologies of the particles were observed by transition electron spectroscope (TEM). The magnetic properties were measured by a vibrating-sample magnetometer at room temperature.

3. Results and discussion

When the reaction was carried out at a temperature lower than 90°C (not shown), no precipitate was obtained. This result is different from those of hydrolysis of ferric nitrate solutions in open systems, where α-FeOOH [6], β-FeOOH [9], or ferrihydrite FeOOH [10] is formed. Fig. 1 shows typical XRD patterns of the products by hydrothermal reactions at temperatures higher than 90°C. At a temperature of 130°C, as shown in Fig. 1a, the sample showed strong diffraction peaks matching well with the standard data for α-Fe_2O_3 (JCPDS 33-664), while two broad peaks centered at ca. 2θ of 17 and 27° demonstrated some amounts of amorphous phases. These broad peaks were located closely near to the strong peaks (1 0 4), (1 1 0), (2 1 4), and (3 0 0) for hematite. We assumed that these broad peaks were probably associated with the presence of amorphous hydrous iron oxide, $Fe_2O_3 \cdot nH_2O$, on the surface of hematite nanocrystals by forming a nanocomposite. This is indicated by the absence of phase separation for crystalline hematite from amorphous iron oxide and by the great agglomeration of the irregular particles shown in the TEM photograph (Fig. 2). It is reasonable that the amorphous layers could have some strong interactions with the hematite nanocrystals, however, we found that these amorphous layers were unstable. As shown in Fig. 1b and c, the diffraction intensity for the broad peaks was drastically weakened by slightly increasing reaction temperature to 250°C. As described in the following part, higher reaction temperature led to larger grain size. Therefore, the above results indicated that relative content of amorphous layers was decreased with the grain growth of hematite nanocrystals.

Grain growth of hematite nanocrystals in the present systems seems to proceed via three steps: (i) homogeneous nucleation of amorphous hydrous iron oxide at a temperature lower than 130°C; (ii) formation of nanocomposite with hematite nanocrystals being modified by surface layers of amorphous hydrous iron oxide; and (iii) dehydration and transformation of amorphous layers into hematite nanocrystals. The transformation process could be estimated from the variation of the particle shape of hematite nanocrystals as calculated from different crystallographic directions [11]: the compatible intensities for diffraction peaks (1 0 4) and (1 1 0) are related to spherical shape of α-Fe_2O_3 particles, while a large intensity difference for both lines could be indicative of an ellipsoidal particle shape. In the present work, no large intensity difference was observed for these peaks. Particle sizes of the hematite nanocrystals evaluated by Scherrer equation from several typical peaks (1 0 4), (1 1 0), (0 2 4), and (1 1 6) are shown in Table 1. We found that the particle sizes

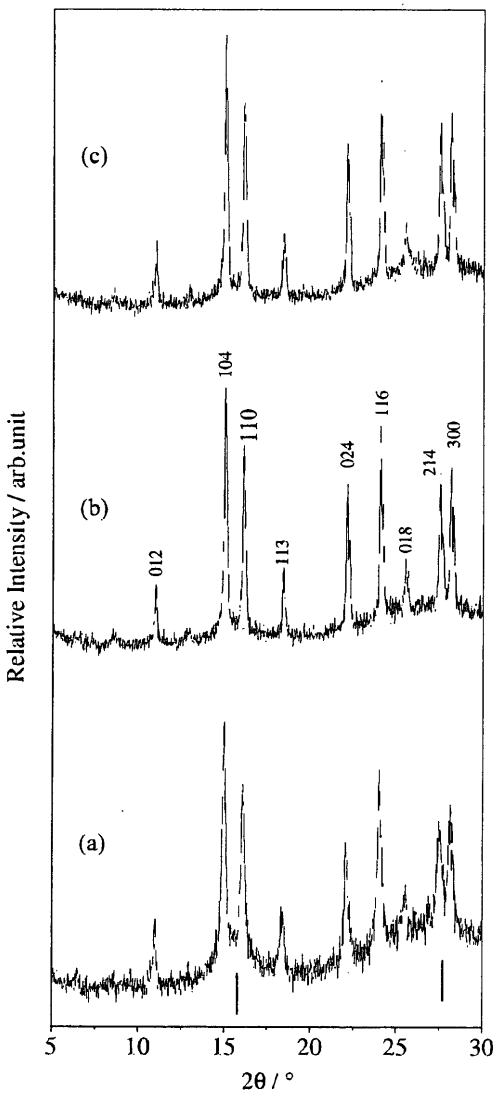

Fig. 1. XRD patterns of the products by hydrothermal reactions of 0.25 M $Fe(NO_3)_3$ solution at (a) 130°C, (b) 250°C and (c) 400°C.

along these four crystallographic directions were similar at the given temperatures, showing evidence of close to spherical shapes. The hematite nanocrystals obtained at 130°C were smallest, while the broad peaks had a strong intensity in Fig. 1a. With increasing reaction temperature, the particles obtained from the peak (1 0 4) increased from 17.1 nm at 130°C to 26.6 nm at 195°C, and then reached a plateau at 250°C. Similar growth trends have been found for other crystallographic directions. The homogeneous grain growth of hematite nanocrystals could be rationalized in terms of the continuous dehydration and transformation of the amorphous hydrous iron oxide layers, because when the temperature was increased to 195°C, the amorphous layers probably dehydrated while the domains for the hematite nanocrystals were enlarged. Above 195°C, the amorphous layers were almost absent, and therefore, the particle size of nanocrystals did not shown any obvious change. Similar

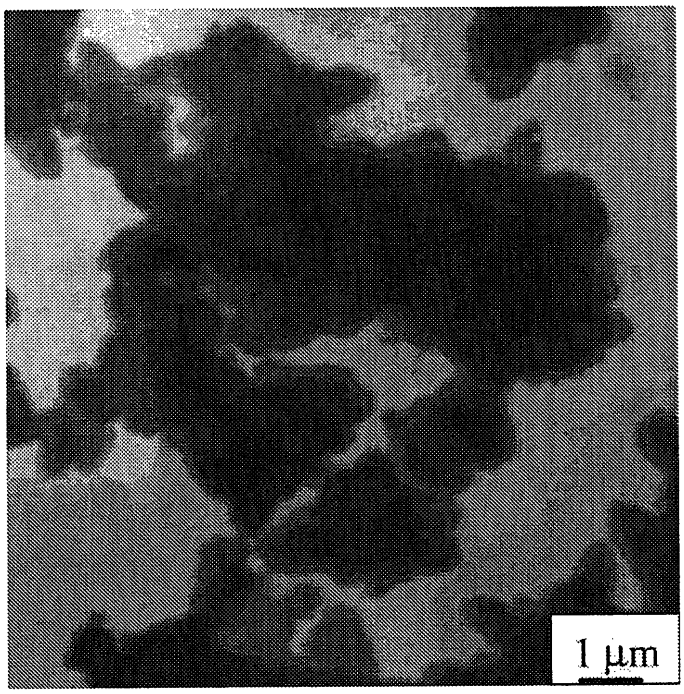

Fig. 2. Morphology of the sample obtained at 130°C.

growth processes have been found in the products from nitrate hydrothermal systems [12].

However, as shown in Table 1, when the reaction temperature reached 400°C, the particle size was slightly reduced, which indicated a re-dissolution process at the high temperature acidic hydrothermal conditions. When the reaction systems involve some amounts of alkali species, the phase behavior of nanocrystals changes [13,14]. For example, in the presence of hydrazine, hydrazine reduction of ferric nitrate produces Fe_3O_4 [13], while in the case of KOH, larger spherical α-Fe_2O_3 particles are formed [14].

Fig. 3 shows a TG curve of the sample prepared at 130°C. It was observed that the sample lost weight continuously up to 600°C. Generally, the physically adsorbed water is evaporated at ca. 120°C, and dehydration of the lattice hydroxyl groups gives a sharp weight loss over a narrow range around 330°C [15]. Therefore, the relatively wide dehydration process observed in Fig. 3 could be due to the strongly bound water from the amorphous layers on the hematite nanocrystals. The total weight loss was about 15.6%, indicating that the amorphous layers were probably $Fe_2O_3 \cdot 1.64H_2O$. The number of hydroxyl groups in the amorphous layers was estimated to be extremely low as revealed by the absence of characteristic hydroxyl absorptions at ca. 3360 cm^{-1} in the corresponding infrared spectrum (not shown). This coated structure could be possible since the iron sites were octahedrally coordinated both in the crystalline hematite and in the amorphous state [8,16]. As a result of partial crystallization, the crystalline hematite particles were covered by the amorphous layers with similar chemical compositions.

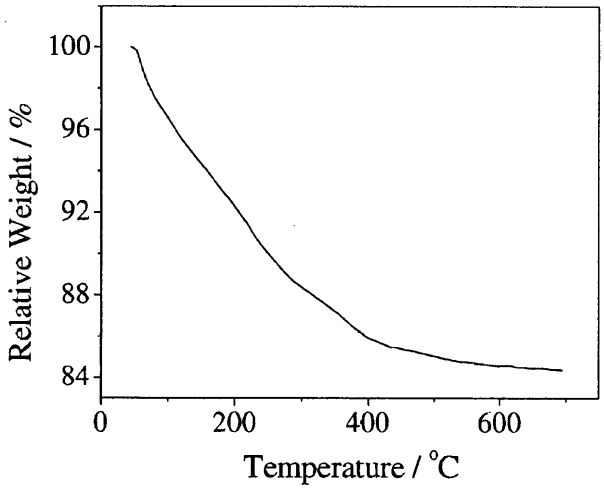

Fig. 3. TG curve of the sample obtained at 130°C.

Fig. 4 shows the room temperature magnetization curve of the sample prepared at 130°C. The hysteresis loop did not reach saturation up to the maximum field employed for present measurement system. The remanent magnetization was determined to be 0.046(2) emu/g, which is smaller than 0.10 emu/g for 40 nm trapezoidal α-Fe_2O_3 [1]. The coercivity was found to be 0.534 kOe, which is slightly larger than the reported values for α-Fe_2O_3 nanocrystals with few agglomerations [1]. It is known that the remanent magnetization is strongly dependent upon the particle shape, while coercivity is inversely proportional to grain size [8]. The smaller remanent magnetization for the present α-Fe_2O_3 nanocrystals modified with amorphous surface layers was probably associated with the fine spherical shape of hematite nanocrystals, while the slightly larger coercivity was consistent with the relatively small particle size. Even though the magnetic property of the present hematite nanocrystals with amorphous layers did not show much enhancement of the magnetic properties compared with that of agglomeration of hematite nanocrystals [1], the finding of

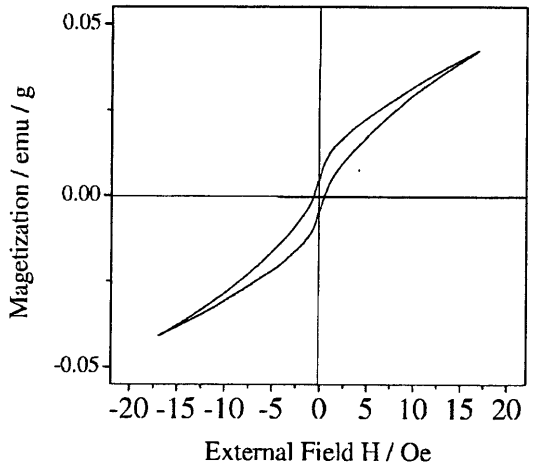

Fig. 4. Magnetization curve of the sample obtained at 130°C.

this work should help to understand the direct formation of magnetic nanocomposites by hydrothermal conditions.

Acknowledgments

The TEM analyses were supported by CREST of JST (Japan Science and Technology).

References

[1] C. Rath, K.K. Sahu, S.D. Kulkarni, S. Anand, S.K. Date, R.P. Das, N.C. Mishra, Appl. Phys. Lett. 75 (1999) 4171.
[2] C.V.G. Reddy, K.K. Seela, S.V. Manorama, Int. J. Inorg. Mater. 2 (2000) 301.
[3] H. Sesigur, E. Acma, O. Addemir, A. Tekin, Mater. Res. Bull. 31 (1996) 1573.
[4] L. Suber, D. Fiorani, P. Imperatori, S. Foglia, A. Montone, R. Zysler, Nanostruct. Mater. 11 (1999) 797.
[5] A.A. Burukhin, B.R. Churagulov, N.N. Oleynikov, A.V. Knotko, in: Proceedings of the 6th International Symposium on Hydro. React. and 4th International Conference on Solvo-therm. React., 2P-54, Japan, 2000.
[6] E. Matijevic, P. Scheiner, J. Colloid Interface Sci. 63 (1978) 509.
[7] M.P. Morales, T.G. Carreno, C.J. Serna, J. Mater. Res. 7 (1992) 2538.
[8] L. Li, G. Li, R.L. Smith Jr., H. Inomata, Chem. Mater. 12 (2000) 3705.
[9] M. Schuttz, W. Burckhardt, S. Barth, J. Mater. Sci. 34 (1999) 2217.
[10] R.A. Eggleton, R.W. Fitzpatrick, Clays Clay Miner. 36 (1988) 111.
[11] M. Ocana, M.P. Morales, C.J. Serna, J. Colloid Interface Sci. 212 (1999) 317.
[12] M. Hirano, Y. Fukuda, H. Iwata, Y. Hotta, M. Inagaki, J. Am. Ceram. Soc. 83 (2000) 1287.
[13] C.V.G. Reddy, K.K. Seela, S.V. Manorama, Int. J. Inorg. Mater. 2 (2000) 301.
[14] L. Diamandescu, D.M. Tarabasanu, N.P. Pogrion, A. Totovina, I. Bibicu, Ceram. Int. 25 (1999) 689.
[15] G. Li, S. Feng, L. Li, X. Li, W. Jin, Chem. Mater. 9 (1997) 2894.
[16] L. Armelao, R. Bertoncello, L. Crociani, G. Depaoli, G. Granozzi, E. Tondello, M. Bettinelli, J. Mater. Chem. 5 (1995) 79.

ELSEVIER

Fluid Phase Equilibria 194–197 (2002) 869–877

FLUID PHASE EQUILIBRIA

www.elsevier.com/locate/fluid

Temperature dependence of dielectric spectra of carbon dioxide and methanol mixtures at high-pressures

Richard L. Smith Jr.*, Chie Saito, Sachio Suzuki, Sung-Bong Lee, Hiroshi Inomata, Kunio Arai

Department of Chemical Engineering, Research Center of Supercritical Fluid Technology, Tohoku University, Aoba-ku, Aramaki Aza Aoba-07, Sendai 980-8579, Japan

Received 20 May 2001; accepted 1 August 2001

Abstract

Dielectric spectra can quantify how the solution structure of hydrogen-bonding solutions changes with composition and thermodynamic state. In our research, [Rev. Sci. Instrum. 71 (2000) 4226–4230], we developed a new dielectric probe and apparatus that can be applied to high-pressure liquids and gases. In this work, we study carbon dioxide and methanol mixtures over the temperature range of 313–333 K and at pressures up to 15 MPa. The characteristic relaxation times of methanol were found to exhibit a maximum in composition that persisted with increasing temperature. The increase in the relaxation time of carbon dioxide and methanol mixtures over that of pure methanol indicates that attraction occurs between the methanol dipole and the carbon dioxide quadrupole. Data are analyzed using experimental volumetric behavior of the system and according to the theory of Eyring. Regions of composition where carbon dioxide is incorporated into the methanol hydrogen-bonding structure are identified and an estimation is made on the region where the methanol associated structures probably dissociate.

Keywords: Dielectric constant; Spectroscopy; Mixtures

1. Introduction

Carbon dioxide and methanol mixtures find a wide range of use in the analytical [1], pharmaceutical [2], metal ion extractions [3], environmental [4] fields, and also in many chemical processing applications [5]. When methanol is added to supercritical carbon dioxide in low concentrations (1–10%), it acts as a co-solvent and enhances the extraction of solutes [3]. On the other hand, when supercritical carbon dioxide is added to liquid chromatography solvents such as methanol, it not only lowers the mobile phase viscosity, but also allows the mobile phase properties to be varied with pressure. The modified

* Corresponding author.
E-mail address: smith@scf.che.tohoku.ac.jp (R.L. Smith Jr.).

0378-3812/02/$ – see front matter
PII: S0378-3812(01)00714-2

mobile phase has been termed pressure enhanced fluidity by Shows and Olesik in the field and is leading to the development of many new bio- and chiral-separation techniques [6,7]. The interactions between methanol and carbon dioxide play a key role in these applications. In studies of dilute concentrations of methanol in carbon dioxide, Fulton et al. [8] found that methanol tends to form tetrameric aggregates in the supercritical carbon dioxide phase and attributed this to the probable strong interaction between the large quadrupole of CO_2 and the dipole of methanol. In studies on pure methanol, Asahi and Nakamura [9] used NMR and MD simulation and found that hydrogen-bonded clusters of methanol persisted up to the critical region. Yamaguchi et al. [10] investigated hydrogen-bond of methanol at subcritical and supercritical conditions with X-ray, neutron diffraction, and simulation methods. From their results, they concluded that methanol at ambient conditions have a non-linear hydrogen-bonded chain structure whereas at subcritical and supercritical conditions, the hydrogen-bonds are mostly associated with clusters of three to five methanol molecules. In contrast to these detailed research works, few studies exist on changes in the methanol environment when some amount of supercritical carbon dioxide is added to the system at constant temperature and pressure. In previous work, we developed a probe that allows dielectric spectroscopy measurements of supercritical fluid solutions. With this technique, it is possible to determine the distribution of dipole–dipole interactions in the presence of an electric field, and thus, quantify the change of molecular interactions that is occurring in solution. In this work, our objective was to study the interaction that methanol has with carbon dioxide using dielectric spectroscopy and solution properties and to apply Eyring's theory for interpreting the temperature dependence of the relaxation time constants.

2. Dielectric spectroscopy

The electric polarization of a polar molecule is made up of orientation, atomic and electric polarization. The orientation polarization can be determined from complex permittivity or so-called dielectric spectroscopy measurements. The complex permittivity, $\varepsilon^*(\omega)$ is a function of the angular frequency ($\omega = 2\pi f$) and is defined as

$$\varepsilon^*(\omega) = \varepsilon'(\omega) - i\varepsilon''(\omega) \tag{1}$$

where $\varepsilon'(\omega)$ and $\varepsilon''(\omega)$ are the real and imaginary contributions, respectively. As the frequency of the applied field is varied from low frequency to high frequency, dielectric storage capacity given by $\varepsilon'(\omega)$, decreases, and energy loss given by $\varepsilon''(\omega)$, increases. The frequency at which the greatest number of dipoles convert their motion into heat is characteristic of a molecule and its environment and defines the relaxation time constant

$$\tau = \frac{1}{2\pi f_{\max}} \tag{2}$$

The relaxation time constant data determined from dielectric spectra has found use in quantifying local composition regions of hydrogen-bonding mixtures [11].

3. Materials and methods

Methanol (99.8%) and water (HPLC grade) used were obtained from Wako Chemical (Osaka) and were used without further purification. CO_2 (99.99%) was obtained Nihon Sanso (Sendai). The appara-

tus and probe have been described previously [12]. Briefly, the apparatus consisted of a custom-made high-pressure co-axial probe and network analyzer, a 30 cm^3 cell, densimeter, magnetic pump and a 30 cm^3 pressure generator. The main components were housed in a constant temperature convection oven. The magnetic pump provided agitation while the pressure generator allowed variation of density at constant composition. Calibration fluids were water, methanol and air. After loading mixtures at a given temperature and pressure, dielectric spectra were taken after equilibration had been achieved.

4. Results and discussion

Numerous dielectric spectra and density data were taken in the single phase region of methanol+carbon dioxide at pressures from 0.1–18 MPa and at temperatures from 313.2–323.2 K. From the $\varepsilon'(\omega)$ and $\varepsilon''(\omega)$ versus frequency data, the Cole–Cole equation was fit to the data to determine τ. Details on the general procedure are given in our previous work [11]. Our emphasis in this work is to analyze the thermal dependence of the relaxation time constant data of methanol in the presence of a fluid in a highly compressible state. The pressure chosen was 11 MPa due to considerations of the single phase region. Another work in preparation will cover the spectral distributions, data reduction and their analysis [13].

4.1. Relaxation time constants

The variation of the relaxation time τ with composition and temperature is shown in Fig. 1. The lines in Fig. 1 are discussed in a later section. At 313.2 K, pure methanol had a relaxation time of 34.5 ps. This value means that with an applied sinusoidal electric field of 4.6 GHz approximately $1/\varepsilon$ of the methanol dipoles can just follow the change in the electric field according to the relaxation theory of Debye [14].

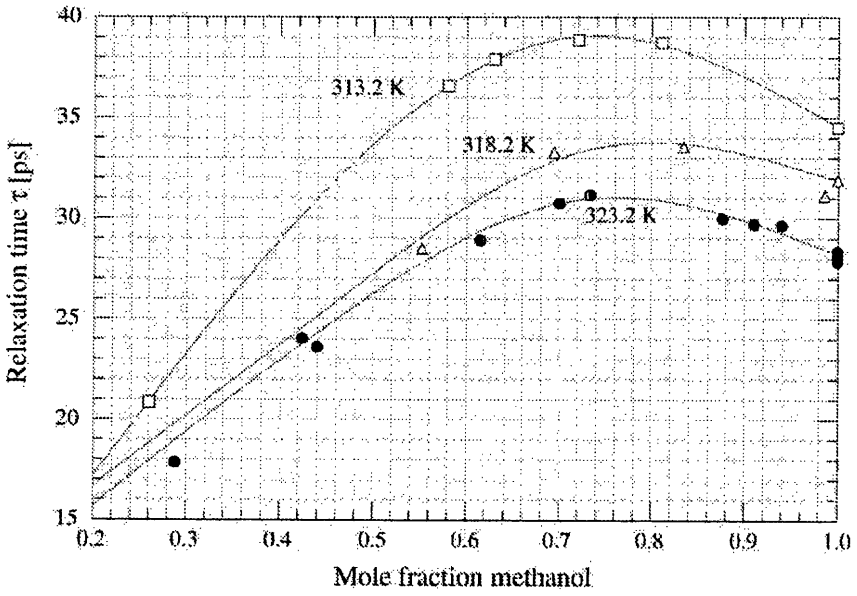

Fig. 1. Relaxation time constants vs. methanol composition for carbon dioxide and methanol mixtures at 11 MPa for temperatures from 313.2 to 323.2 K.

As the temperature was increased, the relaxation time decreased to about 28 ps at 323.2 K. When carbon dioxide was added to the pure methanol solutions, the relaxation times initially increased and exhibited a maximum according to methanol mole fraction as shown in Fig. 1.

The hydrodynamic theory of the Stokes–Einstein–Debye (SED) equation [15] is useful to discuss the various trends of the relaxation time data although is it is only valid for dilute solutions of a solute in a solvent:

$$\tau = \left\{\frac{4\pi r^3}{3k_B}\right\}\left(\frac{\eta}{T}\right) \tag{3}$$

where r is the radius of a solute, k_B the Boltzmann constant η the solvent viscosity and T is the absolute temperature. In the present case, R refers to methanol in the carbon dioxide and methanol solvent mixture. Eq. (3) predicts that τ is inversely proportional to temperature which is qualitatively followed by the pure methanol data in Fig. 1. At constant temperature, as carbon dioxide is added to pure methanol at constant pressure, the solution viscosity can be expected to monotonically decrease and this was confirmed by estimations that we made with the equations of Chung et al. [16]. According to Eq. (3), then, as the carbon dioxide mole fraction increases, the relaxation time should monotonically decrease. In contrast to the expected behavior, the relaxation time increased and exhibited a maximum. This implies that, along with all of the many assumptions of Eq. (3), that the solute volume r^3 is a function of the solvent environment. Next, we examined solution volumetric behavior.

4.2. Excess volumes

The volumetric data measured were correlated with a two-constant Redlich–Kister expansion:

$$V^E = x_{CO_2}x_m[A + B(x_{CO_2} - x_m)] \tag{4}$$

where x_m and x_{CO_2} refer to the methanol and carbon dioxide mole fractions, respectively. Constants A and B for Eq. (4) for each isotherm are given in Table 1. According to the observed behavior, the excess volume was found to be negative over all conditions examined as shown by our measurements in Fig. 2 according to the technique in [12].

4.3. Partial molar volume (PMV)

Use of standard thermodynamic relations with Eq. (4) allows determination of component partial molar volumes. These results are shown in Figs. 3 and 4 for methanol and carbon dioxide, respectively. Table 2 gives the pure component volumes used. In Fig. 3, it can be seen that the methanol PMV undergoes little change over the composition region from pure methanol to x_m of about 0.6. As the methanol mole fraction

Table 1
Parameters for the excess volume (Eq. (4)) for mixtures of carbon dioxide and methanol at 11 MPa

T (K)	A (m^3/mol) × 10^6	B (m^3/mol) × 10^6
313.2	−32.1487	−15.7370
318.2	−44.2108	−18.1521
323.2	−74.7464	−51.1840

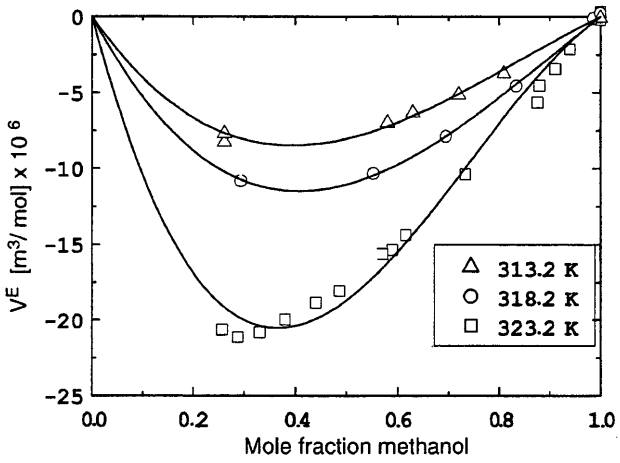

Fig. 2. Excess volume of methanol and carbon dioxide mixtures at 11 MPa and at temperatures from 313.2 to 323.2 K.

becomes low, the methanol PMV goes negative which has been attributed in very early work to the local density enhancement of fluids in their supercritical state [17]. In Fig. 4, over the composition region from pure methanol to x_m of about 0.6, the carbon dioxide PMV initially decreased with increasing carbon dioxide mole fraction and all isotherms exhibited a distinct minimum. This means that carbon dioxide was initially incorporated into the methanol solution structure. A close examination of Fig. 3 does show that the methanol PMV all slightly increase over the same composition region.

The densities for all three isotherms (not shown) exhibited maxima at about a methanol mole fraction of 0.6, which leads us to believe that the trend of relaxation time with composition can be described by a free-volume model. This will be examined in a later more comprehensive work.

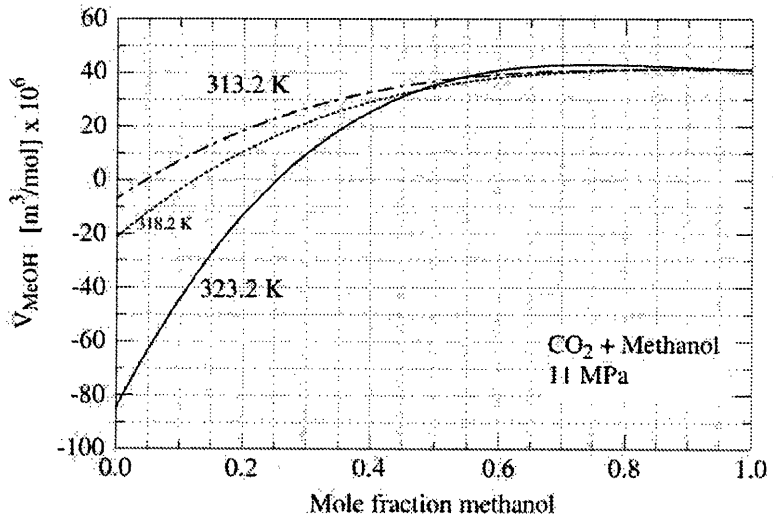

Fig. 3. Partial molar volume of methanol in carbon dioxide at 11 MPa and at temperatures from 313.2 to 323.2 K.

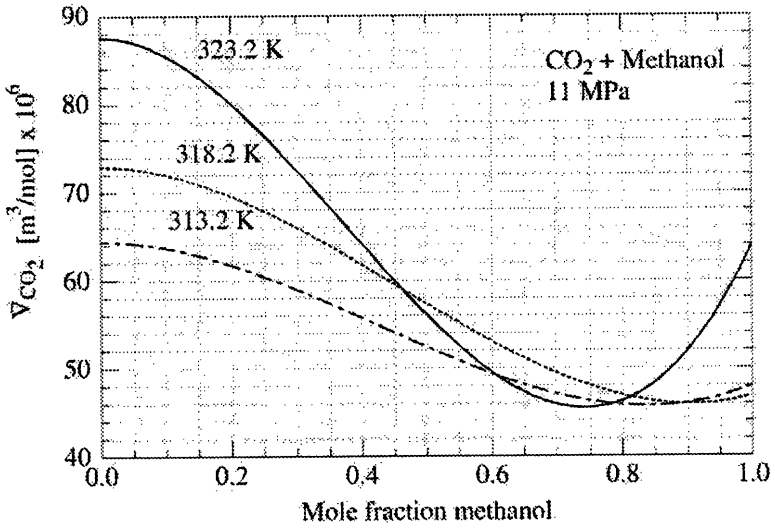

Fig. 4. Partial molar volume of carbon dioxide in methanol at 11 MPa and at temperatures from 313.2 to 323.2 K.

Table 2
Pure component molar volumes used [22,23] for the calculation of the partial molar volumes

T (K)	V^0 CO_2 (m^3/mol) × 10^6	V^0 methanol (m^3/mol) × 10^6
313.2	64.39	40.95
318.2	72.91	41.14
323.2	87.56	41.39

4.4. Activation free energy, enthalpy and entropy

It is of interest to determine the activation free energy, enthalpy and entropy of the relaxation processes. Following the procedure of Sato et al. [18] who used Eyring's theory for relating relaxation processes to activation energies:

$$\Delta G^* = RT\left(\ln\tau - \ln\left(\frac{h}{k_B T}\right)\right) \tag{5}$$

$$\Delta H^* = R\left(\frac{\mathrm{d}\ln\tau}{\mathrm{d}(1/T)}\right) - RT \tag{6}$$

$$T\Delta S^* = \Delta H^* - \Delta G^* \tag{7}$$

where h is Planck's constant and ΔG^*, ΔH^*, and ΔS^*, refer to the activation Gibbs free energy, enthalpy and entropy, respectively. From the data in Fig. 1, smooth curves were drawn to approximately fit their trend. These curves allowed interpolation at convenient composition intervals and differentiation with inverse temperature. Excess values of the activation energies were calculated according to

$$\Delta F^{*E} = \Delta F - [x_{CO_2}\Delta F_{CO_2} + x_m \Delta F_m] \tag{8}$$

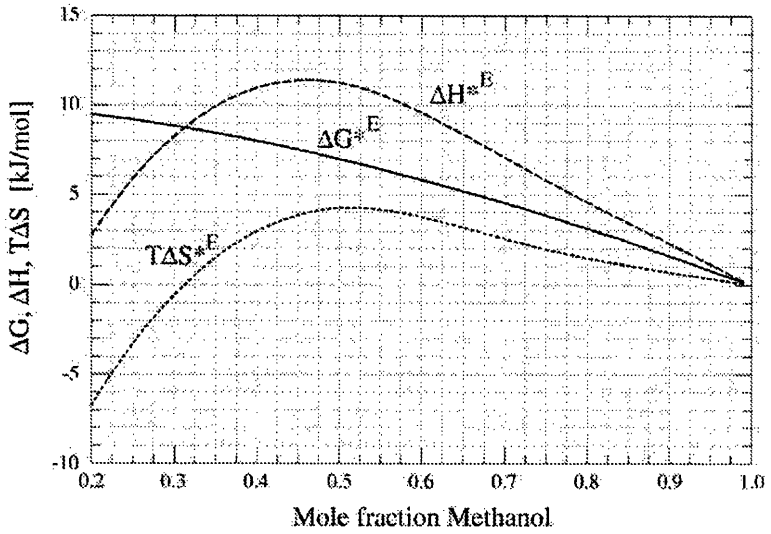

Fig. 5. Activation energies and entropies for methanol and carbon dioxide mixtures at 11 MPa determined from application of the theory of Eyring and differentiation of the smoothed relaxation time constant data.

where F is equal to G, H, or S and ΔF_{CO_2} and ΔF_m refer to pure component values. For carbon dioxide, which only has a quadrupole moment, values of ΔF_{CO_2} were set equal to zero. For methanol, values of ΔF_m could be derived from the relations given by Eqs. (5)–(7) and the pure methanol data of Fig. 1. Application of Eqs. (5)–(8) to the curves in Fig. 1 gave the results as shown in Fig. 5. From Fig. 5, over most of the composition region ($x_m = 0.3$ to $x_m = 1$), the contributions of ΔG^*, ΔH^*, and $T\Delta S^*$ were large positive values indicating strong interactions. Although ΔG^* did not show any unusual features, the ΔH^*, $T\Delta S^*$ each exhibited a maximum in composition which indicates a change in the solution structure.

The solution structure of pure methanol is of interest in discussing the above trends. It has been suggested that methanol contains a large fraction of hexamer associated structures in its liquid state at room temperature [19]. However, in view of the detailed analyses of Yamaguchi et al. [20,21], methanol solution structure consists of groups of three to five methanol molecules are associated in a non-linear fashion. According to the analysis of this work, the increase in the relaxation times when CO_2 is added to pure methanol shows incorporation of carbon dioxide into the methanol hydrogen-bonding network until at least the maximum in the relaxation time of each isotherm is reached ($x_m = 0.7$–0.8). Then, as more carbon dioxide is added, the population of dimer, trimer or associated structures increase, which eventually leads to breakup of the larger associated groups and decreases in the excess activation enthalpy and entropy along with negative values of the partial molar volumes.

5. Conclusions

The temperature dependence of the dielectric spectra of carbon dioxide and methanol mixtures has been summarized and analyzed with solution properties and consideration of the rate theory of Eyring. It is found that when carbon dioxide is initially added to pure methanol at 11 MPa and 313.2–323.2 K, that the CO_2 is incorporated into the methanol hydrogen-bonding structure as observed by an increase

in the characteristic relaxation time constant of the methanol dipole. Further addition of CO_2 leads over the maximum mole fractions given by the relaxation time data probably leads to a break-up of the associated structures. Dielectric spectroscopy data on hydrogen-bonding systems, especially with carbon dioxide, should help to develop new local composition theory and to refine molecular dynamics simulation models.

List of symbols

A, B	constants in Eq. (4) (m^3/mol)
i	$\sqrt{-1}$
f_{max}	frequency of maximum in ε'' (Hz)
F	G, H, or S
ΔG	molar Gibb's free energy (J/mol)
h	Planck's constant (6.626×10^{-34} J s)
ΔH	molar enthalpy (J/mol)
k_B	Boltzmann constant (1.38×10^{-23} J/K)
r	solute radius (m)
R	gas constant (8.314 J/mol K)
ΔS	molar Entropy (J/mol K)
T	absolute temperature (K)
V	molar volume (m^3/mol)
x	mole fraction

Greek letters

ε^*	complex permittivity
ε'	real contribution of Eq. (1)
ε''	imaginary contribution of Eq. (1)
η	viscosity (P)
τ	relaxation time (s)
ω	angular velocity ($=2\pi f$)

Subscripts

CO_2	carbon dioxide
m	methanol

Superscripts

0	pure
*	activation
E	excess property

Acknowledgements

The authors wish to gratefully acknowledge financial support from Genesis Research Institute, Inc. and the Ministry of Education, Science, Sports and Culture Japan.

References

[1] M. Ashraf-Khorassani, M.T. Combs, L.T. Taylor, J. Chromatogr. A 774 (1997) 37–49.
[2] F.P. Lucien, N.R. Foster, J. Supercrit. Fluids 17 (2000) 111–134.
[3] C. Erkey, J. Supercrit. Fluids 17 (2000) 259–287.
[4] G. Anitescu, L.L. Tavlarides, J. Supercrit. Fluids 14 (1999) 197–211.
[5] W.H. Hauthal, Chemosphere 43 (2001) 123–135.
[6] M.E. Shows, S.V. Olesik, J. Chromatogr. Sci. 38 (2000) 399–408.
[7] Q. Sun, S.V. Olesik, Anal. Chem. 71 (1999) 2139–2145.
[8] J.L. Fulton, G.G. Yee, R.D. Smith, J. Am. Chem. Soc. 113 (1991) 8327–8334.
[9] N. Asahi, Y. Nakamura, J. Chem. Phys. 109 (1998) 9879–9887.
[10] Y. Yamaguchi, C.J. Benmore, A.K. Soper, J. Chem. Phys. 112 (2000) 8976–8987.
[11] R.L. Smith Jr., S.B. Lee, H. Komori, K. Arai, Fluid Phase Equilib. 144 (1998) 315–322.
[12] S.B. Lee, R.L. Smith Jr., H. Inomata, K. Arai, Rev. Sci. Instrum. 71 (2000) 4226–4230.
[13] R.L. Smith Jr., C. Saito, S. Suzuki, S.-B. Lee, H. Inomata, K. Arai, J. Chem. Phys., 2001, submitted for publication.
[14] P. Debye, Polar Molecules, Chemical Catalog Co. Inc., New York, 1929.
[15] M. Nakahara, K. Emi, J. Chem. Phys. 99 (1993) 5418–5425.
[16] T.-C. Chung, M. Ajlan, L.L. Lee, K.E. Starling, Ind. Eng. Chem. Res. 27 (1988) 671–679.
[17] C.A. Eckert, D.H. Ziger, K.P. Johnston, T.K. Ellison, Fluid Phase Equilib. 14 (1983) 167.
[18] T. Sato, A. Chiba, R. Nozaki, J. Chem. Phys. 112 (2000) 2924–2932.
[19] S. Sarkar, R.N. Joarder, J. Chem. Phys. 99 (1993) 2032–2039.
[20] T. Yamaguchi, K. Hidaka, A.K. Soper, Mol. Phys. 96 (1999) 1159–1168.
[21] T. Yamaguchi, K. Hidaka, A.K. Soper, Mol. Phys. 97 (1999) 603–605.
[22] R. Span, W. Wagner, J. Phys. Chem. Ref. Data 25 (1996) 1509–1596.
[23] R.D. Goodwin, J. Phys. Chem. Ref. Data 16 (1987) 799–892.

March 2002

ELSEVIER

Materials Letters 53 (2002) 175–179

MATERIALS LETTERS

www.elsevier.com/locate/matlet

Synthesis and thermal decomposition of nitrate-free boehmite nanocrystals by supercritical hydrothermal conditions

Guangshe Li, R.L. Smith Jr., H. Inomata*, K. Arai

Research Center of Supercritical Fluid Technology, Department of Chemical Engineering, Tohoku University, Sendai 980-8579, Japan

Received 2 February 2001; received in revised form 21 June 2001; accepted 29 June 2001

Abstract

Single-phase boehmite nanocrystals that are free of nitrate contamination could be prepared at supercritical hydrothermal conditions at 400 °C and 35 MPa for 30 min. XRD analysis showed that the single phase boehmite was formed in the absence of alkali species. Two well-defined and strong absorption bands observed at 3300 and 3092 cm^{-1} in the present infrared spectra showed that the boehmite by supercritical hydrothermal conditions was highly crystallized. Furthermore, IR spectra confirmed that the boehmite samples were free of NO_3^--related impurities in contrast to boehmite produced by hydrothermal conditions as reported by Music et al. [Mater. Lett., 40 (1999) 269] and Mishra et al. [Mater. Lett., 42 (2000) 38]. At a temperature of 725 °C, the present boehmite powders were decomposed into 10 nm γ-Al_2O_3. Further heating of the samples to 1250 °C led to the formation of single-phase α-Al_2O_3.

Keywords: Nanocrystals; Boehmite; Supercritical; Hydrothermal; γ-Al_2O_3

1. Introduction

Boehmite AlOOH is frequently employed as the precursor for preparation of advanced catalysts, coatings, alumina, and alumina-derived ceramics [1,2]. It has a layered structure with adjacent layers being bound by hydrogen bonds. At higher temperatures, this layered structure is decomposed by breakage of the hydrogen bonds and transformed into alumina with different structures. Each structure exhibits different physical properties such as catalyst support of γ-Al_2O_3 and structural ceramic of α-Al_2O_3. The purity, particle size, and calcination history of boehmite determine the particular characteristics and sinterability of the final alumina [3].

Traditionally, boehmite is prepared via the hydrolysis reactions of inorganic/organic aluminum salts in the basic medium according to the following procedure [4,5]: (i) precipitation of amorphous aluminum hydroxides in the presence of several neutralizing agents such as urea and NaOH, and (ii) transformation of the hydroxides into crystalline $Al(OH)_3$ by heating at higher temperatures or into boehmite by hydrothermal crystallization. These types of synthetic routes have several drawbacks, notably, incomplete transformation reactions that can give unwanted amorphous phases, and possible sample contamination from the nitrate species for the cases when reactants in the form of nitrates are used. It is clear that control of the formation reactions for nanocrystalline boehmite is a great challenge to the alumina industry. In this paper, we report on the supercritical hydrothermal synthesis of single-phase

* Corresponding author.
E-mail address: inomata@scf.che.tohoku.ac.jp (H. Inomata).

00167-577X/02/$ - see front matter
PII: S0167-577X(01)00472-4

boehmite nanocrystals using $Al(NO_3)_3 \cdot 9H_2O$ as the starting material.

2. Experimental

Only a limited set of conditions were examined. A typical experimental procedure can be described briefly as follows: 5 ml of 0.25 M $Al(NO_3)_3$ solution was charged into a stainless steel autoclave of 10 ml capacity. The autoclave was sealed and immersed in a molten salt bath at 400 °C for 30 min. For reference, the pressure would be ca. 35 MPa for a loaded density pure water and the system temperature of 400 °C. The autoclave is then cooled to room temperature in a water bath. The sample was washed with deionized water and dried in air at 60 °C, which gave a white powdered sample.

For comparison, the boehmite samples were also prepared by hydrothermal conditions. Ten milliliters of 0.25 M $Al(NO_3)_3$ solution was mixed with 2 ml of 2 M NaOH while stirring. The mixture was sealed into the 17-ml Teflon-lined stainless steel autoclave with a capacity of 50% and then allowed to react at 200–240 °C for several hours. The washing procedure is the same as that for supercritical conditions.

XRD patterns for the samples were recorded on a diffractometer (Model 2013, MAC Science, Tokyo) with MoKα radiation ($\lambda_{k\alpha 1}$ = 0.70932 Å). The scan rate was 1°/min. The particle sizes were determined by Scherrer's equation and the lattice parameters were refined by least-squares methods.

The infrared (IR) spectra of the samples were recorded in air using the KBr technique. The thermal stability of the boehmite samples was detected by TG-DTA at a heating rate of 20 °C/min in air. The samples that were used in the TG measurements were subsequently examined by XRD.

3. Results and discussion

XRD pattern for the typical sample prepared at supercritical hydrothermal conditions is shown in Fig. 1. It can be seen that the XRD data for the product matched with the standard diffraction data for boehmite [6], which indicated that the present boehmite sample had an orthorhombic structure. The

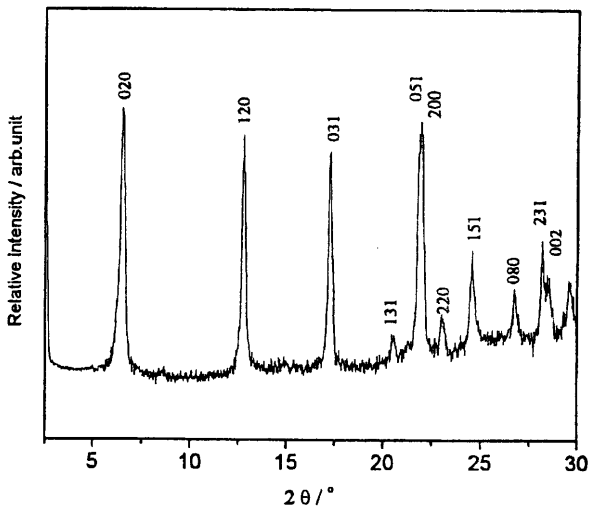

Fig. 1. X-ray diffraction pattern of boehmite prepared at supercritical hydrothermal conditions.

broadening effect for the XRD pattern in Fig. 1 reflected the fine nature of the boehmite particles. The average particle size was determined to be in a narrow range of 13–16 nm. The diffraction line (020) had a maximum intensity and the particle size determined from this peak was ca. 13 nm, while lines (120) and (031) gave comparable particle sizes of ca. 16 nm. These results showed that the boehmite particles were uniform in dimension. In addition, the relative intensities for both peaks (120) and (031) are, respectively, 91% and 85%, much different from 65% and 55% for the boehmite given in Ref. [6]. The peak position for line (020) was found to vary in the range of d-spacing, 6.10–6.28 with the reaction time (not shown), which was closely related to the stacking fault between layers of the boehmite structure [7] by forming a modified boehmite intermediate. These data confirmed that supercritical hydrothermal conditions seem to be efficient in producing single-phase boehmite with changeable layered structures. In contrast, boehmite prepared by traditional hydrothermal conditions (160–220 °C) in the presence of a high concentration of urea usually shows a strong impurity peak at a d-spacing of ca. 0.93 nm [4]. When the hydrothermal conditions contained NaOH or KOH, an extraordinary growth of the (020) diffraction line is observed, which could be associated with the predominant adsorption of Na^+ or K^+ ions on the ac planes of the boehmite lattice [8].

The infrared spectrum of a typical boehmite sample by supercritical hydrothermal conditions is shown in Fig. 2. The IR spectrum for the boehmite by traditional hydrothermal conditions is also illustrated for comparison (inset). From Fig. 2, it is clear that the boehmite prepared by supercritical hydrothermal conditions showed absorption bands at 641, 737, 1071, 1161, 1974, 2100, 3092, and 3300 cm^{-1}, which agreed precisely with those reported in the literature [9]. The band at 641 cm^{-1} corresponded to the vibration mode of AlO_6 while other bands characterized the OH^- bonds in the boehmite lattice. Two strong but well-separated absorption bands at 3092 and 3300 cm^{-1} indicated that the present boehmite was highly crystalline [10]. It should be noted that the boehmite by supercritical hydrothermal conditions did not show absorption at ca. 1380 cm^{-1} (Fig. 2a, inset), which demonstrated that the present boehmite was free of contamination by nitrate species introduced by the reactant aluminum salt. This was further confirmed by the TG measurements as discussed later. In contrast, boehmite samples prepared at traditional hydrothermal conditions from nitrate reactants contains strong absorption from nitrate species [4,10], which is also shown for the boehmite prepared at hydrothermal conditions in this work (Fig. 2b, inset). It should be noted that boehmite

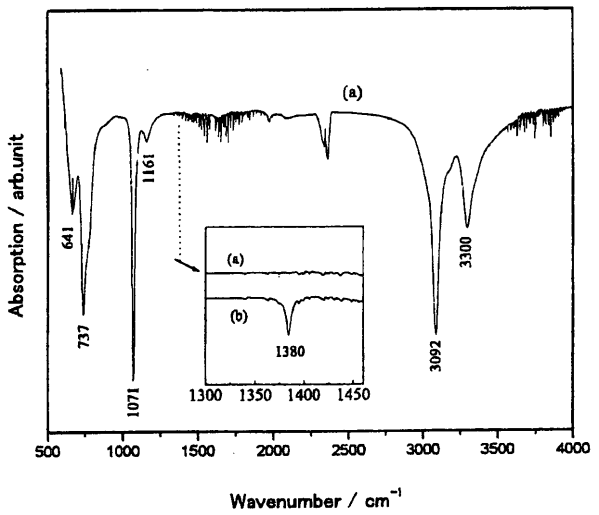

Fig. 2. IR spectrum of boehmite prepared at supercritical hydrothermal conditions. Inset shows the enlargement of the region for nitrate impurity in the boehmite by (a) supercritical hydrothermal conditions and (b) traditional hydrothermal conditions.

produced under traditional hydrothermal conditions contains nitrate species that cannot be completely washed away, even though the boehmite sample can be regarded as single phase in terms of X-ray diffraction [4,10]. As mentioned above, boehmite produced by alkali hydrothermal conditions can contain some amount of alkali species on the ac planes of the boehmite lattice by producing a net charge, which can be balanced by occupation of the nitrate species in the layers of the boehmite lattice. Such a layered structure could also be modified by other species such as alkyl pendant groups [11].

The thermal behavior of the boehmite was studied by TG. Fig. 3 showed the TG curve for a boehmite sample prepared under supercritical hydrothermal conditions. Two weight losses were observed at ca. 70 and 510 °C. The first weight loss is due to desorption of the physically sorbed water, while the second weight loss is ascribed to the condensation of adjacent Al–OH groups. Similar assignments have been found for the decomposition of boehmite, as is confirmed by solid state ^1H and ^{27}Al NMR [12]. From the first-order derivative (dotted line), no obvious thermal effect was observed at ca. 220 °C, which was strong evidence that the present boehmite did not contain amorphous aluminum hydroxide. This result was clearly different from the boehmite prepared by base hydrolysis of aluminum nitrate solutions at 85 °C [5]. In the latter case, a thermal effect at ca. 220 °C was observed and assigned to the strongly bound water associated with a transitional (amorphous) $Al(OH)_3$. We also observed the thermal behaviors of the boehmite samples obtained using different reaction times and found similar decomposition processes except for a slight difference in the total weight loss. From the total weight loss, we found that the hydrated water in $Al_2O_3 \cdot xH_2O$ varied in a range of $1.3 < x < 1.5$, which is exactly the same as that obtained by hydrothermal conditions [4]. The TG measurements also confirmed that the boehmite samples were essentially free of nitrate species on the basis of weight loss related to combustion of nitrate species at ca. 310 °C [13]. No thermal effect in this temperature range was observed.

The structural evolution of the boehmite samples by supercritical hydrothermal conditions was followed with XRD after TG measurements above the

de-hydroxylation point. Fig. 4 shows the XRD patterns for the decomposition products of the boehmite. It can be seen that at a temperature of 725 °C, the boehmite transformed into γ-Al_2O_3. From the broadening effect of the peak (400), the particle size of γ-Al_2O_3 could be calculated to be ca. 10 nm. The γ-Al_2O_3 crystallized in a defective spinel lattice with aluminum located in tetragonal positions. Such a lattice is metastable and should transform into a stable form at high temperatures. It is known that the preparative conditions of the precursor boehmite have shown a pronounced effect on the structural stability and furthermore the structural evolution of γ-Al_2O_3 [14]. For the present work, as shown in Fig. 4, increasing temperature to 900 °C led to the appearance of traces of δ-Al_2O_3 as characterized by the main peak at 2θ of ca. 21°, which is an essential intermediate phase for the phase transformation of γ-Al_2O_3 at higher temperatures. These results demonstrate that γ-Al_2O_3 was stable below 900 °C. Such a relatively low structural stability provides indirect evidence of pure boehmite being formed under supercritical hydrothermal conditions. For example, it has been shown that when there are alkali species such as Na^+ located in the layered lattice, then the addition of defects from the sodium cations stabilizes the metastable spinel lattice of γ-Al_2O_3 up to 1100 °C [15]. At a temperature higher than 1250 °C, single-phase α-Al_2O_3 was obtained with a high crystalline as is reflected by the highly relative intensity of the diffraction peaks.

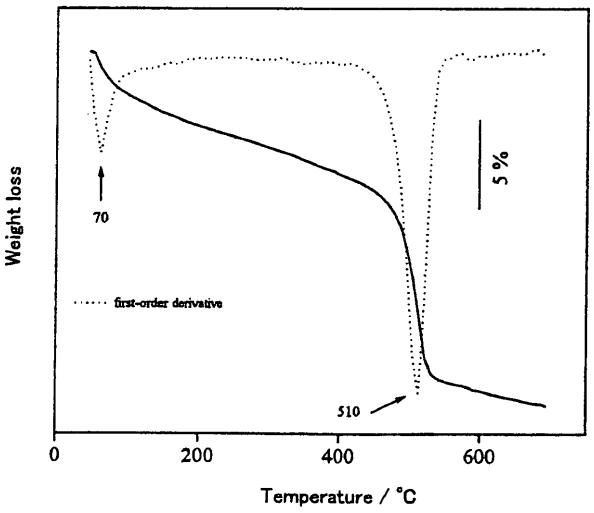

Fig. 3. TG curve of boehmite prepared at supercritical hydrothermal conditions.

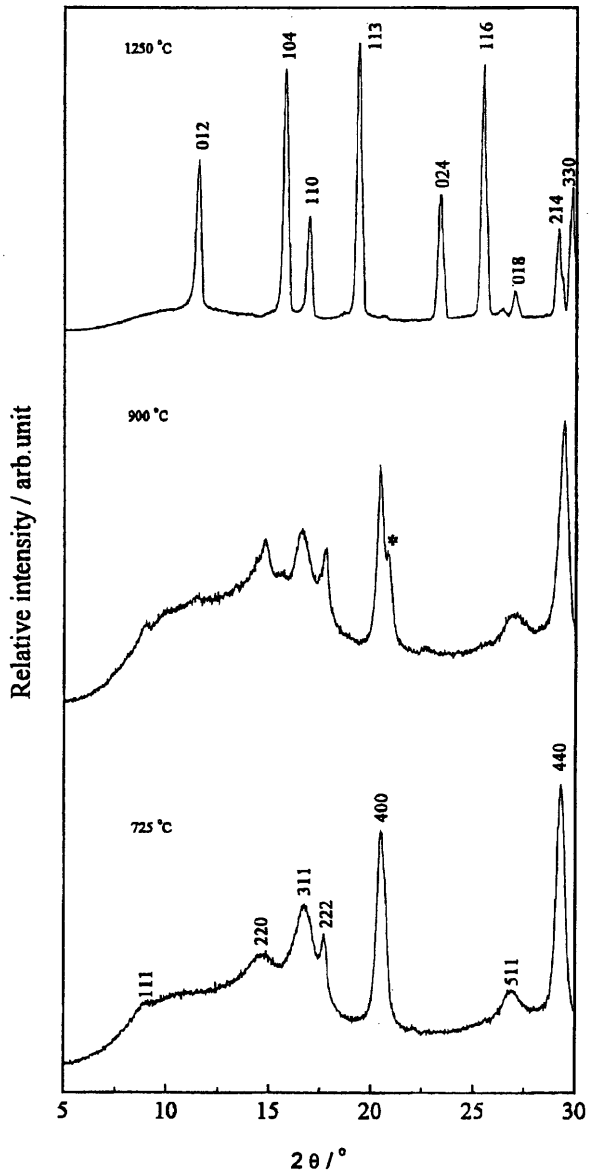

Fig. 4. XRD patterns of boehmite decomposition products after TG measurements at 725, 900, and 1250 °C. * Denotes an intermediate phase of δ-Al_2O_3.

4. Conclusions

Nitrate-free boehmite nanocrystals can be formed under supercritical hydrothermal conditions. The

nanocrystals were highly crystalline and the resulting material could be decomposed into γ-Al_2O_3 nanocrystals at 725 °C and single-phase α-Al_2O_3 at 1250 °C.

Acknowledgements

The authors would like to acknowledge financial support of the Ministry of Education, Science, Sports and Culture for support of this research.

References

[1] K. Strenge, U. Bollmann, Colloids Surf. Eng. 57 (1991) 139.
[2] B.E. Yoldas, Am. Ceram. Soc. Bull. 54 (1975) 289.
[3] T.V. Mani, P.K. Pillai, A.D. Damodaran, K.G.K. Wattier, Mater. Lett. 19 (1994) 237.
[4] D. Mishra, S. Anand, R.K. Panda, R.P. Das, Mater. Lett. 42 (2000) 38.
[5] E. Morgado Jr., Y.L. Lam, F.L. Nazar, J. Colloid Interface Sci. 188 (1997) 257.
[6] W.F. McLung, Powder Diffraction File: Inorganic Phase, JCPDS, International Center for Powder Diffraction Data: Swarthmore, PA, 1989, Card No. 21-1307.
[7] D. Grebille, J.F. Berar, J. Appl. Crystallogr. 19 (1986) 249.
[8] T. Tsuchida, J. Eur. Ceram. Soc. 20 (2000) 1759.
[9] A.B. Kiss, G. Keresztury, L. Fakas, Spectrochim. Acta 36A (1980) 653.
[10] S. Music, D. Dragcevic, S. Popovic, Mater. Lett. 40 (1999) 269.
[11] M. Inoue, M. Kimura, T. Inui, Chem. Mater. 12 (2000) 55.
[12] J.J. Fitzgerald, G. Piedra, S.F. Dec, M. Seger, G.E. Maciel, J. Am. Chem. Soc. 119 (1997) 7832.
[13] L. Li, G. Li, R.L. Smith Jr., H. Inomata, Chem. Mater. 12 (2000) 3705.
[14] C. Pecharroman, I. Sobrados, J.E. Iglesias, T.G. Carreno, J. Sanz, J. Phys. Chem. 103B (1999) 6160.
[15] R.S. Zhou, R.L. Snyder, Acta Crystallogr. 47B (1991) 617.

Activation of oxide-ion conduction in $KNbO_3$ by addition of Mg^{2+}

Liping Li[a)]
Department of Physics, Jilin University, Changchun 130023, People's Republic of China

Guangshe Li,[b)] R. L. Smith, Jr., and H. Inomata
Research Center of Supercritical Fluid Technology, Department of Chemical Engineering, Tohoku University, Sendai 980-8579, Japan

(Received 28 February 2002; accepted 15 August 2002)

Niobate perovskite oxides of $KNb_{1-x}Mg_xO_{3-\delta}$ were synthesized directly at high temperature and pressure. X-ray diffraction confirmed the formation of single-phase orthorhombic structures. High-temperature Raman spectroscopy in combination with thermal analysis showed that phase transitions occurred from orthorhombic to tetragonal, to pseudo cubic, and finally to cubic, in sequence. Addition of Mg^{2+} at the Nb^{5+} sites of perovskite $KNbO_3$ lattice led to a dramatic enhancement of oxide-ion conduction. This enhancement in oxide-ion conduction was through the suppression of the contribution from p-type holes, which shows that these high-temperature phases can be promising candidates as conductive materials. © *2002 American Institute of Physics.* [DOI: 10.1063/1.1512957]

Niobate-based perovskite oxides are of great interest to the physics community, since these materials have physical properties that are highly dependent on structure.[1] For example, rhombohedral ferroelectric $KNbO_3$ transforms to a paraelectric cubic phase at high temperatures[1] and by structural modification, the properties of $KNbO_3$ can be further tailored for specific applications. The K^+-site substitutions by elements such as Ba^{2+} can yield semiconducting behavior,[2] while substitutions at the Nb^{5+} site with Mg^{2+} enhance optical properties.[3] Niobate-based perovskite oxides such as $PbMg_{1/3}Nb_{2/3}O_3$ show dielectric enhancements, while their ionic conduction is poor. Research on Mg^{2+} doping at the octahedral site shows enhanced ionic conduction in perovskite lattices.[4,5] If oxide-ion conduction can be activated and phase transitions can be modified by doping $KNbO_3$, then this could open the door to a new technological era.

Current perovskite lattices with Mg^{2+} and Nb^{5+} simultaneously at octahedral sites have to be prepared through two-step sintering processes that have $MgNb_2O_6$ as the key intermediate phase. It is of great interest to develop a single-step route to highly crystallized Mg niobate-based perovskite oxides and to determine the oxide-ion conduction enhancement in these lattices.

In this letter, we report on a single-step synthesis and oxide-ion conduction of $KNb_{1-x}Mg_xO_{3-\delta}$ that was obtained by high-temperature and high-pressure conditions.

The synthesis of $KNb_{1-x}Mg_xO_{3-\delta}$ was achieved with the following procedure. $KHCO_3$, MgO, and Nb_2O_5 were used as the starting materials, and were grinded fully at molar ratios of K : Nb: Mg = 1: $1-x$: x with $x = 0.05-0.30$. This mixture was placed into a high-pressure chamber as described in our previous article.[6] Pressure was set to 4.0 GPa and then the temperature was increased gradually to 870 °C. After maintaining these conditions for 40 min, the specimens were quenched to room temperature under high pressure and subsequently, the pressure was released.

X-ray diffraction (XRD) data of samples were measured at room temperature at a scan rate of 0.3°2 θ/min. The lattice parameters for the samples were calculated by least-squares methods. Phase transitions were determined by high-temperature Raman spectroscopy. Phase transitions were determined by differential thermal analysis (DTA). The ionic conductivities for the pellet samples were measured using ac impedance spectroscopy with an alternating current at a frequency between 10 Hz and 9 MHz at an amplitude of 50 mV in the temperature range of 400–800 °C in air. The impedance spectra were also measured at different oxygen partial pressures.

XRD data (Fig. 1) of the samples $KNb_{1-x}Mg_xO_{3-\delta}$ consisted of several split diffraction peaks, indicating a low symmetric structure. The double lines that can be observed at ~23° and 47° are characteristic of the orthorhombic perovskites. The XRD patterns were scaled for $x < 0.30$ but this did not result in any weak peaks arising from $MgNb_2O_6$ or $Mg_4Nb_2O_9$. These phases are, however, key intermediates during the formation of Mg niobate-based perovskite oxides.[7] These results clearly demonstrated that high-temperature and high-pressure conditions provided a single-step synthesis route to orthorhombic perovskite lattice $KNb_{1-x}Mg_xO_{3-\delta}$.

The substitution of Mg^{2+} at the Nb^{5+} sites was also evident from the diffraction peak shifts under the lattice volume variation. The lattice volume increased with the dopant content of Mg^{2+} (inset of Fig. 1) mainly due to Mg^{2+} being larger than Nb^{5+} in octahedral coordination. Doping Mg^{2+} at Nb^{5+} sites would most likely produce a larger lattice distortion for lattice expansion. The large charge difference between Nb^{5+} and Mg^{2+} may produce some negative charge centers on a local scale around Mg^{2+}, since this would have to be balanced by oxygen vacancies. Each two Mg^{2+} ions should yield three oxygen vacancies $V\ddot{o}$, which would be attracted to the nearest neighboring positions of Mg^{2+} under

[a)]Present address: Department of Materials Science and Engineering, California Institute of Technology, Pasadena, California 91106.
[b)]Author to whom correspondence should be addressed; present address: C302 BNSN, Department of Chemistry and Biochemistry, Brigham Young University, Provo, UT 84604; electronic mail: guangshe@hotmail.com

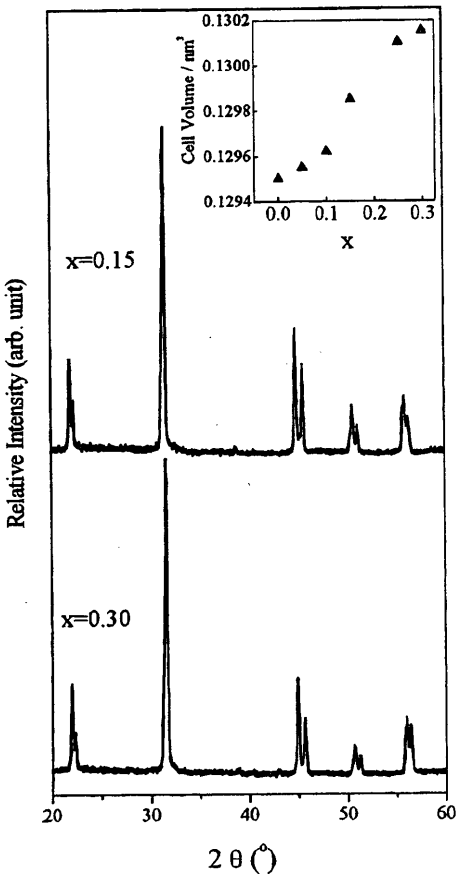

FIG. 1. XRD patterns for $KNb_{1-x}Mg_xO_{3-\delta}$ at typical compositions $x=0.15$ and 0.30. Inset illustrates the variation of the lattice volume with dopant content.

Coulombic forces. In our samples, the concentration of oxygen vacancy $V\ddot{o}$ would increase with Mg^{2+} content. The cationic substitutions and variations for the relative content of oxygen vacancy $V\ddot{o}$ and defect associations $\{Mg_{Nb}'''V\ddot{o}\}$ were, therefore, assumed to be the main factors for the increase in lattice volume. This follows similar reasoning as that has been proposed to explain the nonlinearity for solid solutions of $Ce_{1-x}RE_xO_{2-x}$ (RE=Eu,Tb).[8]

Figure 2 shows Raman spectra for $KNb_{0.85}Mg_{0.15}O_{2.78}$ at given temperatures. The Raman spectra recorded at temperatures below 150 °C were nearly the same as those of undoped $KNbO_3$.[9] When the temperature was increased to 200 °C (Fig. 2), the intensity for the weak sharp phonon mode at 190 cm^{-1} was decreased, and the mode at ~280 cm^{-1} became asymmetric due to asymmetric $Nb(Mg)O_6$ octahedra at B sites,[10] indicating that the orthorhombic phase was not predominant. The phonon mode at 530 cm^{-1} vanished, while the mode at ~580 cm^{-1} exhibited a single mode of high symmetry. With an increase in temperature, the weak sharp phonon mode associated with the orthorhombic structure disappeared at ~190 cm^{-1} and the phonon modes centered at ~280 and 580 cm^{-1} became two symmetric modes, while the mode at ~830 cm^{-1} was further weakened. A tetragonal phase was formed at a temperature above 200 °C. The phase transition of orthorhombic to tetragonal corresponded to an endothermic process, as indicated by the thermal peak at 203 °C in the DTA curve (inset of Fig. 2). When the temperature was increased to 400 °C, the mode at ~830 cm^{-1} lost most of its intensity, indicating the formation of a pseudo-cubic phase.[11] The phase transition of tetragonal to pseudo cubic was also endothermic, as demonstrated by the thermal peak at 378 °C in DTA (inset of Fig. 2). At temperatures above 500 °C, both phonon modes at ~280 and 580 cm^{-1} further broadened and lost intensity, which could be associated with the transition of pseudo cubic to cubic. Above 600 °C, both phonon modes further weakened at ~280 and 580 cm^{-1}. The mode at ~830 cm^{-1} disappeared completely. These results are evidence for the formation of a cubic phase.[12] The thermal effect for the phase transition of pseudo cubic to cubic is not obvious. Similar phase transitions were also observed at other compositions in $KNb_{1-x}Mg_xO_{3-\delta}$.

The transition from tetragonal to pseudo cubic could be associated with the change from tetragonal mode to triply degenerated cubic F_{1u} mode. $KNbO_3$ modified by larger Mg^{2+} substitution could give a large displacement for Nb^{5+}, and the oxygen vacancies adjacent to Mg^{2+} could produce distorted polyhedra around Nb^{5+}. Pseudo-cubic $KNb_{1-x}Mg_xO_{3-\delta}$ contained a partial lattice order, whereas B-site ions in the cubic phase are assumed to be distributed disorderly at eight off-center sites along the ⟨111⟩ axes due to the potential-energy minima at these sites.[13] The presence of these Raman modes confirmed some disordered arrangements in the lattice. Similar distributions of Mg^{2+} and Nb^{5+} can probably be expected at one to eight off-center sites along the ⟨111⟩ axes in the presence of some lattice distortions due to the size mismatch of Mg^{2+}/Nb^{5+}. Further, oxygen vacancies or oxygen vacancy clusters adjacent to Mg^{2+} could give rise to an inhomogeneous distribution of the electrical field at B sites. The different static displacements of Mg^{2+} and Nb^{5+} decreased the local symmetry around B site ions. With increasing temperature, a rapid increase in the disorder of Nb^{5+}/Mg^{2+} at B sites favored preservation of the highly symmetric average cubic structure at high temperature. Large amounts of oxygen vacancies $V\ddot{o}$ and defect associations $\{Mg_{Nb}'''V\ddot{o}\}$ at higher dopant contents exhibited strong interactions with the framework ions and mobile oxygen ions. The transition of order–disorder of oxygen vacancies was thus suppressed.

The impedance spectra clearly showed bulk and grain boundary conduction as well as electrode polarization (not shown). The total conductivity data derived from the impedance spectra were separated into two linear regions, corresponding to the high-temperature phases, respectively (Fig. 3). The ionic conduction at lower temperatures showed a lower activation energy of 0.58 eV at 500 °C at $x=0.1$, while above the transition temperatures, there was a break in the conductivity data showing an increase in the activation energy to 0.83 eV at temperatures greater than 700 °C. Theoretical modeling reported in the literature[14] has noted oxide-ion or cation conduction in perovskite lattices. However, for the present samples, cation conduction associated with K^+, Mg^{2+}, and Nb^{5+} is most unlikely to occur via cation vacancies. This can be reasoned from the comparison of the measured activation energies and the theoretical values for cation conduction. The activation energies of our samples were relatively lower having values of around 1.0 eV, which is

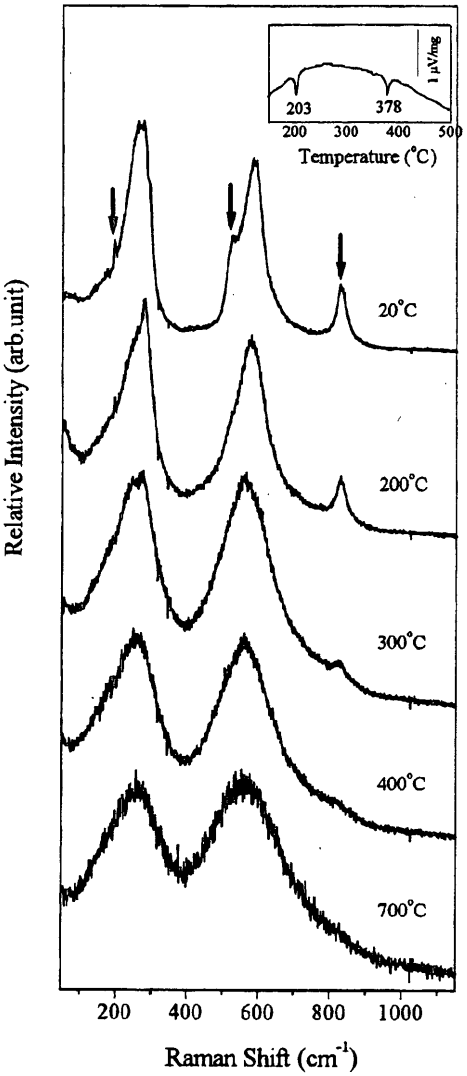

FIG. 2. Raman spectra for $KNb_{0.85}Mg_{0.15}O_{2.78}$ at the given temperatures. Inset shows a DTA curve that demonstrates the endothermic nature of the phase transitions from orthorhombic to tetragonal at 203 °C and to pseudo cubic at 378 °C.

characteristic for migration of oxygen vacancies. Assuming cation conduction was present in the samples, the extremely large ionic size of 1.64 Å for K^+ at A site would probably yield an activation energy larger than 4.0 eV.[14] For the *B*-site ions such as Mg^{2+} and Nb^{5+}, the migration energy along the diagonal direction ⟨110⟩ would be even higher and would have a value, most likely, around 14 eV. Therefore, cation vacancy formation and, furthermore, cation conduction by vacancy migration between the neighboring sites should be highly unfavorable as expected for the close-packed perovskite lattice. The conductivity data for a typical sample of $KNb_{0.90}Mg_{0.10}O_{2.85}$ were measured at 500 °C under several oxygen partial pressures around that of air (Fig. 3, inset). No pronounced variations were observed in conductivity, which shows the ionic nature of primary oxide-ion conduction. Even though there was a small increase in the conductivity at higher oxygen partial pressures, the slope $\partial \log \sigma / \partial \log PO_2$ in this oxygen partial pressure region was much smaller than

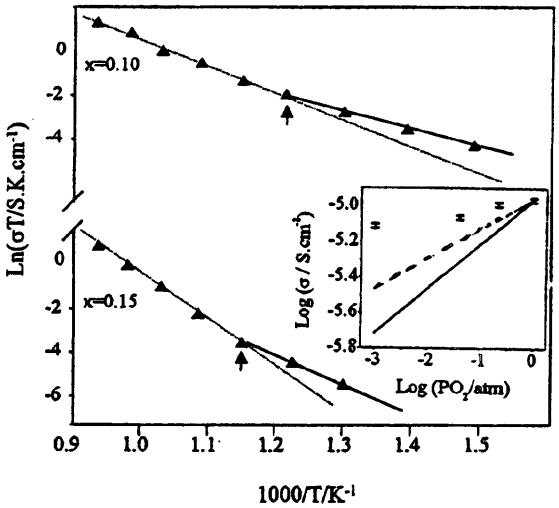

FIG. 3. Temperature dependence of total conductivity for $KNb_{1-x}Mg_xO_{3-\delta}$ at $x=0.10$ and 0.15. Inset shows the conductivity dependence on oxygen partial pressure at 500 °C for $x=0.10$.

1/4 or 1/6, which makes it likely that the *p*-type electronic contribution is extremely small in this region.[15] The ionic conductivity data varied systematically with the dopant content and can be associated with the relative content of oxygen vacancies and defect associations as well as the order-to-disorder transitions, and will be described elsewhere. $KNb_{0.90}Mg_{0.10}O_{2.85}$ was determined to exhibit the most favorable conduction characteristics such as a relatively high conductivity ($\sigma_{700\,°C}=1.10\times10^{-3}$ S cm^{-1}) and low activation energy ($E_a=0.83$ eV).

This project is financially supported by a fund from NSFC (No.19804005) (L.L.). G.L. thanks Dr. S. Haile at Caltech for access to oxygen partial pressure imedance measurements.

[1] M. D. Fontana, G. Metrat, J. L. Servoin, and F. Gervais, J. Phys. C **16**, 483 (1984); R. Sommer, N. K. Yushin, and J. J. van der Klink, Phys. Rev. B **48**, 13230 (1993); D. L. Orauttapong, J. Toulouse, J. L. Robertson, and Z. G. Ye, Phys. Rev. B **64**, 212101 (2001).
[2] D. Hamada, M. Machida, Y. Sugahara, and K. Kuroda, J. Mater. Chem. **6**, 69 (1996).
[3] L. E. Busse, L. Goldberg, M. R. Surette, and G. Mizell, J. Appl. Phys. **75**, 1102 (1994).
[4] K. Q. Huang and J. B. Goodenough, J. Alloys Compd. **303**, 454 (2000).
[5] S. M. Choi, K. T. Lee, S. Kim, M. C. Chun, and H. L. Lee, Solid State Ionics **131**, 221 (2000).
[6] D. Lu, L. Li, J. Miao, H. Liu, and W. Su, Rev. High Pressure Sci. Technol. **7**, 1031 (1998).
[7] S. L. Swartz and T. R. Shrout, Mater. Res. Bull. **17**, 1245 (1982).
[8] L. Li, G. Li, Y. Che, and W. Su, Chem. Mater. **12**, 2567 (2000).
[9] A. M. Quittet, M. I. Bell, M. Krauzman, and P. M. Raccah, Phys. Rev. B **14**, 5068 (1976).
[10] I. J. Clark, T. Takeuchi, N. Ohtori, and D. C. Sinclair, J. Mater. Chem. **9**, 83 (1999).
[11] M. D. Fontana, G. E. Kugel, J. Vamvakas, and C. Carabatos, Solid State Commun. **45**, 873 (1983).
[12] M. D. Fontana and M. Lambert, Solid State Commun. **10**, 1 (1972).
[13] T. P. Dougherty, G. P. Weiderrecht, K. A. Nelson, M. H. Garrett, H. P. Jenssen, and C. Warde, Phys. Rev. B **50**, 8996 (1994).
[14] M. S. Islam, J. Mater. Chem. **10**, 1027 (2000).
[15] T. Shimura, S. Fujimoto, and H. Iwahara, Solid State Ionics **143**, 117 (2001).

ELSEVIER

Hydrometallurgy 65 (2002) 159–175

hydrometallurgy

www.elsevier.com/locate/hydromet

Reactive phase behavior of aluminum nitrate in high temperature and supercritical water

Tao Wang [1], Richard L. Smith Jr. *, Hiroshi Inomata, Kunio Arai

Research Center of Supercritical Fluid Technology, Department of Chemical Engineering, Tohoku University, Aoba-ku Aza Aramaki Aoba-04, Sendai 980-8579, Japan

Received 5 September 2001; received in revised form 4 March 2002; accepted 3 June 2002

Abstract

Batch hydrothermal reaction of $Al(NO_3)_3$ in water was investigated at temperatures up to 421 °C and pressures up to 850 MPa by direct visual observation of reactive solutions in a 50-nL microreactor. A number of gelatinous phase transitions were observed that seem to play a key role in boehmite formation. At high $Al(NO_3)_3$ concentrations (0.32 M) and high densities (1060 kg/m^3), high pressure induced formation of a gel-like phase and the phase formed seemed to be much less reactive than solutions at lower densities (400–670 kg/m^3). At densities closer to the critical density of water, as heating occurred, the gelatinous material precipitated and redissolved into solution prior to intense precipitation around the apparent critical point. A model for the aluminum hydroxocomplexes in solution was developed which showed that cationic species were the main species present at high-density conditions. Nitrate ion seems to play a key role in the gel-like phase formation and boehmite particle production.

Keywords: Aluminum nitrate; Boehmite; Phase behavior; Supercritical water

1. Introduction

Methods for producing boehmite represent an important industrial topic in hydrometallurgical applications (Schimanski, 1998; Whittington, 1996; Diblitz et al., 1998). Much effort has been put on determining accurate solubility behavior for the industrial process (Panias et al., 2001) and on statistical optimization of precipitation conditions for applications associated with catalysts, coatings and alumina-derived materials (Mishra et al., 2000). In a Gordon conference on solid-state chemistry, a new hydrothermal crystallization technique was proposed by Arai (1999) that used water at supercritical conditions (T>374 °C, P>22.1 MPa) to produce catalysts, phosphorus, magnetic materials, energetic materials, ceramics, and boehmite.

The most attractive feature of the supercritical hydrothermal technique is the simplicity of the method for producing sub-micron particles rapidly and continuously. Adschiri et al. (1992) provided an early example for the production of boehmite. Hakuta et al. (1999) proposed that boehmite crystals in super-

* Corresponding author. Tel./fax: +81-22-217-5863.
E-mail address: smith@scf.che.tohoku.ac.jp (R.L. Smith).
[1] Permanent address: Department of Chemical Engineering, Tsinghua University, Beijing 100084, PR China.

0304-386X/02/$ - see front matter © 2002 Elsevier Science B.V. All rights reserved.
PII: S0304-386X(02)00085-3

critical water formed through selective adsorption of positively charged species on negatively charged faces of the crystal, and this was a primary factor in determining particle morphology.

In the supercritical hydrothermal crystallization technique, reactants in the form of aqueous nitrates are combined in one or more mixing points under flow conditions at constant pressure. The reaction is initiated by mixing the combined reactants with supercritical water and terminated rapidly by mixing the products with cooling water. Reducing or oxidizing agents can be added to combine with water to form a homogeneous reaction environment. Under these conditions, however, very little is known on the phase behavior and how the phase changes occur at elevated temperatures and pressures.

In previous work, we developed a method for studying the reactive phase behavior of polymer–water systems at temperatures up to 670 °C and at pressures up to 2600 MPa (Fang et al., 1999). The method uses a microsize 50-nL volume reactor with opposing diamond anvils to contain the solutions. In this work, our objective was to determine the reactive phase behavior of $Al(NO_3)_3$ solution in water at conditions favorable for producing boehmite.

2. Materials and methods

Aluminum nitrate was used in an enneahydrate form ($Al(NO_3)_3 \cdot 9H_2O$) and was obtained from Wako (Osaka). Water was HPLC grade from Aldrich (Tokyo). Aluminum nitrate solution concentrations were prepared by weight and confirmed by inductively coupled plasma (ICP) spectroscopy (SPS-1200, Seiko, Tokyo).

The apparatus used in this work (Fig. 1) was a diamond anvil cell (DAC) that has been proposed for hydrothermal systems (Bassett et al., 1993). In our DAC apparatus, the sample was sealed inside the chamber hole of a gasket by two opposing diamond anvils with 1-mm face, which were held in mounts and pressed together by tightening three diametrically spaced screws. The gasket (inconel) hole diameter and thickness were 0.5 and 0.25 mm, respectively. Wetted materials were diamond and inconel. The voltage to the two microheaters which heat the sample to the reaction temperature was controlled by a high-speed (0.1-s sampling) temperature controller. A reducing gas mixture consisting of argon and 1% hydrogen was introduced into the cell to protect the diamond anvils from oxidation at temperatures higher than 300 °C. Temperature was measured by K-type thermocouples attached to the diamond anvils and was recorded every second by a scanner and software (Model 34970A, Benchlink 1.1, Agilent, Palo Alto). The temperature of the upper anvil was reported as the experimental temperature. More details can be found in Fang et al. (2000) and Smith et al. (2000).

2.1. Pressure determination

For high density loadings (>1000 kg/m^3), ruby fluorescence was used to determine pressure at the room temperature by the method of Forman et al. (1972). Initial pressures were set to approximately 30 MPa. For low-density loadings (< 1000 kg/m^3), the homogeneous temperature (vapor disappearance) during heating and the heterogeneous temperature (vapor formation) during cooling were used to estimate the density from the saturated liquid phase boundary of pure water. From the density of the system, the isochore could be used to estimate the pressure with the equation of state of Wagner and Pruß (1997) assuming that the solvent was pure water.

In the speciation calculations performed, the system pressure was estimated as follows. First, the system temperature and density were known from the loading and the ruby provided the initial system pressure (ca. 30 MPa). The equation of state of water was used to calculate the pressure from the initial loading density and temperature of the solution assuming that the solution was pure water. Since the solution contained some concentration of aluminum nitrate, the calculated pressure would be systematically high. However, by using the pressure determined from the ruby, a pressure correction could be estimated that was subtracted from each subsequent data obtained. The corrected pressures were used in the estimation of the dielectric constant required for the activity coefficient model as described below.

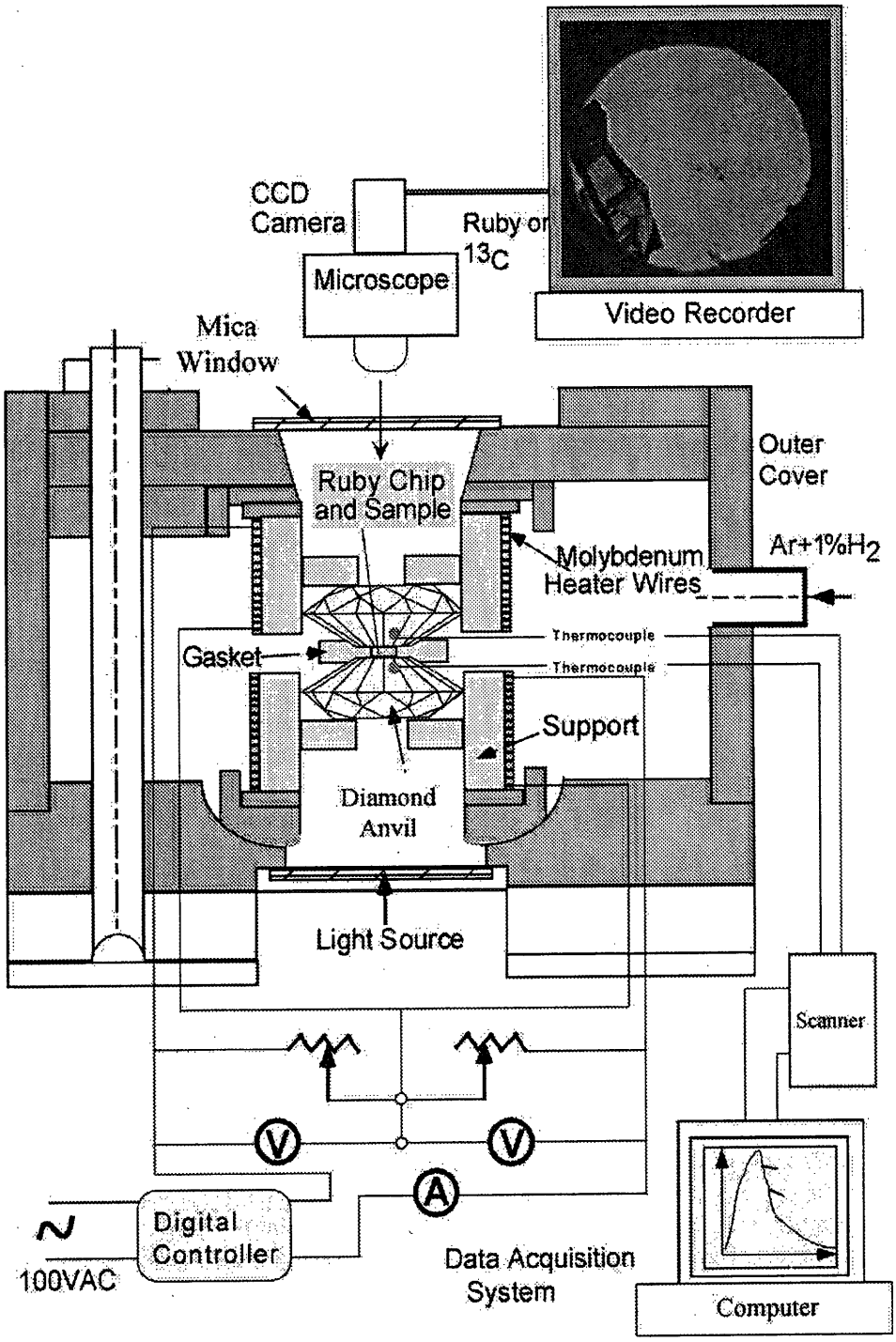

Fig. 1. Experimental set up showing microreactor and diamond anvil cell.

Table 1
Summary of experimental conditions and observations

		Group A: low concentration, high density		Group B: low concentration, intermediate density			Group C: high concentration, intermediate to high densities		
		Subcritical	Supercritical	Supercritical			Supercritical		
		Run 1	Run 2	Run 3	Run 4	Run 5	Run 6	Run 7	Run 8
Initial conditions and experimental details	Solution concentration C_s (mol/L)	0.10	0.10	0.10	0.10	0.10	0.30	0.30	0.30
	Loading density, ρ_l (kg/m^3)	1010	950	950	800	400	400	670	1060
	Corrected concentration C_l (mol/l)	0.101	0.095	0.095	0.080	0.036	0.12	0.20	0.32
	Temperature T (°C)	282–304	396–421	396–421	377–415	378–387	378–389	377–384	376–388
	Average heating rate (°C/s)	7.4	5.1	5.1	7.5	5.9	9.2	7.5	8.1
	Run time for heating (s)	38	78	78	50	64	41	50	46
	Run time before cooling (s)	601	602	602	902	299	56	180	89
Solvent phase	Homogeneous T (°C) during heating	–	190	190	196	383	367	319	–
	Heterogeneous T (°C) during cooling	–	108	108	247	374	359	318	–
Solid precipitate	Appearance run time (s)	90	31	31	20	100	31	36	–
	Apparent time of precipitation completion (s)	420	90	90	50	146	43	37	–
	Solid precipitation Time period (s)	330	59	59	30	46	12	1	
	Appearance Temperature (°C)	282	250	250	201	380	311	313	–
	Apparent temperature of precipitation completion (°C)	290	396	396	377	382	346	319	–

2.2. Loading procedure

Loading for each of the steps discussed below was confirmed with a 10–100 × microscope (Olympus SZH10 Tokyo). After cleaning the diamond anvils, a gasket was centered and temporarily fixed on the lower anvil of the diamond anvil cell (DAC) assembly with thin strands of tape. For the high loading density (>1000 kg/m^3) runs, a ruby chip was placed into the sample chamber of the gasket. Static electricity on a pair of fine pointed tweezers was used to assist in transferring 25–100 micron-sized ruby chips into the chamber. After the ruby was placed into the gasket chamber, solution was introduced into the chamber by either placing a small drop on the upper anvil and combining the top and bottom anvil or by direct placement of the solution drop onto the gasket hole with a microsyringe. Observation of the sample after slight application of pressure to the DAC assembly confirmed whether the loading was successful.

For low-density runs (< 1000 kg/m^3), a ruby chip was not used in general. For these cases, the solution was introduced into the sample chamber by placing a small liquid drop-off center from the gasket hole. The screws of the DAC were tightened carefully and at same time, the sample was observed with the microscope.

To begin the experiments, thermocouples heaters and Ar + 1% H_2 gas flow were connected to the DAC. The controller temperature and input voltages for the microheaters were set at about 2 V AC. After heating the sample to the desired temperature for a given period of time, the sample was rapidly cooled by cutting off the power to the heaters while maintaining the gas flow. During the entire process of pressurization, heating, and cooling, the sample was observed at 100 × magnification and the images were recorded by a CCD camera (KY-F55M, Olympus, Tokyo) onto tape recording media.

2.3. Solution concentrations

For the high-density runs, overall solution concentrations contained within the sample chamber are fixed due to the constant volume system. For the low-density runs, however, a certain amount of gas space exists and therefore, a correction was necessary to determine the solute concentration at the homogeneous temperature. The corrections to the concentrations for the low-density runs are defined as follows:

$$\rho_l = m_s/V \quad (1)$$

$$C_l = N_s/V = \rho_l C_s/\rho_s \quad (2)$$

where ρ_l is the loading density, m_s is the mass of sample solution, V is the volume of the sample chamber, C_l is the loading concentration, N_s is the mole number of the solute and C_s are the concentration and density of the prepared solution, respectively. To apply Eqs. (1) and

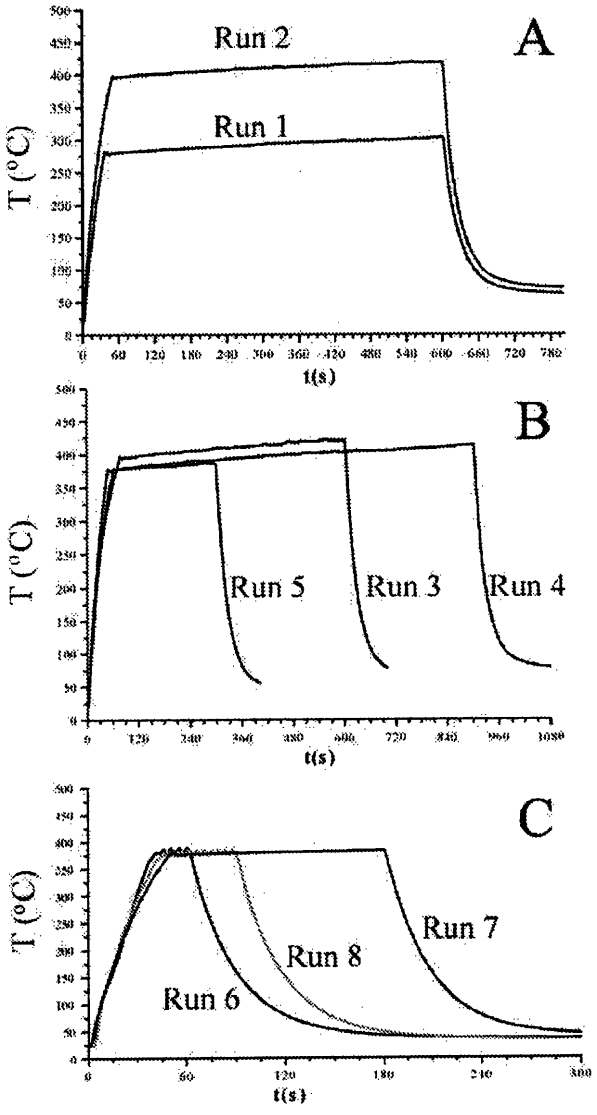

Fig. 2. Time–temperature profiles for the experimental runs (Groups A, B, and C). Refer to Table 1 for conditions.

(2), the temperature at which the cell contents became homogeneous (gas disappearance) was used as discussed earlier.

2.4. Digital imaging analysis

The recorded photos were edited with video imaging software (VideoMotion 1.0, Sony, Tokyo) and analyzed with digital imaging software (Image-Pro Plus 4.1, Media Cybernetics, Silver Spring, MD). Two types of image analyses were performed. The first analysis is called color table subtraction. Digital imaging analysis was used to examine the solvent phase at various temperatures by using one image as a background for the color table and taking differences between successive photos. This provided some information on the change in the refractive index of the sample. The second image analysis performed was with custom software to obtain 2-D information on the relative amounts of the phases or solids formed.

Experimental runs were performed at subcritical and supercritical conditions for examining the phase behavior during reaction of aqueous aluminum nitrate for three cases: Group A—low concentration, high density; Group B—low concentration, intermediate density; Group C—high concentration, intermediate to high densities. Runs and conditions are summarized in Table 1 and temperature profiles for each run are given in Fig. 2. Results for the three groups are discussed in the next sections.

3. Results

3.1. Low concentration and high density (Group A)

For the experimental runs in Group A (Table 1), loading density and sample concentration were 1010 kg/m^3 and 0.10 M, respectively. Reaction temperature was set to be subcritical (ca. 300 °C) for run 1 and supercritical (ca. 420 °C) for run 2. Fig. 2 shows the temperature profiles for Group A experiments which were similar in terms of heating rate and reaction time.

Fig. 3 shows direct visual observations for two different times for the subcritical (Fig. 3a) and supercritical (Fig. 3b) runs. Pressure at room temperature was approximately 28 MPa as estimated by the ruby sensor for the subcritical experiment. Density of the supercritical run was about 950 kg/m^3 as estimated from the temperature at which the solution became homogeneous upon heating (not shown). Comparing the two sets of photos (Fig. 3a and b), it can be seen that at supercritical conditions, a large number of fine particles formed compared with the subcritical case. This is in agreement with the results of Adschiri et al. (2000) and Hakuta et al. (1999).

According to our observations and the digital imaging analysis, particle sizes for the supercritical run (run 2) were much finer than those for the subcritical run (run 1). For both runs, the first solids appeared at temperatures lower than the critical temperature of water. However, precipitation increased dramatically as the temperature rose above 300 °C. For both cases, the solid product appeared stable and did not appear to re-dissolve into the liquid phase. In these experiments, the only phases that could be observed were the homogeneous liquid solvent and the solid particles.

3.2. Low concentration and intermediate density

For the experimental runs in Group B (Table 1), loading densities were varied from 400 to 950 kg/m^3 through the introduction of air bubbles into the sample. Corrected concentrations were calculated from Eqs. (1) to (2) as shown in Table 1. Maximum temperatures used were all above the critical temperature of pure water. Temperature profiles for these runs are given in Fig. 2.

In run 4, a gas bubble that was loaded with the sample solution is shown in Fig. 4. For this case, no ruby was loaded due to the low density used. Pressurization resulted in the formation of a gel-like phase around the chamber periphery. Upon heating, the gas bubble became smaller and the gel-like particles grew along weakly defined boundaries as the temperature increased up to about 139 °C. As the temperature increased further to 148 °C, the gel-like particles began to dissolve and leave a residue. The gas bubble disappeared completely at 196 °C, and at 201 °C, the gel-like particles had completely dissolved. Precipitation of numerous solid particles began at 22 s and 217 °C. The precipitation

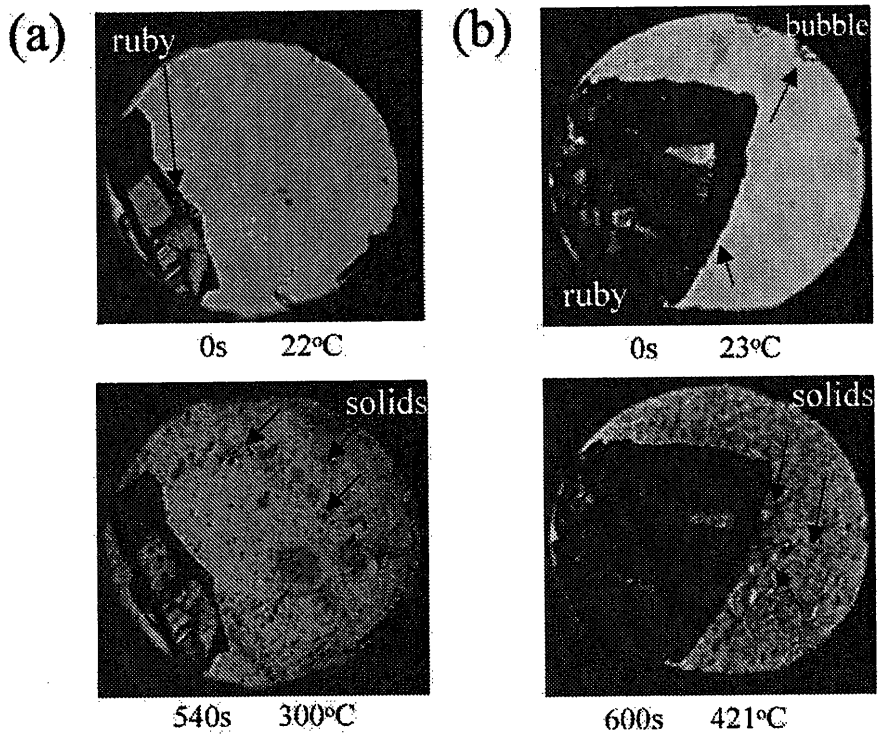

Fig. 3. Direct observation of boehmite formation from $Al(NO_3)_3$ in water at high pressure: (a) Subcritical temperature (Run 1, ρ_l: 1010 kg/m^3; C_l: 0.101 M); (b) Supercritical temperature (Run 3, ρ_l: 950 kg/m^3; C_l: 0.095 M).

appeared to be complete at 50 s and 377 °C. The sample became molted in appearance. Further heating and cooling did not seem to change the appearance of the precipitated particles. Upon cooling, numerous small gas bubbles that look like black dots in the image (Fig. 4) appeared and these grew in size as the temperature decreased.

3.3. High concentration and intermediate to high densities

For the experimental runs in Group C (Table 1), prepared solution concentrations of 0.3 M were used. Densities were varied from 400 to 1060 kg/m^3 with maximum temperatures being higher than that of the critical temperature of pure water. Temperature profiles are given in Fig. 2C.

In run 6, the solution was loaded as a liquid droplet on the top anvil. Upon heating, the solution turned cloudy and broke up into a myriad of fine liquid regions as shown in the photo at 5 s, 59 °C (Fig. 5). At 124 °C, the solution appeared as three liquid regions that collapsed into a single droplet surrounded by a vapor region at 253 °C. As the system approached 311 °C, the droplet changed colors from clear to orange and precipitation was noted around the droplet. As the temperature increased further, the liquid droplet became smaller and the vapor phase became much denser. A large number of solids were left behind in a ring-like pattern as shown by the images up to 379 °C. At 379 °C (43 s), the precipitation appeared to be complete and the remaining bulk phase was homogeneous. Repeated heating and cooling did not affect the precipitated solids but caused intense light scattering that is typical of gas–liquid critical temperatures (Smith et al., 1990). Upon cooling, the solution turned clear and many fine particles were apparent.

In run 7 (Fig. 6), two phases (liquid and air) existed at the beginning of the experiment (0 s, 21 °C). In the initial stage of heating, gel-like particles appeared at the bottom of the liquid droplet (10 s, 122 °C). As heating continued, the liquid drop

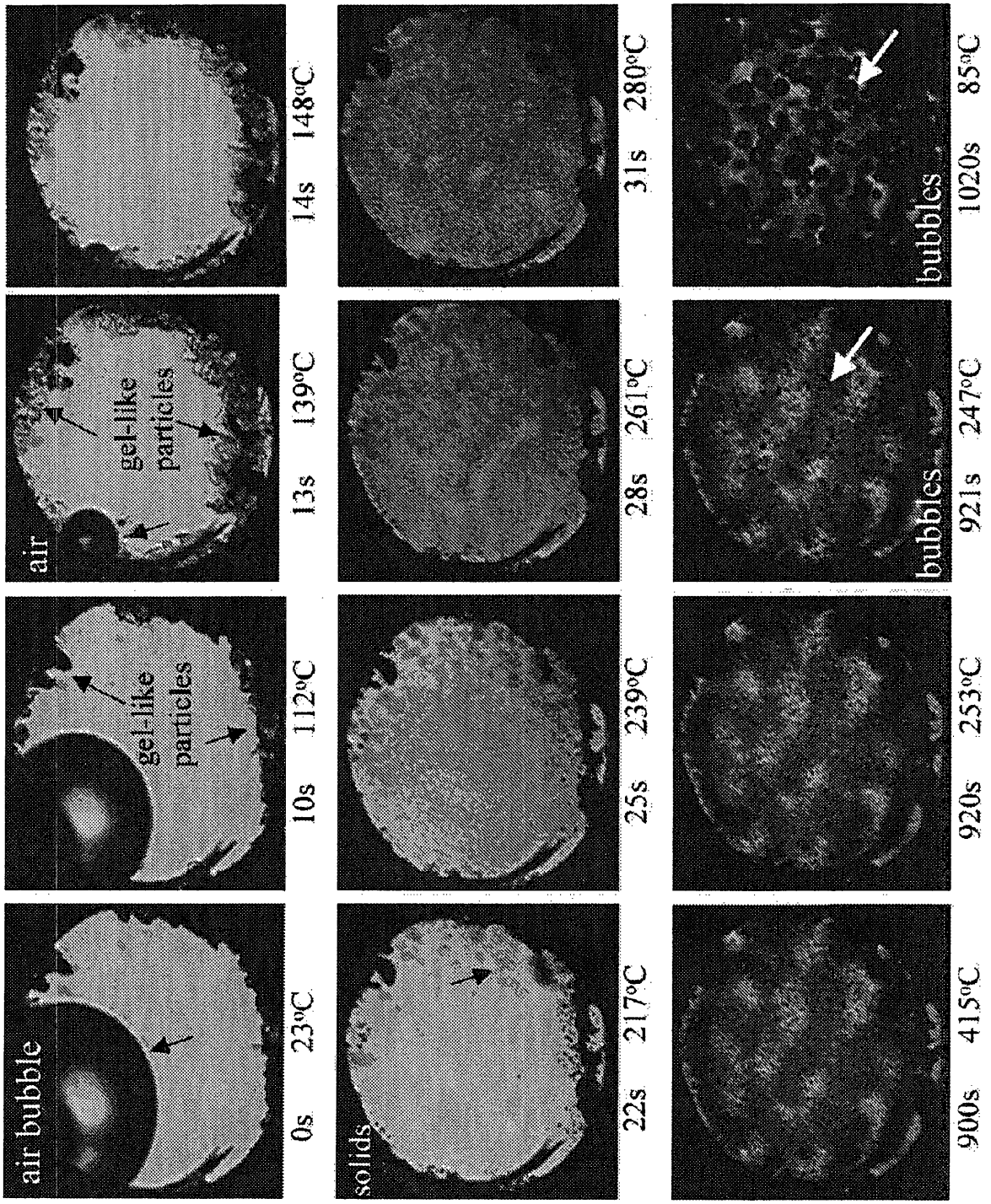

Fig. 4. Direct observation of $Al(NO_3)_3$ reacting at supercritical temperatures at an intermediate density (Run 4, ρ_i: 800 kg/m^3; C_i: 0.080 M).

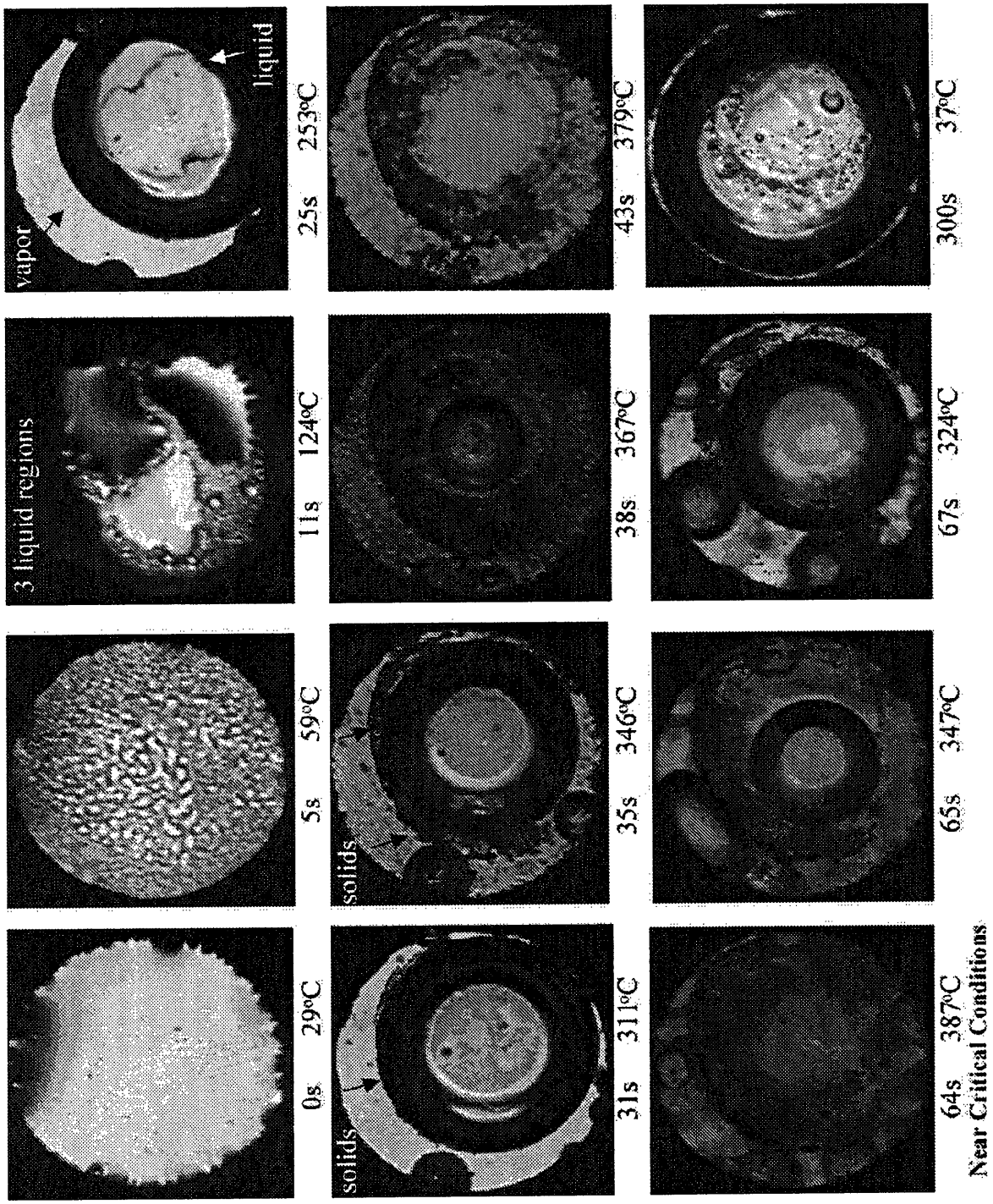

Fig. 5. Direct observation of $Al(NO_3)_3$ reacting at conditions near the critical point (Run 6, ρ_i: 400 kg/m^3; C_i: 0.12 M).

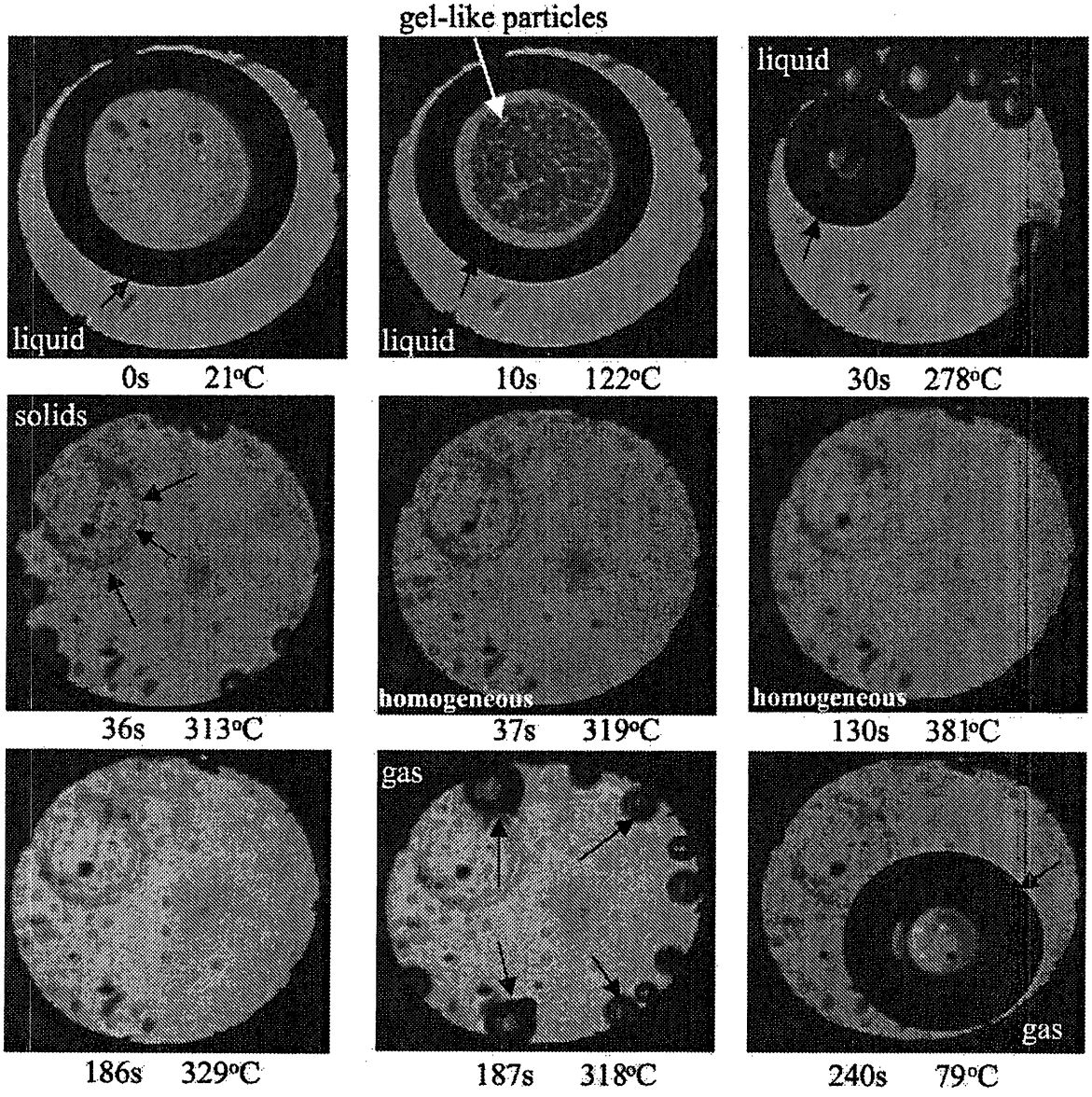

Fig. 6. Direct observation of $Al(NO_3)_3$ reacting in the supercritical region (Run 7, ρ_f: 670 kg/m^3; C_f: 0.2 M).

moved violently and dispersed to smaller droplets (30 s, 278 °C). Solid precipitate appeared at 36 s and 313 °C as noted in Fig. 6 by the arrows. The liquid droplets along the edge of the gasket disappeared at 37 s and 319 °C, and the solvent became homogenous. At these conditions, the precipitation seemed to be complete. As the heating continued up to 381 °C (130 s), no changes in the solvent phase or the solid were observed. When the temperature was lowered, the solvent separated into vapor and liquid at 187 s and 318 °C. The fraction of this vapor phase increased as the temperature decreased. Finally, the vapor drops coalesced into a large bubble. Solid particles that had formed did not seem to change during the cooling.

In Group C, high concentration and intermediate density conditions were examined. In run 8, after loading the solution and applying pressure to about 30 MPa, gel-like areas formed as shown in the image at 0 s and 24 °C (Fig. 7). Upon heating the

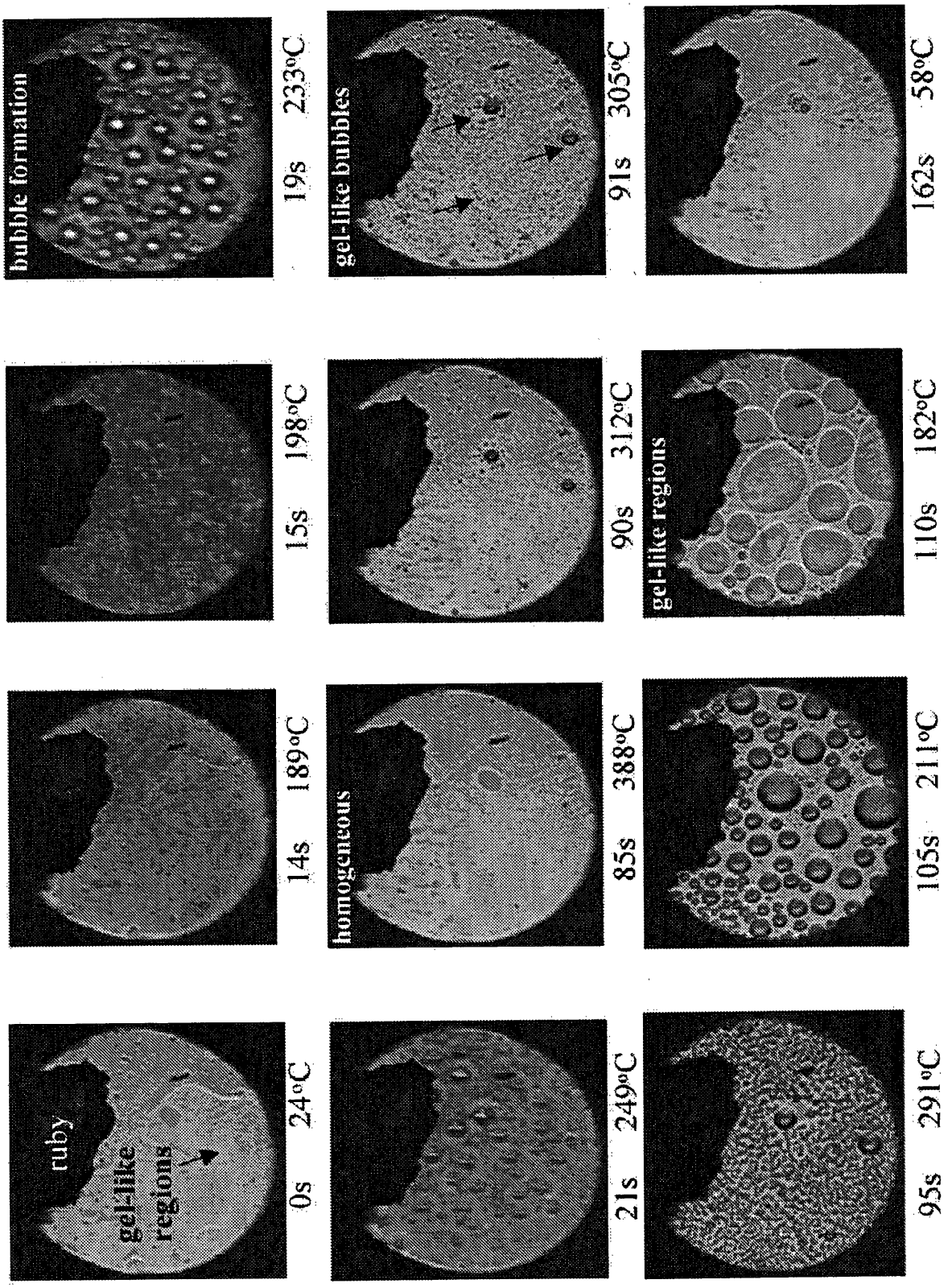

Fig. 7. Direct observation of $Al(NO_3)_3$ reacting at high concentration and at high density at supercritical temperatures (Run 8, ρ_i: 1060 kg/m^3; C_i: 0.32 M).

sample, the solution darkened and turned cloudy at 189 °C (14 s) and then there was an obvious change in the refractive index. Numerous gel-like spheres formed at 233 °C. The spheres dissolved completely into the bulk phase at 388 °C (85 s). No obvious particles or precipitates were observed. Upon cooling, liquid spheres formed and coalesced and appeared to be much more gel-like in appearance than those observed during heating. Estimated pressure at the highest temperature condition was 850 MPa based on the equation of Wagner and Pruß (1997). As room temperature was approached, the spheres coalesced into a film.

4. Discussion

4.1. Reaction pathway and modeling

The overall reaction pathway for aluminum nitrate in water to form boehmite and aluminum oxide can be written in terms of a hydrolysis reaction that is followed by one or more dehydration reactions:

$$\text{Hydrolysis}: \quad Al(NO_3)_3 + 3H_2O \rightarrow Al(OH)_3 + 3HNO_3 \tag{3}$$

$$\text{Dehydration I}: \quad Al(OH)_3 \rightarrow AlOOH + H_2O \tag{4}$$

$$\text{Dehydration II}: \quad 2AlOOH \rightarrow Al_2O_3 + H_2O \tag{5}$$

In the supercritical hydrothermal synthesis technique, the forward reaction of Eq. (3) is highly favored (Arai and Adschiri, 1999), which means that the dissociation of nitric acid has to be considered. The speciation reactions of Eqs. (3) and (4) are summarized in Table 2. In Table 2, aluminum nitrate dissociates to form nitrate ions that can serve as oxidizing agents. The aluminum hydrolyzes to hydroxocomplexes depending on the system pH and solvent dielectric constant. Details of the boehmite hydroxocomplexes have been discussed by Castet et al. (1993), Palmer et al. (2001), Panias et al. (2001) and specifically for supercritical systems by Hakuta et al.(1999). For interpreting some of the images obtained in this work, we developed a set of chemical equilibrium constant expressions based on the density model of Anderson et al.

Table 2
Equilibrium constants for reaction of $Al(NO_3)_3$ in water

$AlOOH + 3H^+ \overset{K_{S0}}{\rightleftharpoons} Al^{3+} + 2H_2O$
$AlOOH + 2H^+ \overset{K_{S1}}{\rightleftharpoons} Al(OH)^{2+} + H_2O$
$AlOOH + H^+ \overset{K_{S2}}{\rightleftharpoons} Al(OH)_2^+$
$AlOOH + H_2O \overset{K_{S3}}{\rightleftharpoons} Al(OH)_3^0$
$AlOOH + 2H_2O \overset{K_{S4}}{\rightleftharpoons} Al(OH)_4^- + H^+$
$Al(NO_3)_3 \overset{K_{Al}}{\rightleftharpoons} Al^{3+} + 3NO_3^-$
$HNO_3 \overset{K_{HNO_3}}{\rightleftharpoons} H^+NO_3^-$
$H_2O \overset{K_w}{\rightleftharpoons} H^+OH^-$

(1991) that can be used at the extreme conditions (420 °C, 850 MPa) studied.

In the density model, the equilibrium constant, K, for a given speciation reaction is represented as a function of temperature and density:

$$\ln K = p_1 + p_2/T + (p_3 \ln\rho)/T \tag{6}$$

where the p_1, p_2, and p_3 in Eq. (6) depend only upon the thermophysical properties of the reaction and the coefficient of thermal expansion of water, α, and its temperature derivative as follows:

$$p_1 = \ln K_r + \frac{\Delta H_r^0}{RT_r} - \frac{\Delta C_{P_r}^0 \alpha_r}{RT_r(\partial\alpha/\partial T)_{P_r}} \tag{7}$$

$$p_2 = -\frac{\Delta H_r^0}{R} + \frac{(T_r\alpha_r + \ln\rho_r)\Delta C_{P_r}^0}{RT_r(\partial\alpha/\partial T)_{P_r}} \tag{8}$$

$$p_3 = -\frac{\Delta C_{P_r}^0}{RT_r(\partial\alpha/\partial T)_{P_r}} \tag{9}$$

In this work, the reference state was taken to be 25 °C and 0.1 MPa. At these conditions, ρ_r, α_r, and $(\partial\alpha/\partial T)_{P_r}$ were calculated to be 997.05 kg/m^3, 2.573×10^{-4} K^{-1}, and 9.626×10^{-6} K^{-2}, respectively, from the IAPWS formulation of Wagner and Pruß (1997). For the aluminate species, Eqs. (6)–(9) were used with the tabulated values for the free energies, enthalpies, entropies, and heat capacities summarized in Table 3. The C_p^0 for $Al(NO_3)_3$ was unavailable and was set equal to zero. Variation of this property by +100 J/mol K had a negligible effect on the calculated $Al(NO_3)_3$ equilibrium constants and only shifted the general trend of the curve to slightly lower values. For water, K_w was calculated from the relationship of Marshall and Franck (1981). For nitric acid at elevated

Table 3
Thermochemical properties used and their literature source

No.	Species	ΔG_f^0 [kJ/mol]	ΔH_f^0 [kJ/mol]	S^0 [J/mol K]	C_p^0 [J/mol K]	Ref.
1	H^+	0.0	0.0	0.0	0.00	a
2	AlOOH (c)	−917.82	−992.19	49.4	54.23	b
3	$Al(NO_3)_3$ (aq, $m=1$)	−820.0	−1155.0	117.60	–	c
4	HNO_3	−103.47	−190.0	178.66	75.31	a
5	Al^{3+}	−487.2	−539.4	−342.4	−96.00	b
6	$Al(OH)^{2+}$	−696.0	−769.7	−181.5	−21.00	b
7	$Al(OH)_2^+$	−900.2	−998.3	−30.6	54.00	b
8	$Al(OH)_3^0$	−1110.4	−1270.7	−5.7	179.00	b
9	$Al(OH)_4^-$	−1305.7	−1503.0	−103.7	160.00	b
10	NO_3^-	−110.91	−206.81	−146.94	−68.62	a
11	OH^-	−157.3	−230.02	−10.71	−137.19	a
12	H_2O (l)	−237.14	−285.83	69.95	75.35	a

(a) Shock et al. (1997).
(b) Bénézeth et al. (2001) and Palmer et al. (2001).
(c) Dean (1998).

temperatures and pressures, Oscarson et al. (1992) presented a relationship for its ionization from about 218–319 °C that could be reliably extrapolated to higher temperatures:

$$\log_e K_{HNO_3} = 86083/T + 173.72\ln T + 31.264\ln(\rho/1000) + 1247.57 \quad (10)$$

where T is the absolute temperature in Kelvin and ρ is the density in kg/m^3. Eq. (10) was extrapolated to the conditions analyzed by Chlistunoff et al. (1999) and agreement was within 35% in $\log_{10} K_{HNO_3}$, which was considered to be acceptable for the present analysis. Eq. (10) was used to determine K_{HNO_3} instead of the thermodynamic values given in Table 3.

In the present analysis, 11 species (H^+, AlOOH, $Al(NO_3)_3$(aq), HNO_3, Al^{3+}, $Al(OH)^{2+}$, $Al(OH)_2^+$, $Al(OH)_3^0$, $Al(OH)_4^-$, NO_3^-, OH^-) plus water were assumed to be present as numbered in Table 3. The activity of water was set equal to 1. For the ionic species, activity coefficients were calculated from the Davies (1977) revision of the Debye–Hückel equation:

$$\ln\gamma_i = -\frac{z_i^2 A\sqrt{I}}{1+\sqrt{I}} + 0.2Az_i^2 I \quad (11)$$

where z_i is the charge of the ionic species, I is the true ionic strength representing the concentrations of all species, and A is the Debye–Hückel parameter that was calculated from:

$$A = \frac{1.8248\times 10^6(\rho_0/1000)^{1/2}}{(\varepsilon_0 T)^{3/2}} \quad (12)$$

where ρ_0 and ε_0 are the density (kg/m^3) and dielectric constant, respectively, of pure water at the temperature and pressure of interest.

To determine the concentrations of the M (=11) species, the set of N (=8) equations (Table 2) with mass–action relations given by Eqs. (6)–(10), the $M-N-1$ material balances (Al, NO_3), and the electroneutrality condition were solved simultaneously by a Newton–Raphson technique. First, the chemical equilibrium constants and the Debye parameter A were calculated for a given temperature and density. Then compositions were iterated and species activities were calculated from Eq. (11). Activities that became negative during the iteration were reinitialized to a concentration of 1×10^{-12}. The iteration was terminated when the concentrations reached constant values that satisfied the simultaneous equations.

4.2. Calculations

Chemical equilibrium constants were calculated from the thermodynamic data in Table 3 and Eqs. (6) and (10). Fig. 8 shows a plot of the chemical equilibrium constants versus temperature at the density of 1060 kg/m^3. The equilibrium constant for aluminum

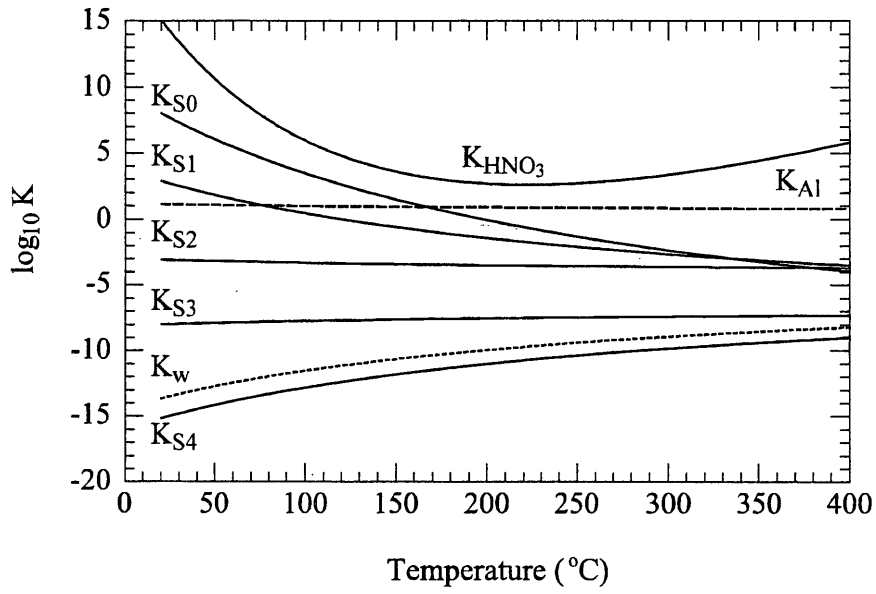

Fig. 8. Chemical equilibrium constants calculated from the density model as a function of temperature at high concentration and high-density conditions (Run 8, ρ_l: 1060 kg/m^3; C_i: 0.32 M). See Table 2 for equilibrium constant definitions.

nitrate (K_{Al}) and for the cationic hydroxocomplexes (K_{S0}–K_{S2}) decreased with temperature. The equilibrium constants for the neutral species $Al(OH)_3^0$, K_{S3}, and negatively charged hydroxocomplex (K_{S4}) increased with temperature. The equilibrium constant for nitric acid exhibited a minimum at about 222 °C. At this high density, the ion product (K_w) monotonically increases with temperature as can be calculated from the equation of Marshall and Franck (1981) or as demonstrated by Xiang and Johnston (1994).

Speciation calculations at high density (1060 kg/m^3) using the equilibrium constants of Fig. 8 are shown in Fig. 9 as a function of temperature. Pressure was estimated to increase from 30 MPa at room temperature to about 850 MPa at 388 °C. As shown in the figure, aluminum nitrate steadily dissociated with temperature while undissociated nitric acid exhibited a maximum at about 230 °C. Conditions of the solution at equilibrium were highly acidic so that cationic aluminates were the main hydrolytic species in solution. The anionic $Al(OH)_4^-$ species and uncharged $Al(OH)_3^0$ species were virtually nonexistent. This is in contrast with the work of Hakuta et al. (1999), who found that the main species in supercritical water at 30 MPa and 400 °C were the uncharged $Al(OH)_3^0$ species (95%) and anionic $Al(OH)_4^-$ species (5%). These differences can be explained by considering the differences in the solution physical properties. At the conditions of 388 °C and 850 MPa, the density and estimated dielectric constant (1060 kg/m^3, 28.8) were considerably greater than those in the supercritical region of 30 MPa, 400 °C (357 kg/m^3, 5.9). In other words, at the high-density conditions of run 8, water could support a much greater concentration of the high-valence species than at the low-density conditions of the supercritical region.

4.3. Phase behavior

The previous calculations provided an estimation of the ions present under equilibrium conditions at high temperatures and pressures. Although the equilibrium results cannot be directly related to the observed reactive phase behavior that occurs under dynamic conditions, the calculations can be used to aid in discussion of the more likely possibilities.

At high densities and low solute concentrations (Group A, Table 1), the solvent phase remained homogeneous up to precipitation regardless of whether the temperature was subcritical or supercritical. Direct observations and digital analysis showed that there was little visible change in the solvent phase during the heating period up to the point of precipitation. From the previous calculations, the solution can be seen to be acidic with very low concentrations ($< 10^{-9}$ m) of

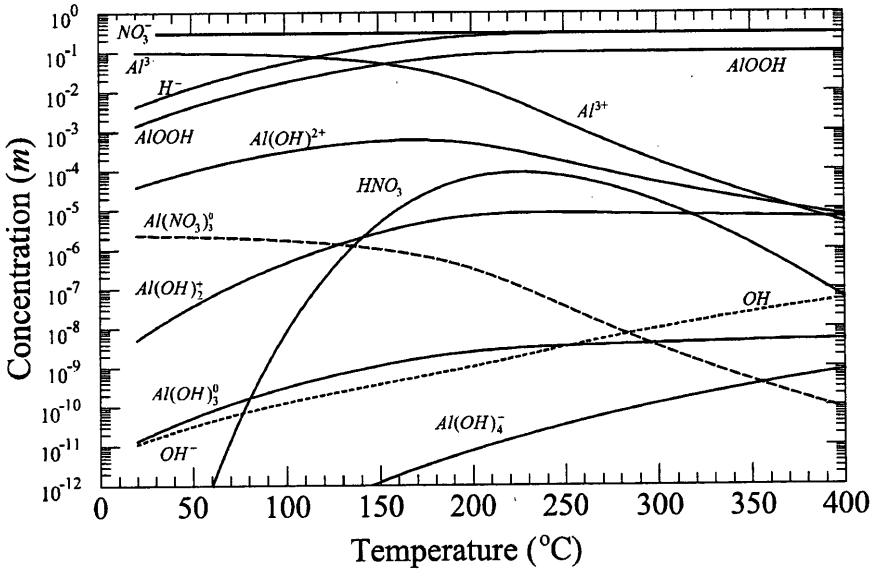

Fig. 9. Speciation calculation as a function of temperature using chemical equilibrium constants determined from the density model at high concentration and high-density conditions (Run 8, ρ_l: 1060 kg/m^3; C_l: 0.32 M).

$Al(OH)_3^0$ and $Al(OH)_4^-$ anions. This means that conditions are less favorable for the formation of a gelatinous precipitate under the range of conditions summarized by Musić et al. (1999). According to Mishra et al. (2000), who studied the formation of boehmite from $Al(NO_3)_3$ and urea under hydrothermal conditions, precipitation of crystalline boehmite takes place almost instantaneously at temperatures above 180 °C when a neutralizing agent (urea) is present. For our case, no neutralizing agents were used and so this probably led to the high precipitation temperatures observed. As water is heated, the solvent has less ability to support ion–ion separation due to its lower dielectric constant. Further, water becomes less able to support higher charge cations in solution, as shown in Fig. 9 as the temperature is increased. This means that at some point, there is probably an abrupt transition to $Al(OH)_3$ products and subsequent transformation to AlOOH. Evidence for this type of behavior has been reported by Adschiri et al. (2000) for a wide range of particle materials formation under hydrothermal conditions including boehmite and for experimentally measured solubilities of oxides in supercritical water and their modeling by Sue et al. (1999, 2000). It should be pointed out that the quality of the boehmite for these runs is unknown due to the extreme conditions and small amount of material produced. However, as discussed below, single-phase boehmite is expected under low densities (400 kg/m^3) and supercritical conditions and this has been confirmed with larger-scale experiments by Li et al. (2002).

At lower densities, the phase behavior was striking. According to the images of Group B experiments, as the system was heated and became homogeneous, an intermediate gel-like phase formed. At densities of 800 kg/m^3 (Fig. 6), many gel-like particles formed and subsequently dissolved. Digital imaging analysis of the solvent phase by subtracting the background of the color tables showed large changes in the values indicating significant refractive index differences. For the low-density run in this group (400 kg/m^3), there seemed to be an intermediate gel-like phase (Fig. 5, 253 °C) at the bottom of the liquid droplet.

At the lower densities of Group B experiments, the solvent phase has even less capacity to support charged species compared with the solvent phase at high-density conditions of Group A experiments. Therefore, it is probable that there was a shift in the concentration of higher charged cationic species to lower charged anionic species or uncharged hydrolytic species as the system attained homogeneous conditions. These general trends have been noted for many systems by Ziemniak (1994) and with measurements and detailed calculations for several species in

the supercritical region by Sue et al. (1999, 2000). The lowering of the population of highly charged anionic species could be through paths K_{S0}–K_{S3} listed in Table 2, or through the formation of complexes such as aluminate cation–nitrate pairs (e.g., $Al^{3+}(H_2O)_x(NO_3^-)_y$ or $Al(OH)^{2+}(H_2O)_x(NO_3^-)_y$). In situ spectroscopic measurements and more detailed thermodynamic data would be required to explore these possibilities. We have studied the formation of boehmite from $Al(NO_3)_3$ aqueous solutions at 400 °C and pressures of roughly 35 MPa in larger scale (10 cm^3) batch reactors at supercritical conditions similar to those reported in this work (Li et al., 2002). XRD, FT-IR, and thermal gravimetric methods were used to characterize the particles and it was found that at supercritical conditions, single-phase boehmite nanocrystals free of nitrate contamination were formed. This is in contrast to hydrothermal methods, where nitrate contamination of the solid phase readily occurs and is difficult or impossible to just wash away (Musić et al., 1999). Therefore, we suspect that the nitrate ion plays an important role in the gelatinous material formation and its inclusion in the final precipitated solids. In terms of Eqs. (3) and (4) and Fig. 9, the nitrate ion probably provides a stabilizing element allowing formation of a weakly stable gel at hydrothermal conditions and at conditions of high density. At supercritical conditions, however, the nitrate probably reacts with the aluminate species and prevents or reduces the formation of any type of aluminate cation–nitrate networks.

Another point regarding Group B experimental results (Table 1, Fig. 4) is that of a gas–antisolvent effect. In gas–antisolvent methods, crystallization of a solute occurs as the result of gaseous component being added to a solvent–solute mixture. The gaseous component causes the solvent phase to expand and thus reduces the solvent power of the solvent for the solute as discussed by de la Fuente Badilla et al. (2000). In this case, it is a gelatinous precipitate that would be forced out of solution, which is probably made up of a three-dimensional network such as $Al^{3+}(H_2O)_x(NO_3^-)_y$ or $Al(OH)^{2+}(H_2O)_x(NO_3^-)_y$.

For Group C experiments, higher concentrations of $Al(NO_3)_3$ were used. At the highest density examined (Fig. 7), it is clear that formation of the gel was promoted with application of pressure. Further, even though the temperature was increased to 388 °C for a short period of time, the gelatinous material remained stable, which is evidence that the gel network was much less reactive at high densities than at the lower densities in this group. At the lower densities in the group (runs 6 and 7), the number of particles that formed was large, which clearly shows the merits of producing particles in the supercritical region.

5. Conclusions

The reactive phase behavior of aluminum nitrate in high temperature and supercritical water has been characterized by direct visual observation of solutions contained in a microreactor. The observed phase behavior greatly depended on the solvent density and solute concentration. As the solvent density became closer to the apparent critical density, particle formation greatly increased. Gelatinous regions were found to form during the experiments for various reasons. At high $Al(NO_3)_3$ concentrations, pressure induced gel formation and the solutions were found to have less reactivity compared with solutions at lower densities. At the low densities, heating promoted gel formation probably through a gas–antisolvent effect, which subsequently reacted. Such a gel was probably weakly linked through nitrate ions that stabilize the cationic species. Nitrate appears to play a key role in the boehmite formation mechanism in aqueous aluminum nitrate solutions.

Acknowledgements

The authors gratefully acknowledge the Ministry of Education, Science, Sports and Culture for financial support of this research. A portion of this research was also supported by Genesis Research Institute.

References

Adschiri, T., Kanazawa, K., Arai, K., 1992. Rapid and continuous hydrothermal synthesis of boehmite particles in subcritical and supercritical water. J. Am. Ceram. Soc. 75 (9), 2615–2618.

Adschiri, T., Hakuta, Y., Arai, K., 2000. Hydrothermal synthesis of metal oxide fine particles at supercritical conditions. Ind. Eng. Chem. Res. 39, 4901–4907.

Anderson, G.M., Castet, S., Schott, J., Mesmer, R.E., 1991. The

density model for estimation of thermodynamic parameters of reactions at high temperatures and pressures. Geochim. Cosmochim. Acta 55, 1769–1779.

Arai, K., 1999. Continuous hydrothermal synthesis of metal oxides in sub- and supercritical water. Presentation at the Gordon Research Conference of Solid State Chemistry, Queen's College, Oxford, England, September, 19–24.

Arai, K., Adschiri, T., 1999. Importance of phase equilibria for understanding reactions in supercritical fluids. Fluid Phase Equilib. 158, 673–684.

Bassett, W.A., Shen, A.H., Bucknum, M., 1993. A new diamond anvil cell for hydrothermal studies to 2.5 GPa and from −190 to 1200 °C. Rev. Sci. Instrum. 64, 2340–2345.

Bénézeth, P., Palmer, D.A., Wesolowski, D.J., 2001. Aqueous high-temperature solubility studies. II. The solubility of boehmite at 0.03-m ionic strength as a function of temperature and pH as determined by in situ measurements. Geochim. Cosmochim. Acta 65, 2097–2111.

Castet, S., Dandurand, J.L., Schott, J., Gout, R., 1993. Boehmite solubility and aqueous aluminum speciation in hydrothermal solutions (90–350 °C). Experimental study and modeling. Geochim. Cosmochim. Acta 57, 4869–4884.

Chlistunoff, J., Ziegler, K.J., Lasdon, L., Johnston, K.P., 1999. Nitric/Nitrous acid equilibria in supercritical water. J. Phys. Chem., A 103, 1678–1688.

Davies, P.C.W., 1977. The Physics of Time Asymmetry; Thermodynamics and Cosmology. University of California Press, Berkeley, pp. 80–111.

Dean, J.A. (Ed.), 1998. Lange's handbook of chemistry, 15th ed. McGraw-Hill, New York, p. 6.82.

de la Fuente Badilla, J.C., Peters, C.J., de Swaan Arons, J., 2000. Volume expansion in relation to the gas antisolvent process. J. Supercrit. Fluids 17, 13–23.

Diblitz, K., Feldbaum, T., Ludemann, T., 1998. Manufacturing of raw materials for the catalyst industry. Stud. Surf. Sci. Catal. 113, 599–611.

Fang, Z., Smith Jr., R.L., Inomata, H., Arai, K., 1999. Phase behavior and reaction of polyethylene terephthalate–water system at pressures up to 173 MPa and temperatures up to 490 °C. J. Supercrit. Fluids 15, 229–243.

Fang, Z., Smith Jr., R.L., Inomata, H., Arai, K., 2000. Phase Behavior and Reaction of Polyethylene in Supercritical Water at Pressures up to 2.6 GPa and Temperatures up to 670 °C. J. Supercrit. Fluids 16, 207–216.

Forman, R.A., Piermarini, G.J., Barnett, J.D., Block, S., 1972. Pressure measurement made by the utilization of ruby sharp-line luminescence. Science 176, 284.

Hakuta, Y., Adschiri, T., Hirakoso, H., Arai, K., 1999. Chemical equilibria and particle morphology of boehmite (AlOOH) in sub- and supercritical water. Fluid Phase Equilib. 158–160, 733–742.

Li, G., Smith Jr., R.L., Inomata, H., Arai, K., 2002. Synthesis and thermal decomposition of nitrate free boehmite nanocrystals by supercritical hydrothermal conditions. Mater. Lett. 53, 175–179.

Marshall, W.L., Franck, E.U., 1981. Ion product of water substance, 0–1000 °C, 1–10,000 bars. J. Phys. Chem. Ref. Data 10, 295–304. See also, http://www.iapws.org, Release on the ion product of water substance, May 1980.

Mishra, D., Anand, S., Panda, R.K., 2000. Statistical optimization of conditions for the hydrothermal precipitation of boehmite. Hydrometallurgy 58 (2), 169–174.

Musić, S., Dragčević, Đ, Popović, S., 1999. Hydrothermal crystallization of boehmite from freshly precipitated aluminium hydroxide. Mater. Lett. 40, 269–274.

Oscarson, J.L., Gillespie, S.E., Izatt, R.M., Chen, X., Pando, C., 1992. Thermodynamic quantities for the ionization of nitric acid in aqueous solution from 250 to 319 °C. J. Solution Chem. 21, 789–801.

Palmer, D.A., Bénézeth, P., Wesolowski, D.J., 2001. Aqueous high-temperature solubility studies. I. The solubility of boehmite as functions of ionic strength (to 5 molal, NaCl), temperature (100–290 °C), and pH as determined by in situ measurements. Geochim. Cosmochim. Acta 65, 2081–2095.

Panias, D., Asimidis, P., Paspaliaris, I., 2001. Solubility of boehmite in concentrated sodium hydroxide solutions: model development and assessment. Hydrometallurgy 59 (1), 15–29.

Schimanski, J., 1998. Production of dispersible aluminas and their use in different applications. Key Eng. Mater. 150, 161–169.

Shock, E.L., Sassani, D.C., Willis, M., Sverjensky, D.A., 1997. Inorganic species in geologic fluids: correlations among standard molal thermodynamic properties of aqueous ions and hydroxide complexes. Geochim. Cosmochim. Acta 61, 907–950.

Smith Jr., R.L., Negishi, E., Arai, K., Saito, S., 1990. Measurement of critical temperatures of terpenes. J. Chem. Eng. Jpn. 23 (1), 99–102.

Smith Jr., R.L., Fang, Z., Inomata, H., Arai, K., 2000. Phase behavior and reaction of Nylon 6/6 in water at high temperatures and pressures. J. Appl. Polym. Sci. 76 (7), 1062–1073.

Sue, K., Hakuta, Y., Smith Jr., R.L., Adschiri, T., Arai, K., 1999. Solubility of lead(II) oxide and copper(II) oxide in subcritical and supercritical water. J. Chem. Eng. Data 44, 1422–1426.

Sue, K., Aida, T.M., Hakuta, Y., Smith Jr., R.L., Adschiri, T., Arai, K., 2000. Measurement and correlation of metal oxide solubilities in sub- and supercritical water. In: Tremaine, P.R., Hill, P.G., Irish, D.E., Balakrishnan, P.V. (Eds.), Steam, Water, and Hydrothermal Systems: Physics and Chemistry Meeting the Needs of Industry. Proceedings of the 13th International Conference on the Properties of Water and Steam, NRC Research Press, Ottawa, pp. 782–789.

Wagner, W., Pruß, A., 1997. Die Neue Internationale Standard-Zustandsgleichung für Wasser für den Allgemeinenen und Wissenschaftlichen Gebrauch. Jahrbuch 97, VDI-Gesellschaft Verfahrenstechnik und Chemieingenieurwesen. VDI-Verlag, Dusseldorf, pp. 134–156. See also, http://www.iapws.org. IAPWS Formulation 1995 for the Thermodynamic Properties of Ordinary Water Substance for General and Scientific Use.

Whittington, B.I., 1996. The chemistry of CaO and Ca(OH)(2) relating to the Bayer process. Hydrometallurgy 43 (1–3), 13–35.

Xiang, T., Johnston, K.P., 1994. Acid–base behavior of organic compounds in supercritical water. J. Phys. Chem. 98, 7915–7922.

Ziemniak, S.E., 1994. Metal oxide solubility behavior in high temperature aqueous solutions. J. Solution Chem. 21, 745–760.

Densities of Carbon Dioxide + Methanol Mixtures at Temperatures from 313.2 to 323.2 K and at Pressures from 10 to 20 MPa

Richard L. Smith, Jr.,* Sung B. Lee, Sachio Suzuki, Chie Saito, Hiroshi Inomata, and Kunio Arai

Research Center of Supercritical Fluid Technology, Department of Chemical Engineering, Tohoku University, Aoba-ku, Aza Aramaki Aoba-07, Sendai 980-8579 Japan

Densities of carbon dioxide (1) + methanol (2) mixtures were measured with a variable-volume static type of apparatus at three temperatures (313.2, 318.2, and 323.2 K) over a range of pressures (10 to 20 MPa) for methanol-rich mole fractions ($x_2 > 0.257$). Molar volumes could be correlated to within about ±0.1 $cm^3 \cdot mol^{-1}$ by combining a Redlich−Kister expression with a Tait type of equation.

Introduction

The addition of compressed gases to polar liquids leads to an enhancement in the fluid properties such as viscosity, diffusion coefficient, and density and this effect is being studied for new chromatographic applications[1] and for particle design with gas antisolvent techniques.[2] Methanol and carbon dioxide are two of the most widely used solvent pairs and, thus, properties of these mixtures are of great interest. Some of the studies that have been made on methanol−CO_2 systems include Frank et al.[3] who measured diffusion coefficients and viscosities, Dai et al.,[4] who measured excess enthalpies, and Yeo et al.,[5] who measured critical properties. Bezanehtak et al.[6] summarize vapor−liquid equilibria of methanol−CO_2 systems. Densities at various compositions and temperatures of methanol in the presence of carbon dioxide have been measured by Roškar et al.,[7] Chang et al.,[8] Galicia-Luna et al.,[9,10] and Goldfarb et al.[11] We have begun to measure dielectric spectra of methanol−CO_2 mixtures,[12] and in the data reduction, the mixture density is needed. As a result, we have measured densities of methanol−CO_2 mixtures at temperatures from 313.2 K to 323.2 K at pressures from 10 MPa to 20 MPa with emphasis on compositions in the methanol-rich region. In this work, our objective is to report on our methanol−CO_2 density measurements and to provide a suitable correlating equation for the data.

Experimental Section

Materials. Anhydrous methanol (99.8%) and water (HPLC-grade) were obtained from Wako Pure Chemicals (Osaka) and were handled to avoid contamination with air and moisture. Methanol purity was checked with gas chromatography. CO_2 (99.99%) was obtained Nihon Sanso (Sendai) and was dried by passing the gas through a column of silica gel and then filtered with a 0.5-μm sintered filter.

Apparatus. The apparatus used for the density measurements was developed in our research on dielectric spectra and uses a vibrating tube densimeter (model DMA 512 P and DMA 60, Anton Paar, Graz).[12,13] The vibration period of the tube and its contents are proportional to the square root of its mass times an instrument constant that is determined by measurement of the vibration period for known reference fluids at given conditions of temperature and pressure. The calibration procedure is described in the next section. The apparatus consisted of a variable volume (≈110 cm^3) static system in which a magnetic pump was used to circulate CO_2 and methanol mixtures through the densimeter until equilibrium was reached. The entire apparatus was enclosed in a constant temperature forced convection air bath (model FV-450, Advantec, Tokyo) in which temperature was controlled to within ±0.1 K. Further details are given in ref 13.

Temperature was measured inside the system and outside of the system with a three-wire platinum resistance thermometer (PRT) (model TF-A31, Keyence, Osaka) and a four-wire PRT (model RMB-100SY02, Yamari, Osaka), respectively. Accuracy of the temperature probes was confirmed within the system by comparison with a secondary temperature standard that was NIST traceable to 0.01 K. Temperature gradients in the system were no greater than 0.05 K. Pressure of the system was measured with a digital sensor (model SPX-G, Sokken, Tokyo) to an accuracy of 0.05 MPa. Accuracy of the pressure sensor was confirmed by comparison with a dead weight tester that was accurate to 0.5 kPa. Temperatures and pressures reported are estimated to have reproducibilities of ±0.12 K and ±0.07 MPa, respectively, due to gradual temperature and pressure cycling of the system. Composition of the system was determined by trapping the entire system contents in a 125-cm^3 bomb with liquid nitrogen that was followed by weighing the loaded substances before and after slow depressurization into a second trap filled with water. Compositions reported are estimated to be accurate to 0.005 in mole fraction. Replicate measurements and some analyses are given in the discussion.

Calibration. In this work, air, water, and methanol were used as the reference fluids. Air was used as a reference fluid at atmospheric pressure with properties being determined from the Kyushu University physical property package PROPATH.[14] Pure water and pure methanol were used as reference fluids at pressures up to 20 MPa with properties being determined from the IAPWS-95 formulation of Pruβ and Wagner[15] and the IUPAC equation of state of de Reuck and Craven,[16] respectively. It was noticed that some curvature existed between pure water, pure methanol, and air at atmospheric pressures.

* To whom correspondence should be addressed. E-mail: smith@scf.che.tohoku.ac.jp. Fax: +81-22-217-7293.

10.1021/je010207n CCC: $22.00
Published on Web 03/30/2002

Table 1. Experimental Densities for the CO_2 (1) + Methanol (2) System at 313.2 K

P	x_2	ρ	V_{mix}	V_{mix} (eq 4)	deviation (eq 4)
MPa		kg·m^{-3}	cm^3·mol^{-1}	cm^3·mol^{-1}	%
10.50	0.580	845.39	43.848	43.876	0.064
10.56	0.580	845.34	43.851	43.867	0.037
10.57	0.580	845.41	43.847	43.866	0.043
10.89	0.580	846.19	43.806	43.819	0.028
10.95	0.630	843.03	43.261	43.244	−0.039
10.96	0.630	842.87	43.269	43.242	−0.062
10.96	0.630	842.96	43.264	43.242	−0.051
10.97	0.630	843.00	43.262	43.241	−0.049
11.01	0.580	846.43	43.794	43.801	0.017
11.02	0.580	846.59	43.786	43.800	0.032
11.03	0.580	846.56	43.787	43.799	0.025
11.08	0.720	835.34	42.370	42.364	−0.014
11.09	0.720	835.45	42.364	42.363	−0.004
11.12	0.720	835.57	42.358	42.360	0.005
11.14	0.810	823.90	41.651	41.687	0.087
11.16	0.810	824.05	41.643	41.686	0.102
11.18	0.720	835.74	42.350	42.355	0.013
11.18	0.810	824.13	41.639	41.684	0.108
11.18	0.810	824.16	41.638	41.684	0.112
12.41	0.630	846.32	43.093	43.076	−0.039
12.41	0.630	846.28	43.095	43.076	−0.043
12.42	0.630	846.34	43.091	43.075	−0.038
12.43	0.630	846.37	43.090	43.074	−0.038
12.90	0.810	826.27	41.531	41.567	0.086
12.97	0.580	851.86	43.515	43.531	0.037
12.97	0.810	826.43	41.523	41.562	0.094
12.99	0.810	826.51	41.519	41.561	0.100
13.00	0.810	826.55	41.517	41.560	0.104
13.01	0.580	851.92	43.512	43.526	0.032
13.02	0.580	851.93	43.511	43.524	0.030
13.03	0.580	852.00	43.508	43.523	0.035
13.11	0.630	847.80	43.017	42.999	−0.043
13.11	0.630	847.80	43.017	42.999	−0.043
13.18	0.630	848.11	43.002	42.991	−0.024
13.18	0.720	838.68	42.201	42.185	−0.038
13.26	0.630	848.28	42.993	42.983	−0.025
13.27	0.720	838.95	42.187	42.177	−0.024
13.29	0.720	839.03	42.183	42.176	−0.018
13.29	0.720	838.99	42.186	42.176	−0.023
14.83	0.580	856.43	43.283	43.295	0.028
14.88	0.580	856.53	43.278	43.289	0.025
14.88	0.810	828.55	41.417	41.437	0.048
14.89	0.720	841.22	42.073	42.047	−0.063
14.89	0.810	828.57	41.416	41.436	0.049
14.89	0.810	828.58	41.415	41.436	0.051
14.90	0.720	841.22	42.074	42.046	−0.066
14.92	0.720	841.24	42.073	42.044	−0.067
15.02	0.580	856.89	43.259	43.272	0.028
15.11	0.580	857.32	43.238	43.261	0.053
15.11	0.720	841.87	42.041	42.029	−0.028
15.26	0.630	852.20	42.795	42.773	−0.051
15.30	0.630	852.28	42.791	42.769	−0.052
15.32	0.630	852.31	42.790	42.767	−0.052
15.34	0.630	852.35	42.788	42.765	−0.052
15.35	0.630	852.46	42.782	42.764	−0.042
16.81	0.810	830.58	41.316	41.316	0.000
16.87	0.810	830.72	41.309	41.312	0.008
16.92	0.580	861.55	43.026	43.049	0.055
16.92	0.810	830.81	41.304	41.309	0.013
16.94	0.580	861.61	43.022	43.047	0.058
16.95	0.580	861.68	43.019	43.046	0.062
16.99	0.580	861.74	43.016	43.041	0.060
17.05	0.720	844.50	41.910	41.881	−0.070
17.07	0.720	844.53	41.908	41.879	−0.069
17.09	0.720	844.58	41.906	41.878	−0.067
17.10	0.720	844.64	41.903	41.877	−0.062
17.13	0.720	844.74	41.898	41.875	−0.055
17.69	0.630	857.15	42.548	42.537	−0.026
18.03	0.630	857.72	42.520	42.506	−0.033
18.06	0.630	857.78	42.517	42.503	−0.033
18.09	0.630	857.87	42.512	42.500	−0.028

Since all measurements were at super-atmospheric conditions and at methanol-rich mole fractions, methanol and water were used mainly in regressing the constants for the calibration equations at a given temperature. The form of the calibration equations were

$$\rho = AT^2 + BT + C + DT^2P \qquad (1)$$

where ρ (kg·m^{-3}) is the density, T is the period (s), P is the absolute pressure (MPa), and A, B, C, and D are fitted parameters in consistent units. At each temperature, 60 to 70 points were used to determine the constants in eq 1, and in all fits, maximum deviations were less than 0.05% with many deviations being less than 0.01%. For all temperatures, the 95% confidence interval of the density residuals contained zero.

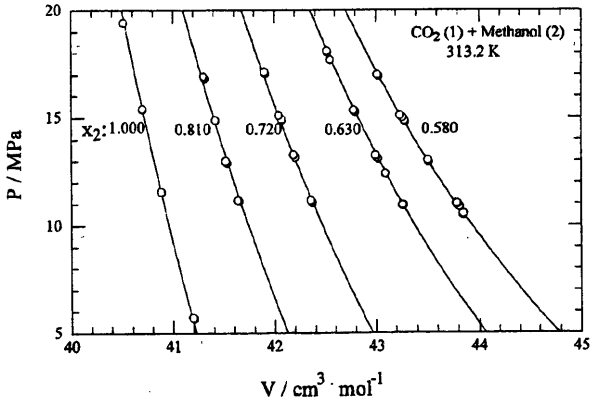

Figure 1. Pressure–volume diagram for the CO_2 (1) + methanol (2) system at 313.2 K; lines calculated from eq 4.

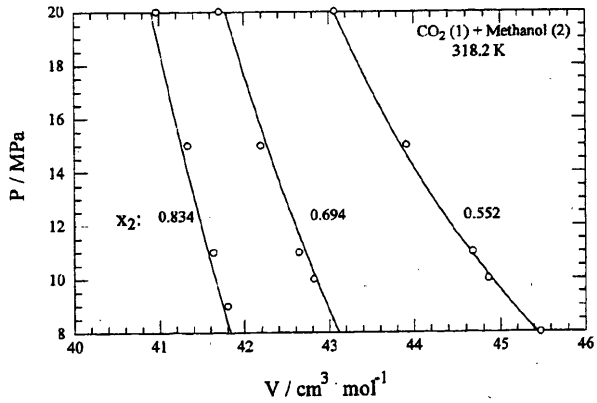

Figure 2. Pressure–volume diagram for the CO_2 (1) + methanol (2) system at 318.2 K; lines calculated from eq 4.

Results and Discussion

Tables 1–3 show the experimental data at 313.2 K, 318.2 K, and 323.2 K, respectively. The correlated values and the residuals are discussed in the next section. From the data, it can be seen that all densities in the range of 750 to 870 kg·m^{-3}, which is intermediate to those of pure methanol and pure water at the same temperature and pressure. The methanol and CO_2 system exhibits a maximum in density versus composition for a given temperature and pressure[17] and thus pressure–molar volume plots show the trend of the data more clearly. A maximum in density for the 2-propanol and CO_2 system has also been noted by Yaginuma et al.[18] Figures 1–3 show all data plotted in P–V coordinates at given mole fractions of methanol. From the

Table 2. Experimental Densities for the CO_2 (1) + Methanol (2) System at 318.2 K

P	x_2	ρ	V_{mix}	V_{mix} (eq 4)	deviation (eq 4)
MPa		$kg \cdot m^{-3}$	$cm^3 \cdot mol^{-1}$	$cm^3 \cdot mol^{-1}$	%
8.0	0.552	822.37	45.477	45.440	−0.080
9.0	0.834	814.10	41.799	41.744	−0.132
10.0	0.552	833.71	44.859	44.897	0.085
10.0	0.694	833.84	42.813	42.846	0.077
11.0	0.552	837.04	44.680	44.657	−0.052
11.0	0.694	837.25	42.639	42.721	0.192
11.0	0.834	817.35	41.633	41.573	−0.144
15.0	0.552	851.62	43.915	43.847	−0.154
15.0	0.694	846.17	42.190	42.266	0.182
15.0	0.834	823.35	41.330	41.259	−0.172
20.0	0.552	868.44	43.064	43.063	−0.003
20.0	0.694	855.99	41.705	41.781	0.182
20.0	0.834	830.59	40.969	40.908	−0.150

Table 3. Experimental Densities for the CO_2 (1) + Methanol (2) System at 323.2 K

P	x_2	ρ	V_{mix}	V_{mix} (eq 4)	deviation (eq 4)
MPa		$kg \cdot m^{-3}$	$cm^3 \cdot mol^{-1}$	$cm^3 \cdot mol^{-1}$	%
11.00	0.257	748.05	54.721	54.579	−0.260
11.51	0.257	759.51	53.896	53.894	−0.002
12.61	0.257	776.47	52.718	52.738	0.037
13.20	0.257	784.57	52.174	52.236	0.120
14.17	0.257	794.05	51.551	51.533	−0.035
14.74	0.257	800.56	51.132	51.173	0.081
15.51	0.257	806.00	50.787	50.736	−0.101
15.96	0.257	810.05	50.533	50.501	−0.063
16.57	0.257	814.88	50.233	50.205	−0.057
17.16	0.257	819.23	49.966	49.938	−0.056
17.78	0.257	823.58	49.703	49.677	−0.052
18.25	0.257	826.84	49.507	49.490	−0.034
11.20	0.288	769.29	52.728	52.695	−0.063
11.90	0.288	777.90	52.145	52.139	−0.012
12.10	0.331	795.59	50.338	50.324	−0.029
12.65	0.331	800.73	50.015	50.065	0.101
13.40	0.331	806.56	49.653	49.741	0.176
14.65	0.331	814.48	49.171	49.258	0.178
15.78	0.331	821.89	48.727	48.872	0.297
16.95	0.331	829.12	48.303	48.512	0.433
15.31	0.380	824.71	47.850	47.741	−0.226
18.14	0.380	839.56	47.003	47.060	0.122
10.57	0.486	817.09	46.743	46.654	−0.191
11.00	0.486	819.64	46.598	46.551	−0.101
11.15	0.486	819.63	46.598	46.515	−0.178
12.07	0.486	823.23	46.395	46.307	−0.188
12.09	0.486	825.25	46.281	46.303	0.046
13.12	0.486	827.25	46.169	46.085	−0.183
11.00	0.570	823.34	45.168	45.237	0.153
13.00	0.570	828.19	44.903	44.902	−0.003
15.00	0.570	833.26	44.630	44.598	−0.071
17.00	0.570	837.79	44.389	44.322	−0.151
20.00	0.570	844.14	44.055	43.947	−0.244
13.00	0.700	821.39	43.381	43.499	0.271
15.00	0.700	825.14	43.184	43.274	0.209
17.00	0.700	829.15	42.974	43.064	0.209
20.00	0.700	834.91	42.678	42.775	0.226
10.50	0.880	796.86	42.013	42.086	0.174
11.00	0.880	796.83	42.014	42.041	0.064
13.00	0.880	800.29	41.833	41.868	0.086
15.00	0.880	802.69	41.708	41.705	−0.006
17.00	0.880	805.35	41.570	41.550	−0.047
20.00	0.880	808.84	41.391	41.333	−0.140
10.70	0.940	785.76	41.693	41.674	−0.045
11.00	0.940	786.19	41.670	41.649	−0.049
13.00	0.940	788.61	41.542	41.492	−0.121
15.00	0.940	790.77	41.428	41.342	−0.209
17.00	0.940	793.16	41.304	41.200	−0.252
20.00	0.940	796.43	41.134	40.998	−0.329

figures, it can be seen that the methanol liquid $P-V$ lines had very steep slopes for methanol mole fractions of about 0.5 or higher. However, as the CO_2 mole fraction increased, the $P-V$ lines exhibited greater curvature.

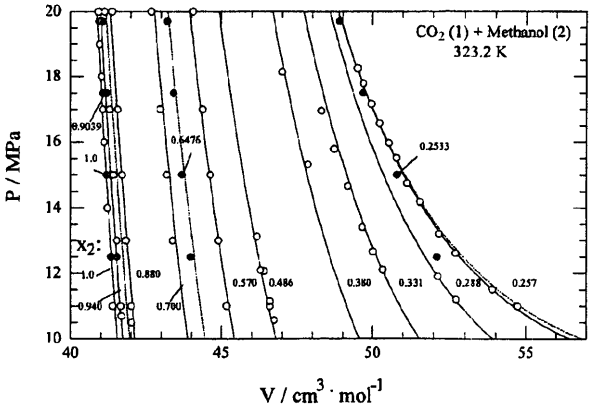

Figure 3. Pressure–volume diagram for the CO_2 (1) + methanol (2) system at 323.2 K; white circles, this work; filled circles, Galicia-Luna et al.;[9,10] lines calculated from eq 4; dashed lines calculated from eq 4 at compositions of ref 9.

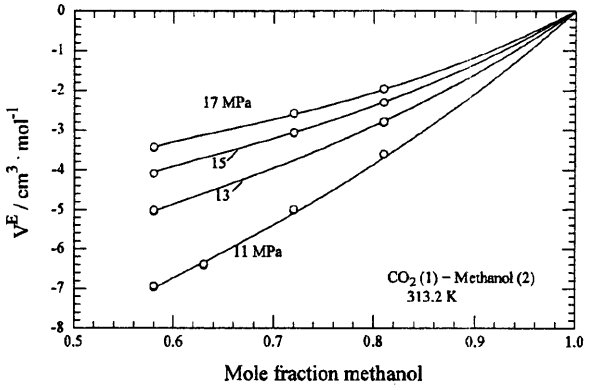

Figure 4. Excess molar volumes for the CO_2 (1) + methanol (2) system at 313.2 K; lines calculated from eq 4.

The precision of the data can be estimated from replicate measurements made at 313.2 K. From Table 1 and Figure 1, maximum variabilities of 0.1 $kg \cdot m^{-3}$ were observed by comparing density measurements made at the same pressures or pressures within about 0.01 MPa. In general, the variations in the density were much less than 0.1 $kg \cdot m^{-3}$. Due to errors in the mole fraction determination and temperature and pressure cycling in the system, however, accuracy in density is estimated to be no higher than about 0.5 $kg \cdot m^{-3}$ with the higher errors occurring for the higher CO_2 mole fractions.

Some measurements were performed at specific pressures of nominally 11, 13, 15, 17, and 20 MPa to allow analysis of the excess molar volumes. Pure component molar volumes were obtained from the equations of Span and Wagner[19] for pure CO_2 and IUPAC relations of de Reuck and Craven[16] for pure methanol. Results are shown plotted in Figures 4–6 along with correlation equation results. The excess volumes can be seen to be negative over the composition region measured. Development of the correlation equations is discussed next.

Correlation. Data correlation was somewhat more difficult than at first anticipated. Forms of the Tait equation can be fitted to the experimental data at a given composition but do not allow interpolation at other compositions. The excess volumes at a given temperature and pressure can be fit with Redlich–Kister expansions or remarkably well with van-Laar-type expressions but do not allow interpolation at other pressures. Since our objective

Table 4. Parameter Values for Eq 4 and Their Standard Deviation

	313.2 K		318.2 K		323.2 K	
parameter	values	standard deviation	values	standard deviation	values	standard deviation
P_0 (MPa)	11		11		11	
c	0.07		0.07		0.07	
A_1 ($cm^3 \cdot mol^{-1}$)	−11.92293	0.095	−19.22192	0.585	−63.90117	1.249
A_2 ($cm^3 \cdot mol^{-1}$)	0		0		−48.13704	1.527
A_3 ($cm^3 \cdot mol^{-1}$)	0		0		−25.21391	1.189
V_1 ($cm^3 \cdot mol^{-1}$)	54.71537	0.062	59.56155	0.349	83.07311	0.612
V_2 ($cm^3 \cdot mol^{-1}$)	40.90840	0.002	41.18354	0.025	41.46474	0.012
B_1 (MPa)	−41.32487	0.939	−39.67061	4.277	−21.30546	0.378
B_2 (MPa)	47.59646	0.496	36.72802	3.267	28.94383	1.082

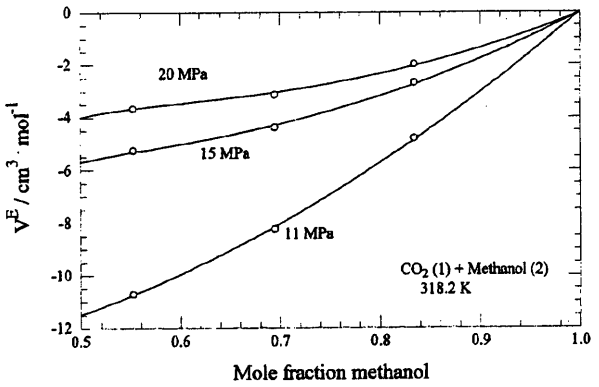

Figure 5. Excess molar volumes for the CO_2 (1) + methanol (2) system at 318.2 K; lines calculated from eq 4.

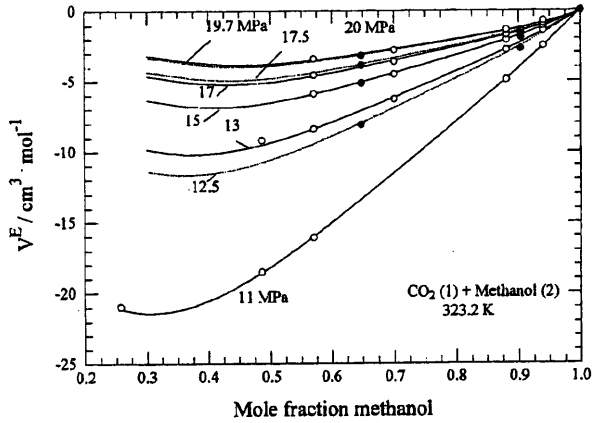

Figure 6. Excess molar volumes for the CO_2 (1) + methanol (2) system at 323.2 K; lines calculated from eq 4; white circles, this work; filled circles, Galicia-Luna et al.;[9,10] dashed lines calculated from eq 4 at the pressures of ref 9.

in this section was to provide a correlation for interpolation, *not extrapolation*, of the data, we combined the Redlich–Kister expansion with the Tait form of equation to give the set of empirical correlating equations,

$$B = x_1 B_1 + x_2 B_2 \tag{2}$$

$$V_0 = x_1 V_1 + x_2 V_2 + x_1 x_2 (A_1 + A_2(x_1 - x_2) + A_3(x_1 - x_2)^2) \tag{3}$$

$$V_{mix} = V_0(1 - c\ln((B + P)/(B + P_0))) \tag{4}$$

where x_1 and x_2 are the mole fractions of carbon dioxide and methanol, respectively, and V_{mix} is the mixture molar volume. The V_1, V_2, B_1, B_2, A_1, A_2, and A_3 are empirical parameters determined by a least-squares fit of the $P-V$ data at a given temperature. The V_1 and V_2 should not be confused with the pure component molar volumes at the given temperature and pressure since eq 4 can only be applied over a limited composition range. The c and P_0 in eq 4 could have been used as fitting parameters, but in this work, we assigned values of c to be a constant independent of temperature and the reference pressure, P_0, to be 11 MPa, according to initial evaluations and parameter sensitivities. It should be noted that eq 4 cannot be extrapolated to the saturation region or to CO_2-rich mole fractions due to its functional form and choice of reference state, P_0 and V_0.

Fitted values for eq 4 are summarized in Table 4 and calculated deviations for each point are shown in Tables 1–3 with the average percent deviation of the correlation from the data for all data points being 0.08%. Percent deviations of the model versus the data are shown for each point in the tables. Parameter standard deviations were calculated and are given in Table 4 and can be used to calculate the 95% confidence interval of the parameters (not shown). Standard deviations of the A and V parameters were smaller compared with those of the B parameters and indicated a lower range of variability. Values of the covariance matrix indicated low correlation between the parameters. The χ^2 values (correlation coefficients) were 0.00984 (0.999968), 0.0363 (0.99988), and 0.3179 (0.99989) for the 318.2 K, 318.2 K, and 323.2 K data, respectively. Higher variability for the 323.2 K data set was probably due to the wider range of carbon dioxide mole fractions studied.

Comparison with Other Data. Several other researchers have reported densities of carbon dioxide + methanol mixtures as noted in the Introduction. Brunner et al.[20] measured densities along the CO_2 + methanol saturation curve with a static apparatus to a nominal precision of 2.5 digits whereas in this work densities in the compressed regions were measured and therefore these data cannot be directly compared. Roškar et al.[7] reported CO_2 + methanol molar volumes at 308.2 K, 323.2 K, and 338.2 K with a static apparatus to a nominal precision of 2.5 digits. However, the region of measurement of Roškar et al.[7] extends into the two-phase region of Brunner et al.,[20] indicating some inconsistency in the compositions reported, specifically, $x_2 = 0.571$ and $x_2 = 0.781$. The data of Goldfarb et al.[11] are mainly in the region of CO_2-rich mole fractions, where we have not made measurements and show excess volumes that are positive. The data set that we chose for comparison are the high-precision measurements of Galicia-Luna et al., who used a vibrating tube method.[9,10] The data applicable to our region of measurement are plotted in Figures 3–6 and calculations made with eq 4 at the compositions reported by those authors are shown by the dashed lines. Good agreement (0.25%) between the molar volumes of this work and those of the literature can be seen at the methanol mole fraction of 0.6476 but only fair

agreement (0.8%) is apparent in the methanol mole fraction of 0.9039 and for one point at high CO_2 mole fractions at 12.5 MPa. The data are also compared in Figure 6, where experimental data and calculated excess molar volumes are shown. Good agreement can be seen between the two data sets.

Conclusions

We have reported density data for methanol + CO_2 mixtures, where methanol is in its expanded liquid state. The data should find use in the analyses of dielectric spectra data as well as in other fields related to liquid chromatography and gas antisolvent crystallization. A simple correlation equation was developed for interpolating within the conditions of measurement. Extreme caution should be used when extrapolating values, specifically, extrapolation to lower pressures or to higher carbon dioxide mole fractions. Extrapolation of the correlating equation to higher pressures, on the other hand, can probably provide acceptable results.

Acknowledgment

The authors wish to thank Mr. Mikio Kikuchi for assistance with construction of the apparatus.

Literature Cited

(1) Zhao, J.; Olesik S. V. Phase Diagram Studies of Methanol-CHF_3 and Methanol-H_2O-CHF_3 Mixtures. *Fluid Phase Equilib.* **1999**, *154*, 261–284.

(2) Jung, J.; Perrut, M. Particle Design using Supercritical Fluids: Literature and Patent Survey. *J. Supercrit. Fluids* **2001**, *20*, 179–220.

(3) Frank, M. J. W.; Kuipers, J. A. M.; van Swaaij, P. M. Diffusion Coefficients and Viscosities of CO_2 + H_2O, CO_2 + CH_3OH, NH_3 + H_2O, and NH_3 + CH_3OH Liquid Mixtures. *J. Chem. Eng. Data* **1996**, *41*, 297–302.

(4) Dai, W.; Kojima, K.; Ochi, K. Measurement and Correlation of Excess Molar Enthalpies of CO_2 + CH_3OH System in the Vicinity of Critical Point of Carbon Dioxide. *J. Chem. Eng. Data* **1999**, *44*, 161–164.

(5) Yeo, S.-D.; Park, S.-J.; Kim, J.-W.; Kim, J.-C. Critical Properties of Carbon Dioxide + Methanol, + Ethanol, + 1-Propanol, and + 1-Butanol. *J. Chem. Eng. Data* **2000**, *45*, 932–935.

(6) Bezanehtak, K.; Combes, G. B.; Dehghani, F.; Foster; N. R.; Tomasko, D. L. Vapor-Liquid Equilibrium for Binary Systems of Carbon Dioxide + Methanol, Hydrogen + Methanol, and Hydrogen + Carbon Dioxide at High Pressures. *J. Chem. Eng. Data* **2002**, *47*, 161–168.

(7) Roškar, V.; Dombro, R. A.; Prentice, G. A.; Westgate, C. R.; McHugh, M. A. Comparison of the Dielectric Behavior of Mixtures of Methanol with Carbon Dioxide and Ethane in the Mixture-Critical Region and Liquid Regions. *Fluid Phase Equilib.* **1992**, *77*, 241–259.

(8) Chang, C. J.; Day, C.-Y.; Ko, C.-M.; Chiu, K.-L., Densities and P-x-y Diagrams for Carbon Dioxide Dissolution in Methanol, Ethanol, and Acetone Mixtures. *Fluid Phase Equilib.* **1997**, *131*, 243–258.

(9) Galicia-Luna, L. A.; Richon, D.; Renon, H. New Loading Technique for a Vibrating Tube Densimeter and Measurements of Liquid Densities up to 39.5 MPa for Binary and Ternary Mixtures of the Carbon Dioxide-Methanol-Propane System. *J. Chem. Eng. Data* **1994**, *39*, 424–431.

(10) Galicia-Luna, L. A.; Richon, D.; Renon, H. Corrections: New Loading Technique for a Vibrating Tube Densimeter and Measurements of Liquid Densities up to 39.5 MPa for Binary and Ternary Mixtures of the Carbon Dioxide-Methanol-Propane System. *J. Chem. Eng. Data* **1995**, *40*, 528–529.

(11) Goldfarb, D. L.; Fernandez, D. P.; Corti, H. R. Dielectric and Volumetric Properties of Supercritical Carbon Dioxide (1) + Methanol (2) Mixtures at 323.15 K. *Fluid Phase Equilib.* **1999**, *158–160*, 1011–1019.

(12) Smith, R. L., Jr.; Saito, C.; Suzuki, S.; Lee, S.-B.; Inomata, H.; Arai, K. Temperature Dependence of Dielectric Spectra of Carbon Dioxide and Methanol Mixtures at High-Pressures. *Fluid Phase Equilib.* **2002**, *194–197*, 869–877.

(13) Lee, S. B.; Smith, R. L., Jr.; Inomata, H.; Arai, K. Coaxial Probe and Apparatus for Measuring the Dielectric Spectra of High-Pressure Liquids and Supercritical Fluid Mixtures. *Rev. Sci. Instrum.* **2000**, *71*, 4226–4230.

(14) PROPATH Group. *PROPATH: A Program Package for Thermophysical Properties, version 10.2*; Kyushu University: Fukuoka, 1997.

(15) Pruß, A.; Wagner, W. *Release on the IAPWS Formulation 1995 for the Thermodynamic Properties of Ordinary Water Substance for General and Scientific Use*; The International Association for the Properties of Water and Steam (www.iapws.org), 1996.

(16) de Reuck, K. M.; Craven, R. J. B. *Methanol. International Thermodynamic Tables of the Fluid State-12, International Union of Pure and Applied Chemistry*; Blackwell Scientific Publications: Oxford, 1993.

(17) Lee, S.-B. Dielectric Spectroscopy and Thermodynamic Behavior of Supercritical Fluid Solutions, Ph.D. Thesis, Tohoku University, 2000.

(18) Yaginuma, R.; Nakajima, T.; Tanaka, H.; Kato, M. Densities of Carbon Dioxide + 2-Propanol at 313.15 K and Pressures to 9.8 MPa. *J. Chem. Eng. Data* **1997**, *42*, 814–816.

(19) Span, R.; Wagner, W. A New Equation of State for Carbon Dioxide Covering the Fluid Region from the Triple-Point Temperature to 1100 K at Pressures up to 800 MPa. *J. Phys. Chem. Ref. Data* **1996**, *25*, 1509–1596.

(20) Brunner, E.; Hültenschmide, W.; Schlichthärle, G. Fluid Mixtures at High Pressures IV. Isothermal Phase Equilibria in Binary Mixtures Consisting of (Methanol + Hydrogen or Nitrogen or Methane or Carbon Monoxide or Carbon Dioxide). *J. Chem. Thermodyn.* **1987**, *19*, 273–291.

Received for review July 23, 2001. Accepted February 27, 2002. The authors wish to gratefully acknowledge support of the Genesis Research Institute. A portion of this work was supported by a Ministry of Education, Science, Sports, and Culture grant.

JE010207N

Available online at www.sciencedirect.com
SCIENCE DIRECT®
Fuel 82 (2003) 1231–1239
FUEL
www.fuelfirst.com

Upgrading of asphalt with and without partial oxidation in supercritical water☆

Takafumi Sato[a], Tadafumi Adschiri[a], Kunio Arai[a], Garry L. Rempel[b], Flora T.T. Ng[b,*]

[a]*Department of Chemical Engineering, Tohoku University, 07 Aoba, Aramaki-Aza, Aoba-ku, Sendai 980-8579, Japan*
[b]*Department of Chemical Engineering, University of Waterloo, 200 University Avenue West, Waterloo, Ont., Canada N2L 3G1*

Received 1 July 2002; revised 6 January 2003; accepted 10 January 2003; available online 13 February 2003

Abstract

Supercritical water and supercritical water partial oxidation treatments were applied to the upgrading of asphalt. Asphalt was converted at 613–673 K, 0–0.5 g/cm^3 water density under argon or air atmosphere. Under an argon atmosphere and 0.5 g/cm^3 water density, both the asphaltene conversion and desulfurization increased with increasing temperature. At 673 K, the asphaltene conversion and the yield of CO_2 increased with an increasing water density. Water apparently participated in the reaction and its hydrogen was used for capping the free radicals generated during the upgrading of asphalt resulting in an increased yield of maltene. Under an air atmosphere at 673 K, asphaltene conversion was lower but desulfurization was higher than those obtained in an argon atmosphere.

Keywords: Supercritical water; Desulfurization; Partial oxidation; Asphaltene; Asphalt; Upgrading; Steam reforming

1. Introduction

The world-wide demand for petroleum oil is directed towards light hydrocarbons with low sulfur content because of environmental problems. On the other hand, the supply of light oil is decreasing and feedstocks are becoming heavier and have a high sulfur content. Canada has a vast reserve of oil sands, heavy oil/bitumen resources. Utilization of these heavy hydrocarbons is of great interest. Hydroprocessing is the current route for upgrading heavy feedstocks, however, hydrogen supply is a major cost in hydroprocessing. Therefore, alternative upgrading processes that do not use externally supplied hydrogen are desirable.

Supercritical water (SCW) ($T_c = 647$ K and $P_c = 22.1$ MPa), also known as dense steam, can become miscible with light gases, oils and aromatics to form a homogeneous phase [1,2]. SCW not only participates in a reaction as a solvent but also as a reactant [3,4]. C–O bonds such as in ethers and esters, and the aliphatic C–S bonds are easily broken in high temperature or hydrothermal water including SCW [3,5].

The conversion of coal and oil shale has been studied in SCW. Coal conversion in SCW was higher than that in supercritical toluene because of the hydrolysis of ether or ester bonds in coal [6,7]. Treatment of oil shale with SCW has resulted in a higher conversion and a larger oil recovery than that obtained from toluene extraction [8]. Furthermore, more facile decomposition of the polar components in SCW compared with supercritical toluene was obtained [9]. These results indicate that SCW can be an effective solvent for the extraction and decomposition of heavy hydrocarbons. However, essentially no attention has been given to desulfurization in previous studies. Recently a study on the desulfurization of gas oil in SCW was reported by Vogelaar et al. [10]. They evaluated the desulfurization and demetalization of gas oil in SCW and concluded that SCW itself is not sufficient for the reforming of gas oil.

Supercritical water oxidation (SCWO), that is, the oxidation at 673–873 K in SCW, is an effective method for the conversion of organics. SCWO has been mainly applied to the decomposition of harmful organics and there are various publications in this research area [3,11]. The objective of the SCWO process is to convert organics into CO_2 and H_2O and not to recover chemicals from the starting materials.

* Corresponding author. Tel.: +1-519-8851211; fax: +1-519-7464979.
E-mail address: fttng@cape.uwaterloo.ca (F.T.T. Ng).
☆ Published first on the web via Fuelfirst.com—http://www.fuelfirst.com

0016-2361/03/$ - see front matter © 2003 Elsevier Science Ltd. All rights reserved.
doi:10.1016/S0016-2361(03)00019-X

On the other hand, partial oxidation occurs around the critical temperature of water in supercritical condition. Watanabe et al. [12] reported that the amount of partial oxidation products such as CO, aldehyde and ketone increased with increasing water density in the partial oxidation of *n*-hexadecane at 673 K in SCW. Furthermore, hydrogenation of hydrocarbons during partial oxidation is also observed in SCW [13] since partial oxidation produces CO which could undergo a water gas shift reaction to produce in situ hydrogen for hydrogenation and desulfurization [14,15]. Furthermore, the in situ hydrogen is more active than molecular hydrogen for desulfurization [14,15]. In addition, we have found that in the presence of CO, hydrogen was generated in a bitumen emulsion via the water gas shift reaction to generate H_2 in situ for upgrading [16]. These results suggest that SCW partial oxidation may also be suitable for upgrading heavy hydrocarbons.

In particular, SCW has potential application in the upgrading of heavy oil/bitumen emulsions produced from the recovery of heavy oil/bitumen using steam injection techniques and the bitumen extracted from oil sands using hot water. Water may be a cheaper source for the hydrogen that is required in upgrading heavy oil/bitumen and provides the incentive for this investigation. For hydrocarbon resources containing water, upgrading in SCW eliminates the need for the separation of hydrocarbon from water. Furthermore, upgrading in SCW with partial oxidation will provide additional heat and in situ hydrogen for upgrading and hence potentially reduce the cost of upgrading. Due to the inherent high pressure and the corrosive nature of SCW, the cost of the special material needed for the construction of the reactor and the associated equipment have to be considered in the economic analysis of the process.

This paper reports our exploratory research on the upgrading of asphalt in SCW with and without oxygen. The effect of water and oxygen on the conversion and desulfurization of asphalt will be discussed.

2. Experimental

2.1. Materials

The asphalt from Esso Imperial Oil was used for upgrading studies. The asphalt is a solid at room temperature and completely soluble in toluene. Asphalt was ground into a powder with a mortar and pestel before being used in the experiments. The asphalt was found to consist of maltene (defined as the class of hydrocarbon soluble in *n*-pentane) and asphaltene (defined as the class of hydrocarbon insoluble in *n*-pentane and soluble in toluene). The maltene and asphaltene were found to be 37.2 ± 3.9 and 62.8 ± 3.9 wt% of the raw asphalt, respectively. The sulfur content was determined using X-ray fluorescence equipment (XRF: Lab-X3000, Oxford). The sulfur content in maltene and asphaltene was 2.05 ± 0.20 and 5.36 ± 0.31 wt% of raw asphalt, respectively.

n-Pentane (99.8%) was purchased from Fisher Scientific and toluene (technical grade) was obtained from the University of Waterloo. Argon (Ar: 99.998 %) and air (ultra zero ambient monitoring, O_2 20.9%) were purchased from Praxair.

2.2. Procedures

The experiments were conducted with a 316 SS tube bomb reactor (6 cm^3) with a high pressure valve and a thermocouple at the center of the reactor. Before the experiment, each reactor was loaded with 3.0 g of 3.0 wt% hydrogen peroxide aqueous solution and heated at 673 K for up to 10 h. This procedure is used to oxidize and passivate the reactor wall. The reactor was loaded with 0.6 g of asphalt and 0.6–3 g of water corresponding to 0.1–0.5 g/cm^3 water density. At 673 K, these amounts of water loaded corresponded to pressures of 20.0 to 37.0 MPa based on the pure water data of Haar et al. [17]. Then the reactor was pressurized with argon or air and these gases were released through the high pressure valve. This purging procedure was repeated several times. After that, the reactor was pressurized with 0.10 g of argon gas or 0.08 g of air. The loaded amount of gases corresponded to 60 and 66 cm^3 at STP, respectively. For experiments with air, the amount of oxygen was 0.0185 g. We also conducted experiments without water for reference.

The reactor, loaded with reagents, was submerged in a fluidized sand bath (Fisher Scientific) that was heated to the reaction temperature (613–673 K). The heat up time for the tube bomb reactor to reaction temperature was 3 min. During the reaction, the reactor was shaken once per second using a mechanical device. The reaction was conducted for 60 min and ended by quenching the reactor in a water bath at room temperature.

Fig. 1 shows the analysis procedure. After the reaction, the gas products were collected into the syringe via the sampling valve and the volume was measured. The oxygen content and the gas products were analyzed by a GC (a Perkin Elmer Model 8500 Gas Chromatograph) with TCD and with a 1.52 m × 3.175 mm o.d. Hayesep C column and 1.5 m × 3 mm o.d. Molecular Sieve 5A column. The liquid and solid products were collected in a beaker by rinsing the reactor with 30 g of *n*-pentane. The products in the beaker were filtered with a 1.5 μm glass microfiber filter (VWR Canlab) and separated from the solid. The filtrate contained *n*-pentane and water phases. The content in the *n*-pentane fraction was defined as maltene. The water phase was collected by using a Pasteur pipette and diluted to 10 cm^3 with water for analysis. The *n*-pentane phase and water phase were analyzed by X-ray fluorescence (XRF: Lab-X3000, OXFORD) to determine the sulfur content. The water phase was also analyzed by TOC (TOC-5050A, SHIMADZU) to measure the organic carbon content.

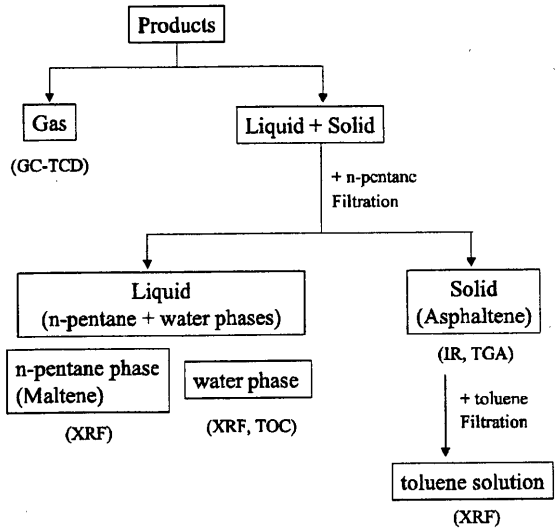

Fig. 1. The procedure for product analysis.

The solids on the filter were put into a petri dish with a filter, dried at 60 °C overnight and weighed. Then, 0.05 g of the solid was dissolved in 40 g of toluene and filtered. A very small amount of toluene insoluble (coke) was produced and was trapped inside the filter. Since the coke yield was negligible, the solids in the reactor are defined as asphaltene. Asphaltene was analyzed by FT-IR (FTS6000, Bio-Rad) using diffuse reflectance IR techniques (DRIFT). Thermal analysis of the asphaltene was conducted under a helium atmosphere with a TGA instrument (SDT2960, TA Instruments). The temperature program was set over a temperature range of 333–973 K at 10 K/min followed by an isothermal stage at 973 K for 5 min. The sulfur content in asphaltene was analyzed by XRF using a solution of asphaltene in toluene. The asphaltene conversion, sulfur concentration, changes in sulfur, sulfur content, desulfurization, gas yield and oxygen conversion are defined as follows

Asphaltene conversion (wt%)

$$= 100 - W_{AS}/(W_{AS} \text{ of raw asphalt}) \times 100 \quad (1)$$

Sulfur concentration (wt%)

$$= (W_S \text{ in maltene or asphaltene})/(W_{MA} \text{ or } W_{AS} \text{of raw asphalt}) \times 100 \quad (2)$$

where W_{MA}, W_{AS} is the weight of maltene and asphaltene (g) and W_S is the weight of sulfur (g).

Change in sulfur (wt% of S)

$$= (W_S \text{ in maltene or asphaltene})/(W_S \text{ in maltene or asphaltene of raw asphalt}) \times 100 - 100 \quad (3)$$

Desulfurization from asphalt (wt% of S)

$$= 100 - (W_S \text{ in maltene} + W_S \text{ in asphaltene})/(W_S \text{ in raw asphalt}) \times 100 \quad (4)$$

Sulfur content (wt% of S)

$$= (W_S \text{ in maltene or asphaltene})/(W_S \text{ in raw asphalt}) \times 100 \quad (5)$$

Gas *yield* (*wt%*)

$$= (\text{net weight of gas (g)})/(\text{weight of raw asphalt loaded (g)}) \times 100 \quad (6)$$

Oxygen conversion (%)

$$= 100 - \left(\frac{\text{oxygen in the reactor (g)}}{\text{oxygen introduced into reactor (g)}}\right) \times 100 \quad (7)$$

3. Results and discussion

The properties of the asphalt are shown in Table 1. After the reaction, upon the addition of pentane to the reactor, an amber solution containing some black solid was obtained. The water phase was clear and colorless. In all the experiments in this study, the water phase contained a small amount of organics (<0.14 wt% to raw asphalt loaded) based on TOC analysis and no sulfur was found in this phase. For this reason, the sulfur removal was calculated based on the results obtained from the asphaltene, *n*-pentane phases and gas. We could not obtain complete S balance due to a small amount of asphalt used for the reaction and a larger number of separation and dilution steps are used for the separation of the different phases of the products (Fig. 1). However, we feel that we could discuss the trends obtained on S removal. No attempt was made to determine the carbon balance in this preliminary study and it is not included in our discussions.

3.1. Effect of temperature

We conducted the asphalt conversion experiments with 3 g of water at 613–673 K for 60 min under Ar atmosphere, and with air at 673 K. We also conducted the experiments without water at 673 K. The experiments at 613 and 633 K were conducted under subcritical conditions to compare the results obtained under supercritical conditions. Table 1 summarizes the experimental results. In these experiments, the gas yield was relatively low, less than 2.32 wt%, except for the experiment carried out under air without water at 673 K, which produced 6.27 wt% of gases. Due to the small amount of gases produced and the inherent experimental difficulty in quantifying the small amount of gases

Table 1
Summary of experimental results on the upgrading of asphalt at 613–673 K for 60 min

	Raw asphalt	Loaded gas (Temperature, K)						
		Ar (613)	Ar (633)	Ar (653)	Ar (673[a])	Ar (673)	Air (673[a])	Air (673)
Asphalt loaded (g)	0.60	0.60	0.60	0.60	0.60	0.60	0.60	0.60
Water loaded (g)	–	3.08	3.02	3.02	3.02	0	3.01	0
Maltene (g)	0.22	0.32	0.35	0.37	0.40	0.37	0.37	0.34
Asphaltene (g)	0.38	0.28	0.25	0.23	0.20	0.23	0.23	0.26
Sulfur ($\times 10^2$ g)								
In maltene	1.23	1.64	1.74	1.52	1.60	1.53	1.41	1.45
In asphaltene	3.22	2.08	1.97	2.25	1.69	1.71	1.36	1.72
In H_2S	–	0.05	0.06	0.12	0.24	0.43	0.13	0.36
Asphaltene conversion (wt%)	0	25.7	33.7	39.0	46.9	39.0	39.0	31.0
Sulfur concentration (wt%)								
Maltene	5.6	5.1	5.0	4.1	4.0	4.1	3.8	4.3
Asphaltene	8.5	7.4	7.9	9.8	8.4	7.4	5.9	6.6
Change in sulfur amount (wt% of S)								
Maltene	0	+33.5	+41.2	+23.2	+30.3	+24.3	+14.8	+18.2
Asphaltene	0	−35.4	−38.7	−30.0	−47.6	−46.8	−57.6	−46.6
Desulfurization from asphalt (wt% of S)	0	16.3	16.6	15.3	26.0	27.1	37.6	28.7
Sulfur removal as H_2S (wt% of S)	–	1.2	1.4	2.7	5.4	9.7	2.9	8.1

[a] Average values.

produced, the amount of maltene listed in Table 1 was calculated based only on the difference of the weight of asphalt and asphaltene.

The experiments carried out at different temperatures in water under an Ar atmosphere will be described first. The asphaltene conversion and the weight of maltene increased as the temperature was increased. At 400 °C in the presence of SCW, 48.7 wt% conversion of asphalt to maltene was obtained while 39 wt% conversion of asphaltene was obtained without SCW. Therefore, SCW enhanced the conversion of asphaltene.

The concentration of sulfur in maltene was decreased by about 16 wt%; therefore water also reduces the sulfur concentration in the maltene fraction and improves the quality of the maltene fraction. However, there is no clear trend on the changes of the concentration of sulfur in the asphaltene fraction as the temperature was increased. The desulfurization obtained from the asphalt was 16.3–26.0 wt% and the sulfur removed as H_2S was only 1.2–5.4 wt% based on the gas phase analysis. The sulfur balance based on the H_2S determined in the gas phase and the S content in the maltene and asphaltene showed that about 0.004–0.009 g of sulfur was unaccounted for. This amount of missing sulfur is probably in the small amount of toluene insoluble and the H_2S dissolved in the water that were not quantified. Although we could not obtain a complete S balance, we feel that we could discuss the general trend based on the observed result. The desulfurization obtained at 673 K was the highest and the sulfur removed as H_2S increased with increasing temperature. The increase of temperature enhanced the conversion of asphaltene, production of H_2S and the desulfurization from asphalt.

Table 2 shows the gas yield of the experiments carried out at 613–673 K for 60 min. The gases produced were CO_2, CO, H_2S, CH_4, C_2H_6 and C_3H_8. No hydrogen was detected. No carbon or sulfur was found in the water phase by TOC and XRF analysis; this maybe due to a combination of low levels of CO_2 and H_2S and the volatility of these gaseous compounds since we could not analyze for these compounds immediately after the reaction and separation. In the gaseous products, the main component was CO_2 while H_2S was the second highest component. The yield of total gas ranged from 0.33 to 2.1 wt% and a higher gas yield was observed at a higher temperature as expected. The significant amount of CO_2 in the gas phase obtained in the absence of air suggests that water participates in the steam reforming reaction. In the presence of air, the amount of CO_2 was higher which indicates oxidation of some of the asphalt to CO_2 as would be expected. Belgrave et al. [18] also reported that CO_2, CO, H_2S, hydrocarbons and a small amount of hydrogen was produced in the aquathermolysis of heavy oils at 633–693 K.

The increase of temperature enhanced the decomposition of asphalt and desulfurization via removal as H_2S and/or the accumulation of sulfur in the heavier components (i.e. the toluene insolubles or the asphaltene). Schlepp et al. [19] conducted the conversion of asphalt in high temperature water at less than 623 K. They reported that both the

Table 2
Gas yield obtained from the upgrading of asphalt at 613–673 K for 60 min

Temperature (K)	Gas	Water (g)	Yield (wt%)						
			CO_2	CO	H_2S	CH_4	C_2H_6	C_3H_8	Total
613	Ar	3.08	0.14	0.02	0.10	0.01	0.01	0.05	0.33
633	Ar	3.02	0.40	0.03	0.11	0.02	0.01	0.08	0.65
653	Ar	3.02	0.41	0.02	0.21	0.06	0.04	0.07	0.81
673[a]	Ar	3.02	1.03	0.02	0.42	0.16	0.16	0.31	2.10
673	Ar	0	0.34	0.09	0.77	0.17	0.18	0.41	1.95
673[a]	Air	3.01	1.29	0.08	0.23	0.16	0.17	0.39	2.32
673	Air	0	4.46	0.31	0.64	0.20	0.22	0.43	6.27

[a] Average values.

conversion of asphalt to gas and the formation of heavier components were enhanced with increasing temperature, but there is no report on the sulfur removal.

We also conducted the partial oxidation experiment at 673 K in SCW. There was no previous report on the partial oxidation of asphalt in SCW. Asphaltene conversion in air was less than that in Ar. However, it is interesting to note the S concentration in the maltene and asphaltene fraction are less than the experiments carried out under argon. Hence partial oxidation apparently enhances the S removal from the asphalt. The amount of H_2S detected is also less and this suggests that the sulfur in the asphalt was concentrated in the toluene insoluble fraction and/or removed into the water phase. Oxygen slightly reduced the yield of maltene but increased the desulfurization from asphalt.

3.2. Effect of water and oxygen on the asphaltene conversion and S removal from asphalt

Since high asphaltene conversion and S removal were obtained at 673 K and a water density of 0.5 g/cm^3 in Ar and air, respectively, we conducted other experiments at 673 K at various water densities to examine the effect of water on this reaction.

Fig. 2 shows the effect of water density on asphaltene conversion at 673 K and 60 min. The conversion of asphaltene increased with the increase of water density although the conversion of asphaltene was quite high without any water indicating that pyrolysis is the dominant pathway for asphaltene conversion. Yasar et al. [20] studied the pyrolysis of asphaltene, and reported that asphaltene was converted selectively to maltene at 673 K. We also found that only a very small amount of toluene insoluble was produced. Asphaltene conversion obtained in Ar was higher than that in air. While the asphaltene conversion increased slightly with increasing water density in both cases, oxygen inhibited the conversion of asphaltene to maltene in SCW while SCW itself enhanced the conversion of asphaltene to maltene. It appears that the water density does not have a significant effect on asphaltene conversion although it was reported that an increase of water density usually promotes the conversion of organics in SCWO [3]. However, our upgrading of asphalt was carried out either under argon or under air with a very small amount of oxygen (i.e. weight of oxygen/weight of asphalt = 0.03) and hence we anticipate that the effect of water density on conversion should be more similar to the trend obtained in partial oxidations in SCW rather than SCWO. It was reported that for the partial oxidation of hydrocarbons in SCW, an increase of water density suppresses the reaction through the direct oxidation pathway and increases the amount of partial oxidation products [12]. Asphalt contains a complex mixture of hydrocarbons, further studies are required to elucidate the effect of water density on upgrading in SCW.

Table 2 shows the composition of the gases produced at different temperatures. The gases detected are CO_2, CO, H_2S, CH_4, C_2H_6 and C_3H_8. Fig. 3 shows the effect of water density on the gas yield in Ar at 673 K. In this Figure, C1–C3 represents the sum of CH_4, C_2H_6 and C_3H_8. It is interesting to note that the yield of CO_2 increased with increasing water density hence resulting in an increased total gas yield. The increase of CO_2 with increasing water density suggests that steam reforming of asphalt occurs during the

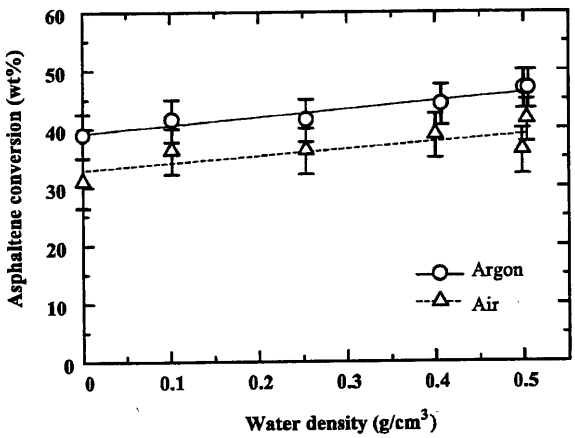

Fig. 2. Effect of water density on asphaltene conversion in Ar at 673 K for 60 min.

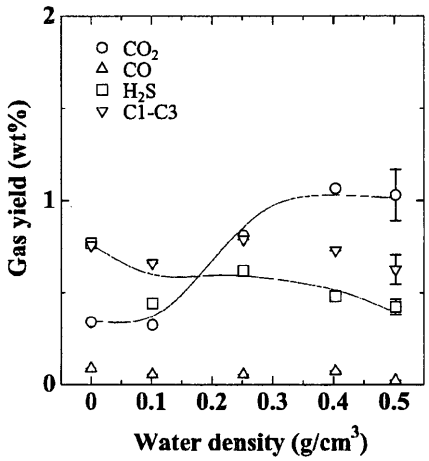

Fig. 3. Effect of water density on gas yield in Ar at 673 K for 60 min.

upgrading. It is reasonable that increased water density could enhance the steam reforming reaction. No further increase in CO_2 was observed when the water density was above 0.4 gm/cm^{3}and this may be due partly to the higher solubility of CO_2 when the water density increased. The yield of H_2S in the gas phase slightly decreased with increasing water density which was probably due to the increased amount of H_2S dissolved in the water. The yield of C1–C3 gases were almost constant over these water densities.

It was reported that SCW supplies hydrogen in the thermal cracking of polyethylene and the yield of oil is higher than the thermal cracking of polyethylene [21]. Our results also suggest that water reacted with asphalt since the yield of maltene was higher in the presence of water. Water probably provided a source of hydrogen atoms which was used to cap the reactive radicals produced during the decomposition of asphalt and hence resulting in a higher conversion to maltene.

Fig. 4 shows the gas yield for upgrading in air as a function of water density at 673 K and 60 min. The produced gases were the same as that obtained in an Ar atmosphere, that is, CO_2, CO, H_2S, CH_4, C_2H_6 and C_3H_8. The yield of CO_2 was significantly larger than the yield of other gases. The yield of CO, H_2S, CH_4, C_2H_6 and C_3H_8 were at the same level as those obtained in an Ar atmosphere. At water densities less than 0.5 g/cm^3 the yield of CO_2 obtained in an air atmosphere was much larger than that obtained in the argon atmosphere and this could be attributed to the oxidation of asphalt in the presence of air. The reason for the large drop off of oxygen conversion and CO_2 yield at 0.5 g/cm^3 is not clear, but it is likely related to the suppression of the direct oxidation pathway of asphalt possibly due to the competition from the steam reforming reaction and/or the dissolution of CO_2 in the water phase. The oxygen conversion decreased with increasing water density and follows the same trend as the formation of CO_2. These results indicate that SCW moderates the direct oxidation of asphalt.

Fig. 5 shows the effect of water density on desulfurization for reactions carried out at 673 K for 60 min. Although there is considerable scatter in the data, it appears that desulfurization slightly increased with increasing water density. It is worth noting that desulfurization in the presence of air was about 10 wt% larger than that obtained in Ar. Oxygen apparently enhanced the desulfurization of asphalt. Fig. 6 shows the variation of the sulfur content in the maltene and asphaltene fraction as a function of water density. Both the H_2S and the sulfur content in the maltene obtained in air and argon were essentially the same. On the other hand, the sulfur content in asphaltene obtained from upgrading in air was generally smaller than that in Ar. The difference in sulfur yield in asphaltene between those obtained in air and that in Ar could be due to the higher sulfur content in the toluene insoluble fraction obtained in air.

The results described above indicate that the properties of asphaltene changed during the reaction. Fig. 7 shows the DRIFT powdered spectra of the raw asphalt and the asphaltenes obtained from upgrading at 673 K and 60 min. There are six spectra in this figure, namely (1) raw asphalt,

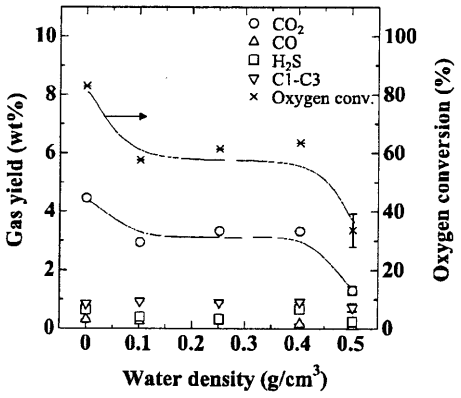

Fig. 4. Effect of water density on gas yield and oxygen conversion in air at 673 K for 60 min.

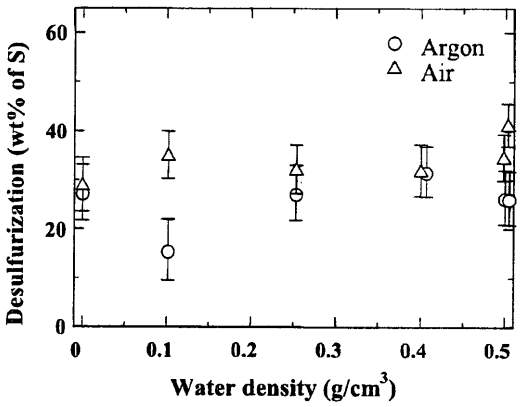

Fig. 5. Effect of water density on desulfurization at 673 K for 60 min.

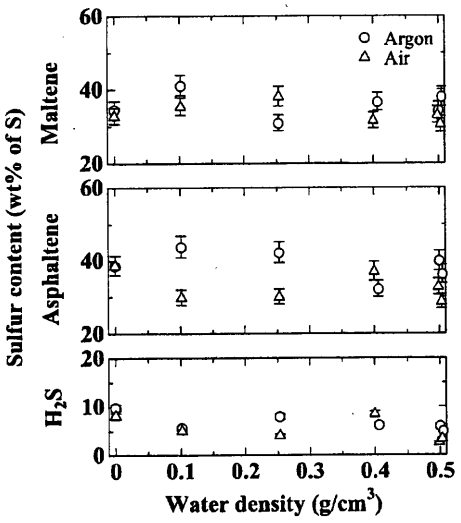

Fig. 6. Effect of water density on sulfur content at 673 K for 60 min.

(2) asphaltene obtained without reaction, (3) asphaltene obtained without water in Ar, (4) asphaltene obtained at 0.5 g/cm^3 water density in Ar, (5) asphaltene obtained without water in air, and (6) asphaltene obtained at 0.5 g/cm^3 water density in air.

A spectrum of raw asphalt shows some characteristic bands [22]. The bands at 2800–2900 and 1450 cm^{-1} were due to the stretching and bending modes of saturated aliphatic hydrocarbons, respectively. The band at around 1600 and 800 cm^{-1} are assigned to the stretching of aromatic C=C bond and the substitution on the aromatic rings. A relatively broad weak band at 3100–3500 cm^{-1} corresponds to the strong OH stretching mode. The absorption around 1050 cm^{-1} is due to the C=S bond [23]. Spectra (1) and (2) are essentially the same, which indicates that the extraction of asphalt with *n*-pentane does not change the distribution of the functional group. The spectra (3)–(6) were also almost the same. The distribution of the functional group was independent of the reaction condition. However, spectrum (2) differs from those of (3)–(6) in the range of 3000–3500 cm^{-1}. Spectrum (2) shows broad peaks from 3100 to 3500 cm^{-1}, however, those of (3)–(6) have almost disappeared. In addition, the peak at 3050 cm^{-1} of (3)–(6) were sharper than that of (2). This peak corresponds to the stretching of aromatic groups. The peak around 1050 cm^{-1} of (3)–(6) were weaker than (1). These findings suggest that the OH functional group in asphaltene reacts and is consumed, however, the aromaticity increased. The C=S bond also decreased after reaction at 673 K which could be related to bond cleavage or the saturation of the C=S which is part of the process for S removal.

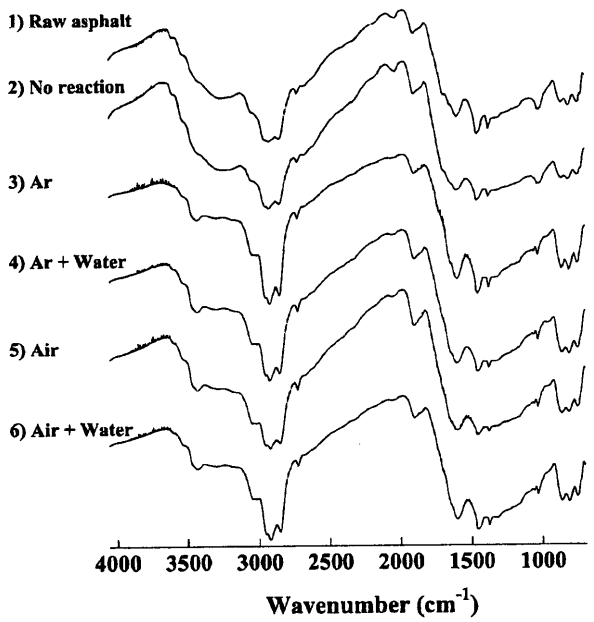

Fig. 7. DRIFT spectra of asphalt and asphaltene.

Fig. 8 shows the TGA results for the asphaltene obtained at 673K and 60 min under various reaction conditions: (1) No reaction, (2) obtained without water in Ar, (3) obtained at 0.5 g/cm^3 water density in Ar, (4) obtained without water in air, and (5) obtained at 0.5 g/cm^3 water density in air. In this figure, the weight change is expressed on the raw asphalt basis. In all curves, the weight change was not significant at temperatures below 650 K. There was a large weight loss between 650 and 800 K. The final weight for (1)–(5) were 15.0, 18.8, 18.2, 21.4 and 21.4 wt%, respectively. The weight was in the order as (4), (5) > (2), (3) > (1). Clearly, asphaltene became heavier after reaction. This result supports that the asphaltene conversion in air was less than that in argon. The effect of water was small but upgrading in air increases the molecular weight of asphaltene. Therefore, it is reasonable to assume that

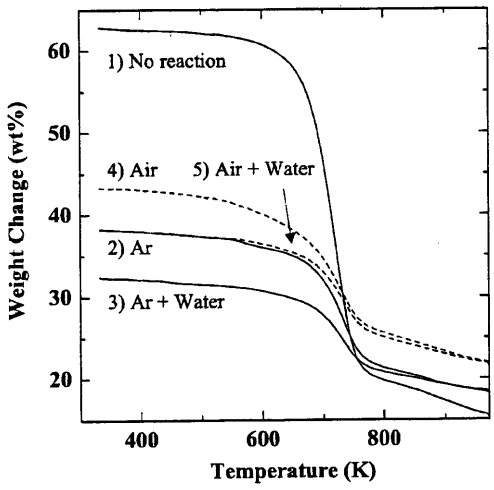

Fig. 8. TGA result of the asphaltenes.

the toluene insoluble produced in air with SCW could be very heavy and contains a high sulfur content.

3.3. Role of water and oxygen on conversion of asphaltene

The structure of asphaltene is very complex and it consists of relatively large polycyclic units, in which the units of 4–5 aromatic fused ring are connected to each other by an alkyl bond or heteroatoms [24]. Sulfur exists as a bridge between core segments as sulfides or disulfides and in heterocycles such as thiophenes [25] and the polycyclic units aggregate by intra- and intermolecular bonds to produce the asphaltene [26].

In general, S–S and C–S bonds are thought to play a key role in asphaltene conversion because S–S and C–S bonds are weaker than C–C bonds. The C–S bonds in thiophenes are quite stable in SCW at 733 K [27] and 673 K [11,28]. On the other hand, the aliphatic C–S bond cleaves easier [4,11, 27]. Therefore, it is expected that over the temperature range of this study (613–673 K), the cleavage of the aliphatic sulfur linkage is the major pathway for S removal.

We will first discuss the role of water in the reactions carried out under Ar. It has been reported that during pyrolysis, sulfur compounds are cleaved to form free radicals and these sulfur-containing radicals abstract hydrogen atoms and form H_2S [29]. Conversion of asphalt probably proceeds through a free radical mechanism. In the absence of water, asphalt itself was decomposed to sulfur-containing free radicals which subsequently formed H_2S through the abstraction of hydrogen from other hydrocarbons. This abstraction of the hydrogen atom will also result in polymerization and eventually will lead to coke formation because of the combination of some of the large radicals unless there is a readily available hydrogen source to cap the radicals.

For the conversion of asphaltenes in various solvents, hydrogen donating ability of solvent is an important factor [30]. The kinetics of the decomposition of sulfur compounds in high temperature water has been explained using a free radical mechanism [4,27]. It is interesting to observe in this study that the CO_2 formation and asphaltene conversion to maltenes both increased with increasing water density. This suggests that hydrogen was supplied by water for upgrading during the aquathermolysis of asphalt. It is possible that water effectively reacted with the free radicals produced during the thermolysis of the asphalt to produce maltene and hence prevented polymerization between the radicals resulting in an increased asphaltene conversion to maltene. The mechanism for the supply of hydrogen from water is not clear. Steam reforming of asphalt by water could also occur under the upgrading conditions to produce CO which then undergoes a water gas shift reaction to produce hydrogen and CO_2. The hydrogen is used in situ to cap the radicals generated in the reaction leading to the formation of maltenes. Since more CO_2 was produced at a higher water density in the absence of O_2, one may speculate that a steam reforming reaction occurred during the upgrading. It is surprising that the amount of H_2S detected did not increase with increasing water density since it is likely that the removal of S as H_2S will also increase with increasing water density due to an increased available hydrogen source. The lower amount of H_2S detected at a higher water density could be due to the fact that a larger amount of H_2S is dissolved when the amount of water is higher. It is also known that hydrodesulfurization of thiophenic compounds requires a catalyst, therefore it is not surprising that S removal was not enhanced when the water density was increased since no catalyst was used.

The thermolysis reaction carried out in the presence of air showed that O_2 plays a role in the upgrading of asphalt. In general, oxygen reacts readily with the radicals (e.g. $R^{\cdot} + O_2 \rightarrow RO_2^{\cdot}$) and increases the reactivity of species [31]. In the absence of water, decarboxylation of this radical could occur to produce CO_2. Alternatively, direct oxidation of the hydrocarbon will also produce CO_2. Oxygen can also produce the sulfones ($R-SO_2-R'$) by the reaction such as $RO_2^{\cdot} + R'O_2^{\cdot} \rightarrow RO_2R' + O_2$ where R' is a radical containing S [31]. However, it is also possible for the S containing radicals to react with O_2 directly to produce RSO_2 radicals which could couple with other radicals resulting in a high molecular weight S containing coke like species.

In SCWO, a number of elementary reactions involving free radicals have been proposed [3,32]. The OH radical is one of the important species in SCWO. The reaction related to OH radicals such as ($R^{\cdot} + OH^{\cdot} \rightarrow$ products) is an important reaction in SCWO [3]. Although the mechanism for upgrading asphalt in SCW in air is not known, water probably affects the oxidation kinetics by inhibiting the pathway for the direct oxidation of asphalt to CO_2. This may be one of the reasons that the yield of CO_2 and oxygen conversion decreased with increasing water density.

Yamaguchi et al. [33] reported that aromatic hydrocarbons polymerized with methylene, biphenyl-type bonds during the oxidation with air at 603 K. Therefore in the presence of oxygen, it is possible that the reactive sulfur containing radicals polymerized and formed toluene insolubles. The sulfur components were apparently concentrated into the heavier components and hence even though the sulfur removal was higher in the presence of oxygen, the amount of H_2S detected was less.

4. Conclusion

Asphalt was upgraded at 613–673 K, 0–0.5 g/cm^3 water density under argon or air atmosphere. Asphaltene conversion, the gas yield and desulfurization increased with increasing temperature in Ar. Higher temperature promoted both the conversion of asphalt to gaseous products and the formation of heavier components. Sulfur was removed either as H_2S and/or transferred to the toluene insoluble

fraction. Asphaltene conversion and the yield of CO_2 increased with increasing water density in Ar. Water apparently provided an additional hydrogen source to cap the radicals generated during the thermolysis of asphalt and increased the maltene yield.

Oxygen affects the conversion of asphalt under conditions of partial oxidation in SCW. The asphaltene conversion was lower but desulfurization was higher than those obtained in an Ar atmosphere. The asphaltene was heavier, however, the sulfur content in asphaltene was lower than that obtained in the absence of oxygen. From the experimental findings, we propose that the reactive sulfur containing radicals polymerized, following which sulfur was removed to the toluene insoluble fraction.

Acknowledgements

The authors acknowledge the financial support of both the Ministry of Education, Culture, Sports, Science and Technology through a Grant-in-Aid for Scientific Research on Priority Areas and the Natural Sciences and Engineering Research Council of Canada, Strategic Research Program. We would also like to thank Esso Imperial Oil for supplying the asphalt.

References

[1] Frank EU. Special aspects of fluid solution at high pressures and sub- and supercritical temperatures. Pure Appl Chem 1981;53: 1401–16.
[2] Schneider GM. Phase behavior and critical phenomena in fluid mixtures under pressure. Ber Bunsenges Phys Chem 1972;76:325–31.
[3] Savage PE. Organic chemical reactions in supercritical water. Chem Rev 1999;99:603–21.
[4] Katritzky AR, Nichols DA, Siskin M, Murugan R, Balasubramanian M. Reactions in high-temperature aqueous media. Chem Rev 2001; 101:837–92.
[5] Lachance R, Paschkewitz J, DiNaro J, Tester JW. Thiodiglycol hydrolysis and oxidation in sub- and supercritical water. J Supercrit Fluids 1999;16:133–47.
[6] Li L, Egbiebor NO. Oxygen removal from coal during supercritical water and toluene extraction. Energy Fuels 1992;6:35–40.
[7] Adschiri T, Sato T, Shibuichi H, Fang Z, Okazaki S, Arai K. Extraction of Taiheiyo coal with supercritical water–HCOOH mixture. Fuel 2000;79:243–8.
[8] Hu H, Zhang J, Guo S, Chen G. Extraction of Huadian oil shale with water in sub- and supercritical states. Fuel 1999;78:645–51.
[9] Funazukuri T, Yokoi S, Wakao N. Supercritical fluid extraction of Chinese Maoming oil shale with water and toluene. Fuel 1988;67(1): 10–14.
[10] Vogelaar BM, Makkee M, Moulijn JA. Applicability of supercritical water as a reaction medium for desulfurisation and demetallisation of gasoil. Fuel Process Technol 1999;61:265–77.
[11] Savage PE, Gopalan S, Mizan TI, Martino CJ, Brock EE. Reactions at supercritical conditions: applications and fundamentals. AIChE J 1995;41:1723–78.
[12] Watanabe M, Mochiduki M, Sawamoto S, Adschiri T, Arai K. Partial oxidation of *n*-hexadecane and polyethylene in supercritical water. J Supercrit Fluids 2001;20:257–66.
[13] Arai K, Adschiri T, Watanabe M. Hydrogenation of hydrocarbons through partial oxidation in supercritical water. Ind Engng Chem Res 2000;39:4697–701.
[14] Ng FTT, Milad IK. Catalytic desulphurization of benzothiophene in an emulsion via in situ generated H_2. Appl Catal, A: Gen 2000;200: 243–54.
[15] Adschiri T, Shibata R, Sato T, Watanabe M, Arai K. Catalytic hydrodesulfurization of dibenzothiophene through partial oxidation and a water-gas shift reaction in supercritical water. Ind Engng Chem Res 1998;37:2634–8.
[16] Ng FTT, Tsakiri SK. US Patent 5055175. Upgrading crude oil emulsions; 1991.
[17] Haar L, Gallagher JS, Kell GS. NBC/NRC steam tables. New York: Hemisphere; 1984.
[18] Belgrave JDM, Moore RG, Ursenbach MG. Gas evolution from the aquathermolysis of heavy oils. Can J Chem Engng 1994;72:511–6.
[19] Schlepp L, Elie M, Landais P, Romero MA. Pyrolysis of asphalt in the presence and absence of water. Fuel Process Technol 2001;74: 107–23.
[20] Yasar M, Trauth DM, Klein MT. Asphaltene and resid pyrolysis. 2. The effect of reaction environment on pathways and selectivities. Energy Fuels 2001;15:504–9.
[21] Moriya T, Enomoto H. Characteristics of polyethylene cracking in supercritical water compared to thermal cracking. Polym Degrad Stab 1999;65:373–86.
[22] Akrami HA, Yardim MF, Akar A, Ekinci E. FT-i.r characterization of pitches derived from Avgamasya asphaltite and Raman–Dincer heavy crude. Fuel 1997;76:1389–94.
[23] Conley RT. Infrared spectroscopy, 2nd ed. Boston: Allyn & Bacon; 1972.
[24] Artok L, Su Y, Hirose Y, Hosokawa M, Murata S, Nomura M. Structure and reactivity of petroleum-derived asphaltene. Energy Fuels 1999;13:287–96.
[25] Strausz OP, Mojelsky TW, Faraji F, Lown EM, Peng P. Additional structural details on athabasca asphaltene and their ramifications. Energy Fuels 1999;13:207–27.
[26] Kowalewski I, Vandenbroucke M, Huc AY. Preliminary results on molecular modeling of asphaltenes using structure elucidation programs in conjunction with molecular simulation programs. Energy Fuels 1996;10:97–107.
[27] Katritzky AR, Barcock RA, Balasubramanian M, Greenhill JV. Aqueous high-temperature chemistry of carbo- and heterocycles. 21. Reations of sulfur-containing compounds in supercritical water at 460 °C. Energy Fuels 1994;8:498–506.
[28] Ogunsola OM, Berkowitz N. Removal of heterocyclic S and N from oil precursors by supercritical water. Fuel 1995;74(10):1485–90.
[29] Attar A. Chemistry, thermodynamics and kinetics of reactions of sulfur in coal-gas reactions: a review. Fuel 1978;57:201–12.
[30] Rahmani S, McCaffrey W, Gray MR. Kinetics of solvent interactions with asphaltenes during coke formation. Energy Fuels 2002;16: 148–154.
[31] Attar A, Corcoran WH. Desulfurization of organic sulfur compounds by selective oxidation. Ind Engng Chem Prod Res Dev 1978;17(2): 102–9.
[32] Brock EE, Savage PE. Detailed chemical kinetics model for supercritical water oxidation of C_1 compounds and H_2. AIChE J 1995;41:1874–88.
[33] Yamaguchi C, Mondori J, Matsumoto A, Honma H, Kumagai H, Sanada Y. Air-blowing reactions of pitch. I. Oxidation of aromatic hydrocarbons. Carbon 1995;33(2):193–201.

ELSEVIER

Bioresource Technology 86 (2003) 301–304

BIORESOURCE TECHNOLOGY

Short communication

Fractionation of sugarcane bagasse by hydrothermal treatment

Mitsuru Sasaki [a,b,*], Tadafumi Adschiri [b], Kunio Arai [b]

[a] *Genesis Research Institute, Inc., 4-1-35 Noritake-shinmachi, Nishi-ku, Nagoya, 451-0051, Japan*
[b] *Department of Chemical Engineering, Faculty of Engineering, Tohoku University, 7 Aza-Aoba, Aramaki, Aoba-ku, Sendai, Miyagi 980-8579, Japan*

Received 8 May 2002; received in revised form 7 July 2002; accepted 27 July 2002

Abstract

Hydrothermal treatment of sugarcane bagasse was conducted using a semi-batch reactor to develop a new biomass fractionation method that has low impact in the environment. A continuously increasing temperature was used in this treatment. It was found that hemicellulose and lignin could be mainly extracted as a water-soluble fraction at 200–230 °C, while the cellulose fraction was hydrolyzed at higher temperatures (230–280 °C) or recovered as solid residue from this treatment. Detailed analyses of the solid residue indicated that the crystal structure and the chemical composition of the residue were in good accordance with those of untreated crystalline cellulose. These experimental and analytical findings show that this method is promising for removal of hemicellulose and lignin from woody biomass without any catalyst and organic solvent.

Keywords: Sugarcane bagasse; Fractionation; Hydrothermal treatment; Semi-batch reactor; Cellulose; Lignin; Hemicellulose

1. Introduction

Chemical composition, structure and water content of biomass differ with species. Also, even in the same kind of woody biomass, chemical structure and water content of the biomass differ with the habitat area and climate. So far, there have been various conventional techniques for biomass fractionation or solubilization with various alcohols (Cemek and Küçük, 2001; Cruz et al., 1999) and alkalies (Sun et al., 1998, 2000) as solvents, which require considerable waste treatment.

Recently, some researchers have studied the development of a new biomass 'clean fractionation' technique with steam (Ibrahim and Glasser, 1999; Avellar and Glasser, 1998; Glasser and Wright, 1998; Rubio et al., 1998) and hot-compressed water (Mok and Antal, 1992; Allen et al., 1996, 2001). Particularly, Allen et al. (1996, 2001) have studied the fractionation of various woody biomass species such as sugarcane bagasse and corn fiber using only hot (190–230 °C), compressed ($P > P_{sat}$), liquid water. They adopted a semi-batch reactor as the experimental apparatus. In this treatment, hot compressed liquid water of constant temperature was loaded into the reactor so that hemicellulose and lignin could be solubilized. From the result, it was found that hemicellulose was completely solubilized and cellulose was almost entirely recovered as a solid fraction: but lignin could not be completely liquefied. This was probably because this extraction was conducted under low and constant temperature.

In the present study, fractionation experiments on sugarcane bagasse using a semi-batch reactor with water at hydrothermal condition were investigated. In this treatment, a continuously increasing program was used to remove hemicellulose and lignin from sugarcane bagasse. From this experiment, the possibility of this technique as a biomass fractionation method was evaluated.

2. Methods

2.1. Material

Sugarcane bagasse which had been ground prior to the semi-batch treatment was used as a starting material, composition: cellulose 35.0%, hemicellulose 35.8%, lignin 16.1%, water content 3.5%.

* Corresponding author. Tel.: +81-22-217-7248; fax: +81-22-217-7246.
E-mail address: sasaki@arai.che.tohoku.ac.jp (M. Sasaki).

0960-8524/03/$ - see front matter
PII: S0960-8524(02)00173-6

2.2. Experimental apparatus and procedure

The apparatus was composed of several units: solvent loading unit, solvent preheating unit, reactor, heat exchanger, bypass line, pressure control unit and solution recovery unit. Maximum working conditions of the apparatus were 450 °C and 45 MPa. Prior to the treatment, 4.0 g of sugarcane bagasse was placed in a reactor tube, and then stainless steel gauze (400 mesh) was placed in both tube ends to keep the bagasse in the reactor. Distilled water was introduced to the by-pass line at a flow rate of 10 ml/min by two high performance liquid chromatography (HPLC) pumps (GL science Co., Ltd., Model PUS-8), pressurized in the system up to 15 MPa by a back-pressure regulator (TESCOM, Model 26-1721-24) and heated by an electric furnace (Seiwa-Rico Co., Ltd., Model FTO-6). As the temperature of the distilled water reached 200 °C at the inlet of the reactor, the reactor was put into a metal-salt bath at 200 °C, and the preheated water was simultaneously loaded to the reactor by switching a three-way valve. Temperatures of both the metal-salt bath and the extraction solvent were then increased at a slow heating rate of 0.51 °C/min up to 330 °C. At the outlet of the reactor, an extract fraction was rapidly quenched by a cooling jacket and subsequently collected continuously into sampling bottles changed every 20 min.

2.3. Analysis

After the extraction, solid residue, which had settled in the reactor, was recovered, dried at 60 °C for 24 h, and then weighed, W (g). Its chemical composition was determined by an elemental analysis. Water-solubilization rate of the sugarcane bagasse, X, was calculated as a ratio of weight of the residue to the initial weight of the untreated bagasse by Eq. (1).

$$X = \frac{W_0 - W}{W_0} \tag{1}$$

In order to examine the macromolecular structure of the residue, X-ray diffraction (XRD) analysis was performed using an XRD analyzer (MAC Science Co. Ltd., Model M18XHF^{22}-SRA).

The carbon concentration in the aqueous extract solution was measured using a total organic carbon (TOC) analyzer (Shimadzu Co., Ltd., Model TOC-5000A). Xylose, galactose and glucose in this aqueous extract solution were identified and quantified by a HPLC system (Thermoquest, Co., Ltd., Model AS3000) with a RI detector and a UV detector. Details of product analyses were described in our previous work (Sasaki et al., 2000). Yield of product i, Y_i, was determined by Eq. (2).

$$Y_i = \frac{W_i}{W_0} \tag{2}$$

In this study, we confirmed that almost all the organic carbons existed in the collected aqueous extract solutions. So, we did not analyze gaseous products.

3. Results and discussion

3.1. Extract

In the hydrothermal semi-batch treatment, the integrated carbon yield of the extract and the yield at each temperature as a function of treatment temperature are displayed in Fig. 1. Organic compounds (about 60% of the initial bagasse) were extracted as a water-soluble fraction at low temperatures (200–230 °C), and about 30% was extracted at higher temperatures (230–280 °C). At 200–230 °C, hydrolysates of hemicellulose (galactose, arabinose and xylose) and aromatic compounds mainly existed in the extract solution. At this stage, hardly any glucose and cellobiose, which are normally formed via hydrolysis of cellulose, was extracted. At 230–280 °C, glucose and cellobiose were yielded and a few aromatic compounds were formed.

3.2. Residue

Chemical composition of the residues was measured. Table 1 shows the result. Chemical compositions of untreated sugarcane bagasse, crystalline cellulose and organosolv lignin are displayed in the same table. In the case that the carbon number is fixed to 6, the ratios of C:H:O in all the untreated materials was as follows: 6:9.44:4.44 in sugarcane bagasse; 6:10.71:5.25 in crys-

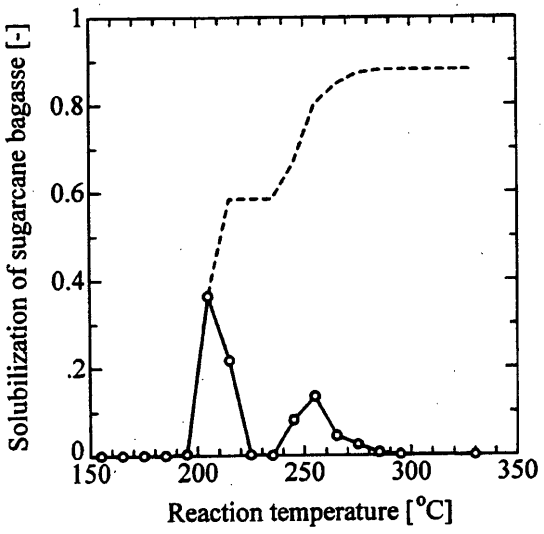

Fig. 1. Relationship between the solubilization of sugarcane bagasse and the reaction temperature in the semi-batch treatment. The broken line shows the integral solubilization and the continuous line represents the solubilization of every 10 °C.

Table 1
Comparison of the chemical compositions of the residues recovered after the semi-batch treatment with those of untreated sugarcane bagasse, crystalline cellulose and organosolv lignin

Material	Chemical composition (C value was fixed 6)			
	C	H	O	N
Untreated sugarcane bagasse	6	9.44	4.44	0.02
Untreated crystalline cellulose	6	10.71	5.25	0.01
Untreated organosolvlignin	6	6.48	1.72	0.03
Residue	6	10.42	5.03	0.02

talline cellulose; 6:6.48:1.72 in organosolv lignin. The chemical composition of the residue recovered after the semi-batch treatment was in good accordance with that of the untreated crystalline cellulose, indicating that removal of hemicellulose and lignin was successfully achieved.

For clarifying the macromolecular structure of the residue, the XRD was measured. Fig. 2 shows the diffraction patterns of untreated sugarcane bagasse, the solid residue recovered after the hydrothermal extraction and untreated crystalline cellulose. Untreated sugarcane bagasse had a broad diffraction pattern because it was a mixture of carbohydrates (cellulose and hemicellulose) and lignin. However, after the hydrothermal extraction of the sugarcane bagasse, the XRD pattern of the solid residue (Fig. 2(b)) had three major peaks at $2\theta = 6.6°$, 6.8° and 9.9° and it became similar to that of untreated crystalline cellulose (Fig. 2(c)). This result

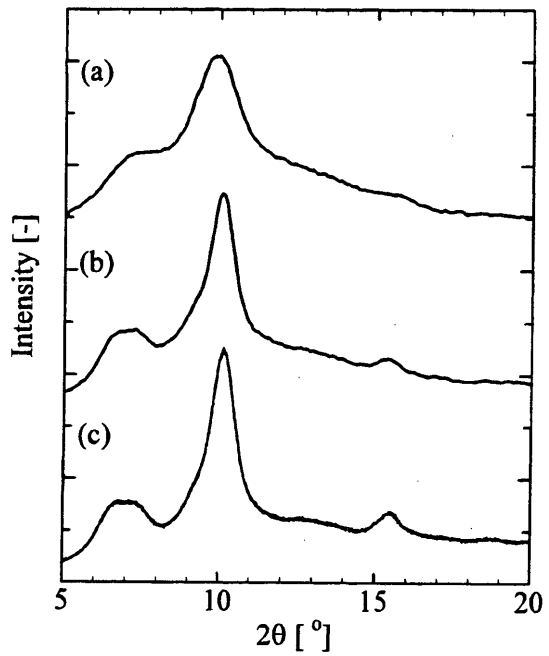

Fig. 2. The XRD patterns: (a) untreated sugarcane bagasse; (b) the residue recovered after the hydrothermal extraction of sugarcane bagasse; (c) untreated crystalline cellulose (cellulose I crystal).

indicates that both hemicellulose and lignin were extracted during the extraction to form water-soluble products, while crystal structure of cellulose I remained as a solid state. With regards to macromolecular structure of cellulose, some workers had already reported that crystalline cellulose, which has crystal modification of cellulose I, is mainly hydrolyzed on its crystal surface under hydrothermal conditions and therefore the internal crystal structure of the cellulose was maintained without any change in crystal modification (Sakaki et al., 1998a,b; Sasaki et al., 1998). From this analytical finding, it can be concluded that crystalline cellulose having cellulose I crystal modification was successfully isolated from sugarcane bagasse with the semi-batch hydrothermal extraction. In future, we will conduct analyses of products formed in this treatment so as to evaluate any possibility for a new biomass fractionation technique without catalyst.

Acknowledgements

The authors gratefully acknowledge support by a Grand-in-Aid for Scientific Research on Priority Area (#11450295) from the Ministry of Education, Culture, Sports, Science and Technology.

References

Allen, S.G., Kam, L.C., Zemann, A.J., Antal Jr., M.J., 1996. Fractionation of sugar cane with hot, compressed, liquid water. Ind. Eng. Chem. Res. 35, 2709–2715.

Allen, S.G., Schulman, D., Lichwa, J., Antal Jr., M.J., 2001. A comparison between hot liquid water and steam fractionation of corn fiber. Ind. Eng. Chem. Res. 40, 2934–2941.

Avellar, B.K., Glasser, W.G., 1998. Steam-assisted biomass fractionation. I. Process consideration and economic evaluation. Biomass Bioenergy 14 (3), 205–218.

Cemek, M., Küçük, M.M., 2001. Liquid products from *Verbascum* stalk by supercritical fluid extraction. Energy Conversion Mange. 42 (2), 125–130.

Cruz, J.M., Dominguez, J.M., Dominguez, H., Parajo, J.C., 1999. Solvent extraction of hemicellulosic wood hydrolysates: a procedure useful for obtaining both detoxified fermentation media and polyphenols with antioxidant activity. Food Chem. 67, 147–153.

Glasser, W.G., Wright, R.S., 1998. Steam-assisted biomass fractionation. II. Fractionation behavior of various biomass resources. Biomass Bioenergy 14 (3), 219–235.

Ibrahim, M., Glasser, W.G., 1999. Steam-assisted biomass fractionation. Part III. A quantitative evaluation of the "clean fractionation" concept. Bioresour. Technol. 70, 181–192.

Mok, W.S.-L., Antal Jr., M.J., 1992. Uncatalyzed solvolysis of whole biomass hemicellulose by hot compressed liquid water. Ind. Eng. Chem. Res. 31, 1157–1161.

Rubio, M., Tortosa, J.F., Quesada, J., Gomez, D., 1998. Fractionation of lignocellulosics: solubilization of corn stalk hemicelluloses by autohydrolysis in aqueous medium. Biomass Bioenergy 15 (6), 483–491.

Sakaki, T., Shibata, M., Miki, T., Yasuda, S., Hirosue, H., Hayashi, N., 1998a. Saccharification of cellulosic biomass with hot

compressed water and alcohol fermentation. Nippon Energy Gakkaishi 77 (3), 241–247.

Sakaki, T., Shibata, M., Miki, T., Hirosue, H., 1998b. Oligosaccharification of cellulose using a hot-compressed-water flow type reactor and enzymatic hydrolysis of formed oligosaccharide. Nippon Energy Gakkaishi 77 (11), 1111–1115.

Sasaki, M., Kabyemela, M.B., Malaluan, R.M., Hirose, S., Takeda, N., Adschiri, T., Arai, K., 1998. Cellulose hydrolysis in subcritical and supercritical water. J. Supercrit. Fluids 13, 261–268.

Sasaki, M., Fang, Z., Fukushima, Y., Adschiri, T., Arai, K., 2000. Dissolution and hydrolysis of cellulose in subcritical and supercritical water. Ind. Eng. Chem. Res. 39 (8), 2883–2890.

Sun, R.C., Fang, J.M., Goodwin, A., Lawther, J.M., Bolton, A.J., 1998. Fractionation and characterization of polysaccharides from abaca fibre. Carbohydr. Polym. 37, 351–359.

Sun, R.C., Tomkinson, J., Ma, P.L., Liang, S.F., 2000. Comparative study of hemicelluloses from rice straw by alkali and hydrogen peroxide treatments. Carbohydr. Polym. 42, 111–122.

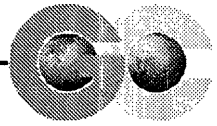

Conversion of the hydroxyl group in 1-hexyl alcohol to an amide group in supercritical water without catalyst

Mitsuru Sasaki,*[a] Junko Nishiyama,[b] Munehiro Uchida,[b] Kohtaro Goto,[c] Kiyohiko Tajima,[c] Tadafumi Adschiri[b] and Kunio Arai*[b]

[a] *Genesis Research Institute, Inc, 4-1-35 Noritake-shinmachi, Nishi-ku, Nagoya 451-0051, Japan. E-mail: sasaki@arai.che.tohoku.ac.jp; Fax: +81 22 217 7246; Tel: +81 22 217 7248*

[b] *Department of Chemical Engineering, Tohoku University, 7 Aza-Aoba, Aramaki, Aoba-ku, Sendai 980-8579, Japan. E-mail: karai@arai.che.tohoku.ac.jp; Fax: +81 22 217 7246; Tel: +81 22 217 7245*

[c] *Noguchi Institute, 1-8-1 Kaga, Itabashi-ku, Tokyo 173-0003, Japan*

Received 22nd November 2002
First published as an Advance Article on the web 27th January 2003

The main reaction pathway in the reaction between 1-hexyl alcohol and acetamide in subcritical and supercritical water without catalyst is proposed and the optimum conditions where amidation of 1-hexyl alcohol can selectively occur are explored.

Water can be considered as a promising solvent that is benign to the environment.[1] If water can be utilized under its supercritical condition (T_c = 374.2 °C, P_c = 22.1 MPa, ρ_c = 0.32 g cm^{-3}), it can act like most organic solvents by manipulating the reaction temperature and pressure. Recently, a large number of researches regarding not only hydrolysis of polymers (*e.g.* polyethylene terephthalate[2] and cellulose[3]) and hazardous organic chemicals,[4] but also synthesis of organic materials[5] in subcritical and supercritical water have been reported. Katritzky *et al.*[6] and Chandler *et al.*[7] found that Friedel–Crafts alkylation of phenol and *p*-cresol occurred at 275 °C under a catalyst free condition by adding *tert*-butyl alcohol and isopropyl alcohol. Sato *et al.*[8] found that reaction of phenol and isopropyl alcohol could successfully form isopropyl phenol under non-catalytic conditions in supercritical water. Akiya *et al.*[9] reported that dehydration of cyclohexanol to cyclohexene took place in near-critical water in a selective manner. Experimental results for Diels–Alder reactions,[10] aldol condensation,[11] Claisen rearrangement,[11] and the Rupe rearrangement[11] in supercritical water have also been reported.

Notably, Ikushima *et al.*[12] reported that ε-caprolactam could be quantitatively synthesized by the Beckmann rearrangement of cyclohexanone oxime in supercritical water in the absence of catalyst. This finding is of great importance to solve the problem of emission of ammonium sulfate, which is a by-product of the conventional synthetic processes, and to develop an efficient method of ε-caprolactam production. Another production method for ε-caprolactam is a UCC (Union Carbide Co.) method,[13] in which cyclohexanone is oxidized by Baeyer–Villiger oxidation to form ε-caprolactone, followed by the formation of ε-caprolactam *via* the reaction between ε-caprolactone and ammonia under hydrothermal conditions. This method seemed to be promising from the viewpoint of green chemistry,[14] but the yield and purity of ε-caprolactam obtained were low. Ito *et al.*[15] carried out this reaction in supercritical water and proposed that in the main reaction pathway ε-caprolactone hydrolyzed to 6-hydroxyhexanoic acid and subsequently reacted with ammonia to form 6-hydroxyhexanamide. They also found that a high yield of ε-caprolactam (87%) could be achieved at temperatures of 400–450 °C, over 10–60 min using water densities of 0.3–0.5 g cm^{-3}.

In the above study, an interesting point is that an amide bond can form by intramolecular dehydration between a hydroxyl group and an amide group in 6-hexylhexanamide. In general, this reaction does not occur in water under catalyst free conditions. This finding suggests that hydroxyl groups in primary alcohols can be converted to amide groups in supercritical water without catalyst. In this communication, we report results of the reactions between 1-hexyl alcohol and acetamide in subcritical and supercritical water without catalyst for determining the optimum conditions where amidation can occur in a selective manner in the absence of catalyst.

Reactions were conducted using a 6.0 cm^3 stainless steel 316 tube bomb reactor. 1-Hexyl alcohol (99.0% purity, Wako Pure Chem. Ind., Ltd.) and acetamide (99.0% purity, Wako Pure Chem. Ind., Ltd.) were loaded into the reactor and a given amount of distilled water, which corresponds to a density of water of 0–0.5 g cm^{-3}, was introduced. The air in the reactor was substituted to argon gas by repeated purging and then the reactor was sealed. The molar ratio of acetamide to 1-hexyl alcohol was 5–50, corresponding to concentrations of 0.33 mol L^{-1} for 1-hexyl alcohol (**1**) and 1.66–16.6 mol L^{-1} for acetamide (**7**). The reactor was submerged into a sand-bath heated to 300–450 °C. After 5–60 min, the reactor was quickly quenched. Products were identified by GC-MS and by comparing their GC and HPLC retention times with those of standards. Quantitative analysis of the products was performed using HPLC. The conversion of **1** (X) and the yield of product ***i*** (Y_i) are defined as $X = ([\mathbf{1}]_0 - [\mathbf{1}])/[\mathbf{1}]_0$ and $Y_i = [i]/[\mathbf{1}]_0$. The selectivity of the product ***i*** was also calculated using $S_i = Y_i/X$.

Fig. 1 shows the yield of the main products derived from **1** at 400 °C, 0.5 g cm^{-3} and $[\mathbf{7}]_0$ = 1.66 mol L^{-1}. Products

Green Context

Supercritical water is a fascinating material, which has been used for several organic transformations recently (see *e.g.* Hamley *et al.*, *Green Chem.*, 2002, 4, 235). Here, it is shown that it is possible to alkylate amides at the N atom using alcohols in supercritical water without catalyst. Selectivity was very good, especially considering the potential number of side-reactions which could occur. ***DJM***

DOI: 10.1039/b211451h

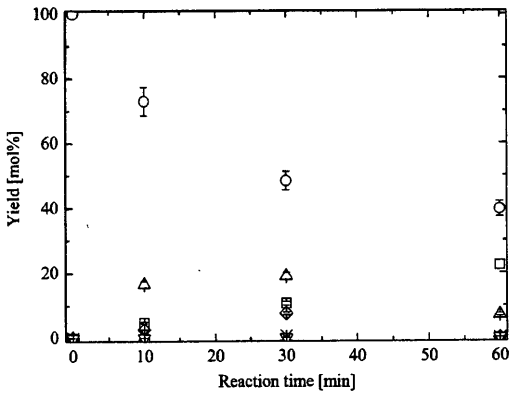

Fig. 1 Yields of the main products at 400 °C, 0.5 g cm^{-3}, 1-hexyl alcohol $[1]_0$ = 0.33 mol L^{-1} and acetamide $[7]_0$ = 1.66 mol L^{-1}: (○) 1-hexyl alcohol (**1**); (□) *N*-hexylacetamide (**2**); (△) hexanal (**3**); (◇) hexene (**4**); (×) hexylamine (**5**); (▽) hexanoic acid (**10**); (+) hexyl acetate (**6**).

identified in this study were *N*-hexylacetamide (**2**), hexanal (**3**), hexene (**4**), hexylamine (**5**), hexylacetate (**6**), acetic acid (**8**) and hexanoic acid (**10**). Conversion X increased with time and reached about 60% at 60 min. The yield Y_2 was 21.9% at 60 min while the yields Y_3 and Y_4 reached about 20% and 8% at 30 min and then decreased with time. Yield Y_6 was 4.4% at 10 min and then decreased to 0.8% at 60 min. The yield of **5**, a hydrolysis product of **2**, was low (1.5%), although it was expected that **2** should easily hydrolyze to **5** in supercritical water. The reason for the low level of **5** may be that **2** is stablized over **5** due to solvation in supercritical water, or that **2** is converted to **1** and **7** by the reverse reaction of amidation. Under the used reaction conditions, about 70% of **7** hydrolyzed to form **8** at 10 min and the yield Y_8 scarcely changed even for extended reaction times. In summary, amidation between **1** and **7** took place in supercritical water. Moreover, we evaluated any possibility of the formation of **2** and/or **5** from the reaction between **4** and **7** in subcritical and supercritical water and found that they did not form.

Based on these results, we propose the main reaction pathway in the 1-hexyl alcohol–acetamide–water system in subcritical and supercritical water as shown in Scheme 1. The main

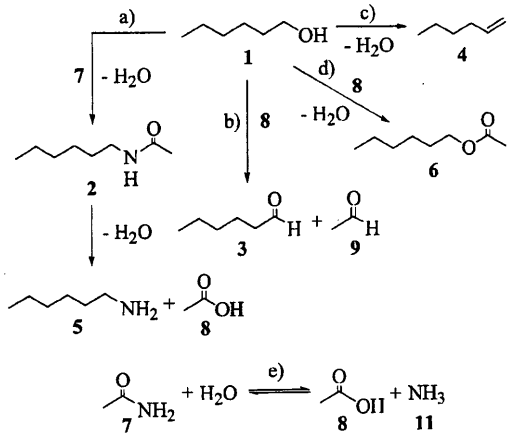

Scheme 1 Main reaction pathway in the 1-hexyl alcohol (**1**)–acetamide (**7**)–water system in subcritical and supercritical water.

reaction paths are (a) intermolecular dehydration between **1** and **7**, (b) a reverse Cannizzaro reaction between **1** and **8** formed by the dissociation of **7**, (c) intramolecular dehydration to **4**, (d) intermolecular dehydration (esterification) between **1** and **8**, and (e) hydrolysis of **7** to **8** and ammonia (**11**). It has already been reported that the Cannizzaro reaction takes place in supercritical water under catalyst free conditions.[16] From a preliminary experiment, we also confirmed that the reverse Cannizzaro reaction can take place in supercritical water.[13]

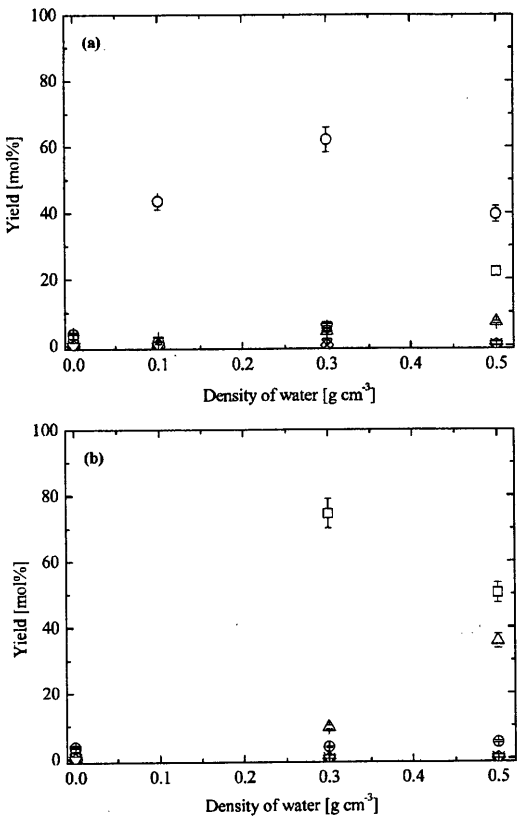

Fig. 2 Water density dependence of the product distributions at 400 °C, 60 min, $[1]_0$ = 0.33 mol L^{-1} and water densities ranging 0 to 0.5 g cm^{-3}: (a) $[7]_0$ = 1.66 mol L^{-1}; (b) $[7]_0$ = 16.6 mol L^{-1}: (○) 1-hexyl alcohol (**1**); (□) *N*-hexylacetamide (**2**); (△) hexanal (**3**); (◇) hexene (**4**); (×) hexylamine (**5**); (▽) hexanoic acid (**10**); (+) hexyl acetate (**6**).

The effect of the density of water on amidation was examined under the conditions: 400 °C, 60 min and $[1]_0$ = 0.33 mol L^{-1}. Fig. 2(a) and (b) shows the results at $[7]_0$ = 1.66 and 16.6 mol L^{-1}, respectively. At low $[7]_0$, as shown in Fig. 2(a), gaseous products were mainly formed by pyrolysis of **1** in argon atmosphere and low water densities of 0.1 and 0.3 g cm^{-3}. By contrast, at a higher water density (0.5 g cm^{-3}), gaseous products were scarcely detected and liquid products, especially **2**, mainly formed. With increasing $[7]_0$ (see Fig. 2(b)), the yield Y_2 became higher at 0.3 and 0.5 g cm^{-3}. This experimental finding demonstrates that amidation of **1** can be promoted at high water densities in supercritical water.

Next, the effect of the reaction temperature on amidation was examined under the condition of $[1]_0$ = 0.33 mol L^{-1}, $[7]_0$ = 1.66 mol L^{-1} and 0.3 g cm^{-3}. Table 1shows the experimental

Table 1 The effect of the reaction temperature on the main products with $[1]_0$ = 0.33 mol L^{-1} and $[7]_0$ = 16.6 mol L^{-1}; at 400 °C; at water density 0.3 g cm^{-3} and 60 min (300 and 400 °C), or at water density 0.35 g cm^{-3} and 10 min (450 °C)

		Y (mol%)				
T/°C	100 − *X* (mol%)	**2**	**3**	**4**	**5**	**6**
300	60.8	11.3	14.2	n.d.	4.0	7.1
400	3.6	74.5	9.6	n.d.	n.d.	2.0
450	3.8	57.2	10.1	n.d.	n.d.	n.d.

results conducted at temperatures of 300, 400 and 450 °C. At 300 °C, X was 31% and S_2 was low (29%). **3** was formed at a similar level to **2** by a reverse Cannizzaro reaction between **1** and **8**. In this case, the yield Y_5 was 4.0%. At 400 °C, X was over 96% and Y_2 reached 74.5% (selectivity: 77%) at 60 min with **5** not forming at all. At 450 °C and 10 min, X became even higher while Y_2 was comparatively high (57.2%). In this case,

however, the carbon recovery of liquid products was low. This is probably because gaseous products form by the thermal degradation of **1** and its primary products. From these experimental results, it was confirmed that the amidation of 1-hexyl alcohol in supercritical water was more suitable than that in subcritical water from the view point of a rapid and selective process. Also, it was suggested that subcritical water might be applicable as a reaction medium for hydrolyzing amides to amines.

Further, reactions of **1** with other amidation reagents (benzamide and hexanamide) were conducted and results are shown in Table 2. With both reagents, the amide compounds (*N*-hexylbenzamide and *N*-hexylhexanamide, respectively) could be synthesized, but the selectivity of these products were low compared with the case of acetamide. This is probably because the thermal stabilities of the amide compounds are not high under the used conditions.

Table 2 Experimental results of reactions of **1** with other amidation agents in supercritical water. *Conditions*: 400 °C, 0.3 g cm^{-3}, initial concentration of each amidation agent $[R]_0$ = 0.33 mol L^{-1} and 60 min

R	$[R]_0/[1]_0$	$100 - X$ (mol%)	Y_{Amide} (mol%)	S_{Amide} (mol%)
Benzamide	10	25.3	18.6	24.9
Hexanamide	20	4.1	16.7	17.4

In summary, we have demonstrated the conversion of the hydroxyl group in 1-hexyl alcohol to an amide group in supercritical water without catalyst. This experimental finding leads to the development of a new method for efficient production of amide compounds from primary alcohols. Future efforts will be directed to elucidate the reaction mechanism further and to explore optimum conditions for rapid and selective amidation in supercritical water.

Acknowledgement

The authors gratefully acknowledge support for a Grand-in-Aid for Scientific Research on Priority Area (Grant 11450295) from the Ministry of Education, Culture, Sports, Science and Technology.

References

1 (*a*) J. M. DeSimone, *Science*, 2002, **297**, 799; (*b*) M. Poliakoff, J. M. Fitzpatrick, T. R. Farren and P. T. Anastas, *Science*, 2002, **297**, 807.

2 (*a*) T. Adschiri, O. Sato, K. Machida, I. Saito and K. Arai, *Kagaku Kogaku Ronbunshu*, 1997, **23**(4), 505; (*b*) Z. Fang, R. L. Smith, H. Inomata and K. Arai, *J. Supercrit. Fluids*, 1999, **15**(3), 229; (*c*) S. G. Kazarian and G. G. Martirosyan, *Phys. Chem. Chem. Phys.*, 2002, **4**(15), 3759; (*d*) A. T. Quitain, M. Faisal, K. Kang, H. Daimon and K. Fujie, *Hazard. Mater.*, 2002, **93**(2), 209.

3 (*a*) T. Adschiri, S. Hirose, R. M. Malaluan and K. Arai, *J. Chem. Eng. Jpn.*, 1993, **26**(6), 676; (*b*) O. Bobleter, *Prog. Polym. Sci.*, 1994, **19**, 797; (*c*) T. Sakaki, M. Shibata, T. Miki, H. Hirosue and N. Hayashi, *Energy Fuels*, 1996, **10**, 684; (*d*) T. Sakaki, M. Shibata, T. Miki, H. Hirosue and N. Hayashi, *Bioresour. Technol.*, 1996, **58**, 197; (*e*) M. Sasaki, B. M. Kabyemela, R. M. Malaluan, S. Hirose, N. Takeda, T. Adschiri and K. Arai, *J. Supercrit. Fluids*, 1998, **13**, 261; (*f*) S. Saka and T. Ueno, *Cellulose*, 1999, **6**(3), 177; (*g*) K. Sakanishi, N. Ikeyama, T. Sakaki, M. Shibata and T. Miki, *Ind. Eng. Chem. Res.*, 1999, **38**(6), 2177; (*h*) M. Sasaki, Z. Fang, Y. Fukushima, T. Adschiri and K. Arai, *Ind. Eng. Chem. Res.*, 2000, **39**(8), 2883; (*i*) X. Y. Lu, A. Sakoda and M. Suzuki, *Chinese J. Chem. Eng.*, 2000, **8**(4), 321; (*j*) M. Sasaki, K. Iwasaki, T. Hamaya, T. Adschiri and K. Arai, *Kobunshi Ronbunshu*, 2001, **58**(10), 527; (*k*) T. Sakaki, M. Shibata, T. Sumi and S. Yasuda, *Ind. Eng. Chem. Res.*, 2002, **41**(4), 661.

4 (*a*) J. C. Meyer, P. A. Marrone and J. W. Tester, *AIChE J.*, 1995, **41**(9), 2108; (*b*) J. D. Taylor, J. I. Steinfeld and J. W. Tester, *Ind. Eng. Chem. Res.*, 2001, **40**(1), 67; (*c*) T. Moriyoshi, K. Sakai and Y. Uosaki, *High Pressure Res.*, 2001, **20**(1–6), 491; (*d*) R. Lachance, J. Paschkewitz, J. DiNaro and J. W. Tester, *J. Supercrit. Fluids*, 1999, **16**(2), 133; (*e*) J. D. Taylor, F. A. Pacheco, J. I. Steinfeld and J. W. Tester, *Ind. Eng. Chem. Res.*, 2002, **41**(1), 1.

5 (*a*) J. B. Dunn and P. E. Savage, *Ind. Eng. Chem. Res.*, 2002, **41**(18), 4460; (*b*) P. A. Hamley, T. Ilkenhans, J. M. Webster, E. Garcia-Verdugo, E. Venardou, M. J. Clarke, R. Auerbach, W. B. Thomas, K. Whiston and M. Poliakoff, *Green Chem.*, 2002, **4**(3), 235; (*c*) M. Sasaki, K. Goto, K. Tajima, T. Adschiri and K. Arai, *Green Chem.*, 2002, **4**(3), 285.

6 A. R. Katritzky, S. M. Allin and M. Siskin, *Acc. Chem. Res.*, 1996, **29**(8), 399.

7 K. Chandler, F. Deng, A. Dillow, C. L. Liotta and C. A. Eckert, *Ind. Eng. Chem. Res.*, 1997, **36**(12), 5175.

8 T. Sato, G. Sekiguchi, T. Adschiri and K. Arai, *Chem. Commun.*, 2001, 1566.

9 N. Akiya and P. E. Savage, *Ind. Eng. Chem. Res.*, 2001, **40**(8), 1822.

10 J. An, L. Bangnell, T. Cablewski, C. R. Strauss and R. W. Trainor, *J. Org. Chem.*, 1997, **62**(8), 2505.

11 M. B. Korzenski and J. W. Kolis, *Tetrahedron Lett.*, 1997, **38**(32), 5611.

12 Y. Ikushima, K. Hatakeda, O. Sato, T. Yokoyama and M. Arai, *J. Am. Chem. Soc.*, 2000, **122**, 1908.

13 J. Nishiyama, M.S. Thesis, Tohoku University, Sendai, Japan, 2002.

14 (*a*) P. T. Anastas and J. C. Warner, *Green Chemistry: Theory and Practice*, Oxford University Press, Oxford, 1998; ch 1 & 2; (*b*) D. T. Allen and D. R. Shonnard, *Green Engineering: Environmentally Conscious Design of Chemical Processes*, Prentice Hall PTR, Upper Saddle River, NJ, 2001.

15 H. Ito, J. Nishiyama, T. Adschiri and K. Arai, *Kobunshi Ronbunshu*, 2001, **58**(12), 679.

16 Y. Tsujino, C. Wakai, N. Matsubayashi and M. Nakahara, *Chem. Lett.*, 1999, 83.

Available online at www.sciencedirect.com
SCIENCE DIRECT®
Fuel 82 (2003) 545–552
FUEL
www.fuelfirst.com

Catalytic effects of NaOH and ZrO_2 for partial oxidative gasification of *n*-hexadecane and lignin in supercritical water☆

Masaru Watanabe[a], Hiroshi Inomata[a,*], Mitsumasa Osada[b], Takafumi Sato[a], Tadafumi Adschiri[c], Kunio Arai[a,b]

[a]*Research Center of Supercritical Fluid Technology, Tohoku University, 07 Aoba Aramaki, Aoba-ku, Sendai 980-8579, Japan*
[b]*Department of Chemical Engineering, Tohoku University, 07 Aoba, Aramaki, Aoba-ku, Sendai 980-8579, Japan*
[c]*Institute of Multidisciplinary Research for Advanced Materials Tohoku University, 2-1-1, Katahira, Aoba-ku, Sendai 980-8577, Japan*

Received 18 April 2002; accepted 29 August 2002; available online 22 October 2002

Abstract

Partial oxidative gasification of *n*-hexadecane (*n*-C_{16}) and organosolv-lignin (lignin) was studied by use of a batch type reactor in supercritical water: 673 K, 0.52 cm^{-3} of water density (40 MPa of water pressure at 673 K), and 0.3 of O/C ratio for the *n*-C_{16} experiments; 673 K, 0.35 cm^{-3} of water density (30 MPa of water pressure at 673 K), and 1.0 of O/C ratio for the lignin experiments. The experiments without O_2 were also conducted for lignin (lignin decomposition). For all the cases (*n*-C_{16} partial oxidation, lignin decomposition, lignin partial oxidation), NaOH or zirconia (ZrO_2) was added in the system as catalysts. Through *n*-C_{16} studies, the catalytic effect of NaOH and ZrO_2 on partial oxidation in supercritical water were examined. In the case of lignin partial oxidation, we studied the possibility of partial oxidation in supercritical water for gasification technique of wastes. The yield of H_2 from *n*-C_{16} and lignin with zirconia was twice as same as that without catalyst at the same condition. The H_2 yield with NaOH was 4 times higher than that without catalyst. Thus, a base catalyst has a positive effect on partial oxidation of *n*-C_{16} and lignin to produce H_2. The catalytic effect of NaOH and ZrO_2 was found to be enhancement of decomposition of intermediate (aldehyde and ketone) into CO, through *n*-C_{16} studies. In the case of lignin studies, the enhancement of decomposition of the carbonyl compounds by catalytic effect of NaOH and ZrO_2 inhibit char formation and promotes CO and thus H_2 formation.

Keywords: Gasification; Partial oxidation; Hydrocarbon; Lignin; Supercritical water; Sodium hydroxide; Zirconia

1. Introduction

In these days, an innovative, effective, and low cost process for organic compound gasification to produce hydrogen (H_2) has been required significantly because fuel cell, that is a new energy supplier, is almost ready to use in near future. So far, an industrial gasification process has been operated at higher than 1073 K. The high temperature process requires a lot of energy and thus a decrease of operating temperature has been desired for developing a low cost process for energy production. Recently, some researchers show that a low temperature gasification process of biomass can be archived by use of supercritical water as a reaction media and a reactant [1–3]. Kruse et al. [1], for instance, show that alkali salt like potassium hydroxide (KOH) and potassium carbonate (K_2CO_3) promote gasification of a biomass model compound (pyrocatechol) in supercritical water even at a low temperature (773 K). We also reported that sodium hydroxide (NaOH) is an effective catalyst for gasification of glucose and cellulose in low temperature (673 K) of supercritical water [3]. In the report [3], we reported that zirconia (ZrO_2) was also effective for H_2 production from these biomass model compounds in supercritical water.

On the other hand, hydrocarbon (a main component of waste plastics) and lignin (a main component of wood biomass consists of phenolic structure) is known to be difficult to gasify even in supercritical water [4–6]. Adschiri et al. [7], Arai et al. [8], and Watanabe et al. [9] reported that partial oxidation of hydrocarbon (both a linear chain

* Corresponding author. Tel.: +81-22-217-7283; fax: +81-22-217-7282.
E-mail address: inomata@scf.che.tohoku.ac.jp (H. Inomata).
☆ Published first on the web via Fuelfirst.com—http://www.FuelFirst.com

0016-2361/03/$ - see front matter © 2002 Elsevier Science Ltd. All rights reserved.
PII: S0016-2361(02)00320-4

hydrocarbon and an aromatic hydrocarbon) in high density (more than 0.25 g/cm^3 of water density) and low temperature (673 K) supercritical water is favored to produce H_2 and CO selectively. However, the H_2 yield from hydrocarbon is still low (less than 2% of the hydrogen atom basis of a raw material) [9]. Watanabe et al. [9] suggested that partial oxidation of hydrocarbon in supercritical water proceeds via formation of aldehyde and ketone (namely carbonyl compounds). Kabyemela et al. [10] showed that key compounds of glucose decomposition are also aldehyde and ketone (such as glyceraldehyde, dihydroxyacetone, and so on). As mentioned above, since NaOH and ZrO_2 are effective for the decomposition of glucose to produce H_2 [3], these catalysts are expected to be also effective catalysts for partial oxidative gasification of hydrocarbons.

In this study, we performed partial oxidative gasification of *n*-hexadecane (*n*-C_{16}) and organosolv-lignin (lignin) in supercritical water (673 K and 40 MPa for *n*-C_{16} or 673 and 30 MPa for lignin) with and without catalyst. The reason why *n*-C_{16} and lignin are selected in this study is as follows: (1) the decomposition *n*-C_{16} in supercritical water has been studied by the authors [8,9] and thus we can consider the catalytic effect of a catalyst in more detail, (2) lignin is a main component wood biomass and well known to be a compound that is difficult to decompose into gaseous products [5,6]. Thus we consider that we can show the possibility of partial oxidation for gasification of waste treatment technique through the lignin studies. We focused on the degree of gasification and H_2 yield, and thus quantitative analyses of liquid product of the reaction had not been performed in the study. Firstly, we conducted *n*-C_{16} experiments and compared with the previous data [9]. From the results of the *n*-C_{16} experiments, we discussed the catalytic effect of NaOH and ZrO_2 on partial oxidation in supercritical water. Next, lignin decomposition in supercritical water was also performed with and without catalyst. Further, partial oxidation of lignin with NaOH and ZrO_2 was also conducted and then the effect of these catalysts on partial oxidation of lignin in supercritical water was examined. The mechanism of partial oxidation of lignin in supercritical water and the effect of catalysts on it was considered based on *n*-C_{16} partial oxidation. Finally, we discussed the possibility of partial oxidation in supercritical water for waste treatment technique.

2. Experimental

n-Hexadecane (*n*-C_{16}: $C_{16}H_{34}$) was obtained from Wako Chemical and organosolv-lignin (lignin) was purchased from Aldrich and these compounds were used as received. The molecular formula of lignin is $C_{3.25}H_{3.54}O$, which was revealed by ultimate analysis. Sodium hydroxide (NaOH, 1 M aqueous solution) and used without further purification. Distilled water was obtained from a water distillation apparatus (Yamato Co., model WG-220). Zirconia (ZrO_2) catalyst was prepared by calcination of zirconium hydroxide (Nakarai Tesque, Inc.) at 673 K for 3 h in air. The mean value of surface area of ZrO_2 catalyst was 110 m^2/g from BET analysis. The structure of zirconia observed by X-ray was monoclinic and tetragonal mixture.

The reaction was carried out in a SUS 316 stainless steel tube bomb reactor with an inner volume of 6 cm^3 [8]. One can see the experimental procedure elsewhere [8]. Briefly, the loaded amounts of samples (*n*-C_{16} and lignin) were all 0.3 g. After loading of liquid and solid samples, O_2 gas was introduced from gas cylinder through 1/16 line and a high-pressure stop valve. The amount of loaded O_2 was calculated by the loaded pressure of O_2 and the vacant volume of the reactor. In the case of *n*-C_{16} experiments, the loaded amount of water was 3.1 g (0.52 g/cm^3) and the ratio of O (oxygen atom of O_2, not including O of H_2O) to C (carbon atom of the loaded organic compound) was 0.3 (O/C = 0.3). From the literature [6], char formation was observed at lignin decomposition in supercritical water, while a little char formation at *n*-C_{16} decomposition [9]. Therefore, required O_2 for the lignin gasification must be higher than that for *n*-C_{16} and O/C was set to be 1.0. Water density was 0.35 g/cm^3 for lignin experiments. For the experiments using alkali, 0.1 mol/l of NaOH aqueous solution was loaded instead of pure water. In the case of the ZrO_2 catalyst experiments, 0.3 g of a catalyst was loaded. The reaction temperature was 673 K. The reaction time of *n*-C_{16} experiments was always 5 min. Since the catalytic effect of the catalysts on partial oxidation was examined through the *n*-C_{16} experiments, the experiments at the same reaction time were needed for comparison [9]. For examining the decomposition mechanism of lignin, the reaction time of lignin experiments without O_2 (lignin decomposition) ranged from 15 to 60 min. The experiments at 15 min with O_2, that was the shortest residence time for lignin decomposition without O_2, was conducted because the possibility of partial oxidation as a low temperature gasification technique was discussed through lignin experiments.

The identification and quantification of produced gas was conducted by GC-TCD (Shimadzu, model GC-7A, and Hitachi, model GC163). For recovering liquid and solid in the reactor, the reactor was washed with THF for both *n*-C_{16} and lignin studies. Before washing of the reactor with THF, an amount of water was added to recover water soluble compound for lignin experiments. THF insoluble (THFI, including char and/or the metal oxide catalyst) was divided by filtration with membrane filter. THF soluble (THFS) and water soluble was roughly analyzed with GC-FID (Hewlett-Packard, model 6890) and GC-MS (JEOL, model Automass 20). The amount of carbon (both inorganic and organic) in the water solution was evaluated using TOC (total organic carbon detector, Shimadzu, model TOC-5000A) for the lignin studies.

For n-C_{16} experiments, the product yield was evaluated from carbon base and the H_2 yield was evaluated from hydrogen base of a loaded amount of n-C_{16} ($C_{16}H_{34}$):

$$\text{yield (mol\%)} = \frac{\text{the recovered amount of carbon (or hydrogen) in a product}}{\text{the loaded amount of carbon (or hydrogen) in } n\text{-}C_{16}H_{34}} \times 100 \quad (1)$$

For lignin experiments, the yield of gas and water-soluble product containing C atom was evaluated from carbon base and the H_2 yield was evaluated from hydrogen base of a loaded amount of lignin ($C_{3.25}H_{3.54}O$):

$$\text{yield (mol\%)} = \frac{\text{the recovered amount of carbon (or hydrogen) in a product}}{\text{the loaded amount of carbon (or hydrogen) in } C_{3.25}H_{3.54}O} \times 100 \quad (2)$$

The yield of THF insoluble was evaluated from weight base:

$$\text{yield (wt\%)} = \frac{\text{the weight of THF insoluble}}{\text{the weight of loaded } C_{3.25}H_{3.54}O} \times 100 \quad (3)$$

3. Results and discussion

3.1. Study of n-C_{16}

3.1.1. Effect of ZrO_2 and NaOH on partial oxidation of n-C_{16} in supercritical water

First of all, we conducted partial oxidation of n-C_{16} with and without NaOH and ZrO_2 catalyst at 673 K, 0.52 g/cm^3, 5 min, and 0.3 of O/C. For all the cases of n-C_{16} experiments, (1) the main products were H_2, CO, CO_2, C_1–C_{15} n-alkanes, C_2–C_{15} 1-alkenes, some oxygenated organic compounds (alcohol, aldehyde, carboxylic acid, and ketone; in particular, aldehyde and ketone were the main oxygenated organic products); (2) conversion of O_2 was always more than 90%; (3) conversion of n-C_{16} was always around 15%, as same as reported previously [9]. Thus, the catalyst addition does not increase the conversion of n-C_{16}. In this work, since we focus on H_2 formation from hydrocarbon, the gas product was firstly discussed.

Figs. 1 and 2 shows carbon compound yield and H_2 yield in the gas products, respectively. As shown in Fig. 1, CO yield with the catalysts was higher than that without catalyst. The order of CO yield is as follows: NaOH > ZrO_2 > without catalyst. This order was the same as the order of H_2 yield, as shown in Fig. 2. This means that H_2 formation was closely related to CO formation. Fig. 3 shows the ratio of H_2 yield to CO_2 yield (H_2/CO_2 ratio). When H_2 is formed only from water gas shift reaction ($CO + H_2O \leftrightarrow CO_2 + H_2$), the H_2/CO_2 ratio must be unity. Although the H_2/CO_2 ratio without catalyst was 0.3, those with ZrO_2 and NaOH were 0.75 and 1.76, respectively. Ross et al. [11] and Elliott et al.

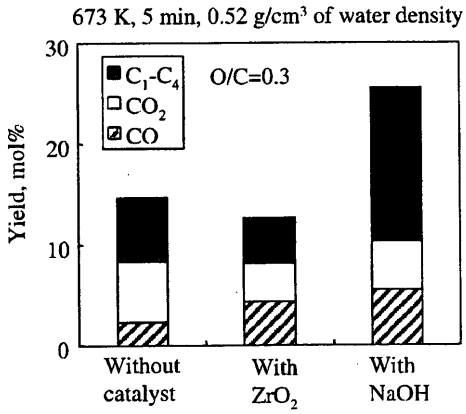

Fig. 1. Gas products (carbon compound) yield of n-C_{16} partial oxidation in supercritical water with and without catalyst.

[12] suggested that the water gas shift reaction must be promoted by alkali (such as NaOH) in sub- and supercritical water. At the short residence time for the n-C_{16} experiments, CO conversion into CO_2 was not so high probably. As suggested before [3,13], ZrO_2 can work as base catalyst even in supercritical water since the H_2/CO_2 ratio was almost unity. Furthermore, the increase of H_2/CO_2 ratio with the catalyst suggests that ZrO_2 and NaOH inhibited the direct oxidation into CO_2 because CO_2 formation was possibly only from water gas shift reaction. One of the reasons why the H_2/CO_2 ratio with NaOH was close to 2 were possibly incompleteness of CO_2 recovery because CO_2 is well known to dissolve into alkaline (such as NaOH) solution. We analyzed the amount of dissolved CO_2 by use of TOC at the lignin studies as described below, but we did not analyze dissolved CO_2 in the n-C_{16} studies. As mentioned below in the lignin studies, there might be a possibility of another pathway of H_2 formation besides water gas shift reaction, for example, the contribution of thermal decomposition of hydrocarbons. At this time, we consider that the above results indicates that these base catalysts (ZrO_2 and NaOH) promote partial oxidation into

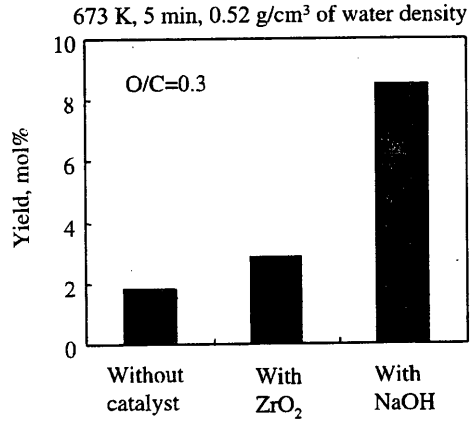

Fig. 2. H_2 yield of n-C_{16} partial oxidation in supercritical water with and without catalyst.

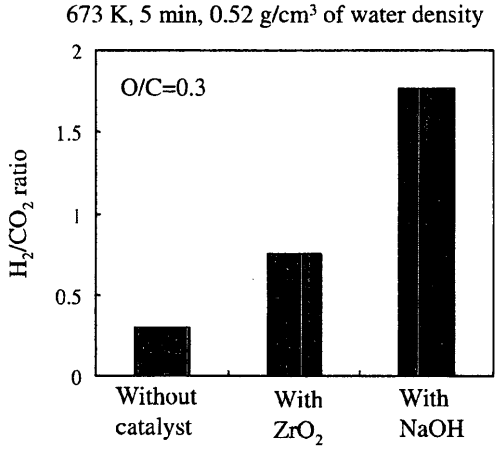

Fig. 3. H_2/CO_2 ratio of n-C_{16} partial oxidation in supercritical water with and without catalyst.

CO, water gas shift reaction, and decompose some organic compounds into CO and H_2.

Fig. 4 shows the ratio of n-alkane to 1-alkene (n-alkane/1-alkene ratio) in the THF soluble. The n-alkane/1-alkene ratio with ZrO_2 was slightly lower than that without catalyst. The n-alkane/1-alkene ratio with NaOH was much lower than that with ZrO_2 and without catalyst. Thus the CO and H_2 formations were considered to relate to the n-alkane/1-alkene ratio. As shown in our previous studies [4,9], the n-alkane/1-alkene ratio implies the ratio of the rate of unimolecular reaction (decomposition) to that of bimolecular reaction (hydrogen abstraction), based on pyrolysis mechanism [14, 15]. According to this idea, the rate of decomposition was enhanced by adding base catalyst (ZrO_2 and NaOH). Buhler et al. [16] suggest that CO was formed via HCHO decomposition with OH radical at glycerol decomposition in supercritical water and that the formation of HCHO from some intermediates (an aldehyde) was enhanced by OH ion in supercritical water. As reported on gas phase pyrolysis [17, 19,20], a ketone was also a precursor of CO. According to these suggestions, decomposition of an aldehyde and a ketone into CO was enhanced by adding OH ion (namely base catalyst such as ZrO_2 and NaOH). Since n-alkane/1-alkene ratio decreased by adding base catalyst as shown in Fig. 4, a by-product of decomposition of an aldehyde and a ketone was assumed to be 1-alkenes.

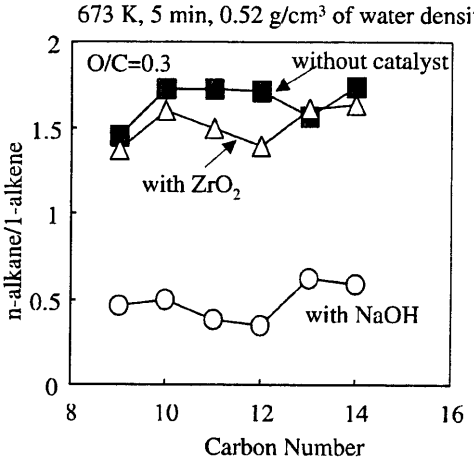

Fig. 4. Ratio of n-alkane/1-alkene of n-C_{16} partial oxidation in supercritical water with and without catalyst.

Thus, though the n-C_{16} studies, we suggest the pathways of partial oxidation and the effects of ZrO_2 and NaOH on n-C_{16} partial oxidation as follows.

Partial oxidation into intermediates:

$$\text{hydrocarbon} \xrightarrow{O_2} \text{aldehyde} + \text{ketone} + \text{others} \quad \text{(R-1)}$$

HCHO formation from intermediate:

$$\text{aldehyde and ketone} \xrightarrow[\text{base}]{} \text{HCHO} + \text{others (probably 1-alkene)} \quad \text{(R-2)}$$

HCHO decomposition into CO:

$$\text{HCHO} \xrightarrow[\text{base}]{\text{OH radical}} \text{CO} \quad \text{(R-3)}$$

Water gas shift reaction:

$$\text{CO} + \text{H}_2\text{O} \xrightarrow[\text{base}]{} \text{CO}_2 + \text{H}_2 \quad \text{(R-4)}$$

3.2. Study of lignin

3.2.1. Effect of ZrO_2 and NaOH on lignin decomposition in supercritical water

The overall reaction of lignin including gas products in supercritical water (at around critical point of water) has not been reported so far. In order to clarify the effect of partial oxidation on lignin reaction and the effect of catalyst on partial oxidation, we first performed the lignin decomposition in supercritical water. The experiments for lignin decomposition were conducted with and without ZrO_2 and NaOH at 673 K, 0.35 g/cm^3 of water density, and 15–60 min. The products were categorized into gas, water soluble, THF soluble, and THF insoluble products. The gas products include H_2, CO, CO_2, and C_1–C_4 alkane and alkene. The water soluble include CO_2 and some phenolic compounds (catechol, guaiacum, and so on). In the THF soluble products, there were some aromatic compounds (toluene, propyl benzene, and so on) in addition of phenolic compounds. All the yields of identified phenolic and aromatic compounds were very low (less than 1 mol%). Figs. 5–7 show the product distribution without catalyst, with ZrO_2, and with NaOH, respectively. Except for THF insoluble, the yield of each compound was evaluated by mole base to a loaded amount of lignin. The yield of THF insoluble was evaluated by weight base. The water soluble was from TOC value. At this moment, we did not evaluate the amount of the yield of THF soluble. As shown in

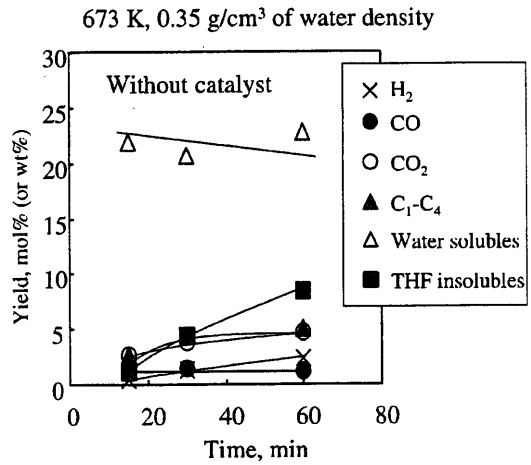

Fig. 5. Product distribution of lignin decomposition in supercritical water without catalyst.

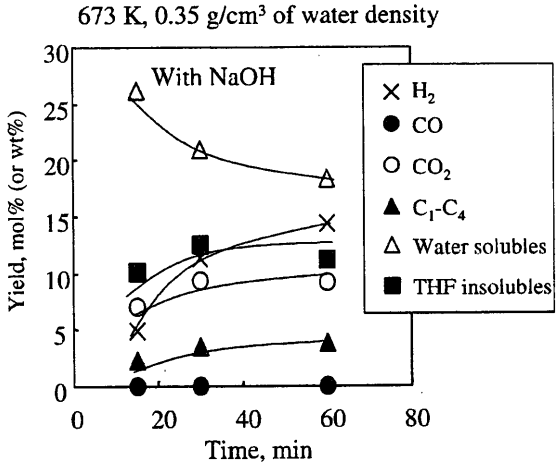

Fig. 7. Product distribution of lignin decomposition in supercritical water with NaOH catalyst.

Figs. 5–7, although the water-soluble yields were almost same 20–25 mol%, the THF insoluble yield with catalyst (4–13 wt%) was higher than that without catalyst (1–8 wt%). Lundquist and Ericsson [18] observed HCHO and phenolic compounds formation at lignin degradation (Eq. (R-5)).

HCHO formation:

$$\text{Lignin} \rightarrow \text{HCHO} + \text{phenolic compounds} + \text{others} \qquad \text{(R-5)}$$

It is well known that phenolic compound can react with HCHO to form phenolic resin (polymerization) [19].

Polymerization:

$$\text{HCHO} + \text{phenolic compound} \rightarrow \text{resins} \qquad \text{(R-6)}$$

Thus we consider that the formation of HCHO Eq. (R-5) was probably enhanced by base catalyst, as a result, the yield of THF insoluble with base catalyst was higher than that without catalyst. Next, H_2 formation from lignin will be discussed.

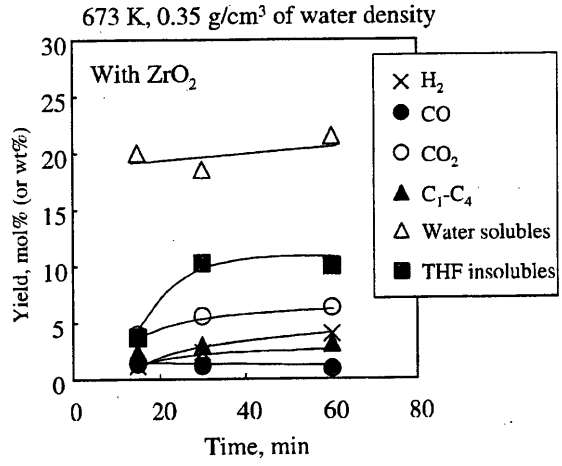

Fig. 6. Product distribution of lignin decomposition in supercritical water with ZrO_2 catalyst.

As shown in Fig. 5, the yield of H_2 and CO_2 slightly increased with increasing reaction time, on the other hand, the yield of CO has a maximum (1.26 mol% at 15 min, 1.41 mol% at 30 min, and 1.14 mol% at 60 min). This indicates that water gas shift reaction proceeds gradually even without catalyst. With ZrO_2 (Fig. 6), the yield of H_2 and CO_2 increased with increasing reaction time as well as without catalyst. The yields of H_2 with ZrO_2 (4.0 mol% at 60 min) were almost twice as much as that without catalyst (2.3 mol% at 60 min). The yield of CO with ZrO_2 linearly decreased with increasing reaction time. Comparing with the time profile of CO and CO_2 yield without catalyst, the rate of water gas shift reaction was enhanced by adding ZrO_2. By adding NaOH (Fig. 7), the formation of H_2 and CO_2 was significantly enhanced. The yield of H_2 and CO_2 (15 and 9.3 mol% at 60 min, respectively) was quite higher than that without catalyst (2.3 and 4.7 mol% at 60 min, respectively). The CO yield with NaOH was remarkably low at all the reaction time. This means that the rate of water gas shift reaction was remarkably promoted by alkali. At 60 min of reaction time, the yield of CO_2 was also enhanced by adding ZrO_2 (6.3 mol%, Fig. 6) and NaOH (9.3 mol%, Fig. 7) compared to without catalyst (4.7 mol%, Fig. 5). This indicates that the yield of CO which is the precursor of CO_2 was also enhanced by base catalyst (ZrO_2 and NaOH). This is possibly due to enhancement of the decomposition rate of aldehyde and ketone, which are assumed to be intermediates of lignin decomposition as well as n-C_{16} partial oxydation, to form HCHO by base catalyst Eq. (R-2). In addition, HCHO thermally decomposes into H_2 and CO at a low HCHO concentration (less than 0.1 mol/L at 673 K) in the absence of O_2 in supercritical water [20]:

HCHO thermal decomposition:

$$\text{HCHO} \rightarrow \text{CO} + \text{H}_2 \qquad \text{(R-7)}$$

Fig. 8 shows the time profile of the H_2/CO_2 ratio with and

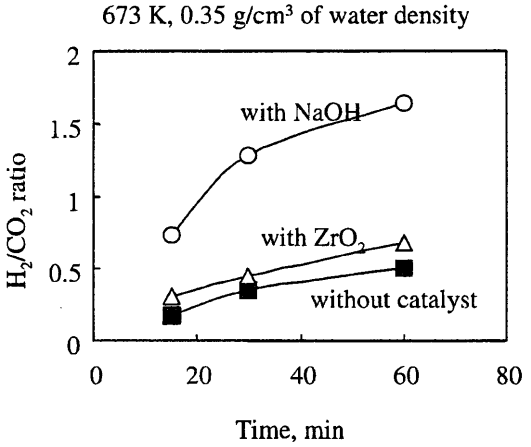

Fig. 8. H_2/CO_2 ratio of lignin decomposition in supercritical water with and without catalyst.

without catalyst. The ratio was enhanced by adding ZrO_2 and NaOH. In the case of NaOH, the H_2/CO_2 ratio was 1.6 at 60 min. This means that there is another pathway of H_2 formation besides water gas shift reaction as mentioned above (at the results of n-C_{16} studies, for example Eq. (R-7)).

3.2.2. *Effect of ZrO_2 and NaOH on lignin partial oxidation in supercritical water*

Through the above lignin decomposition studies without O_2, the formation of HCHO (Eq. (R-5)) must be enhanced by adding base catalyst, as a result, formation of CO (Eq. (R-3) or (R-7)) and THF insoluble (Eq. (R-6)) was also enhanced. For promotion of gasification and H_2 formation, HCHO must be decomposed more effectively before polymerization with phenolic compound to form THF insoluble. Buhler et al. [16] suggested that HCHO decomposition into CO was enhanced by OH radical (Eq. (R-3)). Thus, partial oxidation of lignin with and without catalyst was performed to examine the effect of partial oxidation on promotion of gasification and H_2 formation from lignin at 673 K, 0.35 g/cm^3 of water density, 1.0 of O/C, and 15 min.

The main products were almost the same as without O_2 experiments. In this case, we also categorize the products into gas, water soluble, THF soluble, and THF insoluble products. As same as the case without O_2, the yield of THF soluble was not evaluated at this moment.

Fig. 9 shows the product distribution of carbon compound. The yield of THF insoluble was calculated by weight base and the others were by mole base, as well as Figs. 5–7. For comparison, the results without O_2 were also shown in this figure. Without O_2, the highest gasification yield (CO and CO_2 yield with NaOH) was 7 mol% at 15 min. In the case of partial oxidation, gasification (CO and CO_2 yield) was achieved more than 40 mol% regardless of the presence or absence of catalyst. While the THF insoluble yield without catalyst was enhanced by adding O_2 (1.2 → 6.0 wt%), that with catalyst was inhibited by partial oxidation

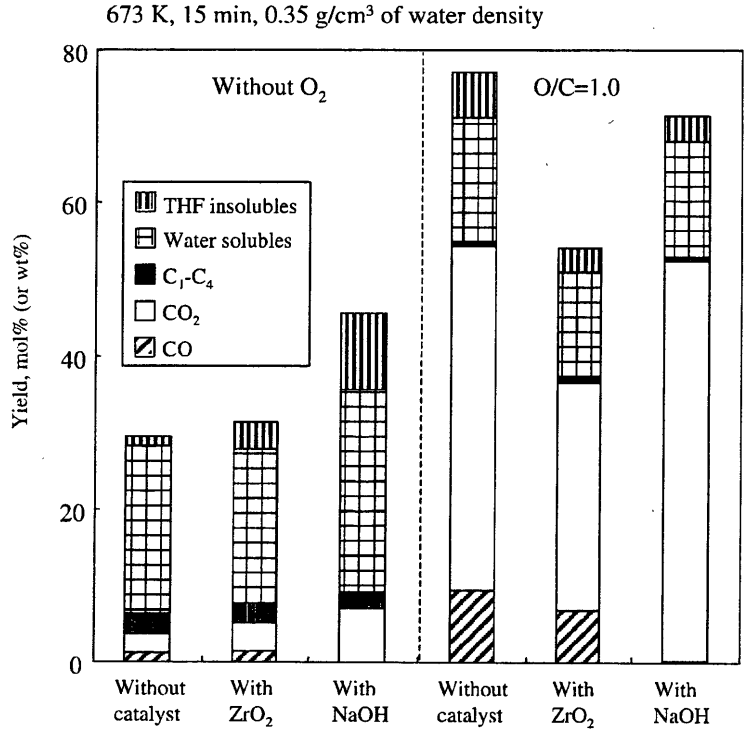

Fig. 9. Product distribution of lignin thermal decomposition and partial oxidation in supercritical water with and without catalyst.

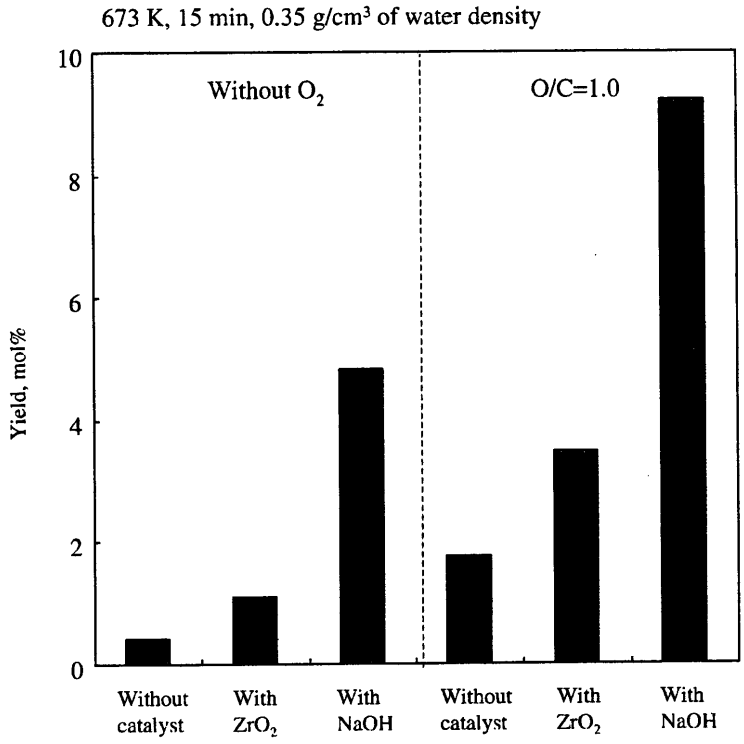

Fig. 10. H_2 yield of lignin thermal decomposition and partial oxidation in supercritical water with and without catalyst.

(3.6 → 3.2 wt% with ZrO_2 and 10 → 3.3 wt% with NaOH). The water soluble decreased by partial oxidation with and without catalyst. These phenomena indicate that HCHO formation from lignin (Eq. (R-8)) proceeds by O_2 as well as n-C_{16} partial oxidation (Eqs. (R-1) and (R-2)) and HCHO decomposition was enhanced by partial oxidation as shown in Eq. (R-3).

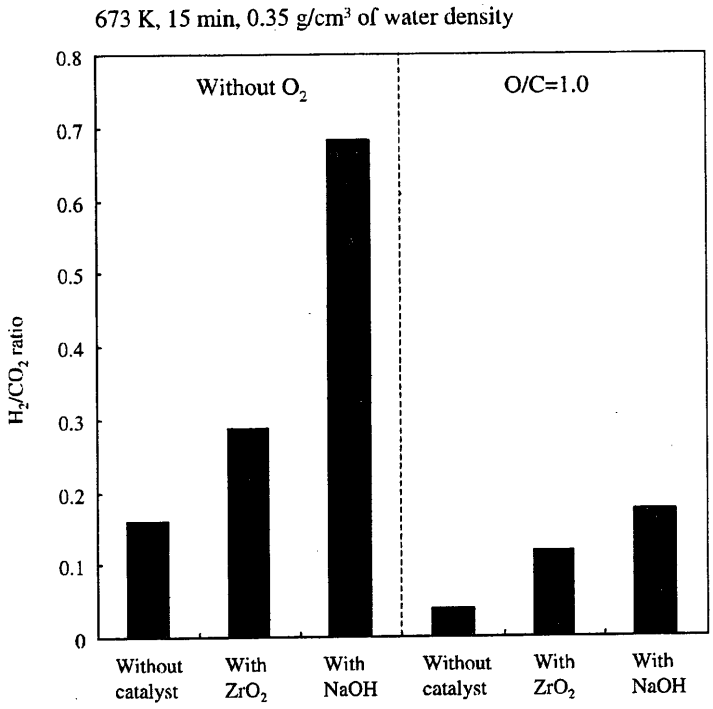

Fig. 11. H_2/CO_2 ratio of lignin thermal decomposition and partial oxidation in supercritical water with and without catalyst.

HCHO formation through partial oxidation:

$$\text{lignin} \xrightarrow{O_2} \text{HCHO} + \text{others} \quad \text{(R-8)}$$

Fig. 10 shows the H_2 yield with and without O_2. By adding O_2, H_2 formation was enhanced at all the cases, as shown in Fig. 10. With ZrO_2, the H_2 yield (3.5 mol%) was twice as much as that without catalyst (1.8 mol%). As well as the case of n-C_{16} partial oxidation and lignin decomposition, the H_2 yield with NaOH (9.2 mol%) was 4 times higher than that without catalyst (1.8 mol%). Fig. 11 shows the H_2/CO_2 ratio. Although H_2 yield was enhanced with O_2 (Fig. 10), the H_2/CO_2 ratio was inhibited at all the cases (Fig. 11). This means that CO_2 formed not only water gas shift reaction but also direct oxidation. The another reason of low H_2/CO_2 ratio was probably due to H_2 combustion with excess O_2 because the partial oxidation was carried out at 1.0 of O/C. In the case of 0.3 of O/C at n-C_{16} partial oxidation, H_2/CO_2 ratio with catalyst was almost or more than unity as described above. Thus, there is possibility that we can get much H_2 yield and H_2/CO_2 ratio by changing O/C value. Through this study, it was found that partial oxidation with base catalyst in supercritical water can be applied for H_2 formation from hydrocarbon (plastics) and lignin (biomass), by due to enhancement of HCHO formation (Eqs. (R-2) and (R-5)), HCHO decomposition (Eqs. (R-3) and (R-7)), and water gas shift reaction Eq. (R-4).

4. Conclusion

Partial oxidation of n-hexadecane and organosolv-lignin was studied by use of a batch type reactor in supercritical water. The n-hexadecane experiments were carried out at 673 K, 0.52 cm^{-3} of water density (40 MPa of water pressure at 673 K), and 0.3 of O/C ratio, to examine the effect of base catalyst (ZrO_2 and NaOH). As the result, the addition of catalyst did not increase the conversion of n-C_{16} and promoted the formation of 1-alkenes and H_2. Since the H_2/CO_2 ratio was almost or more than unity, partial oxidation into CO and water gas shift reaction was possibly enhanced by base catalyst.

The lignin experiments were performed at 673 K, 0.35 cm^{-3} of water density (30 MPa of water pressure at 673 K), 1.0 of O/C. The experiments without O_2 were also conducted for lignin. The yield of H_2 from lignin with zirconia was twice as same as that without catalyst at the same condition for both with and without O_2. The H_2 yield with sodium hydroxide (NaOH) was almost 4 times higher than that without catalyst (with and without O_2). Thus, a base catalyst has a positive effect on decomposition and partial oxidation of lignin to gaseous product such as H_2.

Acknowledgements

The authors thank for the Grant-in-Aid for Scientific Research (13750707) of the Ministry of Education and Culture of Japan.

References

[1] Kruse A, Meier D, Rimbrecht P, Schacht M. Ind Engng Chem Res 2000;39:4842.
[2] Minowa T, Ogi T. Catal Today 1998;45:411.
[3] Watanabe M, Inomata H, Arai K. Biomass Bioenergy 2002;22:405.
[4] Watanabe M, Hirakoso H, Sawamoto S, Adschiri T, Arai K. J Supercrit Fluids 1998;13:247.
[5] Funazukuri T, Wakao N, Smith JM. Fuel 1990;69:349.
[6] Yokoyama C, Nishi N, Nakajima A, Seino K. Sekiyu Gakkaishi 1998; 41:243.
[7] Adschiri T, Shibata R, Sato T, Watanabe M, Arai K. Ind Engng Chem Res 1998;37:2634.
[8] Arai K, Adschiri T, Watanabe M. Ind Engng Chem Res 2000;39:4697.
[9] Watanabe M, Mochiduki M, Sawamoto S, Adschiri T, Arai K. J Supercrit Fluids 2001;20:257.
[10] Kabyemela BM, Adschiri T, Malaluan RM, Arai K. Ind Engng Chem Res 1999;38:2888.
[11] Ross DS, Blessing JE, Nguyen QC, Hum GP. Fuel 1984;63:1206.
[12] Elliott DC, Hallen RT, Sealock Jr. JL. Ind Engng Chem Prod Res Dev 1983;22:431.
[13] Watanabe M, Inomata H, Smith Jr. RL, Arai K. Appl Catal A Gen 2001;219:149.
[14] Watanabe M, Tsukagoshi M, Hirakoso H, Adschiri T, Arai K. AIChE J 2000;46:843.
[15] Watanabe M, Adschiri T, Arai K. Ind Engng Chem Res 2001;40:2027.
[16] Buhler W, Dinjus E, Ederer HJ, Kruse A, Mas C. J Supercrit Fluids 2002;22:37.
[17] Berces T. The decomposition of aldehydes and ketones. In: Bamford CH, Tipper CF, editors. Comprehensive chemical kinetics, vol. 5. Amsterdam: Elsevier; 1972.
[18] Lundquist K, Ericsson L. Acta Chem Scand 1970;24:3681.
[19] Billmeyer Jr.FW. Textbook of polymer science, 3rd ed. New York: Wiley; 1984.
[20] Watanabe M, Osada M, Inomata H, Arai K, Kruse A. Submitted to Appl Catal A Gen..

Estimation of the degree of hydrogen bonding between quinoline and water by ultraviolet–visible absorbance spectroscopy in sub- and supercritical water

Mitsumasa Osada, Katsunori Toyoshima, Takakazu Mizutani, Kimitaka Minami, Masaru Watanabe, Tadafumi Adschiri, and Kunio Arai[a)]
Department of Chemical Engineering, Tohoku University, 07 Aza-Aoba, Aramaki, Aoba-ku, Sendai, 980-8579, Japan

(Received 16 October 2002; accepted 18 December 2002)

UV–visible spectra of quinoline was measured in sub- and supercritical water (25 °C$<T<$430 °C and 0.1 MPa$<P<$40 MPa), and the degree of hydrogen bonding between quinoline and water was estimated from solvatochromic shifts in the $\pi-\pi^*$ absorbance band. Hydrogen bonding decreased with increasing temperature from 25 to 360 °C. At supercritical conditions (380 °C$<T<$400 °C), hydrogen bonding abruptly decreased where the isothermal compressibility of water was large ($0.5<\rho_r<1.5$). In this condition, local density around quinoline was lower than bulk density, namely negative solvation, and it led to the cleavage of hydrogen bonding between quinoline and water. © *2003 American Institute of Physics.* [DOI: 10.1063/1.1545099]

I. INTRODUCTION

The local solvation structure around solutes in supercritical fluids can be attributed to the balance between kinetic energy of molecules and solute–solvent interactions (dispersion, induction, and dipole–dipole).[1,2] For the case of supercritical water, hydrogen bonding adds to the above-described solute–solvent interactions and is an important factor to control the solvation structure. Further, the solvent properties of water such as dielectric constant change greatly with temperature and density, which probably leads to the great change of hydrogen bonding between solute and water. Hence, the estimation of the dependence of solute–solvent hydrogen bonding and other interactions (dispersion, induction, and dipole–dipole) on temperature and water density is essential for evaluating the solvation structure in supercritical water.

UV–visible spectroscopy has been employed for the estimation of solute–solvent interactions with their solvatochromic shifts and the shifts can be represented by the physical properties of the solvent. In general, the frequency of maximum absorbance, ν(max), can be expressed by the McRae–Bayliss expression[3] as follows:

$$\nu(\max)=A+B\frac{n^2-1}{2n^2+1}+C\left(\frac{\epsilon-1}{\epsilon+2}-\frac{n^2-1}{n^2+2}\right), \tag{1}$$

where n is the refractive index and ϵ is the dielectric constant of the solvent. The first term (A term) is ν(max) in the condition where no solute–solvent interaction exists, such as in a vacuum. The second term (B term) is for the interaction between the solute dipole and induced dipole of the solvent, and the third term (C term) expresses the dipole–dipole interactions. These constants (A, B, and C) are correlated from spectral shift data in ordinary liquids that do not form hydrogen bonding to the probe. For the case where solvent forms hydrogen bonding, ν(max) can be expressed by the Kamlet–Taft π^*, α, β scale[4] as follows:

$$\nu(\max)=A+S\pi^*+D\alpha+E\beta, \tag{2}$$

where the second term (π^* scale) is for the interactions that combine the solvent dipolarity and polarizability. The α and β scale describes the solvent hydrogen bond donor acidities, and the solvent hydrogen bond acceptor basicities, respectively. There are dual contributions of hydrogen bonding to solvatochromic shifts. The first contribution comes via the macroscopic n and ϵ, and the second contribution originates from the specific interactions between the solute and water. Because of hydrogen bonding, the dielectric constant of water is quite large as compared with other molecules with same size of dipole moment. However, this contribution works as a whole on solvatochromic shift and is therefore included in Eq. (1). On the other hand, specific hydrogen bonding interactions between the solute and water should be extracted as the difference between the experimentally obtained shifts and that can be estimated by Eq. (1). In this work, we attempted to extract the latter contribution, namely hydrogen bonding between solute and water.

In supercritical fluids, the difference between the estimated ν(max) from Eq. (1) and the experimental ν(max) is often observed even for solvents that do not form hydrogen bonding. Some researchers attribute this difference to the specific solvation around the solute and estimated local density around the solute.[1,2,5–35] Kajimoto[1] studied the charge transfer state formation for (*N*,*N*-dimethylamino)-benzonitrile in CF_3H and attributed the larger spectral shift to the occurrence of aggregation of solvent molecules around the solute. As the bulk density increased, the bathochromic shift asymptotically converged to that observed in the liquid phase. Kim and Johnston[5] also found local density enhancement, namely positive solvation, through UV–visible spectra of phenol blue in supercritical ethylene, chlorotrifluo-

a)Electronic mail: karai@arai.che.tohoku.ac.jp

romethane, and fluoroform. They reported that the local density to the bulk density is related linearly to the isothermal compressibility. In supercritical water, the difference probably includes the effect of hydrogen bonding between solute and solvent as well as solvation. Bennett and Johnston[6] observed UV–visible spectra of acetone in supercritical water and reported the importance of estimating the dependence of solute–solvent hydrogen bonding on temperature and water density. Lu *et al.* determined the Kamlet–Taft π^*, α, β scale of near critical water based on solvatochromic measurements and reported that the polarity and hydrogen bonding of water are highly tunable properties with temperature.[7,8] To evaluate the solvation around the solute in supercritical water, a separation of the contributions of solute–solvent hydrogen bonding and solvation is required.

The first objective of this work is to estimate the solvatochromic shifts over a wide range of temperatures (25 °C $< T <$ 430 °C) and pressures (0.1 MPa $< P <$ 40 MPa). The second objective is to evaluate the difference of the spectrum for the estimation and discuss the effect of hydrogen bonding between quinoline and water and the solvation structure around the quinoline. In this work, quinoline was chosen as a probe to quantify these interactions. Quinoline is the spectral probe that is stable in supercritical water (460 °C) for about 1 h,[36] and the $\pi-\pi^*$ absorbance bands are known to be sensitive to hydrogen bond interactions.[37–39]

II. EXPERIMENT

A. Materials

Distilled and de-ionized water was used with resistivity of 18.2 MΩ cm. Deoxygenation was conducted with LABOC GASTORR GT-102. Quinoline used was of 95.0% of purity from Wako Pure Chemical Industries, Ltd. Solvents used were with the highest purity available (hexane: 99.0%, heptane: 99.0%, cyclohexane: 99.5%, diethyl ether: 99.5%, isobutyl nitrile: 97.0%, DMF: 99.5%, acetonitrile: 99.0%, DMSO: 99.0%, methanol: 99.8%, and ethanol: 99.5 mol %). Carbon dioxide of 99.99 mol % was purchased from Nihon Sanso.

B. Apparatus

A flow-type apparatus was used to allow *in situ* UV–visible absorbance spectroscopic measurement in supercritical water as shown in Fig. 1. UV–visible spectra were obtained with a polychromator/spectrograph (JASCO, CT-25TP) with a 0.12 nm resolution. The spectroscopic cell was fabricated from hastelloy C-276 and contained two 8-mm diam, 5.0-mm-thick sapphire windows sealed with gold foil. The path length of the cell was 7.6 mm. The temperature of the cell was maintained at measurement temperature to an accuracy of ±1.0 °C by a temperature controller (RKC, REX-F900) and *K*-type thermocouples (Sukegawa Denki, 1.6 mm o.d.) inserted directly into the cell body. The cell was heated with a thermostatic unit (JASCO, 6762-1001-KIYO). The pressure was controlled electronically with a HPLC pump (JASCO, PU-987) combined with a backpressure regulator (TESCOM, model 26) and was measured by an analog pressure gauge (NAGANO KEIKI Co.) with an accuracy of ±0.15% F.S.

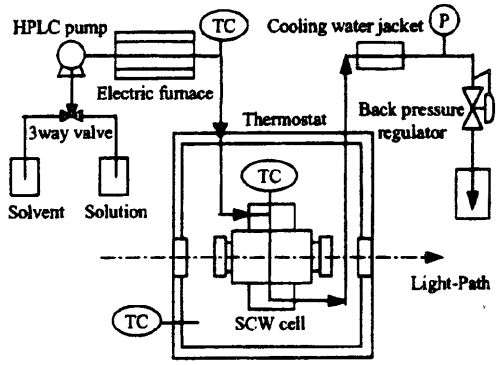

FIG. 1. Flow apparatus for transmission spectroscopy.

III. METHOD FOR UV–VISIBLE MEASUREMENTS

Measurements were performed according to the following procedure. The solvent without solute was fed at 5 mL/min into the system. After the temperature and pressure fluctuations became smaller than 1 °C and 0.1 MPa, respectively, a reference spectrum of solvent was measured. Next, the quinoline solution was fed at 5 mL/min into the system, and a sample spectrum of solution was measured. An absorbance spectrum was obtained by subtracting the reference spectrum from the sample spectrum at the same temperature and pressure. The reference and sample spectrum were recorded only when baseline fluctuations were less than 0.1% in the wave number range from 30 000 to 40 000 cm^{-1}, since quantitative discussion required high reproducibility in the absorbance spectra. The concentrations (2.63, 4.18, 7.59×10^{-4} or 1.93×10^{-3} mol/L) used were well below the saturated solubility limits of quinoline in each solvent. The spectral shift also occurs by the solute–solute interaction (multimerization). It is reported that the quinoline follows Beer's law without the spectral shift in the cyclohexane solvent at the concentration from 1.00×10^{-4} to 4.32×10^{-2} mol/L at 25 °C and 0.1 MPa.[40] We observed ν(max) in aqueous solution at different concentrations (2.63 and 7.59×10^{-4} mol/L) from 25 to 400 °C and obtained the same ν(max) which absorbance could be expressed by Beer's law. Spectroscopic research in the past using quinoline was carried out at the equivalent concentration to our experiment.[37–39] In this work, we assumed that the solute–solute interactions could be neglected at our experimental concentrations.

IV. RESULTS

Figure 2 shows the $\pi-\pi^*$ absorption spectra of quinoline in water at various temperatures and 25 MPa. The signal/noise ratios of the spectrum were from 150 (360 °C) to 350 (25 °C). With an increase in temperature, the $\pi-\pi^*$ absorption band shifted to higher energies (blueshift). Figure 3 shows experimentally obtained ν(max) in water over a wide range of temperature versus pressure. In the liquid phase (25 °C $< T <$ 360 °C), the variation of ν(max) with pressure was negligible, while at supercritical conditions

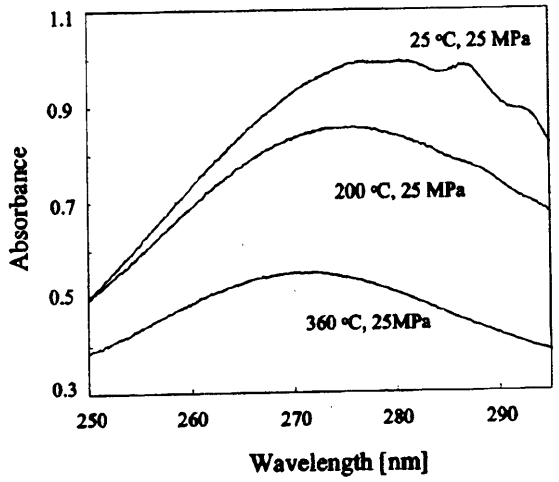

FIG. 2. The $\pi-\pi^*$ absorption spectra of quinoline in water (solute concentration 4.18×10^{-4} mol/L).

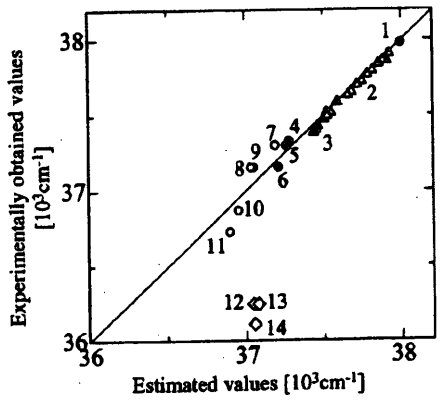

FIG. 4. Experimentally obtained values vs estimated values by A, B, C terms at 25 °C. (1) Argon, (2) CO_2 (63 °C, 8–30 MPa), (3) CO_2 (25 °C, 6–30 MPa), (4) hexane, (5) heptane, (6) cyclohexane, (7) diethyl ether, (8) isobutyl nitrile, (9) acetonitrile, (10) DMF, (11) DMSO, (12) ethanol, (13) methanol, (14) water.

(380 °C$<T<$400 °C) a significant decrease of ν(max) with increasing pressure was observed. In particular, near the critical point (380 °C$<T<$400 °C, 20 MPa$<P<$30 MPa), the decrease of ν(max) with pressure was drastic, but at high pressures, namely in the high density region, the pressure dependence became smaller. At 430 °C, namely in the low density region, the change of ν(max) with increasing pressure was smaller.

First, solute–solvent interactions (dispersion, induction, and dipole–dipole) except hydrogen bonding between quinoline and water were estimated from the spectrum shift in nonhydrogen bonding solvents or in gaseous phase (Ar, CO_2) from Eq. (1). The value of ν(max) in argon was employed as the constant A (38.0×10^3 cm^{-1}), although the accuracy of ν(max) might not be so high due to the weak spectrum in the dilute gas phase measurement. The constant B (-3.85×10^3 cm^{-1}) of the equation was correlated with the experimentally obtained ν(max) in nonpolar solvents (hexane, heptane, cyclohexane) by using refractive index (n) and dielectric constant (ϵ) of the solvent and the value of A

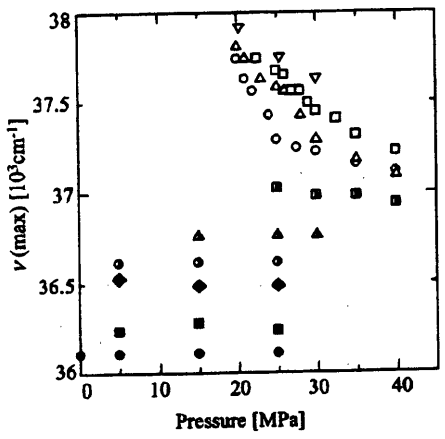

FIG. 3. The ν (max) of quinoline in water vs pressure. (●) 25 °C, (■) 100 °C, (◆) 200 °C, (◑) 250 °C, (▲) 300 °C, (◨) 360 °C, (○) 380 °C, (△) 390 °C, (□) 400 °C, (▽) 430 °C.

evaluated earlier. The constant C (-0.383×10^3 cm^{-1}) was correlated with experimentally obtained ν(max) in polar solvents that do not form hydrogen bonds (diethyl ether, isobutyl nitrile, acetonitrile, DMF, DMSO). In Fig. 4, the experimentally obtained values of nonhydrogen bonding solvents and argon gas were fitted to Eq. (1), with a root-mean-square deviation of about 100 cm^{-1}, which was the same order of magnitude as the experimental error in the determination of band frequencies of the solution spectra (~50 cm^{-1}).

The temperature and pressure dependence of solute–solvent interactions, except hydrogen bonding between quinoline and water, were evaluated. We measured ν(max) in gaseous argon at temperatures ranging from 25 to 300 °C at 0.1 MPa, where no change of ν(max) was observed over this temperature range. The pressure dependence was evaluated by employing CO_2 ($n^2=\epsilon$) as a solvent in a range of pressure from 8 to 30 MPa at constant temperatures of 25 and 63 °C and the correlation of Moriyoshi *et al.*[41] (Fig. 4). Good correlation ($R^2=0.99$) of the experimental results with the estimated values by Eq. (1) with the parameters A, B, and C evaluated earlier could be obtained. These results indicated that the effect of pressure on the A and B values was negligible at pressures up to 30 MPa. Thus, in this analysis we assumed that A, B, and C were constants irrespective of temperature and pressure.

Next, ν(max) values in hydrogen bonding solvents (methanol, ethanol, and water) were compared with the estimated values from Eq. (1) (Fig. 4). The experimental ν(max) had smaller wave numbers than the estimated ν(max). These differences, $\Delta\nu_{\text{difference}}$, for the hydrogen bonding solvents are probably due to hydrogen bonding between quinoline and solvent and may be attributed to the Kamlet–Taft α, β scale.[4]

Figure 5 shows the relation between $\Delta\nu_{\text{difference}}$ and the reduced density, ρ/ρ_c, in water over a wide range of temperatures. The bulk refractive index (n) and the bulk dielectric constant (ϵ) from the literature[42,43] were used for the estimation of ν(max) with Eq. (1). The error bars were obtained from the recalculated ν(max) values by Eq. (1) using ϵ

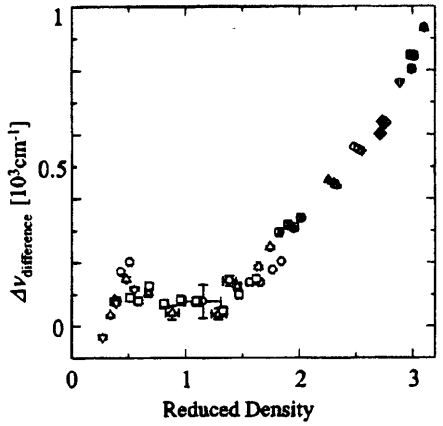

FIG. 5. The $\Delta\nu_{difference}$ in water vs reduced density. (●) 25 °C, (▲) 50 °C, (■) 100 °C, (▼) 150 °C, (♦) 200 °C, (◑) 250 °C, (Δ) 300 °C, (◧) 360 °C, (○) 380 °C, (△) 390 °C, (□) 400 °C, (▽) 430 °C.

and n considering both ±1 °C temperature errors and ±0.1 MPa pressure errors. There was a general trend of decreasing $\Delta\nu_{difference}$ with decreasing water densities.

V. DISCUSSION

Figure 6 shows $\Delta\nu_{difference}$ in supercritical CO_2 (T_c =31.1 °C) in a range of pressure from 8 to 30 MPa at constant temperature of 38 °C. Error bars were given to all experimental results at ±1 °C temperature errors and ±0.1 MPa pressure errors. The $\Delta\nu_{difference}$ observed in supercritical CO_2 was smaller than that for supercritical water. Supercritical CO_2 is a nonhydrogen bonding solvent and thus the difference between the estimated ν(max) by Eq. (1) and experimentally obtained ν(max) can probably be attributed to the difference of the local ϵ and n from the bulk ϵ and n.[1,2,5–35] In supercritical CO_2, the $\Delta\nu_{difference}$ exhibited a peak in a range of $0.5<\rho_r<1.5$.

There are some reports that solvation occurs around the solute which has high local densities.[1,2,5–35] In this paper we refer to this solvation as "positive solvation." The estimated ν(max) by Eq. (1) around the critical density is calculated to

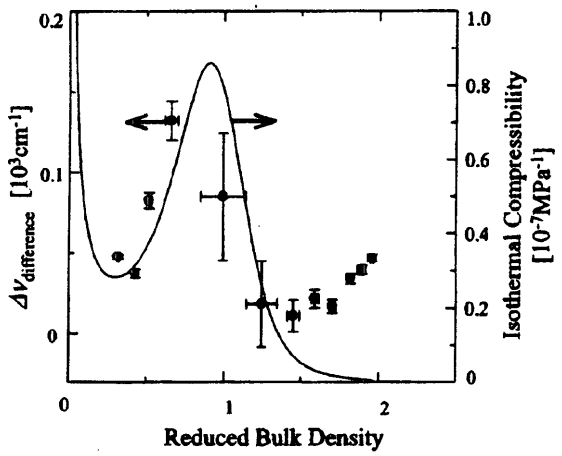

FIG. 6. The $\Delta\nu_{difference}$ in CO_2 and the isothermal compressibility vs reduced density at 38 °C.

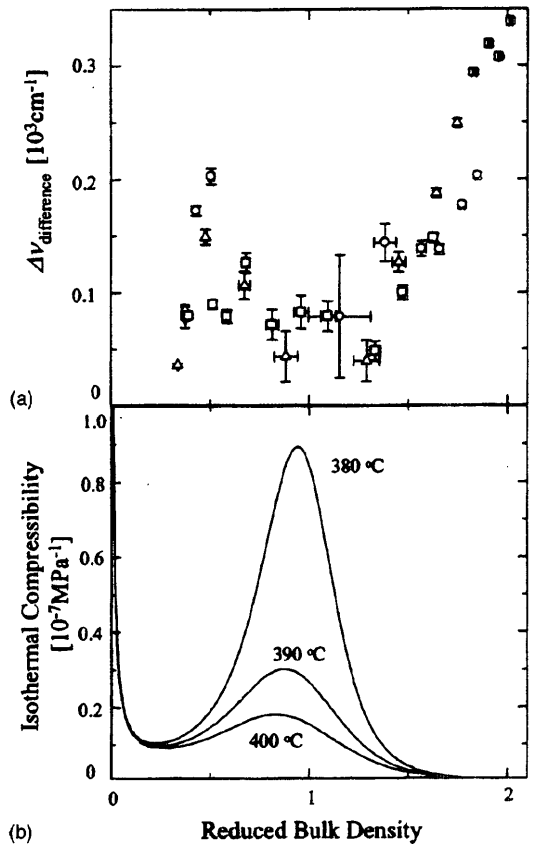

FIG. 7. (a) The $\Delta\nu_{difference}$ in water vs reduced density. (b) Isothermal compressibility. (◧) 360 °C, (○) 380 °C, (△) 390 °C, (□) 400 °C.

be smaller as compared with the correct ν(max), since positive solvation gives an increase in both local n and ϵ. In the present analyses, $\Delta\nu_{difference}$ was evaluated from the bulk n and ϵ, which might underestimate the true n and ϵ, and thus lead to an overestimation in $\Delta\nu_{difference}$. Kim and Johnston[5] claimed that the effect of solvation increased with the isothermal compressibility of fluids. Figure 6 shows a comparison of $\Delta\nu_{difference}$ and the isothermal compressibility of the fluid. In supercritical CO_2, the $\Delta\nu_{difference}$ became significant where the isothermal compressibility of the fluid was large as reported by Kim and Johnston.[5] This result suggests higher local density around quinoline than the bulk. Figure 7 is a magnification of Fig. 5 with the isothermal compressibility of water. The data shown in Fig. 7 exhibited a sigmoidal shape. In a range of $1<\rho_r<2$, the $\Delta\nu_{difference}$ decreased as the ρ_r decreased. Just below the critical density ($0<\rho_r<1.0$), $\Delta\nu_{difference}$ became larger with decreasing density, but then became smaller again at low densities. The peak appearing in the range of density for $0<\rho_r<1.0$ was largest at 380 °C and decreased with increasing temperature. Although there is experimental error in the data, in supercritical water the maximum peak of $\Delta\nu_{difference}$ ($0<\rho_r<1.0$) was observed at lower density region than the maximum of isothermal compressibility ($0.5<\rho_r<1.5$). This trend is different from that observed in supercritical CO_2 in Fig. 6.

The solvation structure around the solute is attributed to the competition between the solvent–solvent interaction and

the solute–solvent interaction. There are three types of solvation in supercritical conditions according to molecular dynamics studies.[44] The first is positive solvation, which is defined as the case where local density is higher than the bulk. The second is weak positive solvation, which is defined as the case where local density is slightly higher than the bulk density. The third is negative solvation, which is defined as the case where local density is lower than the bulk. For the case of nonpolar supercritical CO_2 solvent, quinoline–CO_2 forces are probably higher than that for CO_2–CO_2 forces. However, the affinity of quinoline with water is lower than the water–water interactions. This leads to the probable negative solvation around a quinoline in water.

Although the mechanism of this result has not yet been elucidated, the following hypothesis of negative solvation may be one of the probable explanations. Since quinoline molecule is hydrophobic, water molecules do not preferentially allocate themselves or solvate around quinoline molecules, although solvation may occur in the vicinity of the nitrogen atom. Thus, at a lower density region ($0<\rho_r<0.5$), a kind of positive solvation occurs around the nitrogen atom of quinoline molecules. However, hydrogen bonding between nitrogen atom of quinoline and hydrogen atom of water is weaker than that between water molecules. Thus, at the near critical density region where isothermal compressibility is high, water molecules gathered each other rather than solvated around the nitrogen atom of quinoline. The assembly of water molecules formed especially in the near critical regions ($0.5<\rho_r<1.5$). This assembly of water molecules attracted solvated water molecules around the nitrogen atom of quinoline. Thus, the cleavage of hydrogen bonding between quinoline and water occurred. At high density region ($1.5<\rho_r$) hydrogen bonding formed between the nitrogen atom of quinoline and the hydrogen atom of water, because the bulk density of water molecules was as high as that of local solvation shell.

VI. CONCLUSION

Solvatochromic shifts in the $\pi-\pi^*$ absorption band of quinoline show a strong relationship between hydrogen bonding and other solute–solvent interactions (dispersion, induction, and dipole–dipole) in supercritical water. The degree of hydrogen bonding between quinoline and water decreased with increasing temperature from 25 to 360 °C. In supercritical water, the degree of hydrogen bonding between quinoline and water decreased in water density especially around the critical point. In the critical region, lower local density around quinoline than bulk density, namely negative solvation, was observed.

ACKNOWLEDGMENT

This research was partially supported by the Ministry of Education, Science, Sports and Culture, Grant-in-Aid for Scientific Research (B), 11450295, 2001.

[1] O. Kajimoto, Chem. Rev. **99**, 355 (1999).
[2] S. C. Tucker, Chem. Rev. **99**, 391 (1999).
[3] E. G. McRae, J. Phys. Chem. **61**, 562 (1957).
[4] M. J. Kamlet, J. L. M. Abboud, and R. W. Taft, *Progress in Physical Organic Chemistry* (Wiley, New York, 1981), Vol. 13; C. Reichardt, *Solvent Effects in Organic Chemistry* (Chemie, Weinheim, 1988).
[5] S. Kim and K. P. Johnston, Ind. Eng. Chem. Res. **26**, 1206 (1987).
[6] G. E. Bennett and K. P. Johnston, J. Phys. Chem. **98**, 441 (1994).
[7] J. Lu, J. S. Brown, E. C. Boughner, C. L. Liotta, and C. A. Eckert, Ind. Eng. Chem. Res. **41**, 2835 (2002).
[8] J. Lu, J. S. Brown, C. L. Liotta, and C. A. Eckert, Chem. Commun. (Cambridge) **7**, 665 (2001).
[9] J. Lu, B. Han, and H. Yan, Ber. Bunsenges. Phys. Chem. **102**, 695 (1998).
[10] K. Takahashi, K. Abe, S. Sawamura, and C. D. Jonah, Chem. Phys. Lett. **282**, 361 (1998).
[11] B. L. Knutson, S. R. Sherman, K. L. Bennett, C. L. Liotta, and C. A. Eckert, Ind. Eng. Chem. Res. **36**, 854 (1997).
[12] D. Schwarzer, J. Troe, and M. Zerezke, J. Chem. Phys. **107**, 8380 (1997).
[13] K. P. Hafner, F. L. L. Pouillot, C. L. Liotta, and C. A. Eckert, AIChE J. **43**, 847 (1997).
[14] C. R. Yonker and R. D. Smith, J. Phys. Chem. **92**, 235 (1988).
[15] J. F. Kauffman, J. Phys. Chem. A **105**, 3433 (2001).
[16] J. E. Lewis, R. Biswas, A. G. Robinson, and M. Maroncelli, J. Phys. Chem. B **105**, 3306 (2001).
[17] R. Biswas, J. E. Lewis, and M. Maroncelli, Chem. Phys. Lett. **310**, 485 (1999).
[18] E. D. Niemeyer and F. V. Bright, Energy Fuels **12**, 823 (1998).
[19] E. D. Niemeyer, R. A. Dunbar, and F. V. Bright, Appl. Spectrosc. **51**, 1547 (1997).
[20] J. K. Rice, E. D. Niemeyer, R. A. Dunber, and F. V. Bright, J. Am. Chem. Soc. **117**, 5832 (1995).
[21] Y. Sun, J. Am. Chem. Soc. **115**, 3340 (1993).
[22] Y. Sun, G. Bennett, K. P. Johnston, and M. A. Fox, J. Phys. Chem. **96**, 10001 (1992).
[23] J. F. Brennecke, D. L. Tomasko, J. Peshkin, and C. A. Eckert, Ind. Eng. Chem. Res. **29**, 1682 (1990).
[24] A. Morita and O. Kajimoto, J. Phys. Chem. **94**, 6420 (1990).
[25] P. Lalanne, S. Rey, F. Cansell, T. Tassaing, and M. Besnard, J. Supercrit. Fluids **19**, 199 (2001).
[26] N. Wada, M. Saito, D. Kitada, R. L. Smith, Jr., H. Inomata, K. Arai, and S. Saito, J. Phys. Chem. B **101**, 10918 (1997).
[27] M. Kanakubo, T. Umecky, H. Kawanami, T. Aizawa, Y. Ikushima, and Y. Masuda, Chem. Phys. Lett. **338**, 95 (2001).
[28] M. Kanakubo, T. Aizawa, T. Kawakami, O. Sato, Y. Ikushima, K. Hatakeda, and N. Saito, J. Phys. Chem. B **104**, 2749 (2000).
[29] S. Bai, C. M. V. Taylor, F. Liu, C. L. Mayne, R. J. Pugmire, and D. M. Grant, J. Phys. Chem. B **101**, 2923 (1997).
[30] F. G. Baglin, S. K. Murray, J. E. Daugherty, T. E. Palmer, and W. Stanbery, Mol. Phys. **98**, 409 (2000).
[31] S. A. Egorov, J. Chem. Phys. **113**, 7502 (2000).
[32] J. L. deGrazia, T. W. Randolph, and J. A. O'Brien, J. Phys. Chem. A **102**, 1674 (1998).
[33] F. J. P. Schuurmans, D. T. N. de Lang, G. H. Wegdam, R. Sprik, and A. Langedijk, Phys. Rev. Lett. **80**, 5077 (1998).
[34] J. E. Lewis, R. Biswas, A. G. Robinson, and M. Maroncelli, J. Phys. Chem. B **105**, 3306 (2001).
[35] T. Aizawa, Y. Ikushima, N. Saitoh, K. Arai, and R. L. Smith, Jr., Chem. Phys. Lett. **357**, 168 (2002).
[36] A. R. Katritzky, R. A. Barcock, M. Siskin, and W. N. Olmstead, Energy Fuels **8**, 990 (1994).
[37] M. F. Anton and W. R. Moomaw, J. Chem. Phys. **66**, 1808 (1977).
[38] N. Mataga and S. Tsuno, Bull. Chem. Soc. Jpn. **30**, 368 (1957).
[39] N. Mataga, Y. Kaifu, and M. Koizumi, Bull. Chem. Soc. Jpn. **29**, 373 (1956).
[40] K. R. Hall, R. C. Wilhoit, K. N. Marsh, A. M. Ferguson, and B. Boyed, *Selected Ultraviolet Spectral Data/Thermodynamics Research Center Hydrocarbon Project*, Vol. 3, Serial No. 958 (Thermodynamics Research Center, Texas Engineering Experimental Station, Texas A & M University, College Station, 1945–1977).
[41] T. Moriyoshi, T. Kita, and Y. Uosaki, Ber. Bunsenges. Phys. Chem. **97**, 589 (1993).
[42] P. Schiebener, J. Straub, J. M. H. Levelt Sengers, and J. S. Gallagher, J. Phys. Chem. Ref. Data **19**, 677 (1990).
[43] M. Uematsu and E. U. Franck, J. Phys. Chem. Ref. Data **9**, 1291 (1980).
[44] I. B. Petsche and P. G. Debenedetti, J. Chem. Phys. **91**, 7075 (1989).

Preparation and Transport Properties of New Oxide Ion Conductors $KNb_{1-x}Mg_xO_{3-\delta}$ by High Temperature and Pressure

Liping Li,[†,‡] Guangshe Li,*[,§] Jun Xiang,[†] R. L. Smith Jr.,[§] and H. Inomata[§]

Department of Physics, Jilin University, Changchun 130023, P. R. China, Research Center of Supercritical Fluid Technology, Department of Chemical Engineering, Tohoku University, Sendai 980-8579, Japan, and Department of Materials Science, California Institute of Technology, Pasadena, California 91125

Received May 17, 2002. Revised Manuscript Received October 22, 2002

A series of oxide ion conductors $KNb_{1-x}Mg_xO_{3-\delta}$ ($x = 0.05-0.30$) were prepared at a temperature of 870 °C and a pressure of 4.0 GPa. All samples were thermodynamically stable at ambient pressure and crystallized in an orthorhombic perovskite structure. The lattice volume enlarged with increment of dopant level, which was associated with the ionic substitution, variation of the relative content of oxygen vacancy Vö, and defect associations $\{Mg_{Nb}''Vö\}$, as well as an increase of disorder in Mg^{2+}/Nb^{5+} distribution at B-sites of perovskite lattice. At higher temperatures, $KNb_{1-x}Mg_xO_{3-\delta}$ underwent phase transitions from orthorhombic to tetragonal, pseudocubic, and cubic in sequence, as confirmed by DTA and high-temperature Raman spectra. No thermal effects associated with the decomposition reactions were observed in $KNb_{1-x}Mg_xO_{3-\delta}$ during the successive heating process up to 1000 °C. The high-temperature phase had a relatively high structural stability. Impedance spectra of $KNb_{1-x}Mg_xO_{3-\delta}$ showed bulk and grain boundary conduction. The total conduction was determined to be predominately ionic, while the p-type electronic contribution was extremely small. $KNb_{0.90}Mg_{0.10}O_{2.85}$ was found to provide a highly conductive phase with a conductivity of $\sigma_{700°C} = 1.10 \times 10^{-3}$ S·cm^{-1}. Further, the ionic conductivity data for $KNb_{1-x}Mg_xO_{3-\delta}$ were separated into two linear ranges, corresponding to the pseudocubic and cubic phases, respectively. The variations of conductivity and activation energy for both pseudocubic and cubic phases can be explained in terms of the relative content of the oxygen vacancy and defect associations, delocalization of partial oxygen vacancies, and an order–disorder transition.

Introduction

Perovskite oxides possess a structural unit of ABO_3, in which A represents a larger ion with 12-fold coordination with oxygen ions and B is a smaller ion locating at the octahedral centers.[1] Oxide materials of such structures often show interesting phase transitions and physical properties. $KNbO_3$ is a prototype perovskite ferroelectric material exhibiting phase transitions similar to $BaTiO_3$: from ferroelectric rhombohedral to orthorhombic at −63 °C, to tetragonal at 215 °C, and finally to paraelectric cubic phase at 428 °C.[1] At high pressures, $KNbO_3$ undergoes several irreversible phase transitions,[2] but they are substantially different from those that appeared at higher temperatures. In addition, perovskite structures can be accommodated by doping various kinds of ions at A-sites or B-sites; in this way, structural evolutions and physical properties can be effectively controlled. For example, A-site substitutions in $KNbO_3$ usually lead to a semiconducting behavior,[3] while an oxide ion conduction can be activated when B-site Nb^{5+} is partially replaced by lower valence ions such as Al^{3+}.[4] Similar to other oxide ion conductors, a break is observed in the conductivity data of $KNb_{1-x}Al_xO_3$, which is ascribed to the order–disorder transition of the oxygen vacancies in perovskite lattice.[4]

Dopants in the perovskite oxides alter the microstructures and, furthermore, the physical properties mainly in two ways. The first way is to change the oxygen vacancy concentration in the parent lattice under aliovalent substitution, which forms the possible passages for oxide ion hopping. The second way is to create a large lattice distortion under isovalent substitution with a large difference in ionic size, which produces anti-Frenkel defects and lattice volume variations. In general, a defective perovskite phase with the larger lattice parameters probably shows a higher ionic conductivity.

* Corresponding author. Current address: C302 BNSN, Brigham Young University, Provo UT 84602. E-mail: guangshe@hotmail.com.
† Jilin University.
‡ California Institute of Technology.
§ Tohoku University.

(1) Fontana, M. D.; Metrat, G.; Servoin, J. L.; Gervais, F. *J. Phys.* C **1984**, *16*, 483.
(2) Shen, Z. X.; Hu, Z. P.; Chong, T. C.; Beh, C. Y.; Tang, S. H.; Kuok, M. H. *Phys. Rev.* B **1995**, *52*, 3976.
(3) (a) Hamada, D.; Machida, M.; Sugahara, Y.; Kuroda, K. *J. Mater. Chem.* **1996**, *6*, 69. (b) Kopnin, E. M.; Istomin, S. Y.; Dyachenko, O. G.; Antipov, E. V.; Bordet, P.; Capponi, J. J.; Chaillout, C.; Marezio, M.; Debrion, S.; Souletie, B. *Mater. Res. Bull.* **1995**, *30*, 1379.
(4) Thangadurai, V.; Subbanna, G. N.; Shukla, A. K.; Gopalakrishnan, J. *Chem. Mater.* **1996**, *8*, 1302.

10.1021/cm020582e CCC: $25.00
Published on Web 01/25/2003

As a consequence, strong correlation can be expected between the physical properties and microstructures in perovskite oxides. Busse et al.[5] prepared Mg-doped $KNbO_3$ (0.1 wt % MgO) crystals and found that the absorption loss of the doped sample for the blue light is 40% lower than that of undoped samples, while the infrared absorption is greatly enhanced upon Mg doping. The substitution of Mg^{2+} at B-sites in perovskite lattices can significantly improve the electrical property; e.g., it has been found that enhancement of magnetoresistance occurs in $La_{1-x}Sr_xMn(Mg)O_3$,[6] while for perovskite La(Pr)GaO_3-based electrolytes, addition of Mg^{2+} at B-sites is believed to be one of the most effective methods for increasing the ionic conductivity.[7] Even though $KNbO_3$ has several phase transitions under external fields, however, there are few reports on the phase transitions and transport properties in $KNbO_3$ with B-site Nb^{5+} being partially replaced by Mg^{2+}, which may be due to common problems arising from the phase separation processes during the preparation of Mg niobate-based perovskite oxides.[8]

Mg^{2+} has chemical characteristics that allow it to be easily hydrated and carbonated.[9] Its ionic size (1.34 and 0.72 Å in 12- and 6-fold coordination, respectively) might favor its occupation at A-sites or B-sites in perovskite lattices on the basis of tolerance factor consideration. However, the preparation of such perovskite oxides is rather complex and difficult.[10,11] For example, to obtain the samples containing Nb^{5+} and Mg^{2+} at B-sites in single-phase form, a two-step sintering process with a very long reaction time is necessary.[11] In the synthesis route, the columbite structure compound $MgNb_2O_6$ is a key intermediate phase.[8a] An increase of MgO content in the starting materials usually decreases the relative content of perovskite phase in the final products by forming several separated phases.[11c,d] In addition, Mg^{2+} and Nb^{5+} distribute simultaneously at B-sites in the perovskite lattices (such as $Pb(Nb_{2/3}Mg_{1/3})O_3$ (PMN)),[11g] usually giving excellent ferroelectric properties while the oxide ion conduction in them is considerably poor. Kharton et al.[12] reported on the oxide ion conduction in $LaGa_{0.85-x}Mg_{0.15}(Mg_{0.66}Nb_{0.33})_xO_{3-y}$ ($x = 0.00-0.20$) produced via solid-state reactions at ~1400 °C for 40 h. They found that the ionic conductivity decreases with increasing dopant content, and the samples contain a pronounced amount of impurity phases. Even though such single-phase perovskite oxides could be obtained using a little more complex procedure, X-ray and neutron diffraction methods have not been able to distinguish Nb^{5+} and Mg^{2+} at B-sites (such as in cubic perovskite lattice $Pb(Mg_{1/3}Nb_{2/3})O_3$),[11e,f] and therefore, the local oxygen species or vacancies around Nb^{5+} and Mg^{2+} as well as their effects on the properties remain unclear. With regard to the problems mentioned above, three questions can be raised: (i) Are there any single-step preparation methods for single-phase perovskite oxides with Nb^{5+} and Mg^{2+} at B-sites? (ii) If such methods exist, then what would be the structural stability of the products? (iii) Would the products exhibit any enhancement in ionic conduction having such a lattice? The objective of the present work is to attempt to address these questions.

In this paper, we prepared single-phase $KNb_{1-x}Mg_xO_{3-\delta}$ ($x = 0.05-0.30$) directly by high temperature and pressure and determined the structural stability and oxide ion conduction within this perovskite lattice.

Experimental Section

Analytic reagent grade chemicals $KHCO_3$, MgO, and Nb_2O_5 were used as the starting materials. They were weighed according to the molar ratios of $KNb_{1-x}Mg_xO_{3-\delta}$ ($x = 0.05$, 0.10, 0.15, 0.25, 0.30). After the mixtures were thoroughly ground, each sample was preheated at 700 °C for 5 h at ambient pressure to remove the carbonate species absorbed on the sample surface and to initiate partial reactions. The preheated samples analyzed with a powder X-ray diffraction were mixtures containing component oxides. Each sample was placed into a high-pressure chamber as described in a previous reference.[13] A belt-type apparatus was used for sample preparation. The pressure was set to 4.0 GPa, and then the temperature was increased gradually to 870 °C. After being kept at these conditions for 40 min, the specimens were quenched to room temperature under high pressure. Finally, the pressure was released and the pellet samples were obtained.

Powder X-ray diffraction data for the samples were collected at room temperature on a Rigaku 12kW copper rotating anode X-ray diffractometer. The scan rate was 0.3° 2θ/min. Silica powder (99.99% pure) was used as the internal standard for peak position determination. The lattice parameters for the samples were calculated by least-squares methods. Simultaneous differential thermal analysis (DTA) and thermogravimetric (TG) curves of the samples were recorded on a PE-DTA 1700-TGA7 PC thermoanalyzer at a heating rate of 10 °C/min in air. The compositions for the sample surfaces were measured by X-ray map using scanning electron spectroscopy (JEOL JEM 2000-FX).

Raman spectra of the samples were recorded at a resolution of 2 cm^{-1} on a Dilor Omars 89 spectrometer with an Ar^+ ion laser using an excitation wavelength of 488 nm.

The opposite sides of the pellet samples were coated with silver paste and heated to 550 °C in air for 0.5 h to remove completely the organic components in the paste. The ionic conductivities for the pellet samples were measured using a Solartron 1260 impedance/gain-phase analyzer with the alternating current having a frequency between 10 Hz and 9 MHz at an amplitude of 50 mV in the temperature range of 400–800 °C in air. The impedance spectra were also measured

(5) Busse, L. E.; Goldberg, L.; Surette, M. R.; Mizell, G. *J. Appl. Phys.* **1994**, *75*, 1102.
(6) Anane, A.; Dupas, C.; Le Dang, K.; Renard, J. P.; Veillet, P.; Pinsard, L.; Revcolevschi, A. *Appl. Phys. Lett.* **1996**, *69*, 1160.
(7) (a) Ishihara, T., Matsuda, H., Takita, Y., *J. Am. Chem. Soc.* **1994**, *116*, 3801. (b) Huang, K. Q.; Goodenough, J. B. *J. Alloys Compd.* **2000**, *303*, 454. (c) Goodenough, J. B.; Huang, K. Q. U.S. 6004688 A 21 December, 1999.
(8) (a) Narendar, Y.; Messing, G. L. *J. Mater. Res.* **1999**, *14*, 3921. (b) Swartz, S. L.; Shrout, T. R. *Mater. Res. Bull.* **1982**, *17*, 1245.
(9) Huang, K. Q.; Tichy, R. S.; Goodenough, J. B. *J. Am. Ceram. Soc.* **1998**, *81*, 2565.
(10) (a) Fiquet, G.; Devaele, A.; Andrault, D.; Kunz, M.; Le Bihan, T. *Geophys. Res. Lett.* **2000**, *27*, 21. (b) Yamazaki, D.; Kato, T.; Yurimoto, H.; Ohtani, E.; Toriumi, M. *Phys. Earth Planet. Inter.* **2000**, *119*, 299.
(11) (a) Ananta, S.; Thomas, N. W. *J. Eur. Ceram. Soc.* **1999**, *19*, 2917. (b) Ananta, S.; Thomas, N. W. *J. Eur. Ceram. Soc.* **1999**, *19*, 155. (c) Su, W. F. A. *Mater. Chem. Phys.* **2000**, *62*, 18. (d) Lee, D. Y.; Yoon, S. J.; Yeo, J. H.; Nahm, S.; Paik, J. H.; Whang, K. C.; Ahn, B. G. *J. Mater. Sci. Lett.* **2000**, *19*, 131. (e) Bonneau, P.; Garnier, P.; Husson, E.; Morell, A. *Mater. Res. Bull.* **1989**, *24*, 201. (f) Bonneau, P.; Husson, E.; Morell, A. *Proceedings of the 1st European Ceramic Society Conference*, Maastricht, The Netherlands, 1989. (g) Escribano, P.; Beltran, H.; Cordoncillo, E.; Garcia-Belmonte, G.; Ruiz, L.; Gonzalez-Calbet, J. H.; West, A. R. *Chem. Mater.* **2001**, *13*, 415.
(12) Kharton, V. V.; Yaremchenko, A. A.; Viskup, A. P.; Mather, G. C.; Naumovich, E. N.; Marques, F. M. B. *Solid State Ionics* **2000**, *128*, 79.
(13) Lu, D.; Li, L.; Miao, J.; Liu, H.; Su, W. *Rev. High-Pressure Sci. Technol.* **1998**, *7*, 1031.

at different oxygen partial pressures around that of the oxygen in air. The recorded impedance data were fit to an equivalent circuit model using the least-squares refinement program EQUIVCRT.[14]

Results

Structural Characteristics of $KNb_{1-x}Mg_xO_{3-\delta}$ at Room Temperature. $KNb_{1-x}Mg_xO_{3-\delta}$ ($x = 0.05-0.30$) samples could not be prepared in single phase by solid-state reactions at ambient pressure. XRD data (not shown) analysis indicated that the products obtained by sintering the preheated mixtures at 1000 °C for 32 h and with several intermediate grindings were mixtures containing a main perovskite phase and some unknown impurity phases. Prolonged reaction time had no pronounced influence on the relative content of the mixed phases as estimated from the relative intensity of the most intensive XRD peaks. This is similar to that found for preparation of $K_{1-x}Ba_xNbO_3$ ($0.2 < x < 0.5$).[3b] In this work, we used high temperature and pressure to prepare single-phase $KNb_{1-x}Mg_xO_{3-\delta}$ samples in a single step.

Figure 1 shows XRD patterns of the samples $KNb_{1-x}Mg_xO_{3-\delta}$ ($x = 0.05-0.30$) synthesized at 870 °C and 4.0 GPa. Most of the XRD data for the samples consisted of several split diffraction peaks, which indicated that the present samples had a low symmetric structure. To determine the structure characteristics of these samples, we took undoped $KNbO_3$ as a reference for comparison. At low temperatures, $KNbO_3$ crystallizes in rhombohedral or orthorhombic structures.[2] The rhombohedral phase has the characteristic diffraction lines, such as single lines (012) and (024) at about 23 and 47°, and double lines (110)/(104), (202)/(006), and (122)/(116) at about 33, 41, and 53°, respectively. From Figure 1, it can be seen that the samples exhibited double lines at about 23 and 47°. Therefore, the samples obtained cannot be indexed in rhombohedral. Instead, we found that the XRD data in Figure 1 matched well with the standard data for orthorhombic $KNbO_3$.[15] It is noted that when the dopant content was lower than $x = 0.30$, no diffraction peaks associated with impurity phases such as $MgNb_2O_6$ and $Mg_4Nb_2O_9$ were observed. These impurity phases are, however, key intermediates for the formation of single-phase perovskite oxides (such as $Pb(Nb_{2/3}Mg_{1/3})O_3$) containing Nb^{5+} and Mg^{2+} at B-sites.[8b,16] When the dopant content was larger than $x = 0.30$, some impurity phases were observed (not shown). The indexing of the XRD data in Figure 1 for these single-phase samples indicated that these orthorhombic perovskite structures had a space group of *Cm2m* (*38*). No weak and broad superlattice peaks associated with the long-range ordering distribution of oxygen vacancies were observed. The maximum diffraction intensity at ~32° was contributed by three peaks (020), (200), and (111); it was difficult to obtain the exact line width for these peaks due to their much closer

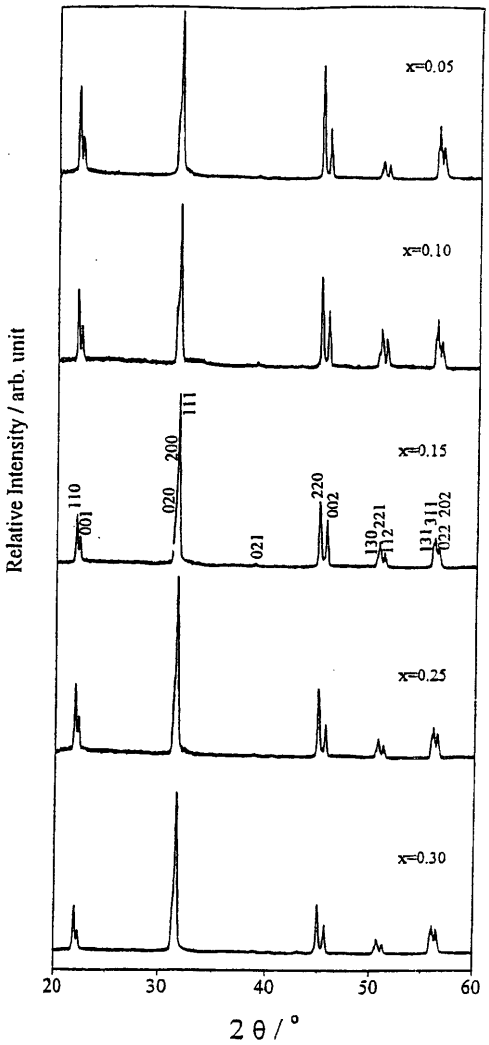

Figure 1. XRD patterns for $KNb_{1-x}Mg_xO_{3-\delta}$ ($x = 0.05-0.30$) prepared directly at 870 °C and 4.0 GPa.

d-spacing values. However, both peaks (220) and (002) centered at ~45° were well separated. Figure 2 shows the relationship between line width of the peak (002) and dopant content. With increasing dopant content, the diffraction peak (002) broadened.

The relationship between lattice volume and dopant content is shown in Figure 3. The lattice volume increased with the dopant content of Mg^{2+}, which seemed to be consistent with the relative ionic size of Mg^{2+} to Nb^{5+} ($r_{Nb(V)} = 0.72$ Å in 6-fold coordination).[17] However, as shown in Figure 3, the relationship between lattice volume and dopant content deviated from the Vegard law. A similar nonlinear relationship has been found in solid solutions $Ce_{1-x}RE_xO_{2-y}$ (RE = Eu, Tb).[18] The reason for this nonlinear relationship will be given in the Discussion section.

Figure 4 shows Raman spectra of the $KNb_{1-x}Mg_xO_{3-\delta}$ samples recorded at room temperature. All samples had Raman bands similar to those of undoped $KNbO_3$,[2,19] namely, a weak sharp band at ~190 cm^{-1}, broad bands

(14) Boukamp, B. B. *Equivalent Circuit*; University of Twente: Twente, The Netherlands, 1988.
(15) McLune, W. F., Ed. *Powder Diffraction File; Inorganic Phases*; JCPDS International Centre for Powder Diffraction Data: Swarthmore, PA, 1989; Card No. 32-822.
(16) (a) Hong, Y. S.; Park, H. B.; Kim, S. J. *J. Eur. Ceram. Soc.* **1998**, *18*, 613. (b) Joy, P. A.; Sreedhar, K. *J. Am. Ceram. Soc.* **1997**, *80*, 770.
(17) Shannon, R. D. *Acta Crystallogr., Sect. A* **1976**, *32*, 751.
(18) Li, L.; Li, G.; Che, Y.; Su, W. *Chem. Mater.* **2000**, *12*, 2567.

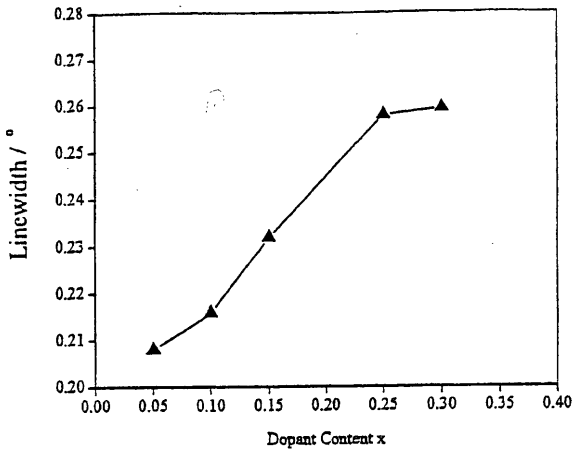

Figure 2. Relationship of line width for diffraction (002) and dopant content x in $KNb_{1-x}Mg_xO_{3-\delta}$ ($x = 0.05-0.30$).

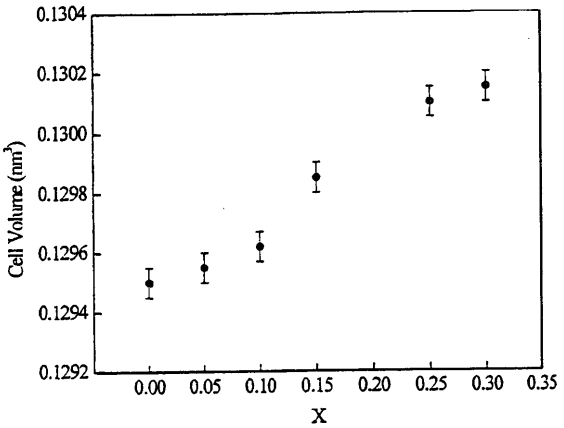

Figure 3. Relationship between lattice volume and dopant content x for $KNb_{1-x}Mg_xO_{3-\delta}$ ($x = 0.05-0.30$).

at 280, 530, and 580 cm^{-1}, and a weak peak at ~830 cm^{-1}. According to the literature,[2] the Raman bands in Figure 4 can be assigned. The weak band at ~190 cm^{-1} is ascribed to the mixed modes of $A_1(TO)$, $A_1(LO)$, and $B_2(TO)$. The broad bands at about 280 and 530 cm^{-1} are associated with the $B_1(TO)$ mode, while the band at ~580 cm^{-1} is due to the $A_1(TO)$ mode and that at ~830 cm^{-1} is due to the $A_1(LO)$ mode. It should be mentioned that $MgCO_3$, Nb_2O_5, and most of the intermediates in the $MgO-Nb_2O_5$ system are Raman active.[20] However, no Raman bands from these impurity phases were observed. These results clearly indicated that the present samples $KNb_{1-x}Mg_xO_{3-\delta}$ ($x = 0.05-0.30$) crystallized in the same orthorhombic structure as that for undoped $KNbO_3$. The samples did not show the presence of impurity phases such as pyrochlore in the preparation of PMN,[8b] which is probably related to the improved reactivity and the great enhancement of the phase transformation rate of pyrochlore to perovskite by an additional driving force provided by high

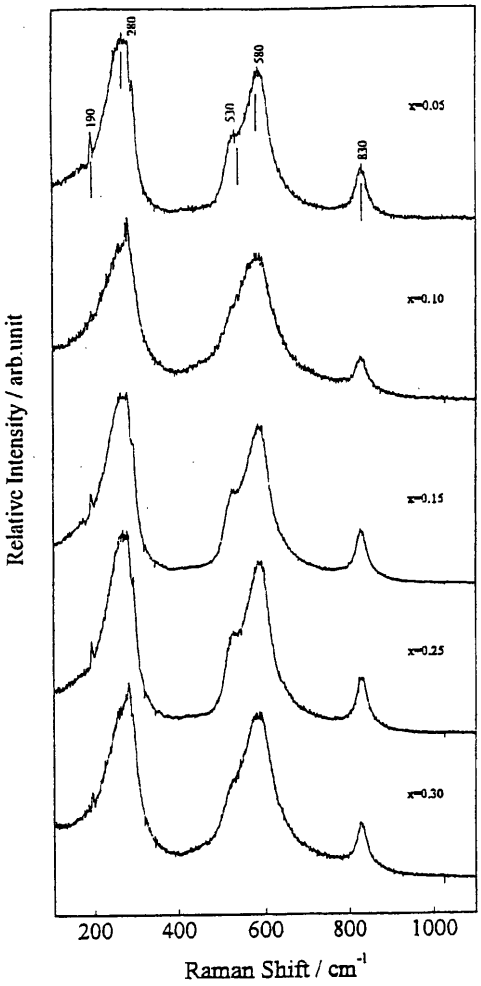

Figure 4. Room-temperature Raman spectra for $KNb_{1-x}Mg_xO_{3-\delta}$ ($x = 0.05-0.30$).

pressures.[21] Many high-pressure phase transitions are reversible when pressure is lowered; however, once the formation reactions are completed at high pressures, especially at high temperatures, the atom arrangements, even in a metastable form, can be stabilized at ambient conditions because the thermodynamically spontaneous reverse reaction is kinetically sluggish or unfavored at lower temperatures.[21d] The preparation of perovskite lattice $KNb_{1-x}Mg_xO_{3-\delta}$ is also associated with its tolerance factor at ~1.01, nearly the same as that of the undoped $KNbO_3$.

Structural Stability of $KNb_{1-x}Mg_xO_{3-\delta}$ at Ambient Pressure and Elevated Temperatures. Single phases of $KNb_{1-x}Mg_xO_{3-\delta}$ were prepared by high temperature and pressure. It is necessary to identify their structural stability at ambient pressure and elevated temperatures. We annealed the samples in air at 900 °C for 5 h and did not observe any change in the XRD patterns (not shown). This fact indicated that the present orthorhombic perovskite structures were kinetically stable at ambient pressure. In general, at elevated

(19) (a) Quittet, A. M.; Bell, M. I.; Krauzman, M.; Raccah, P. M. *Phys. Rev.* B **1976**, *14*, 5068. (b) Bozinis, D. G.; Hurrell, J. P. *Phys. Rev.* B **1976**, *13*, 3109.

(20) (a) Gillet, P. *Am. Mineral.* **1993**, *78*, 1328. (b) Dobal, P. S.; Dixit, A., Katiyar, R. S.; Choosuwan, H.; Gao, R.; Bhalla, A. S. *J. Raman Spectrosc.* **2002**, *33*, 121. (c) Camargo, E. R.; Longo, E.; Leite, E. R. *J. Sol–Gel Sci. Technol.* **2000**, *17*, 111. (d) Bruck, E.; Route, E. K.; Raytmakers, R. J.; Feigelson, R. S. *J. Cryst. Growth* **1993**, *128*, 842.

(21) (a) McMillan, P. F. *Nat. Mater.* **2002**, *1*, 19, (b) Lee, J. H.; Chiang, Y. M. *J. Electroceram.* **2001**, *6*, 7. (c) Demazeau, G. *Chem. Scr.* **1988**, *28*, 21. (d) Yamauchi, H.; Karppinen, M. *Supercond. Sci. Technol.* **2000**, *13*, R33.

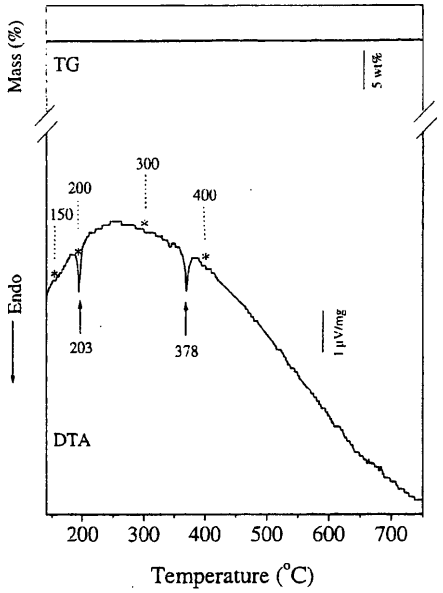

Figure 5. DTA-TG curves for a typical sample $KNb_{0.85}Mg_{0.15}O_{2.78}$. Two endothermic peaks at 203 and 378 °C with no mass variations were ascribed to the phase transitions from orthorhombic to tetragonal and to pseudocubic, respectively. * denotes several points of Raman measurement for identifying both transitions.

temperatures, perovskite oxides or the related lattices of lower symmetry would show several first-order transitions to higher symmetric phases, which are characterized by the transition entropy. An endothermic peak has been observed for a phase transition from tetragonal to cubic in $BaTiO_3$[22] and from monoclinic to cubic in $La_2Mo_2O_9$.[23] The phase stability of $KNb_{1-x}Mg_xO_{3-\delta}$ at elevated temperatures was determined by DTA-TG. Figure 5 shows the DTA-TG curves for a typical sample of $KNb_{0.85}Mg_{0.15}O_{2.78}$ measured in air. Two endothermic peaks centered at about 203 and 378 °C were observed. In the corresponding TG curve, no mass changes were observed. Here, it is hard to distinguish any possible second-order transitions due to the lack of thermal effects; however, these results clearly demonstrated that there were at least two possible high-temperature first-order transitions in $KNb_{0.85}Mg_{0.15}O_{2.78}$, corresponding to the transitions from orthorhombic to tetragonal and from tetragonal to pseudocubic, respectively, which were identified by high-temperature Raman spectra and will be described later. Similar transitions have been found at other compositions of $KNb_{1-x}Mg_xO_{3-\delta}$. During the successive heating process up to 1000 °C, no thermal effects associated with the decomposition reactions were observed in $KNb_{0.85}Mg_{0.15}O_{2.78}$, indicating that the high-temperature phase had a relatively high structural stability. When the temperature was higher than 1077 °C, the $KNb_{0.85}Mg_{0.15}O_{2.78}$ sample melted, accompanied by a large endothermic peak. To identify the high-temperature phases in $KNb_{1-x}Mg_xO_{3-\delta}$, we measured the high-temperature Raman spectra of two typical samples, $KNb_{0.85}Mg_{0.15}O_{2.78}$ and $KNb_{0.70}Mg_{0.30}O_{2.55}$. It should be mentioned that the direct method often used in observing the phase transitions is XRD. However, the broadening effects in the XRD patterns arising from the disordered distribution make it invalid to distinguish the high-temperature phases, especially when those high-temperature phases have a relatively high symmetry. Raman spectroscopy has been demonstrated to be a highly sensitive spectroscopic technique to probe the local structures in perovskite lattices such as $KNbO_3$.[2,24]

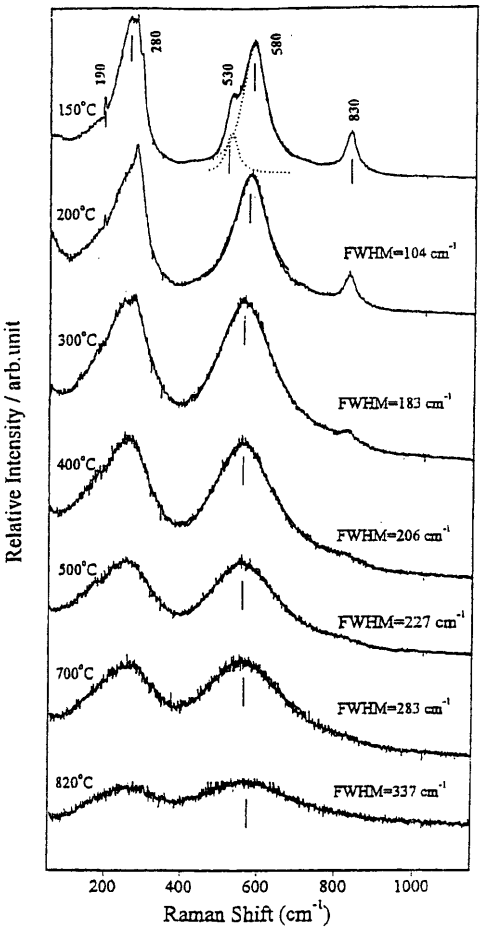

Figure 6. High-temperature Raman spectra for a typical sample $KNb_{0.85}Mg_{0.15}O_{2.78}$. The fwhm for the phonon mode at ~580 cm^{-1} is shown on the corresponding spectrum.

Figure 6 shows the high-temperature Raman spectra for $KNb_{0.85}Mg_{0.15}O_{2.78}$. The Raman spectra recorded at temperatures below 150 °C were nearly the same as the room-temperature spectrum. The phonon modes at about 530 and 580 cm^{-1} could be deconvoluted using Lorentzian shape functions. These results were consistent with the orthorhombic phase. At 200 °C, a point that just falls in the regime for the first endothermic peak in Figure 5, the intensity for the weak sharp phonon mode at 190 cm^{-1} decreased, and the mode at

(22) (a) Asiaie, R.; Zhu, W. D.; Akbar, S. A.; Dutta, P. K. *Chem. Mater.* **1996**, *8*, 226. (b) Didomenico, M., Jr.; Wemple, S. H.; Porto, S. P. S.; Bauman, R. P. *Phys. Rev.* **1968**, *174*, 522. (c) Shimooka, H.; Kuwabara, M. *J. Am. Ceram. Soc.* **1996**, *79*, 2983.

(23) Lacorre, P.; Goutenoire, F.; Bohnke, O.; Retoux, R.; Laligant, Y. *Nature* **2000**, *404*, 856.

(24) Naik, R.; Nazarko, J. J.; Flattery, C. S.; Venkateswaran, U. D.; Naik, V. M.; Mohammed, M. S.; Auner, G. W.; Mantese, J. V.; Schubring, N. W.; Micheli, A. L.; Catalan, A. B. *Phys. Rev. B* **2000**, *61*, 11367.

~280 cm^{-1} became asymmetric, indicating that the orthorhombic phase was not predominant. The phonon mode at 530 cm^{-1} vanished, while the mode at ~580 cm^{-1} became a single mode of high symmetry. We used Lorentzian shape functions to derive the full width at half-maximum (fwhm) of the phonon mode at ~580 cm^{-1}. The fwhm for this mode is shown on the right of Figure 6. It can be seen that the phonon mode at 580 cm^{-1} for $KNb_{0.85}Mg_{0.15}O_{2.78}$ had an fwhm of 104 cm^{-1} at 200 °C. The asymmetric band at ~280 cm^{-1} reflects the presence of asymmetric $Nb(Mg)O_6$ octahedra at B-sites.[25,26] Therefore, the phase transition from orthorhombic to tetragonal in $KNb_{0.85}Mg_{0.15}O_{2.78}$ probably proceeded via the production of asymmetric octahedra for B-site ions.

At 300 °C, a point that is well above the regime for the first endothermic peak in Figure 5, the weak sharp phonon mode associated with the orthorhombic structure disappeared at ~190 cm^{-1} and the phonon modes centered at about 280 and 580 cm^{-1} became two symmetric modes, while the mode at ~830 cm^{-1} was further weakened. Especially, the fwhm for the phonon mode at ~580 cm^{-1} was much broader at 183 cm^{-1} (300 °C) than that at 104 cm^{-1} (200 °C). Therefore, a tetragonal phase was probably formed. At 400 °C, a point that is well above the regime for the second endothermic peak in Figure 5, two highly symmetric phonon modes at about 280 and 580 cm^{-1} were slightly weakened, while the fwhm for the mode at ~580 cm^{-1} increased to 206 cm^{-1}. The mode at ~830 cm^{-1} lost most of its intensity and was too faint to be observed. These results could be associated with a pseudocubic phase.[25] With increasing temperatures above 500 °C, as shown in Figure 6, both phonon modes centered at about 280 and 580 cm^{-1} further broadened and lost intensity, which could be associated with the transition of pseudocubic to cubic. Above 600 °C, both phonon modes further weakened at about 280 and 580 cm^{-1}. The mode at ~830 cm^{-1} disappeared completely. These results were evidence of the formation of a cubic phase. Two similar weak phonon modes are also found for cubic $BaTiO_3$.[27]

High-temperature Raman spectra for $KNb_{0.70}Mg_{0.30}O_{2.55}$ are shown in Figure 7. At temperatures below 150 °C, $KNb_{0.70}Mg_{0.30}O_{2.55}$ gave a very weak phonon mode at ~190 cm^{-1}, which was probably associated with overlapping of some phonon modes and the background under the broadening effect due to an increase of disorder at heavy doping. The phonon mode centered at ~280 cm^{-1} became asymmetric. Both modes at about 530 and 580 cm^{-1} were still observable as deconvoluted by using Lorentzian shape functions shown in Figure 7. These results were associated with an orthorhombic phase below 150 °C. At 300 °C, the weak phonon mode at ~190 cm^{-1} and the stronger one at ~530 cm^{-1} disappeared, while the broad phonon mode at ~580 cm^{-1} became a single mode as fitted by Lorentzian shape functions. Similar to that for $KNb_{0.85}Mg_{0.15}O_{2.78}$, the highly symmetric phonon mode at ~580 cm^{-1} was ascribed to the presence of a tetragonal phase. The fwhm for the phonon mode at ~580 cm^{-1} is shown on the right of Figure 7. At 300 °C, the fwhm of this mode was as wide as 112 cm^{-1}, which showed a jump to 187 cm^{-1} at 400 °C. At 400 °C, the phonon mode at ~830 cm^{-1} became considerably weaker compared with that at 300 °C. These results were probably associated with a pseudocubic phase at 400 °C. Above 600 °C, the broad mode at ~830 cm^{-1} disappeared completely. Both broad phonon modes centered at about 280 and 580 cm^{-1} were shown to have a low S/N ratio and lost intensity gradually with increasing temperature, which was associated with a transition of pseudocubic to cubic phase. It is clear that these transitions were quite similar to those observed for $KNb_{0.85}Mg_{0.15}O_{2.78}$ in Figure 6.

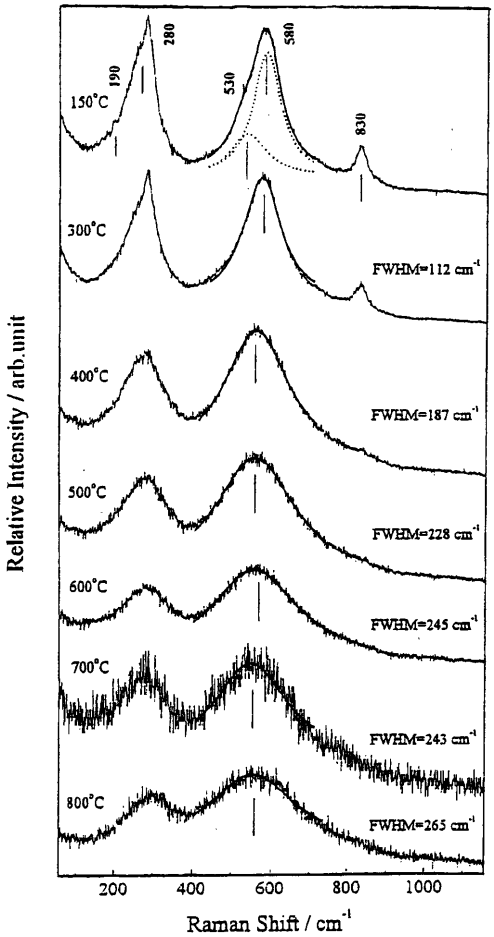

Figure 7. High-temperature Raman spectra for a typical sample $KNb_{0.70}Mg_{0.30}O_{2.55}$. FWHMs are given for the phonon mode at ~580 cm^{-1}. Dashed lines show Lorentzian fits.

Oxide Ion Conduction in $KNb_{1-x}Mg_xO_{3-\delta}$ at Elevated Temperatures. Oxide ion conduction in $KNb_{1-x}Mg_xO_{3-\delta}$ was determined by ac impedance spectroscopy. At temperatures lower than 350 °C, the samples showed extremely large resistance and did not give full arcs. Figure 8 illustrates the impedance spectrum for a typical composition of $KNb_{0.90}Mg_{0.10}O_{2.85}$ that was recorded at 398 °C in air. The impedance data were fit to an equivalent circuit model,[28] in which one Q element and two subcircuits (R and Q in parallel) are

(25) Fontana, M. D.; Kugel, G. E.; Vamvakas, J.; Carabatos, C. *Solid State Commun.* **1983**, *45*, 873.
(26) Clark, I. J.; Takeuchi, T.; Ohtori, N.; Sinclair, D. C. *J. Mater. Chem.* **1999**, *9*, 83.
(27) Fontana, M. P.; Lambert, M. *Solid State Commun.* **1972**, *10*, 1.

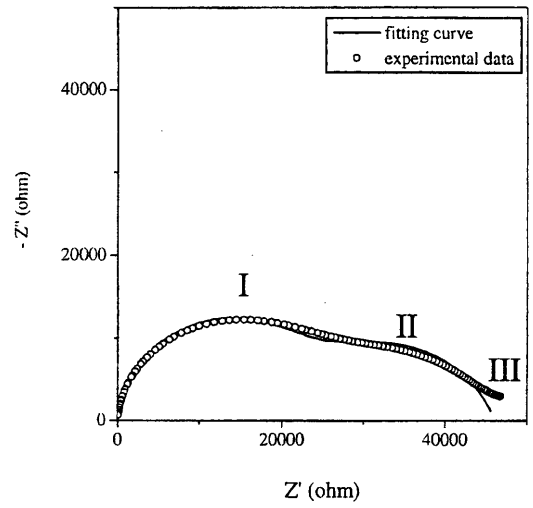

Figure 8. Impedance spectrum for a typical composition of $KNb_{0.90}Mg_{0.10}O_{2.85}$, recorded at 398 °C in air. Solid line shows fit by an equivalent circuit model.

in series with one another, where R represents a resistor and Q is the constant-phase element. The fitting results by this model are also shown in Figure 8. It is seen that the impedance spectrum was mainly composed of two depressed semicircles. The semicircle (I) at higher frequencies can be attributed to the bulk effect, while the intermediate frequency semicircle (II) can be ascribed to the grain boundary conduction. It should be mentioned that, at higher dopant levels, a spike (III) appeared at lower frequencies, which is due to the overall electrode processes. The impedance spectra in Figure 8 can be deconvoluted as overlapped or nonoverlapped semicircles. Mukundan et al.[29] tried fitting the conductivity data of orthorhombic perovskite $SrCe_{0.95}Yb_{0.05}O_{2.975}$ using overlapped semicircles, but the values of their activation energies exhibited large scatter.

In this work, we emphasized the relationship between total conductivity and dopant content by estimating the resistance with nonoverlapped semicircles. The conductivity for $KNb_{1-x}Mg_xO_{3-\delta}$ was determined by the intersection of the semicircles on the real part of the impedance axis. Figure 9 gives ln σT and $1/T$ plots of $KNb_{1-x}Mg_xO_{3-\delta}$. It can be seen that the total conductivity data for all samples were separated into two linear regions. That is, the conduction at lower temperatures had a lower activation energy, while above the transition temperatures, there was a break in the conductivity data, which gave an increase in the conductivity and activation energy. To further confirm the dominant ionic conduction in $KNb_{1-x}Mg_xO_{3-\delta}$ under the present experimental conditions, we measured the impedance spectra of a typical sample $KNb_{0.90}Mg_{0.10}O_{2.85}$ at 500 °C under several oxygen partial pressures around that of air. The dependence of the conductivity on the oxygen partial pressure is shown in Figure 10. No pronounced variation was observed in the conductivity data under the selected oxygen partial pressures. Even though there was a

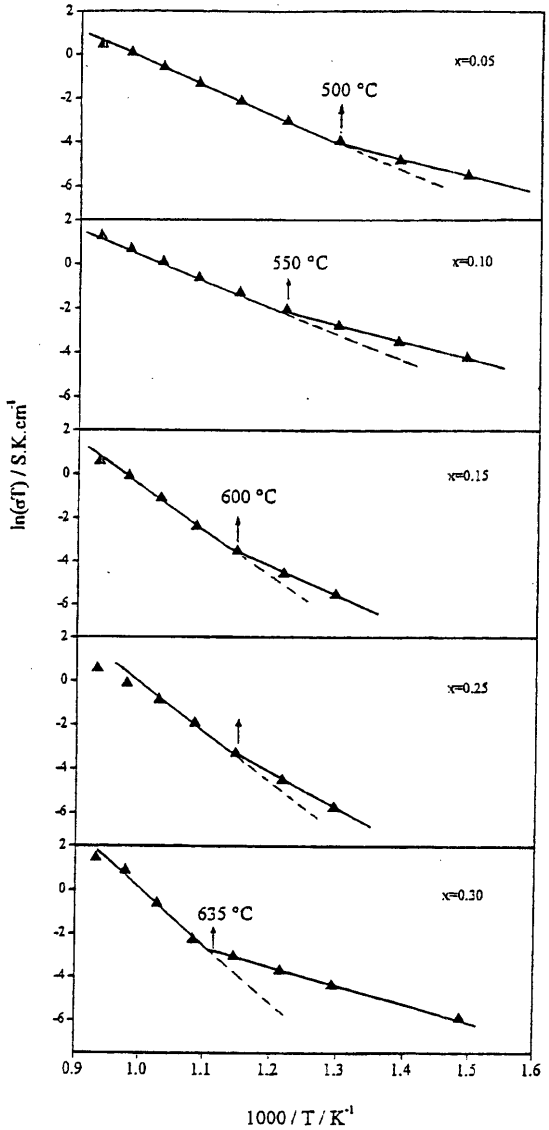

Figure 9. Temperature dependence of total conductivity for $KNb_{1-x}Mg_xO_{3-\delta}$ ($x = 0.05-0.30$).

slight increase in the conductivity at higher oxygen partial pressures, as shown in Figure 10, the slope $\partial \log \sigma / \partial \log PO_2$ in this oxygen partial pressure region was much less than $^1/_4$ or $^1/_6$, the characteristic regime for p-type electronic conduction.[30] The weak PO_2 dependence of the conductivity data was thus probably due to the transition regime between the ionic conductivity with no PO_2 dependence and p-type electronic conductivity with slope $\partial \log \sigma / \partial \log PO_2$ a $^1/_4$ or $^1/_6$. Theoretical modeling has been reported on the oxide ion or cation conduction in perovskite lattices.[31] However, it is highly unlikely that cation conduction for the present $KNb_{1-x}Mg_xO_{3-\delta}$, cation conduction associated with K^+, Mg^{2+}, and Nb^{5+}, occurs via cation vacancies. This can be reasoned from the comparison of the measured activation energies and the theoretical values for cation conduction. The activation energies of $KNb_{1-x}Mg_xO_{3-\delta}$

(28) (a) Haile, S. M.; West, D. L.; Campbell, J. *J. Mater. Res.* **1998**, *13*, 1576. (b) Gerhardt, R.; Nowick, A. S. *J. Am. Ceram. Soc.* **1986**, *69*, 641. (c) Macdonald, J. R. *Impedance Spectroscopy*; Wiley: New York, 1987.

(29) Mukundan, R.; Brosha, E. L.; Birdsell, S. A.; Costello, A. L.; Garzon, F. H.; Willms, R. S. *J. Electrochem. Soc.* **1999**, *146*, 2184.

(30) Shimura, T.; Fujimoto, S.; Iwahara, H. *Solid State Ionics* **2001**, *143*, 117.

(31) Islam, M. S. *J. Mater. Chem.* **2000**, *10*, 1027.

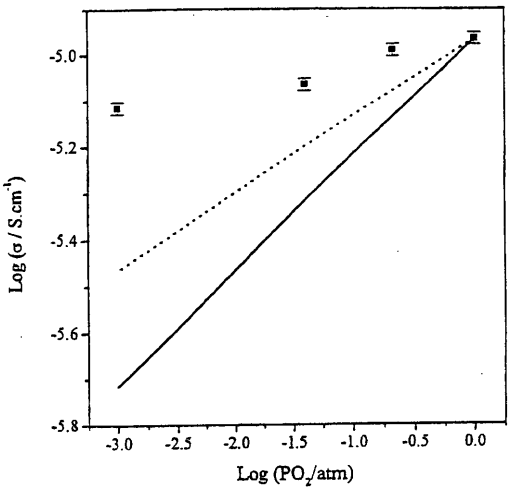

Figure 10. Conductivity dependence on oxygen partial pressure for a typical sample $KNb_{0.90}Mg_{0.10}O_{2.85}$ at 500 °C. Two lines showing $\partial \log \sigma / \partial \log PO_2$ at $^1/_6$ (dotted) and $^1/_4$ (solid) are given to demonstrate the primary ionic nature and extremely small p-type electronic contribution to total conduction in the sample.

Table 1. Conductivities (σ) and Activation Energies (E_a) of $KNb_{1-x}Mg_xO_{3-\delta}$ (x = 0.00–0.30) Measured at 500 and 700 °C. [a]Denotes the Data from Ref 4

x	$\sigma_{500°C}$ (S·cm^{-1})	$E_{a500°C}$ (eV)	$\sigma_{700°C}$ (S·cm^{-1})	$E_{a700°C}$ (eV)
0.00[a]	1.80×10^{-6}	0.89	3.20×10^{-5}	0.89
0.05	2.54×10^{-5}	0.55	5.50×10^{-4}	0.85
0.10	7.90×10^{-5}	0.58	1.10×10^{-3}	0.83
0.15	5.14×10^{-6}	0.93	3.50×10^{-4}	1.35
0.25	4.15×10^{-6}	1.13	4.30×10^{-4}	1.40
0.30	1.65×10^{-5}	0.57	5.50×10^{-4}	1.73

were relatively lower having values of around 1.0 eV, which is characteristic of oxygen migration. Assuming that cation conduction was present in $KNb_{1-x}Mg_xO_{3-\delta}$, the extremely large ionic size of 1.64 Å for K^+ at the A-site of the perovskite lattice would probably yield an activation energy larger than 4.0 eV.[31] For the B-site ions such as Mg^{2+} and Nb^{5+}, the migration energy along the diagonal direction ⟨110⟩ would be even higher and would have a value, most likely, around 14 eV. Therefore, cation vacancy formation and furthermore cation conduction by vacancy migration between the neighboring sites should be highly unfavorable as expected for the close-packed perovskite lattice of $KNb_{1-x}Mg_xO_{3-\delta}$. In consideration of the weak oxygen partial pressure relationship of the conductivity data, it is reasonable that the present samples were a mixed-type conductor of primary oxide ion and traces of electron holes. Similarly, primary oxide ion conduction as well as p-type electronic conduction have been found in several perovskite oxides, such as in Mg-doped $LaGaO_3$.[7b,32]

The conductivities and activation energies for $KNb_{1-x}Mg_xO_{3-\delta}$ at 500 and 700 °C are listed in Table 1. The literature data[4] for $KNbO_3$ at both temperatures are also shown for comparison. At 500 °C, the conductivity increased with the dopant content from 1.80×10^{-6} S·cm^{-1} at x = 0.00 to 7.90×10^{-5} S·cm^{-1} at x = 0.10. When the dopant content was above x = 0.10, the conductivity for $KNb_{1-x}Mg_xO_{3-\delta}$ decreased to 4.15×10^{-6} S·cm^{-1} at x = 0.25. Then, the conductivity increased to 1.65×10^{-5} S·cm^{-1} at x = 0.30. Correspondingly, the activation energy decreased with dopant content from E_a = 0.89 eV at x = 0.00 to 0.55 eV at x = 0.05. Further increasing dopant content led to an increase of the activation energy to E_a = 1.13 eV at x = 0.25. Then the activation energy decreased to E_a = 0.57 eV at x = 0.30.

The conductivity data at 700 °C for $KNb_{1-x}Mg_xO_{3-\delta}$ were much enhanced in comparison with those at 500 °C. With increasing dopant content, the conductivity increased from 3.20×10^{-5} S·cm^{-1} at x = 0.00 to 1.10×10^{-3} S·cm^{-1} at x = 0.10. When the dopant content was higher than x = 0.10, the conductivity decreased to 3.50×10^{-4} S·cm^{-1} at x = 0.15 and then increased to 5.50×10^{-4} S·cm^{-1} at x = 0.30. Correspondingly, the activation energy decreased slightly from E_a = 0.89 eV at x = 0.00 to 0.83 eV at x = 0.10. There was a sharp increase of activation energy to E_a = 1.35 eV at x = 0.15, and then the activation energy increased continuously to E_a = 1.73 eV at x = 0.30. From Table 1, $KNb_{0.90}Mg_{0.10}O_{2.85}$ was found to exhibit most favorable conduction characteristics such as a relatively high conductivity and low activation energy.

Discussion

Correlation of Lattice Volume Variation with Defect Characteristics of $KNb_{1-x}Mg_xO_{3-\delta}$. The lattice volume variation with dopant content for $KNb_{1-x}Mg_xO_{3-\delta}$ could be explained by taking into account the relative ionic size of Mg^{2+} to Nb^{5+} and the charge difference. Doping of larger Mg^{2+} at Nb^{5+} sites in $KNbO_3$ produced a larger lattice distortion, which was the main reason for the lattice expansion. On the other hand, owing to a large charge difference between Nb^{5+} and Mg^{2+}, when a fracture of Nb^{5+} was replaced by Mg^{2+}, there should be some negative charge centers formed in a local scale near Mg^{2+}, which could be balanced by oxygen vacancies produced in the perovskite lattice of $KNb_{1-x}Mg_xO_{3-\delta}$. In this case, every two Mg^{2+} ions in lattice would yield three oxygen vacancies Vö. Mg^{2+} probably attracted the oxygen vacancies to the nearest neighboring positions due to the Coulombic forces. Therefore, an inhomogeneous distribution of oxygen vacancies are expected. With an increase in dopant content of Mg^{2+}, the average concentration of oxygen vacancy Vö would increase. As indicated by the relative variations of the conductivity data (Table 1), it is probable that when the dopant content was further increased beyond x = 0.10, localized defect associations $\{Mg_{Nb}'''Vö\}$ or oxygen vacancy clusters appeared and their content increased at the expense of mobile oxygen vacancies Vö, as has been found in other solid solutions at higher dopant contents.[33] In contrast to cationic substitution, both oxygen vacancies Vö and defect associations $\{Mg_{Nb}'''Vö\}$ or oxygen vacancy clusters were considered to contribute lattice constraints. It should be mentioned that oxygen vacancies Vö and defect associations $\{Mg_{Nb}'''Vö\}$ have different interactions with the framework ions, and the effect from the

(32) Kharton, V. V.; Yaremchenko, A. A.; Viskup, A. P.; Mather, G. C.; Naumovich, E. N.; Marques F. M. B. *J. Electroceram.* **2001**, *7*, 57.

(33) Lidiard, A. B. In *Handbuch der Physik*; Flugge, S., Ed.; Springer-Verlag: Berlin, 1956; Vol. XX.

oxygen vacancies may be slightly larger than the defect associations in reducing the lattice volume.[17] The cationic substitutions and variations for the relative content of oxygen vacancy Vö and defect associations $\{Mg_{Nb}'''Vö\}$ were therefore assumed to be the main reasons for the nonlinearity in Figure 3. Similar reasons have been proposed to explain the nonlinearity for solid solutions $Ce_{1-x}RE_xO_{2-x}$ (RE = Eu, Tb).[17] However, a linear relationship can be expected when the dopants have a much larger ionic size compared with host ions even in the presence of large amounts of defect associations or oxygen vacancy clusters.[34]

Disordered distribution of Nb^{5+}/Mg^{2+} at B-sites also showed some contribution to the nonlinearity in Figure 3. This is because a large amount of oxygen vacancies Vö or defect associations $\{Mg_{Nb}'''Vö\}$ in $KNb_{1-x}Mg_xO_{3-\delta}$ produced lattice distortion on a small scale, which probably yielded some displacements for Mg^{2+} or Nb^{5+} at B-sites. Taking into account the slightly larger ionic radii of Mg^{2+} than Nb^{5+}, the Nb−O bonds were expected to be shorter than the Mg−O bonds, which should generate a distorted BO_6 octahedra network by a slight lattice expansion. Moreover, the Nb−O bonds are more covalent and are more inflexible in comparison with the Mg−O bonds. Therefore, a partial disorder of Mg^{2+}/Nb^{5+} at B-sites can be expected, as is observed in orthorhombic $BaTiO_3$ and $KNbO_3$.[35] As a result, the oxygen vacancies were probably long-range disordered in $KNb_{1-x}Mg_xO_{3-y}$, in good agreement with the absence of superlattice peaks in Figure 2. Such a disordered distribution was also confirmed by the broadening effect in XRD patterns in Figure 2, even though the broadening effect in XRD could be due to a decrease in particle size or an increase in lattice disorder. In this work, all samples were prepared by high temperature and pressure using commercial oxides of several micrometers in dimension as the starting materials; a decrease in particle size is not a likely explanation. Similar results have been found in $(1-x)Pb(Mg_{1/3}Nb_{2/3})O_3 - xPbTiO_3$ containing disordered B-site ions due to Ti^{4+} substitution.[36]

Correlation of Phase Transitions with Lattice Disorder in $KNb_{1-x}Mg_xO_{3-\delta}$. $KNb_{1-x}Mg_xO_{3-\delta}$ underwent phase transitions from orthorhombic, to tetragonal, to pseudocubic, and to cubic. The transition from tetragonal to pseudocubic accompanied by the broadened phonon mode at ~580 cm^{-1} (Figures 6 and 7) could be understood in terms of the change from tetragonal mode to the triply degenerated cubic F_{1u} mode.[37] As described above, substitution of Nb^{5+} by the larger Mg^{2+} could give a larger displacement for Nb^{5+}, and the oxygen vacancies adjacent to Mg^{2+} could produce much distorted polyhedra around Nb^{5+}. As a result, $KNb_{1-x}Mg_xO_{3-\delta}$ exhibited phase transitions different from those in undoped $KNbO_3$ at high temperatures.[1] In the latter case, no pseudocubic was obtained. Pseudocubic $KNb_{1-x}Mg_xO_{3-\delta}$ contained a partial lattice order, whereas B-site ions in the cubic phase can be assumed to be distributed disorderly at eight off-center sites along the ⟨111⟩ axes due to the potential energy minimums at these sites.[38] According to group theory analysis, the irreducible representation of 12 optical phonons for the cubic phase (space group $Pm3m$) is $3F_{1\mu} + F_{2\mu}$. All phonon modes for this highly symmetric structure are Raman inactive. Therefore, the phonon modes such as that at 580 cm^{-1} should be forbidden. The presence of these weak modes can be well explained in terms of the disordered arrangements existing in the lattice of $KNb_{1-x}Mg_xO_{3-\delta}$ for such disordered arrangements could result in removal of the inversion symmetry for the O_h point group and thus activate some Raman modes that are originally inactive.[39]

Similar distributions of Mg^{2+} and Nb^{5+} in $KNb_{1-x}Mg_xO_{3-\delta}$ can be expected at one to eight off-center sites along the ⟨111⟩ axes in the presence of some lattice distortions due to the size mismatch of Mg^{2+}/Nb^{5+} at B-sites. In fact, oxygen vacancies or oxygen vacancy clusters adjacent to Mg^{2+} probably give rise to an inhomogeneous distribution of electrical field at B-sites. The different static displacements of Mg^{2+} and Nb^{5+} decreased the local symmetry for B-site ions.[40] Therefore, with increasing temperature, a rapid increase in the disorder of Nb^{5+}/Mg^{2+} at B-sites was favored to preserve a highly symmetric average cubic structure at high temperatures, which was confirmed by the weakened intensity of both phonon modes for the cubic.[41] At higher dopant contents, large amounts of oxygen vacancies Vö and defect associations $\{Mg_{Nb}'''Vö\}$ showed strong interactions with the framework ions and mobile oxygen ions. The transition of order−disorder of oxygen vacancies was thus suppressed. This is probably the main reason for an increase in transition temperature of pseudocubic to cubic with increasing dopant content shown in Figure 9.

Correlation of Oxide Ion Conduction with Defect Characteristics and Lattice Disorder in $KNb_{1-x}Mg_xO_{3-\delta}$. We addressed first the increased activation energy and conductivity data shown in Figure 9 for the cubic phase in comparison with the pseudocubic phase. Oxide ion conduction in perovskite lattice was achieved by oxide ions passing through a window of a triangle formed by two A-site ions (e.g., K^+) and one B-site ion (e.g., Nb^{5+} and Mg^{2+}) to reach an adjacent oxygen vacant site.[31] It is reasonable that the static displacements of K^+ and neighboring Nb^{5+} or Mg^{2+} as well as the ordering distribution of Nb^{5+}/Mg^{2+} determine the window dimension and therefore strongly influence the activation energy and conductivity of oxide ion hopping in $KNb_{1-x}Mg_xO_{3-\delta}$. It is noted that the energy required for an oxide ion to pass through the window containing one Mg^{2+} will be larger than that in case of one Nb^{5+}. Increasing the symmetry of the perovskite structure allows a higher possibility for B-site Mg^{2+} or Nb^{5+} to be distributed at off-centers along ⟨111⟩.

(34) Li, G.; Mao, Y.; Li, L.; Feng, S.; Wang, M.; Yao, X. *Chem. Mater.* **1999**, *11*, 1259.
(35) Comes, R.; Lambert, M.; Guinier, A. *Solid State Commun.* **1968**, *6*, 715.
(36) Fitzgerald, J. J.; Huang, J.; Shore, J. S. *Ferroelectrics* **1999**, *233*, 187.
(37) Gourdain, D.; Moya, E.; Chervin, J. C.; Canny, B.; Pruzan, P. *Phys. Rev. B* **1995**, *52*, 3108.
(38) Dougherty, T. P.; Weiderrecht, G. P.; Nelson, K. A.; Garrett, M. H.; Jenssen, H. P.; Warde, C. *Phys. Rev. B* **1994**, *50*, 8996.
(39) (a) Laabidi, K.; Fontana, M. D.; Maglione, M.; Jannot, B.; Muller, K. A. *Europhys. Lett.* **1994**, *26*, 309. (b) Laabidi, K.; Fontana, M. D.; Jannot, B. *Solid State Commun.* **1990**, *76*, 765.
(40) Li, L.; Li, G.; Song, X.; Miao, J.; Zhou, X.; Su, W. *Chin. Phys. Lett.* **1998**, *15*, 925.
(41) Choi, S. M.; Lee, K. T.; Kim, S.; Chun, M. C.; Lee, H. L. *Solid State Ionics* **2000**, *131*, 221.

Correspondingly, the efficient dimension of the window for oxide ion hopping probably became narrowed. Therefore, an increase in activation energy could be expected for the cubic phase. Alternatively, the activation energy would be decreased if there was no obvious phase transitions to highly symmetric phases, as is found in $La_{0.9}Ba_{0.1}Ga_{1-x}Mg_xO_{3-y}$.[41] In the latter case, the total activation energy in the low-temperature range is the sum of the migration energy and the association energy. But the contribution of the activation energy term decreases at high temperatures. The increased conductivity for the cubic in Figure 9 can be explained by taking into account the destabilization of part of the defect associations or oxygen vacancy clusters at high temperatures. Some amount of mobile oxygen vacancies released gave rise to the passages for oxide ion hopping.

In regard to the relationship between conductivity and dopant content for $KNb_{1-x}Mg_xO_{3-\delta}$, the ordered distribution of B-site ions should be the main reason for the conductivity variations. According to the order–disorder transition model,[38] orthorhombic and tetragonal phases that appeared at temperatures below 400 °C had a relatively high order of Nb^{5+}/Mg^{2+} at B-sites. The ordered phases are usually less conductive and are transformed into the disordered phases of higher conductivity at higher temperatures.[42–44] The extremely large resistance associated with the ordered B-site ions in both orthorhombic and tetragonal phases makes it very difficult to measure full impedance semicircles over the entire frequency range of interest. Therefore, the relationship between phase transition and oxide ion conductivity could not be reached for orthorhombic to tetragonal to pseudocubic. The conductivity data for both pseudocubic and cubic phases in Table 1 can be rationalized as follows. For the pseudocubic phase, the content of oxygen vacancies increased with dopant content. At lower dopant content, most of these oxygen vacancies Vö were probably mobile. This could explain the gradual decrease of activation energy and increase of conductivity. At high dopant content, defect associations $\{Mg_{Nb}'''Vö\}$ localized near Mg^{2+} begin to form at the expense of the oxygen vacancies Vö. Correspondingly, oxygen sites near Nb^{5+} may become unavailable for hopping. This might explain the increase of activation energy and decrease of conductivity. The variations of the relative content of oxygen vacancies and defect associations could be used to explain the conductivity maximum at $x = 0.10$ and activation energy minimum at $x = \sim 0.05$. The dopant content for the conductivity maximum is closely related to the charge difference between the dopant ions and host ions. A large charge difference should give a conductivity maximum at a smaller dopant level because of the quick increase in the number of oxygen vacancies.[34] In this work, when the defect associations reached a maximum, the strong interactions among these defect associations in the pseudocubic lattice probably ordered the two oxygen vacancies localized near to the adjacent Mg^{2+} ions, while the rest of the oxygen vacancies became delocalized and therefore to some extent mobile, which probably accounts for the increase in conductivity and decrease in activation energy above $x = 0.25$.

For the cubic phase, the conductivity reached a maximum, while activation energy gave a minimum at a lower dopant content of $x = \sim 0.10$, which could be mainly due to the variation of relative content of oxygen vacancies Vö and defect associations $\{Mg_{Nb}'''Vö\}$ as those for the pseudocubic. When the dopant content was increased beyond $x = 0.15$, part of the defect associations $\{Mg_{Nb}'''Vö\}$ localized near Mg^{2+} became unstable under the strong interactions among the defect associations, leading to a transition of order–disorder for the defect associations $\{Mg_{Nb}'''Vö\}$, which accounted for the gradual increases in activation energy and ionic conductivity.

Conclusions

This paper reports on the preparation of oxide ion conductors $KNb_{1-x}Mg_xO_{3-\delta}$ ($x = 0.05–0.30$) by high temperature and pressure. There are clear advantages of the high-temperature and -pressure approach for single-step preparation of single-phase perovskites with Nb^{5+}/Mg^{2+} distributed at B-sites; e.g., the conditions suppress the formation of intermediate phases over those prepared by other synthetic routes. All $KNb_{1-x}Mg_xO_{3-\delta}$ ($x = 0.05–0.30$) samples were kinetically stable orthorhombic perovskite phase at ambient pressure. The lattice volume increased nonlinearly with the dopant content due to the substitution of Nb^{5+} by Mg^{2+}, variation of the relative content of oxygen vacancy and defect associations, and increase of lattice disorder of Nb^{5+}/Mg^{2+} at B-sites. At higher temperatures, $KNb_{1-x}Mg_xO_{3-\delta}$ exhibited phase transitions from orthorhombic to tetragonal, to pseudocubic, and then to cubic. Under the present experimental conditions, the conduction in the samples showed primarily ionic with extremely weak contributions from the p-type holes. $KNb_{0.90}Mg_{0.10}O_{2.85}$ was determined to be a highly conductive phase. The total conductivity data for $KNb_{1-x}Mg_xO_{3-\delta}$ gave two separated linear ranges with different variations of conductivity and activation energy, associating with the relative content of the oxygen vacancies and defect associations, and the order–disorder transitions.

Acknowledgment. This project is financially supported by a fund from NSFC (19804005) (L.L.). G.L. thanks Dr. S. M. Haile at Caltech for access to oxygen partial pressure impedance measurements.

CM020582E

(42) Tien, T. Y.; Subbarao, E. C. *J. Chem. Phys.* **1963**, *39*, 1041.
(43) Goodenough, J. B.; Ruiz-Diaz, J. E.; Zhen, Y. S. *Solid State Ionics* **1990**, *44*, 21.
(44) (a) Kendall, K. R.; Navas, C.; Thomas, J. K.; zur Loye, H. C. *Solid State Ionics* **1995**, *82*, 215. (b) Goodenough, J. B.; Manthiram, A.; Kuo, J. F. *Mater. Chem. Phys.* **1993**, *35*, 221.

APPLIED CHEMISTRY

Conversion of a Used Poly(ethylene terephthalate) Bottle into Oxalic Acid and Terephthalic Acid by Oxygen Oxidation in Alkaline Solutions at Elevated Temperatures

Toshiaki Yoshioka,* Masaki Ota, and Akitsugu Okuwaki

Department of Applied Chemistry, Graduate School of Engineering, Tohoku University, Aramaki Aza Aoba 07, Aoba-ku, Sendai 980-8579, Japan

Chemical recycling of poly(ethylene terephthalate) (PET) flakes to terephthalic acid (TPA) and oxalic acid was investigated by simultaneous hydrolysis and oxygen oxidation in concentrated NaOH. PET flakes were hydrolyzed to sodium terephthalate and ethylene glycol (EG) in NaOH solutions before oxygen introduction. Because sparingly soluble sodium terephthalate in concentrated NaOH solutions was stable to the oxidation, the TPA yield was approximately 100 mol % under all conditions. In contrast, EG was oxidized to oxalate and CO_2, and the maximum oxalic acid yields were 60.7 mol % using flakes from the bodies of transparent bottles and 65.9 and 71.4 mol % using commercial transparent flakes and a mixture of transparent and green flakes from PET, respectively. If the gate fee (83.3¢/kg of PET) can be obtained as a waste PET recycling subsidy from the Japanese government, this process will generate a profit of $1,134.20 for the treatment of 1000 kg of PET as a net profit for 70 mol % of oxalic acid yield.

1. Introduction

Recently, disposal of waste materials has come into focus as an environmental problem that affects everyone. Setting up intermediate treatment plants, such as incinerators, or obtaining the land for reclamation is difficult. Poly(ethylene terephthalate) (PET) resin is inexpensive, light, transparent, tough, and easy to process and, as a result, is used not only in several industries but also in daily life. In particular, PET is used for beverage bottles, the demand for which is increasing year by year. In 2000, domestic production of PET bottles reached 401 000 tons in Japan.

Currently used PET is recycled chemically by solvolysis such as methanolysis[1−3] and glycolysis.[4−8] In these methods, PET is converted to dimethyl terephthalate (DMT) and ethylene glycol (EG) and/or a monomer such as dihydroxyethyl terephthalate (DHET) and a low-molecular-weight oligomer.

Terephthalic acid (TPA) and EG can be obtained by hydrolysis[9−14] in acidic and basic conditions. The hydrolysis rate of PET in water was measured from 60 to 175 °C by Golike and Lasoski[15] and from 260 to 285 °C by Campanelli et al.[16] Zimmerman and Kim[17] investigated the effect of metal catalysts, such as Sb, Zn, Mn/Sb/Pb, Zn/Sb, and Ca/Sb, on the hydrolysis from 280 to 300 °C. Sanders and Zeronian,[18] Schlts and Lhymn,[19] and Dave et al.[20] studied the alkaline hydrolysis of PET fiber in a PET/glass composite with respect to the stabilization of PET.

A number of researchers have studied the chemical recycling process of PET by alkalis in anhydrous conditions in the presence of alcohol or glycol and aprotic solvent to recover the monomeric components and sodium terephthalate.[21−23] Paszun and Spychaj have presented a review of investigations of PET chemical recycling.[24] However, the development of a new process to promote the recycling of waste PET by recovering more valuable chemicals is necessary. One strategy is the conversion of TPA and EG units in PET into more expensive chemicals during the recycling process. Oxalic acid, which not only is used as a semifine raw chemical but also is thought to be a raw chemical of oxamide ($(CONH_2)_2$, which is a slow-releasing nitrogenous fertilizer[25]), is produced from EG.

In the present study, used PET flakes were oxidized by oxygen in NaOH solutions, PET was hydrolyzed to TPA and EG, and only EG was oxidized simultaneously to oxalic acid. The optimum conditions under which to obtain TPA and oxalic acid from used PET flakes are reported.

2. Experimental Section

2.1. Materials. Additive-free PET flakes (0.4 × 5 × 5 mm) were prepared from the bodies of used transparent PET bottles and did not contain crystallized cap or bottom parts. The average molecular weight was approximately 30 000. In the experiment of section 3.3, PET flakes were prepared from both the bodies and crystallized cap parts of used transparent bottles and green bottles. The flakes were washed in water under ultrasonic irradiation for 10 min. All chemicals used were reagent grade.

2.2. Oxygen Oxidation in Alkaline Solutions. A mixture of 0.67 g of PET flakes, 20 cm^3 of water, and a

10.1021/ie010563z CCC: $25.00
Published on Web 01/28/2003

prescribed amount of NaOH was placed in a poly(tetrafluoroethylene) (PTFE) beaker (wall thickness of 2 mm, o.d. of 30 mm, and depth of 120 mm). The PTFE beaker was placed into a 316 stainless steel autoclave of 100 cm^3 in volume which was fitted with a magnet-driven stirrer. The air was then replaced with N_2, and the beaker was heated to 160−250 °C at 3 °C/min in an electric furnace. After reaching the prescribed temperature, the oxygen oxidation was started by pressurized oxygen at 1−10 MPa, and this time was defined as the reaction start. The time at which the autoclave was removed from the electric furnace was defined as the reaction end time, after which air cooling of the autoclave to room temperature was performed compulsorily. The product in the beaker was washed out with water, filtrated using a 1G4 glass filter, diluted to 500 cm^3, and then stocked as a reaction solution for analysis.

2.3. Analysis and Definition. Sodium terephthalate in the reaction solution was precipitated as TPA by the addition of 2 M H_2SO_4, filtered with a glass filter, and washed with cold water. The TPA on the glass filter was dried at 105 °C for 2 h in an oven.

After removal of sodium ions in the reaction solution using a cation-exchange column, the amount of oxalate ion was determined by ion chromatography (Dionex Quic; columns AG4 and AS4) and that of EG and other C_2 substrates was determined by high-performance liquid chromatography (column, Shodex Ionpac 810P-KC 811; detector, RI; 30 °C) and total organic carbon analysis (Shimadzu TOC 5000). The amount of CO_2 was determined by gas chromatography (Hitachi 164; column, stainless steel−silica; detector, TCD; 40 °C), after evolution of CO_2 by adding 6 M H_2SO_4.

The degree of weight loss and yields of terephthalate, EG, oxalate, and CO_2 are defined as follows:

$$\text{degree of weight loss (wt \%)} = \{(W_0 - W_t)/W_0\} \times 100 \quad (1)$$

$$\text{TPA yield (mol \%)} = (m_{TPA}/m_{PET}) \times 100 \quad (2)$$

$$\text{EG yield (mol \%)} = (m_{EG}/m_{PET}) \times 100 \quad (3)$$

$$\text{oxalic acid yield (mol \%)} = (m_{ox}/m_{PET}) \times 100 \quad (4)$$

$$\text{CO}_2\text{ yield (mol \%)} = (m_{CO_2}/2m_{PET}) \times 100 \quad (5)$$

where W_0 is the initial weight of PET, W_t is the weight of the PET residue, m_{PET} is the initial number of moles of PET-based monomeric units, and m_{TPA}, m_{EG}, m_{ox}, and m_{CO_2} are moles of TPA, EG, oxalic acid, and CO_2, respectively.

3. Results and Discussion

3.1. Effects of Reaction Conditions on the Yields of TPA, Oxalic Acid, and CO_2. 3.1.1. Oxidation Curve. A typical oxidation curve of PET flakes is shown in Figure 1. Both TPA and EG yields were quantitative at 0 h, which indicates that the hydrolysis of PET flakes progressed satisfactorily. The TPA yield remained quantitative, indicating that PET was hydrolyzed easily to sodium terephthalate and EG before oxygen introduction (eq 6). In contrast, EG was oxidized rapidly to oxalic acid and CO_2 until 1 h after the oxygen introduction. The oxalic acid yield increased linearly, having a small slope corresponding to a decrease of the EG yield after

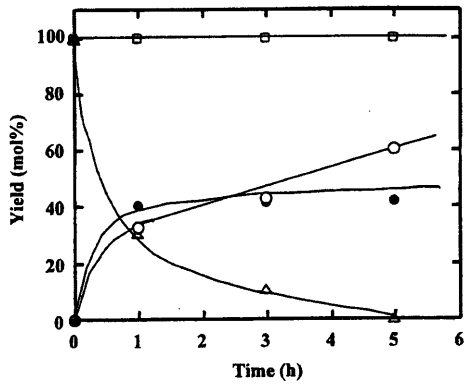

Figure 1. Effect of the reaction time on the TPA (□), EG (△), oxalate (○), and CO_2 (●) yields in 27.5 M NaOH at 250 °C and 5 MPa P_{O_2}.

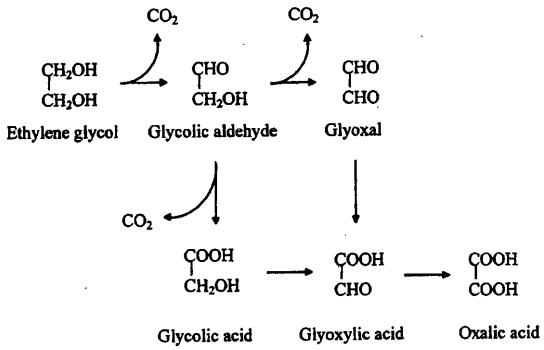

Figure 2. Effect of the NaOH concentration on the TPA (□), EG (△), oxalic acid (○), and CO_2 (●) yields at 250 °C and 5 MPa P_{O_2} for 5 h.

1 h. The CO_2 yield increased little after 1 h, indicating that oxalic acid is formed from released EG and primarily that CO_2 may be produced in the very beginning of the oxidation of EG.

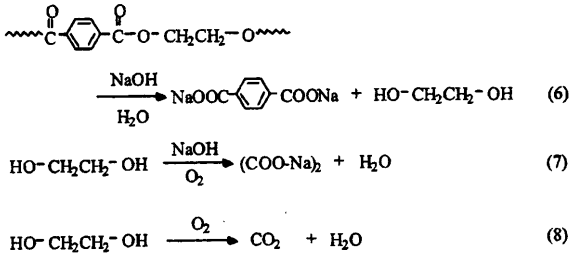

Some chemicals, such as glycolic aldehyde, glyoxal, glycolic acid, and glyoxylic acid, are produced until the formation of oxalic acid in the oxidation of EG. For example, when each substrate was oxidized as a starting material, oxalic acid was quantitatively formed from glyoxal, glycolic acid, and glyoxylic acid without the formation of CO_2. In contrast, CO_2 and oxalic acid were formed from EG and glycolic aldehyde. Therefore, in the oxidation method of EG to oxalic acid, the majority of CO_2 may be produced in the beginning of the oxidation as shown in Figure 2.

3.1.2. NaOH Concentration. The effect of NaOH concentration on TPA, EG, oxalic acid, and CO_2 yields is shown in Figure 3. EG was not measured until reaching 27.5 mol/kg_{H_2O} NaOH due to the complete oxidation and the EG yield increased beyond 27.5 mol/

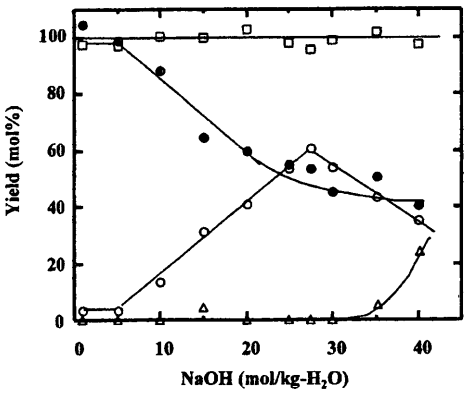

Figure 3. Effect of the NaOH concentration on the TPA (□), EG (△), oxalic acid (○), and CO_2 (●) yields at 250 °C and 5 MPa P_{O_2} for 5 h.

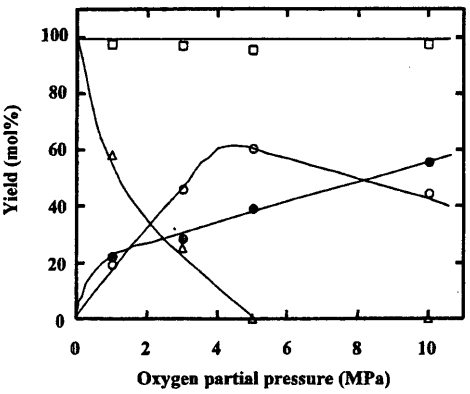

Figure 4. Effect of the oxygen partial pressure on the TPA (□), EG (△), oxalic acid (○), and CO_2 (●) yields in 27.5 M NaOH at 250 °C for 5 h.

kg_{H_2O}. Oxalic acid was formed just below 5 mol/kg_{H_2O} NaOH, indicating that the base-catalyzed oxygen oxidation does not work because free alkali was absent because of the neutralization of NaOH using TPA and CO_2. The oxalic acid yield increased linearly from 3.5 mol % at 5 mol/kg_{H_2O} NaOH to 60.7 mol % at 27.5 mol/kg_{H_2O} NaOH. The sharp linear increase in the oxalic acid yield indicates that oxalic acid is formed by the base-catalyzed oxygen oxidation of EG because the oxidation rate is proportional to the first-order function of the OH^- concentration.[26]

Over 27.5 mol/kg_{H_2O} NaOH, the oxalic acid yield decreased whereas the EG yield increased remarkably. This is caused by lowering the rate of oxidation of EG because of the decrease in the solubility of oxygen in concentrated NaOH solutions, and some mass transfer, such as the transfer of oxygen, controlled the base-catalyzed oxygen oxidation.

3.1.3. Oxygen Partial Pressure. The effect of the oxygen partial pressure on TPA, EG, oxalic acid, and CO_2 yields in 27.5 mol/kg_{H_2O} NaOH is shown in Figure 4. The TPA yield was also quantitative and was not affected by the oxygen partial pressure. The EG yield was quantitative at 0 MPa P_{O_2} but decreased rapidly by 0 mol % at 5 MPa with increasing oxygen partial pressure. In contrast, the oxalic acid yield increased with increasing oxygen partial pressure up to 5 MPa but decreased at 10 MPa, indicating the possible production of less oxalic acid because of a stronger oxidation of EG.

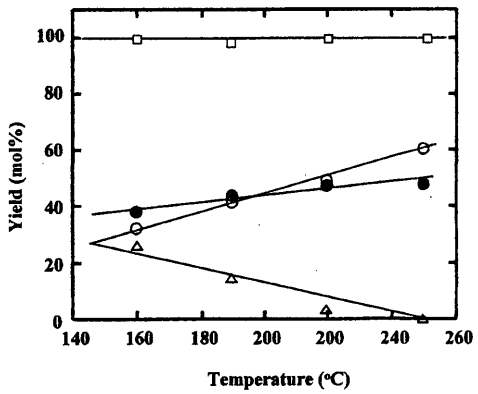

Figure 5. Effect of the reaction temperature on the TPA (□), EG (△), oxalic acid (○), and CO_2 (●) yields in 27.5 M NaOH at 5 MPa P_{O_2} for 5 h.

Table 1. Oxalic Acid Yield from Various PET Flakes (NaOH, 27.5 M; P_{O_2}, 5 MPa; 250 °C; 5 h; 1000 rpm)

type	yield (mol %)
PET flakes (clear type, body)	60.7
PET flakes (clear type, cap and body)	65.9
PET flakes (clear and green types, cap and body)	71.4

3.1.4. Temperature. The effect of the reaction temperature on TPA, EG, oxalic acid, and CO_2 yields is shown in Figure 5. TPA was always produced quantitatively. The EG yield decreased, but oxalic acid and CO_2 yields increased linearly with increasing temperature. The slope of the formation of CO_2 was smaller than that of oxalic acid, which means that the selectivity of oxalic acid formation is advantageous at higher temperatures ranging from 160 to 250 °C. However, because the temperature dependence is low, the base-catalyzed oxygen oxidation appears to be controlled by mass transport processes, as shown those in section 3.1.2. Thus, detailed kinetics of the oxidation of EG will be required from this point on.

3.1.5. Effect of Copper(II) Oxide. The oxygen oxidation of acetate in a NaOH solution was reported to be accelerated by transition-metal oxide catalysts such as CuO and NiO,[27] and the yield of oxalic acid is increased. Similarly, the effect of CuO can be held responsible for the improvement in the yield of oxalic acid in this reaction. The catalytic effect of CuO was observed to some extent and the yield of oxalic acid increased from 60.7 to 65.3 mol % in the presence of 5 wt % CuO powder on PET flakes under 250 °C, 27.5 mol/kg_{H_2O} NaOH, 5 MPa P_{O_2}, and 5 h.

3.2. Effect of the Type of PET Flakes Obtained from Postconsumer PET Bottles. Commercial PET flakes from used bottles contain the hard parts of the cap and bottom, the crystallinity of which is higher than that of the body. Two types of flakes containing the hard parts were used as samples. One sample was produced from clear-type bottles, and the other was produced from a mixture of clear and green bottles. These samples were oxidized in 27.5 M NaOH at 250 °C and an oxygen partial pressure of 5 MPa for 5 h. The resulting product solutions were colorless even for the mixture type, indicating that the green dyestuff in PET bottles was sufficiently oxidized. The results are shown in Table 1. The oxalic acid yield was 65.9 mol % for the clear-type sample and 71.4 mol % for the mixture-type sample. These yields were higher than 60.7 mol % for the PET flakes made of the body alone. The reasons for this

Table 2. Total Balance of the Alkaline Hydrolysis–Oxidation Process of Waste PET Bottles (Oxalic Acid Yield = 70 mol %)

	raw materials				product		byproduct
	PET	NaOH	H_2SO_4	O_2	TPA	oxalic acid	Na_2SO_4
molar ratio	1	4	2	4	1	0.7	2
weight ratio	192.18	160.00	196.18	64.00	166.14	63.03	284.10
weight (kg)	1,000	832	1,021	333	865	328	1478
unit price (¢/kg)[a]	−83.3	37.5	19.1	50.1	104.2	345.8	50.1
sum ($)	−833.0	312.0	196.2	166.8	901.3	1134.2	740.5
total ($)			−158.9			1134.2	

[a] Trust money for recycling of waste PET bottles: 83.3¢/kg (1$ = ¥120, 2000 in Japan).

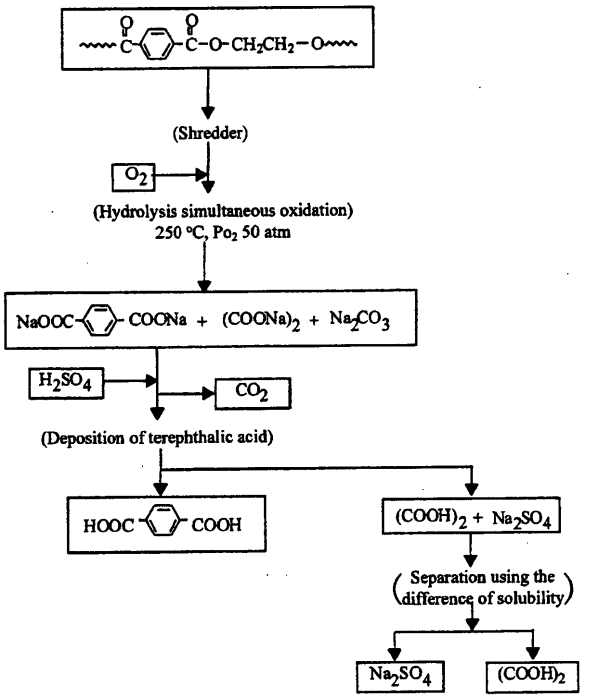

Figure 6. Alkali hydrolysis–oxidation process flow of waste PET bottles.

remain unclear, but the selectivity is thought to have produced oxalic acid according to the effect of base-catalyzed oxygen-oxidation increases at the time of EG release because the rate of hydrolysis of the cap and bottom parts of high crystallinity is too slow. The increase in the oxalic acid yield for green bottles is due to the pigment working as a catalyst. This result indicates that pretreatments such as a water washing and separation between transparent and green bottles are not necessary.

3.3. Chemical Recycling Process for Waste PET. Figure 6 is a flow sheet of a feedstock recycling process for waste PET using simultaneous hydrolysis and oxygen oxidation in alkaline solution, and Table 2 is a balance sheet based only on raw material costs. In this process, the main products are TPA, oxalic acid, and sodium carbonate, with sodium sulfate as a byproduct. Conversion into TPA and oxalic acid as a free acid adding sulfuric acid is necessary because these products are obtained as sodium salts. In contrast, CO_2 was precipitated as Na_2CO_3 using sodium terephthalate and sodium oxalate. However, this can be released as gaseous CO_2 by adding sulfuric acid, and consequently Na_2SO_4 is precipitated. Na_2SO_4 is thus produced as a byproduct. We can obtain the gate fee (83.3¢/kg of PET) as a waste PET recycling subsidy from the Japanese government. Therefore, this process will be able to generate a profit of $1,293.10 for the treatment of 1000 kg of PET as a net profit for 70 mol % of oxalic acid yield. Moreover, the market for TPA, oxalic acid, and Na_2SO_4 with be served.

Acknowledgment

The authors thank Ueyama Works, for supplying the PET flakes.

Literature Cited

(1) Vereinigte Glanzstoff Fabriken A.G. Process for the Conversion of Polyethylene Terephthalate into Dimethyl Terephthalate. Br. Patent 755,071, 1956.

(2) E. I. du Pont de Nemours and Co. Improvements in the Preparation of High Quality Dimethyl Terephthalate. Br. Patent 784,248, 1957.

(3) Grushke, H.; Hammerschick, W.; Nauchem, B. Process for Depolymerizing Polyethylene Terephthalate to Terephthalic Acid Dimethyl Ester. U.S. Patent 3,403,115, 1968.

(4) MacDowell, J. T.; Klusion, N. C. Reclaiming Linear Terephthalate Polyesters. U.S. Patent 3,222,999, 1965.

(5) Vaidya, U. R.; Nadlkarni, V. M. Unsaturated Polyesters from PET Waste: Kinetics of Polycondensation. *J. Appl. Polym. Sci.* **1987**, *34*, 235–245.

(6) Vaidya, U. R.; Nadlkarni, V. M. Polyester Polyols for Polyurethanes from PET Waste: Kinetics of Polycondensation. *J. Appl. Polym. Sci.* **1988**, *35*, 775–785.

(7) Trowell, J. T. Polyols from Scrap Polyethylene Terephthalate and Dimethyl Terephthalate Process Residue. U.S. Patent 4,720,571, 1988.

(8) Gintis, D. Glycolytic Recycle of Poly(ethylene terephthalate) (PET). *Macromol. Chem., Macromol. Symp.* **1992**, *57*, 185–190.

(9) Brown, G. E., Jr.; O'Brien, R. C. Method for Recovery of Trephthalic Acid and Ethylene Glycol from Polyester Materials. U.S. Patent 3,952,053, 1976.

(10) Pusztaseri, S. F. Method for Recovery of Trephthalic Acid from Polyester Scrap. U.S. Patent 4,355,175, 1987.

(11) Yoshioka, T.; Sato, T.; Okuwaki, A. Hydrolysis of Waste PET by Sulfuric Acid at 150 °C for a Chemical Recycling. *J. Appl. Polym. Sci.* **1994**, *52*, 1353–1355.

(12) Yoshioka, T.; Okayama, N.; Okuwaki, A. Kinetics of Hydrolysis of PET powder in Nitric Acid by a Modified Shrinking-Core Model. *Ind. Eng. Chem. Res.* **1998**, *37*, 336–340.

(13) Yoshioka, T.; Motoki, T.; Okuwaki, A. Kinetics of Hydrolysis of Poly(ethylene terephthalate) powder in Sulfuric Acid by a Modifified Shrinking-Core Model. *Ind. Eng. Chem. Res.* **2001**, *40*, 75–79.

(14) Mandoki, J. W. Depolymerization of Condensation Polymer. U.S. Patent 4,605,762, 1986.

(15) Golike, R. C.; Lasoski, S. W., Jr. Kinetics of Hydrolysis of Polyethylene Terephthalate Films. *J. Phys. Chem.* **1960**, *64*, 895–898.

(16) Campanelli, J. R.; Kamal, M. R.; Cooper, D. G. A Kinetics Study of the Hydrolytic Degradation of Polyethylene Terephthalate at High Temperatures. *J. Appl. Polym. Sci.* **1993**, *48*, 443–451.

(17) Zimmerman, H.; Kim, N. T. Investigation on Thermal and Hydrolytic Degradation of Poly(ethylene terephthalate). *Polym. Eng. Sci.* **1980**, *20*, 680–683.

(18) Sanders, E. M.; Zeronian, S. H. An Analysis of the Moisture-Related Properties of Hydrolyzed Polyester. *J. Appl. Polym. Sci.* **1982**, *27*, 4477−4481.

(19) Schlts, J. M.; Lhymn, C. Stress-Rupture Lifetime of a Poly(ethylene terephthalate)/Glass Composite Under an Alkaline Solution Environment. *Polym. Compos.* **1984**, *7*, 208−214.

(20) Dave, J.; Kumar, R.; Stivastave, H. C. Studies on Modification of Polyester Fabrics I: Alkaline Hydrolysis. *J. Appl. Polym. Sci.* **1987**, *33*, 455−477.

(21) Tindall, G. W.; Perry, R. L. Esters Hydrolysis and Depolymerization of Polyesters and Polycarbonate Polymer. U.S. Patent 5,045,122, 1991.

(22) Tindall, G. W.; Perry, R. L.; Spaugh, S., Jr. Depolymerization of Substantially Amorphous Polyesters. U.S. Patent 5,328,982, **1994**.

(23) Oku, A.; Hu, L. C.; Yamada, E. Alkali Decomposition of Poly(ethylene terephthalate) with Sodium Hydroxide in Nonaqueous Ethylene Glycol: A Study on Recycling of Terephthalic Acid and Ethylene Glycol. *J. Appl. Polym. Sci.* **1997**, *63*, 595−598.

(24) Paszun, D.; Spychaj, T. Chemical Recycling of Poly(ethylene terephthalate). *Ind. Eng. Chem. Res.* **1997**, *36*, 1373−1383.

(25) Okuwaki, A.; Okabe, T. Development of a New Route to Oxamide from Coal and Ammonia. *Trends Inorg. Chem.* **1991**, *2*, 145−158.

(26) Wakabayashi, T.; Okuwaki, A. Oxidation of Coals in Liquid Phases. Kinetics of the Base-Catalyzed Oxidation of Acetate Ion by Oxygen at Elevated Temperatures. *Bull. Chem. Soc. Jpn.* **1988**, *61*, 4329−4334.

(27) Ichinose, S.; Okuwaki, A. Oxidation of Coals in Liquid-Phase X. Mechanism of the Cleavage of Benzenecarboxylic Acid to Oxalic Acid and Carbon Dioxide by the Base-Catalyzed Oxygen-Oxidation. *Bull. Chem. Soc. Jpn.* **1990**, *63*, 159−165.

Received for review June 26, 2001
Revised manuscript received December 16, 2002
Accepted December 21, 2002

IE010563Z

PERGAMON

Water Research 37 (2003) 1545–1550

WATER RESEARCH

www.elsevier.com/locate/watres

New method of treating dilute mineral acids using magnesium–aluminum oxide

Tomohito Kameda[a,b,*], Fumiko Yabuuchi[a], Toshiaki Yoshioka[a], Miho Uchida[a], Akitsugu Okuwaki[a]

[a] *Dapartment of Applied Chemistry, Graduate School of Engineering, Tohoku University, Aoba 07, Aoba-ku, Sendai 980-8579, Japan*
[b] *Institute of Multidisciplinary Research for Advanced Materials, Tohoku University, 1, 1 Katahira, 2-Chome, Aoba-ku, Sendai 980-8577, Japan*

Received 21 December 2001; received in revised form 15 July 2002; accepted 25 July 2002

Abstract

Mineral acids, such as H_3PO_4, H_2SO_4, HCl, and HNO_3, were treated with magnesium–aluminum oxide (Mg–Al oxide), which behaved as a neutralizer and fixative of anions. Anion removal increased with increasing Mg–Al oxide quantity, time, Mg/Al molar ratio, and initial acid concentration. Up to 95% removal of anions was achieved in 0.5 N acids using a stoichiometric quantity of $Mg_{0.80}Al_{0.20}O_{1.10}$ for H_3PO_4, 1.75 stoichiometric quantities for H_2SO_4, or 2.5 stoichiometric quantities for HCl or HNO_3 at 20°C over a period of 6 h. The final solutions were found to have a pH in the range of 8–12. Selectivity of acid removal was found to follow the following order: $H_3PO_4 > H_2SO_4 > HCl > HNO_3$. The equivalent of acid removal per 1 g of Mg–Al oxide decreased as the Mg/Al molar ratio of Mg–Al oxide increased.

Keywords: Hydrotalcite; Mg–Al oxide; Dilute mineral acid; Treatment; Intercalation

1. Introduction

In Japan, neutralization is the preferred method of treating acid drainage and exhaust gas. Exhaust gas containing hydrogen chloride generated by incinerators is most commonly treated by dry or wet neutralization methods [1]. The dry method involves converting hydrogen chloride into calcium chloride by blowing slaked lime into the exhaust gas. The wet method uses Venturi scrubbers to wash the exhaust gas, and neutralizes the obtained hydrochloric acid with a caustic soda solution. On the other hand, plating plants generate many acids, including hydrochloric, nitric, sulfuric, and hydrofluoric acid [2]. In addition, waste phosphoric, perchloric, and acetic acids are generated in the process of chemical and electropolishing [2]. These waste acids corrode concrete and drainpipe if they are discharged into drain. Accordingly, the acids must be also treated by neutralization method.

However, neutralization treatment method causes problem of newly produced drainage. For example, the resulting calcium chloride in the dry method is discharged into landfill sites, generating high concentrations of saline leachates. Unless the leachates are treated, severe damage from salt to the surrounding water environment results [3,4]. In the wet method, sewerage must be used to treat the resulting sodium chloride drainage. The neutralization treatment method also generates problems of the high costs of neutralizers, and difficulty in the recovery and reuse of anions. As a result, new waste acids treatment methods, which can solve the above problems, have been desired.

Hydrotalcite (HT) ($[Mg^{2+}_{1-x}Al^{3+}_x(OH)_2](A^{n-})_{x/n}\cdot mH_2O$: $0.20 \leqq x \leqq 0.33$) is a layered double hydroxide with anion

*Corresponding author. Institute of Multidisciplinary Research for Advanced Materials, Tohoku University, 1, 1 Katahira, 2-Chome, Aoba-ku, Sendai 980-8577, Japan. Tel.: +81-22-217-5148; fax: +81-22-217-5148.

E-mail address: kameda@tagen.tohoku.ac.jp (T. Kameda).

0043-1354/03/$ - see front matter
PII: S0043-1354(02)00374-3

exchange properties [5–15]. The crystal structure consists of positively charged brucite-like octahedral hydroxide layers, which are neutralized by the interlayer anion, and water molecules occupy remaining interlayer space. When CO_3^{2-} intercalates into HT (CO_3-HT), magnesium–aluminum oxide (Mg–Al oxide) is obtained when the CO_3-HT is heated to 450–800°C, as expressed in Eq. (1) [16–19].

$$Mg_{1-x}Al_x(OH)_2(CO_3)_{x/2} \rightarrow Mg_{1-x}Al_xO_{1+x/2} + x/2CO_2 + H_2O. \quad (1)$$

The Mg–Al oxide can in turn intercalate anions in solution, reconstructing the HT structure, as expressed in Eq. (2) [16–19].

$$Mg_{1-x}Al_xO_{1+x/2} + x/nA^{n-} + (1 + x/2)H_2O \rightarrow Mg_{1-x}Al_x(OH)_2A_{x/n} + xOH^-. \quad (2)$$

Many studies on this type of reaction for neutral saline solutions, such as NaCl, Na_2SO_4, $NaNO_3$, and Na_2HPO_4 solutions, have shown that the ease with which the anion intercalates increases with increasing its charge density [17–19]. The important feature of the reaction is the release of OH^- with the intercalation of anion in solution. Accordingly, difficulty arises when Mg–Al oxide is applied to the treatment of neutral waste saline solution, due to the strong alkalinity of the resulting solution. Additionally, the quantitative removal of anion is prevented by the intercalation of the released OH^- into Mg–Al oxide [19]. Considering these properties, we evaluated the suitability of using Mg–Al oxide as both a neutralizer and a fixative of anions in the treatment of waste acids.

In this study, dilute solutions of the mineral acids H_3PO_4, H_2SO_4, HCl, and HNO_3 were treated with Mg–Al oxide. The effects of Mg–Al oxide quantity, time, Mg/Al molar ratio, and initial acid concentration were examined in detail.

2. Materials and methods

All reagents used were purchased from Kanto Chemical Co. Inc. CO_3-HTs were prepared by a coprecipitation reaction described previously [20]. $Mg(NO_3)_2$ and $Al(NO_3)_3$ solutions with Mg/Al molar ratios of 2.0, 3.0, or 4.0 were added to 1.0 M Na_2CO_3 solution. The resulting solutions were kept at a pH of 10 by adding a solution of 2.0 M NaOH. After stirring and aging, the product was filtered, washed, dried and calcined at 500°C for 1 h. The CO_3-HTs prepared were $Mg_{0.67}Al_{0.33}(OH)_2(CO_3)_{0.16} \cdot 0.60H_2O$, $Mg_{0.75}Al_{0.25}(OH)_2(CO_3)_{0.13} \cdot 0.61H_2O$, and $Mg_{0.80}Al_{0.20}(OH)_2(CO_3)_{0.10} \cdot 0.78H_2O$, and the calcined products were $Mg_{0.67}Al_{0.33}O_{1.17}$, $Mg_{0.75}Al_{0.25}O_{1.13}$, and $Mg_{0.80}Al_{0.20}O_{1.10}$, respectively.

Ten milliliters of nitric, hydrochloric, sulfuric, or phosphoric acids ranging from 0.1 to 1.0 N were mixed with 0.5–2.5 stoichiometric quantities of $Mg_{1-x}Al_xO_{1+x/2}$ ($x = 0.20$, 0.25, 0.33), as described in Eqs. (3)–(6). These solutions were placed in 50-ml screw-top tubes and shaken at 20°C for 0.2–24 h before being filtered. In Eqs. (5) and (6), the anionic species of phosphate and sulfate ions were estimated as divalent anion considering the dissociative state of H_3PO_4 or H_2SO_4.

$$Mg_{1-x}Al_xO_{1+x/2} + xHNO_3 + (1 - x/2)H_2O \rightarrow Mg_{1-x}Al_x(OH)_2(NO_3)_x, \quad (3)$$

$$Mg_{1-x}Al_xO_{1+x/2} + xHCl + (1 - x/2)H_2O \rightarrow Mg_{1-x}Al_x(OH)_2(Cl)_x, \quad (4)$$

$$Mg_{1-x}Al_xO_{1+x/2} + x/2H_2SO_4 + (1 - x/2)H_2O \rightarrow Mg_{1-x}Al_x(OH)_2(SO_4)_{x/2}, \quad (5)$$

$$Mg_{1-x}Al_xO_{1+x/2} + x/2H_3PO_4 + (1 - x/2)H_2O \rightarrow Mg_{1-x}Al_x(OH)_2(HPO_4)_{x/2}, \quad (6)$$

Two 5-ml portions of 0.5 N acids and stoichiometric quantities of $Mg_{0.80}Al_{0.20}O_{1.10}$ were also shaken at 20°C for 6 h. The pH of the filtrate was measured and the concentration of anions determined using ion chromatography (DIONEX QIC). The precipitates were identified by X-ray diffraction (XRD) using a Rigaku Denki Geiger-flex 2013 diffractometer employing Ni-filtered Cu K_α radiation at 30 kV and 15 mA (scanning rate of 2°/min).

3. Results and discussion

3.1. Mg–Al oxide and acid reactions

Fig. 1 shows the XRD patterns of products following a 6-hour reaction of each acid and 1.75 stoichiometric quantities of $Mg_{0.80}Al_{0.20}O_{1.10}$. Reconstruction of the HT structure from Mg–Al oxide was obtained without by-products at all acids. Even in the case of H_3PO_4, phosphate-HT was produced without $AlPO_4$ or $Mg_3(PO_4)_2$ formation. Table 1 shows the unit layer distance, d_{006}, and the interlayer distance of the products. The interlayer distance was estimated by subtracting 4.77 Å of the brucite layer from the unit layer distance. These interlayer distances were almost similar to that of HT intercalating each anion [17], suggesting that anions were not adsorbed on the surface of HT, but intercalated into the interlayer of HT.

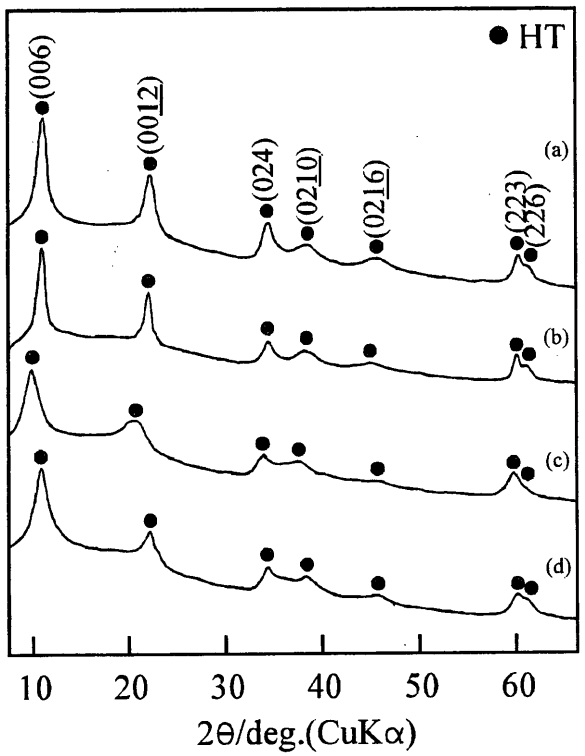

Fig. 1. XRD patterns of products following a 6-hour reaction of each acid and 1.75 stoichiometric quantities of $Mg_{0.80}Al_{0.20}O_{1.10}$. (a) 0.5 M HNO_3, (b) 0.5 M HCl, (c) 0.25 M H_2SO_4, (d) 0.25 M H_3PO_4.

Table 1
The unit layer distance, d_{006}, and the interlayer distance of the products

Acid	Unit layer distance (d_{006})	Interlayer distance (Å)
(a) HNO_3	8.17	3.40
(b) HCl	8.15	3.38
(c) H_2SO_4	8.40	3.63
(d) H_3PO_4	8.22	3.45

3.2. *Effects of Mg–Al oxide quantity, time, Mg/Al molar ratio and initial acid concentration*

Fig. 2 shows the effect of $Mg_{0.80}Al_{0.20}O_{1.10}$ quantity on anion removal. Anion removal increased with increasing $Mg_{0.80}Al_{0.20}O_{1.10}$ quantity. Greater than 95% anion removal was achieved using a stoichiometric quantity of $Mg_{0.80}Al_{0.20}O_{1.10}$ for H_3PO_4, 1.75 stoichiometric quantities for H_2SO_4, and 2.5 stoichiometric quantities for HCl or HNO_3. Removal of SO_4^{2-}, Cl^-, or NO_3^- ranged between 45% and 70% using a single stoichiometric quantity, due to the formation of OH-HT, as described in Eq. (8), following the release of

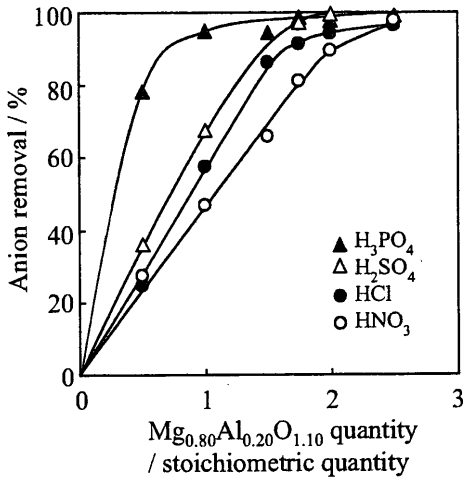

Fig. 2. Effect of $Mg_{0.80}Al_{0.20}O_{1.10}$ quantity on anion removal (time: 6 h, initial acid concentration: 0.5 N).

OH^-, as described in Eq. (7).

$$Mg_{0.80}Al_{0.20}O_{1.10} + 0.20/nA^{n-} + 1.10H_2O \rightarrow Mg_{0.80}Al_{0.20}(OH)_2(A)_{0.20/n} + 0.20OH^-, \quad (7)$$

where A^{n-}: SO_4^{2-}, Cl^-, NO_3^-,

$$Mg_{0.80}Al_{0.20}O_{1.10} + 1.10H_2O \rightarrow Mg_{0.80}Al_{0.20}(OH)_2(OH)_{0.20}. \quad (8)$$

In contrast, phosphate ion was removed above the theoretical value (50%) when 0.5 stoichiometric quantity was used, with the resulting pH being 7.0. This implies that the anionic species formed are a mixture of HPO_4^{2-} (39%) and $H_2PO_4^-$ (62%) in consideration of the dissociation constants of phosphate ($pK_1 = 2.15$, $pK_2 = 7.20$, $pK_3 = 12.33$). This indicates that $H_2PO_4^-$ besides HPO_4^{2-} was intercalated into $Mg_{0.80}Al_{0.20}O_{1.10}$. Assuming that phosphate anionic species, which are intercalated into $Mg_{0.80}Al_{0.20}O_{1.10}$, are monovalent, it means that $Mg_{0.80}Al_{0.20}O_{1.10}$ was added at a stoichiometric quantity into the phosphoric acid, as expressed in Eq. (9).

$$Mg_{0.80}Al_{0.20}O_{1.10} + 0.20H_3PO_4 + 0.90H_2O \rightarrow Mg_{0.80}Al_{0.20}(OH)_2(H_2PO_4)_{0.20}. \quad (9)$$

That is the reason why more phosphate ion was removed than expected relative to the theoretical value. Anion removal followed the sequence $H_3PO_4 > H_2SO_4 > HCl > HNO_3$, while in neutral saline solution, the sequence of $SO_4^{2-} > HPO_4^{2-} > Cl^- > NO_3^-$ has been observed [6,17,19]. Once again, this is due to the intercalation of $H_2PO_4^-$ into $Mg_{0.80}Al_{0.20}O_{1.10}$ during the initial reaction stage.

Fig. 3 shows the effect of time on anion removal by 1.75 stoichiometric quantities of $Mg_{0.80}Al_{0.20}O_{1.10}$. And,

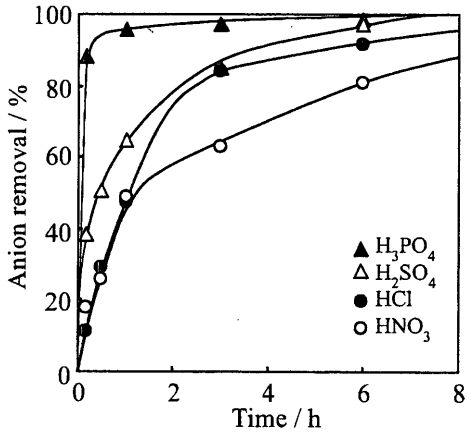

Fig. 3. Effect of time on anion removal by 1.75 stoichiometric quantities of $Mg_{0.80}Al_{0.20}O_{1.10}$ (initial acid concentration: 0.5 N).

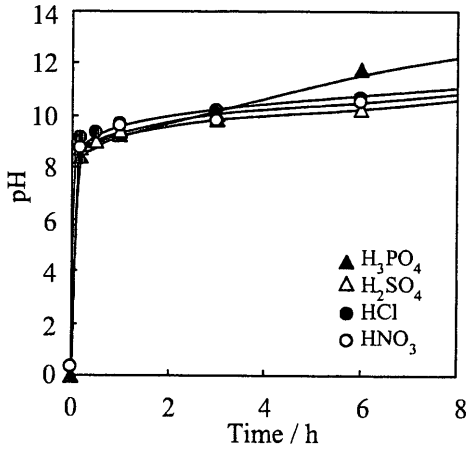

Fig. 4. Effect of time on pH after removing each anion using 1.75 stoichiometric quantities of $Mg_{0.80}Al_{0.20}O_{1.10}$ (initial acid concentration: 0.5 N).

Cl^- and NO_3^- removals at 24 h were 96.3% and 88.5% in case of HCl and HNO_3, respectively. These results reveal that anion removal increased with time, in addition, $Mg_{0.80}Al_{0.20}O_{1.10}$ could remove each anion quickly in the sequence of $H_3PO_4 > H_2SO_4 > HCl > HNO_3$. Fig. 4 shows the effect of time on pH after removing each anion using 1.75 stoichiometric quantities of $Mg_{0.80}Al_{0.20}O_{1.10}$. All solutions were found to have a pH in the range of 8–12. These results suggest that the dissolved Mg^{2+} precipitated as $Mg(OH)_2$, preventing an increase of OH^- concentration. Due to this small amount of OH^-, it can be stated that each anion was easily intercalated into $Mg_{0.80}Al_{0.20}O_{1.10}$.

Fig. 5 shows the effect of the Mg/Al molar ratio on anion removal by 1.75 stoichiometric quantities of

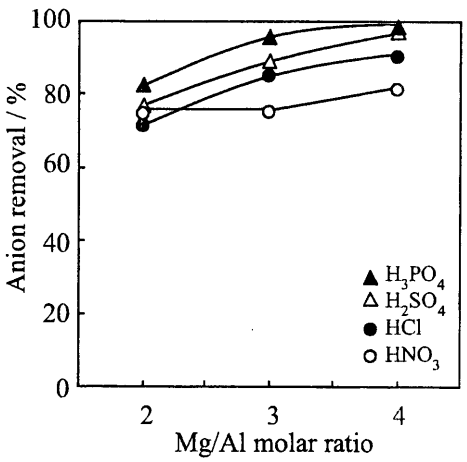

Fig. 5. Effect of Mg/Al molar ratio on anion removal by 1.75 stoichiometric quantities of Mg–Al oxide (time: 6 h, initial acid concentration: 0.5 N).

Mg–Al oxide. Anion removal decreased with decreasing Mg/Al molar ratio. It has previously been observed that a decrease in the Mg/Al molar ratio causes an increase of the positive charge of host layer in the reconstructed HT [18]. In the cases of HCl and HNO_3, intercalation of OH^- whose charge density is larger than that of Cl^- or NO_3^- may occur in order to compensate the increased positive charge. By contrast, it is conjectured that in the cases of H_3PO_4 and H_2SO_4, the phosphate ion and SO_4^{2-} cannot be intercalated sufficiently to balance the increased positive charge due to their larger anionic size. Thus, it is conjectured that OH^- whose anion size is smaller than that of phosphate ion or SO_4^{2-} was intercalated.

Fig. 6 shows the effect of initial acid concentration on anion removal by 1.75 stoichiometric quantities of $Mg_{0.80}Al_{0.20}O_{1.10}$. Anion removal increased with increasing initial acid concentration and removal in excess of 90% was achieved at 1.0 N. It is assumed that as the initial acid concentration increased, the concentration of anions remained higher than that of OH^-, since the reaction was carried out at a pH leading to $Mg(OH)_2$ precipitation. Consequently, it can be concluded that anions were easily intercalated into $Mg_{0.80}Al_{0.20}O_{1.10}$.

3.3. Selectivity of acid removal

Table 2 shows the relative distribution ratios for the removal of two types of acids by $Mg_{0.80}Al_{0.20}O_{1.10}$. The relative distribution ratios, K, were defined as

$$K = K_{d,A}/K_{d,B}[K_{d,A} = m_A(\text{Solid})/m_A(\text{Soln.}),\ K_{d,B} = m_B(\text{Solid})/m_B(\text{Soln.})], \quad (10)$$

where m_A and m_B are the amounts of each anion. The selectivity of acid removal was found to follow the

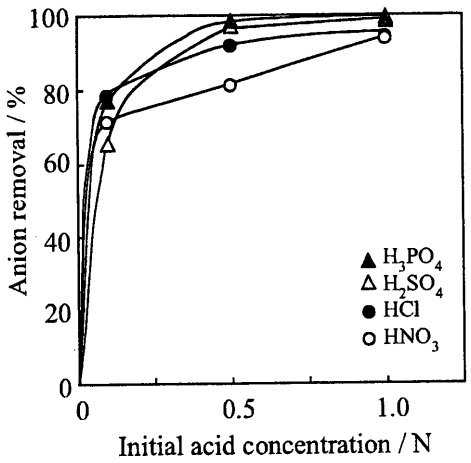

Fig. 6. Effect of initial acid concentration on anion removal by 1.75 stoichiometric quantities of $Mg_{0.80}Al_{0.20}O_{1.10}$ (time: 6 h).

Table 2
Relative distribution ratio for the removal of two types of acids by $Mg_{0.80}Al_{0.20}O_{1.10}$

	Acid	K
A	HNO_3	0.98
B	HCl	
A	HCl	0.18
B	H_2SO_4	
A	HNO_3	0.11
B	H_2SO_4	
A	H_2SO_4	0.043
B	H_3PO_4	
A	HCl	0.027
B	H_3PO_4	
A	HNO_3	0.013
B	H_3PO_4	

following order: $H_3PO_4 > H_2SO_4 > HCl > HNO_3$. This result corresponded with the order of anion removal by the addition of a stoichiometric quantity of $Mg_{0.80}Al_{0.20}O_{1.10}$ into each acid, as seen in Fig. 2.

3.4. Application of Mg–Al oxide to dilute mineral acid treatment

Fig. 7 shows the framework for the treatment of dilute mineral acid using Mg–Al oxide. After treating hydrochloric, sulfuric, or nitric acid by using Mg–Al oxide as a neutralizer and fixative of anion, the produced Cl-, SO_4-, or NO_3-HT can be used as ion exchangers for phosphate ion in order to prevent eutrophication of surface water by an *algae* bloom [21–23]. Phosphorus can be recovered by washing the resulting phosphate-HT with CO_3^{2-} solution. In addition, hydrochloric acid can be obtained

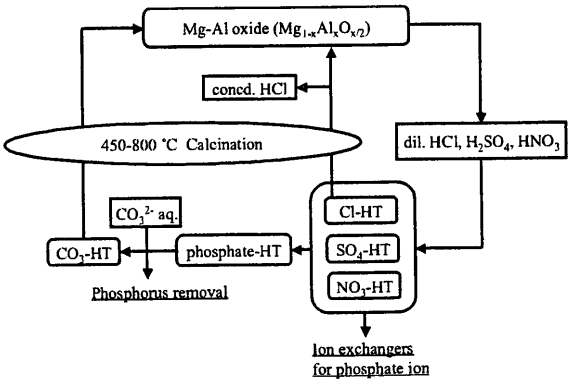

Fig. 7. Framework for the treatment of dilute mineral acid using Mg–Al oxide.

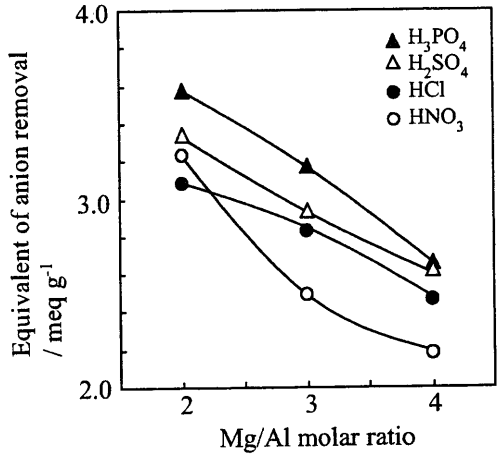

Fig. 8. Effect of Mg/Al molar ratio on equivalent of anion removal per 1 g of Mg–Al oxide.

by calcination of the resulting Cl-HT at 450–800°C [24,25]. The Mg–Al oxide reclaimed by calcining the resulting CO_3-, or Cl-HT can then be reused for dilute mineral acid treatment. In case of phosphoric acid treatment, phosphorus can be similarly recovered from the resulting phosphate-HT. This new treatment method would solve the problems of neutralization treatment that we indicated in "Introduction". Fig. 8 shows the effect of Mg/Al molar ratio on equivalent of anion removal per 1 g of Mg–Al oxide. Contrary to the results seen in Fig. 5, equivalent of anion removal decreased with increasing Mg/Al molar ratio. Efficient use can therefore be achieved using Mg–Al oxide with smaller Mg/Al molar ratio; however, it is necessary to add more Mg–Al oxide for complete anion removal. Additionally, Al is more expensive than Mg. Consequently, the use of Mg–Al oxide with larger Mg/Al molar ratio is recommended.

4. Conclusion

Our studies have shown that Mg–Al oxide can be used as both a neutralizer and a fixative of anions for the treatment of dilute mineral acids. More than 95% of acids could be removed from 0.5 N acids using a stoichiometric quantity of $Mg_{0.80}Al_{0.20}O_{1.10}$ for H_3PO_4, 1.75 stoichiometric quantities for H_2SO_4, or 2.5 stoichiometric quantities for HCl or HNO_3 at 20°C over a period of 6 h. Selectivity of acid removal was found to follow the order: $H_3PO_4 > H_2SO_4 > HCl > HNO_3$. The equivalent of acid removal per 1 g of Mg–Al oxide decreased as the Mg/Al molar ratio of Mg–Al oxide increased.

References

[1] Shigaki M. Etokihaikibutsunosyoukyakugijyutsu. Tokyo: Ohmsha, 1998. p. 87.

[2] Matsutani M. Haisuinokougaitaisaku. Tokyo: Rikougakusya, 1996. p. 4–3.

[3] Takano F, Shoji T, Komatsu T. Management of sanitary landfills in Sendai city, having a high concentration of incinerator residue. Haikibutsugakkaishi 1997;8:523–8.

[4] Horii Y, Higuchi S, Shimaoka T, Hanashima M. The treatment technology of landfill leachates containing condensed inorganic salts. Haikibutsugakkaishi 1997;8:529–39.

[5] Ingram L, Taylor HFW. The crystal structures of sjogrenite and pyroaurite. Mineral Mag 1967;36:465–79.

[6] Miyata S. Anion–exchange properties of Hydrotalcite–like compounds. Clays Clay Miner 1983;31:305–11.

[7] Cavani F, Trifiro F, Vaccari A. Hydrotalcite-type anionic clays: preparation, properties and applications. Catal Today 1991;11:173–301.

[8] Hermosin MC, Pavlovic I, Ulibarri MA, Cornejo J. Hydrotalcite as sorbent for trinitrophenol: sorption capacity and mechanism. Water Res 1996;30:171–7.

[9] Kang MJ, Rhee SW, Moon H. Sorption of MO_4^- (M = Tc, Re) on Mg/Al layered double hydroxide by anion exchange. Radiochim Acta 1996;75:169–73.

[10] Hibino T, Tsunashima A. Synthesis of paramolybdate intercalates of hydrotalcite-like compounds by ion exchange in ethanol/water solution. Chem Mater 1997;9: 2082–9.

[11] Roy AD. Lamellar double hydroxides. Mol Cryst Liq Cryst 1998;311:173–93.

[12] Newman SP, Jones W. Synthesis, characterization and applications of layered double hydroxides containing organic guests. New J Chem 1998;22:105–15.

[13] Olguin MT, Bosch P, Acosta D, Bulbulian S. $^{131}I^-$ sorption by thermally treated hydrotalcites. Clays Clay Miner 1998;46:567–73.

[14] Fetter G, Olguin MT, Bosch P. $^{131}I^-$ sorption from aqueous solutions by nitrated hydrotalcites. J Radional Nucl Chem 1999;241:595–9.

[15] Serrano J, Bertin V, Bulbulian S. ^{99}Mo sorption by thermally treated hydrotalcites. Langmuir 2000;16: 3355–60.

[16] Miyata S. Physico-chemical properties of synthetic hydrotalcites in relation to composition. Clays Clay Miner 1980;28:50–6.

[17] Sato T, Wakabayashi T. Shimada M. Adsorption of various anions by magnesium aluminum oxide ($Mg_{0.7}Al_{0.3}O_{1.15}$). Ind Eng Chem Prod Res Dev 1986;25:89–92.

[18] Sato T, Tezuka M, Endo T, Shimada M. Kinetics of anion uptake by rock salt-type magnesium aluminum oxide solid solutions. React Solids 1987;3:287–95.

[19] Sato T, Onai S, Yoshioka T, Okuwaki A. Causticization of sodium carbonate with rock-salt type magnesium aluminum oxide formed by the thermal decomposition of hydrotalcite-like layered double hydroxide. J Chem Tech Biotechnol 1993;57:137–40.

[20] Yun SK, Pinnavaia TJ. Water content and particle texture of synthetic hydrotalcite-like layered double hydroxides. Chem Mater 1995;7:348–54.

[21] Ookubo A, Ooi H, Hayashi K. Preparation and phosphate ion-exchange properties of a hydrotalcite-like compound. Langmuir 1993;9:1418–22.

[22] Shin H, Kim M, Nam S, Moon H. Phosphorus removal by hydrotalcite-like compounds (HTLcs). Water Sci Tech 1996;34:161–8.

[23] Kawamoto A, Ookubo A, Sato T, Suzuki T. Phosphorus removal from wastewater by layer structure inorganic ion exchanger with high selectivity to phosphate anion. Mizukankyougakkaishi 1999;22:875–81.

[24] Miyata S. The syntheses of hydrotalcite-like compounds and their structures and physico-chemical properties-I: the systems Mg^{2+}–Al^{3+}–NO_3^-, Mg^{2+}–Al^{3+}–Cl^-, Mg^{2+}–Al^{3+}–ClO_4^-, Ni^{2+}–Al^{3+}–Cl^- and Zn^{2+}–Al^{3+}–Cl^-. Clays Clay Miner 1975;23:369.

[25] Constantino VRL, Pinnavaia TJ. Basic properties of $Mg^{2+}_{1-x}Al_x^{3+}$ layered double hydroxides intercalated by carbonate, hydroxide, chloride, and sulfate anions. Inorg Chem 1995;34:883–92.

研究論文

給排水点切り替え上下Uターン水路式生物ろ床法生活排水処理装置の開発

溝口忠昭*・梶山陽介**・佐藤一教**・高本成仁**・村上光正***

要　旨

主として単独浄化槽が使用されている地区の生活排水を対象に，ひも状ろ材を用いた上下Uターン水路（UOS）式生物ろ床法処理装置を開発した．この方式は溶存酸素の確保が容易で，ろ材と液の接触が良好であることが特長である．UOS式において，液流入部のろ材に汚泥が付着して浄化性能が低下した時点でろ材を液後流部にシフトすると，ろ材に付着した汚泥は除去された．この原理に基づいた有効容積1.6 m³で，給排水点の自動切り替えが可能な装置を試作して通年の生活排水処理実験を行った．水温が12℃以上であれば滞留時間6.7hで化学的酸素要求量（COD）は25～30 mg/Lから10～15 mg/L程度まで，生物化学的酸素要求量（BOD）は5 mg/Lまで除去された．場合によっては処理水中に10 mg/L程度の浮遊物質（SS）を認めたが，1年間の実験期間中ろ材の洗浄は不要であった．生活排水中の窒素はもっぱらアンモニア態で存在したが，水温が10℃以上であればその90％以上がろ床内で硝酸態窒素に酸化された．

キーワード：生活排水，生物ろ床，水質浄化，汚泥，給排水点切り替え

1．緒　言

生活排水による水質汚濁問題が全国各地で問題になっている[1-3]．特に，地方都市において，かつて山林や農地として利用されていた土地が宅地に転用され，その地区の生活排水が公共水域に流入すると，流入部では当該有機汚濁物質の嫌気性分解が起こって悪臭が発生する．また湖沼内では富栄養化が進行し，アオコの発生に見られるような景観の悪化，それに伴う悪臭の発生，魚類等生態系への影響等が現れ，またこれを水源とする場合には飲用水が異臭を示すなど生活への影響が無視できない状態となる．その典型的な例を東広島市に見ることができる．市を南北に縦断する黒瀬川の水質が環境基準値である生物化学的酸素要求量（BOD）2 mg/Lの1.5倍に当たる3 mg/Lであるため，東広島市および広島県はその対策に取り組む方針を決定した[4]．

この黒瀬川の上流に位置するため池Nは現在でも農業用水源に供されているが，1970年代から急激に周辺地区の宅地化が進み，生活排水が流入するために夏季にはアオコや悪臭の発生などの問題が起こっている．このため池に流入する水路の水質を調査したところ，住宅地からの集合生活排水は時間帯によってはBOD＞100 mg/L，化学的酸素要求量（COD）＞30 mg/L，全窒素＞10 mg/Lを示すことが明らかになった．このため，この地区の生活排水を対象に処理装置の研究開発を行った．

生活排水を処理するに当たっては生態系への影響が小さく，また運転経費を低減できるという点で微生物処理，中でも生物ろ床法が優れた処理方法とし

*バブコック日立㈱新事業開発本部（現在：東北大学環境保全研究施設）　Tadaaki MIZOGUCHI
**バブコック日立㈱　Yosuke KAJIYAMA, Kazunori SATO, Shigehito TAKAMOTO
***姫路工業大学環境人間学部　Mitsumasa MURAKAMI

2002年9月30日受付
2003年2月5日受理

て期待されている[2,5-8]．そこで，本研究者らは，ろ床部が幅90，水深68，全長3,000㎜の水平水路式装置を用いて処理実験を行った．しかし，水平水路式装置を用いた場合には，(a) 液中の溶存酸素濃度を均一に高めることが難しい，(b)液流れに関してチャンネリング現象が起こり，ろ材の有効利用率が低い，(c) ろ材表面に汚泥が付着した場合，その除去が難しい，(d) 有機汚濁物質の除去は主としてろ床の前半部で進行し，後半部のろ材は浄化にほとんど関与しない，などの問題点が明らかになった．これらの問題点を解決できる給排水点切り替え上下Uターン水路（UOS）式生物ろ床法生活排水処理装置を開発したので，その結果に関して報告する．

2．実験方法

2.1 実験場所

ため池Nの周辺地図およびE地点の概要を図－1に示す．ため池NにはD，E，HおよびS地点で生活排水が流入し，その汚染度はD（COD測定例30 mg/L）≒E（27 mg/L）＞S（10 mg/L）＞H（4 mg/L）である．このうちE地点ではNK団地約80戸相当の生活排水が最初に沈砂池に流入し，次いで縦3 m，横3 m，水深1.5 mの曝気池で処理された後にため池Nに放流されているが，曝気池におけるCOD除去率は20％程度である．D地点の生活排水は約20戸の家庭からのものであり，性状および流量の時間変動が著しいため，本研究における実験はE地点の生活排水を対象に行った．

2.2 実験装置

2.2.1 49L上下Uターン水路式生活排水処理実験装置

装置の概要を図－2に示す．装置本体はメタクリル樹脂製で，縦90，横90，有効深さ1,000㎜の6個の槽区画Z1～Z6から構成され，次の点を特徴とする：(a) 槽区画Z1とZ2，Z3とZ4，Z5とZ6は底部が連通状態にある（連通部高さ100㎜），(b) 槽区画Z2とZ3，Z4とZ5の隔壁は底部まで到達する，(c) 槽区画Z1からZ2へ，Z3からZ4へ，Z5からZ6へは隔壁下部を潜る形で，一方，槽区画Z2からZ3へ，Z4からZ5へはその隔壁上部を越える形で液が移動する，(d) 各槽区画内には長さ1 mのろ材が吊り下げられている，(e) 各槽区画の底部から約50

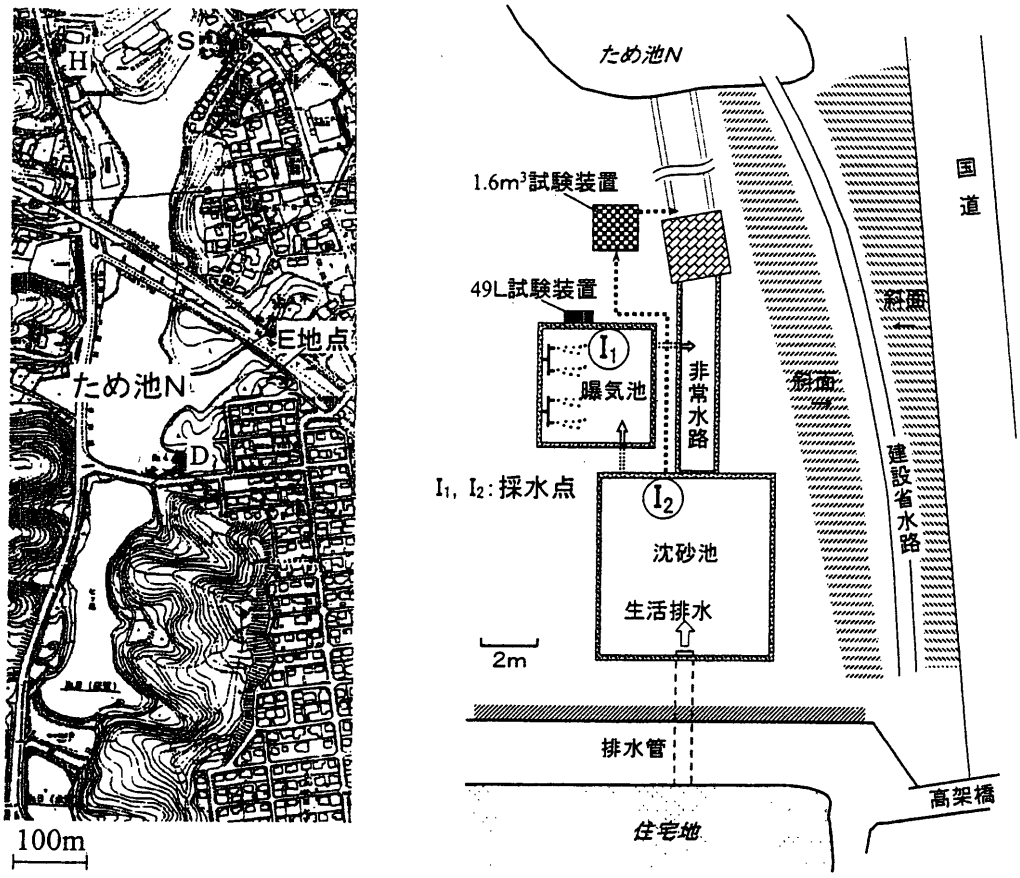

図－1 ため池N周辺（左）および生活排水処理実験実施E地点（右）の概要

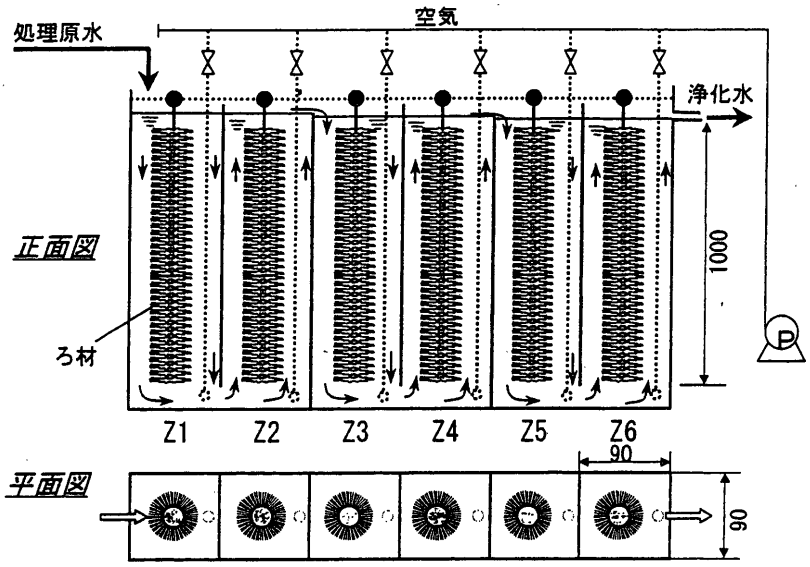

図－2　49LUOS式実験装置

mmの位置からG2焼結ガラス製ボールフィルターを通して空気が供給される．なお，藻類の発生を抑制するために装置全体をアルミ箔付ウレタンシートによって覆い，また給水用チューブも藻発生防止用遮光型チューブによって被覆した．

本装置の有効内容積が約49Lであり，また液が下降流→上昇流→下降流→……→上昇流（上下Uターン流）となって処理槽内を移動することに因んで，本装置を「49L上下Uターン水路（UOS）式生活排水処理実験装置」（以下，「49LUOS式実験装置」と略称）という．

2.2.2　1.6㎥給排水点切り替え上下Uターン水路式生活排水処理実験装置

装置の概要を図－3に示す．装置本体はSUS304

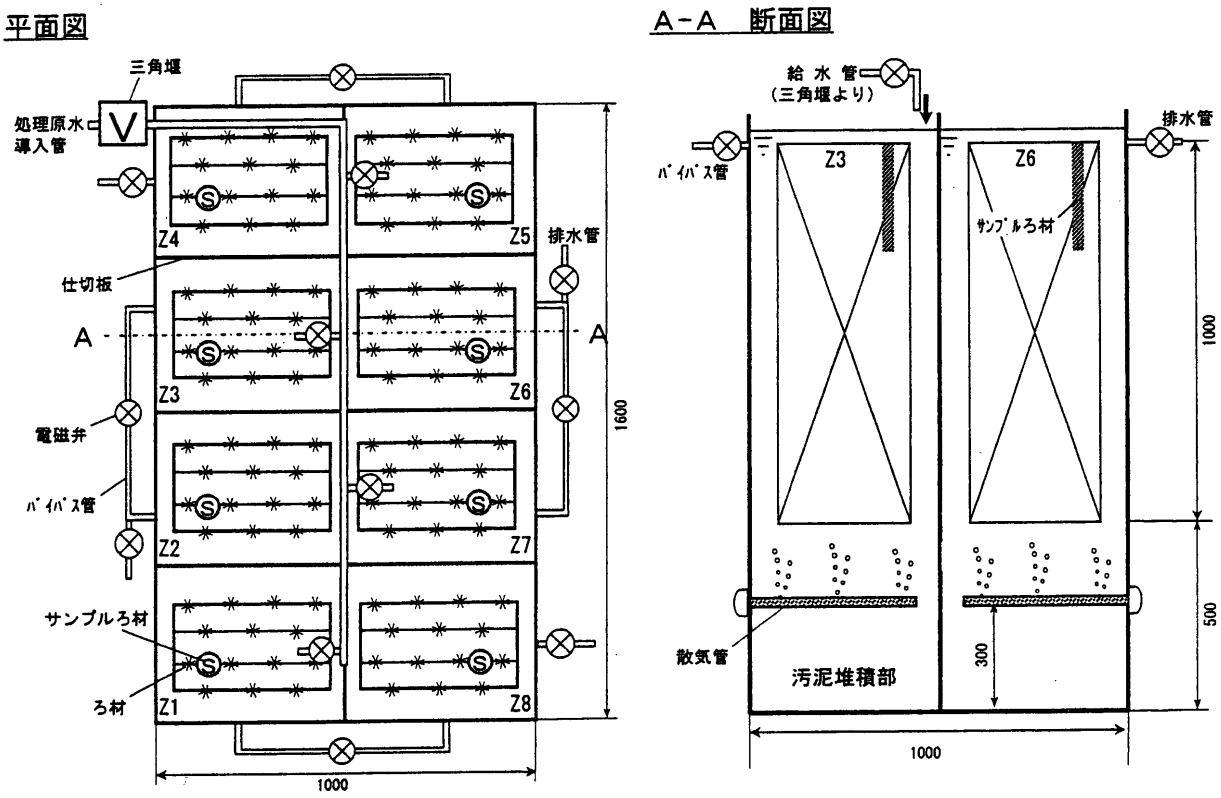

図－3　1.6㎥UOS式実験装置

図－4 1.6㎥UOS式実験装置内部

製で，縦400，横500，有効深さ1,000㎜の8個の槽区画Z1～Z8から構成される．各槽区画内には所定長さ（2001年4月27日以前は24 m/槽区画，2001年4月27日以後は14 m/槽区画）のひも状ろ材を専用枠に固定して静置した．装置内部の様子を図－4に示す．

沈砂池からの処理原水を水中ポンプを用いて三角堰に導き，所定流量（4.0L/min（滞留時間6.7h））に調整した後に槽区画Z1，Z3，Z5またはZ7のいずれかに供給した．Z1，Z3，Z5またはZ7への給水は電磁弁の切り替えによって行った．槽区画Z1とZ2，Z3とZ4，Z5とZ6およびZ7とZ8は底部を連通状態（連通部高さ500㎜）とし，また槽区画Z2とZ3，Z4とZ5，Z6とZ7およびZ8とZ1はバイパス管によって連結し，各バイパス管に電磁弁および電磁弁付排水管を取り付けた．給水点がZ1，Z3，Z5またはZ7の場合，排水点はそれぞれZ8，Z2，Z4またはZ6である．給水点がZ1の場合，液の流れはZ1→Z2→Z3→Z4→Z5→Z6→Z7→Z8（排水点）である．

本装置を用いた生活排水処理実験では汚泥が付着したろ材を懸垂した槽区画が液流出側になるように給排水点を所定間隔（標準的には3日）で順次シフトしたが，この給排水点のシフトは各槽区画に取り付けた給水管およびバイパス管の電磁弁を自動的にオン/オフすることによって行った．なお，エアレーションは三鈴工業㈱製のウレタン製散気管を用いて行った．また，吸水口を目開き10㎜のスクリーン製篭で覆うことによってゴミの吸い込みを防止した．

本装置の有効内容積が約1.6㎥であることに因んで，本装置を「1.6㎥給排水点切り替え上下Uターン水路（UOS）式生活排水処理実験装置」（以下，「1.6㎥UOS式実験装置」と略称）という．

2.3 ろ材

ろ材としてTBR㈱製の紐状「バイオコード」（ϕ 45）を使用した[8]．49LUOS式生活排水処理実験装置用のろ材の調製は次の方法によって行った：長さ1mに切断したろ材をため池NのS地点流入水路に1週間浸漬し，表面に生物膜を付着させた．水路から引き上げたろ材を生物膜調製と同一水路の水に浸漬し，軽く揺り動かしてろ材に付着した大部分の汚泥を除去した後に実験に使用した．1.6㎥UOS式実験装置では新品ろ材を馴致なしに実験に使用した．

2.4 生活排水処理実験操作

2.4.1 49LUOS式実験装置による原理確認実験

E地点の曝気池水（採水点：I_1，図－1参照）または沈砂池水（採水点：I_2）を処理原水とし，これをチューブポンプを用いて処理装置（図－2）の槽区画Z1に供給した．所定時間ごとに各槽区画の上部からCOD測定試料溶液を採取した．COD測定試料採取後に各槽区画内の溶存酸素（DO），pHおよび水温を測定し，必要に応じてBOD分析用試料を採取した．沈砂池水を用いた処理実験では，標準的には3日間隔で試料を採取し，試料採取およびDO等の測定後に，槽区画Z1，Z2，Z3，Z4，Z5およびZ6のろ材をそれぞれZ5，Z6，Z1，Z2，Z3およびZ4に移動した．実験条件等の概要を表1 Run1～3

表1 生活排水処理実験条件概要

Run	装 置	流入水	ろ材充填量 (m/㎥)	液流量 (L/min)	滞留時間 (h)	給排水点シフト	実験期間
1	49LUOS式	曝気池水	123	0.1～0.2	4.0～8.1	なし	00/5/18～00/7/11
2	49LUOS式	沈砂池水	123	0.2	4.0	ろ材移動	00/7/11～00/7/19
3	49LUOS式	沈砂池水	123	0.15	5.4	ろ材移動	00/7/19～00/8/31
4	1.6㎥UOS式	沈砂池水	120	4.0	6.7	自動切り替え	01/1/14～01/4/27
5	1.6㎥UOS式	沈砂池水	70	4.0	6.7	自動切り替え	01/4/27～02/3/30

に示す.

2.4.2 1.6㎥UOS式実験装置による通年スケールアップ実験

E地点沈砂池水（採水点：I_2，図－1参照）を処理原水とし，これを給水，バイパスおよび排水用電磁バルブの切り替えによって処理装置（図－3）の槽区画Z1，Z3，Z5またはZ7のいずれかに供給し，処理水をそれぞれ槽区画Z8，Z2，Z4またはZ6から排出した．たとえば，槽区画Z1に供給した場合，液は槽区画Z1→Z2→Z3→Z4→Z5→Z6→Z7→Z8の順に流れて槽区画Z8から流出した．3日間後に液流入点が槽区画Z3になるように自動的に設定を変更した．6日後まで，液は槽区画Z3→Z4→Z5→Z6→Z7→Z8→Z1→Z2の順に流れ，槽区画Z2から流出した.

実験は，滞留時間6.7h（液流量4.0L/min），曝気量32L/min（4 L/min・槽区画×8槽区画），給排水点シフト間隔3日の条件で行い，通常給排水点シフトの約9時間前に，処理原水（三角堰への流入水）および処理水（処理装置からの流出水）を採取し，CODの分析に供した．本実験装置を用いた場合にも，COD測定試料採取後に装置内の各槽区画内の溶存酸素（DO），pHおよび水温を測定し，必要に応じてBOD，窒素および浮遊物質（SS）を分析した．実験条件等の概要を表1 Run4～5に示す.

2.5 測定方法

液中のCODは，ミリポアフィルターを用いてろ過して得られたろ液を対象に，過マンガン酸カリウム法[9]によって測定した．BODおよびSSはJIS-K0102工場排水試験方法[9]に従って測定した．溶存酸素は溶存酸素計（東亜ディーケーケー，DO-24P）を用い，またアンモニア態窒素（NH_4^+-N）および硝酸態窒素（NO_3^--N）はそれぞれアンモニアイオン電極（電気化学計器，IOL-40）およびイオンクロマトグラフ(DIONEX，DX-100)を用いて測定した.

滞留時間の調整は，所定時間内に処理装置から流出する液量，すなわち液流量を変化させることによって行った．ろ材への汚泥付着量（3.2.2参照）は，次の方法によって測定した．下部に錘を取り付けた長さ約30㎝のろ材（試験ろ材という）を各槽区画内に吊り下げ，必要に応じてこれを取り出した．試験ろ材を日陰に吊るし，水が滴下しきった時点で全体重量を測定した．全体重量から錘および取り付け器材の重量を差し引いた値（ろ材を含む湿重量）を汚泥重量とした.

3．結果および考察

3.1 49LUOS式実験装置による原理確認実験

3.1.1 曝気池水実験

地元住民の要請もあり，またE地点曝気池水（図－1参照）の方が沈砂池水よりも汚濁負荷が小さいために最初の実験には適していると考え，最初に曝気池水を対象に処理実験を行った．曝気池の水を供給し続けたところ，生物ろ床によって処理した水のCODは概して曝気池水の約半分まで低下したが，槽区画Z1およびZ2のろ材への汚泥付着量が次第に増大した．このため，実験開始10日後（6月4日）にろ材を洗浄し，汚泥を除去した．しかし，処理実験を継続すると槽区画Z1およびZ2のろ材には再び汚泥が付着した．ろ材洗浄10日後（6月14日）における各槽区画内のCOD測定結果を図－5に示す．CODの除去は槽区画Z1～Z4のみで進行し，後流側の槽区画Z5およびZ6はCOD除去にほとんど寄与せず，またこの槽区画ではろ材への汚泥付着が見られなかった.

上記の観察結果は，汚泥が付着したろ材を液後流側に移動（以下，「シフト」という）すれば，有機汚濁物質の除去は前流部で進行し，後流側ではむしろ汚泥が分解されるのではないかと期待させた．6月14日に槽区画Z1およびZ2にあったろ材をそれぞれZ5およびZ6に，またZ3，Z4，Z5およびZ6にあったろ材をそれぞれZ1，Z2，Z3およびZ4にシフトした．ろ材シフト2日後（6月16日）には槽区画Z5およびZ6のろ材の汚泥付着量は顕著に減少した．以後，3～5日間隔でろ材を順次シフトしたところ，ろ材の洗浄なしに浄化処理を継続することができた．7月3日～11日の間は大雨がなかったために曝気池水の水質は比較的安定し，この期間のCOD平均値は沈砂池30.2㎎/L，曝気池24.5㎎/L，生物ろ床処理水14.1㎎/Lであった.

3.1.2 沈砂池水実験

沈砂池水を対象とし，ろ材を所定日数間隔でシフトしながら行った生活排水処理実験（2000年7月11日～8月31日）の結果を図－6に示す．CODが25～30㎎/Lの沈砂池水を対象にした場合，滞留時間4 h（液流量200mL/min），ろ材のシフト間隔3日（表1，Run2）では槽区画Z1のろ材に多量の汚泥が付着した．このため，滞留時間の標準値を5.4h

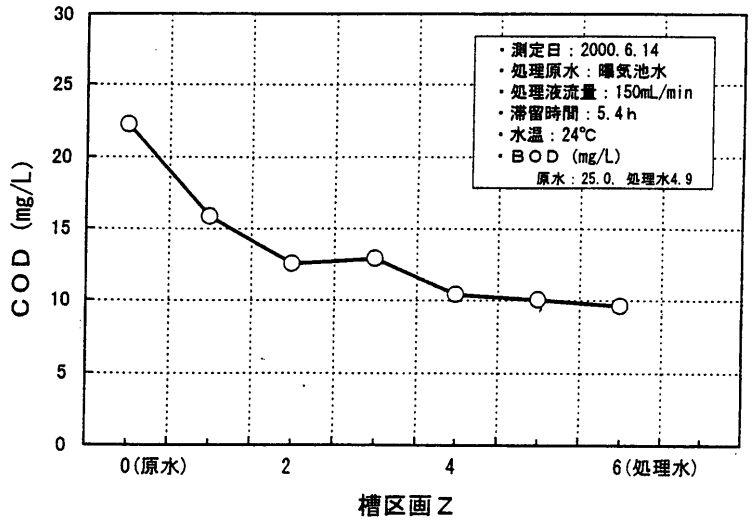

図－5 49LUOS式実験装置内におけるCODの変化

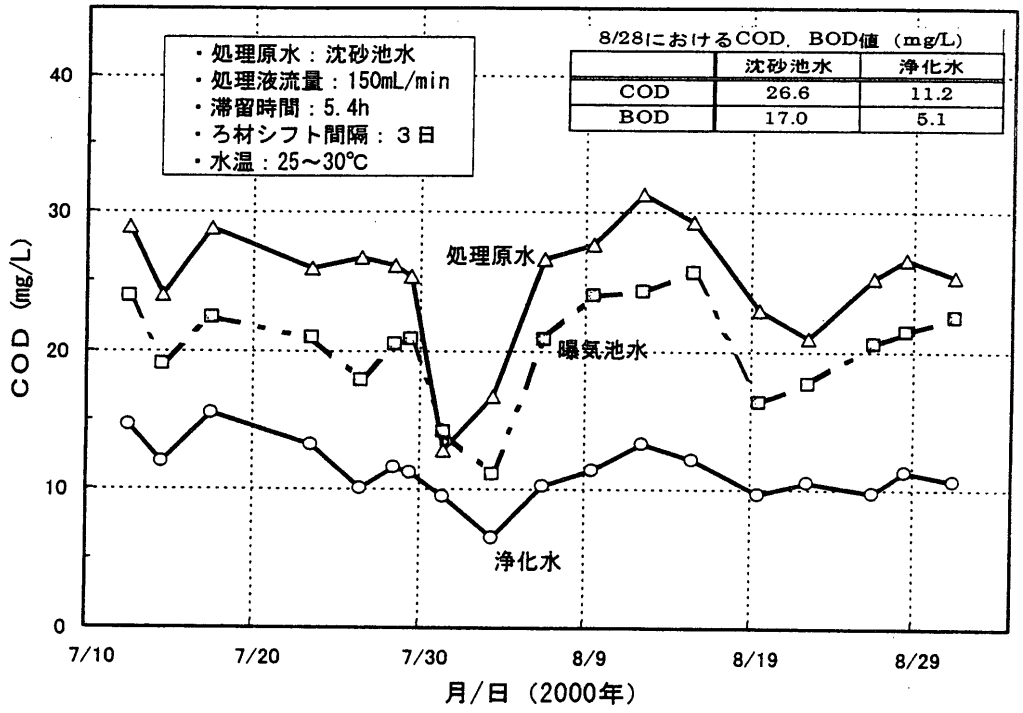

図－6 49LUOS式装置を用いた生活排水処理実験結果

(液流量150mL/min) とした (Run3). 8月初旬は降雨のために原水のCODが低下したが, その後沈砂池水は比較的安定した水質を示した. 試験期間中, ろ材の洗浄は全く不要であった. 8月9日～8月31日におけるCODの平均値は沈砂池水25.8 mg/L, 曝気池水21.5 mg/L, 生物ろ床処理水11.0 mg/Lであった. 8月28日採取試料のCODは沈砂池水26.6 mg/L, 処理水11.2 mg/L, 一方BODは沈砂池水17.0 mg/L, 生物ろ床処理水5.1 mg/Lであり, 沈砂池水も曝気池水を対象とした場合とほぼ同程度の水質まで浄化された.

ろ材への汚泥付着量はろ材のシフトによって顕著に変化した. 図－7に1本のろ材に着目して処理装置内の位置 (槽区画No) と汚泥の付着状況の関係を示す. 槽区画Z2にあったろ材をZ6にシフトして3日間経過すると付着した汚泥の大部分が除去された((1)). これをZ4にシフトして3日経過すると汚泥はほとんど全て除去された((2)). 槽区画Z4にあっ

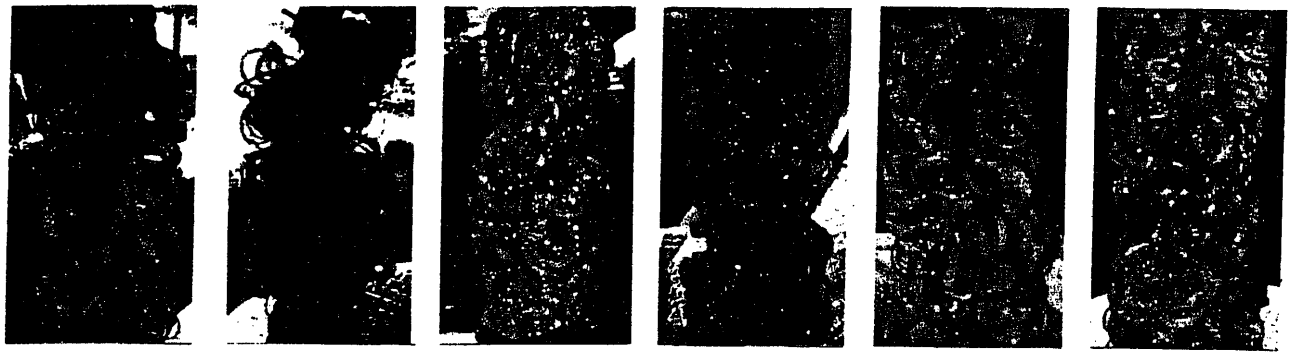

図－7　ろ材のシフトに伴う汚泥付着状態の変化
・写真はいずれもろ材のシフト直前・［　］内はろ材設置槽区画No.・実験条件に関しては図－6参照

たろ材をZ2にシフトして3日経過するとろ材には再び多量の汚泥が付着した（(3)）．このろ材を槽区画Z6にシフトして3日間経過した状態ではまだ汚泥が残存したが（(4)），Z4へシフトして3日経過した時点ではろ材上には汚泥がほとんど存在しなかった（(5)）．これを再び槽区画Z2にシフトして3日経過するとろ材には多量の汚泥が付着した（(6)）．

ろ材から汚泥が除去される機構に関しては今後さらに検討しなければならないが，汚泥が汚濁負荷の小さい条件に置かれると，汚泥そのものが微生物によって分解されることが主原因であると考えられる．貧栄養条件下で汚泥が虫食い状態になり，汚泥の一部がろ材から剥離する現象も起こるものと考えられるが，沈砂池水の処理実験期間（2000年7月11日～8月31日）における装置底部の汚泥堆積量は全区画平均で5cm程度であった．

3.2　1.6㎥UOS式実験装置による通年スケールアップ実験

3.2.1　有機汚濁物質の除去特性

E地点沈砂池水を対象とし，給排水点を3日間隔でシフトしながら行った生活排水処理実験の結果を図－8に示す．実験開始当初，流量調整不良のため

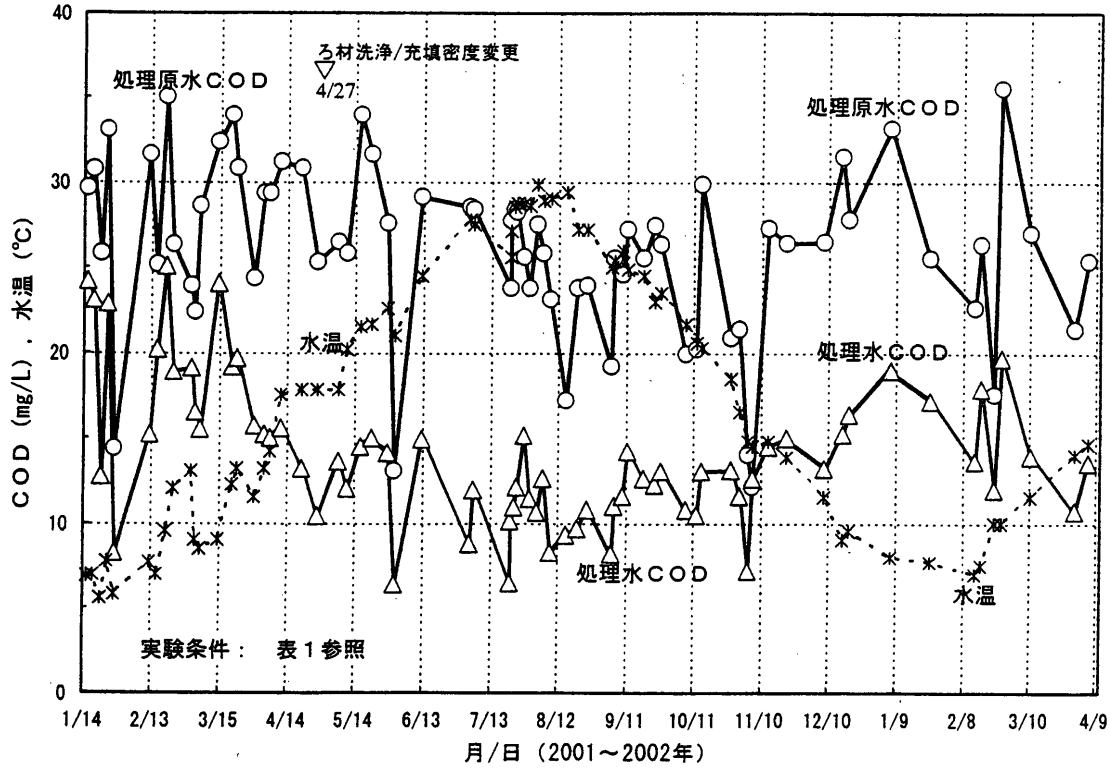

図－8　1.6㎥UOS式装置を用いた生活排水処理実験結果（COD）

に処理装置内に多量の原水が流入し，また水温が10℃またはそれ以下に低下したため，ろ材上に多量の汚泥が付着した．液供給を停止して空気だけを供給するなどの操作を行ったが，付着した汚泥はほとんど減少せず，処理水のCODも15～20 mg/L程度に留まった．

このように所期の処理性能が得られない理由として，(a) 水温が低下した，(b) ろ材に浄化機能を持たない汚泥が付着した，(c) ろ材を密に配置し過ぎたために溶存酸素が全体に行き渡らなかった，などが考えられた．そこで，水温が18℃に上昇した2001年4月27日にろ材を洗浄するとともに，ろ材充填量を24 m/槽区画から14 m/槽区画に減らしたところ（図－4参照），ろ床内でCODが顕著に減少し，またろ材上の汚泥量は給排水点のシフトに伴って増減を繰り返した．2001年4月27日～2002年3月30日までのCOD除去率の平均値は50％であった（図－8参照）．BODの測定点は必ずしも多くないが，17～37 mg/Lが2.4～8.9 mg/Lに低下することが明らかになった（図－9）．なお，2001年4月27日の再スタート後11か月経過した2002年3月末においてもろ材洗浄なしに装置は運転可能であった．

図－10に装置内におけるCOD，溶存酸素（DO），アンモニア態窒素（NH_4^+-N）および硝酸態窒素（NO_3^--N）の変化の様子を示す（NH_4^+-NおよびNO_3^--Nに関しては3.2.3参照）．1.6 ㎥UOS式実験装置は8区画に分割され，装置全体の滞留時間は6.7hであるが，CODの除去は実質的には槽区画Z5（ここまでの滞留時間は4.2h）までに完了することが分かった．Z5～Z8ではDOがほぼ同一であり，この部分では有機汚濁物質の除去に酸素が消費されないことを物語る．

表2の測定項目第1～3段目に水温，pHおよびDOに関する測定データを示す．実験装置は地上に設置され，また処理原水である生活排水がいったん開放型の沈砂池に流入するため，冬季においては水温が6℃付近まで低下した．水温12℃（01/12/8）では，滞留時間6.7h（液流量4.0L/min）で，処理原水：COD26.5，BOD22，処理水：COD13.2，BOD4.4 mg/Lであり，有機汚濁物質の除去性能は維持された．しかし，水温10℃の場合には，一時的に滞留時間を約9 hに長くしたが，CODは20 mg/L程度に低下するだけであった．

3.2.2 汚泥の付着と堆積特性

給排水点のシフトによってろ材が自動クリーニングされることは，ろ材の重量変化からも明らかにされた．槽区画Z1は2001年7月21日には液流入部に当たり，ここに設置した長さ約30 cmの試験ろ材の重量（水分を含む）は3.67 g/cmであったが，液流入部を槽区画Z3，したがって試験ろ材が存在する槽区画Z1が液流入部から数えて7番目に当たる位置に変わって3日目の7月24日には試験ろ材の重量は2.83 g/cmに低下し，再び液流入部に変わった8月2日にはろ材重量は4.1 g/cmに増加した．なお，

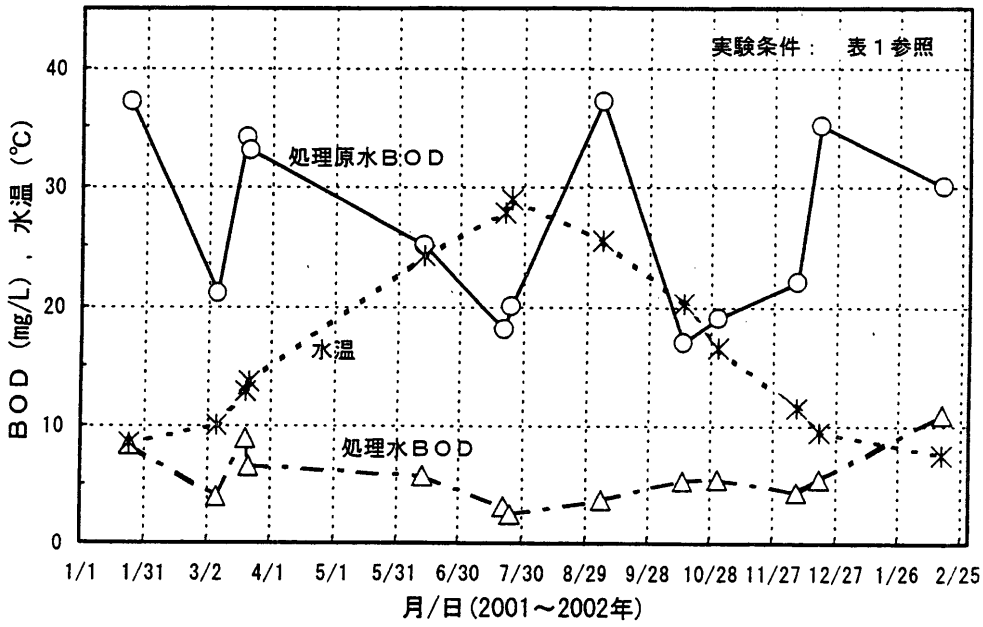

図－9 1.6㎥UOS式装置を用いた生活排水処理実験結果（BOD）

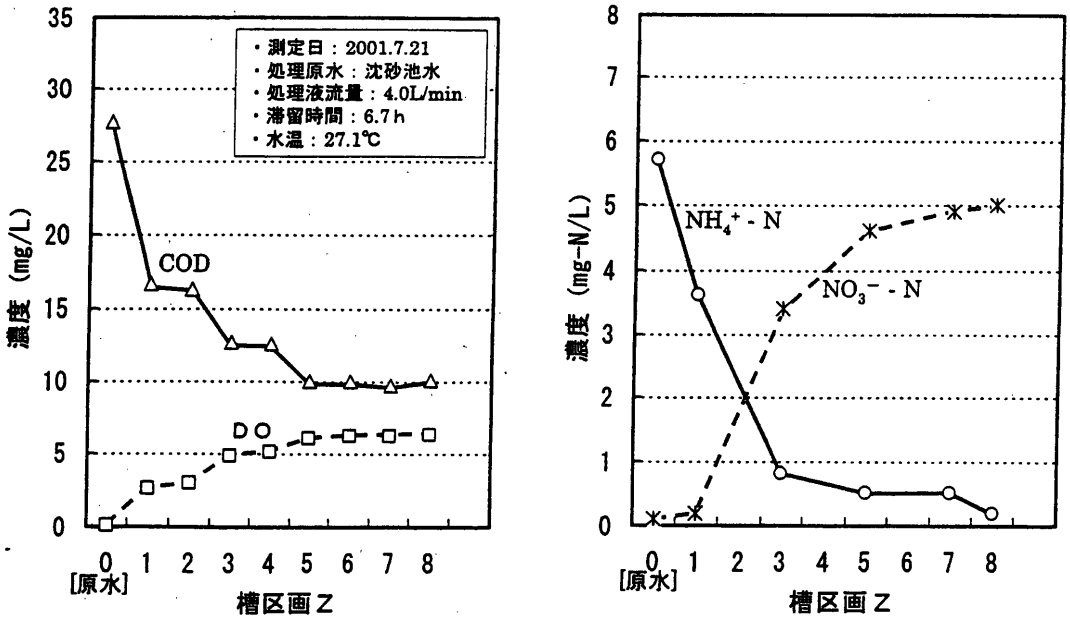

図－10 1.6㎥UOS式実験装置内におけるCOD，DO，NH_4^+-NおよびNO3⁻-Nの変化

表2 1.6㎥UOS式実験装置を用いた生活排水処理における各種特性の測定結果例

測定項目	測定日：01/7/24		01/9/18		01/12/8	
	処理原水	処理水	処理原水	処理水	処理原水	処理水
水温（℃）	28.9	28.7	24.5	24.5	12.2	11.5
pH（mg/L）	7.2	7.1	6.7	6.5	7.3	7.4
DO（mg/L）	0.1	5.8	0.1	7.2	0.1	10.8
COD（mg/L）	28.8	12.1	25.5	12.6	26.5	13.2
BOD（mg/L）	20.0	2.4	14.0	3.6	22.0	4.4
SS（mg/L）	18	11	22	9	31	7

冬季においてはろ材への汚泥付着量が約10 g/cmになったが，給排水点のシフトによるろ材の自動クリーニング現象は確認された．

2001年4月27日以降，装置底部への汚泥の堆積量は高々数cm程度であり，汚泥の抜き出しなしに処理実験を継続できた．このように給排水点のシフトはろ材の洗浄を省略できるという優れた特徴を持つが，汚泥ゼロを保証するものではない．処理水中のSS濃度は，肉眼的に見て比較的高いと判断された数ケースのみ測定した．その結果を表2の最下段に示すが，処理水中のSS濃度は高い場合で10 mg/L程度，通常は5 mg/Lまたはそれ以下であった．

透明度の高い処理水を目標とし，あるいは処理水の放流水路底にSSが沈積するのを回避するためには処理水中のSSを除去する必要がある．本研究で処理原水として用いた生活排水は白濁していたのに対し，処理水中のSSは極めて沈降性がよく，沈殿槽を設置すれば容易にSSを除去できると考えられる．

3.2.3 窒素の挙動

図－10から明らかなように，処理原水中の窒素はそのほとんど全量がNH_4^+-Nであるが，装置内を流下するに従ってNO3⁻-N量が増し，排出口では90％以上の窒素がNO3⁻-Nに酸化された．生物ろ床法ではろ材に付着した汚泥中に硝化細菌が存在するために好気的条件，すなわち液後流側では硝化反応が進行するものと考えられる．なお，図－10の測定日2001年7月21におけるBODは原水18.0 mg/L，処理水3.2 mg/Lであった．

硝化反応に対する温度依存性は極めて大きいことが分かった（図－11）．本装置内におけるNH_4^+-NからNO3⁻-Nへの酸化率は水温が10℃以下になっ

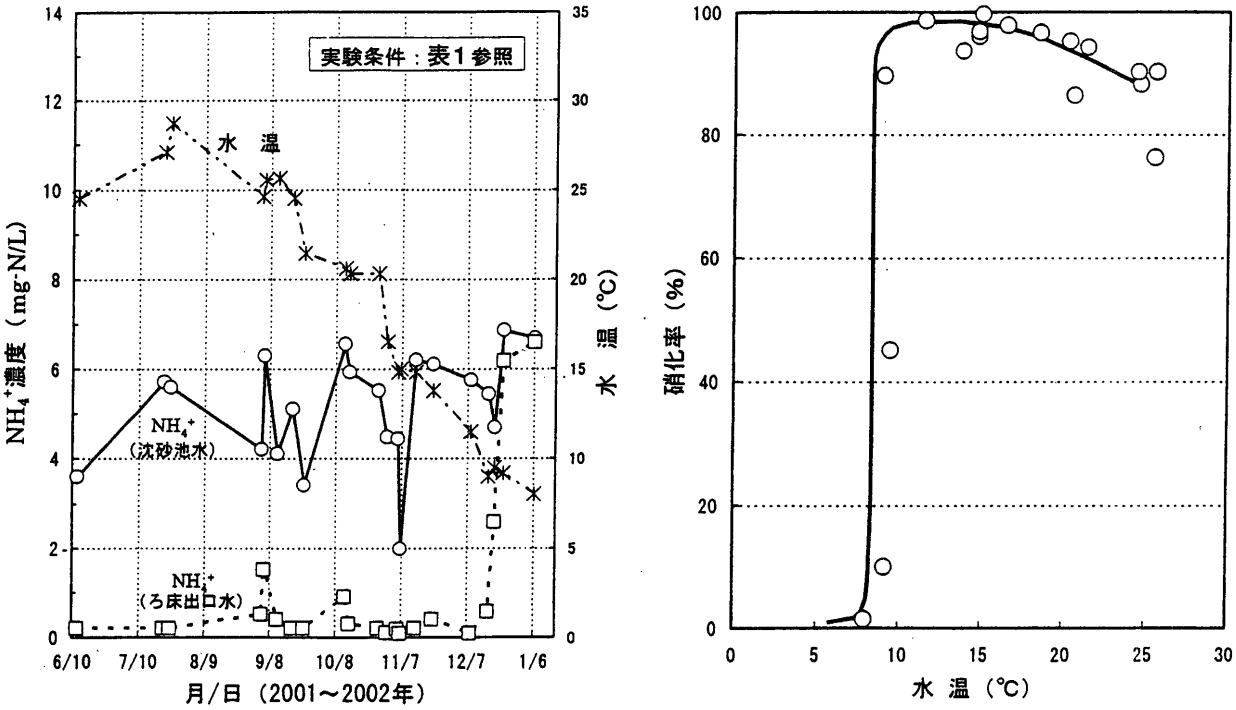

図－11 1.6㎥UOS式実験装置におけるアンモニアの酸化（左：経時変化，右：水温と硝化率）

た12月中旬から急激に低下し，13℃に上昇した3月末には硝化反応が回復した．

排水中の窒素分を除去するためには，まずこれを硝酸イオンに酸化し，次いで有機性還元剤の存在下で脱窒菌の作用によって窒素ガスに還元するのが一般的である．このうち反応し難いと考えられているNH_4^+-NからNO_3^--Nへの酸化反応[10]が生物ろ床内において進行することが分かった．今後，給排水点切り替えUOS式装置をNH_4^+-Nの酸化装置として使用する脱窒法の開発を進めていく予定である．

3.2.4 装置の運転性能

滞留時間6.7hで，送気倍率（＝曝気量（L/min）/処理水量（L/min））＝32/4＝8.0の場合，溶存酸素は液流入部で2～6 mg/L，液流出部で6～10 mg/Lを維持した（図－10，表2参照）．微細気泡の発生手段としてのウレタン製散気管，給排水点の切り替え手段としての専用電磁弁を備えたバイパスラインおよび液流量調整法としての三角堰は所期の性能を発揮し，実験期間中これらに起因するトラブルには一度も遭遇しなかった．

4．結 言

ろ床内を縦方向に多分割し，液を上下Uターン流として移動させるとともに，液流入部のろ材に汚泥が付着した時点でこのろ材を液後流部にシフトすると，ろ材に付着した汚泥が除去されることを明らかにした．ろ材を移動させる代わりに給排水点の自動切り替えが可能な有効容積1.6 ㎥の装置を試作して通年の生活排水処理実験を行ったところ，水温が12℃以上であれば滞留時間6.7hでCODは25～30 mg/Lから10～15 mg/L程度まで，BODは5 mg/Lまで低下した．1年間の実験期間中ろ材の洗浄は不要であり，本装置は運転管理が極めて容易な処理装置として実用に供し得るものであることが確認された．なお，本装置の原理は単に生活排水だけでなく，活性汚泥法の対象となる有機汚濁物質を含む排水の処理に広く適用できるものと期待される．また，ろ床内で数mg/Lのアンモニア態窒素は高効率に硝酸態窒素に酸化された．この現象も生物ろ床法の新たな展開の芽として期待される．

謝辞：本研究を実施するに当たり，東広島市市民部および自らも積極的に生活排水問題への取り組みを行っている東広島市日興苑団地関係者から関連情報および実験場所の提供など多大の協力を戴きました．ここに深謝の意を表します．

参 考 文 献

1）㈳日本水環境学会編集：日本の水環境行政－その歴史と科学的背景－，㈱ぎょうせい（1999）
2）本橋敬之助，立本英機：湖沼・河川・排水路の水質浄化，海文堂出版㈱（1997）

3）村上光正：水はよみがえるか，㈱パワー社（1999）
4）新聞記事：1999年5月16日中国新聞；2000年4月7日朝日新聞
5）斎藤真一他3名：水路における直接水質浄化，新潟理化学，No17，13－19（1991）
6）糟谷真宏他1名：ひも状接触材を充填した接触酸化水路における水質浄化特性：愛知県農業総合試験場研究報告：第23号，313－318（1991）
7）西田保一他8名：ろ材を使った水路浄化とその問題点：環境技術，462－465（1996）
8）崎村誠三：ひも状接触材バイオコードによる河川の直接浄化，用水と廃水，39（3），241－247（1997）
9）日本規格協会：JIS K0102工場排水試験方法（1993）
10）大西彬聰：窒素除去に関する技術動向，環境管理，34（7），643－652（1998）

Development of Under-Over Stream-type Biofilm Reactor Combined with Successive Switching of Inlet and Outlet Points for Treating Domestic Wastewater

Tadaaki MIZOGUCHI, Yosuke KAJIYAMA, Kazunori SATO, Shigehito TAKAMOTO, Mitsumasa MURAKAMI

ABSTRACT

An Under-Over Stream (UOS) -type biofilm reactor equipped with a filtering material in the form of long threads for treating domestic wastewater from a district mainly using a primitive-type wastewater-treating tank was developed. The proposed biofilm reactor in which flow was directed under and over baffles facilitated securing of high levels of dissolved oxygen and gave good contact between the filtering material and wastewater. In the UOS-type reactor, the sludge adhered to the filtering material was removed by shifting the material from the inlet side to outlet side at a point when the cleaning performance at the inlet side is lowered. An year-long test for domestic wastewater treatment was performed with a reactor that had an effective volume of 1.6 ㎥ and with an automatic switching between the wastewater inlet and outlet points at given time intervals. As a result, when the water temperature is 12℃ or higher, the sludge was removed to a level such that COD was lowered from about 25-30 mg/L to about 10-15 mg/L and BOD to about 5 mg/L at a residence time of 6.7h. In few case, the suspended solids were found at a concentration of about 10 mg/L. The filtering material did not require cleaning during the one-year test period. Nitrogen was present mostly in the form of ammonium in the original domestic wastewater. However, when the water temperature is 10℃ or higher, more than 90 % of nitrogen in the form of ammonium was oxidized to nitrate in the biofilm reactor.

Key Words : domestic wastewater, biofilm reactor, wastewater treatment, sludge, inlet and outlet points switching

Flexible Molecular Model of Methanol for a Molecular Dynamics Study of Liquid and Supercritical Conditions

Tetsuo Honma,[†,‡] Chee Chin Liew,[§] Hiroshi Inomata,*[,†] and Kunio Arai[†,∥]

Research Center of Supercritical Fluid Technology, Tohoku University, Sendai, 980-8579, Japan, Supercritical Fluid Research Center, National Institute of Advanced Industrial Science and Technology (AIST), Sendai, 983-8551, Japan, and Research Institute for Computational Sciences (RICS), National Institute of Advanced Industrial Science and Technology (AIST), Tsukuba, 305-8568, Japan

Received: November 27, 2002; In Final Form: February 24, 2003

A new flexible molecular model of methanol was developed for computer simulations applicable to conditions from the liquid to the supercritical state. The proposed model considered methanol as three interaction sites, oxygen atom, methyl group, and hydrogen atom, and was represented as the sum of intramolecular and intermolecular potentials. The intramolecular potential function introduced a Toukan−Rahman potential and the intermolecular potential function applied an OPLS function. The potential parameters were adjusted to represent the experimental saturated liquid density of methanol at 25 °C. The estimated critical point of the proposed model (T_C = 232.2 °C, ρ_C = 0.278 g·cm^{-3}) was found to be close to the experimental critical point. Transport properties and vibrational spectra were in good agreement with the literature values. The fluid structure of methanol was studied via analyses made on the spatial distribution function. Methanol was found to have chainlike structures in the liquid state and perturbed structure at supercritical conditions. From the analyses, roughly half of the hydrogen bonding molecules in the liquid state were preserved even in supercritical conditions.

Introduction

The structure of hydrogen bonding fluids change greatly when fluid conditions are brought from the ambient state to the supercritical state.[1,2] Many researchers have tried to elucidate the hydrogen bonding structure of fluids at higher temperatures and pressures from neutron diffraction,[1,3] X-ray diffraction,[4,5] and theoretical approaches.[6−9] Theoretical approaches have made much progress in describing hydrogen bonding fluids as evident from the many potentials such as SPC,[10] SPC/E,[11] TIPS,[12] OPLS,[13] and other models.[14−16] Our research group has published a flexible model for water denoted as the cm4p-mTR model,[17] which could accurately represent water's critical properties and its hydrogen bonding behavior in the supercritical region.[18]

Most methanol potentials proposed in the literature are rigid models.[19−21] Jørgensen[13,22] and Haughney et al.[23] originally developed methanol models that reproduced thermodynamic properties and the structure substances in the liquid state. However, despite the importance of the critical region, rigid models have lower critical temperatures compared with the experimental values.[24,25] Molecular flexibility may be an important factor to improve the model capability for representing the critical point, because this is one aspect that allows relaxation of the kinetic energy transfer of molecular collisions. In addition, molecular flexibility can provide vibrational spectra that can make a direct comparison with Raman or infrared spectra. Flexible methanol models have been published by Palinkas,[26,27] which are based on the BJH water model.[28] The Palinkas methanol models can change its dipole moment according to the thermodynamic state and exhibit a gas−liquid frequency shift in the vibrational spectrum. However, the functional form of the model is a sum of the CCL model and unique polynomial functions that requires much effort to compose an aqueous system with the currently used water models. Methanol, like water, can be represented in terms of three sites: oxygen atom, methyl group, and hydrogen atom. In a dilute aqueous solution at ambient liquid conditions, for example, it has been suggested that a methanol molecule could replace a water molecule in a hydrogen bonding network and only slightly perturb the hydrogen bond network structure. In this work, we propose a methanol model based on the cm4p-mTR potential that can be conveniently implemented by representing methanol as three sites. We discuss the model's critical point, vibrational spectra, self-diffusion coefficients, and the simulated fluid structure and hydrogen bonding.

Molecular Model

The proposed model considered the methanol molecule as three sites: an oxygen atom (site 1, O), the methyl group as a whole (site 2, Me), and a hydrogen atom (site 3, H), and was represented as the sum of intramolecular and intermolecular potentials. The intramolecular potential functions were based on the angular form of Toukan−Rahman model for water,[29] which was modified for methanol model. We adopted three intramolecular vibrational modes of methanol: O−Me stretching, O−H stretching and H−O−Me bending. The O−Me stretching and H−O−Me bending were assumed harmonic, because the displacement amplitude of these motions from

* Corresponding author. E-mail: inomata@scf.che.tohoku.ac.jp.
† Tohoku University.
‡ Currently at Supercritical Fluid Research Center.
§ Research Institute for Computational Sciences (RICS), National Institute of Advanced Industrial Science and Technology (AIST).
∥ Supercritical Fluid Research Center, National Institute of Advanced Industrial Science and Technology (AIST).

10.1021/jp027578a CCC: $25.00
Published on Web 04/16/2003

TABLE 1: Intramolecular Potential Parameters for the Proposed Methanol Model

$r_{c,12}$/Å	$r_{c,13}$/Å	$\theta_{c,213}$/deg	D_{OH}/kJ·mol^{-1}	α_{13}/Å^{-1}
1.430	0.945	108.5	435.1	2.3083

K_{r12}/kJ·mol^{-1}	β/kJ·mol^{-1}	γ_{12}/kJ·mol^{-1}	γ_{13}/kJ·mol^{-1}	δ/kJ·mol^{-1}
3022.3200	221.1240	139.1369	103.1043	93.2820

TABLE 2: Intermolecular Potential Parameters for the Proposed Methanol Model

interaction site	m/g·mol^{-1}	q/e	ϵ/kJ·mol^{-1}	σ/Å
oxygen	16.000	−0.700	0.7539	3.0645
methyl group	15.034	0.265	1.2307	3.7300
hydrogen	1.008	0.435	0.0100	0.9000

equilibrium geometries was generally small. Consequently, the intramolecular potential functions were expressed as follows:

$$U_{intra} = U_{12} + U_{13} + U_{213} \quad (1)$$

$$U_{12} = K_{r12}\Delta r_{12}^2 \quad (2)$$

$$U_{13} = D_{OH}(1 - \exp[-\alpha_{13}\Delta r_{13}])^2 \quad (3)$$

$$U_{213} = \frac{1}{2}\beta(\Delta\theta)^2 r_{12}r_{13} + \gamma_{r12\theta} r_{12}\Delta\theta\Delta r_{12} + \gamma_{r13\theta} r_{13}\Delta\theta\Delta r_{13} + \delta(\Delta r_{12}\Delta r_{13}) \quad (4)$$

where D_{OH} is the dissociation energy for the O−H bond. Subscripts 1−3 denote oxygen, the methyl group, and the hydrogen site, respectively. The r_{ij} and Δr_{ij} are separation and displacement from the equilibrium distance between atom i and j, and $\Delta\theta$ is the bending angle for H−O−Me subtracted from the equilibrium angle. The K_{r12}, α_{13}, β, γ_{12}, γ_{13}, and δ are potential parameters that were fitted to reproduce vibrational frequencies in the gas phase[37] independently of intermolecular potential.[29] The determined parameters are listed in Table 1.

The intermolecular potential function used was a three-site OPLS-type[13] potential:

$$U_{inter} = \sum_i \sum_j 4\epsilon_{ij}\left[\left(\frac{\sigma_{ij}}{r_{ij}}\right)^{12} - \left(\frac{\sigma_{ij}}{r_{ij}}\right)^{6}\right] + \frac{q_i q_j}{r_{ij}} \quad (5)$$

where i and j denote each interaction site of the methanol, σ and ϵ are the Lennard-Jones (LJ) parameters, and q and r are the partial charge and the separation between interaction sites, respectively. The original OPLS model neglects a LJ parameter on the hydrogen site. However, in presimulations with the flexible model, we found that large O−H stretching occurred, leading to the dissociation of the O−H bond above a critical point. To prevent this phenomenon, a LJ parameter on the hydrogen site was introduced. Moreover, the LJ parameter on the O site was adjusted to fit the experimental liquid saturated pressure of methanol at 25 °C and 0.787 g·cm^{-3}, which were taken from IUPAC.[30] The determined intermolecular potential parameters are listed in Table 2.

MD simulations were performed with *NVT* ensembles containing 500 methanol molecules. The equations of motion were solved using the velocity Verlet algorithm[31] with a reversible reference system propagator (r-RESPA) algorithm.[32] Time steps were 1 fs for the intermolecular motion and 0.2 fs for the intramolecular motion. The total simulation time was 300 ps including 100 ps equilibration. The first 60 ps of simulation, the temperature was maintained at the desired value with momentum scaling and afterward it was controlled with the Nosé−Hoover thermostat. The electrostatic forces were approximated with a cutoff distance of 10 Å for each interaction pair, and energy contributions outside cutoff cavities were treated with a site−site reaction field method[31,33] with a dielectric continuum. For this study, we chose the four state conditions listed in Table 3, three of which had been the target of structural analysis using neutron diffraction H/D substitution by Yamaguchi et al.[5]

TABLE 3: State Points for Simulation

	supercritical	near-critical	subcritical	liquid
T/°C	245	245	195	25
ρ/g·cm^{-3}	0.716	0.463	0.716	0.787

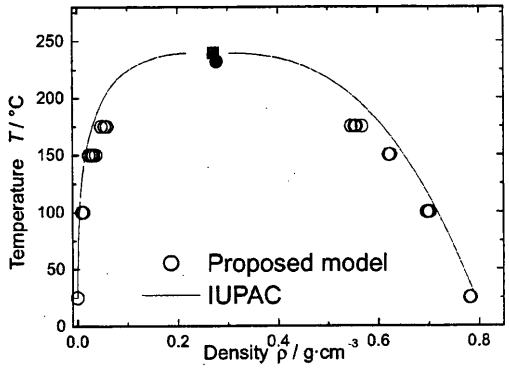

Figure 1. Vapor−liquid coexistence densities. Circles: MD simulation with the proposed model. Filled circle: model's estimated critical point. Solid line: experimental data obtained from IUPAC.[31] Filled square: experimental critical point.

TABLE 4: Critical Temperature and Density of the Proposed Model and Literature

	proposed	OPLS[24]	OPLS[25]	IUPAC[31]
T_c/°C	232.2	220	211.5	239.5
ρ_c/g·cm^{-3}	0.278	0.25	0.262	0.279

TABLE 5: Peak Frequencies in Vibrational Spectra

	libration	Me−O stretching	Me−O−H bending	O−H stretching
supercritical	245	1028	1240	3530
subcritical	193	1025	1240	3590
near-critical	485	1028	1248	3508
liquid	560	1033	1305	3440
liquid (harmonic)	560	1033	1308	3705
exp values[38]				
liquid	655	1029	1420	3337
gas		1034	1346	3687

Critical Properties of Proposed Methanol Model

We estimated the vapor−liquid saturated densities of the proposed model with a direct simulation technique of Alejandre et al.[34] to examine its performance as a methanol model in the subcritical and supercritical region. The obtained vapor−liquid saturated densities are shown in Figure 1. The data had fluctuations in the vicinity of the critical point, but they were in agreement with the saturation data of IUPAC.[30] The critical point of the proposed model was estimated by fitting the coexisting density data using the law of rectilinear diameters and the scaling law with a scaling exponent of 0.325.[35] The critical temperature and density obtained from the proposed flexible model are listed in Table 4. The proposed model was found to reproduce the critical point better than the results of

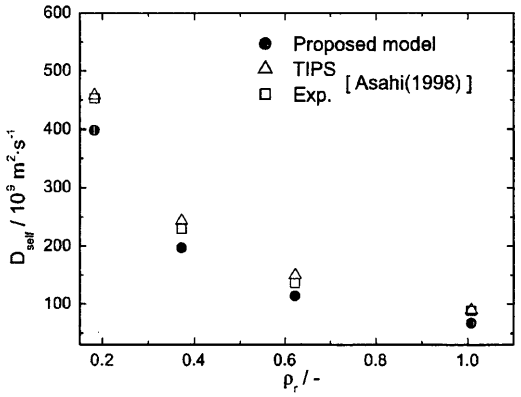

Figure 2. Dependence of self-diffusion coefficient on the densities. Filled circles: estimated from MD simulation of proposed model. Open squares: NMR data.[36] Open triangles: MD simulation[36] (TIPS model).

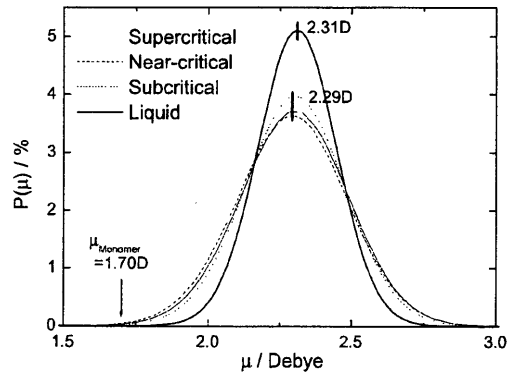

Figure 3. Dipole moment distribution of proposed model.

the current rigid OPLS model,[24,25] which may be attributed to the molecular flexibility that allows relaxation of kinetic energies.

The self-diffusion coefficient, D_{self}, was calculated from the mean square displacement (MSD):

$$D_{self} = \lim_{t\to\infty} \frac{1}{6t} \langle |r(t) - r(0)|^2 \rangle \qquad (6)$$

where $r(t)$ is the position vector at time t. The maximum time for estimating MSD was 0.2 ps, which made MSD a constant slope and was enough time to compute the self-diffusion coefficient. The density dependence of the self-diffusion coefficient determined from the proposed model at a reduced temperature of $T_r = 1.15$ is shown in Figure 2. For comparison, the self-diffusion coefficients of Asahi and Nakamura[36] via MD simulation of the TIPS model and ^{1}H NMR spin−echo techniques measurement are also shown in Figure 2. The self-diffusion coefficient decreased with increasing density, which was qualitatively consistent. However, the proposed model underestimated the self-diffusion coefficient at low densities compared with the literature values, which may be attributed to the TIPS methanol model having about a 10% lower critical temperature.[19]

Figure 3 shows the dipole moment distribution in terms of the density for the proposed model. In the liquid state, the distribution ranged from 1.7 to 3.0 D with the maximum population being around 2.3 D. This was different from that determined by Palinkas et al.[26] and could be attributed to differences in monomer geometries. At higher temperatures, the distributions of the proposed methanol model tended to follow

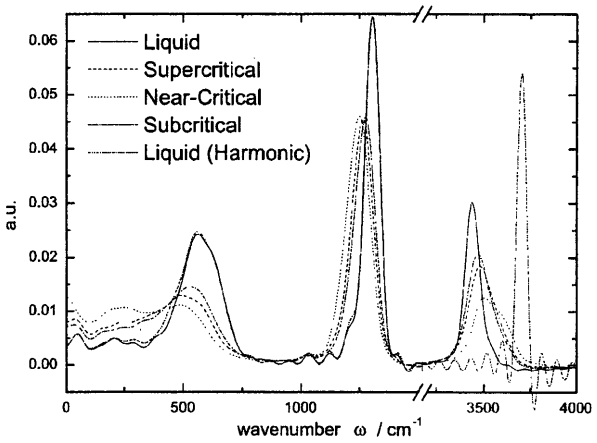

Figure 4. Power spectra of velocity autocorrelation function for H-site.

the Boltzmann distribution, suggesting the validity of the simulation near the critical point.

Power spectra for vibrational modes of three sites of methanol model, $I(\omega)$, were obtained as a Fourier transform of the velocity autocorrelation function as follows:

$$I(\omega) = \int_0^\infty \frac{v(t)\, v(0)}{v(0)\, v(0)} \cos(\omega t)\, dt \qquad (7)$$

where $v(t)$ is the velocity of each atom at time t and ω is the wavenumber. Harmonic potential for O−H vibration was applied to examine the effect of unharmonicity for the intramolecular potential. The peak frequencies of vibrational mode and power spectra for the hydrogen site are shown in Table 5 and Figure 4.

The peak frequencies around 600, 1030, 1250, and 3500 cm^{-1} were assigned as libration, Me−O vibration, Me−O−H bending, and O−H vibration, respectively. Falk and Whalley obtained a gas−liquid frequency shift by infrared spectroscopy that was 250 cm^{-1}.[37] In our simulation, there was a 250 cm^{-1} difference for O−H vibration between the anharmonic (3450 cm^{-1}, liquid) and the harmonic potential (3700 cm^{-1}, liquid harmonic). Molecular anharmonicity permitted a large O−H separation with hydrogen bonding and a red shift of vibrational frequencies.

At higher temperatures, the Me−O and the Me−O−H bending vibrations shifted to lower frequencies. Koda et al. measured Raman spectral shifts at temperatures from ambient to supercritical state and the C−O stretching frequencies decreased with increasing temperature.[38] The vibrational spectra of the proposed model were in good agreement with the experimental data by Koda et al. However, the simulated Me−O frequencies at higher temperatures were not as sensitive to temperature and density as the experimental values. The O−H vibration was composed of the lower (3450 cm^{-1}) and higher (3600 cm^{-1}) vibration peaks. It should be noted that these two peaks were attributed as hydrogen-bonded molecules and nonbonded monomers, respectively, which implied the hydrogen-bonding structure still remained in the critical regions. The vibrational spectra can provide the qualitative degree of hydrogen bonding according to fluid conditions. However, we chose to use the three-dimensional pair distribution function, so-called spatial distribution function, to obtain detailed hydrogen-bonding information such as orientation and coordination.

Fluid Structure

Three-dimensional analysis with a spatial distribution function was conducted for studying fluid structure around an anisotropic

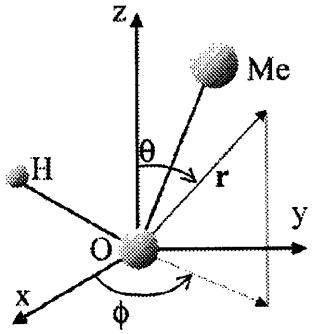

Figure 5. Principal frame coordinates of methanol.

molecule such as methanol. In this study, the definition of the principal frame coordinates described by Svishchev and Kusalik was adopted.[39] As defined in Figure 5, **r** is a position vector pointing toward a site of another molecule from the oxygen site, θ is the angle between the vector **r** and a z-axis bisecting the angle Me−O−H, and ϕ is the angle between the x-axis and the **r**-projection onto the $x-y$ plane. The spatial distribution function at $\theta = 0-360°$ and $\phi = 0°$ was chosen for analysis. According to the definition, it can be expected that linear hydrogen bonding will be observed at $r = 2.8$ Å, $\theta = 60°$, and $\phi = 0°$ defined as LHB1 and $r = 2.8$ Å, $\theta = 180°$, and $\phi = 0°$ defined as LHB2 and an area around methyl group $\theta = 300°$ and $\phi = 360°$.[39]

The oxygen−oxygen spatial distribution function estimated from the proposed model, g_{OO}, in the liquid state is shown in Figure 6a. We also performed additional simulations with the original OPLS model, shown in Figure 6b, which yielded a comparable spatial distribution function. For the case of the first shell, two sharp peaks occurred at LHB1 and LHB2. The peak height at LHB1 for the proposed model was about 130 times higher than that estimated from bulk density. The second solvation shell could be seen at $r = 4.5$ Å, $\theta = 30°$, 90°, and 150°, and broader a third solvation shell occurred at $r = 7$ Å and $\theta \leq 240°$. The two main peaks of the first solvation shell come from linear hydrogen bonding that bound strongly each other. It should be noted that the LHB1 peak of the proposed model was slightly higher than that of the rigid OPLS model. This means that that molecular flexibility changes the molecule's dipole moment and it might promote formation of hydrogen bonding. In the second solvation shell, two peaks at $\theta = 30°$ and 120° at the same separations imply a chainlike structure proposed by Jørgensen.[22] The peak at $\theta = 90°$ relates branches in the chainlike structure. Around the methyl group, it could be seen that only one broad peak was present at $r = 4-7$ Å and $\theta \geq 180°$. The methyl group has a large exclusive volume, and this probably leads to the formation of chainlike structures of methanol rather than three-dimensional networks.

Figure 7a and Figure 7b show spatial distribution functions at supercritical conditions ($T = 245$ °C, $\rho = 0.716$ g·cm^{-3}) obtained from the proposed model and the rigid OPLS model, respectively. The structure obtained from the proposed model was qualitatively in agreement with that determined from the original OPLS model and the neutron diffraction data with H/D substitution treatment estimated by Yamaguchi et al.[5] Two clear peaks occurred at LHB1 and LHB2 and became much broader and lowered compared with those in the liquid state. The hydrogen bonding fluctuated but still remained at supercritical condition, but no long-range liquid structural features such as chainlike structures could be observed. The second shell, $r =$ 4.5 Å, and third shell, $r = 7$ Å, were different and significantly smaller than that in the liquid state. We also estimated the g_{OO}

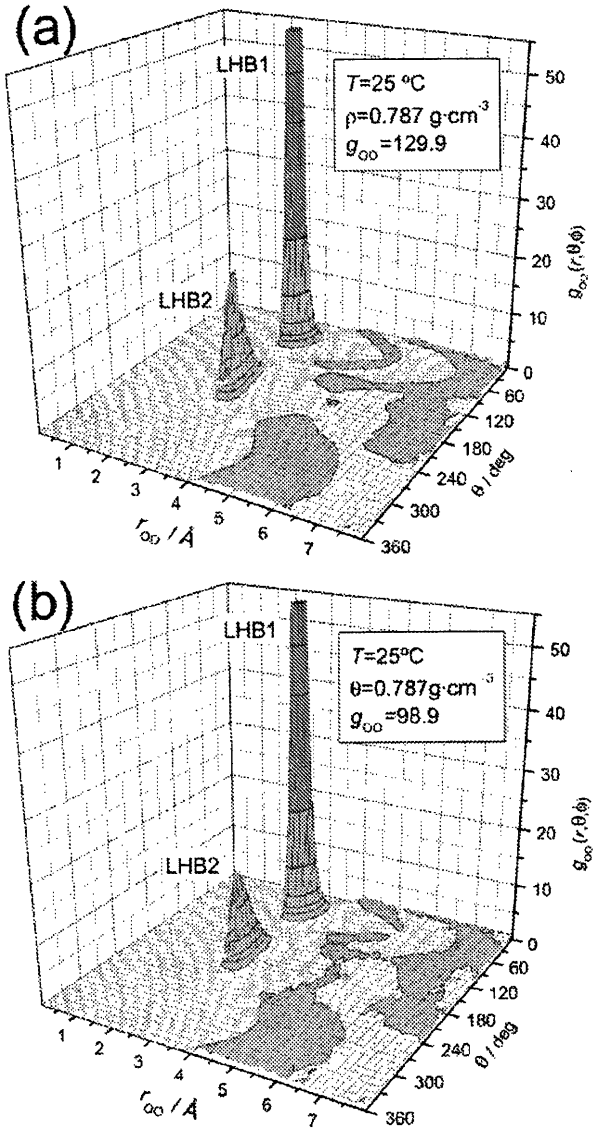

Figure 6. Spatial distribution function in the liquid state. (a) Proposed model. (b) Rigid OPLS model.

at $\phi = 90°$ for methanol, which was perpendicular to its molecular plane. In this plane at $r = 2.8$ Å and $\theta = 180°$ exhibited one peak, which was the same as the peak at LHB2. Therefore, we confirmed that the methanol model could coordinate up to two molecules at LHB1 and LHB2.

For quantitatively discussing the state condition dependence of the hydrogen bonding, we evaluated the average number of hydrogen bonds per molecule. There have been many criteria of hydrogen bonding: geometric definitions,[3,40] energetic definitions,[12,41] and combinations of these.[42,43] In this work, we adopted the geometric definition by Yamaguchi et al.[5] to compare our results with their data. The hydrogen bond between two molecules was defined as follows:

$$2.0 \text{ Å} \leq r_{O\cdots O} \leq 3.4 \text{ Å}$$
$$1.4 \text{ Å} \leq r_{O\cdots H} \leq 2.4 \text{ Å} \quad (8)$$

where $r_{O\cdots O}$ and $r_{O\cdots H}$ are oxygen−oxygen and oxygen−hydrogen separations, respectively. The estimated average numbers of the hydrogen bond are listed in Table 6. The values

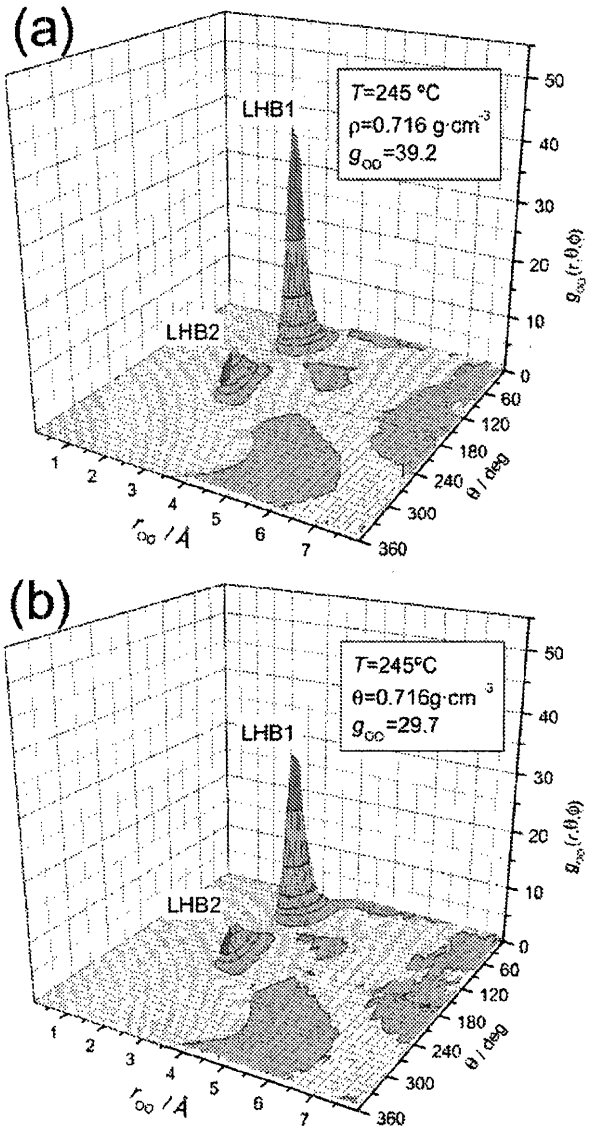

Figure 7. Spatial distribution function in supercritical state. (a) Proposed model. (b) Rigid OPLS model.

TABLE 6: Hydrogen Bonding Analysis From the Geometric Criteria (See Text)[a]

	proposed	rigid OPLS	ref 5	ref 45
liquid	1.90	1.83	1.77	
				(1.0)
supercritical	1.30	1.16	1.6	
	(0.68)	(0.64)	(0.90)	(N/A)
near-critical	0.98	0.89	1.0	
	(0.52)	(0.49)	(0.56)	(0.4)
subcritical	1.43	1.29	1.6	
	(0.75)	(0.71)	(0.90)	(0.6−0.8)

[a] Values in parentheses are normalized values with the value at liquid state.

in brackets are normalized with the liquid state value. The number of hydrogen bonds at each state point showed that the hydrogen bonding decreased with decreasing density and increasing temperature, as expected. At high temperature conditions, roughly half the number of hydrogen bonds still remained compared with that in the liquid state. The average number of hydrogen bonds obtained from the proposed model were 10% higher than those from the original OPLS model, which may be due to the model's temperature dependence of the dipole moment and its flexible nature that contributes to relaxation of kinetic energies. Table 6 contains values by Yamaguchi et al. from the spatial distribution functions from MD simulations of the empirical potentials tuned by the structure refinement approach.[5] They were 1.6, 1.0, and 1.6 at the supercritical, the near-critical, and the subcritical conditions, respectively. In addition, the values determined by Hoffman and Conradi from the ^{1}H NMR chemical shift[44] are also tabulated. Although the average numbers of hydrogen bonding estimated from the proposed model were up to 20% lower than those by Yamaguchi et al., and there are 30% variations in values among researchers. Simulations with the proposed flexible model could represent the qualitative tendency of hydrogen bonding at higher temperatures and probably provides a better estimation of the true solution structure.

Conclusions

A new flexible methanol model was developed that used an angular form of the TR intramolecular and the OPLS intermolecular potentials. The LJ parameter on the H-site prevented dissociation at supercritical conditions, especially higher density conditions. The critical point of the proposed model (T_C = 232.2 °C, ρ_C = 0.278 g·cm^{-3}) was in good agreement with experimental values and provides reliability of the chosen simulation thermodynamic state of methanol, especially at supercritical conditions. The fluid structure of a proposed model had a qualitative agreement with the current model and experiment. In the liquid state, a chainlike structure was formed, but it was perturbed in the critical region. We evaluated the average number of hydrogen bonds via a geometric criteria, it was qualitatively well-reproduced trend and was quantitatively in an error range up to 30% from the literatures. More than half of hydrogen bonds are still preserved in the critical regions according to present simulations. The proposed flexible methanol model could be applied to study supercritical systems and those at extreme conditions of temperature and pressure.

Acknowledgment. This work has been partly supported by CREST of JST (Japan Science and Technology).

References and Notes

(1) Soper, A. K. *Chem. Phys.* **2000**, *258*, 121−137.
(2) Chialvo, A. A.; Yezdimer, E.; Driesner, T.; Cummings, P. T.; Simonson, J. M. *Chem. Phys.* **2000**, *258*, 109−120.
(3) Soper, A. K.; Bruni, F.; Ricci, M. A. *J. Chem. Phys.* **1997**, *106* (1), 247−254.
(4) Yamaguchi, T. *J. Mol. Liq.* **1998**, *78*, 43−50.
(5) Yamaguchi, T.; Benmore, C. J.; Soper, A. K. *J. Chem. Phys.* **2000**, *112* (20), 8976−8987.
(6) Chialvo, A. A.; Cummings, P. T. *J. Chem. Phys.* **1994**, *101* (5), 4466−4469.
(7) Chalaris, M.; Samios, J. *J. Phys. Chem. B* **1999**, *103* (7), 1161−1166.
(8) Jedlovszky, P. *J. Chem. Phys.* **2000**, *113* (20), 9113−9121.
(9) Predota, M.; Nezbeda, I.; Cummings, P. T. *Mol. Phys.* **2002**, *100* (14), 2189−2200.
(10) Berendsen, H. J. C.; Postma, J. P. M.; van Gunsteren, W. F.; Hermans, J. *Intermolecular Forces*; Pullman, B., Ed.; Reidel: Dordrecht, The Netherlands, 1981.
(11) Berendsen, H. J. C.; Grigerarand, J. R.; Straatsma, T. P. *J. Phys. Chem.* **1987**, *91* (24), 6269−6271.
(12) Jørgensen, W. L.; Chandrasek, J.; Madura, J. D.; Impey, R. W.; Klein, M. L. *J. Chem. Phys.* **1983**, *79* (2), 926−935.
(13) Jørgensen, W. L. *J. Phys. Chem.* **1986**, *90* (7), 1276−1284.
(14) Sprik, M.; Klein, M. L. *J. Chem. Phys.* **1988**, *89* (12), 7556−7560.
(15) Rick, S. W.; Stuart, S. J.; Berne, B. J. *J. Chem. Phys.* **1994**, *101* (7), 6141−6156.
(16) Svishchev, I. M.; Kusalik, P. G.; Wang, J.; Boyd, R. J. *J. Chem. Phys.* **1996**, *105* (11), 4742−4750.

(17) Liew, C. C.; Inomata, H.; Arai, K. *Fluid Phase Equilibr.* **1998**, *144*, 287−298.
(18) Liew, C. C.; Inomata, H.; Arai, K.; Saito, S. *J. Supercrit. Fluids* **1998**, *13*, 83−91.
(19) van Leeuwen, M. E.; Smit, B. *J. Phys. Chem.* **1995**, *99* (7), 1831−1833.
(20) Bakó, I.; Jedlovszky, P.; Pálinkas, G. *J. Mol. Liq.* **2000**, *87*, 243−254.
(21) Walser, R.; Mark, A. E.; van Gunsteren, W. F.; Lauterbach, M.; Wipff, G. *J. Chem. Phys.* **2000**, *112* (23), 10450−10459.
(22) Jørgensen, W. L. *J. Am. Chem. Soc.* **1981**, *103* (2), 335−340.
(23) Haughney, M.; Ferrario, M.; McDonald, I. R. *Mol. Phys.* **1986**, *58* (4), 849−853.
(24) Mezei, M. *Mol. Simul.* **1992**, *9* (4), 257−267.
(25) Kettler, M.; Nezbeda, I.; Chialvo, A. A.; Cummings, P. T. *J. Phys. Chem. B* **2002**, *106* (30), 7537−7546.
(26) Palinkas, G.; Hawlicka, E.; Heinzinger, K. *J. Phys. Chem.* **1987**, *91* (16), 4334−4341.
(27) Hawlicka, E.; Palinkas, G.; Heinzinger, K. *Chem. Phys. Lett.* **1989**, *154* (3), 255−259.
(28) Bopp, P.; Janscó, G.; Heinzinger, K. *Chem. Phys. Lett.* **1983**, *98*, 129−133.
(29) Toukan, K.; Rahman, A. *Phys. Rev. B* **1985**, *31* (5), 2643−2648.
(30) de Reuck, K. M., Craven, R. J. B., Eds. *Methanol*, IUPAC Chemical Data Series; Blackwell Science Inc.: Glasgow, 1993.
(31) Allen, M. P.; Tildesley, D. J. *Computer Simulation of Liquids*, 2nd ed.; Oxford University Press Inc.: Oxford, U.K., 1987.
(32) Tuckerman, M.; Berne, B. J.; Martyna, G. J. *J. Chem. Phys.* **1992**, *97* (3), 1990−2001.
(33) Hummer, G.; Soumpasis, D. M.; Neumann, M. *Mol. Phys.* **1992**, *77* (4), 769−785.
(34) Alejandre, J.; Tildesley, D. J.; Chapela, G. A. *J. Chem. Phys.* **1995**, *102* (11), 4574−4583.
(35) Guissani, Y.; Guillot, B. *J. Chem. Phys.* **1993**, *98* (10), 8221−8235.
(36) Asahi, N.; Nakamura, Y. *J. Chem. Phys.* **1998**, *109* (22), 9879−9887.
(37) Falk, M.; Whalley, E. *J. Chem. Phys.* **1961**, *34* (5), 1554−1568.
(38) Ebukuro, T.; Takami, A.; Oshima, Y.; Koda, S. *J. Supercrit. Fluids* **1999**, *15*, 73−78.
(39) Svishchev, I. M.; Kusalik, P. G. *J. Chem. Phys.* **1994**, *100* (7), 5165−5171.
(40) Mezei, M.; Beveridge, D. L. *J. Chem. Phys.* **1981**, *74* (1), 622−632.
(41) Petsche, I. B.; Debenedetti, P. G. *J. Chem. Phys.* **1989**, *91* (11), 7075−7084.
(42) Liew, C. C.; Inomata, H.; Saito, S. *Fluid Phase Equilib.* **1995**, *104*, 317−329.
(43) Kalinichev, A. G.; Bass, J. D. *J. Phys. Chem. A* **1997**, *101* (50), 9720−9727.
(44) Hoffmann, M. M.; Conradi, M. S. *J. Phys. Chem. B* **1998**, *102* (1), 263−271.

Available online at www.sciencedirect.com
SCIENCE DIRECT®
ELSEVIER
J. Anal. Appl. Pyrolysis 00 (2003) 1–12
JOURNAL of ANALYTICAL and APPLIED PYROLYSIS
www.elsevier.com/locate/jaap

Decomposition kinetics of 2-propylphenol in supercritical water

Takafumi Sato [a], Tadafumi Adschiri [b], Kunio Arai [a,c,*]

[a] *Supercritical Fluid Research Center, National Institute of Advanced Industrial Science and Technology, 4-02-1 Nigatake, Miyagino, Sendai 983-8551, Japan*
[b] *Institute of Multidisciplinary Research for Advanced Materials, Tohoku University, 2-1-1 Katahira, Aoba-ku, Sendai 980-8577, Japan*
[c] *Department of Chemical Engineering, Tohoku University, 07 Aoba, Aramaki-Aza, Aoba-ku, Sendai 980-8579, Japan*

Abstract

The decomposition of 2-propylphenol (PP) at 673 K and a water density of 0–0.5 g cm^{-3} yielded 2-isopropylphenol (IPP), phenol and 2-cresol. Gas products were methane, carbon dioxide, ethylene and propene. The decomposition was found to occur through rearrangement and alkylation, that is, (1) rearrangement of the propyl functional group from PP to IPP, (2) dealkylation of PP to phenol, (3) dealkylation of PP to 2-cresol. The decomposition probably occurred by a free-radical mechanism. The reaction rate constants of each pathway were determined and it was found that these were invariant over all the water densities studied at the given temperature.

Keywords: Alkylphenol; Phenol; Dealkylation; Rearrangement; Supercritical water

1. Introduction

Phenolics such as alkylphenols and phenol are important chemicals as pharmaceuticals, dyes, antioxidants and source of phenolic resins. The phenolics were conventionally synthesized from alkylbenzenes of petroleum by oxidation of cumene to produce phenol and alkylation of phenol with corresponding alkene under strong

* Corresponding author. Tel./fax: +81-22-217-7246.
E-mail address: karai@arai.che.tohoku.ac.jp (K. Arai).

0165-2370/03/$ - see front matter © 2003 Elsevier Science B.V. All rights reserved.
doi:10.1016/S0165-2370(03)00051-2

acid catalyst [1]. Due to the structure, coal, lignin and phenolic resins are expected to become a future source of phenolic compounds to replace conventional petroleum [2,3]. Organic hydrogen donor solvents can be used for recovering the phenolic compounds from these starting materials [3], which have the advantage of reducing char formation due to condensation but a clear disadvantage when considering environmental aspects and green chemistry.

Conversion of alkylphenols in water, especially in its supercritical state, might be expected to provide an alternative method to organic solvents. When water is heated above its critical temperature and pressure ($T_c = 647$ K and $P_c = 22.1$ MPa), it becomes highly compressible and is in a supercritical state. Supercritical water is dense steam and can be miscible with gases and hydrocarbons to form a homogeneous mixture [4,5]. Supercritical water is both a solvent and a reactant [6,7] where hydrolysis is usually a major reaction and water molecules often play a role as collision partners [8]. Further, the physical properties of supercritical water such as dielectric constant and ion product can be greatly changed by manipulating density with temperature and pressure. This allows control of reaction rates and chemical equilibrium [9].

Conversion of coal, lignin and phenolic resins has been demonstrated in supercritical water. Coal conversion in supercritical water promotes hydrolysis of coal so that extraction yields have been noted to be higher than those obtained for pure toluene [10]. For the case of lignin, Yokoyama et al. [11] studied its conversion in supercritical water at 648 K and reported that the yield of oil fraction increased and char formation was suppressed with increasing water density. Goto et al. [12] converted phenolic resin in supercritical water and obtained hydrolysis products.

To understand the effects of water on the decomposition kinetics of these substances, the reactions of alkylphenols under neat pyrolysis and in supercritical water are essential. Demirbas [13] reported that the main reaction of the pyrolysis of 4-ethylphenol was the bond cleavage between carbon in benzene ring and α-carbon of alkyl side chain. Zhou et al. [14] conducted the pyrolysis of 2-ethylphenol under nitrogen atmosphere at 623 K. The main product was phenol that was obtained at a yield of about 50%. The decomposition of alkylphenols has been examined in high temperature water. Katritzky et al. [15,16] reported that 2, 3, 4-cresol did not react significantly in water at 523 K for a reaction time over 3 days. Martino et al. [17] reported that decomposition of 2, 3, 4-cresol yielded phenol as a main product in supercritical water at 733 K. Adschiri et al. [18] conducted the decomposition of bisphenol-A in supercritical water at 673 K and reported that this compound was rapidly consumed within 10 min of reaction time by hydrolysis and phenol was produced as the main product. Tagaya et al. [19] examined bisphenol-F in supercritical water at 703 K. Bisphenol-F was completely decomposed at 60 min of reaction time and phenol, cresols and other alkylphenols were produced. We conducted the experiments on the decomposition of 2-isopropylphenol (IPP) in high temperature water at 613–713 K [20]. IPP decomposed through rearrangement to 2-propylphenol (PP) and dealkylation to phenol and propene. The rearrangement rate was independent of water density and the dealkylation rate increased with increasing water density. These results provide evidence that high temperature region especially

supercritical condition is suitable for the decomposition of alkylphenols in water, and that the structure of alkylphenol and water density are important factors governing the reactivity.

In this study, we chose PP as a model compound of alkylphenol and examined the decomposition of PP in the presence and absence of water. PP has an unbranched propyl group attached to phenol that is similar to the unit of lignin. Experiments were conducted at 673 K and at densities up to 0.5 g cm^{-3}. The reaction rates of each pathway at each water density were evaluated.

2. Experimental

The PP was purchased from Tokyo Kasei and had a purity of +98%. The analytical reagents used were tetrahydrofuran (THF, +97%) with 2,6-di-tert-butyl-4-methylphenol inhibitor and naphthalene (+99%) were obtained from Wako Chemical. All chemicals were used without further purification. Experiments at 673 K were conducted in batch type reactors (6 cm^3) that were fitted with a high-pressure valve (Whitey, model SS-3NBF2). The batch type reactors were made of SUS 316 tubes (length: 105 mm; i.d.: 8.5 mm; o.d.: 12.7 mm) that had two SUS 316 1/16–1/2 inch Swagelok reducing unions to a 1/16 inch SUS 316 tube (length: 300 mm; i.d.: 0.59 mm; o.d.: 1.59 mm) for ports. One port was connected to a high-pressure valve, and the other served as a thermocouple well for measuring reactor temperature. The reactor was loaded with 0.204–0.818 g of PP and 0.3–3 g of distilled water that corresponded to water densities, ρ_W, of 0.05–0.5 g cm^{-3}. Calculated pressures at 673 K and the given density were 12.6–37.0 MPa based on the pure water data of Haar et al. [21] Before the reaction, air in the reactor was displaced by purging with argon. Experiments without water as the solvent were also conducted.

After loading the reactor, the tube except valve was submerged into a fluidized sand bath (Takabayashirika Co., model TK-3) that was controlled at the reaction temperature. Heatup time was around 3 min. After a given amount of time (30–720 min), inclusive of the heatup time, the reactor was taken out of the bath and rapidly quenched in a water bath at 293 K.

After cooling, the reactor was submerged in an ultrasonic water bath for 5 min to degas the liquid and allow recovery of gases dissolved in water. The high pressure valve at the end of the reactor was connected to a sampling loop and a syringe. By opening the valve gently and withdrawing the syringe, gas samples could be collected. Further details can be seen in reference [22]. Gas products were analyzed with gas chromatography with thermal conductivity detector, GC-TCD (Shimadzu, model GC-8A). H_2 was analyzed with a molecular sieve 5A column and Ar carrier. CH_4 was analyzed by a molecular sieve 13x column with He carrier. C2–C3 hydrocarbons and CO_2 were analyzed by Porapak Q column with He carrier.

After sampling or displacing the gases, the reactor was opened and washed with THF. The aromatics in the THF solutions were identified by gas chromatography with flame ionization detector, GC–FID (Hewlett–Packard, model 5890, series II) with HP-1 column and gas chromatography-mass spectrometry, GC–MS (Japan

Electron Optics Laboratory, model Automass 20) with HP-5MS column and by comparison with peak standards and mass spec library. The analyses for detecting aliphatic alcohols were conducted with a HP-5 column. Product concentrations were determined by GC–FID with naphthalene as internal standard.

The product yield (Y), PP conversion (X) and product selectivity (S) were evaluated from:

$$Y_{product}(\%) = \frac{\text{amount of product (mol)}}{\text{amount of PP loaded (mol)}} \times 100 \quad (1)$$

$$X = \left(1 - \frac{\text{amount of PP (mol)}}{\text{amount of PP loaded (mol)}}\right) \quad (2)$$

$$S_{product} = \frac{Y_{product}/100}{X} \quad (3)$$

3. Results and discussion

3.1. Product distribution

Table 1 provides a summary of the experimental results for the liquid products at 673 K, $[PP]_0 = 0.5$ mol L^{-1} and 0–0.5 g cm^{-3} water density and Fig. 1 shows the structure of liquid products detected. The sum of the yield of these compounds at each run was above 81.7% and was above 89.4% at around 180 min of reaction time, which means that the phenol structure was relatively stable for these reaction times. For some experiments, that was above 100% because of the difficulty of accurate estimate for large amount of PP. The yield of PP was 77.4–85.0% at 180 min of reaction time, which means that the decomposition of PP was slow at 673 K regardless of the presence of water. The main products were IPP (**2**), phenol (**3**) and 2-cresol (**4**) over all water densities. These yields clearly increased while residual yield of PP, (**1**) decreased with reaction time, which seems to show that IPP was produced through the rearrangement of alkyl group of PP and phenol and 2-cresol produced through the dealkylation of PP. The effect of water density on the initial product distribution was very small. For example, the yield of IPP (**2**) was 4.5–6.4%, that of phenol (**3**) was 2.8–4.2% and that of 2-cresol (**4**) was 2.2–2.4% at 180 min reaction time. Other products detected were 2-ethylphenol (**5**), 2-ethyl-6-propylphenol (**6**), 2-isopropyl-6-propylphenol (**7**), 2,6-dipropylphenol (**8**) and 2-methylbenzofuran (**9**), and 2-propanol (**10**) that was produced in the presence of water, but these yields were always below 3.9%. The alkylation of 2,6-position of phenol was preferred to that of 2,4-position probably due to the contribution of hydroxy group.

Table 2 shows the amount of gas produced at 0 and 0.5 g cm^{-3} water density and $[PP]_0 = 0.5$ mol L^{-1}. Because of the stability of the phenol structure, the gas components were derived from alkyl side chain of alkylphenols. In the absence of

Table 1
Yields of liquid products for PP decomposition at 0–0.5 g cm^{-3} water density, 673 K and $[PP]_0 = 0.5$ mol L^{-1}

Water density (g cm^{-3})	Reaction time (min)	Yield (%)										
		1	2	3	4	5	6	7	8	9	10	Sum of yields
0	30	98.2	1.2	1.2	0.4	0.0	0.2	0.0	0.4	0.0	0.0	101.6
	60	96.2	2.6	1.8	0.9	0.1	0.4	0.1	0.5	0.0	0.0	102.6
	180	82.0	6.4	4.2	2.6	0.6	1.1	0.3	1.0	0.1	0.0	98.3
	360	64.4	9.1	7.4	5.1	1.5	2.1	0.6	1.0	0.4	0.0	91.4
	720	47.8	10.2	11.0	8.8	3.9	2.8	1.0	1.0	1.0	0.0	87.5
0.05	30	90.4	0.8	0.4	0.2	0.0	0.1	0.0	0.1	0.0	0.0	92.9
	60	93.3	2.1	1.6	0.7	0.0	0.3	0.1	0.3	0.0	0.0	98.2
	90	96.2	3.1	1.9	1.1	0.1	0.4	0.1	0.3	0.0	0.0	93.3
	180	84.4	5.9	3.4	2.3	0.3	1.0	0.2	0.4	0.1	0.0	95.7
0.1	30	99.9	1.0	0.4	0.3	0.0	0.1	0.0	0.1	0.0	0.0	101.9
	60	94.7	2.2	0.8	0.8	0.1	0.2	0.0	0.1	0.0	0.0	98.9
	120	90.1	4.2	2.2	1.6	0.2	0.6	0.1	0.2	0.1	0.3	99.2
	180	85.0	5.5	2.8	2.2	0.3	0.9	0.2	0.4	0.1	0.0	97.4
	365	70.5	7.6	5.7	4.1	1.0	1.7	0.5	0.5	0.2	0.0	91.9
	720	47.7	7.7	11.7	7.2	2.8	2.4	0.9	0.8	0.6	0.2	81.7
0.3	30	102.4	1.3	0.4	0.4	0.0	0.1	0.0	0.1	0.0	0.2	104.6
	60	85.1	2.1	0.8	0.7	0.0	0.2	0.1	0.1	0.0	0.3	89.0
	60	88.9	2.1	0.9	0.7	0.1	0.2	0.1	0.1	0.0	0.3	93.1
	90	83.2	2.7	1.7	1.0	0.1	0.3	0.2	0.1	0.0	0.0	89.4
	120	89.3	4.1	2.5	1.7	0.2	0.6	0.2	0.1	0.0	0.8	98.8
	180	87.2	5.4	3.8	2.4	0.3	0.9	0.3	0.3	0.1	0.4	100.7
	360	73.6	6.8	8.1	4.3	0.9	1.6	0.7	0.6	0.2	0.6	96.9
	720	53.3	6.1	15.6	6.9	2.8	2.2	1.1	1.0	0.3	0.3	89.3
0.5	30	97.0	1.0	0.4	0.3	0.0	0.1	0.1	0.1	0.0	0.4	98.9
	60	92.2	1.9	1.0	0.7	0.0	0.2	0.1	0.1	0.0	0.7	96.0
	90	91.0	3.3	1.7	1.2	0.1	0.4	0.2	0.1	0.0	0.0	98.0
	120	90.0	3.8	3.3	1.7	0.1	0.7	0.4	0.2	0.0	2.3	100.3
	180	77.4	4.5	4.2	2.3	0.2	0.8	0.4	0.2	0.1	1.0	90.2
	360	69.5	6.4	11.5	4.8	1.1	1.8	1.1	0.7	0.1	1.4	97.1
	720	50.7	5.9	20.8	7.6	2.9	2.5	1.5	1.4	0.2	3.6	93.4

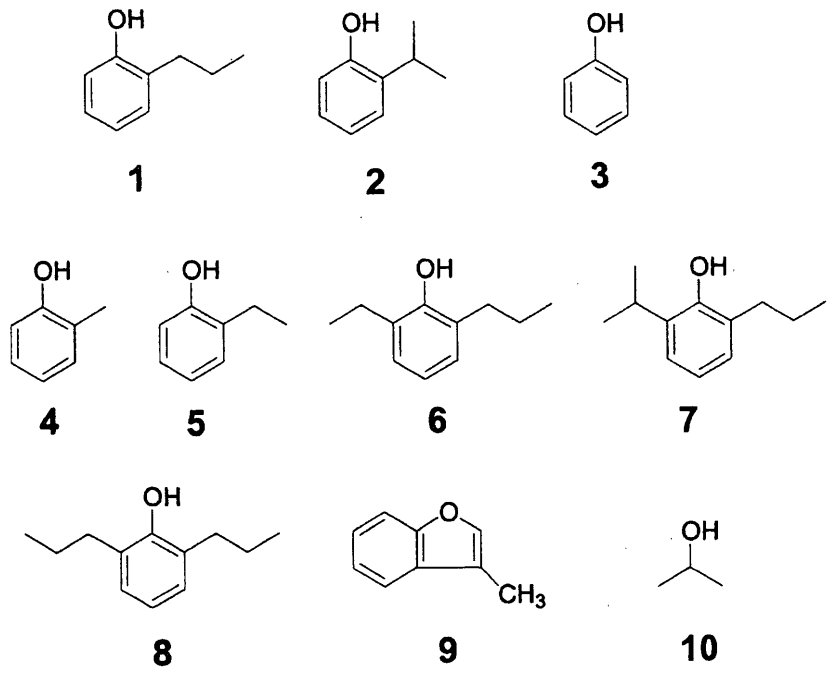

Fig. 1. Liquid products for PP decomposition at 673 K.

water at 30 min, the order of the amount of gases was hydrogen > methane ≈ ethylene > propene ≫ ethane and propane. At 180 min reaction time, this trend was the same and the total amount of gases increased. The data after 360 min of reaction time was probably implying the effect of a secondary reaction. In the presence of water, carbon dioxide was produced and the amounts of hydrogen and methane were less than those obtained in the absence of water. The total amount of carbon atoms and the amount of ethylene, ethane, propene and propane were almost the same with and without water at reaction times less than 180 min. Most likely, this means that carbon dioxide was produced instead of methane in the presence of water. Judging from these results, we propose a reaction pathway of 2-propoyphenol decomposition as Fig. 2. Rearrangement from PP to IPP (k_{IPP}) and dealkylation of PP to phenol (k_{Ph}) and 2-cresol (k_{Cre}) probably occur through the formation of methane, ethylene and propene as a parallel reaction. Rearrangement can proceed from IPP to PP as reported by Sato et al. [20]. Water does not affect the product distribution of alkylphenols significantly but enhances the formation of carbon dioxide instead of methane. From this reaction path, the reaction rate constants were evaluated.

3.2. Reaction kinetics

The rate constant for the rearrangement and dealkylation of PP were determined from the data at reaction times less than 120 min time. We assumed that the reaction was first order with respect to PP to evaluate the rate constants and then made a plot to test this assumption. Fig. 3 shows a plot of $-\ln(1-X)$ versus t where X was evaluated by the sum of the concentration of IPP, phenol and 2-cresol divided by the

Table 2
Amount of gases for PP decomposition at 673 K and $[PP]_0 = 0.5$ mol L^{-1}

Water density (g cm^{-3})	Reaction time	mol ($\times 10^{-5}$)								
		H_2	CO_2	CH_4	C_2H_4	C_2H_6	C_3H_6	C_3H_8	Total	Total carbon atom
0	30	1.29	0	0.64	0.56	0.05	0.29	0.03	2.86	2.82
	180	5.60	0	5.97	3.53	0.76	1.74	0.29	17.89	20.64
	360	6.33	0	12.59	4.18	1.60	4.39	0.76	29.85	39.60
0.5	30	0.18	0.55	0.10	0.51	0.05	0.30	0.02	1.71	2.73
	180	2.04	4.00	0.66	2.17	0.97	3.23	0.22	13.29	21.29
	360	5.75	9.60	2.16	2.14	3.02	6.87	0.74	30.28	44.91

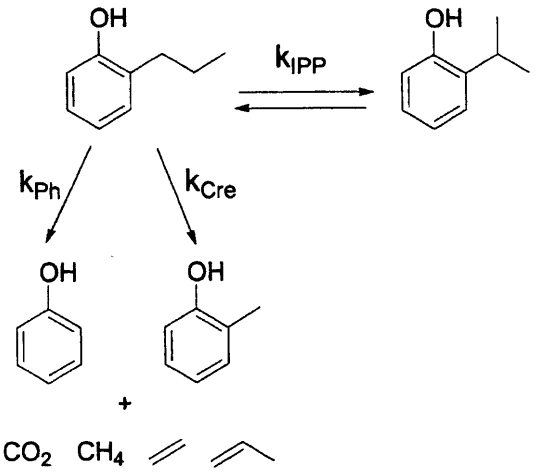

Fig. 2. Main reaction pathways of PP pyrolysis.

initial concentration of PP. These plots include the data of $[PP]_0 = 0.25–1.0$ mol L^{-1} and 0–0.5 g cm^{-3} of water density and the line was obtained with the least squares method. The straight line going through the origin indicated that the reaction rate was the same regardless of water density. From the slope of this line, the rate constant of PP decomposition was determined to be $(1.17 \pm 0.05) \times 10^{-5}$ s^{-1} at 95% C.I.

According to the experimental results, we propose a reaction pathway where the decomposition of PP consists of rearrangement to IPP and dealkylation to phenol and 2-cresol. Thus, the overall rate constant k can be expressed as $k = k_{IPP}$ (rearrangement to IPP) $+ k_{Ph}$ (dealkylation to phenol) $+ k_{Cre}$ (dealkylation to 2-cresol). These reaction rate constants, k_{IPP}, k_{Ph} and k_{Cre} can be related to the

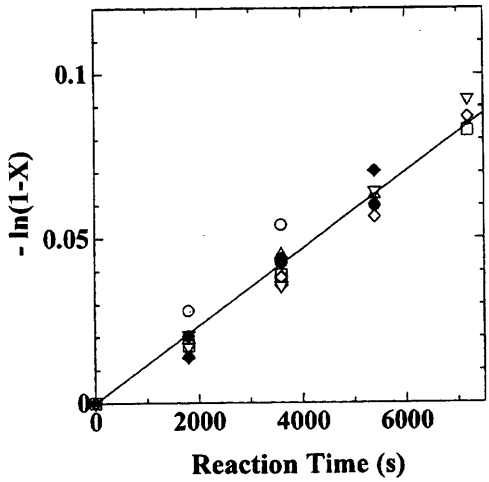

Fig. 3. Plot of $-\ln(1-X)$ vs. reaction time at 0–0.5 g cm^{-3} water density and 673 K for PP decomposition. ○, $[PP]_0 = 0.5$ mol L^{-1}, $\rho_W = 0$ g cm^{-3}; ●, $[PP]_0 = 1.0$ mol L^{-1}, $\rho_W = 0$ g cm^{-3}; △, $[PP]_0 = 0.5$ mol L^{-1}, $\rho_W = 0.05$ g cm^{-3}; $[PP]_0 = 0.5$ mol L^{-1}, $\rho_W = 0.1$ g cm^{-3}; □, $[PP]_0 = 0.5$ mol L^{-1}, $\rho_W = 0.3$ g cm^{-3}; ◇, $[PP]_0 = 0.25$ mol L^{-1}, $\rho_W = 0.5$ g cm^{-3}; ▼, $[PP]_0 = 0.5$ mol L^{-1}, $\rho_W = 0.5$ g cm^{-3}; ◆, $[PP]_0 = 1.0$ mol L^{-1}, $\rho_W = 0.5$ g cm^{-3}.

selectivity of IPP, phenol and 2-cresol at zero conversion level ($S_{0,IPP}$, $S_{0,Ph}$, $S_{0,Cre}$) as [23]:

$$k_{IPP} = S_{0,IPP} \cdot k \quad (4)$$

$$k_{Ph} = S_{0,Ph} \cdot k \quad (5)$$

$$k_{Cre} = S_{0,Cre} \cdot k \quad (6)$$

Fig. 4 shows the relationship between PP conversion and selectivity of IPP, phenol and 2-cresol where the lines shown were obtained by least squares method. The selectivity was in the order of IPP > Phenol > 2-cresol. From the intercept of these lines, the constants $S_{0,IPP}$, $S_{0,Ph}$, $S_{0,Cre}$ and k_{IPP}, k_{Ph}, k_{Cre} were evaluated and are summarized in Table 3. The ratio of the magnitude of reaction rate from PP to product was IPP:Phenol:2-Cresol = 3.5:1.6:1, which shows that rearrangement was fastest reaction. The PP decomposed through rearrangement to IPP and dealkylation to phenol and 2-cresol, and neither rearrangement rate nor dealkylation rate were sensitive to water density in supercritical water.

For rearrangement reaction, the rearrangement from IPP to PP occurs and the reaction rate is also independent of water density [20]. The rearrangement reaction was reversible reaction and probably proceeded through an intramolecular mechanism that was not influenced greatly by the solvent density. Poutsma [24] reported that intramolecular 1,2-shifts of aryl groups of alkylbenzenes occurred through an intermediate spirocyclohexadienyl radical intermediate. The same type of rearrangement possibly occurred in the rearrangement from PP to IPP.

The rate constant of rearrangement is compared for PP to IPP for the forward and reverse direction. At 673 K, the rate constant from PP to IPP was $k_{PP} = 6.70 \times 10^{-6}$ s^{-1} as shown in Table 3. The reported rate constant from IPP to PP was $k_{IPP} = 1.27 \times 10^{-5}$ s^{-1} at 673 K [20]. Hence, the apparent equilibrium constant between PP and IPP ($K = [IPP]/[PP] = k_{PP}/k_{IPP}$) is about 0.53, which means that PP is more stable than IPP at 673 K. In general, IPP should be more stable than PP at room

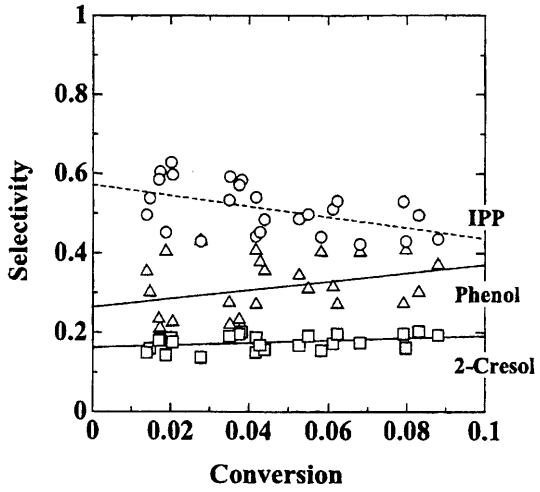

Fig. 4. Relationship between PP conversion and selectivity of IPP, phenol and 2-cresol at 0–0.5 g cm^{-3} of water density at 673 K.

Table 3
Selectivity and rate constants for PP decomposition at 673 K and 0–0.5 g cm^{-3} of water density

i	$S_{0,i}$	95% C.I.	k_i (10^{-6} s^{-1})	95% C.I. (10^{-6} s^{-1})
IPP	0.572	±0.050	6.70	±0.88
Phenol	0.265	±0.065	3.11	±0.91
2-cresol	0.163	±0.016	1.91	±0.27

temperature. We estimated the isobaric heat capacity, standard enthalpy of formation, standard entropy of PP and IPP by the method of Benson [25] and calculated the equilibrium constant between PP and IPP. This estimation is qualitative because the solvent effect of supercritical water was not considered. Fig. 5 shows the dependence of equilibrium constant (K) on temperature. At 298 K, the equilibrium constant is 2.13 and favorable for the formation of IPP. The enthalpy of the reaction decreased and the entropy of the reaction increased with increasing temperature and the magnitude of the change in entropy with temperature was relatively larger than that in enthalpy. For example, the enthalpy and entropy at 673 K were 0.8 and 3.5 times of those at 300 K, respectively. The equilibrium constant shifted to the formation of PP with increasing temperature and reached 0.024 at 673 K. The trend of equilibrium constant was the same as expected although the calculated values contain inaccuracies due to the estimation of the energies. Thermodynamic stability can be one of the reasons that PP was more stable than IPP.

Next, the dealkylation is discussed. The dealkylation of PP yielded phenol and 2-cresol with methane and ethylene, and propene was not the major product derived from alkyl side chain. On the other hand, phenol and propene is the main products in dealkylation of IPP [20]. In supercritical water, the alkylation of phenol with propene yields IPP through an unsaturated ketone as an intermediate [26], which means that the alkylation of phenol with propene and dealkylation of IPP should be

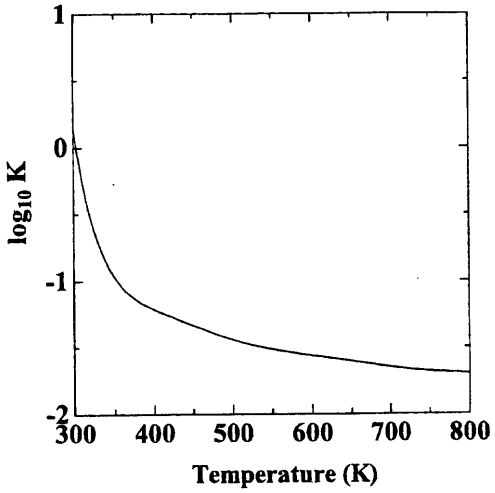

Fig. 5. Calculated equilibrium constant between PP and IPP (K = [IPP]/[PP]) with temperature.

reversible. The mechanism probably occurs through an unsaturated ketone as a common intermediate in which the hydroxy group works as a hydrogen donor or accepter. This means that the kinetics of dealkylation of PP was different from that of IPP and the unbranched alkyl side chain probably lowered the influence of the hydroxy group of phenol structure.

Both dealkylation rates from PP to phenol and from PP to 2-cresol were independent of water density. The rate constants from PP to phenol and 2-cresol were 3.11×10^{-6} and 1.91×10^{-6}, respectively, and were constant at all water densities at 673 K. On the other hand, the dealkylation rate from IPP to propene is known to increase with increasing water density [20]. The rate constant of dealkylation of IPP to phenol increases from 2.02×10^{-5} to 5.76×10^{-5} s^{-1} with increasing water density at 673 K [20]. In general, the rate of reactions with polar intermediate species should be affected by solvent properties such as dielectric constant in the supercritical region of water [27]. In the dealkylation of PP, each bond of alkyl side chain was probably cleaved and the dealkylation rate was slower than that of IPP. Judging from these results, the dealkylation of PP probably occurred through non polar intermediates such as free-radicals.

Dealkylation occurred through the cleavage of C–C bond of alkyl side chain. The energy requirement for breaking a C–C bond is lower than that of a C–H bond [14], thus cleavage of a C–C bond should be preferred. For alkylbenzenes, bond dissociation enthalpy between carbon and carbon atom is in the order of (1) benzene ring and the α-carbon atom of the alkyl side chain > (2) β and γ position of alkyl side chain > (3) α and β position of alkyl side chain [24]. Hence, the cleavage of α and β carbon of alkyl side chain should be more likely to occur. In the dealkylation of PP, this cleavage probably follows the formation of hydoxybenzyl radical and ethyl radical to initiate the reaction. In the presence of water, the reaction rate was the same as that in the absence of water, which implied that the rate determining step with water and that without water were the same. Carbon dioxide was produced instead of methane and small amount of 2-propanol was produced, which means that the oxygen atom of water was incorporated into the products through dealkylation. However, the mechanism of the dealkylation including formation of carbon dioxide in supercritical water will read to the subject of a future work.

References

[1] J.I. Kroschwitz, H.-G. Mary, Encyclopedia of Chemical Technology, fourth ed, Wiley-Interscience, New York, 1991.
[2] J.-Z. Dong, K. Ouchi, Fuel 68 (1989) 710.
[3] E. Dorrstijn, L.J.J. Laarhoven, I.W.C.E. Arends, P. Mulder, J. Anal. Appl. Pyrol. 54 (2000) 153.
[4] E.U. Franck, Pure Appl. Chem. 53 (1981) 1401.
[5] G.M. Schneider, Ber. Bunsenges Phys. Chem. 76 (1972) 325.
[6] P.E. Savage, Chem. Rev. 99 (1999) 603.
[7] A.R. Katritzky, D.A. Nichols, M. Siskin, R. Murugan, M. Balasubramanian, Chem. Rev. 101 (2001) 837.
[8] E.E. Brock, P.E. Savage, AIChE J. 41 (1995) 8.

[9] P.E. Savage, S. Gopalan, T.I. Mizan, C.J. Martino, E.E. Brock, AIChE J. 41 (1995) 1723.
[10] T. Adschiri, T. Sato, H. Shibuichi, Z. Fang, S. Okazaki, K. Arai, Fuel 79 (2000) 243.
[11] C. Yokoyama, K. Nishi, A. Nakajima, K. Seino, Sekiyu Gakkaishi 41 (1998) 243.
[12] J. Goto, T. Adschiri, K. Arai, Proceedings of the First International Symposium on Feedstock Recycling of Plastics, 1999, pp. 231.
[13] A. Demirbas, Energy Conversion Manage. 41 (2000) 633.
[14] P. Zhou, B.L. Crynes, Ind. Eng. Chem. Process Des. Dev. 25 (1986) 898.
[15] A.R. Katritzky, R. Murugan, M. Siskin, Energy Fuels 4 (1990) 531.
[16] A.R. Katritzky, R. Murugan, M. Siskin, Energy Fuels 4 (1990) 538.
[17] C.J. Martino, P.E. Savage, Ind. Eng. Chem. Res. 36 (1997) 1385.
[18] T. Adschiri, R. Shibata, K. Arai, Sekiyu Gakkaishi 4 (1997) 291.
[19] T. Tagaya, Y. Suzuki, J. Kadokawa, M. Karatsu, K. Chiba, Chem. Lett. (1997), 47.
[20] T. Sato, G. Sekiguchi, M. Saisu, M. Watanabe, T. Adschiri, K. Arai:, Ind. Eng. Chem. Res. 41 (2002) 3124.
[21] L. Haar, J.S. Gallagher, G.S. Kell (Eds.), NBC/NRC Steam Tables, Hemisphere, New York, 1984.
[22] M. Watanabe, M. Tsulagoshi, H. Hirakoso, T. Adschiri, K. Arai, AIChE J. 46 (2000) 843.
[23] N.A. Bhore, M.T. Klein, K.B. Bischoff, Ind. Eng. Chem. Res. 29 (1990) 313.
[24] M.L. Poutsma, J. Anal. Appl. Pyrol. 54 (2000) 5.
[25] S.W. Benson, Thermochemical Kinetics, second ed, Wiley, New York, 1976.
[26] T. Sato, G. Sekiguchi, T. Adschiri, K. Arai, Ind. Eng. Chem. Res. 41 (2002) 3064.
[27] M.T. Klein, L.A. Torry, B.C. Wu, S.H. Townsend, S.C. Paspek, J. Supercrit. Fluids 3 (1990) 222.

Available online at www.sciencedirect.com
SCIENCE DIRECT
J. of Supercritical Fluids 00 (2003) 1–7
THE JOURNAL OF Supercritical Fluids
www.elsevier.com/locate/supflu

Water gas shift reaction kinetics under noncatalytic conditions in supercritical water

Takafumi Sato [a,*], Shutaro Kurosawa [b], Richard L. Smith, Jr. [c], Tadafumi Adschiri [d], Kunio Arai [a,b,c,*]

[a] *Supercritical Fluid Research Center, National Institute of Advanced Industrial Science and Technology, 4-2-1 Nigatake, Miyagino, Sendai 983-8551, Japan*
[b] *Department of Chemical Engineering, Tohoku University, 07 Aoba Aramaki-Aza, Aoba-ku, Sendai 980-8579, Japan*
[c] *Research Center of Supercritical Fluid Technology, Tohoku University, 07 Aoba Aramaki-Aza, Aoba-ku, Sendai 980-8579, Japan*
[d] *Institute of Multidisciplinary research for Advanced Materials, Tohoku University, 2-1-1 Katahira, Aoba-ku, Sendai 980-8577, Japan*

Received 7 October 2002; received in revised form 4 March 2003; accepted 5 March 2003

Abstract

The kinetics of the water gas shift reaction was studied under noncatalytic conditions in supercritical water at CO/H_2O ratios of 0.03 and at temperatures from 653 to 713 K. The selectivities of CO_2 and hydrogen were almost equal and did not change with pressure at 673 K. The increase of pressure and water density sensitively promoted the reaction at 653 K from 25 to 30 MPa whereas the pressure and water density did not seem to affect the rate constant at 673 K from 10 to 30 MPa. The first order rate constant for CO conversion was $k = 10^{5.58 \pm 1.38} \exp(-1.16 \pm 0.19 \times 10^5/RT)$ /s at 10–59.6 MPa and 653–866 K.

Keywords: Supercritical water; Water gas shift reaction; Carbon monoxide; Hydrogen; Kinetics

1. Introduction

The water gas shift reaction (WGSR) ($CO + H_2O \rightarrow CO_2 + H_2$) is an important fundamental reaction used in industry for reforming hydrocarbons, producing hydrogen [1]. There is renewed interest in water–gas shift chemistry that originates from applications of hydrogen production for fuels and gasification of biomass as a sustainable route for energy [2]. The WGSR in water under supercritical conditions could provide a noncatalytic route since a large excess of water solvent could possibly drive the reaction to produce hydrogen. Moreover, the partial oxidation of hydrocarbons has been found to be closely related to the WGSR [3]. Watanabe et al. [3] studied the partial oxidation of *n*-hexadecane at 673 K in supercritical water and found that when a carbon to oxygen ratio of 3:1 was used, approximately 40% of the gas product was CO. This means that it is possible to use the partial oxidation of hydrocarbons to produce CO, which can then be

* Corresponding author. Tel./fax: +81-22-217-7246.
E-mail address: karai@arai.che.tohoku.ac.jp (T. Sato).

0896-8446/03/$ - see front matter © 2003 Published by Elsevier Science B.V.
doi:10.1016/S0896-8446(03)00049-4

converted to hydrogen via the WGSR. In other words, it is possible to develop a noncatalytic route for reforming hydrocarbons without requirement of high temperature conditions (1073–1273 K). In such a route, the water–gas reaction ($C+H_2O \rightarrow CO+H_2$) and the WGSR kinetics in the supercritical region of water would be important.

Studies on noncatalytic WGSR in supercritical water are summarized in Table 1 with the high temperature steam [4] and the heterogeneous and homogeneous catalytic case [5,6] being listed for reference. Hirth and Franck [7] measured the equilibrium constant of WGSR from 773 to 873 K at 40 MPa and reported that activity ratio equilibrium constant K_a ($=a_{CO_2}a_{H_2}/a_{CO}a_{H_2O}$) was 2.75 at 773 K and 0.69 at 873 K, where 4.91 and 2.55 at normal pressure, respectively. The K_a was largely different from that in the ideal gas state and the equilibrium shifted to the reactants side with increasing pressure. Holgate et al. [8] conducted the WGSR experiments by using a flow-type apparatus at 712–866 K at 24.6 MPa. They proposed a global rate expression for their conditions. Rice et al. [9] examined this reaction with in situ Raman spectroscopy under batch conditions at 683–793 K and 7–60 MPa. They found that the WGSR was accelerated with increasing pressure and proposed a global rate expression at 20 mol/L of water density. We reported that the reaction rate was influenced with pressure at 653 K and also proposed a global rate expression [10] near the critical temperature. At this temperature, the CO conversion was about 5% at 300 s of reaction time, which indicates that the reaction was relatively slow. These studies evaluated the rate constant over wide range of temperatures and pressures with various expressions. For practical applications, it is convenient if these expressions could be summarized over a wide range of conditions including the supercritical region.

In this study, we report detailed data of WGSR in supercritical water at 653–713 K and 10–30 MPa that was measured with a flow-type reactor. We evaluate the effect of pressure on the product distribution and determine the rate constant from 653 to 713 K at each pressure. By analyzing the rate constants obtained in this study and those reported previously, we propose a global reaction model for the WGSR in supercritical water that can be applied in the critical region of water and over a wider range conditions than previous models.

2. Experimental

Fig. 1 shows the flow-type apparatus in this study. Carbon monoxide (99.95% Nippon Sanso Corporation) was used which contained 2% of neon as internal standard. Carbon monoxide was pressurized with a booster pump (AGT-15/75, Haskel) and introduced into the piston syringe (TOC-30, HIP). Distilled water was supplied with a HPLC pump (PUS-0.5, GL Science) to displace a piston syringe, and carbon monoxide was supplied into the reactor. From another line, distilled water was supplied to preheating tube with a HPLC pump (Model TRI ROTAR-V, JASCO Corporation). Both carbon monoxide and water supply lines were submerged in the

Table 1
Summary of high temperature WGSR studies

Catalyst	Objective	T (K)	P (MPa)	Apparatus	Reference
None (supercritical)	Equilibrium	773–873	40	Batch	[7]
	Rate	712–866	24.6	Flow	[8]
	Rate	683–793	7–60	Batch	[9]
	Rate	653–713	10–30	Flow	[10]
None (gas phase)	Rate	1073–1173	0.06–0.1	Flow	[4]
Heterogeneous	Rate	573–623	0.3–0.9	Flow	[5]
Homogenous	Kinetics	473–673	[a]	Batch	[6]

[a] Initial water density was 0.5 g/cm^3.

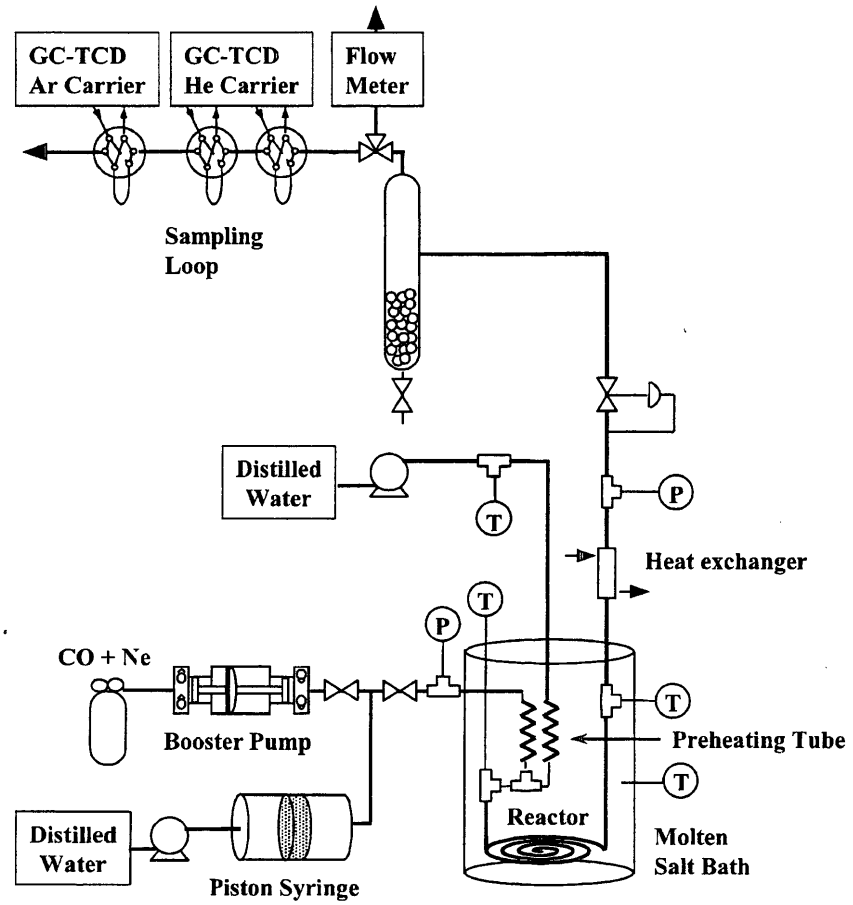

Fig. 1. Experimental apparatus.

molten salt bath (T1, Shinnippo Kagaku) controlled at the reaction temperature from 653 K to 713 K. Gas and water were supplied separately to the reactor and then mixed at the reactor entrance. The initial CO/H_2O molar flow rate ratio was 0.03 ± 0.0065.

The reactor was a coiled length (4 m, 1/4 o.d. thickness 2.15 mm) of stainless 316 tube. The reaction temperature was defined as the average temperature at the entrance and exit of the tube coil and the temperature difference between these two points was within 2 K. The difference of temperature between set values and the average values was within ± 0.1 K. At the end of the reactor, the effluent was cooled down with a water-cooled double-pipe heat exchanger to suppress the reaction. Residence time was estimated from the values of pure water [11] because the ratio of CO and products was very low. The reaction pressure was controlled at set value within ± 0.1 MPa with a back pressure regulator (Model PU-100, JASCO Corporation) and the effluent was separated into gas and liquid streams in a separator.

The flow rate of gas was measured by a flowmeter (Model W-NK-1A, Shinagawa). To prevent contamination of air, the effluent gas stream was introduced into three sampling loops attached to two gas chromatographs as shown in Fig. 1. Hydrogen was analyzed by GC-TCD (Shimadzu GC-8A) with argon carrier and a Molecular Sieve 5A column (GL Science). Carbon monoxide was analyzed by GC-TCD (Shimadzu GC-8A) with helium carrier and a Molecular Sieve 13X column (GL Science). CO_2 was analyzed with helium carrier and a Porapak Q column (GL

Science). The quantities of gases were calculated based on neon internal standard. For the liquid analysis, total organic and inorganic carbon contents were analyzed by TOC (TOC-5000, Shimadzu). The inorganic carbon in the liquid was considered to be CO_2 dissolved in water.

The product yield and CO conversion were defined as follows:

$$\text{Product yield } (\%) = F_{\text{product}}/F_{\text{CO,in}} \times 100 \quad (1)$$

$$\text{CO conversion: } X = (F_{\text{CO}_2} + F_{\text{OC}})/F_{\text{CO,in}} \quad (2)$$

$$\text{Product selectivity } (\%) = \text{Product yield}/X \quad (3)$$

where F_i is flow rate of product (mol/s), F_{OC} is the flow rate of total organic carbon in liquid and $F_{CO,in}$ (mol/s) is flow rate of CO supplied.

3. Results and discussion

Fig. 2 shows the selectivity of CO_2, H_2 and organic carbon with conversion at 673 K and 10–30 MPa and $CO/H_2O = 0.03$. The main products were CO_2 and hydrogen and their selectivities were 78–98% and 75–107%, respectively. A small amount of organic components in liquid were detected by TOC analysis, and the selectivity of organic carbon was below 19%. The selectivity of organic carbon decreased with conversion corresponding to an increase in that for CO_2, which means that the organics such as formic acid as considered by Melius et al. [12] in their calculations were probably produced at the initial stages of the reaction and converted to CO_2.

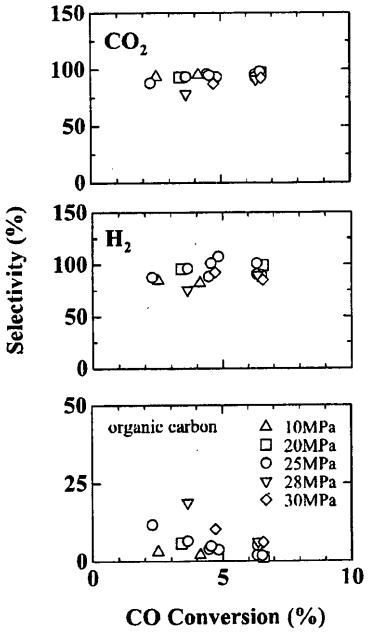

Fig. 2. Selectivities of CO_2, H_2 and organic carbon versus CO conversion in the WGSR at 673 K and $CO/H_2O = 0.03$.

The selectivity of CO_2 and hydrogen seemed to be insensitive to changes in pressure, which means that the kinetics of WGSR were essentially independent of reaction pressure over the range of 10–30 MPa at 673 K. Rice et al. [9] reported that CO conversion increased significantly at pressures above 30 MPa. At the conditions examined in this work, pressures were apparently not high enough to observe the effects reported in Ref. [9]. Further, the ratio of CO/H_2O was constant in this study, although the ratio of CO/H_2O decreased with increasing water density m the case of Rice et al. [9]. The ratio of CO/H_2O used probably caused some differences in pressure dependence.

Table 2 shows CO conversion obtained at temperatures from 653 to 713 K and $CO/H_2O = 0.03$. For all of our experiments, CO conversions were low being below about 11%. For example, at 300-s reaction time and 673 K, CO conversion was 7%. Since the reaction rate of WGSR was relatively slow, it is possible to estimate the rate constant in this conversion range. The reaction rate of the WGSR in supercritical water below 793 K can be described as a first order reaction of CO as $(-d[CO]/dt = k[CO])$ [9,10].

Fig. 3 shows the $-\ln(1-X)$ against residence time at 25 MPa and $CO/H_2O = 0.03$, where X is CO conversion (%). To reduce the data and to estimate the contribution of heat-up, mixing, cool-down and other factors on the reaction, we used the procedure in Ref. [10] that is described here briefly. First, data at 673 K at 25 MPa were plotted and a line was drawn through the points and extrapolated to zero conversion. This provided an estimate for the apparent zero conversion residence time. Then, the 693 K data was extrapolated and it was found that the value was practically the same. Therefore, we took this value as the instrument factor that contains systematic experimental errors such as heating, mixing effects

Table 2
CO conversion in the WGSR at $CO/H_2O = 0.03$

T (K)	P (MPa)	Residence time (s)	CO conversion (%)	Rate constant $(s^{-1})^a$
653	25	194	2.09	8.28×10^{-5}
	27	283	3.84	1.24×10^{-4}
		413	5.97	
	30	269	4.06	1.79×10^{-4}
		414	4.92	
663	25	116	2.93	1.67×10^{-4}
673	10	57	2.50	2.27×10^{-4}
		120	4.12	
	25	58	2.28	1.87×10^{-4}
		129	3.64	
		173	4.47	
		192	4.55	
		232	4.84	
		286	6.34	
		288	6.53	
	28	118	3.64	1.95×10^{-4}
		280	6.37	
	30	210	4.72	1.79×10^{-4}
		299	6.35	
		322	6.58	
693	25	129	5.89	3.26×10^{-4}
		287	10.8	
713	25	59	5.74	4.92×10^{-4}

[a] Considering $\tau = \tau(\exp) + 61.5$ (s).

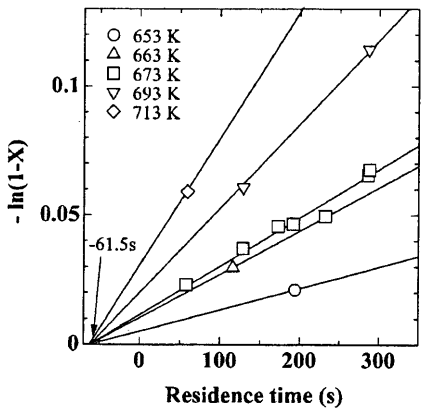

Fig. 3. Plot of $-\ln(1-X)$ against residence time for the WGSR at 25 MPa and $CO/H_2O = 0.03$.

as well as cooling effects. The instrument factor was assumed to be constant over the range of temperatures studied and was used to construct the other lines in all condition. The rate constants obtained are shown in Table 2. At 653 K, the rate constant increased with pressure by a factor of 2.2 from 25 to 30 MPa. However, the rate constant was almost constant as a function of pressure at 673 K from 10 to 30 MPa. The water density increased by a factor of 1.2 at 653 K and 9.4 at 673 K in these pressure ranges. Judging from these results, the increase of pressure and water density sensitively promoted the reaction at 653 K from 25 to 30 MPa whereas the pressure and water density did not seem to affect the rate constant at 673 K from 10 to 30 MPa.

Fig. 4 shows an Arrhenius plot of rate constants for the data in this work and that reported in the literature for WGSR in supercritical water. In this figure, the rate constants of Holgate et al. [8] are in the high temperature range (712–866 K) while those of Rice et al. [9] are in the mid range (683, 723 and 753 K) and those of this study are in the low temperature range (653–713 K). The rate constants of Holgate et al. [8] are obtained at constant pressure, 24.6 MPa. The rate constants of Rice et al. [9] analyzed in this study are of constant water concentration above 20 mol/L, that is, 0.36 g/cm^3 of water density, which corresponds to pressure of 33.2–59.6 MPa [11]. The difference in reaction rate constants in Fig. 4 at 683 K can be attributed to the different reaction pressures studied in Ref. [9]. According to the results in Fig. 4, the rate constants for given temperatures varied by as much as 2 orders in magnitude. In particular, the points at the higher side of 683 K

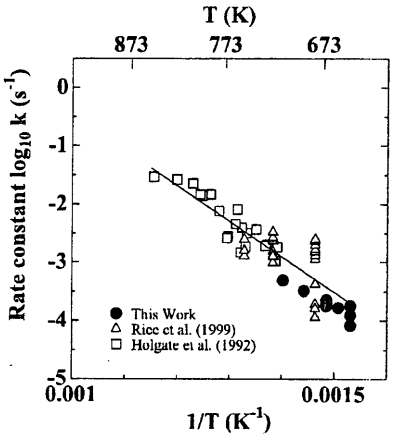

Fig. 4. Arrhenius plot of rate constants for the noncatalytic WGSR in supercritical water.

corresponded to those above 41.2 MPa [11]. The pressure (density) probably affects the reaction rate in high pressure region at 683 K. Above 683 K, rate constants were obtained up to 59.6 MPa [11] at high pressure, however, they were in the same range as those of Holgate et al. [8] The rate constants in this study were obtained at 10–30 MPa and showed the smaller dependence of pressure compared with the results of Rice et al. [9]. Although the reaction pressures for the rate constants were different, a linear relationship could be determined, which means that the rate constant of WGSR in supercritical water is a weak function of pressure over most conditions.

We chose to use an Arrhenius function and fitted the rate constants from 653 to 866 K, 10–59.6 MPa and obtained the following expression:

$$k = 10^{5.58\pm1.38}\exp(-1.16\pm0.19\times10^5/RT) \quad (s^{-1}) \tag{4}$$

where R is gas constant (J/mol/K) and the ± indicates 95% C.I. The Arrhenius parameters reported for WGSR in supercritical water, high temperature steam and catalytic conditions are summarized in Table 3. The apparent activation energy was in the range of 95–283 kJ and pre-exponential factor was different among these studies. For the studies in supercritical water, the Arrhenius parameter obtained in this study was among those of the other works. Although the mechanism of WGSR in supercritical water has been elucidated to some extent by Rice et al. [9], we chose to describe the rate constant with a simple Arrhenius type equation because of its simplicity for describing a wide range of conditions.

In general, the WGSR is carried out under catalytic conditions [13]. At lower temperatures (473–523 K), Cu catalysts are used that provide high activity of the WGSR. However, Cu catalysts readily deactivate and require frequent replacement. At higher temperatures, Fe–Cr catalysts can be used that are more stable but have lower activity. The reaction rate constants under non-catalytic conditions can be compared with those for catalytic conditions. Keiski et al. [5] conducted catalytic WGSR with Fe_3O_4–Cr_2O_3 catalyst at 573–623 K and 0.3–0.9 MPa and proposed the equation of reaction rate as Table 3. The initial reaction rate of CO disappearance at 673 K, 25 MPa and $CO/H_2O = 0.03$ was calculated from both the equation of Keiski et al. [5] and that of this study (Eq. (4)). The former rate was 6.7×10^3 (mol/L/s) and the latter was 1.1×10^{-4} (mol/L/s), which means that reaction rate under catalytic conditions are much higher those under noncatalytic conditions in supercritical water.

Use of catalyst in supercritical water has been studied under those conditions. Antal et al. [2] reported that gasification of biomass accelerated with carbon catalyst in supercritical water under catalyst being stable. Xu et al. [14] conducted the gasification of glucose in supercritical water with and without carbon catalysts. They reported the yield of CO in the presence of various activated carbon was much lower than that in the absence of catalyst and carbon catalyzed WGSR in supercritical water. The reaction rate of WGSR with

Table 3
Summary of rate constants for the WGSR

Catalyst	T (K)	P (MPa) or water density (g/cm^3)	Assumptions: $-$d[CO]/dt (1/s) = [b]	Reference
None (supercritical)	712–866	24.6	$10^{3.3}\exp(-0.95\times10^5/RT)$ [CO]$^{0.71}$	[8]
	683–793	33.2–56.2[a]	$10^{7.2}\exp(-1.45\times10^5/RT)$ [CO]	[9]
	653–713	10–30	$10^{3.9}\exp(-0.98\times10^5/RT)$ [CO]	[10]
	653–866	10–59.6	$10^{5.6}\exp(-1.16\times10^5/RT)$ [CO]	This work
None (gas phase)	1073–1173	0.06–0.1	$10^{12.7}\exp(-2.83\times10^5/RT)$ [CO]$^{0.5}$[H_2O][c]	[4]
Fe_3O_4–Cr_2O_3	573–623	0.3–0.9	$10^{11.3}\exp(-0.95\times10^5/RT)$ [CO]$^{1.1}$[H_2O]$^{0.53}$	[5]

[a] Constant water density of 20 mol/L.
[b] R (J/mol/K).
[c] The terms for hydrogen is omitted.

carbon catalyst in supercritical water has not been elucidated, however, this method is one of the possible alternatives to promoting the WGSR in supercritical water. It is important to note that catalyst deactivation in supercritical water is an active research topic. For example, Ding et al. [15] reported that the deactivation of some solid catalyst could occur due to melting, phase change and lack of hydrothermal stability in supercritical water oxidation.

4. Conclusions

We measured the kinetics of the WGSR at 653–713 K, 10–30 MPa and CO/H_2O ratios of 0.03 without catalyst in supercritical water. The selectivities of CO_2 and hydrogen did not vary much with pressure. In the measurements, only a small amount of liquid compounds were produced. The first order rate constant for CO conversion of this study and those obtained at higher temperatures in supercritical water could be well-described by an Arrhenius plot almost regardless of pressure.

Acknowledgements

The authors wish to thank Dr Steve Rice for providing us some of their analyses. A Grant-in-Aid for Scientific Research on Priority Areas (06246103, 09218205, 09450281 and 10555270) the Ministry of Education, Culture, Sports, Science and Technology, for support of this research is gratefully acknowledged.

References

[1] J.I. Kroschwitz, H.-G. Mary, Kirk–Othmer, Encyclopedia of Chemical Technology, fourth ed., A Wiley-Interscience Publication, New York, 1991.

[2] M.J. Antal, Jr., S.G. Allen, D. Schulman, X. Xu, R.J. Divilio, Biomass gasification in supercritical water, Ind. Eng. Chem. Res. 39 (2000) 4040.

[3] M. Watanabe, M. Mochiduki, S. Sawamoto, T. Adschiri, K. Arai, Partial oxidation of *n*-hexadecane and polyethylene in supercritical water, J. Supercrit. Fluids 20 (2001) 257.

[4] W.M. Graven, F.J. Long, Kinetics and mechanisms of the two opposing reactions of the equilibrium $CO+H_2O = CO_2+H_2$, J. Am. Chem. Soc. 76 (10) (1954) 2602.

[5] R.L. Keiski, T. Salmi, P. Niemisto, J. Ainassaari, V.J. Pohjola, Stationary and transient kinetics of the high temperature water–gas shift reaction, Appl. Catal. A: Gen. 137 (1996) 349.

[6] D.C. Elliott, L.J. Sealock, Jr, Aqueous catalyst systems for the water–gas shift reaction. 1. Comparative catalyst studies, Ind. Eng. Chem. Prod. Res. Dev. 22 (1983) 426.

[7] Th. Hirth, E.U. Franck, Oxidation and hydrothermolysis of hydrocarbons in supercritical water at high pressures, Ber. Bunsenges. Phys. Chem. 97 (1993) 1091.

[8] H.R. Holgate, P.A. Webley, J.W. Tester, Carbon monoxide oxidation in supercritical water: the effects of heat transfer and the water–gas shift reaction on observed kinetics, Energ. Fuels 6 (1992) 586.

[9] S.F. Rice, R.R. Steeper, J.D. Aiken, Water density effects on homogeneous water–gas shift reaction kinetics, J. Phys. Chem. A 102 (1998) 2673.

[10] T. Sato, S. Kurosawa, T. Adschiri, K. Arai, Kinetics of water gas shift reaction in supercritical water, Kagaku Kogaku Ronbunshuu 25 (1999) 993.

[11] E.W. Lemmon, M.O. McLinden and D.G. Friend, In: P.J. Linstrom, W.G. Mallard (Eds.), Thermophysical Properties of Fluid Systems in NIST Chemistry Webbook, NIST Standard Reference Database Number 69, National Institute of Standards and Technology, Gaithersburg, MD 20899, 2001. Available from http://webbook.nist.gov.

[12] C.F. Melius, N.E. Bergan, J.E. Shepherd Effects of water on combustion kinetics at high pressure, 23rd Symposium (International) on Combustion, The Combustion Institute, 1990, pp. 217–223.

[13] G. Ertl, H. Knözinger, J. Weitkamp, Handbook of Heterogeneous Catalysis, VCH Verlagsgesellschaft mbH, Weinheim, 1997.

[14] X. Xu, Y. Matsumura, J. Stenberg, M.J. Antal, Jr., Carbon-catalyzed gasification of organic feedstocks in supercritical water, Ind. Eng. Chem. Res. 35 (1996) 2522.

[15] Z.Y. Ding, M.A. Frisch, L. Li, E.F. Gloyna, Catalytic oxidation in supercritical water, Ind. Eng. Chem. Res. 35 (1996) 3257.

Available online at www.sciencedirect.com
SCIENCE DIRECT®
Applied Catalysis A: General 245 (2003) 333–341
APPLIED CATALYSIS A: GENERAL
www.elsevier.com/locate/apcata

Acidity and basicity of metal oxide catalysts for formaldehyde reaction in supercritical water at 673 K

Masaru Watanabe[a], Mitsumasa Osada[b], Hiroshi Inomata[a,*], Kunio Arai[a,b], Andrea Kruse[c]

[a] *Research Center of Supercritical Fluid Technology, Tohoku University, 07 Aoba, Aramaki, Aoba-ku, Sendai 980-8579, Japan*
[b] *Department of Chemical Engineering, Tohoku University, 07 Aoba, Aramaki, Aoba-ku, Sendai 980-8579, Japan*
[c] *Institut für Technische Chemie (ITC-CPV), Forschungszentrum Karlsruhe GmbH, P.O. 3640, 76021 Karlsruhe, Germany*

Received 16 October 2002; received in revised form 5 December 2002; accepted 5 December 2002

Abstract

Formaldehyde (HCHO) reactions in supercritical water (673 K and 25–40 MPa) with and without acid and base catalysts (homogeneous: H_2SO_4 and NaOH, and heterogeneous: CeO_2, MoO_3, TiO_2, and ZrO_2) were conducted by use of batch reactors. Cannizzaro reaction ($2HCHO + H_2O \rightarrow CH_3OH + HCOOH$) and self-decomposition of HCHO ($HCHO \rightarrow CO + H_2$) were found to be primary reactions for all the cases and the contribution of each reaction depended on the condition. In the case of the homogeneous systems, Cannizzaro reaction became dominant with increasing bulk hydroxyl ion (OH^-). The simple network model can well express the experimental results in the homogeneous conditions. We correlated the ratio of the yield of CH_3OH to that of CO (at 15 min) against bulk OH^- in the homogeneous system. For elucidating acidity and basicity of metal oxide catalysts on HCHO reaction in supercritical water, OH^- concentration on the metal oxide surface was calculated by use of the above correlation and the following order was found: $CeO_2 > ZrO_2 > MoO_3 > TiO_2$ (rutile) > TiO_2 (anatase). At the reaction condition, CeO_2 and ZrO_2 were base catalysts, and MoO_3 and TiO_2 were acid catalysts. The experimental results with the metal oxides can be expressed by the model that was developed under homogeneous systems, with the values of the OH^- concentrations that were calculated from the correlation about the CH_3OH/CO ratio at 15 min of reaction time.

Keywords: Formaldehyde; Supercritical water; Hydroxyl ion; Metal oxide catalyst; Solid acid and base; CeO_2; MoO_3; TiO_2; ZrO_2

1. Introduction

Recently, supercritical water (SCW), that is water above its critical temperature (647 K) and pressure (22.1 MPa), has been noted to be a green chemical environment for organic synthesis because many organic reactions occur without any catalyst [1–5]. Ikushima et al. [1] reported that rearrangements of both pinacol and Beckmann, which are normally reactions with strong acid at ambient temperature, proceeded very rapidly without any catalyst in SCW, in particular, at around the critical point of water. Sato et al. [3] and Chandler et al. [4,5] also found that a reaction which requires a strong acid catalyst, namely Friedel-Crafts alkylation between phenols and alcohols, occurred in SCW without a catalyst. Further, Cannizzaro-type reaction of benzaldehyde, which proceeds with a strong base normally, was also confirmed to proceed in the absence of any catalyst by Ikushima et al. [2]. Similar phenomena have been observed for hydrolysis (some

* Corresponding author. Tel.: +81-22-217-7282; fax: +81-22-217-7282.
E-mail address: inomata@scf.che.tohoku.ac.jp (H. Inomata).

0926-860X/03/$ – see front matter © 2003 Elsevier Science B.V. All rights reserved.
doi:10.1016/S0926-860X(02)00656-7

ethers [6–13] and esters [14,15]) and dehydration [16–20]) in SCW, that is, hydrolysis and dehydration that normally need acid or base catalyst occur rapidly without catalyst in SCW. These organic synthesis and hydrolysis cases without catalyst provided the possibility that SCW must be an acid or base catalyst for the reactions around the critical temperature and pressure [1,2].

However, if one wanted to enhance and control an acidic and basic reaction in SCW, a catalyst would be useful and effective. Because water dissociates into $H^+ + OH^-$ with an equilibrium constant at a temperature and a density, the amounts of H^+ and OH^- in pure water are the same for all temperatures and pressures. Therefore, if one wanted to make an increase of only H^+ concentration or make a huge increase of H^+ concentration in a system, one must add an acid in the system. Indeed, some reactions, such as dehydration of lower alcohols [17–20] and decarboxylation of acetic acid [21], requires acid (for example, H_2SO_4) and base (such as KOH) for the increase of the reaction rate at around the critical point of water. Furthermore, even for the reaction that can proceed without catalyst, increase and control of the reaction rate can be achieved by adding an acid and a base catalyst (for example, the case of hydrolysis of methyl tert-butyl ether in SCW [13]). For the control of pH in water, homogeneous acids (such as H_2SO_4) and bases (such as NaOH and KOH) would be used normally, but the acid and base have a negative impact on the inner wall of a reactor and on the global environment. Thus we must find an ecological friendly method for changing pH of the system, instead of using homogeneous acid and base catalyst.

One of the possibilities for green chemical control of pH is to use a solid and base catalyst in SCW. However, there has been very little information about which sold acid and base catalyst can work in SCW, so far. Recently, we found that ZrO_2 is a solid base catalyst even in SCW through the study with acetic acid [21] and gasification of biomass [22]. Tomita et al. [23] also reported that hydration of propylene to 2-propanol, which usually needs an acidic catalyst, proceeded with MoO_3 catalyst in SCW at around the critical point of water. These results suggest that a metal oxide can work as an acid or a base catalyst in SCW, instead of a homogeneous acid or alkali. For selecting a metal oxide to a reaction, the acidity and basicity of a metal oxide in SCW must be known.

For elucidating acidity and basicity of a metal oxide in an atmosphere, an activity test through a reaction such as dehydration and dehydrogenation of 2-propanol [24] is employed, for example, because the contribution of dehydration and dehydrogenation of 2-propanol can be controlled for acidity and basicity of a metal oxide [24]. In another study, we reported that reaction of HCHO in SCW is governed by the hydroxide ion concentration [25]. If solid acidity and basicity functioned as same as H^+ and OH^- in SCW, the reaction of HCHO could be controlled by solid acid and base catalyst. Thus, we can discover the acidity and basicity of the metal oxide through the study on controllability of HCHO reaction with a metal oxide.

In this study, we conducted HCHO reaction with and without catalyst using batch reactors. At first, for developing a simple network model for HCHO reaction in SCW at 673 K, the effect of concentration of HCHO and that of OH^- on the reaction was examined. Metal oxides were selected in view of hydrothermal and thermal stability [26]; thus CeO_2, MoO_3, TiO_2, and ZrO_2 were used in this study. Through the comparison between the network model and the experimental results, we would like to discuss the acidity and basicity of catalysts on the reaction pathway of HCHO in SCW.

2. Experimental

Paraformaldehyde, which is a linear polymer of HCHO, was used as a source of HCHO. Paraformaldehyde, sodium hydroxide (NaOH), and sulfuric acid (H_2SO_4) were purchased from Wako Pure Chemical and used without further purification. Pure water was obtained by with a water distillation apparatus (Yamato Co., model WG-220). Ceria (CeO_2) was obtained from Merck. Titania (TiO_2) (both anatase form and rutile form) and MoO_3 were purchased from Wako Chemicals. CeO_2, MoO_3, and TiO_2 (anatase and rutile) were used as received. Zirconia (ZrO_2) catalyst was prepared by calcination of zirconium hydroxide ($ZrO_2 \cdot xH_2O$, which was purchased from Nakarai Tesque Inc.), at 673 K for 3 h. The metal oxide catalysts that were used in the study are listed in Table 1 along with information of structure and BET surface

Table 1
Metal oxide catalysts used in the study

	BET (m^2/g)	Structure before HCHO reaction	Structure after the reaction
CeO_2	1.7	Cubic	Cubic
MoO_3	4.9	Orthorombic	Orthorombic
TiO_2(a)	47	Anatase	Anatase
TiO_2(r)	6.8	Rutile	Rutile
ZrO_2	68	Monoclinic and tetragonal mixture	Monoclinic

area. Except for ZrO_2, the structures of the metal oxides did not change from before to after the reaction. For ZrO_2, the monoclinic and tetragonal mixture of ZrO_2 before the reaction was changed into pure monoclinic zirconia after the reaction. This structure change of ZrO_2 probably occurred very rapidly and the activity of monoclinic ZrO_2 was studied in this study, as in the previous study [27].

The reactions were carried out in a SS 316 stainless steel tube bomb reactor (inner volume of 6 cm^3) [27]. The loaded amounts of paraformaldehyde were 0.03–0.3 g (0.15–1.7 mol/l), and the loaded amounts of water were from 1.0 (0.17 g/cm^3) to 3.1 g (0.52 g/cm^3). By changing water density and adding an amount of NaOH and H_2SO_4 in the system, we could make the OH^- concentration range from about 1.0×10^{-12} to 1.0×10^{-4} mol/l at 673 K. In the case of the experiments with solid catalysts (CeO_2, MoO_3, TiO_2, and ZrO_2), 0.3 g of the catalyst was loaded. After samples were loaded, Ar gas was pressurized at about 1 MPa to recover the gas product easily, after purging air in a reactor. The reactor with the samples was submerged in a fluidized sand bath (Takabayashi Rico Co., model TK-3) whose temperature was controlled to keep the reaction temperature (673 K). After a given reaction time (3–30 min), the reactor was taken out of the bath and rapidly quenched in a water bath. After the reactor reached room temperature, it was connected to a syringe that was equipped with gas samplers to collect produced gas and measure its volume. After the sampling of the produced gases, the reactor was opened and washed with pure water. Water-insoluble material (the solid catalyst) was separated by filtration with a membrane filter (1 μm).

The identification and quantification of produced gas was conducted by GC-TCD (Shimadzu, model GC-7A, and Hitachi, model GC163). An external standard (1-propanol) was added to the recovered water solution for GC-FID analysis (Hewlett Packard, model 6890). Some samples were analyzed by use of HPLC with RI and UV detectors (JASCO, model Gulliver series). The amounts of organic and inorganic carbon in the water solution were evaluated using TOC (total organic carbon detector, Shimadzu, model TOC-5000A). Surface areas of metal oxides were measured by single point BET method (Quantachrome Instruments, model ChemBET-3000), and are listed in Table 1. Structure of the solid catalysts before and after the reaction were analyzed by X-ray diffractometer (Mac Science, model M18XHF-SRA) with Mo Kα radiation (the results are also listed in Table 1).

Product yield was evaluated from carbon base. Hydrogen yield was evaluated from hydrogen base of a loaded amount of paraformaldehyde. For all the experiments, H_2, CO, CO_2, CH_3OH, HCHO, and HCOOH were identified and quantified. The yield of HCOOH was always less than 1 mol% and is not shown in this study.

3. Result and discussion

3.1. Effect of HCHO concentration on HCHO reaction in SCW at 673 K

The effect of HCHO concentration on the reaction was examined at 673 K, 0.35 g/cm^3 of water density (30 MPa of water pressure at 673 K), and 3–30 min of reaction time. Figs. 1–3 show the results at HCHO concentrations of 0.15, 0.54, and 1.7 mol/l, respectively.

At the lowest HCHO concentration (0.15 mol/l), while the yield of HCHO gradually decreased with time, the yield of CH_3OH, CO, CO_2, and H_2 increased with time, as shown in Fig. 1. The yield of CH_3OH became the highest amongst all the products after 10 min and finally reached 45%. CO_2 and H_2 were formed simultaneously. The final value of CO_2 and H_2 yield was about 40%. The yield of CO increased up to 10% with reaction time.

As shown in Fig. 2, the trend of the product yield at 0.54 mol/l was similar to that at 0.15 mol/l. However, the CH_3OH yield at 0.54 mo/l was higher than that at 0.15 mol/l and was about 50% at 30 min. The yield of CO_2 was always higher than that of H_2. The differences between the yield of CO_2 and H_2 were always

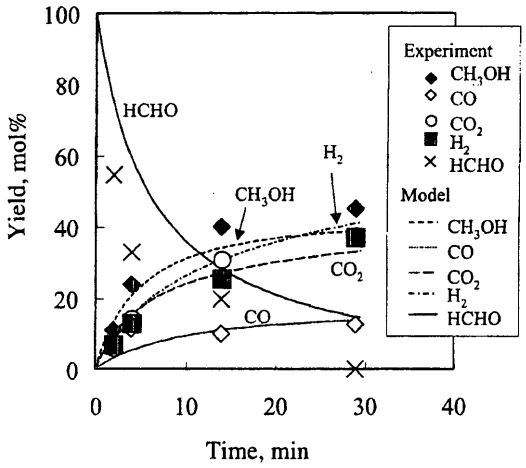

Fig. 1. Reaction time profile of the product distribution at 673 K, 30 MPa, and [HCHO] = 0.15 mol/l.

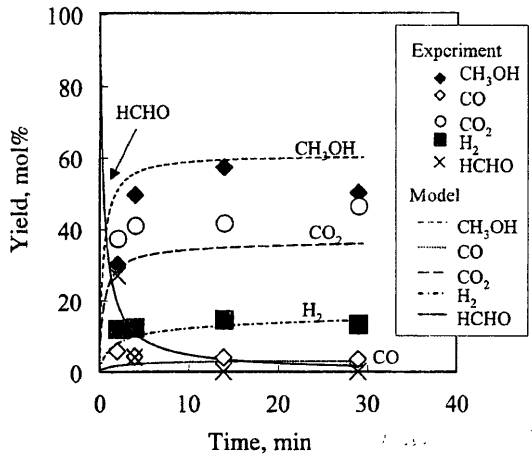

Fig. 3. Reaction time profile of the product distribution at 673 K, 30 MPa, and [HCHO] = 1.7 mol/l.

more than 5%. The yield of CO was always less than 10% at 0.54 mol/l of HCHO concentration.

At the highest concentration (1.7 mol/l), the yield of HCHO rapidly decreased with time. The yields of CH_3OH, CO_2, and H_2 also increased rapidly with time and reached a constant value, as shown in Fig. 3. The yield of CH_3OH was always more than 50%. The yield of CO_2 was always higher than that of H_2, as in Fig. 2. The yield of CO_2 was about 40% at all the reaction time, while that of H_2 was less than 20%. The yield of CO was less than 5% at all the reaction times.

3.2. Effect of bulk OH^- concentration on HCHO reaction in SCW at 673 K

The details of the effect of bulk OH^- concentration on HCHO reaction in SCW at 673 K can be found in another study [25]. Here, we describe only the reaction results at 15 min of reaction time. Fig. 4 shows the dependence of the product distribution at 15 min on bulk OH^- concentration. Concentration of OH^- and ion product of pure water were calculated by the method of Marshall and Franck [28]. The OH^-

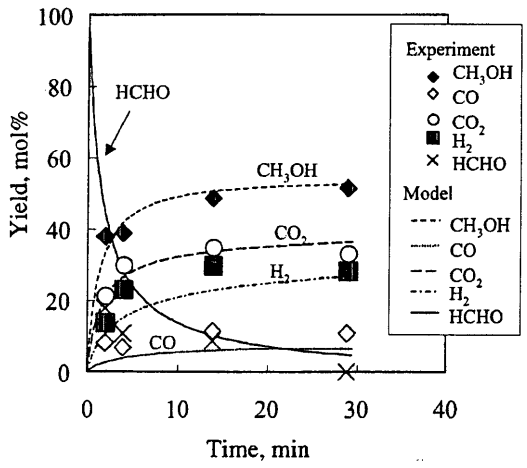

Fig. 2. Reaction time profile of the product distribution at 673 K, 30 MPa, and [HCHO] = 0.54 mol/l.

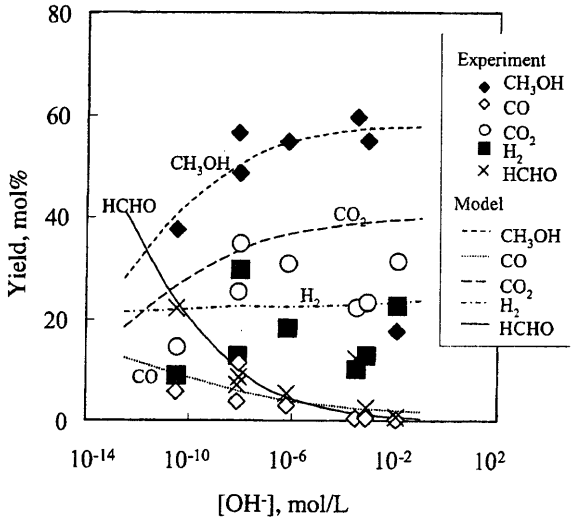

Fig. 4. Effect of OH^- concentration on the product yields at 673 K, 15 min, and [HCHO] = 0.54 mol/l.

concentration with acid and base were obtained from the ion product of the water [28], the equilibrium constant [29,30] and the activity coefficient [31]. In this study, we consider the experimental data at $1.9 < -\log[OH^-] < 10.5$. However, the carbon balances at higher OH^- concentration ($10^{-1.9}$ and $10^{-3.1}$ mol/l) were about 80 mol% and that at the lowest OH^- concentration in Fig. 4 ($10^{-10.5}$ mol/l), namely acidic condition, was about 50 mol%. The low carbon balance means formation of some by-products other than H_2, CO, CO_2, HCOOH, and CH_3OH. The reaction pathways for production of the by-products are not taken into consideration.

As shown in Fig. 4, the yield of CH_3OH gradually increased with increasing OH^-; on the other hand, the yield of CO increased with a decrease of OH^- concentration. Thus HCHO reactions in SCW are governed by the OH^- concentration, as reported elsewhere [25].

3.3. Simple network model for HCHO reaction in SCW

Based on the above experimental results, we developed a simple network model for HCHO reaction in supercritical water, as shown in Fig. 5. The details of the simple network model shown in Fig. 5 are described here.

CH_3OH forms via Cannizzaro reaction in supercritical water, as suggested by Bröll et al. [32]. In the case of benzaldehyde which has no α-hydrogen, Cannizzaro-type reaction also proceeds in supercritical water without catalyst [2]. Thus the Cannizzaro reaction can be taken into account for the model in SCW at 673 K.

$$2HCHO + H_2O \xrightarrow{k_1} CH_3OH + HCOOH \text{ (Cannizzaro reaction)} \quad (1)$$

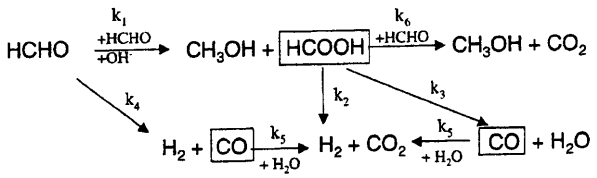

Fig. 5. Proposed HCHO reaction pathways in supercritical water at 673 K.

where k_1 is the rate constant. In the model, the concentration of water is considered to be constant, because the amount of water (about 20 M) is significantly higher than that of the others. For the Cannizzaro reaction, we take OH^- concentration into account because the yield of CH_3OH, which is the product from the Cannizzaro reaction, was strongly affected by OH^- concentration, as shown in Fig. 4.

According to the study by Yu and Savage [33], HCOOH decomposed via two pathways: one of them is decarboxylation (Eq. (2)) and the other is dehydration (Eq. (3)):

$$HCOOH \xrightarrow{k_2} H_2 + CO_2 \text{ (decarboxylation)} \quad (2)$$

$$HCOOH \xrightarrow{k_3} H_2O + CO \text{ (dehydration)} \quad (3)$$

Yu and Savage [33] reported k_2 and k_3 and we employed these rate constants in the model. According to Yu and Savage, the pre-exponential factors of k_2 and k_3 are $10^{8.4}$ and $10^{11.6}$ s^{-1}, respectively, and the activation energies of k_2 and k_3 are 115.3 and 171.9 kJ/mol, respectively. At 673 K, k_2 is 0.26 and k_3 is 1.85×10^{-2} s^{-1}. Thus, under the experimental conditions, decarboxylation of HCOOH is predominant.

HCHO decomposes into CO and H_2 in gas phase [34–36], and thus the following reaction should be taken into consideration:

$$HCHO \xrightarrow{k_4} H_2 + CO \text{ (HCHO decomposition)} \quad (4)$$

In SCW, the water gas shift reaction proceeds [37–39]:

$$H_2O + CO \xrightarrow{k_5} H_2 + CO_2 \text{ (water gas shift reaction)} \quad (5)$$

Sato et al. [39] reported that the pseudo first-order rate constant for CO disappearance is $10^{3.9}$ s^{-1} for the pre-exponential factor and 98.3 kJ/mol for the activation energy. In the model, the value reported by Sato et al. [39] was employed.

As shown in the experimental results (Figs. 1–4), the yield of H_2 is almost always lower than that of CO_2. The above reactions show that the yield of H_2 must be higher than the yield of CO_2 (Eqs. (2), (4) and (5)). Tsujino et al. [40] suggested that HCOOH is reacted with HCHO to produce CH_3OH and CO_2 (hydride transfer reaction: Eq. (6)) in hydrothermal condition.

$$\mathrm{HCOOH} + \mathrm{HCHO} \xrightarrow{k_6} \mathrm{CH_3OH} + \mathrm{CO_2}\ \text{(hydride transfer reaction)} \quad (6)$$

Through the hydride transfer reaction, HCOOH decomposes into CO_2 without forming H_2. Thus, this reaction can be a reason why the H_2 yield is lower than that of CO_2. Another possible reaction of the lower H_2 yield has been pointed out by some researchers [41,42]: that is, direct hydrogenation of HCHO into CH_3OH (Eq. (7)).

$$\mathrm{H_2} + \mathrm{HCHO} \xrightarrow{k_7} \mathrm{CH_3OH}\ \text{(hydrogenation of HCHO)} \quad (7)$$

However, this reaction can be neglected because we verified the H_2 did not affect the product distribution, through an experiment using H_2 instead of argon gas [25]. Further, the direct hydrogenation of HCHO by H_2 might not proceed in SCW without a hydrogenation catalyst, such as a noble metal catalyst, as suggested by Marrone et al. [42]. Therefore, in this study, the hydrogenation of HCHO is neglected.

The disappearance rate of HCHO is calculated by the following equation because all the reactions are assumed to depend on the concentration of each compound by first-order, except for OH^- concentration. Here, the reaction order of OH^- concentration for the Cannizzaro reaction is set to n.

$$-\frac{\mathrm{d[HCHO]}}{\mathrm{d}t} = 2k_1[\mathrm{HCHO}]^2[\mathrm{OH^-}]^n + k_4[\mathrm{HCHO}] + k_6[\mathrm{HCHO}][\mathrm{HCOOH}] \quad (8)$$

The formation rates of the products (CH_3OH, HCOOH, CO_2, CO and H_2) are described as follows:

$$\frac{\mathrm{d[CH_3OH]}}{\mathrm{d}t} = k_1[\mathrm{HCHO}]^2[\mathrm{OH^-}]^n + k_6[\mathrm{HCHO}][\mathrm{HCOOH}] \quad (9)$$

$$\frac{\mathrm{d[HCOOH]}}{\mathrm{d}t} = k_1[\mathrm{HCHO}]^2[\mathrm{OH^-}]^n - k_2[\mathrm{HCOOH}] - k_3[\mathrm{HCOOH}] - k_6[\mathrm{HCHO}][\mathrm{HCOOH}] \quad (10)$$

$$\frac{\mathrm{d[CO_2]}}{\mathrm{d}t} = k_2[\mathrm{HCOOH}] + k_5[\mathrm{CO}] + k_6[\mathrm{HCHO}][\mathrm{HCOOH}] \quad (11)$$

$$\frac{\mathrm{d[CO]}}{\mathrm{d}t} = k_3[\mathrm{HCOOH}] + k_4[\mathrm{HCHO}] - k_5[\mathrm{CO}] \quad (12)$$

$$\frac{\mathrm{d[H_2]}}{\mathrm{d}t} = k_2[\mathrm{HCOOH}] + k_4[\mathrm{HCHO}] + k_5[\mathrm{CO}] \quad (13)$$

Eqs. (8)–(13) were solved by Euler's method. The unknown constants of n, k_1, k_4, and k_6 were determined by fitting the experimental data. The constants in the model are listed in Table 2. The calculated results are also shown in Figs. 1–4. As shown in Figs. 1–4, the model can express the experimental data.

As shown in Table 2, the reaction order for OH^- concentration on the Cannizzaro reaction is 0.2, significantly lower than unity. For this lower reaction order, the following reasons can be considered: (i) Cannizzaro reaction is not an elementary reaction, that is, it is a summary of single reaction steps; (ii) one OH^- can cause some reactions of single HCHO molecules, because it is a catalyst, as mentioned above; (iii) an OH^- can cause reactions of another species such as HCOOH or CO; (iv) the lower reaction order is due to an experimental error, as suggested by Taylor et al. [13]. In a future work, we would like to study the role of OH^- for a reaction in SCW, by means of microscopic experimental and/or computational techniques.

From the next section, we will evaluate an acidity and basicity of a metal oxide for HCHO reaction in SCW. For doing that, it is convenient that an effective OH^- concentration to the reaction can be correlated by a product distribution. As described the above, HCHO reaction is controlled by OH^- concentration. Thus, as shown in Fig. 4, the yield of CH_3OH was higher than that of CO at higher OH^- concentration, on the other hand, the formation of CO became dominant at lower OH^- concentration. Thus the ratio of the yield of CH_3OH to that of CO can tell

Table 2
Reaction order and rate constants of the model at 673 K

n	0.2
k_1 ($l^{1.2}/(mol^{1.2}\,s)$)	0.3
k_2 (s^{-1})	0.26
k_3 (s^{-1})	1.85×10^{-2}
k_4 (s^{-1})	2.5×10^{-4}
k_5 (s^{-1})	1.87×10^{-4}
k_6 (l/(mol s))	1.0

us the amount of OH^- available for the reaction in the system. In other words, the CH_3OH/CO ratio at a reaction time relates to OH^- concentration that can participate to the reaction. If acidity and basicity of metal oxides can function as same as H^+ and OH^- in SCW, we must evaluate the acidity and basicity of the metal oxide for HCHO reaction through the experimental CH_3OH/CO ratio. Using the model, we correlated the CH_3OH/CO ratio at 15 min of reaction time with OH^- concentration and obtained the following equation:

$$\frac{CH_3OH}{CO} = 63\exp(0.26\log[OH^-]) \quad (14)$$

Here, we defined OH^- concentration calculated by the above correlation as "effective OH^- concentration".

3.4. Effect of metal oxides on HCHO reaction in supercritical water

We conducted the experiments for examining of the effect of some metal oxides on HCHO reaction in SCW (673 K and 30 MPa; the loaded amount of all metal oxide catalysts was 0.3 g). CeO_2, MoO_3, TiO_2 (both anatase and rutile), and ZrO_2 are used in this study because they are stable even in SCW, from the viewpoints of hydrothermal and thermal stability [26].

The recovered compounds were H_2, CO, CO_2, CH_3OH, unreacted HCHO, and a small amount of HCOOH with all the metal oxides. As with the results without a solid catalyst, the yield of HCOOH is not shown here because it was less than 1 mol%. The yield of CH_3OH and CO depended on the kind of a metal oxide as well as on OH^- concentration in the absence of a metal oxide catalyst. For evaluating the acidity and basicity on the metal oxide catalysts (CeO_2, MoO_3, TiO_2 (both anatase and rutile), and ZrO_2), we employed the CH_3OH/CO ratio with the catalyst. In the absence of a solid catalyst at 673 K and 30 MPa (0.35 g/cm^3 of water density, the bulk OH^- concentration is 10^{-8} mol/l [28,31]); thus the CH_3OH/CO ratio is calculated as to be 7.9 by the correlation (Eq. (14)). In the presence of CeO_2 and ZrO_2, the CH_3OH/CO ratios were higher than 7.9. On the other hand, the CH_3OH/CO ratios were lower than 7.9 with MoO_3 and TiO_2 (both anatase and rutile).

Table 3
Effective OH^- concentration for HCHO reaction at 673 K and 0.35 g/cm^3 of water density

	CH_3OH/CO	Log([OH^{-1}]) (mol/l)
CeO_2	16	−5
MoO_3	3.7	−11
TiO_2(a)	1.7	−14
TiO_2(r)	2.8	−12
ZrO_2	8	−8

Thus, it was suggested that CeO_2 and ZrO_2 are basic and MoO_3 and TiO_2 (both anatase and rutile) are acidic catalysts for HCHO reaction in SCW at 673 K. Using the CH_3OH/CO ratios with the solid catalysts, we calculated the effective OH^- concentration by use of the correlation (Eq. (14)). The calculated OH^- concentration (effective OH^- concentration) is shown in Table 3 with the CH_3OH/CO ratio.

Fig. 6 shows the plot of the product yields against the effective OH^- concentration (Table 3) with the metal oxides. In this figure, the results calculated with the simple network model are also shown. The trends of the increase of CH_3OH yield and the decrease of CO yield with increasing the effective OH^- concentration are the same for the experimental results and for the model. However, the discrepancy of HCHO yield between the experimental results and the model at

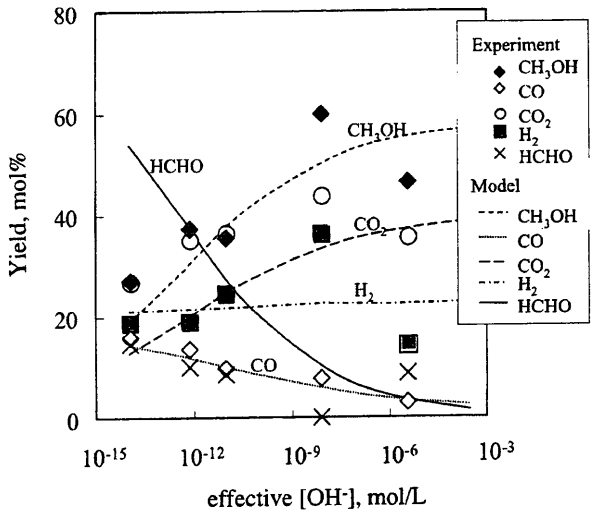

Fig. 6. Relationship between the effective OH^- concentration and the product yields at 673 K, 15 min, 0.35 g/cm^3 of water density, and [HCHO] = 0.54 mol/l.

the lower OH^- concentration (MoO_3 and TiO_2 (both anatase and rutile)) is very huge. The discrepancy may indicate the presence of another reaction pathway that consumes HCHO. At this moment, we consider only the Cannizzaro reaction (Eq. (1)) and the HCHO decomposition (Eq. (4)) as primary reaction pathways of HCHO reaction in SCW (at 673 K and 0.35 g/cm^3 of water density).

Next, we would like to consider the reason why CeO_2 and ZrO_2 are basic and MoO_3 and TiO_2 are acidic catalysts for HCHO reaction in SCW. The acidity or basicity of a metal oxide is related to the nature of the metal ion such as the electronegativity [43]. The generalized electronegativity of a metal ion (χ_i) is calculated by the following equation [43]:

$$\chi_i = (1 + 2Z)\chi_0 \quad (15)$$

where Z is the charge of a metal ion and χ_0 the electronegativity of a neutral atom ($Z = 0$). In this study, we employed the value of electronegativity of neutral atom given by Sanderson [44]. Fig. 7 shows the relationship between the effective OH^- concentration to HCHO reaction and the electronegativity of the metal ion of the metal oxides. One of the reasons for the difference of OH^- concentration on rutile TiO_2 and anatase TiO_2 may be the difference of the surface area (Table 1). The effective OH^- concentration decreases to a minimum and then slightly increases with increasing the electronegativity of the metal ion. This trend is similar to the relationship between the heat of hydration of metal oxides and the electronegativity of metal ion [43]. Further, Shimizu reported that the surface of metal oxide has hydroxyl groups (base site) and oxy-acid groups (acid site) due to the dissociative adsorption of water [45]. According to Shimizu [45], hydroxyl groups exist on a metal oxide surface up to about 13 of electronegativity of the metal ion, while oxy-acid group exist over 13. Then, on CeO_2 and ZrO_2, hydroxyl group (base site) is assumed to be rich, on the other hand, the oxy-acid group (acid site) is assumed to be rich on MoO_3 and TiO_2. Recently, Busca [46] summarized the relationship between acidity and basicity of metal oxide catalyst and the properties of metal ion. The results suggested that high acidity on a metal oxide surface appears when the radius of a metal ion is small and its electronegativity is large. On the contrary, strong basicity appears when the radius of a meal ion is large and its electronegativity is small. Such insistence by Busca [46] is basically the same as that by Shimizu [45].

In this study, a large amount of water always existed in the system with the metal oxide catalysts. Thus we consider that the acidity and basicity of metal oxide catalysts strongly depends on the interaction between water and the metal oxide. As suggested by Shimizu [45] and Busca [46], acidity and basicity of the metal oxide catalysts is found to be related to the electronegativity of the metal ion in this study. Consequently, at this moment, we consider that water is activated as hydroxyl and/or oxy-acid group on the metal oxide surface and then acidity and basicity for HCHO reaction appeares in SCW at 673 K and 0.35 g/cm^3 of water density.

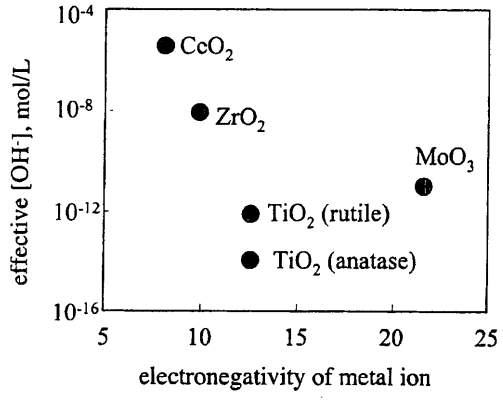

Fig. 7. Relationship between electronegativity of metal ion and the effective OH^- concentration.

4. Conclusion

The experiments of HCHO reaction in SCW (673 K) were conducted by use of batch type reactors. HCHO was mainly converted into CH_3OH through a Cannizzaro reaction at a high OH^- concentration (basic condition), but into CO through self-decomposition at a low OH^- concentration (acidic condition). We developed a simple network model for HCHO reaction in SCW and can express the experimental data by the model.

With MoO_3 and TiO_2 (both anatase and rutile), CO formation was enhanced due to their acidity. On the other hand, in the presence of CeO_2 and ZrO_2, the

Cannizzaro reaction was promoted due to basicity on their surfaces. This trend can be explained by electronegativity of metal ion. This means that the acidity and basicity on a metal oxide surface in SCW are probably due to dissociative absorption of water on the surface.

References

[1] Y. Ikushima, K. Hatakeda, O. Sato, T. Yokoyama, M. Arai, J. Am. Chem. Soc. 122 (2000) 1908.
[2] Y. Ikushima, K. Hatakeda, O. Sato, T. Yokoyama, M. Arai, Angew. Chem. Int. Ed. 40 (2001) 210.
[3] T. Sato, G. Sekiguchi, T. Adschiri, K. Arai, Ind. Eng. Chem. Res. 41 (2002) 3064.
[4] K. Chandler, F. Deng, A.K. Dillow, C.L. Liotta, C.A. Eckert, Ind. Eng. Chem. Res. 36 (1997) 5175.
[5] K. Chandler, C.L. Liotta, C.A. Eckert, D. Schiraldi, AIChE J. 44 (1998) 2080.
[6] S.H. Townsend, M.A. Abraham, G.L. Huppert, M.T. Klein, S.C. Paspek, Ind. Eng. Chem. Res. 27 (1988) 143.
[7] G.L. Huppert, B.C. Wu, S.H. Townsend, M.T. Klein, S.C. Paspek, Ind. Eng. Chem. Res. 28 (1989) 161.
[8] M.T. Klein, L.A. Torry, B.C. Wu, S.H. Townsend, J. Supercrit. Fluids 3 (1990) 222.
[9] T. Funazukuri, R.M. Serikawa, K. Yamaura, Fuel 76 (1997) 865.
[10] J.M.L. Penninger, R.J.A. Kersten, H.C.L. Baur, J. Supercrit. Fluids 16 (1999) 119.
[11] J.M.L. Penninger, R.J.A. Kersten, H.C.L. Baur, J. Supercrit. Fluids 17 (2000) 215.
[12] J.D. Taylor, J.I. Steinfeld, J.W. Tester, Ind. Eng. Chem. Res. 40 (2001) 67.
[13] J.D. Taylor, F.A. Pacheco, J.I. Steinfeld, J.W. Tester, Ind. Eng. Chem. Res. 41 (2001) 1.
[14] P. Krammer, H. Vogel, J. Supercrit. Fluids 16 (2000) 189.
[15] H. Oka, S. Yamago, J. Yoshida, O. Kajimoto, Angew. Chem. Int. Ed. 41 (2002) 623.
[16] N. Akiya, P.E. Savage, Ind. Eng. Chem. Res. 40 (2001) 1822.
[17] R. Narayan, M.J. Antal Jr., J. Am. Chem. Soc. 112 (1990) 1927.
[18] X. Xu, C.D. Almeida, M.J. Antal Jr., J. Supercrit. Fluids 3 (1990) 228.
[19] X. Xu, C.P.D. Almeida, M.J. Antal Jr., Ind. Eng. Chem. Res. 30 (1991) 1478.
[20] X. Xu, M.J. Antal Jr., AIChE J. 40 (1994) 1524.
[21] M. Watanabe, H. Inomata, R.L. Smith Jr., K. Arai, Appl. Catal. A 219 (2001) 149.
[22] M. Watanabe, H. Inomata, K. Arai, Biomass Bioenergy 22 (2002) 405.
[23] K. Tomita, S. Koda, Y. Oshima, Ind. Eng. Chem. Res. 41 (2002) 3341–3344.
[24] D. Haffad, A. Chambellan, J.C. Lavalley, J. Mol. Catal. A 168 (2001) 153.
[25] M. Osada, M. Watanabe, K. Sue, T. Adschiri, K. Arai, J. Supercrit. Fluids, submitted for publication.
[26] Z.Y. Ding, M.A. Frisch, L. Li, E.F. Gloyna, Ind. Eng. Chem. Res. 35 (1996) 3257.
[27] M. Watanabe, M. Tsukagoshi, H. Hirakoso, T. Adschiri, K. Arai, AIChE J. 46 (2000) 843.
[28] W.L. Marshall, E.U. Franck, J. Phys. Chem. Ref. Data 10 (1981) 295.
[29] A.S. Quist, W.L. Marshall, H.R. Jolley, J. Phys. Chem. 69 (1965) 2726.
[30] P.C. Ho, D.A. Palmer, J. Sol. Chem. 25 (1996) 711.
[31] R.T. Pabalan, K.S. Pitzer, Geochim. Cosmochim. Acta 25 (1987) 2429.
[32] D. Bröll, C. Kaul, A. Kramer, P. Krammer, T. Richter, M. Jung, H. Vogel, P. Zehner, Angew. Chem. Int. Ed. 38 (1999) 2998.
[33] J. Yu, P.E. Savage, Ind. Eng. Chem. Res. 37 (1998) 2.
[34] R. Klein, M.D. Scheer, L.J. Schoen, J. Am. Chem. Soc. 73 (1956) 50.
[35] K. Saito, T. Kakumoto, Y. Nakanishi, A. Imamura, J. Phys. Chem. 89 (1985) 3109.
[36] E.A. Irdam, J. Kiefer, Int. J. Chem. Kinet. 25 (1993) 285.
[37] H.R. Holgate, P.A. Webley, J.W. Tester, R.K. Helling, Energy Fuels 6 (1992) 586.
[38] S.F. Rice, R.R. Steeper, J.D. Aiken, J. Phys. Chem. A 102 (1998) 2673.
[39] T. Sato, S. Kurosawa, T. Adschiri, K. Arai, Kagaku Kogaku Ronbunshu 25 (1999) 993 (in Japanese).
[40] Y. Tsujino, C. Wakai, N. Matubayashi, M. Nakahara, Chem. Lett. (1999) 287.
[41] J.K. Walker, Formaldehyde, Reinhold, New York, 1964.
[42] P.A. Marrone, P.M. Gschwend, K.C. Swallow, W.A. Peters, J.W. Tester, J. Supercrit. Fluids 12 (1998) 239.
[43] K. Tanaka, A. Ozaki, J. Catal. 8 (1967) 1.
[44] R.T. Sanderson, Inorganic Chemistry, Reinhold, New York, 1967.
[45] K. Shimizu, Metal Oxide and its Catalytic Ability, Kodansha, Japan, 1978 (in Japanese).
[46] G. Busca, Phys. Chem. Chem. Phys. 1 (1999) 723.

ARTICLE IN PRESS

ELSEVIER

Available online at www.sciencedirect.com

SCIENCE DIRECT®

J. of Supercritical Fluids 00 (2003) 1–9

THE JOURNAL OF Supercritical Fluids

www.elsevier.com/locate/supflu

Analysis of the density effect on partial oxidation of methane in supercritical water

Takafumi Sato, Masaru Watanabe, Richard L. Smith, Jr., Tadafumi Adschiri, Kunio Arai *

Department of Chemical Engineering, Tohoku University, 07 Aoba Aramaki-Aza, Aoba-ku, Sendai 980-8579, Japan

Received 3 August 2002; received in revised form 19 December 2002; accepted 10 January 2003

Abstract

Partial oxidation of methane was conducted in supercritical water at O_2/CH_4 ratios of 0.03 at 673 K with a flow-type reactor. The main products were CO, methanol, formaldehyde and a small amount of CO_2 and H_2. With increasing water density, methane conversion increased due to the formation of formaldehyde. A free radical reaction model was applied to this reaction and it was confirmed that the dependence of selectivities for CO and CO_2 on pressure could be well described. The experimental results and model prediction shows that an increase of water density shifted product distribution to partial oxidation products and formaldehyde was found to play an important role in the product selectivity and the partial oxidation chemistry.

Keywords: Supercritical water; Oxidation; Kinetics; Methane; Aldehyde

1. Introduction

Supercritical water ($T_c = 647$ K and $P_c = 22.1$ MPa) is a promising solvent for upgrading heavy hydrocarbons such as heavy oil and coal [1,2]. Hydrogenation of hydrocarbons through partial oxidation and water gas shift reaction occurs in supercritical water without hydrogen addition [3]. At first, partial oxidation of hydrocarbons leads to CO formation. Then, the water gas shift reaction between CO and water generates hydrogen, which provides a hydrogenation atmosphere. For example, hydrogenation of coal [4] and desulfurization of dibenzothiophene [5] proceed through the water gas shift reaction in supercritical water.

Watanabe et al. [6] conducted partial oxidation of *n*-hexadecane in supercritical water at 673 K and reported that the selectivity of partial oxidation products such as CO, aldehyde and ketone increased with increasing water density. In supercritical water, solvent properties such as dielectric constant and ion product greatly change with density, namely with temperature or pressure, and the change of solvent properties is known to affect reaction kinetics [2]. However, variation of the product selectivities with water density in

* Corresponding author. Tel./fax: +81-22-217-7246.
E-mail address: karai@arai.che.tohoku.ac.jp (K. Arai).

0896-8446/03/$ - see front matter © 2003 Elsevier Science B.V. All rights reserved.
doi:10.1016/S0896-8446(03)00008-1

partial oxidation of hydrocarbons has received much less attention.

Methane is the simplest hydrocarbon and the kinetics of methane oxidation is important to understand the kinetics of oxidation of hydrocarbons in supercritical water. Studies on methane oxidation in supercritical water are summarized in Table 1 in which the research is grouped into total oxidation and partial oxidation experiments.

Total oxidation usually proceeds at high temperature or high O_2/CH_4 ratios. Above about 800 K, the main products are CO and CO_2 [7,8]. Steeper et al. [9] conducted methane oxidation experiments and at O_2/CH_4 ratios of 1–2.6 and at temperatures from 663 to 713 K. The products were CO and CO_2 and these authors reported that the methane conversion rate exhibits a maximum with increasing pressure (density). For these cases, the free radical network model for gas phase was used to interpret the reaction mechanism, the product distribution [8,10] and its pressure dependence [9].

Partial oxidation has been examined in supercritical water at temperatures below about 800 K as shown in Table 1. Hirth and Franck [11] studied the partial oxidation of methane at 653–713 K and obtained the products, CO, methanol and CO_2. Lee and Foster [12] reported that CO and methanol are the main products at O_2/CH_4 ratios of 0.03–0.05. In their studies, methanol selectivities greater than 30% were obtained. Savage et al. [13] conducted the oxidation of methane in supercritical water at 622–754 K and for 1–9 min with batch reactor and reported that low methane conversions give methanol selectivities as high as 75%. The catalytic reaction was also studied. Dixon and Abraham [14] examined methane oxidation over Cr_2O_3 catalyst in supercritical water. They revealed that methane was oxidized to methanol and CO while methanol was oxidized to CO, and then CO was oxidized to CO_2. This reaction pathway was similar to that of the non-catalytic conditions. Further, the yield of methanol in supercritical water was larger than that obtained without water.

In this study, we conducted the partial oxidation of methane in supercritical water at 673 K, 20–35 MPa and at residence times of 29–117 s with a flow-type reactor at shorter residence times than studied previously. Further, since the measurements use a flow-type apparatus, the effect of preheat times inherent in batch-type experiments was eliminated. At first, we evaluated the effect of water density on the product distribution with special attention to reaction intermediates. Next, we applied a radical elementary reaction network model to the partial oxidation system, and propose a reaction pathway that considers the density effect on the product selectivity.

2. Experimental

Fig. 1 shows the flow-type apparatus in this study. Methane (99.999% Nippon Sanso Corporation) was mixed with neon (2%) as an internal

Table 1
Summary of studies for methane oxidation in supercritical water

Methane oxidation	Initial (O_2/CH_4)	T (K)	P (MPa)	Apparatus	References
Total	0.6–3.3	833–923	24.6	Flow	[7]
Total	4.5–19	798–860	25	Flow	[8]
Total	1–2.6	663–713	0.35–27	Batch	[9]
Partial	0.025–0.33	653–713	30–100	Batch	[11]
Partial	0.03–0.05	673–723	25	Flow	[12]
Partial	0.04–0.1	655–754	23–43[a]	Batch	[13]
Total/partial[b]	0.07–8.7	723	43[a,c]	Batch	[14]
Partial	0.03	673	20–35	Flow	This work

[a] Estimated from the reactor volume and the amount of water loaded.
[b] With Cr_2O_3 catalyst.
[c] Experiments without water also performed.

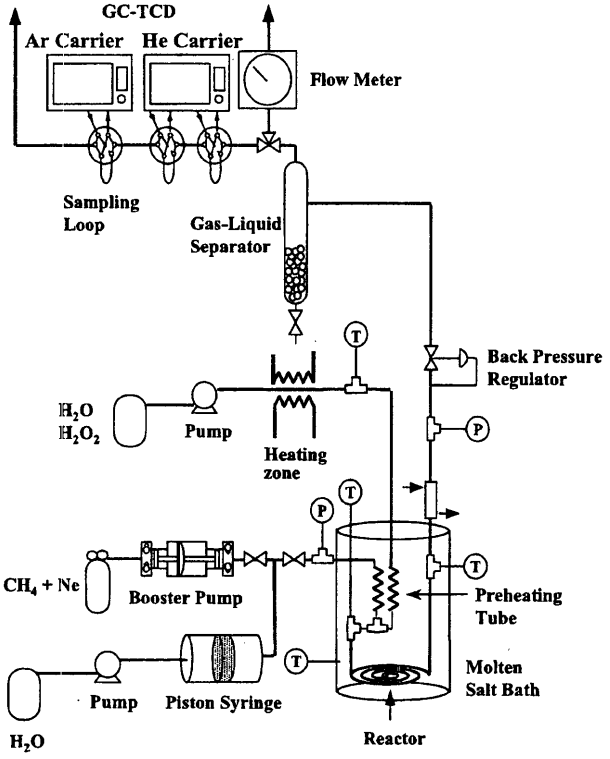

Fig. 1. Experimental apparatus.

standard. Methane was pressurized with a booster pump (AGT-15/75, Haskel) and introduced into the piston syringe (TOC-30, HIP). Distilled water was supplied with a HPLC pump (PUS-0.5, GL Science) to displace a piston syringe, and methane was supplied into the reactor. From another line, hydrogen peroxide aqueous solution was supplied to heating zone with a HPLC pump (Model TRI ROTAR-V, JASCO Corporation). The temperature of outer heating zone was controlled so that hydrogen peroxide was decomposed to oxygen and water at 99.9% conversion as confirmed in separate experiments. Both methane and oxygen-water supply lines were submerged in the molten salt bath (T1, Shinnippo Kagaku) controlled at the reaction temperature. Gas samples were supplied separately to the reactor and then mixed at the reactor entrance. The initial concentration of methane was 0.3 Mol/L and the O_2/CH_4 molar flow rate ratio on a molar basis was 0.03.

The reactor was a coiled length (2 m, 1/8 in. o.d. thickness 0.72 mm) of stainless 316 tube. The reaction temperature was defined as the average temperature at the entrance and exit of the tube coil. The temperature difference between these two points was within 2 K. At the end of the reactor, the effluent was cooled down with a water-cooled double-pipe heat exchanger to suppress the reaction. The residence time of methane was calculated from:

$$\tau = V/(G\rho_W) \quad (1)$$

where V is volume of reactor (cm^3), G is flow rate of water (g/s), ρ_W (g/cm^3) is the water density at the given conditions. Residence time was estimated from the values of pure water available from Ref. [15].

The reaction pressure was controlled with a back pressure regulator (Model PU-100, JASCO Corporation) and the effluent was separated into gas and liquid streams in a separator. The flow rate of gas was measured by a flow meter (Model W-NK-1A, Shinagawa). To prevent contamination of air, the effluent gas stream was introduced into three sampling loops attached to two gas chromatographs as shown in Fig. 1. Hydrogen was analyzed by GC-TCD (Shimadzu GC-8A) with argon carrier and a Molecular Sieve 5A column. Methane, oxygen and carbon monoxide were analyzed by GC-TCD (Shimadzu GC-8A) with helium carrier and a Molecular Sieve 13X column. CO_2 was analyzed with helium carrier and a Porapak Q column. All columns were purchased from GL Science. The quantities of gases were calculated based on neon internal standard.

For the liquid analysis, total organic and inorganic carbon contents were analyzed by TOC (TOC-5000, Shimadzu). The inorganic carbon in the liquid was considered to be CO_2 dissolved in water. Methanol was analyzed by GC-FID (Hewlett Packard HP5850, HP-FFAP column) with 1-propanol as internal standard. We developed the following procedure for analyzing formaldehyde. GC-FID analysis of standard showed that the retention time of methanol and formaldehyde were different. Therefore, we assumed that the carbon content in the liquid phase would be mainly methanol and formaldehyde with traces of CO_2. Samples were subjected to a formaldehyde indicator available commercially (Model WAK-FOR,

Kyoritsu Chemical-check Lab.). Then TOC analysis was (TOC = methanol + formaldehyde) following the method of Brock et al. [16]. In the actual sample analyses, we confirmed that each sample contained formaldehyde in the liquid product with the formaldehyde indicator and then used TOC to quantify the formaldehyde. Consequently, the products measured were CO, CO_2, methanol, formaldehyde and hydrogen.

The following definitions were used for product yield, methane conversion, oxygen conversion and product selectivity:

$$\text{Product yield, } Y(\%) = F_{\text{product}}/F_{\text{CH}_4,\text{in}} \times 100 \quad (2)$$

$$\text{Methane conversion, } X(\%) = (F_{\text{CO}} + F_{\text{CO}_2} + F_{\text{CH}_3\text{OH}} + F_{\text{HCHO}})/F_{\text{CH}_4,\text{in}} \times 100 \quad (3)$$

$$\text{Oxygen conversion (\%)} = 100 - F_{\text{O2}}/F_{\text{O}_2,\text{in}} \times 100 \quad (4)$$

$$\text{Product selectivity (\%)} = Y_{\text{product}}/X \times 100 \quad (5)$$

In Eqs. (2)–(5), F_i is the flow rate of the given reactant or product in mol/s.

3. Results

Fig. 2 shows oxygen conversion and product yield versus residence time at 673 K and 25 MPa. Oxygen conversion was about 20% for 30 s residence time and reached 100% in about 60 s, which is similar to that observed by Lee and Foster [12]. For all samples, the existence of formaldehyde was confirmed. The yield of CO greatly increased with residence time and that of methanol, formaldehyde, CO_2 and hydrogen slightly increased with residence time. From the results, conditions used in this study favored partial oxidation not total oxidation to CO_2. Formaldehyde formation was observed by Savage et al. [16] who studied the oxidation of methanol. However, Lee and Foster [12] studied the partial oxidation of methane at similar conditions did not consider the formation of formaldehyde in their analytical procedure.

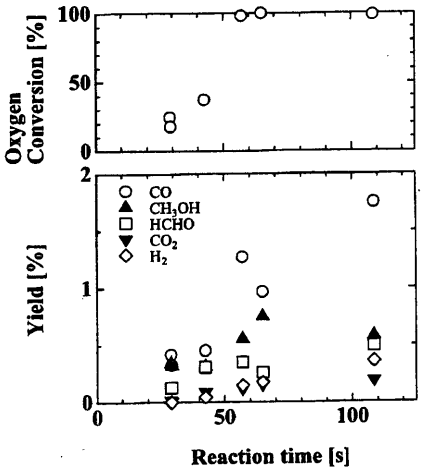

Fig. 2. Yield of products versus reaction time at 673 K, 25 MPa and $O_2/CH_4 = 0.03$.

Table 2 shows that the dependence of methane conversion on pressure at 29 or 30 s of residence time. The methane conversion increased with increasing pressure, namely, water density. The pressure dependence of methane conversion changed with O_2/CH_4 ratio. Steeper et al. [9] reported that the rate constant of methane conversion showed a maximum against reaction pressure at $O_2/CH_4 = 1-2.6$. However, in this work we did not observe such trends, which can probably be attributed to much lower O_2/CH_4 ratios ($O_2/CH_4 = 0.03$) used in this work. Also shown in Table 2 are the yields of formaldehyde that considerably high at the residence times studied, and low yields of hydrogen and CO_2.

Fig. 3 shows the selectivity of the main species versus methane conversion. The selectivities of CO were largest up to 60%, methanol and formaldehyde were larger than those of CO_2. The selectivities of CO and CO_2 slightly increased with methane conversion corresponding to a decrease in the selectivity of methanol and formaldehyde. Methanol and formaldehyde probably formed at an early reaction stage and then oxidized to CO and CO_2. Although the data are scattered, the trend of the sensitivity-conversion data with pressure and density can be seen. The filled symbols in Fig. 3 represent selectivities at 30 and 35 MPa, namely, the high pressure or high density conditions. The selectivities of CO at high pressure were slightly smaller than those at low pressure. The selectivities of formaldehyde at high pressure were greater than those at low pressure. On the other

Table 2
Dependence of methane conversion on pressure at 673 K and $O_2/CH_4 = 0.03$

Pressure (MPa)	Residence time (s)	Yield (%)						Methane conversion (%)
		O_2	CO	CO_2	H_2	CH_3OH	HCHO	
20	30	2.48	0.16	0.01	0.00	0.17	0.17	0.51
25	29[a]	2.51	0.38	0.02	0.00	0.34	0.13	0.85
30	29	2.64	0.41	0.04	0.00	0.22	0.51	1.18
35	29	0.81	0.75	0.12	0.11	0.50	0.88	2.25

[a] Average of two data.

hand, the selectivities of methanol and CO_2 were relatively independent of pressure. These results provide the evidence that the product distribution shifted to these expected for the partial oxidation reaction with increasing water density and that the increase of methane conversion with water density was mainly due to the formation of formaldehyde.

4. Discussion

The stability of each product is an important factor that governs product distribution and selectivities. Thermal decomposition of formaldehyde occurs easily at high temperatures regardless of whether water is present or not [17–19]. Tsujino et al. [18] reported that trioxane, which is the trimer of formaldehyde, is easily decomposed and produces methanol and CO_2 in high temperature water at 523 K for 6 h. Bröll et al. [19] studied the decomposition of formaldehyde at 30 MPa and 573–723 K including supercritical conditions. In their experiments, formaldehyde decomposed almost completely in 2 min and yielded CO, CO_2 and methanol. On the other hand, methanol is fairly stable in supercritical water as shown by Hirth and Franck [11], who reported that the conversion of methanol in supercritical water at 673 K was only about 3.8% at 60 min reaction time.

In our work, CO was the major product and it might be expected to react through the water gas shift reaction after oxygen was almost completely consumed. However, we have reported that the CO conversion at 300 s residence time was about 5% at 673 K in supercritical water [20], which

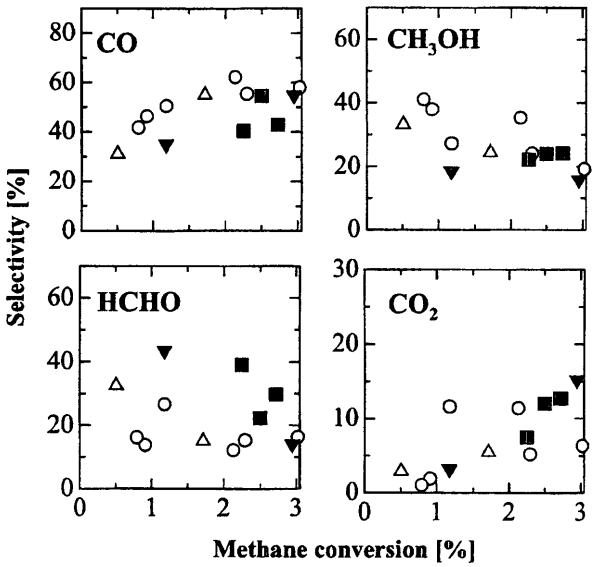

Fig. 3. Selectivities of products versus methane conversion at various water densities at 673 K and $O_2/CH_4 = 0.03$. △: 20 Mpa; ○: 25 MPa; ▼: 30 MPa; ■: 35 Mpa.

means that for the conditions in this work that the conversion of CO through this pathway is low, especially in the absence of oxygen.

Water density greatly affects the reactivity of chemical species and product distribution as described previously. To understand the role of water in the reaction mechanism, researchers have used free radical elementary reaction models. Savage group has been developed a reaction mechanism for the oxidation of C_1 compounds such as methane and methanol in supercritical water [8,10,16,21,22]. The latest version of their model consists of 22 chemical species and 150 elementary reactions [22]. We applied their model

to the system studied in this work. Chemkin III [23] was used for the calculation and ideal gas law was applied the to all chemical species. Thus, following the method of Brock and Savage [10], we set the pressure in the calculation different from that in experiments so that water density and species concentrations in the calculations were the same as those of the experimental conditions.

Fig. 4 shows the methane conversions calculated from the model at 673 K and 25 MPa. The calculated conversions were lower than the experimental data and attained saturation at around 2.5%. However, the calculated methane conversions increased with increasing pressure in a similar manner as the experimental data. Although the experimental data and calculated results were different, the model does seem to show the trends of conversion and selectivities with pressure.

Fig. 5 shows the calculated selectivities of CO, methanol, formaldehyde and CO_2 against methane conversion at various pressures. The model predicted the experimental quantity of methanol and CO_2 fairly well. However, predicted selectivities for CO were higher and that for formaldehyde were lower than experimental those. With increasing pressure, the calculated selectivity of CO decreased and CO_2 also slightly decreased, which shows that the direct oxidation to CO and CO_2 was inhibited with increasing water density. This is the same trend as that found for the experimental

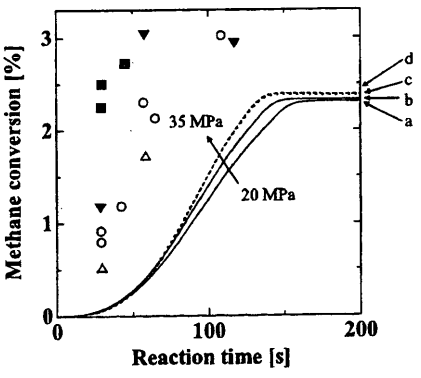

Fig. 4. Calculated methane conversion with reaction time at various pressure at 673 K and $O_2/CH_4 = 0.03$. Symbols for calculation: (a) 20 MPa (dash–dot line); (b) 25 MPa (solid line); (c) 30 MPa (fine dash line); (d) 35 MPa (coarse dash line). Symbols for experimental data: (Δ) 20 MPa; (○) 25 MPa; (▼) 30 MPa; (■) 35 MPa.

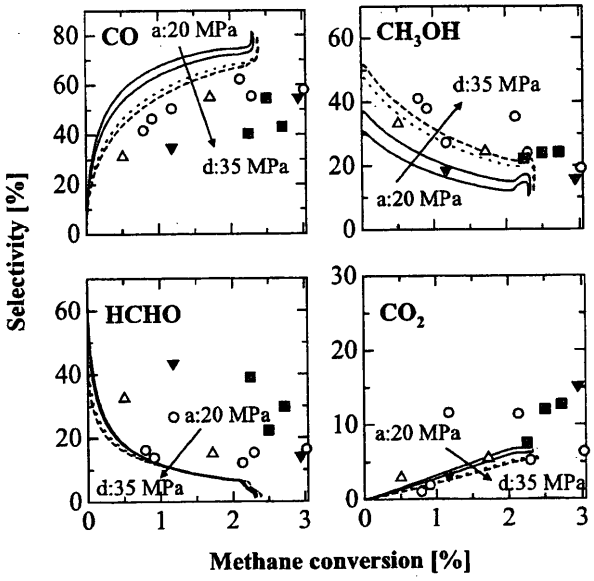

Fig. 5. Calculated selectivity of products with methane conversion at 673 K, $O_2/CH_4 = 0.03$ and various pressure. See Fig. 4 for symbols.

selectivities of CO and CO_2 where those values decreased and almost constant with increasing pressure, respectively. The model correctly predicted that an increase in pressure should shift product distribution to partial oxidation products. On the other hand, the calculated selectivity of methanol increased and that of formaldehyde was roughly constant with increasing pressure whereas the experimental methanol selectivity was constant and formaldehyde selectivity increased with increasing pressure.

Fig. 6 shows the major reaction pathway for the species containing carbon atoms at 673 K and 25 MPa. The flux diagram has been used for understanding reaction pathway [8,24]. The thickness of the arrows indicates the relative reaction rates. Overall, methane was converted to methanol and formaldehyde as shown in the figure. Methanol further reacted to form formaldehyde that reacted to form CO. This is in agreement with previous reports for methane and methanol oxidation in supercritical water [7,8,16]. The fast reactions in Fig. 6 determined by the calculations are shown in Table 3. Methane is consumed through the reaction of R4. Methanol, formaldehyde are produced from CH_3O. CH_3O_2 and CH_3O_2H can be identi-

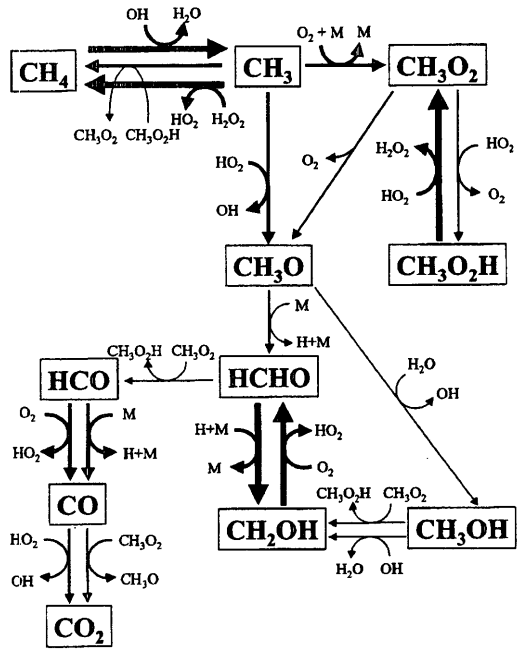

Fig. 6. Major reaction pathway for partial oxidation of methane at 673 K, 25 MPa and $O_2/CH_4 = 0.03$.

fied as key intermediates in the reactions. Methanol is produced from the reverse reaction of R48 denoted as −R48 and consumed through R47 and R53 to formaldehyde. Formaldehyde is produced from −R84 and R40 and consumed through −R95 and R86 to HCO. These reactions seemed to control the ratio of methanol to formaldehyde. CO is produced from HCO through R104 and R109. CO_2 is produced from CO by R118 and R119. This reaction pathway of this study was almost the same as total oxidation of methane in supercritical water at 822 K, except that the reactions related to methanol formation and consumption, reaction from CH_3 to HCHO and that from CH_3O_2H to CH_3O were found to be major reactions and CO is oxidized through the formation of HOCO as in total oxidation [8]. In the proposed partial oxidation pathway, reaction paths related to methanol appeared and HOCO was found not to be a key intermediate.

A sensitivity analysis was performed to evaluate the reaction that controlling the concentration of main compounds. Table 4 shows the four reactions that were found to have the largest maximal normalized sensitivity coefficients for methane,

Table 3
Main reactions for methane oxidation in supercritical water at 673 K, 25 MPa and $O_2/CH_4 = 0.03$

Type	Number[a]	Reaction
Consumption of methane	R4	$CH_4+OH \rightarrow CH_3+H_2O$
	R21	$CH_3+HO_2 \rightarrow CH_3O+OH$
Formation and consumption of methanol	−R48	$CH_3O+H_2O \rightarrow CH_3OH+OH$
	R47	$CH_3OH+OH \rightarrow CH_2OH+H_2O$
	R53	$CH_3OH+CH_3O_2 \rightarrow CH_2OH+CH_3O_2H$
Formation and consumption of formaldehyde	−R84	$CH_2OH+O_2 \rightarrow HCHO+HO_2$
	R40	$CH_3O+M \rightarrow HCHO+H+M$
	−R95	$HCHO+H+M \rightarrow CH_2OH+M$
	R86	$HCHO+CH_3O_2 \rightarrow HCO+CH_3O_2H$
Formation of CO	R104	$HCO+O_2 \rightarrow CO+HO_2$
	R109	$HCO+M \rightarrow H+CO+M$
Formation of CO_2	R118	$CO+HO_2 \rightarrow CO_2+OH$
	R119	$CO+CH_3O_2 \rightarrow CO_2+CH_3O$

[a] Reaction numbers according to Brock et al. [10,16].

CO, methanol, formaldehyde and CO_2 at 673 K and 25 MPa. The normalized sensitivity coefficients were defined as $\partial \ln(X_i)/\partial \ln k_j$ where (X_i) is the concentration of species i and k_j is the rate constant for reaction j. The reactions of R146, R124, R126 and R25 were found to be the four most important reactions for the concentrations of methane, CO, methanol, formaldehyde. Those of R146, R124, R126 and R119 were important for the concentration of CO_2. R146 was found to be one of the reactions that control the concentrations of OH radical and was influenced with pressure. Under partial oxidation conditions, the reactions controlling the concentration of OH such as R146 were also important as well as the case of total oxidation of methane and methanol in SCW [8,16]. The change of reaction pressure would affect this reaction to promote the methane con-

Table 4
Four reactions with largest maximal normalized sensitivity coefficients for each compound at 673 K, 25 MPa and $O_2/CH_4 = 0.03$

Number[a]	Reaction	Maximal normalized sensitivity coefficients				
		CH_4	CO	CH_3OH	HCHO	CO_2
R146	$H_2O_2+M=OH+OH+M$	−0.025	1.192	4.572	−12.82	−0.472
R124	$CH_3O_2+HO_2=CH_3O_2H+O_2$	0.012	−0.545	−2.234	6.266	−0.589
R126	$CH_3O_2+CH_3O_2=CH_3O+CH_3O+O_2$	−0.011	0.507	1.999	−5.587	0.487
R25	$CH_3+CH_3O_2=CH_3O+CH_3O$	−0.007	0.302	1.442	−3.438	–
R119	$CO+CH_3O_2=CH_3O+CO_2$	–	–	–	–	0.553

[a] Reaction numbers according to Brock et al. [10,16].

version and change the selectivities because R146 contains the species of the third body M. The reactions of R124, R126, R25 and R119 involved CH_3O_2 were important reactions for all five species, which means that CH_3O_2 was a key intermediate that controlled product distribution in the partial oxidation of methane in supercritical water.

The model could predict the trend of methane conversion and the dependence of selectivities for CO and CO_2 on pressure, however, it could not provide prediction quantitative of methane conversion and the dependence of selectivities for methanol and formaldehyde on pressure. In addition to various experimental factors (residence times, concentrations, mixing), one possible explanation for these differences may be the change of fugacity in supercritical water. The solvent properties of water probably affect the fugacity of chemical species in particular near the critical point. For supercritical water oxidation, Mizan et al. [25] reported that the fugacity of HO_2 radical changes with pressure in supercritical water. If the fugacity of OH, H_2O_2 and CH_3O_2 in supercritical water could be evaluated, the accuracy of methane conversion and product selectivities would probably be improved. Another possibility may be the effect of ionic reactions, which have not been taken into account in the proposed free radical reaction network model. In the supercritical phase, the number of ionic species, such as protons and hydroxyl ions should be larger than those present in the gas phase. Watanabe et al. [26] reported that methanol oxidation is controlled by ionic behavior due to the formation of ionic species in supercritical water. The contribution of ionic species increases with decreasing temperature corresponding to a decrease in the contribution of radical species.

In this work, the main experimental findings were: (i) formaldehyde was produced in significant quantities at short residence times, and (ii) the product distribution shifted to partial oxidation products with increasing water density, that is, the selectivity of formaldehyde increased with increasing pressure corresponding to decreasing of the selectivity of CO. The radical reaction model could predict the dependence of methane conversion and the selectivities for CO and CO_2 on pressure, but failed to predict quantitative of methane conversion and the dependence of selectivities for methanol and formaldehyde on pressure. Satisfactory theory for describing the fugacity of radical and ionic species in supercritical water is still lacking in the literature. However, the current experimental data will hopefully aid in developing methods for calculating fugacity coefficients and the stability of ionic species in supercritical water.

5. Conclusions

Partial oxidation experiments of methane in supercritical water were conducted at 673 K and O_2/CH_4 ratios of 0.03. The main products were CO, methanol, formaldehyde and a small amount of CO_2 and hydrogen. Formaldehyde was produced at all conditions and the selectivity of CO was as high to 60%. The water density was found to greatly affect the product distribution. Methane

conversion and selectivities of formaldehyde increased with pressure. Product distribution was calculated with a free radical elementary reaction model, which could predict the dependence of selectivities for CO and CO_2 on pressure. The model and reaction sensitivity analysis assisted in formulating the main reaction pathways. The experimental results and model prediction shows that an increase in pressure shifted product distribution to partial oxidation products and formaldehyde was found to a key species in the partial oxidation chemistry.

References

[1] P.E. Savage, Organic chemical reactions in supercritical water, Chem. Rev. 99 (1999) 603.

[2] P.E. Savage, S. Gopalan, T.I. Mizan, C.J. Martino, E.E. Brock, Reactions at supercritical conditions: applications and fundamentals, AIChE J. 41 (1995) 1723.

[3] K. Arai, T. Adschiri, M. Watanabe, Hydrogenation of hydrocarbons through partial oxidation in supercritical water, Ind. Eng. Chem. Res. 39 (2000) 4697.

[4] T. Adschiri, T. Sato, H. Shibuichi, Z. Fang, S. Okazaki, K. Arai, Extraction of Taiheiyo coal with supercritical water–HCOOH mixture, Fuel 79 (2000) 243.

[5] T. Adschiri, R. Shibata, T. Sato, M. Watanabe, K. Arai, Catalytic hydrodesulfurization of dibenzothiophene through partial oxidation and a water–gas shift reaction in supercritical water, Ind. Eng. Chem. Res. 37 (1998) 2634.

[6] M. Watanabe, M. Mochiduki, S. Sawamoto, T. Adschiri, K. Arai, Partial oxidation of *n*-hexadecane and polyethylene in supercritical water, J. Supercrit. Fluids 20 (2001) 257.

[7] P.A. Webley, J.W. Tester, Fundamental kinetics methane oxidation in supercritical water, Energy Fuels 5 (1991) 411.

[8] P.E. Savage, J. Yu, N. Stylski, E.E. Brock, Kinetics and mechanism of methane oxidation in supercritical water, J. Supercrit. Fluids 12 (1998) 141.

[9] R.R. Steeper, S.F. Rice, I.M. Kennedy, J.D. Aiken, Kinetics measurements of methane oxidation in supercritical water, J. Phys. Chem. 100 (1996) 184.

[10] E.E. Brock, P.E. Savage, Detailed chemical kinetics model for supercritical water oxidation of C_1 compounds and H_2, AIChE J. 41 (1995) 8.

[11] Th. Hirth, E.U. Franck, Oxidation and hydrothermolysis of hydrocarbons in supercritical water at high pressures, Ber. Bunsenges. Phys. Chem. 97 (1993) 1091.

[12] J.H. Lee, N.R. Foster, Direct partial oxidation of methane to methanol in supercritical water, J. Supercrit. Fluids 9 (1996) 99.

[13] P.E. Savage, R. Li, J.T. Santini, Jr., Methane to methanol in supercritical water, J. Supercrit. Fluids 7 (1994) 135.

[14] C.N. Dixon, M.A. Abraham, Conversion of methane to methanol by catalytic supercritical water oxidation, J. Supercrit. Fluids 5 (1992) 269.

[15] E.W. Lemmon, M.O. McLinden, D.G. Friend, Thermophysical properties of fluid systems in NIST Chemistry WebBook, NIST Standard reference database number 69, in: P.J. Linstrom, W.G. Mallard, (Eds.), National Institute of Standards and Technology, Gaithersburg MD, July 2001, p. 20899 (http://webbook.nist.gov).

[16] E.E. Brock, Y. Oshima, P.E. Savage, J.R. Barker, Kinetics and mechanism of methanol oxidation in supercritical water, J. Phys. Chem. 100 (1996) 15834.

[17] R. Klein, M.D. Scheer, L.J. Schoen, The pyrolysis of formaldehyde, J. Am. Chem. Soc. 78 (1956) 50.

[18] Y. Tsujino, C. Wakai, N. Matubayashi, M. Nakahara, Noncatalytic Cannizzaro-type reaction of formaldehyde in hot water, Chem. Lett. (1999) 287.

[19] D. Bröll, C. Kaul, A. Krämer, T. Richter, M. Jung, H. Vogel, P. Zehner, Chemistry in supercritical water, Angew. Chem. Int. Ed. 38 (1999) 2998.

[20] T. Sato, S. Kurosawa, T. Adschiri, K. Arai, Kinetics of water gas shift reaction in supercritical water, Kagaku Kogaku Ronbunshuu 25 (1999) 993.

[21] E.E. Brock, P.E. Savage, J.R. Barker, A reduced mechanism for methanol oxidation in supercritical water, Chem. Eng. Sci. 53 (1998) 857.

[22] P.E. Savage, J. Rovira, N. Stylski, C.J. Martino, Oxidation kinetics for methane/methanol mixtures in supercritical water, J. Supercrit. Fluids 17 (2000) 155.

[23] R.J. Kee, F.M. Rupley, J.A. Miller, M.E. Coltrin, J.F. Grcar, E. Meeks, H.K. Moffat, A.E. Lutz, G. Dixon-Lewis, M.D. Smooke, J. Warnatz, G.H. Evans, R.S. Larson, R.E. Mitchell, L.R. Petzold, W.C. Reynolds, M. Caracotsios, W.E. Stewart, P. Glarborg, C. Wang, O. Adigun, CHEMKIN Collection, Release 3.6, Reaction Design, Inc, San Diego, CA, 2001.

[24] S.F. Rice Application of the GRI methane oxidation model to methane and methanol oxidation in supercritical water. The Fourth International Symposium on Supercritical Fluids, 1997, p. 571.

[25] T.I. Mizan, P.E. Savage, R.M. Ziff, Fugacity coefficients for free radicals in dense fluids: HO_2 in supercritical water, AIChE J. 43 (1997) 1287.

[26] M. Watanabe, K. Sue, T. Adschiri, H. Inomata, R.L. Smith, Jr., K. Arai, Control of methanol oxidation by ionic behavior in supercritical water, Chem. Commun. (2001) 2270.

ELSEVIER

Available online at www.sciencedirect.com

SCIENCE DIRECT®

J. of Supercritical Fluids 00 (2003) 1–7

THE JOURNAL OF Supercritical Fluids

www.elsevier.com/locate/supflu

Water density dependence of formaldehyde reaction in supercritical water

Mitsumasa Osada [a], Masaru Watanabe [b], Kiwamu Sue [a], Tadafumi Adschiri [c], Kunio Arai [a,b,*]

[a] *Department of Chemical Engineering, Tohoku University, 07 Aza-Aoba, Aramaki, Aoba-ku, Sendai 980-8579, Japan*
[b] *Research Center of Supercritical Fluid Technology, Tohoku University, 07 Aza-Aoba, Aramaki, Aoba-ku, Sendai 980-8579, Japan*
[c] *Institute of Multidisciplinary Research for Advanced Materials, Tohoku University, 2-1-1, Aoba-ku, Sendai 980-8577, Japan*

Received 9 August 2002; received in revised form 28 December 2002; accepted 14 February 2003

Abstract

The water density dependence of formaldehyde (HCHO) reaction in supercritical water (SCW) was studied with batch experiments. Major products from the reaction were methanol (CH_3OH), formic acid (HCOOH), hydrogen (H_2), carbon monoxide (CO) and carbon dioxide (CO_2). It was found that the Cannizzaro reaction mechanism was the preferred reaction pathway for HCHO reaction in SCW. At higher water densities, CH_3OH yields increased confirming the predominance of the Cannizzaro reaction mechanism. At low water densities, CO yields increased and CH_3OH yields decreased, which indicated that monomolecular decomposition became the main reaction pathway. Addition of base to the reacting mixtures was found to promote the Cannizzaro reaction path whereas addition of acid promoted monomolecular decomposition.

Keywords: Formaldehyde; Supercritical water; Cannizzaro reaction; Water gas shift reaction; Hydroxide ion

1. Introduction

Supercritical water (SCW) is expected to replace many conventional organic solvents in the near future. [1] For example, water can function as an acid or base catalyst in the critical region depending upon its thermodynamic state, and therefore, it is probable that many new chemical processes can be developed. [2–9] In SCW, the reaction mechanism varies from a reaction atmosphere that favors radical reaction to one that favors ionic reactions according to the water density. [10] To control the organic reaction in SCW by the change of the water density, it is important that the understanding of the reaction of the simple organic compounds like formaldehyde (HCHO).

The reaction of aldehydes without α-hydrogen in high temperatures and pressures water was reported. [5,6,11–13] Katritzky et al. [11] studied reaction of benzaldehyde in cyclohexane or water for 5 days at 250 °C. In cyclohexane, benzaldehyde mainly undergoes disproportionation to give ben-

* Corresponding author.
E-mail address: karai@arai.che.tohoku.ac.jp (K. Arai).

0896-8446/03/$ - see front matter © 2003 Elsevier Science B.V. All rights reserved.
doi:10.1016/S0896-8446(03)00042-1

zoic acid as the oxidation product and toluene as the reduction product. In the presence of water, benzaldehyde behaves very similarly, but a small amount of benzyl alcohol is also formed which can be expected from the more polar reaction environment. Ikushima et al. [6] demonstrated that the reaction of benzaldehyde to benzyl alcohol and benzoic acid through the Cannizzaro mechanism proceeds in SCW in the absence of any base catalyst (NaOH). They reported that SCW itself functions as a base catalysis and the pseudo second-order rate constant of the disproportionation of benzaldehyde increases with increasing water density at 377 °C. Tsujino et al. [12] conducted a reaction of s-trioxane, which forms HCHO by ring-opening, under hydrothermal condition at 250 °C and 4 MPa. In the presence of water, methanol (CH_3OH) and formic acid (HCOOH) are produced via the Cannizzaro reaction. HCOOH further undergoes a hydride transfer reaction with HCHO to give CH_3OH at a yield exceeding 50%. Bröll et al. [5] conducted the reaction of HCHO in sub- and SCW to examine its temperature dependence at conditions from 300 to 450 °C at 30 MPa. They reported that the Cannizzaro reaction became predominant at the lower temperatures.

Considering the previous literature results, HCHO should be a good probe for investigating the water density dependence of the reaction pathway because simple organic compounds can be expected to form a smaller number of products, which simplifies the analysis. In this work, we studied the HCHO reaction in SCW over the water density range of 0.17–0.5 g/cm^3 and further, considered the pH dependence of the reaction.

2. Experimental

Distilled and deionized water was used with resistivity of 18.2 MΩ cm. Paraformaldehyde (98% purity) used as the source of HCHO, sodium hydroxide aqueous solution (NaOH, 1.0 mol/dm^3) and sulfuric acid aqueous solution (H_2SO_4, 1.0 mol/dm^3) were purchased from Wako Chemicals and used without further purification.

Reactions were carried out in a SUS 316 stainless steel tube bomb reactors that had an inner volume of 6 cm^3. The loaded amount of paraformaldehyde was 0.1 g, and the loaded amounts of water were 1.0 g (0.17 g/cm^3)–3.0 g (0.50 g/cm^3). For the experiments using acid or base, H_2SO_4 or NaOH aqueous solutions were loaded into the reactor instead of pure water. After loading samples, argon gas (Ar) was pressurized to about 1 MPa after purging air in the reactor. Then the reactor was submerged in a fluidized sand bath (Takahashi Rico Co., model TK-3) that was controlled at 400 °C. For typical experiments, the temperature reached 400 °C within about 2 min; it changes by the loaded amounts of water. Reaction times reported except these heatup times and ranged from 3 to 28 min. After a given reaction time, the reactor was taken out of the bath and rapidly quenched in a water bath and rapidly cooled to below 400 °C. This generally occurred within 1 min. The reactor was connected to a syringe that equipped with gas samplers to collect produced gas and to measure the gas volume. After sampling or displacement of the produced gases, the reactor was opened and washed with pure water.

Identification and quantification of gas products was conducted by GC-TCD (Shimadzu, model GC-7A, and Hitachi, model GC163). The aqueous products were analyzed by HPLC with KC-811 column (Shodex), an ultraviolet (UV detector; JASCO UV-1570) set at 210 nm, and refractive index (RI detector; JASCO RI-1530). The HPLC was operated at an oven temperature of 40 °C with 1 cm^3/min flow of phosphoric acid aqueous solution (0.1 wt.%). Peak identification for the above chromatographic techniques was conducted by comparison of the sample peak retention times with the standard solutions of the pure compounds. Amounts of organic and inorganic carbon in the aqueous phase were evaluated with total organic carbon (TOC detector, Shimadzu, model TOC-5000A).

In all experiments, hydrogen (H_2), carbon monoxide (CO), carbon dioxide (CO_2), CH_4, C_2H_4, C_3H_6, C_3H_8, HCHO, CH_3OH and HCOOH were identified and quantified. Product yield was evaluated from carbon, hydrogen and oxygen base for

a loaded amount of paraformaldehyde. The yield of unknown liquid products (the starting material, paraformaldehyde, and the other products) was determined by subtracting the yields of HCHO, CH_3OH and HCOOH from the TOC value.

3. Result and discussion

Table 1 shows product yields of (a) carbon base, (b) hydrogen base and (c) oxygen base substances at 400 °C and 15 min reaction time. HCHO initial concentration was 0.56 mol/dm^3. Water densities were 0.17, 0.33 and 0.50 g/cm^3, respectively. Under these conditions, paraformaldehyde conversion was 100%, and the major products were HCHO, CH_3OH, HCOOH, H_2, CO and CO_2, and slight amount of CH_4, C_2H_4, and C_3H_6. At the lowest water density (0.17 g/cm^3), a good carbon balance could not be obtained, which probably can be explained from our procedure since volatile HCHO was not determined. At 0.33 and 0.50 g/cm^3, the carbon balance was about 92–93 C%, hydrogen balance (130 H%) and the oxygen balance (120 O%) exceeded 100%. This is strong evidence that water participated in the HCHO reaction.

Figs. 1–3 show reaction time versus product yields obtained at 400 °C and at water densities

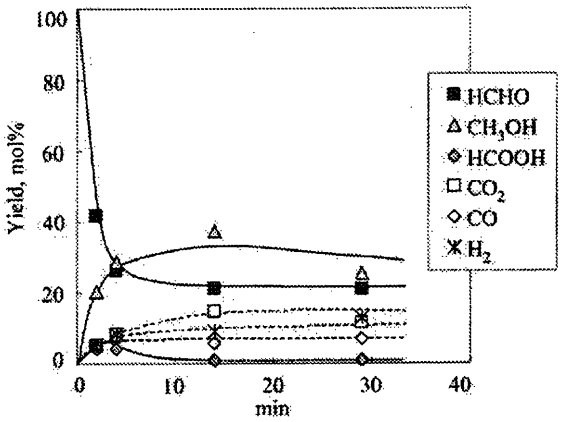

Fig. 1. Reaction time profile of HCHO reaction in SCW. (400 °C, $[HCHO]_0 = 0.56$ mol/dm^3, water density 0.17 g/cm^3).

from 0.17 to 0.5 g/cm^3. Under these conditions, the CH_3OH yields were 30–60 C%, the CO yields were 2–6 C% and the CO_2 yields were 10–30 C%. Bröll et al. [5] conducted HCHO reaction in SCW at 400 °C, water density 0.36 g/cm^3 and shorter reaction time 2 min. They reported that the CH_3OH, CO and CO_2 yield were about 15, 45 and 30%, respectively. Though the paraformaldehyde solid was employed as a starting material in this work, the usage of s-trioxane and HCHO directly was also possible. We conducted HCHO reaction using paraformaldehyde at 250 °C and 4 MPa and confirmed the same product distribution

Table 1
The product yield of HCHO reaction in SCW

Water density (g/cm^3)	Yield (%)						Sum of yields
	HCHO	CH_3OH	HCOOH	CO	CO_2	H_2	
(a) Carbon base							
0.17	21.1	37.4	1.0	5.7	14.6		79.8
0.33	6.7	56.4	0.4	3.8	25.4		92.7
0.50	5.0	54.7	0.4	2.9	30.9		93.9
(b) Hydrogen base							
0.17	21.1	74.8	1.0			8.9	105.8
0.33	6.7	112.8	0.4			12.8	132.7
0.50	5.0	109.4	0.4			18.3	133.1
(c) Oxygen base							
0.17	21.1	37.4	2.0	5.7	29.2		95.4
0.33	6.7	56.4	0.7	3.8	50.8		118.4
0.50	5.0	54.7	0.7	2.9	61.8		125.1

400 °C, $[HCHO]_0 = 0.56$ mol/dm^3. (a) Carbon base, (b) hydrogen base, (c) oxygen base.

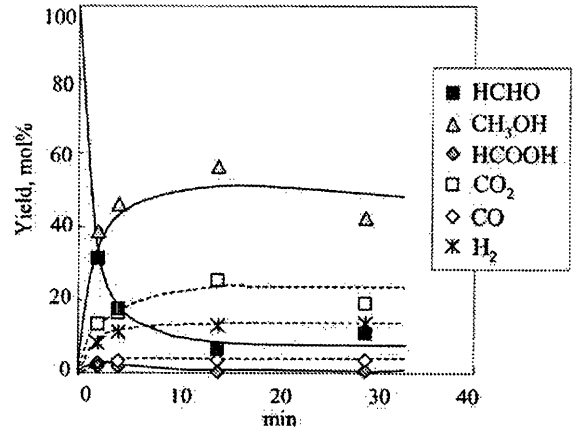

Fig. 2. Reaction time profile of HCHO reaction in SCW (400 °C, $[HCHO]_0 = 0.56$ mol/dm^3, water density 0.33 g/cm^3).

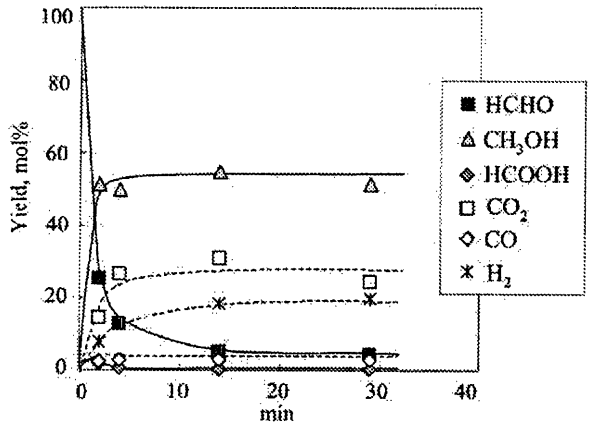

Fig. 3. Reaction time profile of HCHO reaction in SCW (400 °C, $[HCHO]_0 = 0.56$ mol/dm^3, water density 0.50 g/cm^3).

that Tsujino et al. [12] reported by using s-trioxane. There is one of the possibilities that the reaction rate of HCHO was affected by the starting materials and their initial aqueous conditions.

From the results shown in Figs. 1–3, the following reaction pathways probably occurred as given to some extent in the literature [5,12,14–20].

$$HCHO \rightarrow CO + H_2 \quad (1)$$

$$CO + H_2O \rightarrow CO_2 + H_2 \quad (2)$$

$$2HCHO + H_2O \rightarrow CH_3OH + HCOOH \quad (3)$$

$$HCOOH \rightarrow CO_2 + H_2 \quad (4)$$

$$HCOOH \rightarrow CO + H_2O \quad (5)$$

The relationship of these reactions is schematically shown in Fig. 4. Monomolecular decomposition of HCHO shown in Eq. (1) forms H_2 and CO [14–16]. Eq. (2) is the reaction between CO and H_2O to form CO_2 and H_2 [17–19]. The Cannizzaro reaction of between two molecules of HCHO progresses as shown in Eq. (3) and this is indicated by formation of CH_3OH and HCOOH [5]. We confirmed CH_3OH was stable under this experimental condition (400 °C, 30 min, 0.17–0.50 g/cm^3). However, the CH_3OH yield shows a peak around 15 min at 0.17 and 0.33 g/cm^3 conditions, this indicates the possibility of the secondary reaction between CH_3OH and other products. HCOOH probably decomposes by decarboxylation as in Eq. (4) and by dehydration as in Eq. (5). [20] CO probably formed by dehydration as in Eq. (5) and a part of CO became H_2 and CO_2 through the water–gas shift reaction. Another pathway of CH_3OH formation except for the Cannizzaro reaction must be taken into consideration because the CH_3OH yield is over 50 C% at 0.33 and 0.50 g/cm^3 as shown in Figs. 2 and 3. In addition, although the H_2 yield must be higher than the $(CO + CO_2)$ yield from reaction pathway in Fig. 4, the experimental results showed $H_2 < (CO + CO_2)$. These results indicate HCHO undergoes a hydride transfer reaction with HCOOH as shown in Eq. (6), [12]. The hydride reaction is possibly one of the reasons why the CH_3OH yield is over 50 C% and the H_2 yield is low:

$$HCHO + HCOOH \rightarrow CH_3OH + CO_2 \quad (6)$$

Other possibilities for the lower than expected H_2 formation is due to the direct hydrogenation of

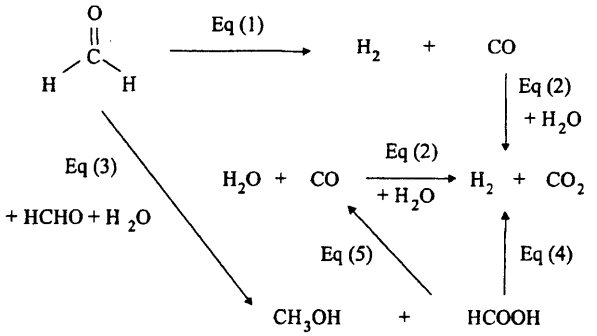

Fig. 4. Reaction pathway of HCHO in SCW.

HCHO into CH_3OH (Eq. (7)) [21] and hydrogenation of CO (Eq. (8)) [22]. This is shown by the following reactions:

$$HCHO + H_2 \rightarrow CH_3OH \quad (7)$$

$$CO + 2H_2 \rightarrow CH_3OH \quad (8)$$

However, these reactions can probably be disregarded because we verified that H_2 did not affect the product distribution, through experiments using H_2 instead of Ar.

As shown in Figs. 1–3, the Cannizzaro reaction became predominant with increasing water density because the CH_3OH, CO_2 and H_2 yields increased with density. At low water density, gas generation from monomolecular decomposition of HCHO probably became the main reaction pathway because the CH_3OH yield was low. Thus, the reaction pathway of the HCHO reaction changed continuously with water density from the monomolecular decomposition at low density, namely radical reaction, to the Cannizzaro reaction at high density, namely ionic reaction.

To investigate acidity and basicity of the water to the HCHO reaction, we examined the pH dependence. The pH and ion product (Kw = 16.2 at 400 °C, 0.33 g/cm^3) of pure water were calculated by the method of Marshall and Franck [23]. The pH values with acid and base were obtained

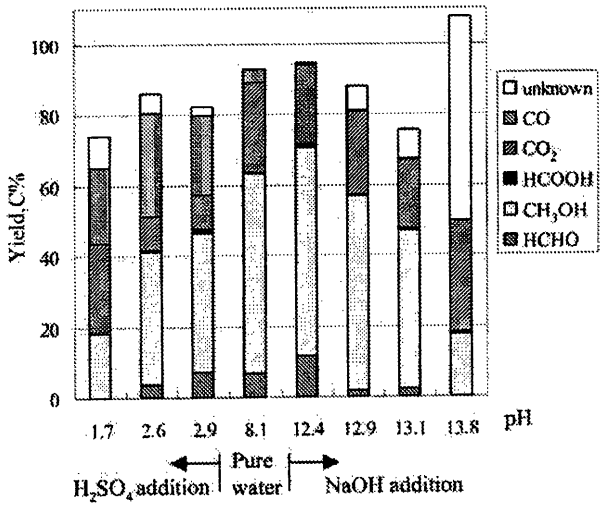

Fig. 5. The pH dependence of HCHO reaction in SCW (carbon base; 400 °C, water density 0.33 g/cm^3, $[HCHO]_0$ = 0.56 mol/dm^3, 15 min).

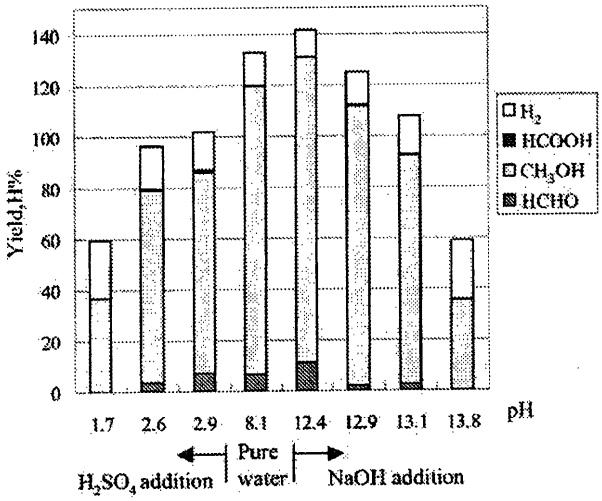

Fig. 6. The pH dependence of HCHO reaction in SCW (hydrogen base; 400 °C, water density 0.33 g/cm^3, $[HCHO]_0$ = 0.56 mol/dm^3, 15 min).

from the ion product of the water [23], the equilibrium constant [24,25] and the activity coefficient [26]. The result is shown in Fig. 5 (carbon base) and Fig. 6 (hydrogen base). As shown in Fig. 5, at $1.7 < pH < 12.4$, the yield of CH_3OH increased with pH. Generally, the Cannizzaro reaction was promoted by base catalyst, and therefore, a high yield of CH_3OH was obtained at $1.7 < pH < 12.4$. Since the water–gas shift reaction is promoted under basic conditions, [27,28] the CO_2 and H_2 yields probably increased. On the other hand, when acid was added, the CH_3OH yield decreased and the product gas yield increased. This showed that the monomolecular decomposition of HCHO was promoted under acidic conditions. In other words, products formed under low pH (acidic) conditions can be thought to correspond to those formed at low water densities. Similarly, products formed at high pH (basic) conditions can be thought to correspond to those formed at high water densities. When excessive NaOH was added ($12.9 < pH$), however, the Cannizzaro reaction seemed to be suppressed and the unknown yield consisting of liquid products except HCHO, CH_3OH and HCOOH increased. This behavior at higher pH was probably due to the other reactions such as the Formose

reaction, which known to occur basic conditions [13], in addition to Eqs. (1)–(6).

Products formed at low pH conditions corresponded to those formed at low water densities, and products at high pH conditions corresponded to those formed at high water densities. These results, both pH and water density dependence of the product, indicate the reaction mechanism of HCHO in SCW is governed by the hydroxide ion concentration.

4. Conclusion

In the reaction of HCHO, the Cannizzaro reaction was dominant at high water densities. At low water densities the monomolecular decomposition of HCHO was main reaction pathway. Thus, the reaction pathway of HCHO reaction varied with water density from monomolecular decomposition mechanism at low density to a Cannizzaro reaction mechanism at high density. From the water density and pH dependence of the products, it was indicated that the hydroxide ion concentration affected the reaction pathway of HCHO reaction.

References

[1] K. Arai, T. Adschiri, Importance of phase equilibria for understanding supercritical fluid environments, Fluid Phase Equilib. 158 (1999) 673.
[2] P.E. Savage, S. Gopalan, T.I. Mizan, C.J. Martino, E.E. Brock, Reactions at supercritical conditions: applications and fundamentals, AIChE J. 41 (7) (1995) 1723.
[3] M.J. Antal, Jr, M. Carlsson, X. Xu, D.G.M. Anderson, Mechanism and kinetics of the acid-catalyzed dehydration of 1- and 2-propanol in hot compressed liquid water, Ind. Eng. Chem. Res. 37 (1998) 3820.
[4] P.E. Savage, Organic chemical reactions in supercritical water, Chem. Rev. 99 (1999) 603.
[5] D. Bröll, C. Kaul, A. Krämer, P. Krammer, T. Richter, M. Jung, H. Vogel, P. Zehner, Chemistry in supercritical water, Angew Chem. Int. Ed. 38 (1999) 2998.
[6] Y. Ikushima, K. Hatakeda, O. Sato, T. Yokoyama, M. Arai, Structure and base catalysis of supercritical water in the noncatalytic benzaldehyde disproportionation using water at high temperatures and pressures, Angew Chem. Int. Ed. 40 (1) (2001) 210.
[7] M. Watanabe, K. Sue, T. Adschiri, H. Inomata, R.L. Smith, Jr, K. Arai, Control of methanol oxidation by ionic behavior in supercritical water, Chem. Commun. 21 (2001) 2270.
[8] J.D. Taylor, J.I. Steinfeld, J.W. Tester, Experimental measurement of the rate of methyl tert-butyl ether hydrolysis in sub and supercritical water, Ind. Eng. Chem. Res. 40 (2001) 67.
[9] T. Sato, G. Sekiguchi, T. Adschiri, K. Arai, Ortho-selective alkylation of phenol with 2-propanol without catalyst in supercritical water, Ind. Eng. Chem. Res. 41 (2002) 3064.
[10] W. Bühler, E. Dinjus, H.J. Ederer, A. Kruse, C. Mas, Ionic reactions and pyrolysis of glycerol as competing reaction pathways in near and supercritical water, J. Supercrit. Fluids 22 (2002) 37.
[11] A.R. Katritzky, D.A. Nichols, M. Siskin, R. Murugan, M. Balasubramanian, Reactions in high-temperature aqueous media, Chem. Rev. 101 (2001) 837.
[12] Y. Tsujino, C. Wakai, N. Matsubayashi, M. Nakahara, Noncatalytic Cannizzaro-type reaction of formaldehyde in hot water, Chem. Lett. 4 (1999) 287.
[13] J.F. Walker, Formaldehyde, Reinhold, New York, 1953.
[14] R. Klein, M.D. Scheer, L.J. Schoen, The pyrolysis of formaldehyde, J. Am. Chem. Soc. 78 (1956) 50.
[15] K. Saito, T. Kakumoto, Y. Nakanishi, A. Imamura, Thermal decomposition of formaldehyde at high temperatures, J. Phys. Chem. 89 (1985) 3109.
[16] E.A. Irdam, J.H. Kiefer, L.B. Harding, A.F. Wagner, The formaldehyde decomposition chain mechanism, Int. J. Chem. Kinet. 25 (1993) 285.
[17] H.R. Holgate, P.A. Webley, J.W. Tester, R.K. Helling, Carbon monoxide oxidation in supercritical water: the effects of heat transfer and the water–gas shift reaction on observed kinetics, Energy Fuels 6 (1992) 586.
[18] S.F. Rice, R.R. Steeper, J.D. Aiken, Water density effects on homogeneous water–gas shift reaction kinetics, J. Phys. Chem. A 102 (1998) 2673.
[19] T. Sato, S. Kurosawa, T. Adschiri, K. Arai, Kinetics of the water–gas shift reaction in supercritical water, Kagaku Kogaku Ronbunshu 25 (1999) 993 (Japanese).
[20] J. Yu, P.E. Savage, Decomposition of formic acid under hydrothermal conditions, Ind. Eng. Chem. Res. 37 (1998) 2.
[21] P.A. Marrone, P.M. Gschwend, K.C. Swallow, W.A. Peters, J.W. Tester, Product distribution and reaction pathways for methylene chloride hydrolysis and oxidation under hydrothermal conditions, J. Supercrit. Fluids 12 (1998) 239.
[22] R.T. Morrison, R.N. Boyd, Organic Chemistry, sixth ed, Prentice Hall, New Jersey, 1992.
[23] W.L. Marshall, E.U. Franck, Ion product of water substance, 0–1000 °C, 1–10 000 bars new international formulation and its background, J. Phys. Chem. Ref. Data 10 (1981) 295.
[24] A.S Quist, W.L. Marshall, H.R. Jolley, Electrical conductances of aqueous solutions at high temperature and

pressure. 2. Conductances and ionization constants of sulfuric acid–water solutions from 0 to 800 °C and at pressures up to 4000 bars, J. Phys. Chem. 69 (8) (1965) 2726.

[25] P.C. Ho, D.A. Palmer, Ion association of dilute aqueous sodium hydroxide solutions to 600 °C and 300 MPa by conductance measurements, J. Solution Chem. 25 (1996) 711.

[26] R.T. Pabalan, K.S. Pitzer, Thermodynamics of concentrated electrolyte mixtures and the prediction of mineral solubilities to high temperatures for mixtures in the system Na–K–Mg–Cl–SO_4–OH–H_2O, Geochim. Cosmochim. Acta 51 (1987) 2429.

[27] D.C. Elliott, L.J. Sealock, Jr, Aqueous catalyst system for the water-gas shift reaction.1. Comparative catalyst studies, Ind. Eng. Chem. Prod. Res. Dev. 22 (1983) 426.

[28] D.S. Ross, J.E. Blessing, Q.C. Nguyen, G.P. Hum, Conversion of bituminous coal in CO/H_2O systems. 2. pH dependence, Fuel 63 (1984) 1206.